SCHOLARLY PUBLICATIONS

A CURRENT AWARENESS BULLETIN
OF RESEARCH OUTPUT

@DTU

(50th Edition)

FEBRUARY 2017

BY: CENTRAL LIBRARY

DELHI TECHNOLOGICAL UNIVERSITY
(FORMERLY *DELHI COLLEGE OF ENGINEERING)*
GOVT. OF N.C.T. OF DELHI
SHAHBAD DAULATPUR, MAIN BAWANA ROAD
DELHI 110042

PREFACE

This is the **Fiftieth** Issue of Current Awareness Bulletin started by Delhi Technological University, Central Library. The aim of the bulletin is to compile, preserve and disseminate information published by the faculty, students and alumni for mutual benefits. The bulletin also aims to propagate the intellectual contribution of Delhi Technological University (DTU) as a whole to the academia.

The bulletin contains information resources available in the internet in the form of articles, reports, presentations published in international journals, websites, etc. by the faculty and students of DTU. The publications of faculty and student which are not covered in this bulletin may be because of the reason that the full text either was not accessible or could not be searched by the search engine used by the library for this purpose.

The learned faculty and students are requested to provide their uncovered publications to the library either through email or in CD, etc to make the bulletin more comprehensive.

This issue contains the information published during **February 2017**. The arrangement of the contents is alphabetical. The full text of the article which is either subscribed by the university or available in the web is provided in this bulletin.

Central Library

CONTENTS

1. A Novel Approach of Multi-Stage Tracking for Precise Localization of Target in Video Sequences, Gurjit Singh Walia, Saim Raza, ***3.Anjana Gupta***, Rajesh Asthana and Kuldeep Singh, Applied Mathematics, DTU

2. A Review on Design and Analysis of the propeller used in UAV, ***7.Yamika Patel*** , ***7.Anant Gaurav***, ***3.Krovvidi Srinivas*** and ***7.Yamal Singh***, Mechanical, DTU

3. A Strongly Trusted Integrity Preservance based Security Framework for Critical Information Storage over Cloud Platform, ***7.Shweta Sharma***, DTU

4. ABC Analysis in the Hospitality Sector, ***3.Nand Kumar*** and ***8.Rohan Soni,*** DTU

5. Analysis on Drag Reduction of Bluff Body using Dimples, ***8.Shabir Grover, 6.B.B.Arora, 8.Vaibhav Khanna, 8.Tushar Kaushik*** and ***3.Akhilesh Arora***, Mechanical Engineering, DTU

6. Application of Gaussian as Edge Detector for Image Enhancement of Ancient Manuscripts, ***3.N.Jayanthi*** and ***3.S.Indu***, ECE Department, DTU

7. Automatic Texture Defect Detection using Gaussian Mixture Entropy Modeling, ***3.Seba Susan*** and ***3.Monika Sharma***, Computer Science & Engineering, DTU

8. Better Approximation Results by Bernstein–Kantorovich Operators, ***6.M. Dhamija*** and ***3.N. Deo***, Applied Mathematics, DTU

9. Charge injection in large area multilayer graphene by ambient Kelvin probe force microscopy, Igor Bdikina, Dhanajay K. Sharma, Gonzalo Otero-Irurueta, María J. Hortigüela, ***3.Pawan K. Tyagi***, Victor Neto and Manoj K. Singh, Applied & Engineering Physics, DTU

10. Compact Model for Ferroelectric Negative Capacitance Transistor With MFIS Structure, ***8.1.Girish Pahwa***, Tapas Dutta, Amit Agarwal, and Yogesh Singh Chauhan, electronics and communication, DTU

11. Design and Pitch Angle Optimisation of Horizontal Axis Hydrokinetic Turbine with Constant Tip Speed Ratio, ***8.Suyash Nigama***, ***8.Shubham Bansal***, ***8.Tanmay Nema***, ***8.Vansh Sharma*** and ***3.Raj Kumar Singh***, Mechanical, Automotive and Production, DTU

12. Detection of Ultrasonic Waves using Resonant Cylindrical Cavity for Defence Application, ***3.Ramesh C. Sharma***, Subodh Kumar and ***8.1Surya K. Gautam***, Electronics and Communication, DTU

13. Dextrose modified flexible tasar and muga fibroin films for wound healing applications, ***7.Chandra Mohan Srivastava***, ***3.Roli Purwar***, Anuradha Gupta and Deepak Sharma, Applied Chemistry and Polymer Technology, DTU

14. Effect of Different Carbon Sources and Elicitors on Shoot Multiplication in Accessions of Centella asiatica, ***7.Koyel Kundu***, ***7.Arpita Roy***, ***3.Gaurav Saxena***, ***8.Lakhan Kumar*** and ***3.Navneeta Bharadvaja***, Biotechnology, DTU

15. Effect of Ratio of Visco-Elastic Material Viscosity to Fluid Viscosity on Stability of Flexible Pipe Flow, ***3.S. ANBUKUMAR*** and ***3.MUNENDRA KUMAR***, Civil Engineering, DTU

16. Efficient music recommender system using context graph and particle swarm, ***3.Rahul Katarya*** & ***3.Om Prakash Verma***, Computer Science, DTU

17. Excellent storage stability and sensitive detection of neurotoxin quinolinic acid, Ranjana Singh, Sunayana Kashyap, ***6.Suveen kumar***, Shiju Abraham, Tejendra K. Gupta, Arvind M. Kayastha, ***3.Bansi D. Malhotra***, Preeti Suman Saxena, Anchal Srivastava and Ranjan K. Singha, Biotechnology, DTU

18. Experimental Investigation of Waste Animal Fat Methyl Ester Blends in Diesel Engine, Sharad Pratap Singh, Harveer Singh Pali and ***3.Naveen Kumar***, DTU

19. Fuzzy-Contextual Contrast Enhancement, ***3.Anil Singh Parihar***, ***3.Om Prakash Verma*** and ***7.Chintan Khanna***, Electronics and Communication, DTU

20. Healant release from microcapsules with varied internal microstructure, ***6.Manorama Tripathi***, ***3.Devendra Kumar*** and Prasun Kumar Roy, Applied Chemistry and Polymer Technology, DTU

21. Hierarchy Influenced Di erential Evolution: A Motor Operation Inspired Approach, ***8.Shubham Dokania***[1], ***8.Ayush Chopra***[2], ***8.Feroz Ahmad***[3] and ***3.Om Prakash Verma***, Applied Mathematics, Computer Science, DTU

22. Highly Sensitive Porous Carbon and Metal/Carbon Conducting Nanofiber Based Enzymatic Biosensors for Triglyceride Detection, Kunal Mondal, Md. Azahar Ali, Chandan Singh, Gajjala Sumana, ***3.Bansi D. Malhotra*** and Ashutosh Sharma, Biotechnology, DTU

23. High-Quality Laser Cavity based on All-Dielectric Metasurfaces, ***6.Nishant Shankhwar***, ***3.Ravindra Kumar Sinha***, ***3.Yogita Kalra***, Sergey Makarov, Alexander Krasnok and Pavel Belov, Applied Physics, DTU

24. Implementation of Lean Manufacturing through Waste Elimination, ***6.Sanjeev Jain*** and ***3.A.K. Madan***, DTU

25. Influence of 100 MeV Au+8 ion on photovoltaic response of BiFeO3/BaTiO3 multilayer structures, ***3.Savita Sharma***, Monika Tomar , Ashok Kumar , Fouran Singh , ***3.Nitin K. Puri*** and Vinay Gupta, Applied Physics, DTU

26. Influence of growth temperature on laser molecular beam epitaxy and properties of GaN layers grown on c-plane sapphire, ***7.Ripudaman Dixit***, Prashant Tyagi, Sunil Singh Kushvaha, Sreekumar Chockalingam, Brajesh Singh Yadav, Nita Dilawar Sharma and M. Senthil Kumar, Applied Physics, DTU

27. Inscription Image Retrieval Using Bag of Visual Words, ***3.N.Jayanthi*** and ***3.S.Indu***, ECE, DTU

28. Investigation of Biocompatible and Protein Sensitive Highly Luminescent Quantum Dots/Nanocrystals of CdSe, CdSe/ZnS and CdSe/CdS, ***6.R.K. Ratnesh*** and ***3.Mohan Singh Mehata,*** Applied Physics, DTU

29. Modelling and Simulation of Thermoelectric Peltier Effect Cooling Unit, ***8.Vineet Mathew***, ***3.Akhilesh Arora***, ***3.B.B. Arora***, ***Saurabh Dubey***, ***8.Rayhan Ali*** and ***8.Sushant Sahasrabuddhe***, Production and Industrial, DTU

30. New agegraphic dark energy model in Brans-Dicke theory with logarithmic form of scalar field, ***6.Pankaj Kumar*** and ***3.C.P. Singh***, Applied Mathematics, DTU

31. Numerical Simulation of Fluid Flow and Heat Transfer in Wavy Micro-Channel at Different Reynolds Number, ***3.Mohammad Zunaid***, Afzal Husain, ***3.NaushadAhmad Ansari***, ***8.Anant Jindal*** and ***7.Avinash Gupchup***, Mechanical Engineering, DTU

32. Performance and emission characteristics of a stationary diesel engine fuelled by Schleichera Oleosa Oil Methyl Ester (SOME) produced through hydrodynamic cavitation process, Ashok Kumar Yadav, M. Emran Khan, ***3.Amit Pal*** and Uttam Ghosh, Mechanical Engineering, DTU

33. P-type multilayer graphene as a highly efficient transparent conducting electrode in silicon heterojunction solar cells, ***6.Kamlesh Patel*** and ***3.Pawan K. Tyagi***, Applied Physics, DTU

34. Review on Morphology and Microstructure Analysis of MGO Reinforced AL Composites For Rame 2016, Surabhi Lata, Nitish Kumar Verma, Chetan Singh, ***3.Roop Lal*** and ***6.Ramakant Rana***, Mechanical, DTU

35. Single layer graphene possessing anomalous dispersion with exotic microwave transmission and dielectric properties, ***6.Kamlesh Patel*** and ***3.Pawan K. Tyagi***, Applied Physics, DTU

36. Single OTRA Based Low Frequency Sinusoidal Oscillator Realization, ***7.Gurumurthy Komanapalli***, ***3.Neeta Pandey*** and ***3.Rajeshwari Pandey***, ECE, DTU

37. Structural and emission properties of Eu3+-doped alkaline earth zinc-phosphate glasses for white LED applications, ***7.Kaushal Jha*** and ***3.Mula Jayasimhadri***, Applied Physics, DTU

38. Transadmittance Mode First Order LP/HP/AP Filter and its Application as an Oscillator, ***3.Deva Nand*** and ***3.Neeta Pandey***, ECE, DTU

39. Universal biquadratic filter using Operational Floating Current Conveyor (OFCC), ***7.1.Divyesh Sachan***, ***3.Deva Nand*** and ***3.Neeta Pandey***, Electronics and Communication, DTU

40. Voltage Mode Single CDBA Based Multifunction Filter, ***7.Priyanka Gupta***, ***3.Rajeshwari Pandey*** and ***3.Neeta Pandey***, Electronics and Communication, DTU

1. *Chancellor*

2. *Pro Vice Chancellor* ***2.1.*** *Ex Pro Vice Chancellor*

3. *Faculty* ***3.1.*** *Ex Faculty*

4. *Teaching-cum-Research Fellow* ***4.1.****Asst. Librarian*

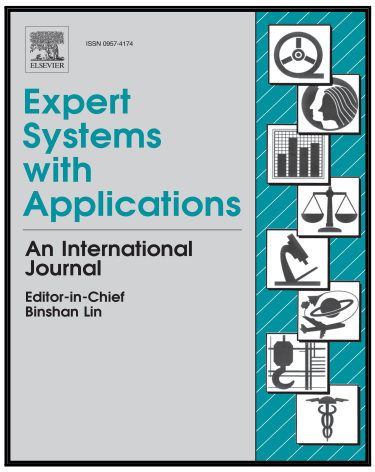
5. *Alumni*

6. *Research Scholar* ***6.1.*** *Ex Research Scholar*

7. *PG Scholar* ***7.1.*** *Ex PG Scholar*

8. *Undergraduate Student* ***8.1.*** *Ex Undergraduate Student*

Accepted Manuscript



A Novel Approach of Multi-Stage Tracking for Precise Localization of Target in Video Sequences

Gurjit Singh Walia , Saim Raza , Anjana Gupta , Rajesh Asthana , Kuldeep Singh

PII: S0957-4174(17)30084-2
DOI: 10.1016/j.eswa.2017.02.007
Reference: ESWA 11114

To appear in: *Expert Systems With Applications*

Received date: 9 September 2016
Revised date: 2 February 2017
Accepted date: 3 February 2017

Please cite this article as: Gurjit Singh Walia , Saim Raza , Anjana Gupta , Rajesh Asthana , Kuldeep Singh , A Novel Approach of Multi-Stage Tracking for Precise Localization of Target in Video Sequences, *Expert Systems With Applications* (2017), doi: 10.1016/j.eswa.2017.02.007

This is a PDF file of an unedited manuscript that has been accepted for publication. As a service to our customers we are providing this early version of the manuscript. The manuscript will undergo copyediting, typesetting, and review of the resulting proof before it is published in its final form. Please note that during the production process errors may be discovered which could affect the content, and all legal disclaimers that apply to the journal pertain.

ACCEPTED MANUSCRIPT

Highlights

- Proposed multi-stage tracker improves accuracy and reduces time complexity
- Spatio-temporal model can handle various challenges of dynamic environments
- Adaptive multicue fusion model effectively combines appearance models
- Quick adaptation due to incorporation of context sensitive reliability
- Robust and real time implementation

ACCEPTED MANUSCRIPT

ACCEPTED MANUSCRIPT

A Novel Approach of Multi-Stage Tracking for Precise Localization of Target in Video Sequences

[1]Gurjit Singh Walia, [2]Saim Raza, [3]Anjana Gupta, [4]Rajesh Asthana, [5]Kuldeep Singh

[1,4]Scientist, Defense Research and Development Organization, Ministry of Defense, Delhi, India
[2]Member Technical, D.E. Shaw India Pvt. Limited, Hyderabad, AP, India
[3]Professor, Department of Applied Mathematics, Delhi Technological University, Delhi, India
[5]Scientist, Central Research Laboratory, Bharat Electronics Limited, Ghaziabad, India

gurjit.walia@gmail.com,saimorsaim@gmail.com,anjanagupta@dce.ac.in,asthana.rajesh30@gmail.com, kuldeep.er@gmail.com

ABSTRACT

Visual tracking methods are mostly based on single stage state estimation that limitedly caters to precise localization of target under dynamic environment such as occlusion, object deformation, rotation, scaling and cluttered background. In order to address these issues, we introduce a novel multi-stage coarse-to-fine tracking framework with quick adaptation to environment dynamics. The key idea of our work is to propose two-stage estimation of object state and to develop an adaptive fusion model. Coarse estimation of object state is achieved using optical flow and multiple fragments are generated around this approximation. Precise localization of object is obtained through evaluation of these fragments using three complementary cues. Adaptation of proposed tracker to dynamic environment changes is quick due to incorporation of context sensitive cue reliability, which encompass its direct application for development of expert system for video surveillance. In addition, proposed framework caters to object rotation and scaling through a random walk state model and rotation invariant features. The proposed tracker is evaluated over eight- benchmarked color video sequences and competitive results are obtained. As an average of the outcomes, we achieved mean center location error (in pixels) of 6.791 and F-measure of 0.78. Results demonstrate that proposed tracker not only outperforms various state-of-the-art trackers but also effectively caters to various dynamic environments.

Keywords: Multicue, Data fusion, Object tracking, Cue Reliability

1. Introduction:

Precise localization of an object in video sequences is imperative due to its wide range of applications in the field of video surveillance and security, traffic monitoring, human-computer interaction, video-indexing, vehicle navigation and many more. However, dynamic environments such as partial or full occlusion, illumination changes, scale changes, rotation, and deformation of object etc. make object tracking in video sequences a challenging task. Time complexity of the tracking algorithm is another indispensable factor for real time applications. The features with high dimensions require high computational power and real time tracking using these features under dynamic environments is a challenge. In the last two decades, object tracking has been explored extensively considering one or more dynamic environment challenges. An extensive review of

ACCEPTED MANUSCRIPT

object tracking methods was reported (Yilmaz, Javed, & Shah, 2006). Further, an experimental survey comparing nineteen state-of-the-art trackers was reported (Smeulders, Chu, Cucchiara, Calderara, Dehghan, & Shah, 2014). A review on multicue based object tracking methods was carried out by (Walia & Kapoor, 2016). Despite these advances in object tracking methods from single cue based solutions to more robust multicue based solutions, most of object tracking solutions based upon only single cue fail to accurately localize objects in real time under dynamic environments (Yilmaz, Javed, & Shah, 2006; Yang & Nevatia, 2014; Smeulders, Chu, Cucchiara, Calderara, Dehghan, & Shah, 2014; Walia & Kapoor, 2016).

Generally, object tracking methods can be categorized on the basis of modalities and features used. Multicue based tracking solutions where multiple features are extracted from single-modal (single sensor) were extensively investigated. Under dynamic environment, cues performing better at one instance of time may get deteriorated at other instance of time. The color cue is invariant to object scaling and can handle partial occlusion, but it gets deteriorated with change in illumination and full occlusion. Inability of color cue to provide spatial information was overcome by considering semi overlapping regions in color space (Maggio & Cavallaro, 2005). Motion feature can be easily extracted but it does not provide any information about the shape of the object. Spatial-temporal motion energy was considered for embedding spatial information in motion cue (Cannons, Gryn, & Wildes, 2010). Texture cue can be easily computed but it gets greatly affected as object moves away from camera. Similarly, gradient cue gets deteriorated under target occlusion. Hence, multiple cues extracted from single sensor were adaptively fused considering different fusion approach such as democratic integration (Triesch & von der Malsburg, 2001), weighted likelihood with cue reliability estimated from previous and present observation (Brasnett, Mihaylova, Bull, & Canagarajah, 2007), and relative discriminative coefficient (Wang, Chen, Chen, & Yang, 2012). However, most of adaptive fusion methods do not resolve conflicts among cues for quick adaption of tracker. Switching among different models on basis of model transition probability was investigated for robust tracking solutions (Dou & Li, 2014) but accuracy of tracker is limited to single model due to dynamic switching. The feature level fusion of multiple cues such as joint height and color histogram (JHCH) and histogram of height difference (HOHD) was also exploited for robust tracking solutions (Thomaidis, Tsgas, Lytrivis, Karaseitanidis, & Amditis, 2013). However, in general, feature level fusion of cues required more computational power.

In another line of research, multi-modal multicue tracking solutions were investigated for extracting complementary features from multiple sensors. Vision based sensors are limited to daytime video surveillance applications. Therefore, vision sensors need to be compensated by other sensors such as IR/Thermal/Radar/audio etc. Recently, Thermal and vision sensors were used for extracting five cues (Conaire, Connor, & Smeaton, 2008) but no adaptive fusion method for individual scores was considered. Context-sensitive reliability was exploited for fusion of color, thermal and motion cues in particle filter framework for adaptive fusion (Erdem, Dubuisson, & Bloch, 2012). Audio sensor array along with vision sensor was considered for tracking active occluded objects under indoor

environment (Kılıç, Barnard, Wang, & Kittler, 2015). In particle filter framework, audio sensor contributed at observation and propagation stage for robust tracking. However, audio sensors assist vision sensor while person is speaking. Performance under highly noisy outdoor environment needs further investigations. In general, multimodal tracking solutions suffer from problems of synchronization and calibration of different modalities. Further, limited information can be extracted from thermal, IR, audio, laser, radar sensors for aiding visual sensor which itself is a rich source of information.

In sum, multicue tracking solutions using either single-modal or multi-modal data have been explored with emphasis of catering to dynamic environments. The real time implementation and adaptive fusion of multicue was studied considering one or more environment scenarios. Considering challenges of visual world, tracking solutions with high precision and quick adaptation still need to be explored. Hence, precise localization of object in video sequences under dynamic environments is partially solved.

1.1 Motivation and Contribution of Present Work

The present research work is aimed at design and development of tracking framework using multi-stage estimation of target location. Our work is motivated from mechanism of object tracking by various living beings in their natural habitats. For instance, visual-motion cues are exploited by falcons to pursue its prey (Kane & Zamani, 2014). Under this study it was shown that location of the prey is made apparent in the visual field and the prey is ultimately caught via motion camouflage. Similarly, Bhagavatula et al. investigated correlation between optic flow and flight velocity of birds (Bhagavatula, Claudianos, Ibbotson, & Srinivasan, 2011). Studies with budgerigars revealed that birds navigate passages safely considering that their eyes experience same rate of optic flow. It was also reported that optical flow field was exploited by insects with compound eyes for defending themselves from incoming predator. Hence, inspired by nature, we considered optical flow for quick rough estimation of target in first stage. The rough estimated location is improved for precise localization of target through multicue based fragment models. Further the calculation of reliability is motivated by the human sensory system. It was reported that in a human sensory system, if particular sensory information is not good the other senses are automatically boosted (Murphy, 1996). We propose fusion model for multicue integration considering above studies on human sensory system. With boosting of good cues and suppressing of discordant cues, adaptation of proposed tracker to dynamic environment is quick and reliable.

The highlights of proposed work can be summarized as follows:

- Multi stage corase to fine estimation improves accuracy and reduces time complexity.
- Proposed spatio-temporal model based upon optical flow and complementary cues can handle various dynamic environments.
- Proposed appearance model can handle object scaling and rotation.

- Proposed adaptive multicue fusion model boosts good appearance models and suppresses discordant models.
- Adaptation of tracker is quick due to incorporation of context sensitive cue reliability.
- Robust and real time implementation.

Further we have organized our proposed work as follows: In Section 2, we introduce proposed multistage multicue tracking algorithm. The adaptive fusion model along with method for handling object rotation and scaling is discussed. Core design of our proposed tracker along with its flow chart and pseudo code is presented in Section 3. Section 4 contains implementation details and testing dataset challenges for conducting experimental simulation. Also, proposed tracker is compared both qualitatively and quantitatively with state of the art tracking solutions on benchmark video sequences. Finally, we have sketched summary of proposed work and future directions in Section 5.

1.2 Related Work: Multicue Object Tracking

In last two decades, object tracking in video sequences has been extensively explored. In general, most of tracking algorithms can be classified either based on appearance model or based on motion estimation between consecutive frames. For appearance based tracking methods, reference model or global template is compared with object models in subsequent frames (Maggio & Cavallaro, 2005; Cannons, Gryn, & Wildes, 2010; Triesch & von der Malsburg, 2001; Brasnett, Mihaylova, Bull, & Canagarajah, 2007; Wang, Chen, Chen, & Yang, 2012; Erdem, Dubuisson, & Bloch, 2012; Dou & Li, 2014; Adam, Rivlin, & Shimshoni, 2006; Zhang & Song, 2013). However, under dynamic environment in subsequent frames, object model mostly deviates from reference model hence impair tracking accuracy. On the other hand, motion based tracking methods such as optical flow calculates object displacement in consecutive frames & hence less affected by dynamic environment (Horn & Schunk, 1981). Hence, considering complementary cues, appearance and motion models were extracted for development of robust multicue tracking solutions. Multicue tracking using democratic integration of motion, color, shape, position, and contrast cues was proposed (Triesch & von der Malsburg, 2001). Democratic integration of cues aims at boosting of good cues and suppression of bad cues. In (Yin, Zhang, Sun, & Gu, 2011), Yin et al. proposed improvement in particle filter framework by embedding Camshift algorithm. Combined probability distribution map was extracted from color and motion cues. Author claimed that combining motion cue with color cue caters not only for illumination changes but also for background clutter. In order to track occluded low saturation object, color and motion cues probability map are adaptively combined in mean shift tracking framework (Liu, Yu, Zha, Zou, & Zhang, 2009). However, in this work, cues reliability estimated from previous frames was used for current state estimation. From calibrated vision and CCD camera, multimodal tracking framework using color, infrared brightness and motion cues was proposed (Liu, Yu, Zha, Zou, & Zhang, 2009). Context sensitive reliability based on current observation is used for quick adaptation of tracker. Using motion and appearance model, multi-target tracking was solved by considering it as energy minimization problem (Yang & Nevatia, 2014). Energy functions were derived from motion and appearance model and association

ACCEPTED MANUSCRIPT

was established under low energy cost. The author claimed that introduced CRF model can efficiently handle spatially close similar targets under camera motion. In (Perez, Vermaak, & Blake, 2004), Perez et al. proposed particle filter framework for combining motion/sound and color cue. Object bearing was determined from time difference of arrival of audio signals and aids main color cue for robust tracking. Exploiting depth information, multicue fusion information was proposed for localization of object in video sequences captured (Wang, Fang, & Yuan, 2014). In the work, optical flow, color and depth information were fused for tracking object in Kinect sequences. However, adaptive fusion of multicue was not considered. Also extraction of depth information from single vision and thermal camera was not employed in most real time scenarios. Ability of stereo vision to provide gesture and invariance to illumination was exploited for robust tracking using condensation algorithm (Nickel & Stiefelhagen, 2008). Proposed approach used stereo, motion, stereo correlation and detector as cues. Target was first localized using stereo cue and position was further refined using adaptive fusion of other cues. But the approach was limited to stereo vision sequences and limitedly tested on a single sequence. In sum, multicue framework using motion cue along with other complementary cues was explored at length. But, adaptive fusion multiple cues under context sensitive reliability of cues was partially solved and discussed. In addition, exploring multistage estimation of target location using single vision or thermal camera needs further investigations.

2. Proposed Multi-stage Tracker

Proposed multistage tracker for precise localization of object in video sequences is based on motion cue and visual features. As shown in Figure 1, Optical Flow is used at first stage for rough estimation of object location. This localization of object is improved in second stage by generating fragments around the approximated location. For each fragment, appearance models are extracted considering their complementary nature. Three cues: RGB color model, rotation invariant Local Binary Pattern (LBP), and Pyramid Histogram of Orientation Gradients (PHOG) are extracted for each appearance model. RGB color model is invariant to scaling, computationally efficient and can handle partial occlusion. However, it could not cater to full occlusion, illumination changes and texture changes. The spatial information is extracted using PHOG, which can efficiently handle object deformation and in-plane rotation. The complementary texture information is obtained using rotation invariant LBP. The rotational invariance of LBP can handle both in-plane and out-of-plane rotation. Hence, in proposed spatial-temporal model complementary cues enlarge its working domain whereas redundant cues enhance its reliability. Further, cue likelihood is subjected to proposed adaptive multicue fusion model, which is based upon Borda count ranking and context sensitive reliability. The final localization of object is determined through weighted sum of fragments, which are evaluated over three complementary appearance models. Before the introduction of core design of proposed tracker, detailed design of Stage-I and Stage-II localization of object in video sequences is illustrated in next section.

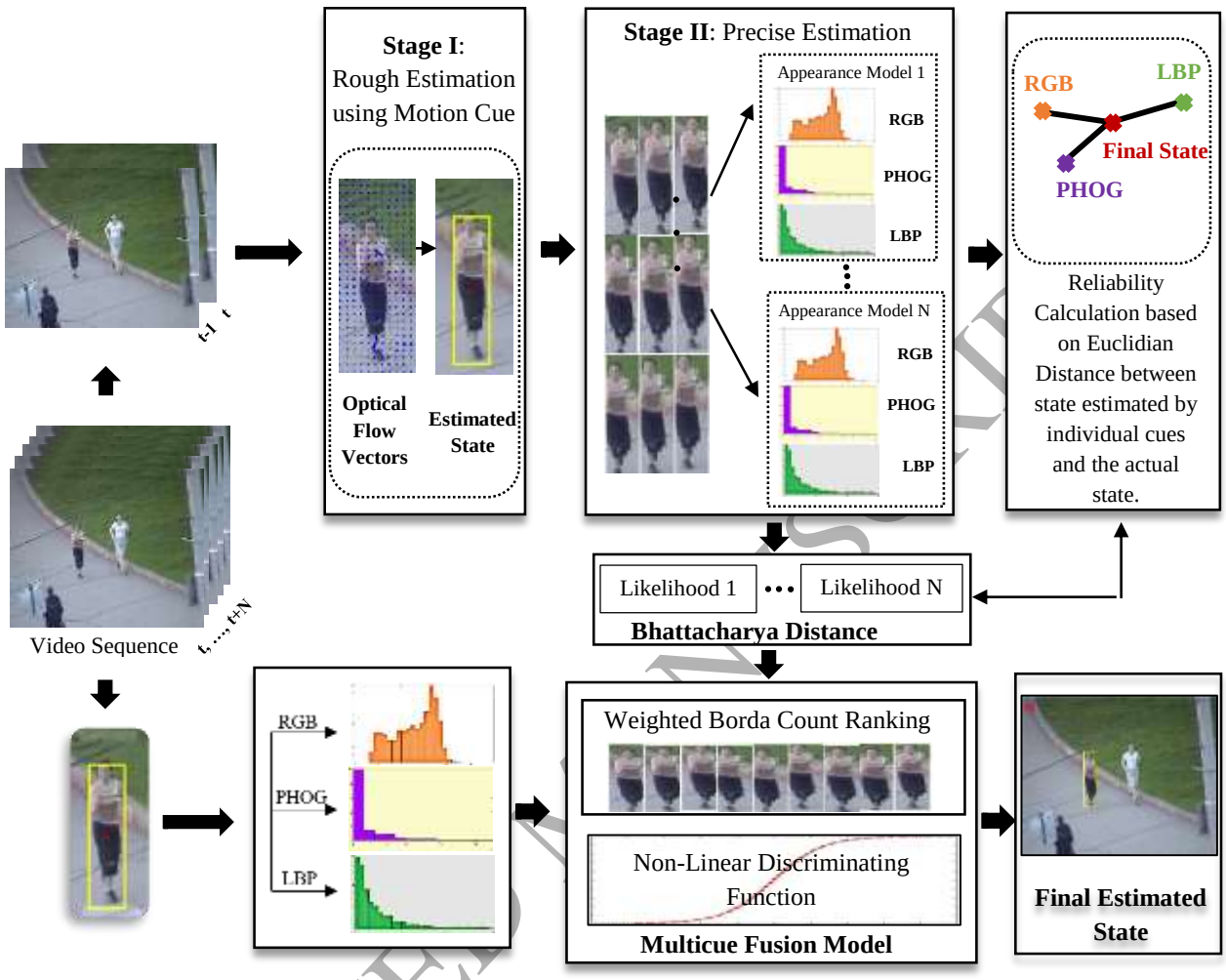


Figure 1: Visualization of Proposed Multistage Tracker

2.1 Stage-I: Rough Localization of Object

In proposed multi-stage tracker, quick rough localization of object is determined through estimation of Optical flow. The idea of rough localization of target is motivated from mechanism of object tracking by various living beings in their natural habitats (Kane & Zamani, 2014; Bhagavatula, Claudianos, Ibbotson, & Srinivasan, 2011). The Optical flow is rate of movement of pixels and their associated direction between consecutive frames. For this, motion vector for each pixel is obtained in a particular frame. Optical flow has been extensively studied due to its applications such as motion estimation, segmentation, time of collision estimation, and many more. In proposed tracker, optical flow is determined using Horn-Schunck (HS) method (Horn & Schunk, 1981). Optical Flow estimation assumes that the brightness is constant between the frames and same can be described using equation (1).

$$\mathcal{F}(x, y, T) \approx \mathcal{F}(x + dx, y + dy, T + dT) \tag{1}$$

In this equation, $\mathcal{F}(x, y, T)$ is the intensity of pixel located at (x, y) at time T. Also, pixel displacement is represented using dx, dy, in x-direction, y-direction respectively and dT is change in time. Equation (1) can be solved by Taylor series expansion as determined in equation (2).

$$\mathcal{F}(x + dx, y + dy, T + dT) = \mathcal{F}(x, y, T) + \frac{\partial \mathcal{F}}{\partial x} dx + \frac{\partial \mathcal{F}}{\partial y} dy + \frac{\partial \mathcal{F}}{\partial T} dT + M \tag{2}$$

Where M represents higher order terms (H.O.T.) and is generally ignored. The approximation of equation (2) can be described using equation (5).

$$\nabla \mathcal{F}. \vec{\mathcal{V}} = -\mathcal{F}_t \tag{3}$$

$$\nabla \mathcal{F}. \vec{\mathcal{V}} + \mathcal{F}_t = 0 \tag{4}$$

$$\mathcal{F}(x, y, T) \approx \mathcal{F}(x + dx, y + dy, T + dT) \tag{5}$$

Where, $\nabla \mathcal{F}$ represents spatial gradient of intensity, $\mathcal{F}_t$ is temporal gradient, and optical flow (velocity) vector is represented as $\vec{\mathcal{V}} = (\mathcal{V}_x, \mathcal{V}_y) = (dx, dy)$. HS method considers smoothness constraint in addition to gradient constraint for minimization of magnitude of optical flow components. The error term for smoothness constraint (global term for smoothing) is determined using equation (6).

$$\mathcal{E}_{HS}^2 = \left(\frac{\partial \mathcal{V}_x}{\partial x}\right)^2 + \left(\frac{\partial \mathcal{V}_x}{\partial y}\right)^2 + \left(\frac{\partial \mathcal{V}_y}{\partial x}\right)^2 + \left(\frac{\partial \mathcal{V}_y}{\partial y}\right)^2 \tag{6}$$

Where, $\frac{\partial \mathcal{V}_x}{\partial x}$, $\frac{\partial \mathcal{V}_x}{\partial y}$ is change of $\mathcal{V}_x$ vector in x and y direction respectively. Similarly, $\frac{\partial \mathcal{V}_y}{\partial x}$, $\frac{\partial \mathcal{V}_y}{\partial y}$ is change of $\mathcal{V}_y$ vector in x and y direction respectively. Hence, total error to be minimized is determined using equation (8).

$$\mathcal{E}_T^2 = \left(\nabla \mathcal{F}. \vec{\mathcal{V}} + \mathcal{F}_t\right) + \left(\mathcal{E}_{HS}^2\right) \tag{7}$$

$$\mathcal{E}_T^2 = \iint \left(\nabla \mathcal{F}. \vec{\mathcal{V}} + \mathcal{F}_t\right) + \epsilon^2 \left(\left(\frac{\partial \mathcal{V}_x}{\partial x}\right)^2 + \left(\frac{\partial \mathcal{V}_x}{\partial y}\right)^2 + \left(\frac{\partial \mathcal{V}_y}{\partial x}\right)^2 + \left(\frac{\partial \mathcal{V}_y}{\partial y}\right)^2\right) dx\, dy \tag{8}$$

In above equation, second term is called the smoothness constraint and constant ϵ^2 is weighing factor. By solving equation (8), values of optical flow vector $\vec{\mathcal{V}} = (u, v)$ for which the error $\mathcal{E}_T$ is minimized are obtained. In proposed tracker for rough localization of object, in Stage-I, we determine the rough centroid location of the object using equation (9).

$$(x_n, y_n) = (x_{n-1} + dx,\ y_{n-1} + dy) \tag{9}$$

ACCEPTED MANUSCRIPT

Where, dx and dy are obtained using equation (10) and (11).

$$dx = \frac{1}{N}\sum_{i} \mathcal{V}_x^i, \quad \forall\, i \in C \tag{10}$$

$$dy = \frac{1}{N}\sum_{i} \mathcal{V}_y^i, \quad \forall\, i \in C \tag{11}$$

In above equations, C is object centroid determined in precise estimation in the previous frame. However, in first frame we manually initialized location of the object. Similarly, $\mathcal{V}_x^i$ and $\mathcal{V}_y^i$ are the optical flow vector associated with i^{th} pixel in C, and N is number of pixels around C that are subjected for evaluation. After rough localization of the target centroid, we precisely localize the target in second stage of estimation. Details of second stage of estimation are illustrated in following sub-section.

2.2 Stage-II: Precise Localization of Object

The precise localization of targeted object is determined through multiple cues extracted from fragments generated around estimated centroid from Stage-I. For fragmentation of target region, object representation is critical factor for robust tracking solutions. Object region for cue extraction is generally represented by different bounding regions such as rectangle, ellipse, circle etc. In proposed fragment based tracking framework, rectangular bounding box is used for extraction of features. Object scaling and rotation is catered using the two factors as random walk modeling and rotation invariant features. Firstly, state $P_t = (\mathrm{s}, \theta)^{\mathrm{T}}$of each fragment is propagated as a random walk as described in equation (12).

$$P_{t+1} = P_t + W_t \tag{12}$$

Here, s and θ are scaling and rotation factors respectively, $W_t \sim \mathcal{N}(0, T)$ is Gaussian noise with zero mean, and $T = diag(\sigma_s, \sigma_\theta)$ is covariance matrix which describes the uncertainty in state vector. During state estimation, each fragment is scaled and rotated using equation (12) and subjected for cues extraction. In addition, we have used rotation invariant Local Binary Pattern and scale invariant PHOG for catering rotation and scaling of object. The details of various cues used for object modeling are illustrated in the following sub sections.

2.2.1 Object and Measurement Model

Localized fragments with incorporation of scaling and rotation factors are subjected for extraction of three complimentary cues. In proposed tracking framework, Color, Edge and Texture cues are considered. Details of these cues along with their likelihood estimation are illustrated below.

Color Cue: Color cue is an effective feature for object tracking due to its invariance to scaling, ability to handle partial occlusion and low computational power demand. However, color model could not distinguish similar color objects and also unable to cater to rotation of object. In proposed

ACCEPTED MANUSCRIPT

framework, we have chosen RGB color model for extracting color cue. As histogram is invariant to appearance change, we extracted color histogram for each fragment region. If $x = \{(x_1, y_1), (x_2, y_2), \dots, (x_m, y_m)\}$ are pixel location in the fragment, its histogram $H = \{H_1, H_2, \dots, H_{N_b}\}$ is determined using equation (13).

$$H_i = K \sum_{j=1}^{m} \delta(b(x_j, y_j) - u), i = 1,2, \dots, N_b \tag{13}$$

Here $\delta(.)$ is Kronecker-delta function, N_b is total number of bins, $b(.)$ relates pixels to histogram bins, and K is a normalizing factor such that $\sum_{i=1}^{N_b} H_i = 1$. First, normalized histogram of reference object is extracted as H_{rc}. Similarly, color histogram for i[th] fragment is determined as H_c^i . In order to assign weights to the fragments using color cue, we calculate Bhattacharya Distance between reference histogram and fragment histogram. The Bhattacharya Distance has been used extensively for measuring similarly between two distributions (Bhattacharyya, 1943). In order to compute Bhattacharya Distance for i[th] fragment, Bhattacharya coefficient $\beta_{i,c}(H_{rc}, H_c^i)$ is determined using equation (14).

$$\beta_{i,c}(H_{rc}, H_c^i) = \sum_{p=1}^{N_b} \sqrt{H_{rc}^p \times (H_c^i)^p} \tag{14}$$

From this, Bhattacharya Distance is determined using equation (15). Lesser the value of distance more is the similarity between distributions.

$$\mathrm{B}_{i,c}(H_{rc}, H_c^i) = \sqrt{1 - \beta_{i,c}(H_{rc}, H_c^i)} \tag{15}$$

The estimation of likelihood using Bhattacharya Distance measure was proposed by Perez et al. (Perez, Vermaak, & Blake, 2004). Color cue likelihood $\tau_{i,c}(H_{rc}, H_c^i)$ for i[th] fragment is determined using equation (16).

$$\tau_{i,c}(H_{rc}, H_c^i) = \frac{1}{\sigma_c \sqrt{2\pi}} e^{\left(-\frac{\left(\mathbf{B}_{i,c}(H_{rc}, H_c^i)\right)^2}{2\,\sigma_c}\right)} \tag{16}$$

Where σ_c is standard deviation and represents Gaussian noise in measurement process. Using equation (16), weights for each fragment of color cue is determined and subjected to fusion model for assigning final weights to the fragments.

Edge Cue: Spatial distribution of shape is considered as prominent feature for object recognition. For extracting image shape along with spatial distribution of shape, image descriptor as Pyramid of Histograms of Orientation Gradients (PHOG) was proposed (Bosch, Zisserman, & Munoz, 2007). In proposed tracking framework, local shape as distribution of edge orientation along with spatial

distribution of edges is extracted for each fragment using PHOG. First, from object region of interest, local shape is extracted as histogram of edge orientation. From given intensity of pixels in object region of interest I, intensity gradient at pixel (x_i, y_i) is determined using equation (17).

$$\mathrm{G}(x_i, y_i) = \sqrt{(\boldsymbol{I}(x_i, y_{i+1}) - \boldsymbol{I}(x_i, y_{i-1}))^2 + (\boldsymbol{I}(x_{i+1}, y_i) - \boldsymbol{I}(x_{i-1}, y_i))^2} \tag{17}$$

In addition for given image, we divided orientation into $18(= 360°/20)$ bins where orientation is determined using equation (18).

$$\alpha = tan^{-1}\left(\frac{(\boldsymbol{I}(x_i, y_{i+1}) - \boldsymbol{I}(x_i, y_{i-1}))}{(\boldsymbol{I}(x_{i+1}, y_i) - \boldsymbol{I}(x_{i-1}, y_i))}\right) \tag{18}$$

Spatial shape is extracted by segmenting image into regions of lower resolution. Zero level indicates original image and C dimensional HOG vector corresponding to C bins. At second level, image is segmented into four regions and corresponding $4C$ HOG vectors are extracted. Similarly, at nth level image is described by $\sum_{l=0}^{l=n} 2^{2l} \left(= \sum_{l=1}^{l=n} 4^l\right)$ vectors each with dimensionality C. Further, these vectors are concatenated to get PHOG descriptor. Finally, PHOG descriptor is normalized and histogram $H = \{H_1, H_2, \dots, H_{N_b}\}$ is extracted using equation (19).

$$H_i = S \sum_{j=1}^{m} G(x_j, y_j) \times \delta(s(x_j, y_j) - u), \qquad i = 1,2, \dots, N_b \tag{19}$$

Here $\delta(.)$ is Kronecker-delta function, N_b is the total number of bins, $s(.)$ relates pixels to histogram bins, and S is a normalizing factor such that $\sum_{i=1}^{N_b} H_i = 1$. For reference object, normalized histogram for edge cue is extracted as H_{re}. Similarly, histogram for edge cue of ith fragment is determined as H_e^i. The similarity of reference histogram with histogram of ith fragment for edge cue is estimated using Bhattacharya Distance which is extensively used for measuring similarity between two distributions (Bhattacharyya, 1943). In order to compute Bhattacharya Distance for ith fragment for edge cue, Bhattacharya coefficient $\beta_{i,e}(H_{re}, H_e^i)$is determined using equation (20).

$$\beta_{i,e}(H_{re}, H_e^i) = \sum_{p=1}^{N_b} \sqrt{H_{re}^p \times (H_e^i)^p} \tag{20}$$

Similarity between reference and fragment distribution is estimated using Bhattacharya Distance equation (21). Lesser the value of distance more is the similarity between distributions.

$$\mathrm{B}_{i,e}(H_{re}, H_e^i) = \sqrt{1 - \beta_{i,e}(H_{re}, H_e^i)} \tag{21}$$

In line with color cue likelihood estimation, edge cue likelihood is determined and its value is

assigned as weight to fragment. Edge cue likelihood $\tau_{i,e}\left(H_{re}, H_e^i\right)$ for i[th] fragment is determined using equation (22).

$$\tau_{i,e}\left(H_{re}, H_e^i\right) = \frac{1}{\sigma_e\sqrt{2\pi}} e^{\left(-\frac{\left(\mathbf{B_{i,e}}\left(H_{re}, H_e^i\right)\right)^2}{2\,\sigma_e}\right)} \tag{22}$$

Where, standard deviation σ_e represents Gaussian noise in measurement process for edge cue. Using equation (22), weights for each fragment of edge cue is determined and subjected to fusion model for assigning final weights to the fragments.

Texture Cue: Texture cue represent spatial arrangement of pixels and contrast in two dimensional image plane. This cue can extract low level features from images. For extraction of texture cue for each fragment we considered rotation invariant Local Binary Pattern (LBP) as proposed (Ojala, Pietikäinen, & Mäenpää, 2002). The generic LBP operator uses a 3x3 grid and slides it over the entire image region. Considering the gray value of centre pixel, neighbourhood pixels are threshold using equation (23).

$$LBP_{(r,n)}(x_c, y_c) = \sum_{p=0}^{n-1} S\left(g_p\left(x_p, y_p\right) - g_c(x_c, y_c)\right).2^p, \tag{23}$$

$$S(z) = \begin{cases} 1, & z \geq 0 \\ 0, & z < 0 \end{cases}$$

Where, $g_p\left(x_p, y_p\right)$ is gray value of p[th] pixel in the radius r. For central pixel, gray value is defined as $g_c(x_c, y_c)$. $S(.)$ is step function. The multi-resolution gray scale rotation invariant analysis was exploited using uniform pattern in image region for extraction of texture cue (Ojala, Pietikäinen, & Mäenpää, 2002). The uniform pattern in image was considered to be strong feature for texture classification. The uniformity is defined using $U\left(LBP_{(r,n)}(x_c, y_c)\right)$, value determines using equation (25), measures number of bit wise transition in generic LBP. The threshold value of uniformity measure is fixed as 2 by statistical analysis of image data.

The rotation invariant LBP is determined using equation (24):

$$LBP_{(r,n)}(x_c, y_c) = \begin{cases} \sum_{p=0}^{n-1} S\left(g_p\left(x_p, y_p\right) - g_c(x_c, y_c)\right), & if\ U\left(LBP_{(r,p)}(x_c, y_c)\right) \leq 2 \\ p+1, & if\ U > 2 \end{cases} \tag{24}$$

$$U\left(LBP_{(r,n)}(x_c, y_c)\right) = \left|S\left(g_{p-1}\left(x_{p-1}, y_{p-1}\right) - g_c(x_c, y_c)\right) - S\left(g_0(x_0, y_0) - g_c(x_c, y_c)\right)\right| \tag{25}$$

ACCEPTED MANUSCRIPT

$$+\sum_{p=0}^{n-1}\left|S\left(g_p(x_p,y_p)-g_c(x_c,y_c)\right)-S\left(g_{p-1}(x_{p-1},y_{p-1})-g_c(x_c,y_c)\right)\right|$$

From extracted LBP operator, histograms are determined for pattern labels which are mapping of uniformity measure of each pixel. First for reference target, normalized histogram for texture cue is extracted as H_{rt}. Similarly, H_t^i histogram for texture cue for i[th] fragment is calculated. In similar line, similarity of histogram of i[th] fragment with reference histogram is estimated using Bhattacharya Distance (Bhattacharyya, 1943). In order to compute Bhattacharya Distance for i[th] fragment, first, Bhattacharya coefficient $\beta_{i,t}(H_{rt},H_t^i)$ is determined using equation (26).

$$\beta_{i,T}(H_{rt},H_t^i)=\sum_{p=1}^{m}\sqrt{H_{rt}^p\times\left(H_t^i\right)^p} \tag{26}$$

Bhattacharya distance is determined from Bhattacharya coefficient using equation (27).

$$\mathrm{B}_{i,t}(H_{rt},H_t^i)=\sqrt{1-\beta_{i,t}(H_{rt},H_t^i)} \tag{27}$$

Finally, Texture cue likelihood is determined and its value is assigned as weight to the fragment. Texture cue likelihood $\tau_{i,t}(H_{rt},H_t^i)$ for i[th] fragment is determined using equation (28).

$$\tau_{i,t}(H_{rt},H_t^i)=\frac{1}{\sigma_t\sqrt{2\pi}}e^{\left(-\frac{\left(\mathrm{B}_{i,t}(H_{rt},H_t^i)\right)^2}{2\,\sigma_t}\right)} \tag{28}$$

Where, standard deviation σ_t represents Gaussian noise in measurement process for texture cue. After the estimation of weights of each fragment using equation (16), (22) (28), weights are subjected to proposed multicue fusion model for assigning a final weight to each fragment. The proposed fusion model not only boosts good performing fragment but also suppresses discordant fragments. The details of proposed multicue fusion model are illustrated in the following section.

2.2.2 Proposed Adaptive Multicue Fusion Model

Likelihood values for each fragment require to be adaptively fused for automatic boosting and suppressing of fragments in accordance with dynamic environment. The fragments with concordant cues are boosted whereas fragments with discordant cues are suppressed. The proposed fusion model considers both fragment likelihood and cue reliability for assigning final weights to each fragment. The details of proposed fusion model are illustrated in this section.

The estimated likelihoods, equation (16), (22), and (28) for each fragment are assigned as preliminary weights to fragments using equations (29), (30) and (31).

ACCEPTED MANUSCRIPT

$$h_{ci} = \tau_{i,c}(H_{rc}, H_c^i), \qquad i = 1 \dots N \tag{29}$$

$$h_{ei} = \tau_{i,e}(H_{re}, H_e^i), \qquad i = 1 \dots N \tag{30}$$

$$h_{ti} = \tau_{i,t}(H_{rt}, H_t^i), \qquad i = 1 \dots N \tag{31}$$

Where N is the number of fragments, h_{ci} is color cue weight, h_{ei} is edge cue weight, and h_{ti} is texture cue weight for i^{th} fragment.

In literature, it was argued that rank level fusion has potential advantages over score level fusion such as scale invariance and simple comparison. The Borda count ranking as proposed by Borda (Borda, 1995) ranks the candidates according to preferences of the voters. The most preferred candidate gets maximum (or minimum) number of votes, the second most preferred gets one less than the maximum number of votes (or one more than the minimum votes) depending upon the model adopted. If k is the total number of candidates and N is the total number of voters, then the Borda count ranking to p^{th} candidate is given by equation (32).

$$J_p = \sum_{i=1}^{N} R_i(p), \qquad p = 1, 2, \dots, k \tag{32}$$

If m is the total number cues and n is the total number of fragments, the matrix representing the likelihood of the all the fragments can be represented using equation (33).

$$\mathrm{M}^{m*n} = \begin{pmatrix} h_{11} & h_{12} & \dots & h_{1n} \\ h_{21} & h_{22} & \dots & h_{2n} \\ \vdots & \vdots & \ddots & \vdots \\ h_{m1} & h_{m2} & \dots & h_{mn} \end{pmatrix} \tag{33}$$

Where h_{ij} is the likelihood of j^{th} fragment for i^{th}cue. From estimated individual cue reliabilities at time $s-1$, the reliabilities at time s can be represented as:

$$r^s = (r_1^{s-1}, r_2^{s-1}, \dots, r_m^{s-1}) \tag{34a}$$

Where r_i^{s-1} is the reliability of i^{th} cue at time $s-1$. For making rank-level fusion adaptive, we multiply each row of matrix M^{m*n} with the reliability of its corresponding cue as done in equation (34).

$$\begin{pmatrix} h_{11} * rel_1^{s-1} & h_{12} * rel_1^{s-1} & \dots & h_{1n} * rel_1^{s-1} \\ h_{21} * rel_2^{s-1} & h_{22} * rel_2^{s-1} & \dots & h_{2n} * rel_2^{s-1} \\ \vdots & \vdots & \ddots & \vdots \\ h_{m1} * rel_m^{s-1} & h_{m2} * rel_m^{s-1} & \dots & h_{mn} * rel_m^{s-1} \end{pmatrix} \xrightarrow{M^{m*n} \to H^{m*n}} \begin{pmatrix} H_{11} & H_{12} & \dots & H_{1n} \\ H_{21} & H_{22} & \dots & H_{2n} \\ \vdots & \vdots & \ddots & \vdots \\ H_{m1} & H_{m2} & \dots & H_{mn} \end{pmatrix} \tag{34}$$

The scores, H^{m*n}, obtained in equation (34) are used to assign ranking to fragments in each row using equation (35).

ACCEPTED MANUSCRIPT

$$\begin{pmatrix} H_{11} & H_{12} & \dots & H_{1n} \\ H_{21} & H_{22} & \dots & H_{2n} \\ \vdots & \vdots & \ddots & \vdots \\ H_{m1} & H_{m2} & \dots & H_{mn} \end{pmatrix} \xrightarrow{\mathfrak{B}: H^{m*n} \to N^{m*n}} \begin{pmatrix} B_{11} & B_{12} & \dots & B_{1n} \\ B_{21} & B_{22} & \dots & B_{2n} \\ \vdots & \vdots & \ddots & \vdots \\ B_{m1} & B_{m2} & \dots & B_{mn} \end{pmatrix} \tag{35}$$

Where $\mathfrak{B} : M^{m*n} \to N^{m*n}$ is a function which assigns with each fragment its ranking B_{ij} in the corresponding row based on its score H_{ij}. The highest ranked fragment in each row gets a score of n, second best gets a score n-1, and so on. Using these rankings we obtain final weights for each fragment by applying an aggregating function $\mathcal{F} : N^{m*n} \to W^{1*n}$ on matrix N^{m*n} using equation (36). The aggregating function not only boosts good fragments but also suppresses bad ones.

$$\begin{pmatrix} B_{11} & B_{12} & \dots & B_{1n} \\ B_{21} & B_{22} & \dots & B_{2n} \\ \vdots & \vdots & \ddots & \vdots \\ B_{m1} & B_{m2} & \dots & B_{mn} \end{pmatrix} \xrightarrow{\mathcal{F}: N^{m*n} \to W^{1*n}} \left(f\left(B_{1,1}, B_{2,1}, \dots, B_{m,1}\right), \dots, f\left(B_{1,n}, B_{2,n}, \dots, B_{m,n}\right) \right) \tag{36}$$

Where f: $P^{1*n} \to \mathbb{R}$ is defined using equation (37).

$$W_i^s = f\left(B_{1,i}, B_{2,i}, \dots, B_{m,i}\right) = sig\left(\frac{\sum_{k=1}^{m} B_{k,i}}{\max_{\forall i} \left(\sum_{k=1}^{m} B_{k,i}\right)}, a, b \right), i = 1,2 \dots n \tag{37}$$

Where W_i^s is the final weight assigned to the i^{th} fragment at time s. Also, the sigmoid function, $sig(.)$, is defined using equation (38):

$$sig(x, a, b) = \frac{1}{1 + e^{-a(x-b)}} \tag{38}$$

Where a and b are constant parameters of sigmoid function. The aim of passing the weights through the non-linear sigmoid function is to boost the fragments with concordant cues and to suppress the fragments with discordant cues. The final estimation of the position of the object state $[X^s = x^s, y^s]$ is done by equation (39):

$$X^s = \sum_{i=i}^{n} W_i^s . X_i^s \tag{39}$$

X_i^s is the centroid of the i^{th} fragment and X^s is the final estimated centroid of the object at time s. The reliabilities of each cue is updated by measuring L2 norm distance between the final estimated state and state estimated through individual cues. Let the state estimated by cue $j = 1, 2, .., m$ at time s is X_j^s, then we define L2 norm distance using equation (40):

$$\lambda_j^s = \left|\left| X_j^s - X^s \right|\right| = \sqrt{\left(x_j^s - x^s\right)^2 + \left(y_j^s - y^s\right)^2} \tag{40}$$

ACCEPTED MANUSCRIPT

Where $\mathfrak{Z}_j^s$ is the Euclidian distance between the centroid of the state estimated using j^{th} cue, $(x_j^s,\ y_j^s)$, and the final estimated state, (x^s, y^s), at time s. Using $\mathfrak{Z}_j^s$, the reliability of each cue is updated using equation (41).

$$r_j^s = \frac{1}{2}\left(\tanh\left(-a.\mathfrak{Z}_j^{t-1} + b\right) + 1\right) \tag{41}$$

In proposed multistage tracker, we have adaptively fused color, edge and texture cues likelihood along with their context sensitive reliabilities. In our experiments, matrix M^{3*n} describing cues is represented using equation (42), and the corresponding ranking matrix B^{3*n} is illustrated using equation (43).

$$\mathrm{M}^{3*n} = \begin{pmatrix} W_{c,1} & W_{c,2} & \dots & W_{c,n} \\ W_{e,1} & W_{e,2} & \dots & W_{e,n} \\ W_{t,1} & W_{t,2} & \dots & W_{t,n} \end{pmatrix} \tag{42}$$

$$\mathrm{B}^{3*n} = \begin{pmatrix} B_{c,1} & B_{c,2} & \dots & B_{c,n} \\ B_{e,1} & B_{e,2} & \dots & B_{e,n} \\ B_{t,1} & B_{t,2} & \dots & B_{t,n} \end{pmatrix} \tag{43}$$

The L2 norm distance for color, edge and texture cue is calculated using equation (44), (45), and (46) respectively.

$$\mathfrak{Z}_c^s = \left|\left|X_c^s - X^s\right|\right| = \sqrt{(x_c^s - x^s)^2 + (y_c^s - y^s)^2} \tag{44}$$

$$\mathfrak{Z}_e^s = ||X_e^s - X^s|| = \sqrt{(x_e^s - x^s)^2 + (y_e^s - y^s)^2} \tag{45}$$

$$\mathfrak{Z}_t^s = ||X_t^s - X^s|| = \sqrt{(x_t^s - x^s)^2 + (y_t^s - y^s)^2} \tag{46}$$

Using above Euclidian distance, reliability of color, edge and texture cue is updated using equation (47), (48), and (49) respectively.

$$r_c^s = \tfrac{1}{2}(\tanh(-a.\mathfrak{Z}_c^{s-1} + b) + 1) \tag{47}$$

$$r_e^s = \frac{1}{2}(\tanh(-a.\mathfrak{Z}_e^{s-1} + b) + 1) \tag{48}$$

$$r_t^s = \frac{1}{2}(\tanh(-a.\mathfrak{Z}_t^{s-1} + b) + 1) \tag{49}$$

These reliability values at time s are used for discounting individual cue likelihood at time s+1. The discounted masses are used for assigning rank to each fragment. Ranked fragments are further subjected to aggregating function and final weight for each fragment is determined. Target precise location is determined using weighted sum of fragments. The localized target is further considered

ACCEPTED MANUSCRIPT

ACCEPTED MANUSCRIPT

for estimation of its next state in this iterative process. The localization of target along with updation of reliability will continue till the object is present in the scene. The core design of proposed multistage tracker follows in next section.

3. Core Design of Proposed Tracker Algorithm

The proposed tracker is based upon two level localization of targeted object in video sequences. From online video sequences, motion along with visual information is exploited for proposed robust tracking solution. In first stage, rough localization of target is carried out through estimation of optical flow. In the second stage, visual features from multiple fragments are extracted and their likelihoods are fused using proposed adaptive fusion model. Novelty in proposed fusion model is incorporated through use of non-linear kernel (sigmoid function) in order to discriminate most likely fragments from the not-so likely fragments. The rotation and scale factors are catered through random walk model in state representation and use of invariant features.

The proposed tracker is initialized with Target ID=0 and target is detected through background subtraction using Gaussian Mixture Model (GMM) considering three Gaussian distribution (Stauffer & Grimson, 1999). The reference histograms are extracted for RGB, PHOG and LBP features viz. H_{rc} , H_{re} , H_{rt} . Initially, reliability of each cue is assumed equal. On the other hand, if the Target ID is not 0, target initialized for reference models is not performed and Stage I estimation of target state is performed. Under this, rough localization of target is performed by determining optical Flow between the consecutive frame. This rough location of target is further used for generation of N fragments around it and three features are extracted for each fragment. For each fragment, three cues are extracted and corresponding histograms are compared with the reference model histograms. Likelihood scores for three cues are calculated using Bhattacharya Distance using equation (16, 22, and 28) and three weights are assigned to each fragment. Fragment weights are discounted with cues reliability estimated in previous frame before applying to proposed fusion model. The discounted weights for each fragment are subjected to the proposed weighted rank based fusion using non-linear kernel as described in Section 2.2. Finally, weights are assigned to each fragment using equation (37).

The precise localization of target is determined using weighted mean of N fragments centroid using equation (39). The reliability of each cue is updated by estimating Euclidean Distance between precise state estimation and individual cue state estimation. These reliability scores are used for discounting individual fragment masses for next state estimation. In order to cater to partial or full occlusion, number of fragments having final weight less than threshold value is determined. Once this count falls below a threshold value (N_{th}), object ID is set to 0 and the object is re-detected using GMM and reference models are reinitialized. This iteration process continues till the target is present in scene. Once target is completely lost, new target is detected through background subtraction and tracker is restarted.

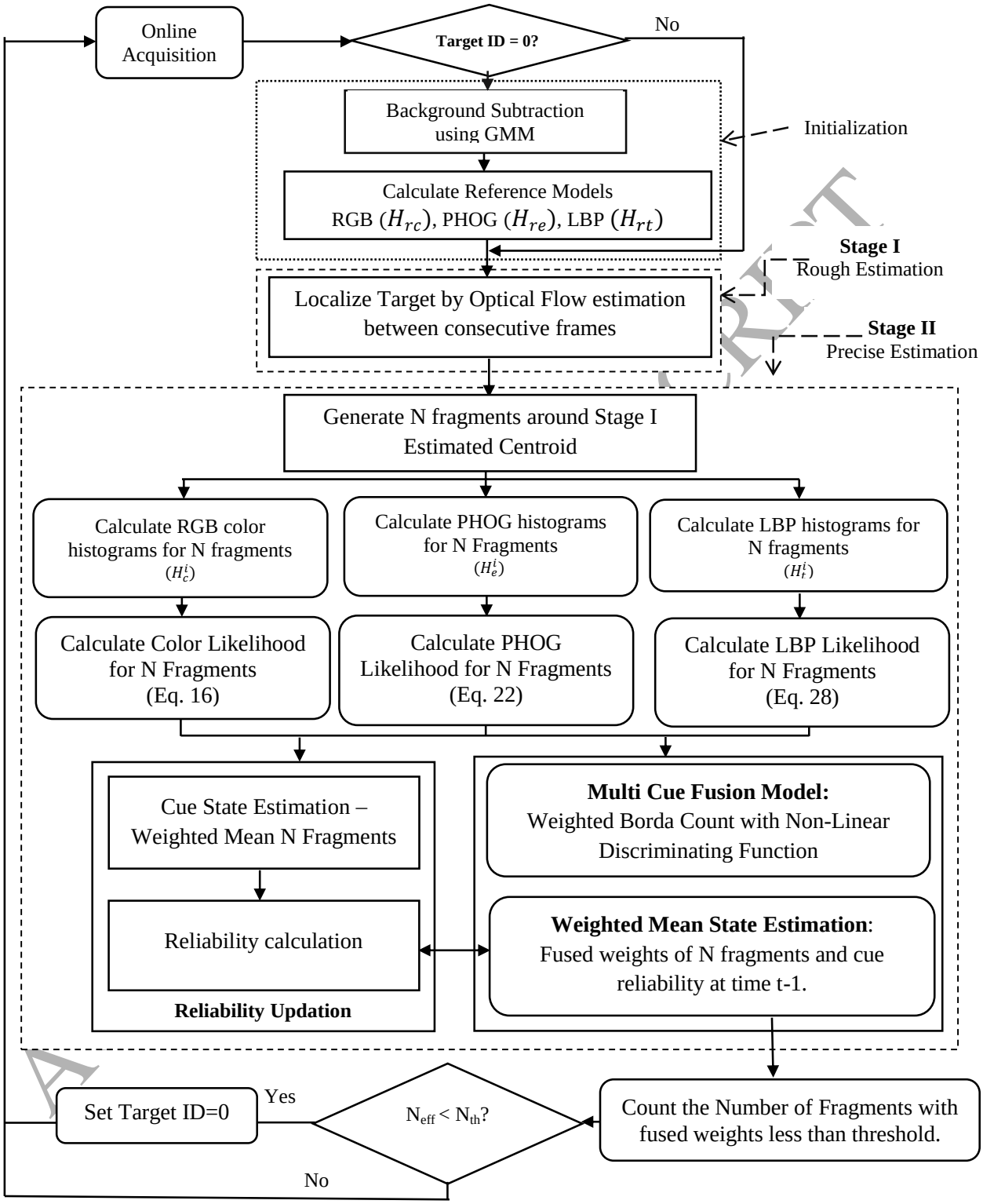


Figure 2: Flow Chart of Proposed Multistage Tracker

The pseudo code for proposed Multi-stage tracker is illustrated as Algorithm 1. The benchmarked video sequences along with our test video sequence are considered for evaluation of proposed tracker under dynamic environment. The detail of experimental validation follows in next section.

Algorithm 1: Proposed Multi-stage Tracker

$[X^s, r_c^s, r_e^s, r_t^s] = MS_Tracter\ [X^{s-1}, r_c^{s-1}, r_e^{s-1}, r_t^{s-1}]$

1. Determine reference histograms viz. H_{rc} (RGB), H_{re} (PHOG), H_{rt} (LBP)
2. *If Target ID=0* Detect Target using GMM
3. Initialize reliability of each cue $[r_c^0 = r_e^0 = r_t^0 = 1/3]$
4. $For\ s = 2 : No_of_frames$
   a. Calculate the Optical Flow vector $\overrightarrow{\mathcal{V}} = (\mathcal{V}_x, \mathcal{V}_y)$between the consecutive frames $s-1$ and s by solving Eq. (8).
   b. Localize target, $[x^s, y^s] = [x^{s-1} + dx, y^{s-1} + dy]$
   c. Generate N fragments around $[x^s, y^s]$as$[(X_i, W_i)_{i=1}^N]$, X_i is the centroid of the i^{th} fragment.
   d. $For\ i = 1{:}N$
      i. Calculate appearance histograms for each fragment, $[H_c^i, H_e^i, H_t^i]$
      ii. Calculate likelihood of fragment as $[\tau_{i,c}, \tau_{i,e}, \tau_{i,t}]$ using Eq.(16, 22, 28)
   e. end
   f. Calculate fragment weights using Eq.(37) as $[(W_i)_{i=1}^N]$, W_i is the weight associated with i^{th} fragment
   g. Calculate individual cue reliability as $r_c^s,\ r_e^s,\ r_t^s$ using Eq.(47,48,49)
   h. Precise Localization of target X^sas weighted mean of all fragment Eq.(39)

   end
5. If $N_{eff} < N_{th}$, Set *Target ID=0, s=1,* go to Step 1.
6. Acquire new frame and set s=s+1, go to Step 4.

---

4. Experimental Validation

Proposed multistage tracker is evaluated both qualitatively and quantitatively on benchmarked video sequences. It is compared using performance metrics with state-of-the-art trackers over length of challenging video sequences. In order to evaluate tracker over extensive dataset captured under different environments, seven videos sequences (S1 – S7) are taken from CVPR2013 tracking benchmark (Wu, Lim, & Yang, 2013). These video sequences are extensively used in different research works and are captured by different authors. The eighth video sequence (S8) titled 'DTU ECE MAIN - 1' is self-generated and captured at DTU campus. Sequences are marked from S1to S8 for further reference in manuscript.

ACCEPTED MANUSCRIPT

The ground truth for S1-S7 is taken from online dataset and that for S8 video sequence it is extracted manually. Video sequences chosen for performance evaluation have both low and high resolution with dynamic tracking challenges. The various tracking challenges for each video sequence are also listed in Table 1. The target subjected for evaluation is marked in Figure 4.

Table 1: Details and Challenges of Video Sequences

Video Sequence	Sequence No.	Frame Resolution	Tracking Challenges
Jogging 1	S1	352 x 288	Occlusion Handling, Deformation in object, Rotation variation
Crossing	S2	360 x 240	Change in Scale, Deformation in object, Rapid Motion, Rotation, Background Confusion
Subway	S3	352 x 288	Occlusion handling, Deformation, Background Confusion
CarScale	S4	640 x 272	Change in Scale, Occlusion Handling, Rapid Motions, Rotation
MountainBike	S5	640 x 360	In-plane rotation and out-plane rotation, background clutter
Human8	S6	320 x 240	Scale change, illumination variation, deformation
Jogging 2	S7	352 x 288	Occlusion Handling, Deformation in object, out of plane rotation
DTU ECE Main - 1	S8	360 x 640	Change in scale, Occlusion Handling, Variation in Illumination, Rotation

The proposed tracker is implemented on MATLAB installed on a PC with Intel® Core™ i5-4210U CPU @1.70GHz 2.40GHz processor having 64-bit platform. The performance of proposed tracker is compared with the following state-of-the-art trackers.

- **FRAG:** fragments based tracking (Adam, Rivlin, & Shimshoni, 2006).
- **IVT:** Incremental learning based tracking (Ross, Lim, Lin, & Yang, 2008).
- **WMIL:** Weighted multiple instances learning (Zhang & Song, 2013).
- **KCF:** Kernelized Correlation Filters (Henriques, Caseiro, Martins, & Batista, 2015).
- **OPTICAL FLOW:** Horn-Schunck based optical flow (Horn & Schunk, 1981).
- **STRUCT:** Structured output tracking (Hare, Saffari & Torr, 2011).
- **CT:** Compressive Tracking (Zhang, Zhang, & Yang, 2012).

Considering implementation of trackers for experimental evaluations, author released source code for FRAG tracker at URL (https://github.com/gnebehay/FragTrack), for IVT at URL (http://www.cs.toronto.edu/~dross/ivt.), for WMIL at URL (https://code.google.com/p/online-weighted-miltracker/), and for KCF at URL (http://www.robots.ox.ac.uk/~joao/circulant/index.html) are used and optical flow tracker based on Horn-Schunck method is implemented on MATLAB. These trackers along with datasets are used for experimental evaluation. The details for various experimental analyses follow in turn.

4.1 Qualitative Analysis

Qualitative performance metric such as handling of partial or full occlusion, illumination change, background clutter, target rotation, scaling and deformation are analyzed for estimation of tracker reliability and robustness. In this section, first, we demonstrate proposed multicue fusion model especially from the aspects of automatic boosting of concordant cues and suppressing of discordant cues for each fragment. As shown in Figure 3, forty appearance models are considered for demonstrating our fusion model in S8 video sequences. The discounted weights of fragments for RGB, PHOG and LBP models are shown along with final fused weight for each fragment. The threshold value of 0.5 is chosen in proposed fusion model. The discounted weight above 0.5 leads to more agreement of detected bounding box with reference bounding box whereas its value less than 0.5 imply that target not localized correctly.

MANUSCRIPT

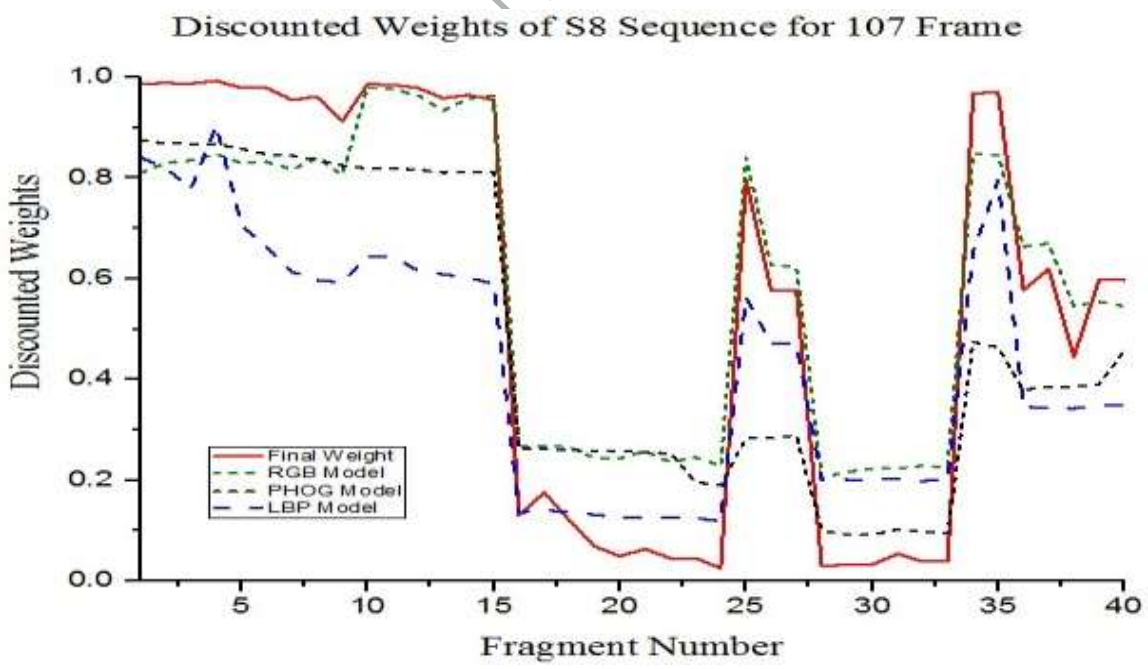


Figure 3: Demonstration of Multicue Fusion of Discounted Weights

ACCEPTED MANUSCRIPT

As shown above, with 0.5 as reference threshold, weights are boosted, suppressed, or resolved for conflicting masses and hence lead to more accurate localization of target in video sequences. Discounted weights of three cues for fragments numbered from 1 to 10 are in concordant with each other and hence these fragments are further boosted towards localization of target state. Due to their placement off the target, fragment numbered from 16 to 24 are in concordant towards non-localization of target state and hence these fragments contribution towards state estimation is further suppressed. Fragment having conflicting weights for different cues are fused adaptively with resolving of conflict among cues. For example, fragments from 25 to 27 have conflict among cues. The conflicting mass is distributed among cues and final fragment contribution towards localization of target is adjusted accordingly. In sum, at fragment level, proposed multicue fusion model automatically boosts concordant cues, suppresses discordant cues and resolves conflict among cues leading to improvement in tracking. The details of video sequences challenges are tabulated in Table 1. For qualitative performance evaluation, we have evaluated our proposed algorithm on CVPR2013 tracking benchmark (Wu, Lim, & Yang, 2013) and our self-captured video sequence. For visual analysis, we have plotted bounding box, Figure 4, on eight video sequences as intermediate tracking results for proposed tracker along with seven state-of-the-art tracking algorithms. Different qualitative attributes such as handling of partial or full occlusion, illumination change, background clutter, target rotation, scaling and deformation are analyzed for convincible evaluation of proposed tracking algorithm.

Illumination and Scale change: The proposed tracker is evaluated for illumination and scale change on different benchmarked video sequences. In reference based tracking algorithm where target estimation is compared with reference appearance model, illumination and scale change drastically reduces tracking accuracy. As shown in Figure 4, targeted object encountered illumination change in sequences *Human8, Subway, DTU ECE Main-1* and *Crossing.* However, due to illumination invariant PHOG feature and rough estimation using optical flow, our tracker faithfully overcome illumination variation. Massive scale change for targeted car is involved in *CarScale* sequence from frame 90 to 190. In *Jogging 1* and *Jogging 2* sequence, targeted object get slight change in scale from frame 84 to 250. In *DTU ECE Main-1* sequence, the targeted object changes in scale from frame 97 to 323. *Human8* and *Crossing* sequences have similar change in targeted object scale. Trackers considering fixed scales search algorithm degrades their performance on large variation of scale. However, our proposed tracker adapts to scale variation of targeted object. Scale adaptation is achieved due to invariant RGB model and incorporation of random walk model, equation (12).

Occlusion and Background Clutter: Partial and full occlusion of targeted object affects appearance model and hence impairs tracking accuracy. In *Jogging 1*, targeted object encounters partial occlusion in frames numbered from 65 to 70 and full occlusion in frames from 71 to 76. Similarly, in *Jogging 2*, full occlusion occurs in frames from 52 to 55 and partial occlusion in frames from 56 to 60. Background clutter occurs when targeted object occluded with similar color objects or with objects with similar texture.

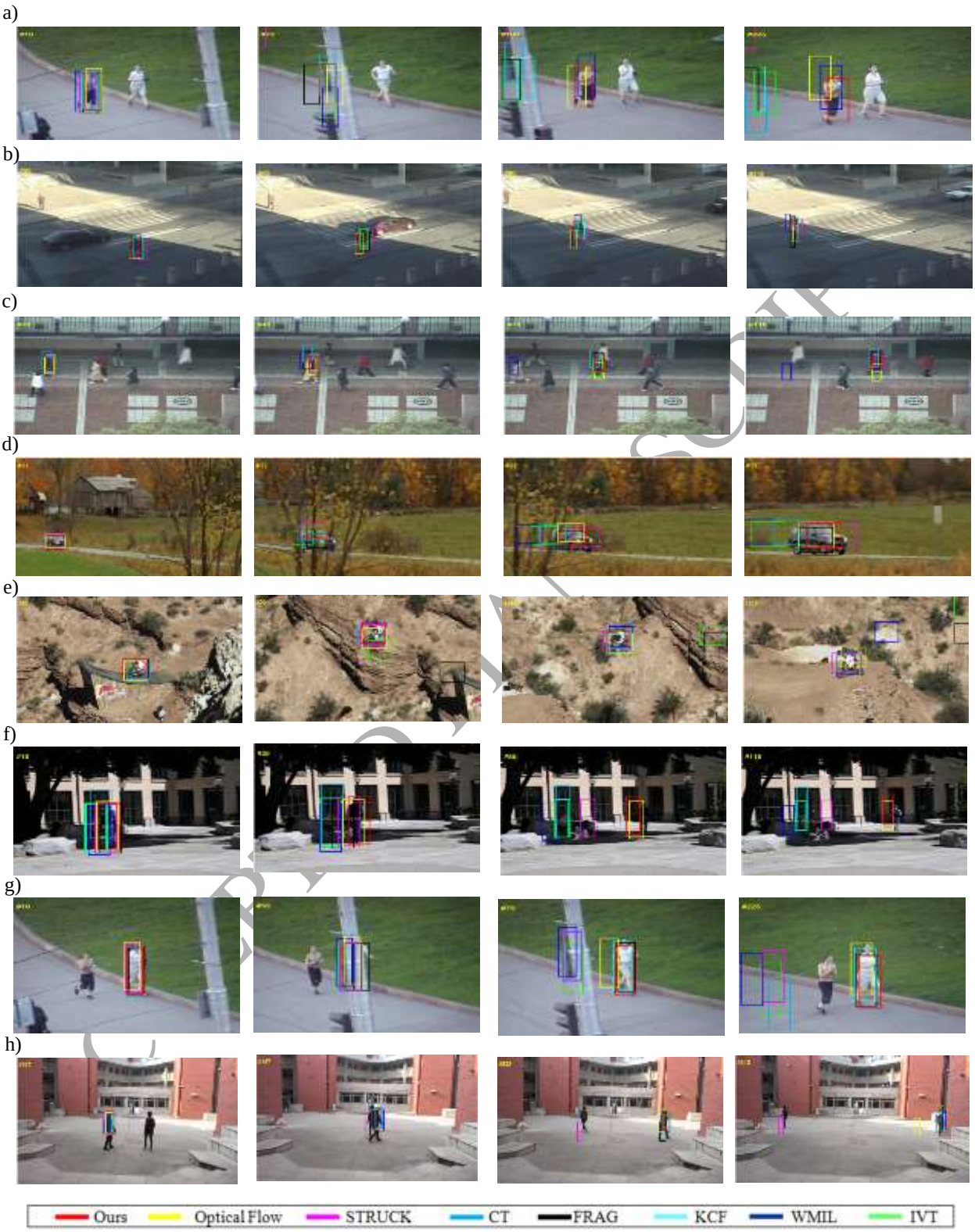


Figure 4: Sample tracking results on eight video sequences a) *Jogging 1* b) *Crossing* c) *Subway* d) *CarScale* e) *MountainBike* f) *Human8* g) *Jogging 2* h) *DTU ECE Main-1* for seven state-of-the-art tracking algorithms (Optical Flow, STRUCK, CT, FRAG, KCF, WMIL, IVT) and Our method

ACCEPTED MANUSCRIPT

In *DTU ECE Main-1* sequence, targeted object occluded with similar color object in frames from 141 to 149 and partial occlusion in frames from 317 to 323. Optical flow (Horn & Schunk, 1981) tracker less affected by occlusion and background clutter and same is depicted in Figure 4. Due to its inherent assumption on observation noise, IVT (Ross, Lim, Lin, & Yang, 2008) tracker deviates less under partial occlusion. In proposed tracker, partial occlusion and clutter are handled efficiently due to automatic boosting of concordant fragments and suppression of discordant fragments. In addition, under heavy occlusion, target is reinitialized and reference appearance models are determined.

Rotation and Deformation: Object rotation along with deformation leads to degradation of tracker accuracy. In *MountainBike* sequence, targeted object encounters rotation in frames from 42 to 118 and further suffer from deformation in frames from 119 to 220. As shown in Figure 4, trackers as FRAG (Adam, Rivlin, & Shimshoni, 2006), IVT (Ross, Lim, Lin, & Yang, 2008) and WMIL (Zhang & Song, 2013) could not correctly localized target during its rotation and deformation. However, due to use of rotation invariant LBP feature and random walk model, equation (12), during fragment initialization, our tracker can quickly adapt to targeted object rotation and deformation. In addition, under heavy deformation ($N_{eff} < N_{th}$), proposed tracker is online updated and reference appearance model is extracted. The qualitative results are further validated with exact estimation of various quantitative metrics. The details of various quantitative metrics are discussed in next section.

4.2 Quantitative Analysis

Quantitative performance metrics such as F-measure, Centre Location Error (CLE) and precision curves are determined for evaluation of tracker robustness and reliability. F-measure, equation (52), is estimated from precision and recall (Lazarevic-McManus, Renno, Makris, & Jones, 2008). Precision, equation (50), is defined as a measure of overlap of bounding box of tracker (B_{TR}) with that of ground truth (B_{GT}) with reference to area of tracker estimated bounding box (B_{TR}). Recall, equation (51), is defined as a measure of overlap of bounding box of tracker (B_{TR}) with that of ground truth (B_{GT}) with reference to area of ground truth bonding box B_{GT}.

$$\mathrm{P} = \frac{B_{TR} \cap B_{GT}}{B_{TR}} \tag{50}$$

$$\mathrm{R} = \frac{B_{TR} \cap B_{GT}}{B_{GT}} \tag{51}$$

$$\mathrm{F} = \frac{2 * \mathrm{P} * \mathrm{R}}{\mathrm{P} + \mathrm{R}} \tag{52}$$

As estimation of precision of state, centre location error (CLE) is determined using equation (53) where, X_{GT} and Y_{GT} are x- and y-coordinates of ground truth state, and X_{TR} and Y_{TR} are x- and y-coordinates of state estimated by tracker.

$$CLE = \sqrt{(X_{GT} - X_{TR})^2 + (Y_{GT} - Y_{TR})^2} \tag{53}$$

Centre Location Error is determined for each estimated state and mean of centre location errors is calculated. In addition, as quantitative measure, we have plotted precision curves (Babenko, Yang, & Belongie, 2011; Wu, Lim, & Yang, 2013). In these plots, precision is estimated as percentage of correctly tracked frames for various distances from ground truth. In precision curves targeted object is regarded as correctly tracked if its centre location error is below a certain threshold distance. Tracker is considered as good if it achieves high precision at low threshold distance from ground truth.

Centre location error for seven state-of-the-art tracker along with proposed tracker is plotted for eight video sequences in Figure 5. In addition, corresponding F-measure are plotted in Figure 6. For experiments, we initialized trackers with default coordinates as provided in benchmarked video sequences. Plots representing centre location error and F-measure are obtained with trackers initialization at frame number as 1 for *Jogging 1*, 1 for *Jogging 2*, 90 for *CarScale*, 10 for *Crossing*, 1 for *Human8*, 1 for *MountainBike*, 1 for *Subway* and 97 for *DTU ECE Main-1*.

In *Jogging 1* sequence, targeted object encounter partial occlusion at frame number 65 and full occlusion at frame 71. Due to this, centre location error increased at frame number 65 but subsequently target is reinitialized leading to decrease in error. Similarly, in *Jogging 2* sequence targeted object encounter full occlusion at frame number 52 leading to increase in error and decrease in F-measure. In *MountainBike* sequence, targeted object encounter rotation in frames from 42 to 118. For this sequence, proposed tracker can handle target rotation due to use of rotation invariant feature and also due to random walk model for initialized fragments. Small value of centre location error for these frames reveal that proposed tracker can handle target rotation more efficiently than most of other trackers.

In *CarScale* sequence, target scaling is overcome better in proposed tracker due to random walk model for fragment scaling. For this sequence, proposed targeted error is lower than other evaluated trackers. FRAG (Adam, Rivlin, & Shimshoni, 2006) tracker could not handle target scaling due to its inherent design limitation and same is reflected in centre location error plot for *CarScale* sequence. The targeted object is redetected in *DTU ECE Main-1* sequence due to its occlusion with background clutters and results of centre location error demonstrate this adaptation. The adaptation of proposed tracker to illumination change and target scaling is also demonstrated in centre location error and F-measure plots of *Human, Subway* and *Crossing* sequence. For these sequences, low value of centre location error for proposed tracker as compared to other evaluated tracker reveal that proposed tracker can better handle illumination change and scaling.

ACCEPTED MANUSCRIPT

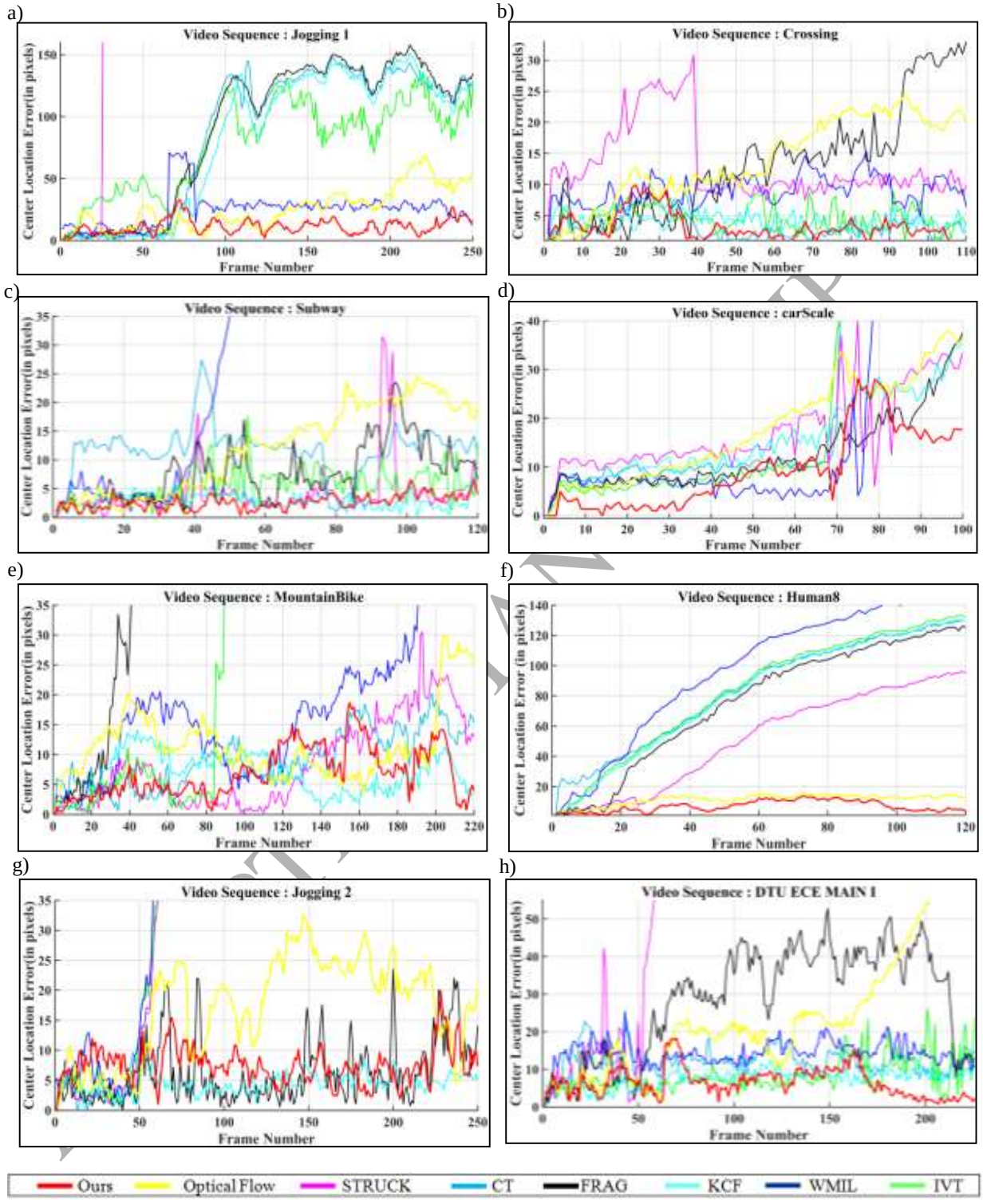


Figure 5: Plots of Centre Location Error (in pixels) as displacement of target centre from ground truth for eight video sequences a) *Jogging 1* b) *Crossing* c) *Subway* d) *CarScale* e) *MountainBike* f) *Human8* g) *Jogging 2* h) *DTU ECE Main-1* for seven state-of-the-art tracking algorithms (Optical Flow, STRUCK, CT, FRAG, KCF, WMIL, IVT) and Our method

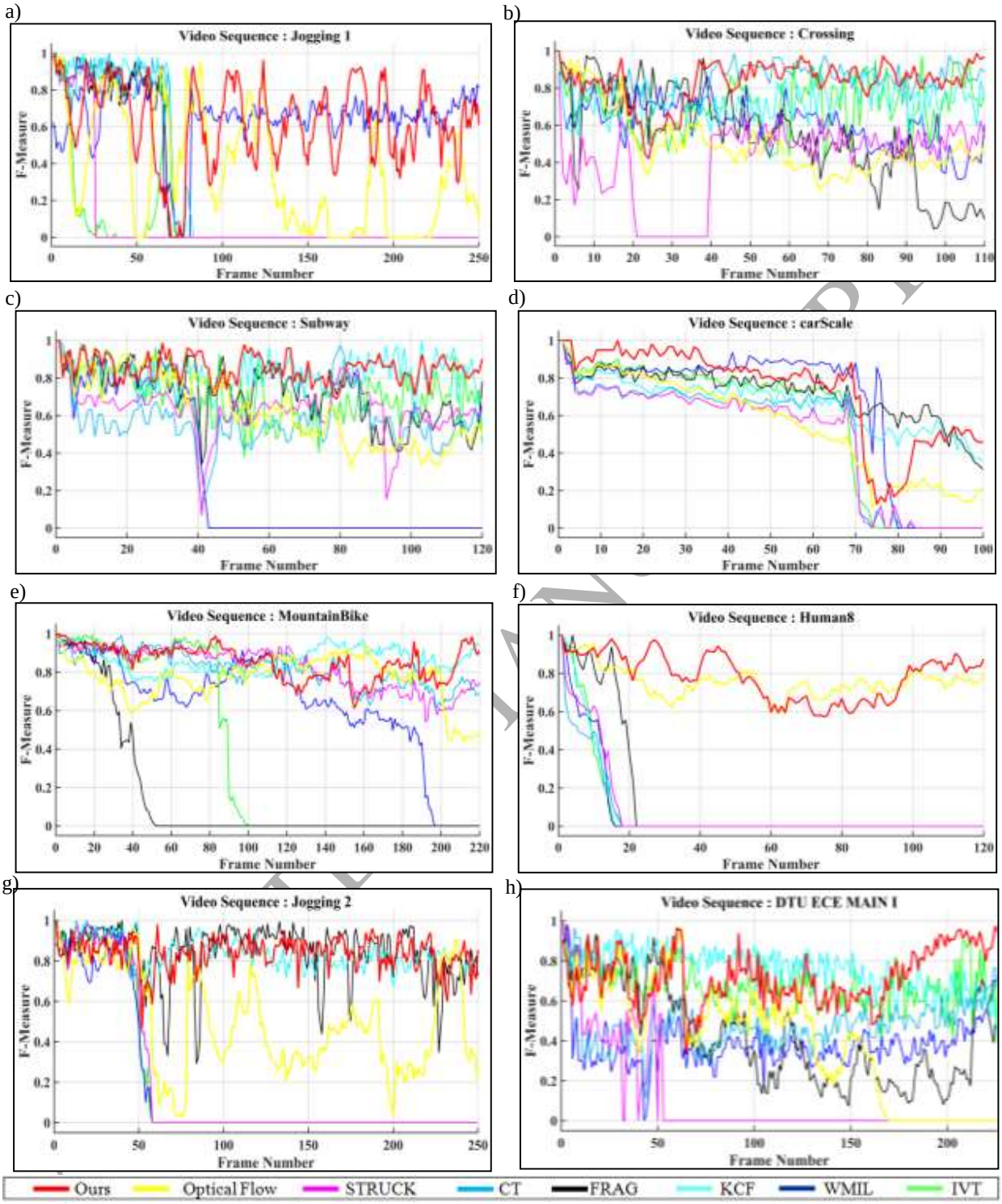


Figure 6: Plots of F-Measure for eight video sequences a) *Jogging 1* b) *Crossing* c) *Subway* d) *CarScale* e) *MountainBike* f) *Human8* g) *Jogging 2* h) *DTU ECE Main-1* for seven state-of-the-art tracking algorithms (Optical Flow, STRUCK, CT, FRAG, KCF, WMIL, IVT) and Our method

In order to gauge more realistic improvement in tracking, mean value of centre location error for eight video sequences is tabulated in Table 2 for eight trackers. Also, mean value of F-measure for eight video sequences is tabulated in Table 3 for eight trackers. In these tables best value is represented by red color and second best is indicated by blue color. Tracker with minimum value of mean centre location error is considered as more precise localizer of targeted object. Also, F-measure close to 1 is considered as best approximation of targeted area. Analysis of tabulated results revealed that our tracker mostly performed better than other evaluated trackers. While considering F-measure as performance matric, in *Jogging 2* sequence, FRAG (Adam, Rivlin, & Shimshoni, 2006) performed best due to little variation in cue. WMIL (Zhang & Song, 2013) performed better in *Jogging 1* sequence and also KCF (Henriques, Caseiro, Martins, & Batista, 2015) performance is better in *MountainBike* sequence. On the other hand, considering centre location error, performance of our tracker is best except for *MountainBike* and *Jogging 2* sequence where KCF (Henriques, Caseiro, Martins, & Batista, 2015) performance is slightly better than our tracker.

Table 2: Mean Centre Location Error (in pixels) for 8 video sequences for 8 trackers. In each row best result is represented by red color and second best by blue color.

Video Sequence	**IVT**	**WMIL**	**KCF**	**FRAG**	**CT**	**STRUCK**	**Optical Flow**	**Ours**
Jogging 1	78.8659	24.9644	81.2377	90.4139	87.4434	183.1063	25.1464	11.3247
Crossing	4.5979	9.0216	4.1730	13.2053	3.2184	13.0888	13.8536	**3.1869**
Subway	5.4390	77.8254	2.9998	7.6033	11.7280	4.2098	12.0001	2.6107
CarScale	35.4594	37.8899	15.7492	12.6884	28.0445	17.2112	17.8404	9.4363
MountainBike	149.9673	28.7800	6.8345	209.7428	9.1927	8.3928	11.5167	6.9097
Human8	83.8614	99.1109	81.7369	76.1450	84.0227	51.3159	13.0644	6.8880
Jogging 2	120.5744	129.4607	4.4591	6.2090	112.2292	129.1537	17.4154	7.4753
DTU ECE Main-1	8.1073	14.2915	7.5592	28.4045	12.1149	206.0251	24.6137	6.4986

Table 3: Mean F-measure for 8 video sequences for 8 trackers. In each row best result is represented by red color and second best by blue color.

Video Sequence	**IVT**	**WMIL**	**KCF**	**FRAG**	**CT**	**STRUCK**	**Optical Flow**	**Ours**
Jogging 1	0.0700	0.6446	0.2604	0.2306	0.2458	0.0878	0.3561	0.6254
Crossing	0.7009	0.6055	0.7214	0.5435	0.8452	0.4062	0.5012	0.8328
Subway	0.7163	0.2695	0.8263	0.7195	0.5679	0.6325	0.6299	0.8522
CarScale	0.5537	0.6482	0.6640	0.7179	0.5004	0.4775	0.5501	0.7281
MountainBike	0.3712	0.6292	0.8657	0.1514	0.8184	0.8236	0.7698	0.8571
Human8	0.0724	0.0704	0.0750	0.1364	0.0600	0.0767	0.7563	0.7865
Jogging 2	0.1840	0.1691	0.8364	0.8449	0.1890	0.1879	0.5049	0.8383
DTU ECE Main-1	0.6780	0.3799	0.7004	0.6036	0.4827	0.1118	0.4054	0.7196

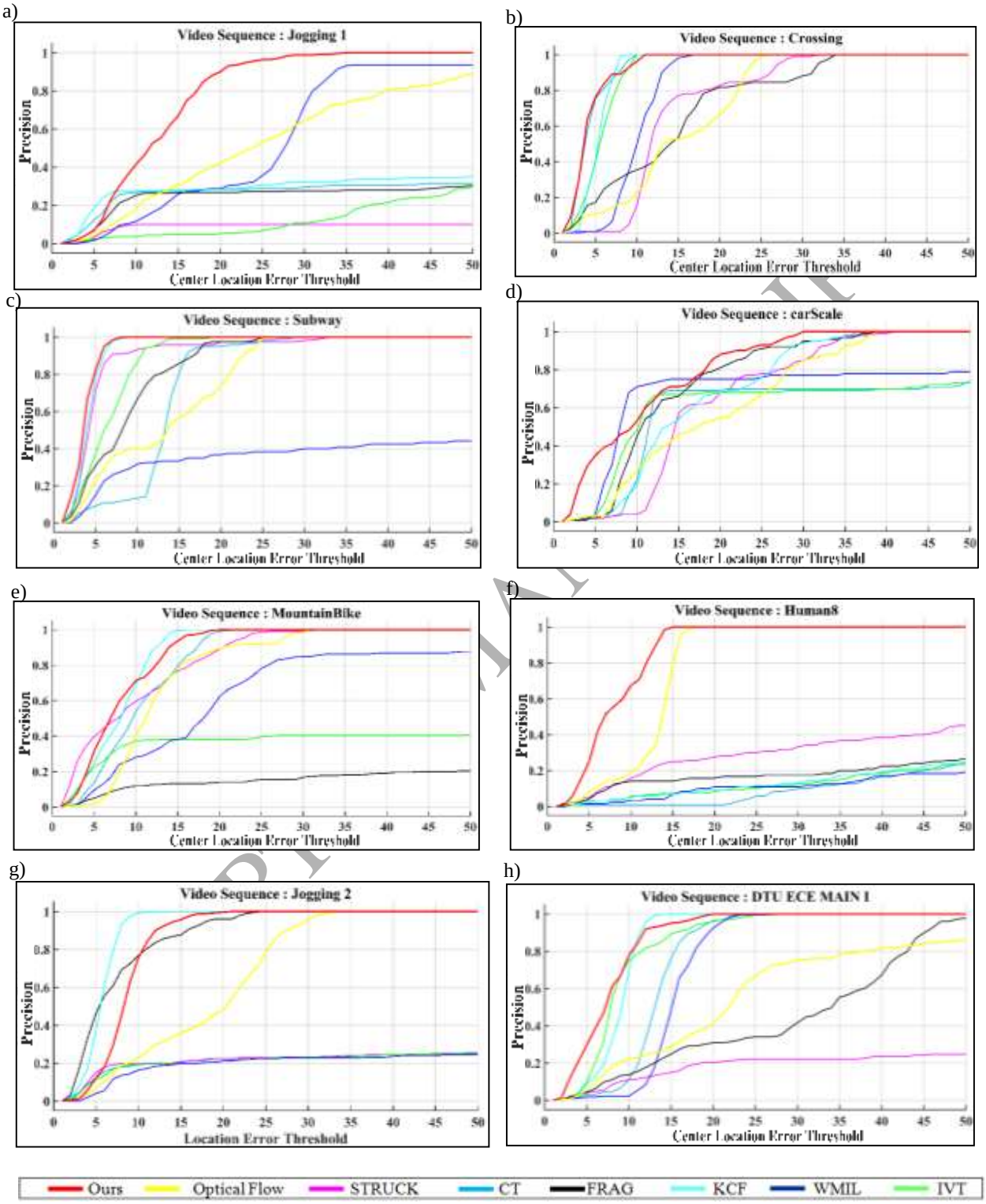


Figure 7: Plots of Precision for eight video sequences a) *Jogging 1* b) *Crossing* c) *Subway* d) *CarScale* e) *MountainBike* f) *Human8* g) *Jogging 2* h) *DTU ECE Main-1* for seven state-of-the-art tracking algorithms (Optical Flow, STRUCK, CT, FRAG, KCF, WMIL, IVT) and Our method

Additionally, we demonstrate robustness and reliability of our tracker through precision curves as shown in Figure 7 for eight video sequences. As precision curves do not require any parameter other than ground truth threshold, they are easy to interpret and act as unambiguous metric for performance evaluation. Analysis of these curves revealed that our proposed tracker achieved high precision with low center location error threshold.

Overall Performance: Proposed tracker is evaluated over eight color video sequences and results are compared with seven trackers namely Optical Flow, STRUCK, CT, FRAG, KCF, WMIL, and IVT. Competitive results are achieved for proposed tracker in terms of mean centre location error and F-measure. Mean centre location error (in pixels) of 6.791 and F-measure of 0.78 is achieved after evaluation of proposed tracking framework on the eight video sequences. The results show precision greater than 0.9 for a threshold error of 15 pixels, which is significant improvement over compared state-of-the-art trackers. As the proposed tracker requires fewer numbers of fragments, average time to process a single frame is 0.0384 sec.

Our tracker tackles the limitations of existing state-of-the-art trackers in various ways. STRUCK tracker (Hare, Saffari & Torr, 2011) effectively handles background clutter and low-resolution sequences, but it is computationally expensive. Its low performance is attributed mainly to its complex learning methods and fixed Haar-like feature. The chosen cues in our tracker are not only dynamic, but also complementary in nature. The optical flow cue in first stage inculcates motion information, which is further assisted by discriminative visual cues in the second stage. In addition, extraction of cues in our method doesn't require any heavy computations and thus can be employed for real time solutions. Optical flow (Horn & Schunk, 1981) based tracking can extract motion cue with high accuracy but fail to incorporate object shape information. However, in proposed tracker we locate target precisely in second stage by its spatial distribution using both PHOG and LBP cues. Furthermore, as FRAG tracker (Adam, Rivlin, & Shimshoni, 2006) does not imbibe discriminative local information, its performance gets hampered in case of object scaling. WMIL (Zhang & Song, 2013) tracker also is unable to overcome target rotation and deformation as it uses random Haar like features. However, in proposed tracking framework, limitations of scaling, rotation, and deformation are tackled by adoption of random walk model and uniform patterns of LBP that are invariant to rotation. In case of large deformation or full occlusion, the online learning of proposed tracker comes into play. CT (Zhang, Zhang, & Yang, 2012) tracker uses an easy to implement and low computation intensive framework. However, it is unable to track object in case of background clutter due to similarity of cues extracted. In case of proposed tracker, discriminative nature of chosen cues is further enhanced because of our fusion model. The non-linear discriminative function introduces a big parity between fragments with high and low likelihood. As mentioned before, rank level fusion is scale invariant and thereby discriminates the fragments effectively. IVT tracker (Ross, Lim, Lin, & Yang, 2008) implements robust particle filter with extended appearance model for target localization. However, large number of appearance model parameters along with initial tracker alignment limits its performance. Although, it was demonstrated that incorporation of multiple modularity in particle filter framework enhanced

ACCEPTED MANUSCRIPT

tracking accuracy, it is computationally expensive due to requirement of large number of particles for high accuracy (Walia & Kapoor, 2016). However, in proposed tracker, due to rough estimation in the first stage, fewer number of appearance models are required and hence reduce computational complexity.

In sum, our tracking framework overcomes various limitations of the state of the art trackers. Proposed multistage tracker enhanced performance is attributed mainly to automatic mechanism of fragment boosting and suppression along with extraction of complementary cues for each fragment. Hence, proposed tracker precisely localize target in all video sequences with overall minimum deviation from ground truth data. However, approximation from optical flow in first stage assumes the brightness to be constant in subsequent frames. Further studies are needed to overcome this limitation.

5. Conclusion and Future Work

In this manuscript, we have proposed a novel multi-stage tracking framework for object tracking under dynamic environment. In each frame, two-stage coarse to fine estimation of target state is performed for achieving high precision. Optical flow based estimation achieved quick approximation of target state. Precise localization of target is achieved through evaluation of multiple fragments initialized around first approximation. For each fragment, RGB, PHOG and LBP histograms are determined and then likelihoods are determined through their respective comparison with reference histograms. For each frame, cues reliability are updated and used to discount likelihoods. The discounted masses are used for assigning rank to each fragment. Ranked fragments are further subjected to aggregating function and final weight for each fragment is determined. Adaption for tracker is quick due to incorporation of context sensitive reliability in proposed fusion model. In addition, automatic boosting of concordant cue fragments and suppression of discordant cue fragments helps in enhancement of overall performance under dynamic environment. Target rotation and scaling is catered by incorporation of random walk model for each fragment and by using rotation invariant feature. Competitive results are obtained for proposed tracker after evaluation over eight benchmarked color video sequences. As an average of the outcomes, we achieved mean center location error (in pixels) of 6.791 and F-measure of 0.78. Experimental results revealed that proposed tracker not only outperforms the mentioned state-of-the-art trackers but can also handle various tracking challenges more reliably and robustly. In future, we will look forward to integrate various types of cues on varying stages. Extending proposed fusion model for multimodal data with incorporation of importance of modality is another dimension to investigate. Larger pose variation along with large-scale non-rigid deformation needs to be studied for robust tracking solutions.

6. References

Adam, A., Rivlin, E., &Shimshoni, I. (2006). Robust Fragments based tracking using the Integral Histogram. In CVPR, 7-22 June 2006

ACCEPTED MANUSCRIPT

.

Babenko, B., Yang, M., & Belongie, S. (2011) . Robust object tracking with online multiple instance learning, IEEE Transactions on Pattern Analysis and Machine Intelligence, Vol 33, issue 8, pp 1619-1632.

Bhagavatula, P. S., Claudianos, C., Ibbotson,M.R., Srinivasan, M.V. (2011). Optic Flow Cues Guide Flight in Birds. Current Biology, Volume 21, Issue 21,Pages 1794-1799.

Bhattacharyya, A. (1943). On a measure of divergence between two statistical populations defined by their probability distributions. Bulletin of the Calcutta Mathematical Society, 35, 99–110.

Borda, J.C. de(1995). Memoire sur les elections au scrutin. Histoire de l'Academie Royale des Sciences, Paris. Available, in: I. McLean, A. Urken (Eds.), Classics of Social Choice, University of Michigan Press, Ann Arbor.

Bosch, A., Zisserman, A., & Munoz, X. (2007). Representing shape with a spatial pyramid kernel. In Proceedings of the 6th ACM international conference on Image and video retrieval (CIVR '07). ACM, New York, NY, USA, 401-408.

Brasnett, P., Mihaylova, L., Bull, D., Canagarajah, N. (2007). Sequential Monte Carlo tracking by fusing multiple cues in video sequences. Image Vision Computer, 25(8), 1217–1227.

Cannons, K., Gryn, J., Wildes,R.(2010). Visual tracking using a pixel wise spatio-temporal oriented energy representation. In : Proceedings of the11th European Conference on Computer Vision, pp. 511–524.

Conaire, C.O., Connor, N.E. O, Smeaton, A.(2008). Thermo-visual feature fusion for object tracking using multiple Spatiogram trackers. Machine Vision Applications, 19, 483‑494.

Dou, J., Li, J.(2014). Robust visual tracking based on interactive multiple model particle filter by integrating multiple cues. Neurocomputing, 135, 118-129.

Erdem, E., Dubuisson,S., Bloch, I. (2012). Visual Tracking by fusing multiple cues with context-sensitive reliabilities. Pattern recognition, 45, 1948-1959.

Hare S., Saffari A., and Torr. P. H. S. (2011). Struck: Structured Output Tracking with Kernels. In ICCV, 6-13 Nov. 2011.

Henriques, J. A. F., Caseiro, R., Martins, P., Batista J. (2015). High speed tracking with Kernelized correlation filters. IEEE Transaction of Pattern Analysis Machine Intelligent, Vol 37, 583-596.

Horn, B.K.P., Schunk, B.G.(1981). Determining optical flow. Artificial Intelligence 17, 185-203.

Kane, S.A., Zamani, M.(2014). Falcons pursue prey using visual motion cues: new perspectives from animal-borne cameras. *J. Exp. Biol.* 217, 225–234.

Kılıç, V., Barnard, M., Wang, W., Kittler, J.(2015). Audio Assisted Robust Visual Tracking with Adaptive Particle Filtering. IEEE Transactions on Multimedia, 17(2),186-200.

Lazarevic-McManus, N., Renno, J. R., Makris, D., Jones, G. A.(2008). An object based Comparative methodology for motion detection based on the F-measure. Computer Vision and Image Understanding, 111, 74‑85.

Liu, H., Yu, Z., Zha, H., Zou, Y., Zhang, Y.(2009). Robust human tracking based on multi-cue integration and mean shift. Pattern Recognition Letters , pp 827-837 , Vol 30.

Maggio, E., Cavallaro, A.(2005). Multi-part target representation for color tracking. In Proc. IEEE Int. Conf. Image Process., Genoa, Italy, vol. 1, pp. 729–732.

Murphy, R.R.(1996). Biological and cognitive foundations of intelligent sensor fusion. IEEE Trans System Man Cybernetic A System Hum, 26(1), 42–51.

Nickel, K., Stiefelhagen, R.(2008). Dynamic Integration of generalized cues for person tracking, ECCV 2008, Part IV, LNCS 5305, pp 514-526.

Ojala, T., Pietikäinen, M., Mäenpää, T. (2002). Multi-resolution gray-scale and rotation invariant texture classification with local binary patterns. IEEE Trans. Pattern Anal. Mach. Intell, 24(7), 971–987.

Perez, P., Vermaak, J., Blake, A. (2004). Data fusion for visual tracking with particles. Proceeding of IEEE 92(3), 495–513.

Ross, D., Lim, J., Lin, R.S., Yang, M.H.(2008). Incremental Learning for Robust Visual Tracking. IJCV, 77(1), 125–141.

Smeulders, A. W. M., Chu, D. M., Cucchiara, R., Calderara, S., Dehghan, A., Shah, M. (2014). Visual Tracking: An Experimental Survey. In IEEE Transactions on Pattern Analysis and Machine Intelligence, vol. 36, no. 7, pp. 1442-1468.

Stauffer, C., Grimson, W. E. L. (1999). Adaptive background mixture models for real-time tracking. In Computer vision and pattern recognition conference, Fort Collins, CO. , pp. 246‑252.

Thomaidis, G., Tsgas, M., Lytrivis, P., Karaseitanidis, G., Amditis, A. (2013). Multiple hypothesis tracking for data association in vehicular networks. Information fusion, 14, 374-383.

Triesch, J., von der Malsburg, C.(2001). Democratic Integration: Self-Organized Integration of Adaptive Cues. Neural Computation 13, 2049–2074.

Walia, G.S., Kapoor, R. (2016). Recent Advances on multicue object tracking: a survey", Artificial Intelligence Review, Springer, vol 46, issue 1, pp 1-39.

Walia, G.S, Kapoor, R.(2016). Robust object tracking based upon adaptive multi-cue integration for video surveillance, Multimedia Tools and applications, vol 75, issue 23, pp 15821–15847.

Wang, J.T., Chen, D.B., Chen, H.Y., Yang, J. Y. (2012). On pedestrian detection and tracking in infrared videos. Pattern Recognition Letters 33(6), 775–785.

Wang, Q., Fang, J., Yuan, Y. (2014). Multi-cue based tracking. Neurocomputing, 131, 227-236.

Wu, Y., Lim, J. , Yang, M. H. (2013). Online object tracking: A benchmark. In CVPR, pp. 2411–2418, available at URL http://cvlab.hanyang.ac.kr/tracker_benchmark/datasets.html.

Yang, B., Nevatia, R. (2014). Multi-target tracking by online learning a CRF model of appearance and motion patterns. Int. J.Comput. Vis., vol. 107, no. 2, pp. 203-217.

Yilmaz, A., Javed, O., Shah, M. (2006). Object tracking: A survey. ACM Computer Survey. 38, 4, Article 13, 45 pages.

Yin, M., Zhang, J., Sun, H., Gu, W. (2011). Multi-cue based camshaft guided particle filter tracking. Expert System Application, 38(5), 6313–6318.

Zhang, K., Song, H. (2013). Real-time visual tracking via online weighted multiple instance learning. Pattern Recognition, 46, 397-411.

Zhang, K., Zhang, L., Yang, M.H. (2012). Real time Compressive Tracking. In ECCV, Italy.

Available online at www.ijapie.org

International Journal of Advanced
Production and Industrial Engineering

IJAPIE-SI-IDCM 605 (2017) 20–23

Special Issue on

INNOVATIVE DESIGN
&
COMPUTATIONAL
MODELLING

A Review on Design and Analysis of the propeller used in UAV

Yamika Patel[1*] , Anant Gaurav[2], Krovvidi Srinivas[3], Yamal Singh[4]
(Department of Mechanical Engineering, Delhi Technological University, New Delhi-110042, India.)
Email: yamika.patel013@gmail.com

Abstract : UAV (unmanned aerial vehicle) known as the quadrotor, has more dynamic stability than the helicopters. It is an aerial vehicle which is a remote controlled and does not require the pilot. They are predominantly used in different areas like civilian purposes such as agriculture, logistics, military exercises, fire sensing etc. Propeller is an integrated propulsion device of UAV, generates thrust for vertical take off and landing of the vehicle. Finite element analysis and solid works have been used to estimate the dynamical properties of the propeller.. The concept of propeller having a variable speed is introduced and the techniques of propeller selection is discussed. The process of analysing drag lift and thrust force over propeller through computational fluid dynamics is very complex and intricate. Different CFD methods are used to simulate the full 3-D viscous and turbulent flow for various propeller geometry. This force is important in selecting the motor to be used in the UAV model. Effect of thrust force along with pressure, velocity, and coefficient of viscosity on the surface of propeller can be analysed by CFD and these parameter helps to optimize the geometry, material selection and practicality of using the propeller.

Keywords: Aerofoil Structure, Lift-Drag force, computational fluid dynamics, solid works

INTRODUCTION

At the present time the development of small UAV is under the interest of many researchers and want to discover the application. There is currently a variety of projects and research topics rising in this field. Research has shown that the most versatile and mechanically easy to construct UAV which is a quadrotor helicopter.

Quadrotor aerial robot is an automatic system which is an unmanned VTOL (vertical take-off and landing) helicopter. Quadrotors can be controlled by varying the speed of the four rotors and there is no need of any mechanical linkages to vary the rotor blade pitch angles as compare to a conventional helicopter.

Propeller is a machine element which transmit power by converting its rotation into thrust force. It has a profile of aerofoil shape. This profile utilises Bernoulli's principle to leviate the aerial vehicle. As the fluid flows over the blade, a pressure difference in formed between the rear and front side of the blade. This causes a net force to develop in the direction opposite to the gravity.

The function of the propeller is to change the mechanical energy from the motor (in the electric propulsion system, the chemical energy stored inside the battery) into thrust. Therefore the propeller directly effects the aircraft's performance and drives the design of the propulsion system. Ideally the propeller will be designed such that the required thrust is always produced while being driven by the motor and battery when both are operating at their peak efficiencies, due to the nature of fixed-pitch propellers this is not always possible.

Principle of design of aerofoil:

1.1 Classical Momentum Theory:
Propellers have been used since the earliest attempts at flight to drive powered aircraft. Their operation can be explained by the classical momentum theory
Classical momentum theory assumes that thrust is produced due to a difference in the static pressure across an infinitely thin actuator disc. It is further assumed that

- The velocity and pressure over the disc are constant and uniform;
- The air flows straight through the disc without rotation;
- The flow through the propeller is constrained to a well-defined stream tube;
- The flow is incompressible

1.2 Blade element momentumTheory:
The BEMT was first introduced by Gustafson and Gessow in 1946 and it is a hybrid theory for hovering rotors that combines the basic principles from the Momentum Theory and from the Blade Element Theory (BET), in an attempt to estimate the inflow distribution along the blade.

In this theory the following assumptions are made,

1) Blade assume as actuator disc.

2) Conservation of mass, momentum and energy is applied.

3) Conservation laws are applied to a annulus.

The coefficient of lift force and coefficient of drag force generated over the surface of the propeller blades are calculated and utilised to calculate thrust to power ratio.

A quadrotor is an aircraft heavier than air, capable of vertical take-off and landing (VTOL), which is propelled by four rotors, positioned in the same plane ,parallel to the ground. In contrast with helicopters, a quadrotor make use of fixed-pitch blades in its rotors and its motion through the air is achieved by varying the relative speed of each propeller as is shown in fig 1. In a quadrotor, rotors positioned at opposite ends rotates in the same direction, rotors one and three rotates in clockwise direction whereas rotors two and four rotates in a anti-clockwise direction. This kind of motions in the quadrotor is necessary so that the torque produced by each couple is cancelled by the other, making the control of a quadrotor symmetric.

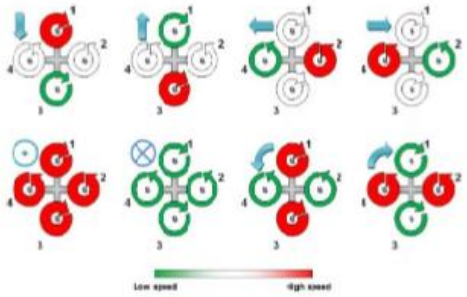


Fig 1: Possible motion of regular quadrotor

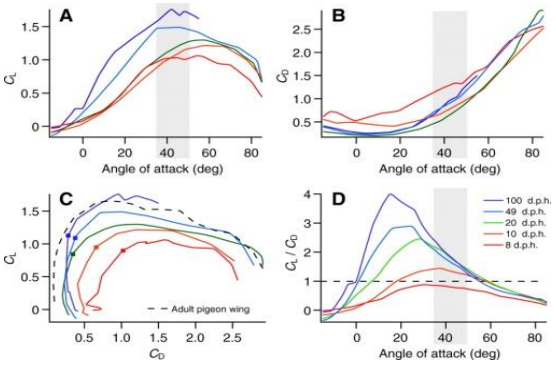


Fig 2: Relationship between coefficient of drag, coefficient of lift with angle of attack

LITERATURE REVIEW:

Pradeep Shetty et al. (2016) [1] This paper predict and correlate the mass flow rate of propeller type axial fan used in condenser unit using Computational Fluid Dynamics (CFD) technique. Computation is done for the axial fan speed of 820 rpm for the steady state condition using moving reference frame approach. The flow rate is correlated with the test results to validate the CFD modelling approach. The correlation level found closer with tested results, hence which will help to improve the futuristic model during conceptual design itself.

Brian Rutkay et al. (2016) [2] The aim of this research was to develop a process for the designing and manufacturing of propellers for small UAV. This aim was achieved by creating a computer program to design a propeller that meets user-defined aircraft performance requirements within the limitations of the electric motor capacity, user-selected materials, and manufacturing techniques. The feasibility of 3D printing technique in making flight worthy propellers was checked through material testing, manufacturing trials, and by testing the propellers in a wind tunnel. The results shows that the propeller performance generated approximates the predicted design thrust but the efficiency and power consumption could not be accurately measured.

Karna S. Patel et al. (2014) [3] In this paper the lift and the drag forces are obtained using CFD which are also experimently obtained using wind tunnel testing. The wind tunnel experiment is a laborious one and also costs more than CFD technique for the same problem. Thus first the data was obtained through analytical method then it cross checked by experimental testing. The analysis of the two dimensional subsonic flow over a NACA 0012 airfoil at various angles of attack and operating at a Reynolds number of 3×E06 is presented. The CFD simulation results show close agreement with those of the experiments, thus suggesting a reliable alternative to experimental method in determining drag and lift.

Mark W. Mueller et al. (2014) [4] Here the analysis of quadrotor is done under a condition that each propeller gets out of service respectively. This paper has sequentially tried to establish the modalities/capabilities of the quadrotor in terms of its height, position, time of flight etc with limited no of propeller in operation, where one, two and three propellers get down and out. . The stability is analysed using the deviation or the tilt in the primary axis with respect to the stable position control axis, along with the changes in altitude are used to design the quadrocopter with proper validiation from experimental data.

S. M. Mahbobur Rahman et al. (2014) [5] In this paper study of fluid flow characteristics for the flow over a propeller used in vertical takeoff and landing (VTOL) radio controlled (RC) aircrafts. Simulation investigation has been conducted through SolidWorks flow simulation using a propeller model. Design can be modified.

Shlok Agarwal et al. (2014) [6] In this paper structural design and manufacturing of twinrotor AVs has been detailed down. Individual component parts have been thoroughly describe and studied which would help in development of trirotor type unmanned aerial vehicle. Here the cost and dimension constraints are the main design feature that would would provide for practical applications. Thrust vector is directly explained and illustrated . On the basis of rolling pitching and yawing a stable rotor design and propeller orientation has been proposed for the trirotor system.

Kalpesh N. Shah et al. (2014) [7] In this paper payload capacity of UAVs is the area of research. Additional payloads on the accounts of design improvement leads to more functionality in a UAV. In order to do such, different basic design structures of UAVs were compared to developed enhanced payload capacities and choose a quadrotor. On

rough estimate a quadrotor has a pay load capacity around 4 kg which gives it additional features for military and other applications. Calculation of aerodynamic drag-lift forces has been done. The stresses generated in the body of quadrotor is not more than 22.5 MPa in "Box" sectional chassis and 22.2 MPa in "C" Sectional chassis as per the practical testing. To validate these results, the stress analysis of two types of body of quadrotor ("Box" and "C" section) is carried out in ANSYS static structural solver. As per the Static Structural solver the stress generated are 15.4 MPa and 16.97 MPa in "Box" and "C" sectional chassis respectively.

S. Subhas et al. (2012) [8] The paper predominantly focuses on CFD analysis of the propeller, forsay ship propeller is used here for CFD. Cavitation and fluid dynamics solution are the parameter are the under consideration. Fluent solution have been implemented here such that the local pressure reduces below surrounding pressure in order to simulate cavitation result. The CFD result are used to establish the design criteria only after experimental validation of the result. The optimization of vibration in flow domain and burrs is done using the above analysis. Varriant boundary conditions, fluid computational domain and grid refinement is considered for improvement in mesh generation methods.

John B. Brandt et al. (2011) [9] In this paper a full scale research on propeller has been done which has earlier been done for aircraft but with growing needs of UAVs, it has highly become imperative to perform such analysis on it too. UAVs use propeller that operate under conditions of low Reynolds number ranging from 5000 to 100000 based on the propeller chord at 75% propeller blade station. Experiments were done at university of Illinios to evaluate the efficiency of propeller under these conditions. 9 to 11 inches was the diameter range for set of 79 propellers under the test. In test conditions at constant rpm. of propeller varied velocities of wind tunnel were used to sweep over a vast range of advanced ratios until a zero thrust condition was reached i.e. windmill state. To study the effect of variable low Reynolds number over the propeller , a range of 1500 to 7500 rpm of propeller revolution, depending upon the nature of propeller was the velocity set used. The results of efficiency varied from 0.68 for best condition to 0.28 under worst possible scenario, implicated that propeller design has a huge impact over the aircraft and UAVs operations.

W.Shawn Westmoreland et al. (2008) [10] In this paper propeller modelling using CFD is done to simulate fluid flow condition over it. Research with the support NLOS-T (Non Line Of Sight Transportation) is published here. The NLOS-T is a conceptual vehicle that will be canister launched, deploy wings and control surface, and then fly to a destination within approximately 15-20 minute of the launch point. The scientific investigation was undertaken over the propeller i.e. spinning geometry of UAV, excluding the rest of air frame structure. The result of CFD over the rotorcraft propeller structure is validated with the help of experimental data.

K.C. Wong et al. (2006) [11] This paper includes the instrumentation of off-the-shelf Remote-Controlled flight platforms, the design development and operation of flight research platforms, innovative airframe concepts, of Micro Air Vehicles (MAVs), and exploring commercial applications for UAV.

Bruno Herisse et al. (2008) [12] In this paper a controller of nonlinear nature to control flight and touchdown operations of a vertical take-off and landing unmanned aerial vehicle is presented. The VTOL is a rigid body equipped with only a camera and IMU circuit which moves over textured flat plane. Stability of hovering flight and automatic landing of the unmanned aerial vehicle using optical flow feedback system is achieved. Results shows that the proposed control strategy is a successful one.

Abdellah Mokhtari et al. (2006) [13] In this paper, a nonlinear quadrotor unmanned aerial vehicle is combined with a feedback linearised controller. The most unfavorable case of control is analysed by introducing Actuator saturation and by constrain on state output. Parameter uncertainities and external disturbances causes performance issues of a controller which is shown through a simulation study. The results shows that the system becomes robust depending upon the selection of weighted functions.

Peter G. Ifju et al. (2002) [14] This research shows the effects of windy environment and unsteady aerodynamics over the micro air vehicle. The introduction of flexible wing on this vehicle improves its flight stability and durability and its performance in adverse weather conditions. The flexible wing has a operating range wingspan of 18 inches to 5 inches. In addition with the concept of flexible wing, aerodynamic assessment, and flight data analysis, fabrication method are also shown in this research.

T. A. Maitre et al. (1991) [15] Circulation around **lifting** body is modelled through a non linear function in this paper. The circulation potential is well defined inside the body and evaluation is made for the flow over the body. This method is well suited for the flow analysis over the propeller of UAVs which are consider to be extremely thin. This method is applied over non cavitating fluid flow condition in a marine propeller. Here the researcher deeply tried to solve the problem pertaining to Joukowski condition, problem of propeller mesh, wake region analysis and the influence of wake region over the hub is numerically analysed.

Jonathon Bell et al. () [16] This project has undertaken the task of designing and constructing a test rig for the purpose of experimental analysis of SUAVs coaxial rotor system. The focus is led on the importance to highlight aero mechanical components and variable that dictate the co-axial flight performance with the aim of optimizing the propulsion system to be used for HALO coaxial SUAVs manufactured by Middlesex university. The chief contribution of the paper is to design and optimize the co-axial configuration with respect to motor and propeller variation. Inter rotor spacing

has been detailed out with the help of H/D ratio that is in between 0,41 to 0.65.

Pierre Jean Bristeaue et al. (2009) [17] Here different models of quadrotor UAV have been studied. Aerodynamic effects of the propellers and their interaction with rigid body motion of the UAV has been modelled. The main assumptions are the twisting of the propellers in such a way that the local angle of attack is constant along the blades in stationary flight and, secondly the local induced velocity is invariable along the blade, these conditions are used to optimize the hovering rotor and hence conclude that the dynamics of the UAV is prominently dependent on the flexibility propeller design (location of centre of gravity) thereby playing important role in designing close loop controller**.**

S. Norouzi Ghazbi et al. (2016) [18]This paper reviews and gives an overview of various works done on quadrotor with dynamic modelling and control features.

A.V. Javir et al. (2015) [19] This paper focuses on the aerodynamic effects of quadcopter. It addresses all the aspects of quadcopter ranging from mechanical design to electronics used. It provides backup to the selection of different components with the help of various formulas from research papers. It also gives clear results with respect to weight of components and their corresponding costs. Along with this, finite element analysis is done on the frame so as to sustain the loads generated in the vehicle and concluded that small deformation occurred on the center plates are safe and within the limit.

CONCLUSION

In this paper we have tried to cover the recent research in the field of propeller specially design for usage in quadrotor with payload capacities of 4kg and above. This review paper has tried to chronologically illustrate the development of propeller advancement in the field of quadrotor. Here optimum design and stability features has been reviewed by researchers is compiled together. This review revealed that the performance of a propeller degrades at low RPM values when the significant value of Reynolds number is used. Numerical Simulation using CFD methods proves to be the most effective method to stimulate full three-dimensional viscous and turbulent flow for various propeller geometries.

REFERENCE

[1] Shetty Pradeep, “computational fluid dynamics simulation of propeller fan”, IJESRT, October 2016 IJSS7.

[2] Rutkay Brian, “Design and manufacture of propellers for small unmanned aerial vehicles”, Department of Mechanical and Aerospace Engineering, Carleton University, 3135 Mackenzie Building, 1125 Colonel By Drive, Ottawa, Ontario, Canada K1S 5B6

[3] S. Patel Karana, B. Patel Saumil, “CFD Analysis of an Aerofoil”, International Journal of Engineering Research, Volume No.3, Issue No.3, pp : 154-158,2014.

[4] W. Mueller Mark, “Stability and control of a quadrocopter despite the complete loss of one, two, or three propellers”, International Conference on Robotics & Automation (ICRA) Hong Kong Convention and Exhibition Center, 2014 IEEE

[5] S. M. Mahbobur Rahman, “ Simulation investigation on flow characteristics for the flow over a propeller used in VTOL RC aircrafts”, International Conference on Mechanical, Industrial and Energy Engineering 2014.

[6] Agarwal Shlok, “Design,Construction And Structure Analysis Of Twinrotor UAV”, International Journal of Instrumentation and Control Systems (IJICS) Vol.4, No.1, January 2014

[7] Kalpesh N. Shah, "Quadrotor – An Unmanned Aerial Vehicle", 2014 IJEDR , Volume 2, Issue 1, ISSN: 2321-9939

[8] Subhas.S, “CFD Analysis of a Propeller Flow and Cavitation”,2012 , Visakhapatnam International Journal of Computer Applications (0975 – 8887)

[9] Brandt John B., “Modeling of Flow Around a Marine Propeller Using a PotentialBased Method”,2011, University of Illinois at Urbana-Champaign, Urbana, IL 61801, USA

[10] W. Shawn Westmoreland, Robert W. Tramel, and Jennie Barber, “Modeling Propeller Flow-Fields Using CFD”, 46th AIAA Aerospace Sciences Meeting and Exhibit, AIAA 2008-402, 7-10 January 2008, Reno, Nevad.

[11] Wong K.C, “UAV Design Activities in a University Environment” School of Aerospace, Mechanical and Mechatronic Engineering University of Sydney NSW 2006

[12] Herisse Bruno, “Hovering and vertical landing control of a VTOL unmanned aerial vehicle using optical flow”, International Conference on Intelligent Robots and Systems”, ANR-06-ROB-0007, 2008

[13] Abdellah Mokhtari,” Robust feedback linearization and GH_{∞} controller for a quadrotor unmanned aerial vehicle”, journal of electrical engineering, vol. 57, no. 1, 2006, 20–27.

[14] Peter G. Ifju, “Flexible-Wing-Based Micro Air Vehicles”, AIAA 2002-0705

[15] Maitre T. A., “Modeling of Flow Around a Marine Propeller Using a PotentialBased Method”, Journal of Ship Research, Vol. 35, No. 2, June 1991, pp. 114-126

[16] Bell Jonathon, “Optimizing Performance Variables for Small Unmanned Aerial Vehicle Co-Axial Rotor Systems”, Middlesex University, School of Engineering and Information Sciences, Trent Park Campus, Bramley Road, London N14 4YZ, United Kingdom

[17] Bristeaue Pierre Jean, “The role of propeller aerodynamics in the model of quadroter UAV”, European control conference 2009

[18] S. Norouzi Ghazbi, “Quadrotors Unmanned aerial vehicles: A review” International journal on smart sensing and Intelligent Systems vol 9. No.1 March 2016.

[19] A.V.Javir,” Design, Analysis and Fabrication of Quadcopter”, Journal of The International Association of Advanced Technology and Science, Vol. 16 | MARCH 2015

[20] A. A. Johnson and T. E. Tezduyar, “Advanced mesh generation and update methods for 3D flow simulation”, Computational Mechanics 23(1999) 130-143, © Springer-Verlag 1999.

[21] Anderson, J. D. (1991), “Fundamentals of Aerodynamics”, McGraw-Hill Companies, 2nd

[22] Anderson John D (1995), Computational Fluid Dynamics, Basics with Applications, McGraw Hill Publications, ISBN 0-07- 113210-4.

International Journal of Applied Information Systems (IJAIS) – ISSN : 2249-0868
Foundation of Computer Science FCS, New York, USA
Volume 11 – No. 6, November 2016 – www.ijais.org

A Strongly Trusted Integrity Preservance based Security Framework for Critical Information Storage over Cloud Platform

Shweta Sharma
M .Tech, Delhi Technological University
Delhi

ABSTRACT
During last few years, the demand of cloud computing has immensely arisen among the Corporate/Business organizations. The cloud computing concept brings exclusive monetary benefits to the corporate houses through its pay-as per use facility. The incurred cost only lies in the consumption of hardware and software resources for any particular available business applications[1].For any particular project, all the web applications are deployed on available physical servers ,dispersed throughout the countries ,connected through cloud service providers. This mega scale growth in the adoption of cloud platform leads to extreme revenue benefits to the involved parties. But at the same time, information security also requires to be well enveloped in the cloud environment [2].In this research work, we have incorporated various cryptographic algorithms to improve the authentication module such as Challenge response Authentication protocol and file data storage using suitable and efficient Digital Signature Standard scheme along with effective encryption schemes such as AES as well. The proposed framework represents proper client –server authentication and secured & trusted architecture for stored information on cloud server. We have done research work to alleviate the security of stored information with in the cloud and also to protect it from any outside attack during information exchange between client and server.

General Terms
Information Security, Cloud Platform, File Integrity.

Keywords
Cryptography,Authentication Protocol, Digital Signature Standard Scheme (DSS), Diffie -Hellman Key Exchange scheme.

1. INTRODUCTION
In today's computing world, cloud security has emerged as an immense requirement in business projects. There have been variety of prevailing security attacks which needs to be fixed to ensure proper protection of stored client's information over cloud server[3].The Security attacks includes distributed denial of service attack (DDoS), replaying, masquerading, side channel attacks, phishing and geographical implications .In cloud computing platform, corporate organizations outsource the computing resources from other cloud vendors. The companies may decide to transfer their business applications/tools/databases on Cloud platform [4]. They are required to follow certain configurations and technical parameters related to their software and hardware needs before deciding to move to the cloud. According to [2][5], there have been various developed features of cloud computing, enforced and provided to the organizations if security and privacy risks are minimized. These features are as:-

Limitless Flexibility: The various software applications/databases can easily be accessed through cloud computing platform. This provides better scalability.

Reliability & Security: Both these features are imparted to the clients dealing with cloud Platform. These requirements serve the purpose of quality improvements in terms of service delivery to the users.

Collaboration of application units*:* Various software applications/UIs/Executable gets collaborated together on same platform to perform desirable computing functions. Thus benefits the user's adaptability.

Portability: Remote servers store and access client's data based on constraints. The client may avail its stored data and applications as per his/her requirements.

Simpler Devices: Devices such as PDAs, cellphones, video recorders etc. may be used to interface with cloud platform and thus becomes easily accessible. The true benefits of cloud computing can be utilized if real time privacy and security issues can be addressed to protect information part of the cloud platforms.

2. RELATED WORK & LIMITATIONS
In order to provide significant amount of information security for storage on cloud server, various research frameworks have been proposed and analyzed to ensure quality schemes to sustain high level security for client's data. There have been various functional models of Cloud. In case of private cloud, there exists confidential and sensitive information such as – credit cards, Intellectual property/trade secrets, Financial, Health, State/Government secrets, Proprietary/Sensitive and Personally Identifiable. Thus, Enhancing Information Security levels become the top most priority to support Cloud Computing for running businesses in IT trade.

Following summarization indicates the literature survey on distinguished proposed research work related to information integrity within the cloud platform during recent years.

2.1 Information storage using Tripwire [12]
It is a type of Intrusion Detection System tool which was used to store the hash values of a particular file within the associated Database. Any intrusion leads to recompilation of latest hash values and comparison with original values from databases. The major drawback is the requirement of

databases to store the computed hash values at any point of time.

2.2 Flogger (A File centric logger to monitor file access in cloud) [11]

This tool accesses various system logs by establishing physical and virtual subnets. Their component includes various services in the form of:-File Sender daemon, File sender client program, Database loader, Windows and Linux floggers. The tool monitors every file/folder accesses briefly, keeps check on online generated system logs. The major drawback is huge database requirements which deteriorate cost effectiveness.

2.3 I3FS Tool (Intrusion detection file system [9] [10])

It consists of Berkeley Databases (Transaction based and High level performance dB).The file integrity gets verified after qualifying security and cache policies criterias.The checksums are stored in Berkeley databases against corresponding access policies. The limitation of this tool is the requirement of Berkeley databases and maintenance of database servers which may lead to server overheads in cloud environment.

2.4 Light weight File Monitoring Tool [6] [7]

It provides a light weight file integrity maintenance tool which computes the checksum of the client's stored file and saves within the file/folder. It verifies the information integrity in a cost effective manner as compared with other tools(already discussed).But it has its own limitations:-

- Absence of transparency to client in reference with determination of checksum by the server.
- There is no client involvement present during calculation of checksum by the server.
- It doesn't cater to the availability of backup replica (if in case, file integrity gets lost/disturbed).
- Client-server trust bond has no significance in this model. The attacker could impersonate as server.
- There exists a requirement of extra effective client—server relationship in order to enhance the overall quality of this model.

3. PROPOSED DESIGN FOR IMPROVISED AND RELIABLE INFORMATION INTEGRITY FRAMEWORK FOR CRITICAL INFORMATION STORAGE UNDER CLOUD PLATFORM [8] [20]

In this proposed work, we elaborate a client-server scenario for cloud computing. To provide information security to the saved client entity record on the cloud server, we have designed the following procedural events .This tool proves to be cost-effective and light weight without any additional database requirements. The Algorithm below illustrates the events sequentially in a given cloud computing scenario [14] [15] [16]

1. Initialize Client Process as P1 and Server Process as P2 (for a given cloud computing scenario).
2. P1 authenticates itself to the server (P2) using Zero Authentication Protocol.
3. If the authentication is valid, P2 allows P1 to get logged into the server and both processes exchanges secret key SP using Diffie-Hellman Key exchange method.
4. P1 selects file storage functionality (with a motive to store its own data on cloud server).
5. P2 saves the file F into shared hard disk and applies hash algorithm (SHA-1) in order to compute the final checksum output X.
6. X is stored in <output>tags in F only. (saves memory).
7. Apply AES encryption algorithm to encrypt the X.
8. Transfer X to P1.P1 applies AES decryption algorithm using secret key SP.
9. P1 applies DSS (Digital Standard Signature) algorithm using P1 private key p on X to produce FX.
10. P2 sends computed output FX to P2 for storage on cloud.
11. If P1 logged in again and applies for Integrity Verification of F.
12. P2 applies Integrity verification ( ) on X to produce FX'.
13. If FX==FX', Integrity Intact. File Preserved.
14. Else Integrity attacked. Apply Back-up Replica functionality.
15. Original File F available.
16. Integrity verification () ends.
17. Program Ends.

3.1 Advantages Of Proposed Information Integrity Model In Cloud Computing [17] [18] [19]

There are certain advantages related to given models which are as listed below:

- This research work generates trust and reliability between client and server entities.
- The client process gets directly connected with server process to compute the final checksum value to be stored in <output> tags within the file.
- This model eliminates the probability of an attacker who could even impersonate as server on the cloud platform.
- Transparency level exists between client and server entities while executing business acts. This leads to inculcation of trusted values.
- For proper secure key exchange procedures, Use of Diffie-Hellman Key exchange technique has also been collaborated into this model.

- This model proves to be economical, reliable, and trustworthy and secure for critical information storage over cloud.
- The client authenticates itself with server using proper valid Zero-Authentication Protocol which has been designed such that claimant does not reveal anything which will endanger the confidentiality of the secret. The claimant proves the verifier that he knows a secret without leaking it
- The Digital Signature Standard (DSS)scheme has been incorporated to enhance the security of the computed checksum as its smaller in size and fast in speed in terms of execution(on comparison with other signatures).

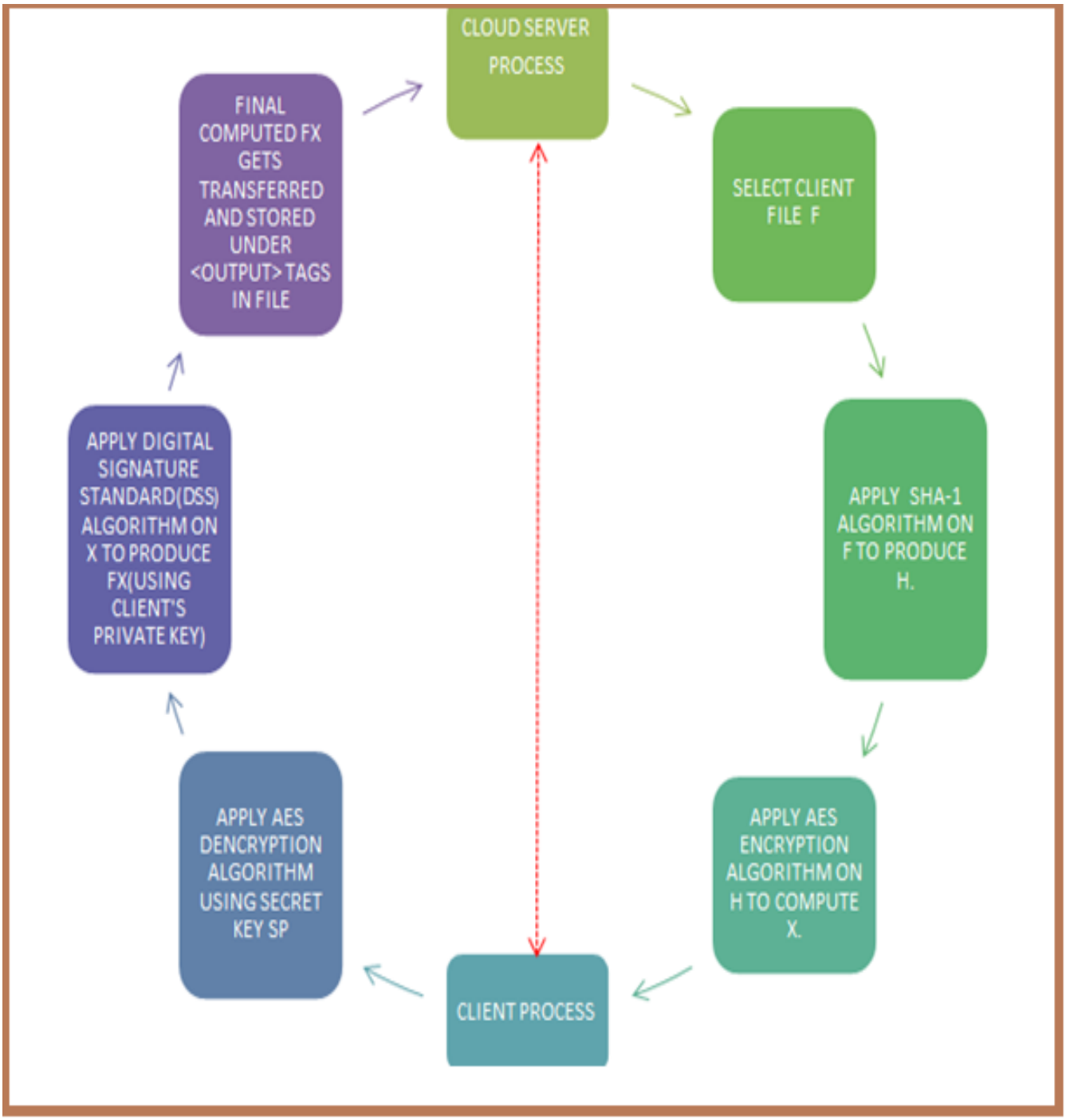


Figure1. Diagrammatic representation of strongly trusted integrity security framework for critical information storage inside cloud

4. OUTPUTS OF NEWLY PROPOSED TOOL TO ENSURE SECURITY FOR CRITICAL INFORMATION OVER CLOUD PLATFORM

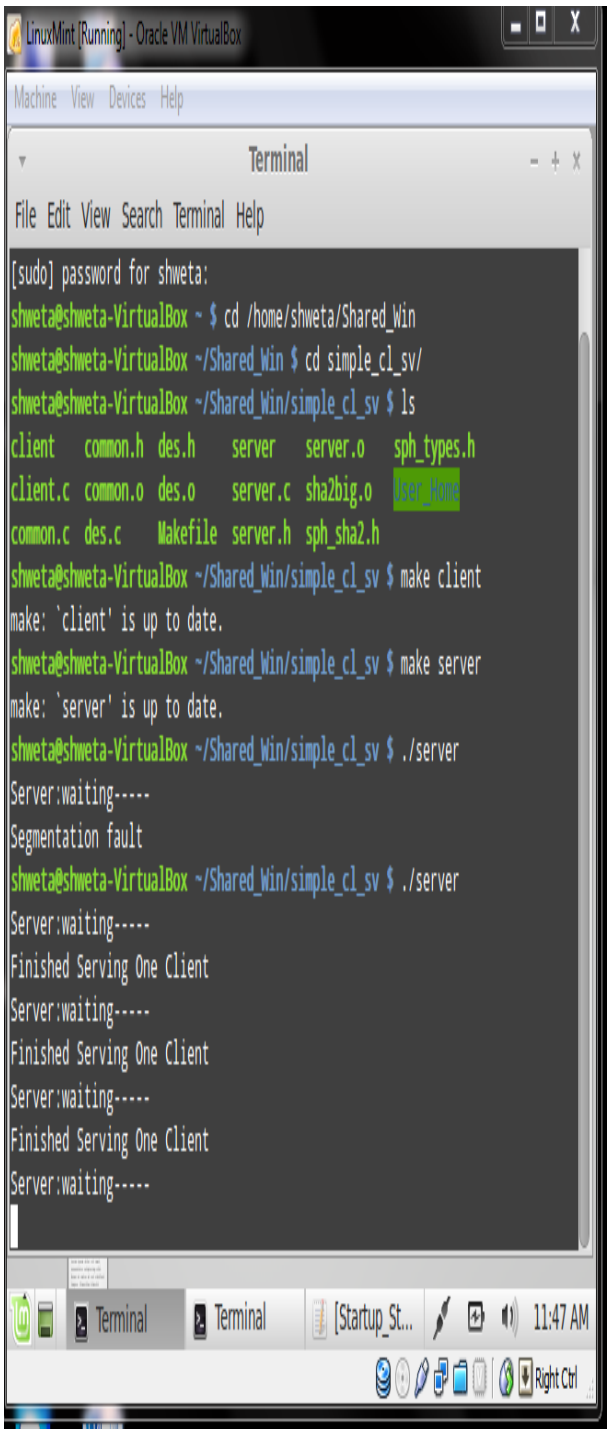


Figure 2: Screenshot for Server Process Initialization Mode

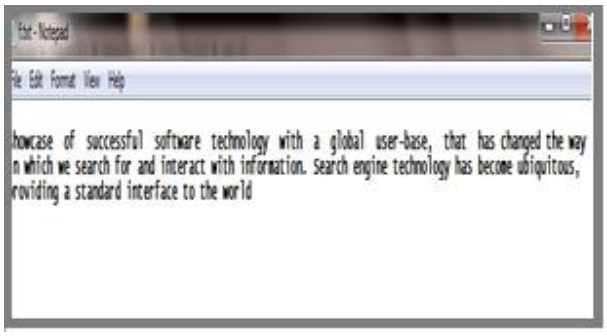


Figure 3: Screenshot of Original client's data stored on server

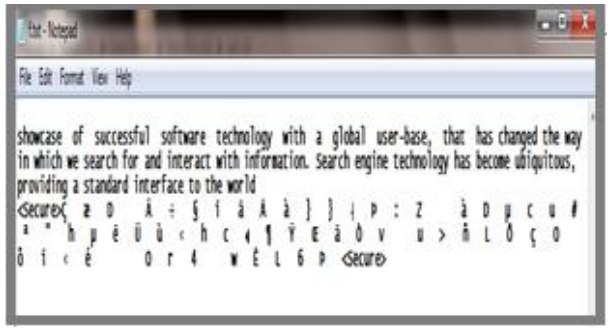


Figure 4: Screenshot of Original Client's data stored after Integrity Calculation (stored within shown tags)

5. CONCLUSION

This proposed tool work had been executed in Oracle VM virtual box (based on LINUX, win7 Platform).The client and server processes have been developed using socket programming and specific socket address based structures. This tool performs regular integrity checks and thus supervises the intact integrity of the client's information over the cloud with better client –server communications .Thus, it can be observed that it proves to be time efficient and cost effective as it executes integrity calculation in approximately 1000 microseconds for 600 byte file which proves to be a minimal requirement as compared to long duration delays(in minutes/hours) consumed by server to perform integrity checks on client's stored information. This tool works without database software on the server. It satisfies light weight and secures storage tool criteria for cloud platform.

6. REFERENCES

[1] GA Solanki, Welcome to the Future of Computing: Cloud Computing and Legal Issues, International Journal of Scientific & Technology Research 2012, vol1, issue 9.

[2] Nelson Gonzalez, Charles Miers, Fernando Redigolo, Marcos Simplicio, Tereza Carvalho, Mats Naslund, Makan Pourzandi, A quantitative analysis of current security concerns and solutions for cloud computing, Gonzalez et al. Journal of Cloud Computing: Advances, Systems and Applications 2012.

[3] Lijun Mei, W .K .Chan, T .H .Tse, A Tale of Clouds: Paradigm comparisons and some thoughts on research issues, 2008 IEEE Asia-Pacific Services Computing Conference.

[4] Balachandra Reddy Kandukuri, Ramakrishna Paturi V, Dr. Atanu Rakshit, Cloud security Issues 2009, IEEE.

[5] M. Sudha, M. Monika, Enhanced Security Framework to Ensure Data Security in Cloud Computing Using Cryptography, Advances in Computer Science and its Applications 32 Vol. 1, No. 1, March 2012, Copyright © World Science Publisher, United States. www.worldsciencepublisher.org.

[6] Sanchika Gupta, Anjali Sardana, Padam Kumar, A light Weight Centralized File Monitoring Approach for Securing Files in Cloud Environment ,The 7th International Conference for Internet Technology and Secured Transactions (ICITST-2012) ,IEEE 2012.

[7] Sanchika Gupta, Anjali Sardana, Padam Kumar , Ajith Abraham, A secure and light weight approach for critical data security in cloud, 2012 Fourth International Conference on Computational Aspects of Social Networks (CA Sons).

[8] Forouzan, Cryptography and Network Security, TMH 2012.

[9] S. Patil, A. Kashyap, G. Sivathanu and E. Zadok, I3FS: An in-kernel integrity checker and intrusion detection file system.

[10] Q. Nguyen Anh and T. Yoshiyasu, A novel approach for a file-system integrity monitor tool of Xen virtual machine, Book A novel approach for a file-system integrity monitor tool of Xen virtual machine, Series A novel approach for a file-system integrity monitor tool of Xen virtual machine, ed.,Editor ed.ls\eds., ACM, 2007.

[11] R.K.L. Ko, P. Jagadpramana and L. Bu Sung, Flogger: A File-Centric Logger for Monitoring File Access and Transfers within Cloud Computing Environments, Trust, Security and Privacy in Computing and Communications (TrustCom), 2011 IEEE 10th International Conference on , pp. 765-771.

[12] H. K. Gene and H. S. Eugene, The design and implementation of tripwire: a file system integrity checker,Book The design and implementation of tripwire: a file system integrity checker, Series The design and implementation of tripwire: a file system integrity checker, ed., Editors, ACM, 1994.

[13] Meiko Jensen, Jorg Schwenk, Nils Gruschka, Luigi Lo Iacono, On technical security issues in cloud computing 2009, IEEE Computer Society.

[14] Tina Francis, S. Vadivel, Cloud Computing Security: Concerns, Strategies and Best Practices: Proceedings of 2012 Intemational of Cloud Computing, Technologies, Applications & Management, 2012 IEEE.

[15] Mr. Prashant Rewagad, Ms. Yogita Pawar, Use of Digital Signature with Diffie Hellman Key Exchange and AES Encryption Algorithm to Enhance Data Security in Cloud Computing, 2013 International Conference on Communication Systems and Network Technologies.

[16] Wang Jun-jie, MuSen, Security Issues and Countermeasures in Cloud Computing, 2011 IEEE.

[17] Balachandra Reddy Kandukuri , Ramakrishna Paturi V, Dr. Atanu Rakshits , “Cloud Security Issues”, 2009 IEEE International Conference on Services Computing,2009 IEEE.

[18] Mrs. G. Nalinipriya ME, (PhD), Mr. R. Aswin Kumar, “Extensive Medical Data Storage with Prominent Symmetric Algorithms On Cloud “, A Protected Framework: 2013.

Available online at www.ijapie.org

International Journal of Advanced
Production and Industrial Engineering

IJAPIE-SI-OSCM 701 (2017) 01–03

Special Issue on

OPERATIONS
&
SUPPLY CHAIN
MANAGEMENT

ABC Analysis in the Hospitality Sector: a Case Study

Nand Kumar[1], Rohan Soni[2]
(Delhi Technological University, Delhi, India)
Email: nandkumar@dce.ac.in

Abstract : The main objectives of this study is to analyze the inventory management techniques employed and get possible solutions to overcome the inefficiency of the inventory management. ABC analysis is used in the study to analyze the data of the XYZ hotel. It is found that ABC analysis is helpful in determining the value of the stocks present in the inventory. Through this classification, the hotel identifies the hot spots, and separates them from the rest of the items that have lower sales. The study was found to be beneficial for the hospitality industry to competently manage their inventory levels and keep a track of the items that have a significant impact.

Keywords: Inventory, Inventory management, Hospitality industry, ABC analysis

INTRODUCTION

The study is to determine the appropriate inventory levels that should be kept in order to reduce the costs of inventory and maintain the required inventory in the hospitality industry.

The inventory management involves supervising and controlling of the ordering, storage and uses of components that the company needs for sale in order to minimize the inventory cost and to guarantee smooth process. Organizations maintain inventories because it is almost impossible to forecast the demand and usage needs precisely. Inventories that are mismanaged can create significant financial problems for a business.

An inventory is an important asset of a company and is an integral part of the operations. A firm must have an optimum level of inventories. Several companies have adopted, embraced the methods and realized the impact of the same. There are different categories of inventories. The first is the raw materials, the units that have been purchased and stored for the future. The second category is the WIP or work in progress goods, which are in the intermediate stages of productions and lastly, the finished goods which are ready to be purchased by the consumer.

A company needs to know the precise number of items on their inventories in order to place orders or control losses. There are several techniques which are employed depending on type of business.

An accurate accounting system with up-to-date records is essential. Companies use perpetual system to maintain accurate inventory records, wherein a continuous record of changes in inventory is maintained. Organizations that capitalize on inventory and procurement functions as means of achieving competitive advantages often resulting in increased profitability and increased market responsiveness. [1]

LITERATURE REVIEW

The company purchases different types of items from different suppliers. There are several types of inventory control analysis techniques such as ABC, XYZ, FSN, VED, HML etc. The concept of ABC model can be used to form a rational inventory policy which would help in the reduction of the minimization of inventory costs, including storage and manpower costs.

The process of ABC analysis classifies inventory items into A, B, or C categories based on so-called annual dollar usage. Annual dollar usage is calculated by multiplying the dollar value per unit by the annual usage rate [2]. The ABC analysis follows a simple rule of thumb: "vital few and trivial many"[3].

The class 'A' items are the ones that are relatively smaller in number, but account for the greatest amount of dollar annual usage. The class 'C' items are the ones which are relatively large in number, but they make up a rather small amount of annual dollar usage. The items in the class 'B' are defined as those items between the classes 'A' and 'B'.

The ABC analysis offers a tool for identifying items that will have a significant impact on overall inventory cost, while also offering a tool for the identification of different categories of stock that will require different management and controls techniques. [4]. The ABC analysis is very useful as it clearly suggests that the inventories are not of equal values. [5].

It is seen from the above categorization that class A items are the ones with higher consumption, class B items are the ones with moderate consumption and the class C items are the ones with low consumption values. It has been seen that the items that belong to category C are not paid much attention

and more focus should be on these items so that their sales are increased.

- Class 'A' items account for the 70% of the total annual consumption value and 10%-15% of all the inventory items.
- Class 'B' items account for the 20% of the total annual consumption value and 15%-20% of all the inventory items.
- Class 'C' items account for the 10% of the total annual consumption value and 70%-75% of all the inventory items.

The cutoffs for the ABC analysis can be modified by the management to classify the inventory. ABC analysis helps in the realizing the significance of each item of inventory in terms of the value of each item. It implies that a small portion of the stock contributes to maximum revenue.

RESEARCH METHODOLOGY

The study is focused at the hospitality industry. Three years data was extracted to study the trends and patterns of the inventory of the hotel. ABC analysis and Pareto analysis was also used to identify the top items for the different categories.
Implementation of ABC analysis involves:

1. Preparation of list of items and their annual consumption value.
2. Arrangement of the items in the descending order of their annual usage in value.
3. Calculation of the percentage of the share of each item.
4. Separation of items into A, B, and C categories.

Method of data collection:

i. The relevant data needed for the analysis was obtained by the sales reports; purchasing reports generated by the finance department of the company collected using the SAP SE(System Analyses and Programme) software. The data was extracted from the SAP SE software by suing certain T-codes for the different materials.
ii. Interviews with the personnel in the stores, and the managers in the purchase and finance departments
iii. Background knowledge information was obtained by review of the related literature on the ABC analysis.

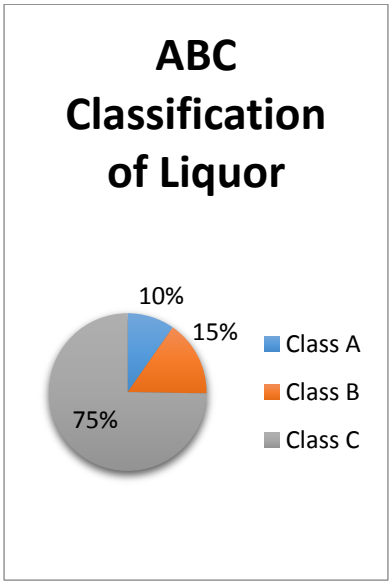
CASE ILLUSTRATION

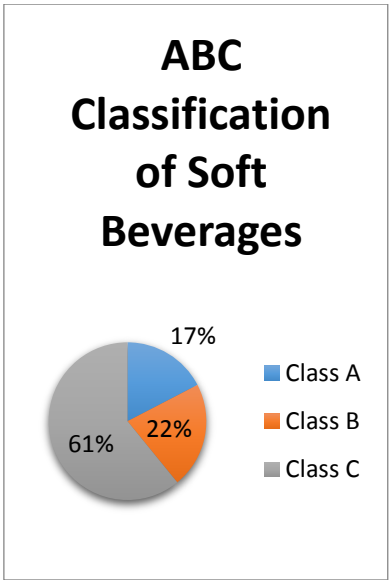
The inventory is bifurcated into 5 types:

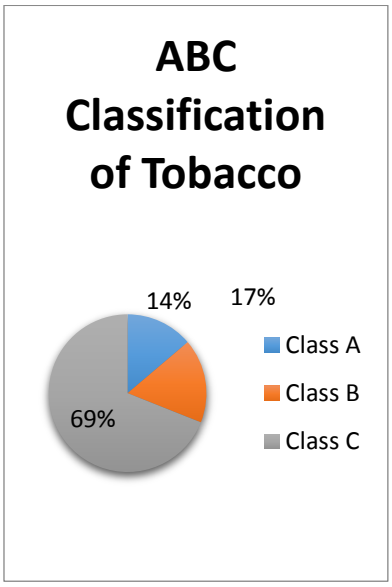
1. Liquor
2. Food
3. Soft beverages
4. Tobacco
5. General and stationery items

We have considered only the "liquor", "soft beverages" and the "tobacco" inventory data.
The following details were obtained:

a) The lead time of the stocks is highly variable according to the demand but to be on a safer side, this is assumed to be 7 days for all the stocks except for imported liquor which has the lead time at 15 days.
b) No theft of stock is possible due to the stringent policies of the XYZ hotel including periodic tracking of the items present in the inventory owing to the use of fully automated inventory system and perpetual inventory.
c) Possibility of a stock out is nil on the account of the use of the software SAP which alerts the operator if the minimum stock level is breached.







CONCLUSIONS

The inventory of liquor is higher than the minimum level that should be maintained. Brand strength of liquor is high and no new brand introduction is necessary. After the ABC analysis of the data obtained, it was found that the Hotel maintained the required inventory for the class 'A' items. However, the level of inventory of the class 'C' items is higher than the optimum level for the same category. Steps have been taken to reduce the class 'C' item stock in the inventory by moving the class 'C' items by giving it away in complementary or in hampers. In order to push the recognized items, promotional events and activities can be conducted

REFERENCES

[1] M. Victoire (2015). Inventory Management Techniques and its contribution on better management of manufacturing companies in Rwanda. European Journal of Academic Essays 2(6): 49-58.
[2] M.A. Cohen & R. Ernst, (1988). Multi-item classification and generic inventory stock control policies. Production and Inventory Management Journal, 29(3), 6–8.
[3] Yu, Min-Chun (2010). Multi-criteria ABC analysis using artificial –intelligence- based classification techniques. Expert Systems with Applications.
[4] Vollmann, T. E., (2004). Manufacturing planning and control systems for supply chain management. McGraw-Hill Education.
[5] Lun, Lai, Cheng (2010) Shipping and Logistics Management, Springer, p. 158
[6] Nadkarni, R. & Ghewari, A. An Inventory Control using ABC Analysis and FSN Analysis. International Journal of Engineering, Business and Enterprise Applications.
[7] S. Mitra, M.S. Reddy, K. Prince. Inventory Control using FSN Analysis – A Case Study on a Manufacturing Industry. International Journal of Innovative Science, Engineering & Technology [April 2015 , Vol. 2 Issue 4
[8] J.B. Hmida, S. Parekh, J. Lee. Integrated Inventory Ranking System for Oilfield Equipment Industry. Journal of Industrial Engineering and Management.

ResearchGate

See discussions, stats, and author profiles for this publication at: https://www.researchgate.net/publication/312219667

International Journal of Advanced Production and Industrial Engineering INNOVATIVE DESIGN & COMPUTATIONAL...

Article · January 2017

CITATIONS
0

READS
37

5 authors, including:



Shabir Grover
Delhi Technological University
2 PUBLICATIONS **0** CITATIONS
SEE PROFILE



B B Arora
Delhi Technological University
30 PUBLICATIONS **36** CITATIONS
SEE PROFILE



Vaibhav Khanna
Delhi Technological University
1 PUBLICATION **0** CITATIONS
SEE PROFILE



Tushar Kaushik
Delhi Technological University
1 PUBLICATION **0** CITATIONS
SEE PROFILE

Some of the authors of this publication are also working on these related projects:



Dates Extended for Full manuscript Submission at ICAPIE 2016, Delhi, India View project

All content following this page was uploaded by Shabir Grover on 12 January 2017.

The user has requested enhancement of the downloaded file. All in-text references underlined in blue are added to the original document and are linked to publications on ResearchGate, letting you access and read them immediately.

Available online at www.ijapie.org

International Journal of Advanced
Production and Industrial Engineering

IJAPIE-SI-IDCM 602 (2017) 04–11

Special Issue on

INNOVATIVE DESIGN
&
COMPUTATIONAL
MODELLING

Analysis on Drag Reduction of Bluff Body using Dimples

Shabir Grover[1,*], B.B.Arora[1], Vaibhav Khanna[1], Tushar Kaushik[1], Akhilesh Arora[1]
[1]*Department of Mechanical Engineering, Delhi Technological University, New Delhi-110042, India.*

Email: shabirgrover_2k14@dtu.ac.in

Abstract : A comparative study based on numerical modelling of airflow over a smooth generic bluff body against a dimpled one has been taken up in the present study using a reformed CFD FLUENT code. The investigation of flow is carried out using an Ahmed body, 25 degrees rear slant with dimples incorporated on its top as well as rear slant surface with specifications, AR equal to 6.25, and diameter (Φ) 25mm. The turbulent characteristics of the air stream were examined using the reliable two equation k-ε model. For an enhanced study of adverse pressure gradients near surfaces, a non-equilibrium state was assumed for the wall interface. All in all, the simulation results show that a drag reduction of 0.3% was obtained by employing dimples with elliptical profile.

Keywords: Reynolds number, Turbulent flow, Flow separation, Drag Coefficient, Dimples, Form Drag

I. INTRODUCTION

Nowadays, the rapid diminution of fossil fuels has posed a tremendous challenge for designers and engineers working in the automotive field to develop more fuel efficient vehicles. Implementing modifications to the exterior form of the vehicles has become paramount to decrease the drag force acting on them thereby, minimizing fuel consumption and maximizing efficiency.
Moreover, the ever increasing worries about ecological concerns over the past two decades, as well as the recent emergence of the energy crisis have accelerated this endeavour of drag reduction.

It has been established that for a medium sized European car, the aerodynamic drag force accounts for nearly 80% of the total road resistance at a 100 km/hr cruise speed. [16]

$$F_D = C_D \times A \times \frac{\rho}{2} \times V^2$$ [19]

Where C_D is the non-dimensional drag coefficient; A is the projected frontal area of the vehicle and ρ is the density of the surrounding air and $F_D$is the Drag force acting on the body.

Drag reduction attained through controlling air flow effects over a surface seems to be an answer to the above problems. Experimentally, this procedure of drag reduction and the development of the methods to control it were first carried out. But due to the higher costs involved in fabrication of wind tunnels and the inaccuracies achieved in similarity matching, experimental methods are proving to be unfeasible. Nowadays, the analysis of an engineering system relies heavily on computer-based solution algorithms which utilize numerical techniques to obtain approximate solutions for the governing partial differential equations (PDE). Computational fluid dynamics (CFD) has emerged as one such essential tool, which is more than widely employed in the automotive industry. Due to the massive advances in computational power, the time and costs required to carry out simulations have reduced significantly.

There has been several work carried out in the past for drag reduction using both active and passive flow control devices. Although, active flow devices have shown greater improvement in efficiency and performance during all phases of operation, but passive flow control devices have proved themselves to be more desirable due to their greater reliability, short profile and no external energy requirement. Active flow control, on the other hand, involves addition of energy or momentum to the system in a regulated manner and has shown a tendency to increase the complexity and weight of the system drastically.

One such passive method is the use of dimples as a means for increasing surface roughness to reduce drag. Previous work has shown that the total drag force experienced by a generic bluff body is a combination of pressure drag and skin friction drag in which the former predominates the latter. The application of dimples on golf balls has shown that dimpled golf balls have a lower coefficient of drag, C_D than non-dimpled ones, which is due to the delaying of the flow separation at the rear end. Thus, the dimpled golf balls are able to travel relatively longer distances. This favourable reduction in drag is caused by the dimples on its surface which “trip” the boundary layer to transition from laminar to turbulent flow, whose mechanism is similar to vortex generators. This happens because turbulent flow stays attached for a longer period due to the greater component of momentum in the direction of flow and this delays flow separation. This delay in flow separation decreases form

drag, which in turn leads to a decrease in the total drag force acting on it. Total drag force is composed of form drag and drag due to skin friction.

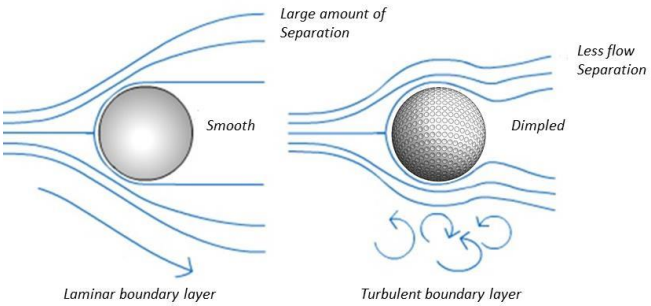


Fig. 1 Effect of dimples on golf ball

While there is an increase in surface roughness due to the presence of dimples, the skin friction component of total drag gets scaled up. Since the golf ball is a bluff body, the component of form drag is more dominant as compared to drag due to skin friction. Overall, the combined effect of dimples on the surface of the golf ball translates in to a reduced total drag coefficient.

$$C_D^{Total} = C_D^{Form} + C_D^{Skin\ Friction}$$

Where $C_D^{Skin\ Friction}$ and C_D^{Form} are the non-dimensional coefficients of skin friction drag and pressure/form drag respectively. Their algebraic sum along with taking into account interference drag, gives the coefficient of parasitic drag or in this case total drag coefficient i.e. C_D^{Total}.

In spite of this work, the underlying mechanisms through which the dimpled surfaces affect the transition of the boundary layer from laminar to turbulent have not been fully explored to the extent that accurate prediction of aerodynamic forces of lift and drag and their corresponding moments is possible. The present work is intended to assess the flow regime, total coefficient of drag value and to ascertain the fact that the result obtained lies in close proximity with the experimentally determined value.

II. Literature Survey

The study undertaken is a mere consequence of the present day situation of road cars and the fuel availability. Extensive development in the automotive arena has led to increased average cruising speeds for road cars. This consequently has brought the problem of aerodynamic drag to the forefront which was earlier considered imperceptible. It thus turns out that significant drag force experienced by cars has led to investigation into the techniques using which the coefficient of drag value for vehicles can be reduced.

A thorough study of previously published research papers has revealed that vehicle parameters alone do not affect total drag; operational parameters have a large effect as well. Here, only passive methods have been researched.

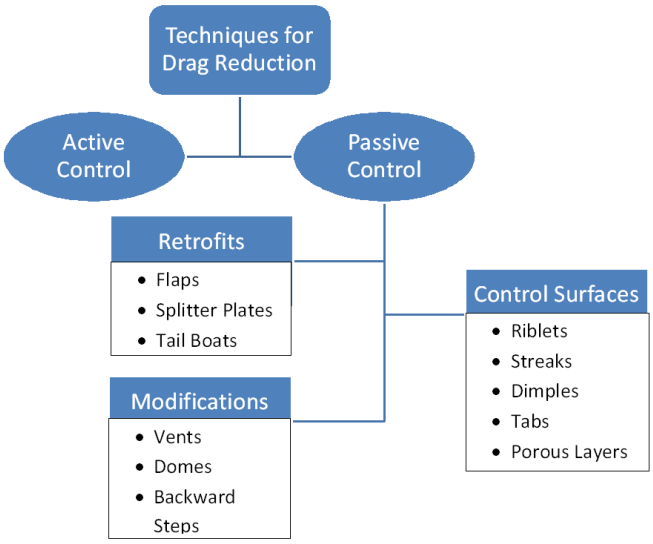


Fig. 2 Methods for drag reduction

A. *Retrofits*

A. Fillippone and Muhammed-Kassim (2008) conducted a numerical study on various drag reducing retrofits with the aim of saving fuel. It was found that using aerodynamics devices is beneficial only when the vehicles travel at high speeds as weight does not have any direct effect on drag. In other cases such as city driving condition their usage is not justifiable. Commonly used retrofits are splitter plate, boat tails, flaps or deflectors.

B. *Control Surfaces*

Katsumi Aoki et al (2012) tried to clarify the mechanism of drag reduction for a sphere with arc type dimples. Pressure and velocity distributions were measured inside and between the dimples and the flow over the sphere was visualised by an oil filling method.

C. *Modifying and Optimizing Existing Designs*

Hsu and Davis (2008) found that by adding humps on the top, bottom and/or sides of trailer along with boat-tail flaps can reduce drag by about 50.9%. But the method isn't viable for real automobiles.

All the above examples are a testimony to the fact that reasonably good amount of investigation has been carried out in this field but still the hypothesis of turbulent boundary layer remaining attached to the body surface for long has not found a sound explanation. Thus extensive research work is still being carried out.

III. METHODOLOGY

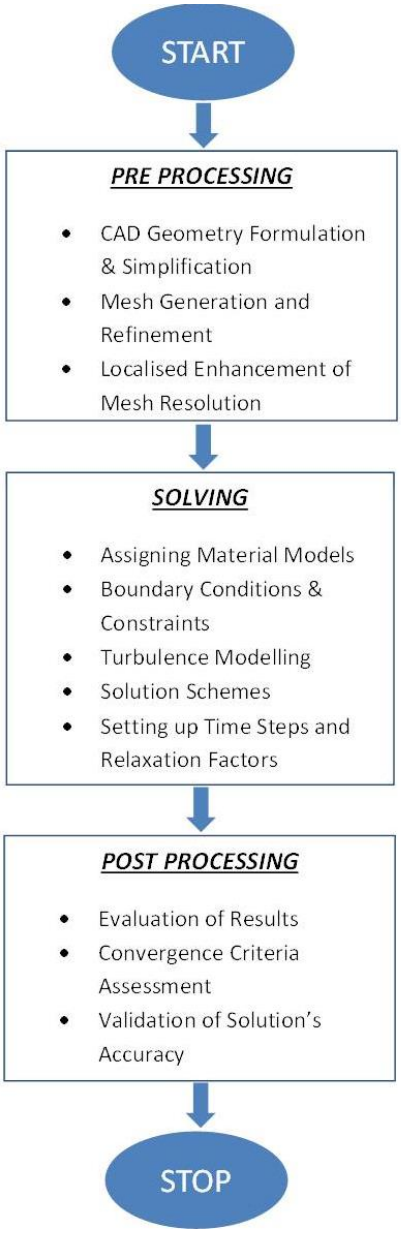


Fig. 3 Framework of CFD

A. *Vehicle Body*

In the present study, a typical bluff body called as the Ahmed body with 25 degrees rear slant angle was utilized. The Ahmed body is a simplified car model which is used for studying the flow simulation carried over the body. But it still retains the prominent features of a car namely, a curved fore body, a straight centre section and the angled rear end. The 3 dimensional CAD model of the body was drafted by using DS Solidworks using the dimensional details available from the research carried out by S.R. Ahmed. After the default model is drafted, it will be added with the formulated profile of dimple at the top surface or roof. For the placement of the dimples on the top surface, a linear patterned configuration was put in to use.

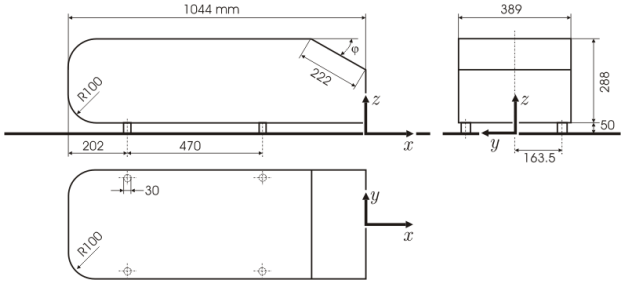


Fig. 4 Dimensions of Ahmed body, given slant angle φ = 25 degrees

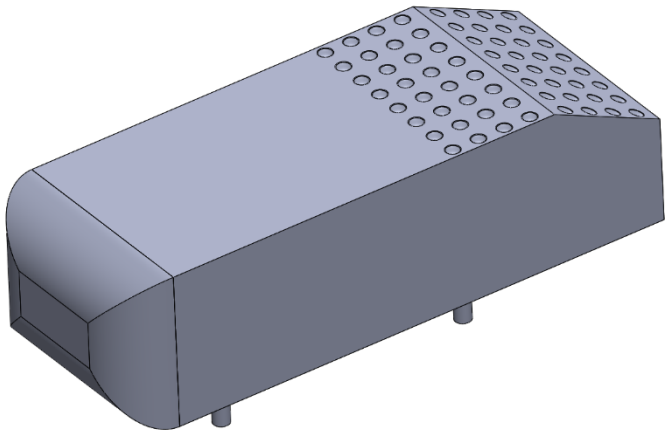


Fig. 5 Trimetric view of dimpled Ahmed body

B. *Aspect Ratio*

In order to completely define the dimple specifications, the parameter Aspect Ratio (AR) has been introduced. This quantity is the ratio of the diameter of the dimple to its depth i.e. (D/h).This implies that for a given dimple Diameter (Φ) and its AR, the dimple depth can be determined.

Significant differences in dimple geometry – due to variations in diameter, aspect ratio, fillet radius, relative positioning of dimples and the profile implicitly determine by how much the Coefficient of Drag will be affected.

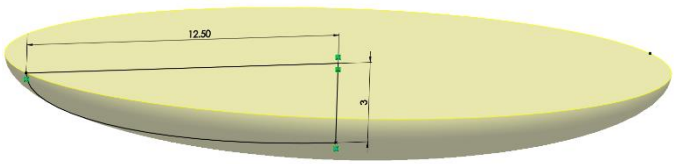


Fig. 6 Dimple geometry incorporated on the Ahmed body

C. *Meshing*

The meshing is done by using ICEM CFD ANSYS meshing software. The computational domain exists between 13.544m X 6.389m X 3.338m. Blockage area ratio of 0.539% is used, which is significantly lesser than the maximum limit of 7.5%. In order to decrease the total computational time, a symmetry plane passing through the Ahmed Body's longitudinal axis is created. This effectively reduces the number of elements and nodes by half. A hybrid mesh topology was adopted –

comprising of both structured and unstructured grids. For regions of inviscid flow, such as the region pertaining to the outside of the boundary layer where local shear stresses are negligible, tetrahedral elements are more dominant. In the regions of viscid flow, like the boundary layers around Ahmed Body's surface, prismatic elements are utilized in order to effectively resolve the velocity profiles for the analysis. For a typical car-like shape, pressure drag is dominant over skin friction, so the accuracy of the drag predictions are largely determined by the accuracy of the predicted static pressure distribution on the body. This pressure distribution is strongly affected by the locations of flow separation and reattachment.

Therefore it is important that the surface mesh resolves all relevant details of the geometry and satisfies the requirements of the physical models used in the simulation.

Prismatic elements provide good alignment with the flow near wall boundaries. This is beneficial for reducing numerical diffusion. Thus, flat regions, especially on the front part of the under-body as well as the top surface containing dimples should be resolved using prismatic layers. The transition between the two types of elements was also kept gradual so as to prevent the distortion of the elements, while also merging the nodes at the interfaces. This not only kept the number of elements low, but at the same time increased the accuracy of the results.

TABLE I
SETUP DETAILS FOR MESH AND SOLVING SCHEME

Particulars	Type of Body	
	Uncontrolled	Controlled
Element Type	Tetra/Prismatic (Flat Base)	Tetra/Prismatic (Flat Base)
Elements	4137591	5787095
Nodes	818485	1288770
Skewness (Maximum)	0.8959	0.8618
Orthogonal Quality (Minimum)	0.2009	0.227
Scheme Deployed	COUPLED	SIMPLE →COUPLED
Cores Utilized (Processors)	4	4
Computational Time	9 Hours	15 Hours
Processing Type	Parallel (Single Precision)	Parallel (Single Precision)

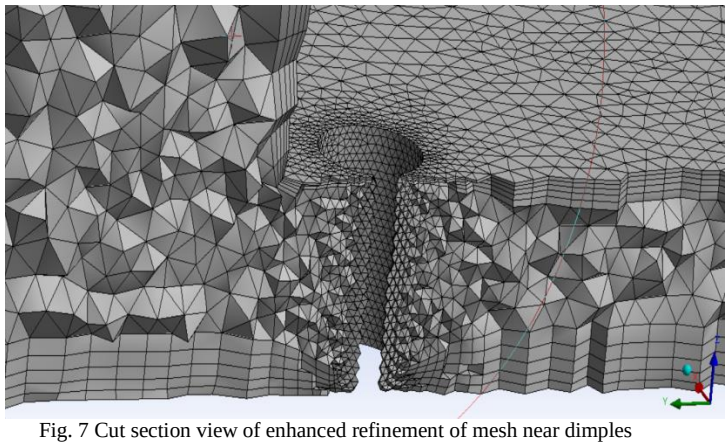


Fig. 7 Cut section view of enhanced refinement of mesh near dimples

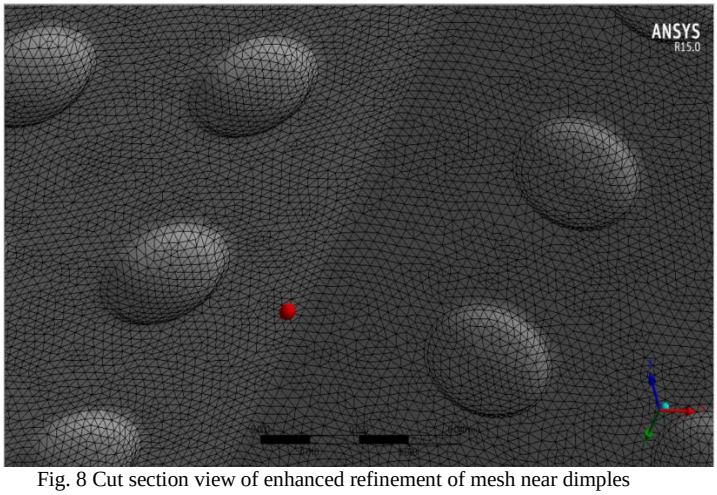


Fig. 8 Cut section view of enhanced refinement of mesh near dimples

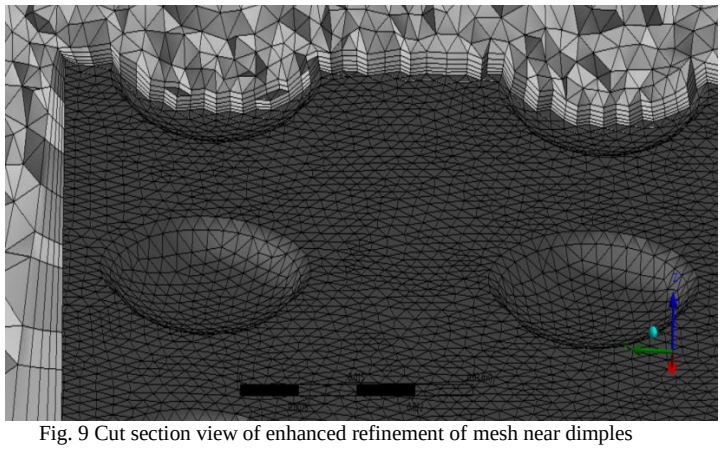


Fig. 9 Cut section view of enhanced refinement of mesh near dimples

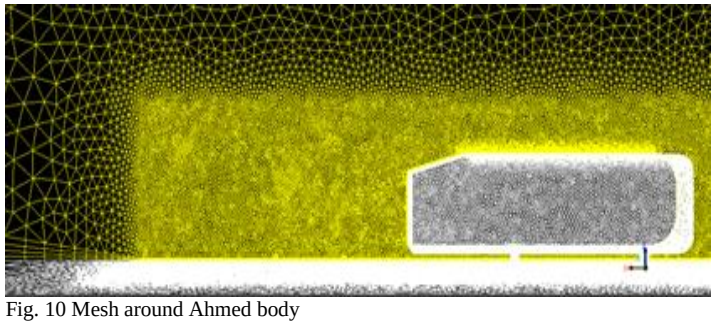


Fig. 10 Mesh around Ahmed body

D. *Turbulence Model*

In this paper, the turbulence model chosen was a realizable *k-ϵ* model with non-equilibrium wall functions. This was done due to its robustness and high degree of versatility, which tends to produce accurate solutions. Also the computational time required for performing Large Eddy Simulation (LES) was proving to be infeasible as compared to Reynolds Averaged Navier-Stokes (RANS) model. Similarly, Direct Numerical Simulation (DNS) would've required a grid with an enormously high level of mesh resolution. All of the above reasons led to the selection of RANS equations with the *k-ϵ* turbulence model. It comprises of two transport equations to represent the turbulent properties of the flow. The first transport variable is the kinetic energy term, *k*. It is the variable to determine the turbulent energy production.

$$\frac{\partial}{\partial t}(\rho k) + \frac{\partial}{\partial x_i}(\rho k u_j) = \frac{\partial}{\partial x_i}\left[\left(\mu + \frac{\mu_t}{\sigma_k}\right).\frac{\partial k}{\partial x_j}\right] + G_k + G_b - \rho\epsilon - Y_M + S_k$$

The second transport variable is the turbulent dissipation term, ϵ. It is the variable to determine the scales of the turbulence.

$$\frac{\partial}{\partial t}(\rho\epsilon) + \frac{\partial}{\partial x_j}(\rho\epsilon u_j) = \frac{\partial}{\partial x_j}\left[\left(\mu + \frac{\mu_t}{\sigma_\epsilon}\right).\frac{\partial \epsilon}{\partial x_j}\right] + \rho C_1 S_\epsilon - \rho C_2 \frac{\varepsilon^2}{k+\sqrt{\upsilon\epsilon}} + C_{1\epsilon}\frac{\epsilon}{k}C_{3\epsilon}G_b + S_\epsilon$$

In the equations above, G_k is the generation of turbulence kinetic energy due to the mean velocity gradients. G_b is the generation of turbulence kinetic energy due to buoyancy. Y_m is the contribution of the fluctuating dilatation in compressible turbulence to the overall dissipation rate. $C_{1\epsilon}$ and C_2
σ_k and σ_ϵ re constants and turbulent Prandtl numbers for *k* and ϵ respectively. S_k and S_ϵ are user defined source terms.

E. *Governing Equations* [20]

1) *Continuity Equation:*

$$\frac{\partial \rho}{\partial t} + \nabla.(\rho V) = 0$$

2) *Conservation of Momentum in x –direction:*

$$\frac{\partial(\rho u)}{\partial t} + \frac{\partial(\rho u^2)}{\partial x} + \frac{\partial(\rho uv)}{\partial y} + \frac{\partial(\rho uw)}{\partial z} = -\frac{\partial p}{\partial x} + \frac{\partial\left(\lambda\nabla.V + 2\mu\frac{\partial u}{\partial x}\right)}{\partial x} + \frac{\partial\left(\mu\left[\frac{\partial v}{\partial x} + \frac{\partial u}{\partial y}\right]\right)}{\partial y} + \frac{\partial\left(\mu\left[\frac{\partial u}{\partial z} + \frac{\partial w}{\partial x}\right]\right)}{\partial z} + \rho f_x$$

3)

4) *Conservation of Momentum in y –direction:*

$$\frac{\partial(\rho v)}{\partial t} + \frac{\partial(\rho uv)}{\partial x} + \frac{\partial(\rho v^2)}{\partial y} + \frac{\partial(\rho vw)}{\partial z} = -\frac{\partial p}{\partial y} + \frac{\partial\left(\mu\left[\frac{\partial v}{\partial x} + \frac{\partial u}{\partial y}\right]\right)}{\partial x} + \frac{\partial\left(\lambda\nabla.V + 2\mu\frac{\partial v}{\partial y}\right)}{\partial y} + \frac{\partial\left(\mu\left[\frac{\partial w}{\partial y} + \frac{\partial v}{\partial z}\right]\right)}{\partial z} + \rho f_y$$

5) *Conservation of Momentum in z –direction:*

$$\frac{\partial(\rho w)}{\partial t} + \frac{\partial(\rho uw)}{\partial x} + \frac{\partial(\rho vw)}{\partial z} + \frac{\partial(\rho w^2)}{\partial y} = -\frac{\partial p}{\partial z} + \frac{\partial\left(\mu\left[\frac{\partial u}{\partial z} + \frac{\partial w}{\partial x}\right]\right)}{\partial x} + \frac{\partial\left(\mu\left[\frac{\partial w}{\partial y} + \frac{\partial v}{\partial z}\right]\right)}{\partial y} + \frac{\partial\left(\lambda\nabla.V + 2\mu\frac{\partial w}{\partial z}\right)}{\partial z} + \rho f_z$$

F. *Boundary Conditions*

In this work, the free stream velocity has been set to 40 m/s at the inlet (with a turbulence intensity of 1%), related to the overall length of the model that gives the Reynolds number as;

$$R_e = \frac{\rho UL}{\mu} = \frac{1.225 \times 40 \times 1.044}{1.789 \times 10^{-5}} = 2.86\times 10^6$$

Where ρ is the density of air; is the flow velocity; *L* is the characteristic length of the car model; μ is the coefficient of dynamic viscosity of air.

The pressure outlet is maintained at a gauge pressure of 0 Bar with 5% turbulence intensity at the exit.

In case of the mid-plane which is parallel to the longitudinal axis of the Ahmed Body and passes through the geometric centre, it was kept as a symmetry plane, which eased up the calculation time required for the simulation.

No slip conditions as applicable on the surfaces of the body, along with zero shear stresses acting on the walls of the fluid domain or the control volume were taken into consideration.

Reference values were computed from the velocity inlet with respect to the global/absolute co-ordinate system.

IV. Setup

Parallel processing was employed for finding out the solution up to single precision. A total of four threads were run simultaneously to carry out the simulations.

Upon defining the conditions in the setup instead of Density based, Pressure Based Navier Stokes (PBNS) was utilised (gravitational effects neglected). Originally, PBNS was used for working with incompressible flows, also since the maximum velocity in the flow-field will be less than Mach number 0.3, relative density changes will be less than 5 per cent. Another reason is that the convergence in density based heavily depends upon several factors since density is derived from the equation of continuity, whereas the state equation is used to obtain the values of pressure.

The solution scheme employed is the coupled scheme for the entire iterations of the uncontrolled (non-dimpled) case while for the controlled case the solution was initially solved using the simple scheme (first order upwind) so as to ensure a decreasing trend for continuity. Later after about 1200 iterations the solving scheme was shifted to the coupled scheme (second order upwind), which takes second order approximations for solving the turbulent kinetic energy and dissipation terms i.e. k and ϵ for ultimately solving the drag value.

Hybrid initialisation was used. The convergence criteria were kept up to e^{-5}. This gives considerably accurate solutions.

Also oscillation of continuity provided an indicator that the result was converged.

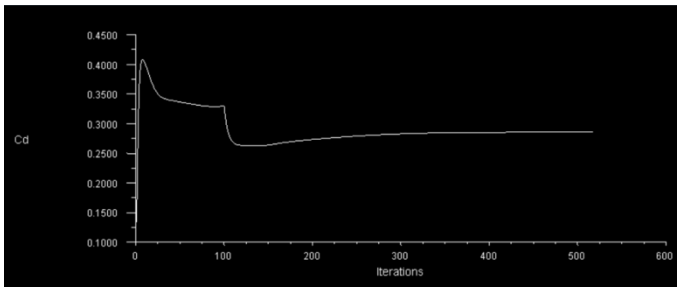


Fig. 11 Cd convergence history for the non-dimpled Ahmed body

V. Results

A. Static Pressure Contour

Figures 11 and 12 depict the distribution of static pressure over the grooved surfaces. The static pressure at velocity inlet and the pressure outlet of the domain is taken to be 0 Bar (gauge pressure). Although its distribution over the surface is rather uniform for almost the entire surface expect a few regions which are of specific interest. As the flow passes over the leading edge of the slant face it accelerates thereby reducing the static pressure value all along the edge. Also, along the direction of flow the periphery of the dimples reflect a greenish ting showing that the pressure value has mellowed down at those points. This phenomenon is observed due to acceleration in the flow both upstream as well as downstream of the dimple as it encounters the depression, thus creating a low pressure region just around the periphery of the dimple. This pressure differential is higher in the longitudinal direction of flow. Another fact worth mentioning is that the intensity of the low pressure increases as we move towards the outer end/edge of the body. This is due to the stream-wise counter rotating vortices which are formed because of the low pressure prevailing on the slant surface compared to side face. The axis of the vortices so formed is along the direction of the slant.

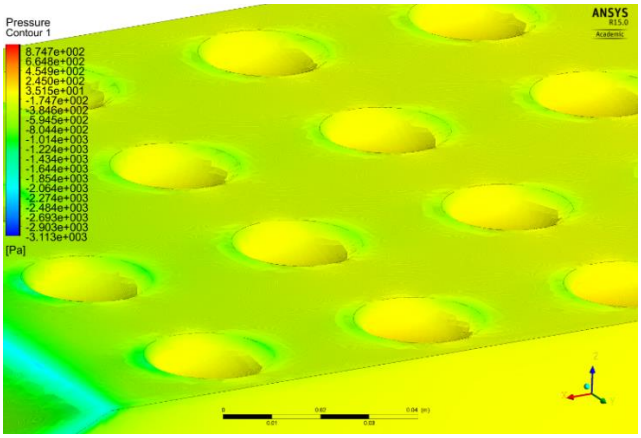


Fig. 12 A surface plot showing the static pressure variation on the top surface and the leading edge of the slant surface

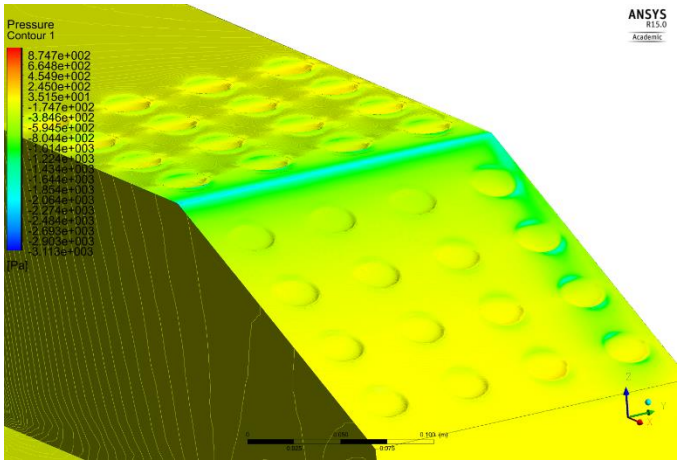


Fig. 13 Low pressure zone created towards the outer edge of the slant surface due to the edge rotating vortices

B. Velocity Volume Rendering

Figure 13 gives a 3-D partially transparent velocity distribution to describe the flow characteristics over the body. As can be seen, there exist 2 major regions of low velocity zone (less than 40m/s) i.e. the one just before the front face or upstream of the body and the other just downstream of the body. The former zone is due to the stagnation of flow at the front face with the highest intensity at the centre point as the flow collides with the body head on. As we move away from the epicentre the intensity subsides as the flow starts gliding over the curved faces though in a constrained manner. The latter low velocity zone is formed due to flow separation taking place and the flow reversals incurred as the flow no longer remains attached to the surface. However, the flow lines ultimately meet further downstream and thus a gradual increase in intensity can be seen. The flow accelerating over the curved faces and over the leading slant edge as well as

remaining attached to the top and bottom faces due to no slip condition are some of the key features visible.

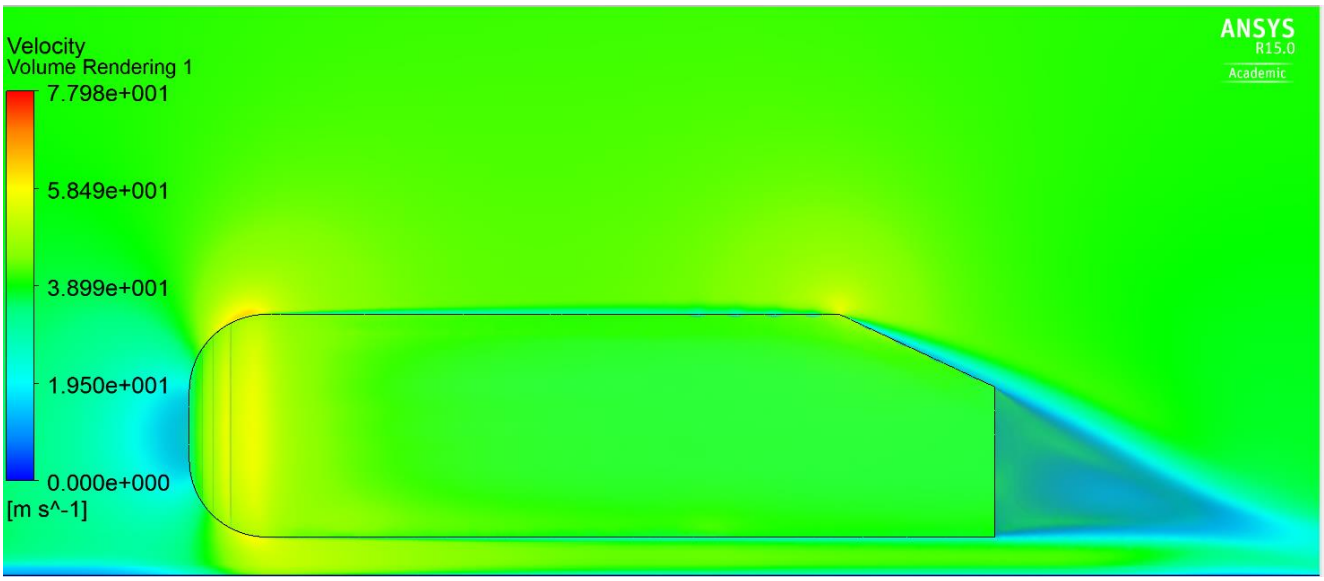
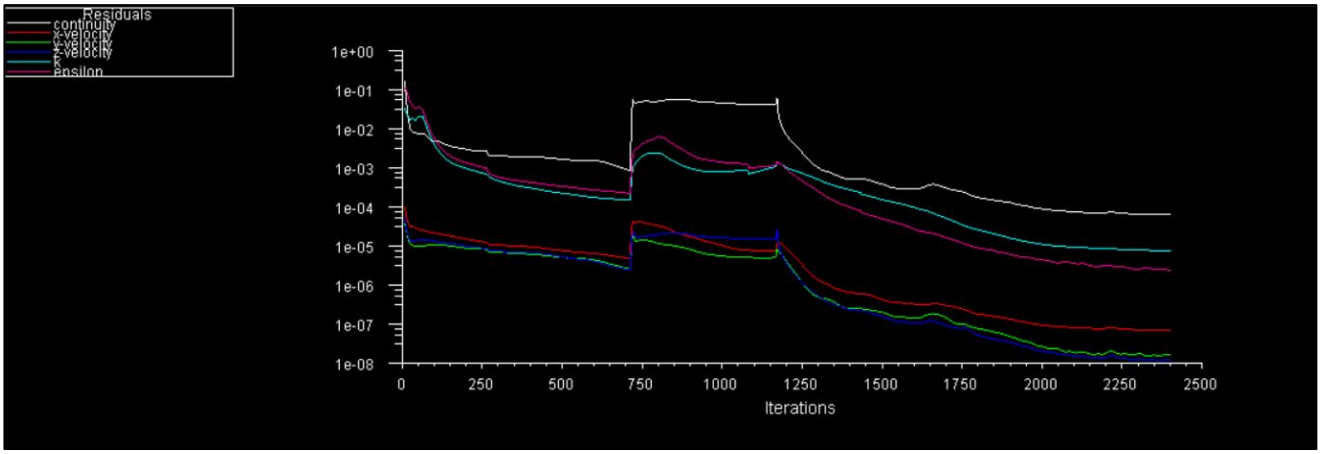


Fig. 14 Velocity volume rendering for the grooved body showing low velocity zones including the most prominent wake region




```
2389  6.6163e-05  7.2066e-08  1.7207e-08  1.2605e-08  7.6109e-06  2.5090e-06  3.6794e-01  2.8781e-01 -1.7449e+02  0.0000e+00  7.5426e+
2390  6.5770e-05  7.2126e-08  1.7186e-08  1.2551e-08  7.5965e-06  2.4926e-06  3.6794e-01  2.8781e-01 -1.7449e+02  0.0000e+00  7.5425e+
2391  6.5584e-05  7.1883e-08  1.7177e-08  1.2469e-08  7.5998e-06  2.4718e-06  3.6794e-01  2.8781e-01 -1.7449e+02  0.0000e+00  7.5425e+
2392  6.5258e-05  7.1981e-08  1.7181e-08  1.2429e-08  7.5855e-06  2.4594e-06  3.6794e-01  2.8781e-01 -1.7449e+02  0.0000e+00  7.5424e+
2393  6.5278e-05  7.1748e-08  1.7210e-08  1.2389e-08  7.5884e-06  2.4410e-06  3.6794e-01  2.8781e-01 -1.7449e+02  0.0000e+00  7.5425e+
2394  6.5281e-05  7.1762e-08  1.7264e-08  1.2321e-08  7.5733e-06  2.4233e-06  3.6794e-01  2.8781e-01 -1.7449e+02  0.0000e+00  7.5425e+
2395  6.5678e-05  7.1649e-08  1.7338e-08  1.2306e-08  7.5774e-06  2.4073e-06  3.6794e-01  2.8781e-01 -1.7449e+02  0.0000e+00  7.5425e+
2396  6.5035e-05  7.1640e-08  1.7311e-08  1.2265e-08  7.5612e-06  2.3887e-06  3.6794e-01  2.8781e-01 -1.7449e+02  0.0000e+00  7.5426e+
iter  continuity  x-velocity  y-velocity  z-velocity           k     epsilon        Cl-1        Cd-1  surf-mon-1  surf-mon-2  surf-mor
2397  6.4760e-05  7.1555e-08  1.7146e-08  1.2267e-08  7.5656e-06  2.3719e-06  3.6794e-01  2.8781e-01 -1.7449e+02  0.0000e+00  7.5426e+
2398  6.5111e-05  7.1681e-08  1.6978e-08  1.2219e-08  7.5500e-06  2.3541e-06  3.6794e-01  2.8781e-01 -1.7449e+02  0.0000e+00  7.5426e+
2399  6.5118e-05  7.1532e-08  1.6821e-08  1.2210e-08  7.5551e-06  2.3434e-06  3.6793e-01  2.8781e-01 -1.7449e+02  0.0000e+00  7.5426e+
iting "| gzip -2cf > C:\Users\Shabir Grover\Desktop\5th sem\minor project\Good simulations\donald trump\donald trump_files\dp0\FFF\Flu
iting temporary file C:\Users\SHABIR~1\AppData\Local\Temp\fluntgz-41968 ...
ne.

2400  6.4859e-05  7.1669e-08  1.6681e-08  1.2172e-08  7.5398e-06  2.3310e-06  3.6793e-01  2.8781e-01 -1.7449e+02  0.0000e+00  7.5425e+
```

Fig. 15 Convergence history graph for the controlled case - abruptness due to change in solving scheme procedure.

VI. Conclusions

The velocity renderings and the pressure variations observed are in synchronisation with the experimental results. The dimple parameters were chosen based on the theoretical study of the flow around the body and the past results which led to a 0.3 % reduction in drag value. But there exists even greater scope for optimisation of the dimple geometry and its positioning over the body surfaces which can lead to a massive reduction in the drag coefficient.

Acknowledgment

The success of the completion of this project is strongly attributed to Dr. B.B. Arora under whose guidance the project has been taken. His knowledge on the subject and the constant motivation provided did go a long way which shaped the outcome in a beautiful manner. Also not to

forget the constant support provided by the parents, by the lab assistant, by our class peers and the blessings of the Almighty.

REFERENCES

[1] Hsu, F.-H., Davis, R. L., Drag reduction of tractor-trailers using optimized add-on devices, Journal. Fluids Engineering, 132(8), 084504. doi:10.1115/1.4001587

[2] C. K. Chear, S. S. Dol, Vehicle Aerodynamics: Drag Reduction by Surface Dimples, International Journal of Mechanical, Aerospace, Industrial, Mechatronic and Manufacturing Engineering Vol: 9, No: 1, 2015.

[3] S. F. Wong, S. S. Dol, Simulation study on vehicle drag reduction, International Journal of Mechanical, Aerospace, Industrial, Mechatronic and Manufacturing Engineering Vol:10, No:3, 2016

[4] Katsumi Aoki, Koji Muto, Hiroo Okanaga, Mechanism of Drag Reduction by Dimple Structures on a Sphere, Journal of Fluid Science and Technology Vol. 7, No. 1, 2012.

[5] Seong-Ho Seo, Chung-Do Nam, Cheol-Hyun Hong, Drag Reduction of a Bluff Body by Grooves Laid Out by Design of Experiment, Journal of Fluids Engineering, Nov. 2013, Vol. 135 / 111202-1.

[6] Laurent Dumas, Optimization and Computational Fluid Dynamics, pp 191-215, Springer Berlin Heidelberg Germany, 2008.

[7] Alaman Altaf, Ashraf A. Omar and Waqar Asrar, Review of Passive Drag Reduction Tecniques for Bluff Road Vehicles, IIUM Engineering Journal, Vol. 15, No. 1, 2014.

[8] Marco Lanfrit, Best practice guidelines for handling Automotive External Aerodynamics with FLUENT, Fluent Deutschland GmbH Germany.

[9] Mohamed-Kassim and Filippone, A. "Fuel savings on a heavy vehicle via aerodynamic drag reduction", Transportation Research Part D Vol.15. pp 275-285. (2010).

[10] Chainani. A and Perera. N, CFD Investigation of Airflow on a Model Radio Control Race Car, WCE 2008 Vol II, July 2 - 4, 2008, London, U.K.

[11] Yeung, W. W. H. and Parkinson, G. V., Analysis and Modeling of Pressure Recovery for Separated Reattaching Flows, ASME Journal of Fluids Engineering, Vol. 126, No. 3, pp. 355–361, 2004.

[12] Manoj Kumar, Arora, B. B. and Subhashis Maji, "Analysis of flow separation in wide angle annular diffusers," International Journal of Applied Engineering Research, Vol.5, No.20. (2010) pp. 3419-3428, ISSN 0973-4562

[13] B. B. Arora, Manoj Kumar and Subhashis Maji, "Study of Inlet conditions on Diffuser Performance," International Journal of Theoretical and applied Mechanics, Vol.5, No.2. (2010) pp. 201-221, ISSN 09736085.

[14] Noor, M. M., Wandel, Andrew P. and Yusaf, Talal, "Detail guide for CFD on the simulation of Biogas combustion in bluff body mild burner," International Conference on Mechanical Engineering Research (ICMER2013), 1-3 July 2013

[15] Yiping Wang, Cheng Wu, Gangfeng Tan and Yadong Deng, "Reduction in the aerodynamic drag around a generic vehicle by using a non-smooth surface", Journal of Automobile Engineering.

[16] Wolf-Heinrich Hucho, "Aerodynamics of Road Vehicles", SAE International, 1998.

[17] Joseph Katz, "Race Car Aerodynamics: Designing for Speed", 1995.

[18] Ahmed, S.R., Ramm, R., Faltin, G. : Some salient features of the time averaged ground vehicle wake, SAE Paper 840300 (1984)

[19] Yunus A. Çengel, John M. Cimbala, "Fluid Mechanics: Fundamentals and Applications", 2006.

[20] John D. Anderson, Jr. "Computational Fluid Dynamics: The Basics with Applocations", 1995

View publication stats

International Conference on Advanced Material Technologies (ICAMT)-2016

27th and 28th December 2016

Dadi Institute of Engineering and Technology (DIET), Visakhapatnam, Andhra Pradesh, India.

Application of Gaussian as Edge Detector for Image Enhancement of Ancient Manuscripts

N.Jayanthi[1] and S.Indu[2]

1. Assistant Professor, ECE Department, Delhi Technological University, Delhi-110042, India

2. Professor, ECE Department, Delhi Technological University, Delhi-110042, India

Abstract: Binarization is an essential step for the Digitization of Ancient Manuscript images. Degradations in the manuscripts, such as, uneven light, low complexity, smears and high noise densities frequently make thresholding of the manuscript images a troublesome task. The purpose of study is to preserve the information contained in documents in digital form. To improve the accuracy of machine reading for camera-based Manuscript images, a simple and novel approach has been proposed based on Difference of Gaussians: a second order edge detector, followed by modified Niblack's local thresholding. The proposed strategy has been correlated with existing techniques. The numerical result stating average PSNR value 19.21dB validates that the performance of proposed method is superior to other five well known binarization techniques.

Keywords: ***Binarization, Difference of Gaussians, global thresholding, Local thresholding, edge detection.***

1. INTRODUCTION

The evolution of modern imaging devices for Image enhancement and restoration plays a key part in manuscript document processing related applications, for example text recognition and image retrieval. In many cases the documents are deteriorated because of age, dust or due to ink smudging. The fundamental task is to digitize a manuscript image so that, background and foreground content are unmistakably isolated. In binarization there is a need of segmenting the document into two grayscale levels, which can be performed either locally [4], [6], [9],[10] or globally [1], [7], [8].

In the past a great deal of global thresholding concepts were proposed (e.g. Otsu's method [2], Illingworth and Kittler's method [3]). But global thresholding fails to remove noise from highly degraded images because of local degradation, poor illumination and complex background texture. Local thresholding is being utilized in [7] to achieve the goal of extracting a foreground part (text) from background (non text). Local thresholding achieves binarization by considering each and every pixel with neighborhood pixels [4]. Niblack proposed a local thresholding procedure by computing a threshold factor using local statistical parameters namely mean and standard deviation [4].

In this manuscript, we present a concept based on difference of Gaussian followed by modified Niblack's local thresholding [4] and morphological post processing. Where the difference of Gaussian results in preservation of the edge information and thresholding using modified Niblack's local algorithm produces binarized image, the final binarized image can be digitized with the help of OCR.

The paper is indexed as: Section 2.1 and 2.2 clarifies the importance of Gaussian Filter and difference of Gaussian also depicts Niblack's thresholding algorithm. Section 2.3 introduces the

proposed algorithm. Section 3 states the results of proposed strategy to access the framework. Section 4 finally concludes the work.

2. METHODOLOGY

2.1 Gaussian Filter and Difference of Gaussians:

As a gray image is a two dimensional object, two dimensional Gaussian functions is defined below.

$$g(a,b) = \frac{1}{2\pi\sigma^2} e^{-\frac{a^2+b^2}{2\sigma^2}} \quad (1)$$

Where a and b are the distances from the origin in the horizontal axis and in the vertical axis respectively, and σ represents the standard deviation of the Gaussian distribution [5 6].

In image processing, difference of Gaussians (DoG) is a second order edge detection algorithm which performs the subtraction between two blurred versions of the image with different blur amounts (σ). Hence DoG acts as a band pass filter for preserving the edge information in an image. Application of Gaussian functions on an image causes reduction in only high frequency spatial information. Subtracting one image from the other conserves spatial information which falls between the ranges of frequencies conserved in the two blurred images.

2.2 Niblack's Local Thresholding Algorithm:

Niblack's thresholding algorithm computes a threshold factor to each pixel by moving a rectangular window over the gray level image [4]. The dimensions of rectangular window can be changed depending upon the complexity of the background. The threshold value is calculated using the local mean and standard deviation of all the pixels in the window and is given by following equations [4]:

$$T_{Niblack} = M + K * SD \quad (3)$$

$$T_{Niblack} = M + K * \sqrt{\frac{\sum (p_i - m)^2}{NP}} \quad (4)$$

Here NP is the total pixels present in gray scale image, T represents the threshold value, M is the mean of gray levels of pixels and k is fixed depending upon the noise in the background and is - 0.2.

2.3 Proposed Method:

The proposed method for enhancement and restoration for manuscript images is described in this section. The flow diagram is shown in Fig.1 and each step is explained in detail in sub-sections.

2.3.1 Difference in Gaussians:

The difference of Gaussian edge detector eliminates high frequency details that generally include random noise removal. It reduces noise in the image by blurring and also preserves the edge information in the image. DoG also removes the low frequency background blotches. Finally the resultant image is normalized to [0, 1].

Equation for DoG is:

$$\Gamma(x,y) = I * (g_{\sigma 1} - g_{\sigma 2}) \quad (5)$$

The output image after application of DoG is denoted by $\Gamma(x,y)$, I is the input gray scale image, $g_{\sigma 1}$ and $g_{\sigma 1}$ are Gaussian functions, provided σ2 > σ1.

2.3.2 Modified Niblack's Local Thresholding Algorithm:

In the proposed method threshold value is calculated using variance instead of standard deviation and the constant k is chosen in the range 0.15 to 0.30. Hence modified equation for calculation of threshold is:

$$T_{Niblack} = M + K * Var \quad (6)$$

***2.3.3** Post Processing:*

In the last step, the binarized image is applied with morphological operation to sharpen the text details in the image.

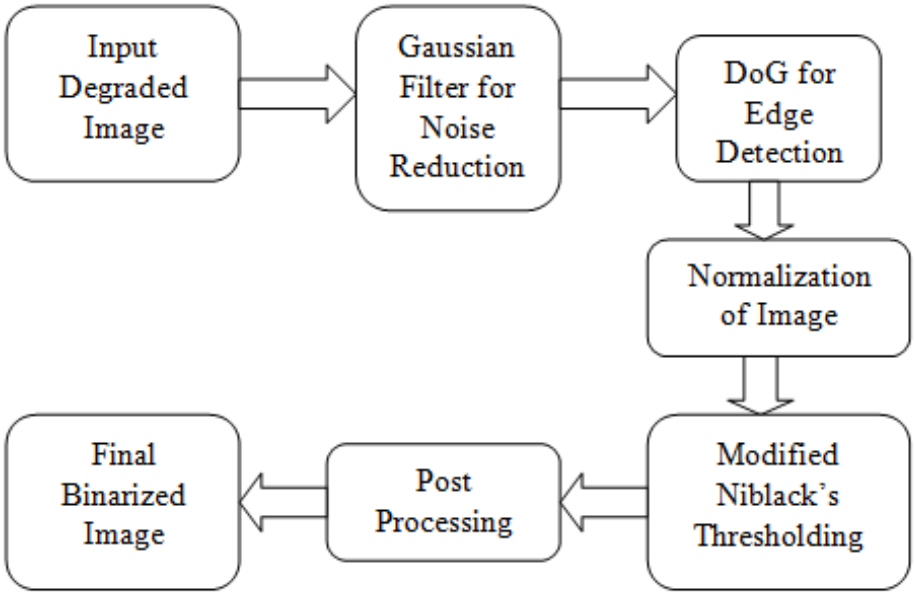
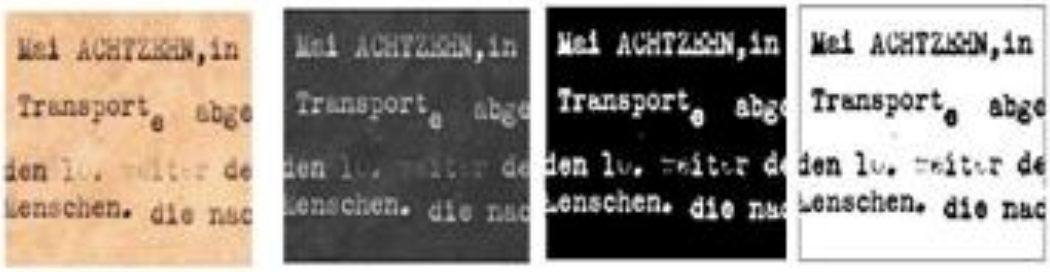


Figure 1: Flow Chart

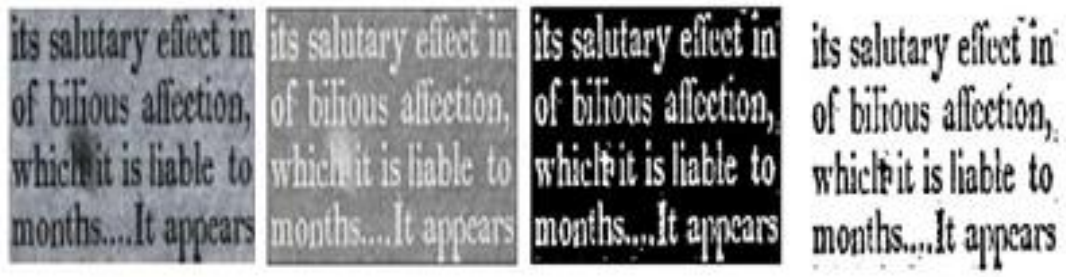
3. EXPERIMENTAL RESULTS

The proposed method is evaluated on a set of 80 images including DIBCO-2009 [11] standard data set. Table 1 shows comparison of PSNR value of proposed technique with the existing binarization methods. Figure 4 and 5 shows that the proposed strategy is superior to contemporary Global and Local thresholding methods. Experimental results show that most of the documents are satisfactorily denoised. Figure 2 and 3 shows output and intermediate stages of the proposed method.



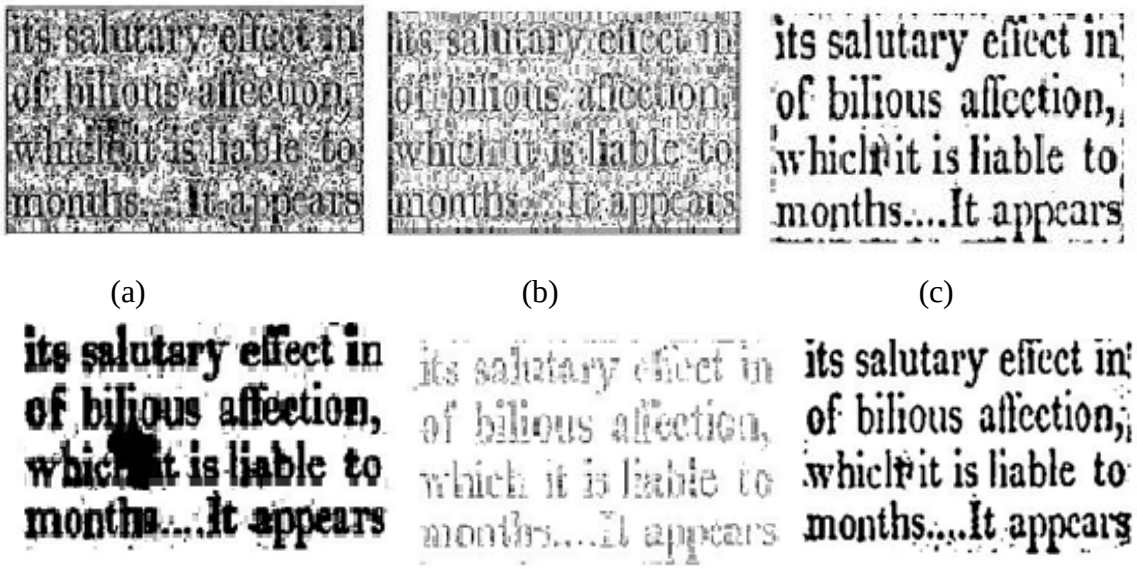
(a) (b) (c) (d)

Figure **2** (a) Input Image, (b) output after application of DoG (c) Result of applying modified Niblack thresholding on fig 2(b), (d) Final resultant image of proposed method



(a) (b) (c) (d)

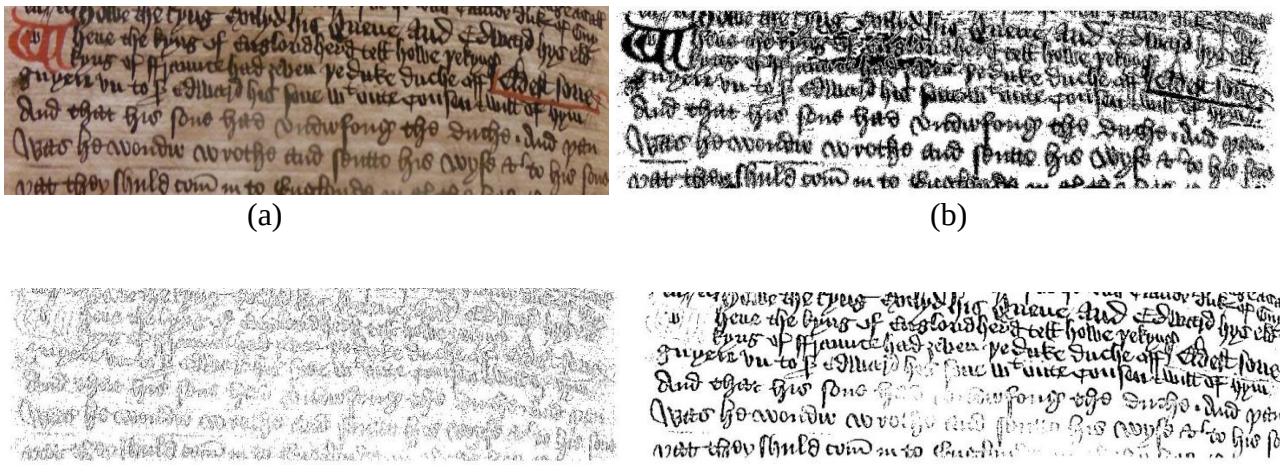
Figure 3: (a) Input Image, (b) output after application of DoG (c) Result of applying modified Niblack thresholding on fig 2(b), (d) Final resultant image of proposed method



(a) (b) (c)

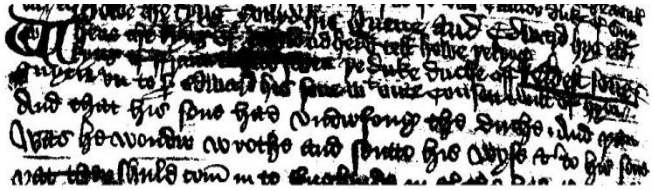
(d) (e) (f)

Figure 4: Result of proposed binarization method in comparison with some well known methods of fig 3a. (a) Bernsen's method, (b) Niblack's method, (c) Nick's method, (d) Otsu's method, (e) Sauvola's method and (f) proposed method.



(a) (b)

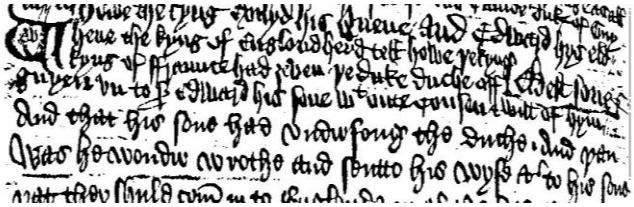
(c) (d)



(e)



(f)



(g)

Figure 5: Result of proposed method in comparison with some well known methods. (a) Input image (b) Bernsen's method, (c) Niblack's method, (d) Nick's method, (e) Otsu's method, (f) Sauvola's method and (g) proposed method

The performance is validated by calculating Peak Signal Noise Ratio (PSNR) and Mean Square Error (MSE). The mathematical formula for MSE and PSNR are:

$$MSE = \frac{1}{MN}\sum\sum\left(k(x,y) - g(x,y)\right)^2 \tag{7}$$

$$PSNR = 10\log\left(\frac{mxi * mxi}{MSE}\right)dB \tag{8}$$

Where k(x, y), g(x, y) and mxi are the output image, input image and maximum intensity of the pixels in image respectively. In table 1 the PSNR value of proposed method (performed on DIBCO 2009 data set) is compared with some standard binarization methods. The numerical results stating average PSNR value 19.21dB validates that the execution of proposed strategy is better than other five binarization methods.

TABLE 1: COMPARATIVE RESULTS

Method	**PSNR(dB)**
OTSU [2]	15.89
NIBLACK'S [4]	10.89
SAUVOLA [9]	9.39
BERSEN [10]	15.01
NICK [12]	18.98
Proposed Method	19.21

4. CONCLUSION

In this paper, hybrid technique by linking the difference of Gaussian and modified Niblack's local thresholding method has been proposed to improve the legibility of manuscript images for better binarization. Results state that the proposed method is producing a binarized image in which background noise is eliminated and the texture information is enhanced. The performance is validated using MSE and PSNR values. Figure 4 and 5 also validates the superiority of proposed method over well known methods. However the method fails to produce better binarization if the manuscript images

having very low contrast between text and the non text portion. Hence addressing the ancient manuscripts with the above said problem will be taken up as future work.

ACKNOWLEDGMENT

We would like to thank Mr. Abhilash Gaur for the data collection of the manuscript images.

REFERENCES

[1] P. K. Sahoo, S. Soltani, A. K. C. Wong, A survey of thresholding techniques, Computer Vision, Graphics Image Processing, 41 (2), 233&260, 1988

[2] N.Otsu, "A threshold selection method from a gray level histograms", IEEE Trans.Systems, Man, Cybernet., 9(1),1979, pp.62- 66

[3] J. Kittler and J. Illingworth , " Minimum error thresholding", Pattern Recogn. 19, 1986, pp. 41-47.

[4] W. Niblack, "An Introduction to Image Processing", Prentice-Hall, Englewood Cliffs, NJ, 1986, pp. 115-116.

[5] R. C. Gonzalez., R. E. Woods, Digital Image Processing,Third Edition,Pearson Education Inc.,2008

[6]. B Gangamma, Srikanta Murthy K, Arun Vikas Singh, "Restoration of Degraded Historical Document Image", Journal of Emerging Trends in Computing and Information Sciences, Vol. 3,I ssue. 5,M ay 2012,I SSN 2079-8407,p ages 792-798

[7] B. Sankur and M. Sczgin. "Image thrcsholdirig techniques. A survey over categories", Pattern Recognition, :!001

[8] Oivind Due Trier , Torfinn Taxt, "Evaluation of Binarization Methods for Document lmages", IEEE Transactions on Pattern Analysis and Machine intelligence, v.17 n.3, p.312-315. March 1995.

[9] J. Sauvola and M. Pietikainen, " Adaptive Document Image Binarization", Pattern Recognition, 33(2), pp.255-236, 2000.

[10] J. Bersen, "Dynamic Thresholding of Gray-level Images", Proc. International Conference on Pattern recognition, 1215-1255, 1986

[11] Document Image Binarization Contest DIBCO", 2009.

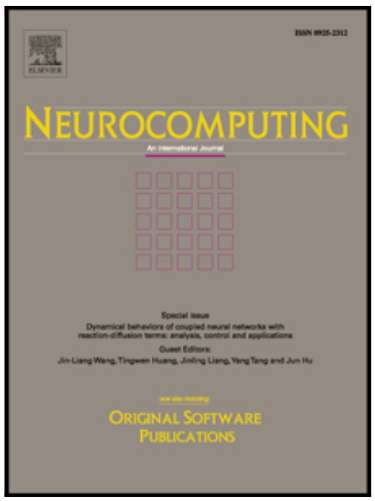


N. Jayanthi received her M.Tech. degree in 2007 from Department of Electronics and Communication Engineering, National Institute of Technology, Tiruchirappalli, Tamilnadu. She had been working as a Assistant Professor for the past 9 years in the Department of Electronics and Communication Engineering, Delhi Technological University, Delhi. Currently she is working towards her Ph.D degree in Image Processing and Applications. Her area of interest is Image Processing, Machine Learning and Communication System.



Dr. S. Indu received her PhD. degree in 2012 from Department of Electronics and Communication Engineering, Delhi University, Delhi. She is working as Professor having 18 years of teaching experience and presently holds the position of Head of the Department in the Department of Electronics and Communication Engineering, Delhi Technological University, Delhi. Her area of interest is Image Processing, Computer Vision and Wireless Sensor Networks and in these areas she has published several research papers. She also holds position of Branch Counsellor IEEE DTU Branch and worked on several DST sponsored projects.

Accepted Manuscript



Automatic Texture Defect Detection using Gaussian Mixture Entropy Modeling

Seba Susan , Monika Sharma

PII: S0925-2312(17)30291-6
DOI: 10.1016/j.neucom.2017.02.021
Reference: NEUCOM 18087

To appear in: *Neurocomputing*

Received date: 15 July 2015
Revised date: 27 May 2016
Accepted date: 6 February 2017

Please cite this article as: Seba Susan , Monika Sharma , Automatic Texture Defect Detection using Gaussian Mixture Entropy Modeling, *Neurocomputing* (2017), doi: 10.1016/j.neucom.2017.02.021

This is a PDF file of an unedited manuscript that has been accepted for publication. As a service to our customers we are providing this early version of the manuscript. The manuscript will undergo copyediting, typesetting, and review of the resulting proof before it is published in its final form. Please note that during the production process errors may be discovered which could affect the content, and all legal disclaimers that apply to the journal pertain.

ACCEPTED MANUSCRIPT

Automatic Texture Defect Detection using Gaussian Mixture Entropy Modeling

Seba Susan, Monika Sharma
Department of Computer Science & Engineering,
Delhi Technological University, New Delhi, India

***Abstract*—In this paper we propose a new unsupervised, automated texture defect detection that does not require any user-inputs and yields high accuracies at the same time. To achieve this end we use the non-extensive entropy with Gaussian gain as the regularity index computed locally from texture patches through a sliding window approach. The optimum window size is determined by modeling the entropy values by a two-mode Gaussian mixture model and checking for the minimum entropy of the mode-probabilities. The outlier entropy values corresponding to defective areas are defined as those that exceed thrice the standard deviation as is the norm in statistics. The result is automatic defect detection with no manual intervention. Empirical results on defective texture images from the Brodatz database provide accurate localization of the defect as compared to Chetverikov and Hanbury's maximal regularity method, which requires manual setting of threshold parameters for each type of texture despite of being a benchmark for texture defect detection.**

Keywords- Gaussian Mixture Model, Non-Extensive Entropy with Gaussian Gain, Texture defects, Sliding window approach, Texture Regularity

I. INTRODUCTION

Texture defect detection finds its uses in the textile industry for automatic fabric inspection, and also has the potential for contributing to modern day video-surveillance and abnormality detection. Texture defect detection techniques are broadly classified into statistical methods that are based on gray-level co-occurrence matrices and the transform methods an example being Gabor filters [1]. A more explicit categorization in [2] groups fabric defect detection techniques into motif-based methods, which consider the characteristics of the smallest pattern unit or motif, and the non-motif based methods. The non-

ACCEPTED MANUSCRIPT

ACCEPTED MANUSCRIPT

motif methods are further categorized into statistical, spectral or transform-based, model-based, learning, structural and hybrid approaches. Texture is a nebulous concept based on the human perception of the arrangement of threads in a woven fabric [3]. Equivalently, the definition extends to the arrangement of pixels in an image in the form of a repetitive pattern. The degree of repetitiveness of the pattern decides how regular the texture is. Several measurements have been proposed in literature to represent the regularity of a texture. One measure that is of significance is Maximal Regularity (MR) defined by Chetverikov and Hanbury [4] which indicates the dominant direction for strongest periodicity. The irregular regions of the texture having lower values of MR were labeled as texture defects. In an earlier work [5], Chetverikov had discriminated between position, intensity and directional regularity in textures with the latter being a combination of the former two. The Maximal Regularity is in fact the maximum directional regularity, and the defects so labeled are stated to agree with human perception. Texture periodicity is used in [6] to decide the size of the Gabor kernels, and hierarchical clustering in the Gabor space extracts the texture defects. In [7] two methods are proposed for texture defect detection based on the regularity of the texture. An optimal Gabor filter with parameters being optimized by the Genetic algorithm is proposed for random textures. For regular textures, a distance matching function computes the size of the patterned unit which in turn is used to identify defective patterns.

Segmentation of defects directly from images without any regularity measurement is not successful in all cases as observed from the works of [8] which uses median based thresholding, [9] which combines edge detection with dilation and blob analysis and [10] which proposes a fast bi-level thresholding for defect segmentation. Segmentation procedures perform poorly for complex defects. Learning of defects was achieved using the neural networks in [11] and support-vector machines in [12]. In both cases gray-level neighboring pixel values with dimensionality reduction was applied as training input. Supervised detection of defects was also proposed in [13] using an Adaptive Subspace Self-Organizing Map architecture. The real-time computation of defects [14] is a major hurdle for learning techniques along with the additional requirement for adequate training of the defects whose possibilities are infinite. In [15] defect-free fabric images are used to build the over-complete basis set via sparse coding. The projections of the defective fabric patch over the over-complete basis set are the features of interest which together with the features of the neighboring patches are compared with the standard features for defect-free images. Gabor and Fourier transformations constitute the spectral techniques used to localize defects. A Gabor filter bank with principal component analysis is applied on texture patches in [16] and the Euclidean norm of features is used to detect a defect. Localized frequency components in the Fourier Transform in non-overlapping, concentric rings have been used for texture defect detection in [17]. Only certain types of defects are detected efficiently through such Fourier analysis

ACCEPTED MANUSCRIPT

such as: missing end, broken fabric and oily fabric [18]. Defect segmentation is viewed as a foreground (defect) versus background (texture) separation problem in [19] and is solved by low-rank matrix reconstruction in which the corrupt entries correspond to defects. A real-time defect detection is proposed in [20] using Gabor filters whose parameters are optimized using composite differential evolution.

The regularity of a texture pattern can also be construed from the ambiguity associated with the pattern. A common measure for uncertainty or ambiguity is entropy. Lower the entropy the higher the repetitivity of the pattern and the more regular is the texture. Entropy has been used in the past as a part of feature sets for texture identification [21] and texture defect detection [22]. However recently, a new form of entropy was used successfully as a single feature for texture identification and categorization [23]. The referred entropy is the non-extensive entropy with Gaussian gain, which being non-additive can represent the long-range correlations in periodic textures. In this paper we utilize this entropy for localizing texture defects through Gaussian mixture entropy modeling. The organization of our paper is as follows: The automated texture defect detection is proposed in Section II, the experimental results are discussed in Section III and the overall conclusions are drawn in Section IV.

II. AUTOMATIC TEXTURE DEFECT DETECTION BY GAUSSIAN MIXTURE ENTROPY MODELING

The non-extensive entropy with Gaussian gain as a regularity indicator

The non-extensive entropy with Gaussian gain [23] is defined by

$$H = \sum_{i=1}^{n} p_i e^{-p_i^2} \qquad (1)$$

The distribution $P = \{p_1, p_2, ..., p_n\}$ involved in the entropy computation in (1) pertains to the results of a n-outcome experiment, and it is a complete probability distribution with all the probabilities summing to one. The entropy in (1) was proved in [23] to be a good indicator of the regularity quotient in texture images since its Gaussian information gain function represents accurately the higher probability events in sparse data that fall within the bell of the Gaussian curve. Its ability to detect patterns was utilized in [28] for matching keywords in automata.

Outlier definition for the Non-extensive entropy and the Motivation for our work

The non-extensive entropy with Gaussian gain in (1) can be interpreted as the weighted average of single-sided zero mean Gaussian functions with standard deviation of $1/\sqrt{2}$. The non-extensive entropies of the same texture class approximate a

ACCEPTED MANUSCRIPT

normal distribution for a regular texture since the sum of Gaussians is non-additive [26] and outliers with very low probabilities that deviate more than thrice the standard deviation would not disturb the weighted sum significantly. According to the three-sigma rule in Central Limit Theorem [27], the values exceeding thrice the standard deviation in a normal distribution are labeled as outliers. In this work we aim to detect outliers in texture images which can be interpreted as texture defects. The weighted sum of non-extensive entropies computed from all the windows is stable in a state of order and deviations or spikes indicate some form of abnormality which in our application corresponds to texture defects. The abnormality detection property of the non-extensive entropy with Gaussian gain within a state of order has already been utilized for the detection of alarms in normal crowd movement [26] and the detection of anomalic training patterns in the incremental training of dynamic neural networks [29].

Deciding on the optimum window size for the computation of the entropy is an important part of our work. The defective part of the texture would assume a normal distribution in a similar manner to the non-defective part. The overall probability graph of the defective texture image would thus resemble a two-peak distribution which is modelled by a two-mode Gaussian mixture model. For the optimum window size, the mode probabilities would be highly non-uniform since the defect is a small part of the texture image. The minimum entropy of the mode probabilities would thus indicate the most optimum window size. The corresponding defects are segmented out. The procedure is described below in more detail.

Segmentation of the texture defects from outlier entropy values

The sliding-window approach is followed for entropy computation in which a window of pre-determined size is slided through the image starting from top-left till bottom right. Each time the window slides by 1 pixel position. For a window w of size $N \times N$ in a texture image of size $L \times M$, the entropy in (1) is computed from each of the gray-level co-occurrence matrices along four directions: $0°, 45°, 90°, 135°$ and an offset distance of $offset_dist = round\left(\frac{N}{4} - 1\right)$ (in case of asymmetric texture windows N is the lesser dimension) where the function $round(\cdot)$ rounds off the fraction to the next highest integer. The four entropies are subsequently averaged to obtain a single entropy feature for the window w, as per the procedure outlined in [23]. In this manner, the entropy is computed by sliding the window w throughout the image starting from the top-left corner and ending with the bottom-right corner of the image spanning over W windows. Let $\{H_w\}$ be the set of entropies computed from W windows for the window size $N \times N$ such that $\{H_w\} = \{H_1, H_2, ..., H_W\}$. To

ACCEPTED MANUSCRIPT

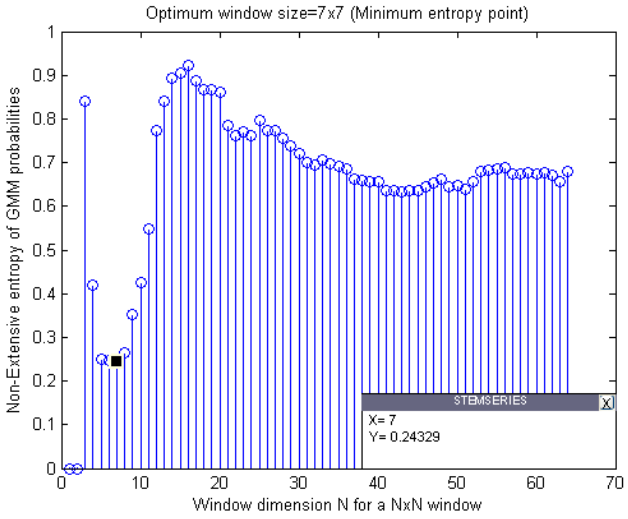
differentiate the defective windows from the normal texture windows we refer to the statistical definition of an outlier in a normally distributed data. The outliers are those whose distance from the mean of the distribution $\overline{H_w}$ exceeds thrice the standard deviation (square-root of the variance: $\text{var}(H_w)$). In the context of our work, the defective windows are those whose entropies' distance from the mean exceed thrice the standard deviation of the entropy distribution. A texture window w is thus declared as defective if

$$\left|H_w - \overline{H_w}\right| > 3\sqrt{\text{var}(H_w)} \qquad (2)$$

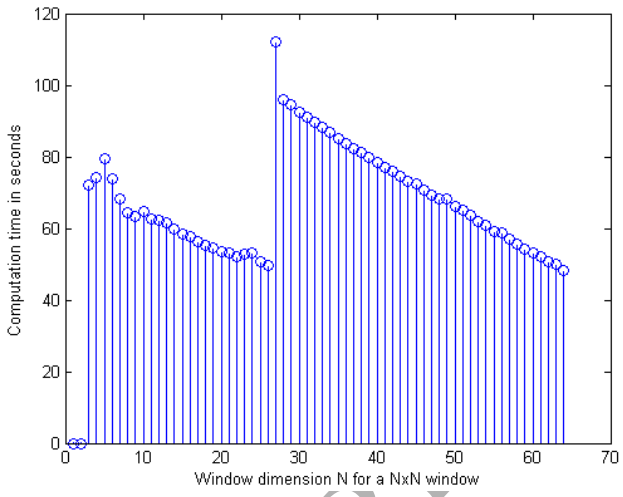
Determining the optimum window size for the computation of entropies

The optimum window size for accurate defect segmentation is determined by modeling the entropy distribution emanating from each window size (window sizes ranging from 3 to 64 tested for a 256x256 image) by a two-component Gaussian mixture model (GMM) [24] and testing for the minimum entropy of the mode probabilities. The number of components or modes is fixed at two since there are two categories: defective and non-defective texture windows. The minimum entropy of the fitted model checks for a condition in which most of the texture windows belong to the first component while the defective windows which are in a minority form the second component of the GMM model. At the non-optimum window sizes, some of the normal texture windows may get classified to the second component resulting in increased uniformity and hence higher entropy. The fact is demonstrated through Fig.1 (a) which shows the entropy graph for different window sizes (for texture sample (v) in our experiment). Fig.1 (a) indicates the optimum window size as 7×7. The computational complexity graph shown in Fig. 1(b) for different window sizes, indicates that the entire process of the computation of entropy from all windows of the texture image takes about 60 seconds (in a 2.6 GHz PC).

ACCEPTED MANUSCRIPT



(a)



(b)

Fig. 1: (a) The entropy graphs based on the GMM probabilities for different window sizes ranging from 3x3 to 64x64 for Sample (v) texture defect image (b) Computational time (in secs) for window sizes ranging from 3x3 to 64x64 for one of the texture images

The fitting of the 2-component Gaussian mixture model (GMM) to the entropy distribution emanating from a defective texture image is a maximum likelihood problem, with the parameters of the model being estimated by the Expectation Maximization (EM) algorithm. GMM has been used in the context of textures before for identifying the class of textures [24]

ACCEPTED MANUSCRIPT

and not for classifying texture patterns as being defective or non-defective. The process of fitting a Gaussian Mixture to unlabelled data is explained below.

Let $\{x\}$ be the unlabelled data and let the number of clusters/Gaussian components be two (number of components is pre-determined by the user). In order to fit a mixture of two Gaussians to the data, we maximize the log-likelihood of the data given by

$$\ln p(x|\pi,\mu,\Sigma) = \ln\left[\sum_{k=1}^{2}\pi_k \mathrm{N}(x|\mu_k,\Sigma_k)\right] \qquad (3)$$

where π_k is the mixing coefficient or the weight assigned to the k[th] Gaussian component $\mathrm{N}(x|\mu_k,\Sigma_k)$ with $\sum_{k=1}^{2}\pi_k = 1$, and $\{\mu_k,\Sigma_k\}$ are the Gaussian parameters (mean and co-variance matrix respectively) to be estimated by the EM algorithm along with the mixing coefficient π_k.

The steps of the proposed automated texture defect detection algorithm are as follows.

1. Read the gray-level input texture image of size $L \times M$
2. For an image window w of size $N \times N$ where $N = 3:64$ do:
   i. Find the four 256x256 gray-level co-occurrence probability matrices corresponding to the angles $0°, 45°, 90°, 135°$ at an offset distance of $offset_dist = round\left(\frac{N}{4} - 1\right)$
   ii. Average the four values of the non-extensive entropies with Gaussian gain, derived from the co-occurrence matrices (using Eq. (1)) and let this value be denoted by H_w.
   iii. Slide the image window across the entire image starting from the top left corner and ending at the bottom right corner. Let the set of entropies computed across all windows be $\{H_w\}$.
   iv. Fit a two-component Gaussian mixture model to the entropy values $\{H_w\}$ with the model parameters being optimized using the Expectation-Maximization algorithm, and also determine the mixing coefficients $\{\pi_k\}, k = 1,2$ which form a probability distribution since $\sum_{k=1}^{2}\pi_k = 1$.
   v. Find the non-extensive entropy of the mixing coefficients as shown below

ACCEPTED MANUSCRIPT

$$H_N = \sum_{k=1}^{2} \pi_k e^{-\pi_k{}^2} \qquad (4)$$

This value is the entropy associated with the GMM model fitted to the window entropy values $\{H_w\}$. Ideally this entropy should be as low as possible for a 'best fit', since defect probabilities are generally much lower than the normal texture probabilities.

3. The optimum window size is the one for which the entropy of the GMM model H_N is minimum in Step 2.

$$optimum_windowsize = \arg\min_{\forall N} H_N \qquad (5)$$

4. The entropies $\{H_w\}$ computed for the optimum window size is the final set of entropies. Let the mean of these entropies be denoted by $\overline{H_w}$ and the variance be denoted by $\mathrm{var}(H_w)$. The defective windows would be those that satisfy the outlier criterion in Eq. (2). The defective windows are highlighted by white and the non-defective windows by black in the result image which is of the same size as that of the original image.

III. EXPERIMENTAL RESULTS AND DISCUSSIONS

The experiments are conducted on complex natural defects in Brodatz texture images downloaded from websites such as [25] which is also used by Chetverikov and Hanbury [4]. The proposed automatic defect detection outlined in the previous section is executed in MATLAB 7.10 on a Pentium 2.6 GHz processor and takes around less than a minute for execution as shown in the computational complexity graph in Fig. 1 (b). The segmented defects are shown in Fig. 2 for eight texture samples, for the proposed method and also for the comparison methods of Chetverikov and Hanbury's Maximal Regularity method [4], Gray-Level Co-occurrence Matrix (GLCM) features [21], Sivabalan and Ghandurai's defect segmentation technique [8]. Fig. 2 indicates visually correct segmentations for the proposed method that tallies with the high *Ncorr:Nfalse* ratios in Table 1 for the proposed method. *Ncorr* is the number of texture windows correctly classified as defective. *Nfalse* is the number of texture windows falsely classified as defective. A high *Ncorr:Nfalse* ratio is preferable. In the absence of ground-truths for defect segmentation we followed the procedure in [4] for the calculation of this ratio and evaluation of the segmentation, by manually taking a decision for each window as being defective or non-defective. All types of defects are successfully segmented by our method as seen from Fig. 2 -linear defects (i,iii,v,vii), blob-shaped defects (ii,iv,vi,viii). The results highlight the utility of our technique for automated and accurate defect detection and segmentation. Chetverikov and

ACCEPTED MANUSCRIPT

Hanbury's Maximal Regularity method [4] though second best requires manual setting of parameters for each texture, and the segmented blocks are large since the minimum allowed window size is around 40x40 resulting in lower precision. The proposed method does not perform as well, in the cases of the defects in Samples (vii) and (viii), due to these defects being random and grainy in nature. The more commonly found defects such as holes or stains in Samples (i) to (vi) are of constant or similar intensity levels and therefore contribute to low entropy for the defective windows. These negative entropy spikes easily pass as outliers satisfying Eq.(2) hence the excellent defect detection results for our method. Random or grainy defects on the other hand are associated with equally likely intensities contributing to high entropy and chaos in the defective region. All of these high entropies may not necessarily satisfy the criterion in (2) and hence are not declared outliers. We also test our algorithm on a defect free image *D101* from the Brodatz database and the results are shown in Fig. 3. A false alarm rate of 7.76% is noted for the proposed method (Fig. 3(b)) for an optimum window size of 3x3. The false alarm rates induced by the other methods are 30.53% for Sivabalan and Ghandurai's segmentation technique [8], 0.006% for GLCM [21] and 0% for Chetverikov and Hanbury's Maximal Regularity method [4] (best performance for defect-free images due to the very small window sizes of the order of 3x3 not being considered at all for the defect computations). Improvising our results on random defects and further reducing the false alarm rates of defect-free textures is the future-scope of our work. Also parallel architectures for the real-time implementation of the sliding window approach for all window sizes shall be explored in future.

IV. CONCLUSION

The non-extensive entropy with Gaussian gain identifies regularity in textures. We propose the outlier definition for this entropy and use it to successfully localize defects or anomalies in textures with high accuracy. The process for finding the optimal window size for localizing defects is automated by Gaussian mixture entropy modeling. Comparisons with state of the art methods for complex defects establish the efficiency of our proposed automated texture defect segmentation.

ACCEPTED MANUSCRIPT

ACCEPTED MANUSCRIPT

REFERENCES

[1] Raheja, Jagdish Lal, Sunil Kumar, and Ankit Chaudhary. "Fabric defect detection based on GLCM and Gabor filter: a comparison." *Optik-International Journal for Light and Electron Optics* 124, no. 23 (2013): 6469-6474

[2] Ngan, Henry YT, Grantham KH Pang, and Nelson HC Yung. "Automated fabric defect detection—a review." *Image and Vision Computing* 29.7 (2011): 442-458.

[3] Nixon, Mark. *Feature extraction & image processing*. Academic Press, 2008.

[4] Chetverikov, Dmitry, and Allan Hanbury. "Finding defects in texture using regularity and local orientation." *Pattern Recognition* 35, no. 10 (2002): 2165-2180.

[5] Chetverikov, Dmitry, "Pattern regularity as a visual key", *Image and Vision Computing* 18 (2000) 975–985.

[6] Asha, V., Nagappa U. Bhajantri, and P. Nagabhushan. "Automatic detection of texture defects using texture-periodicity and Gabor wavelets." *Computer Networks and Intelligent Computing*. Springer Berlin Heidelberg, 2011. 548-553.

[7] Kang, Xuejuan, Panpan Yang, and Junfeng Jing. "Defect Detection on Printed Fabrics Via Gabor Filter and Regular Band⋆." *Journal of Fiber Bioengineering and Informatics* 8, no. 1 (2015): 195-206.

[8] K.N. Sivabalan, Dr. D. Ghanadurai, "Detection of defects in digital texture images using segmentation", *International Journal of Engineering Science and Technology* Vol. 2(10), 2010, 5187-5191.

[9] A. Conci and C. B. Proença, "A computer vision approach to textile inspection," *Text. Res. J.*, vol. 70, pp. 347-350, Apr. 2000.

[10] C-S. Cho, B-M.Chung and M-J. Park, "Development of real-time vision-based fabric inspection system," *IEEE Trans. Industrial Electronics*, vol. 52, no. 4, Aug. 2005.

[11] A. Kumar, "Neural network based detection of local textile defects," *Pattern Recognition*, vol. 36, pp. 1645-1659, 2003.

[12] A. Kumar and H. C. Shen, "Texture inspection for defects using neural networks and support vector machines," Proc. *Intl. Conf. Image Process., ICIP*-2002, pp. 353-356, Rochester, New York, Sep. 2002.

[13] Ruiz-del-Solar, Javier. "TEXSOM: texture segmentation using self-organizing maps." *Neurocomputing* 21, no. 1 (1998): 7-18.

[14] Li, Pengfei, Zhuo Zhao, Lei Zhang, Hongwei Zhang, and Junfeng Jing. "The Real-Time Vision System for Fabric Defect Detection with Combined Approach." In *Image and Graphics*, pp. 460-473. Springer International Publishing, 2015.

[15] Zhu, Qiuping, Minyuan Wu, Jie Li, and Dexiang Deng. "Fabric defect detection via small scale over-complete basis set." *Textile Research Journal* 84, no. 15 (2014): 1634-1649.

[16] Bissi, Lucia, Giuseppe Baruffa, Pisana Placidi, Elisa Ricci, Andrea Scorzoni, and Paolo Valigi. "Automated defect detection in uniform and structured fabrics using Gabor filters and PCA." *Journal of Visual Communication and Image Representation* 24, no. 7 (2013): 838-845.

[17] H. Sari-Sarraf and J. S. Goddard, "On-line optical measurement and monitoring of yarn density in woven fabrics," Proc. *SPIE* 2899, pp. 444-452, 1996.

[18] R.M. Haralick, K.Shanmugam, and I. Dinstein, "Textural Features for Image Classification" , *IEEE Trans. On Systems, Man and Cybernetics*, 1973, pp.610-621.

[19] Cen, Yi-Gang, Rui-Zhen Zhao, Li-Hui Cen, Li-Hong Cui, Zhen-Jiang Miao, and Zhe Wei. "Defect inspection for TFT-LCD images based on the low-rank matrix reconstruction." *Neurocomputing* 149 (2015): 1206-1215.

ACCEPTED MANUSCRIPT

ACCEPTED MANUSCRIPT

[20] Tong, Le, W. K. Wong, and C. K. Kwong. "Differential evolution-based optimal Gabor filter model for fabric inspection." *Neurocomputing* 173 (2016): 1386-1401.

[21] Popescu, Dan, Radu Dobrescu, and Maximilian Nicolae. "Texture classification and defect detection by statistical features." *International Journal of circuits, system and signal processing* 1, no. 1 (2007): 79-84.

[22] I. S. Tsai and M. C. Hu, "Automated inspection of fabric defects using an artificial neural networks," Text. Res. J., vol. 66, pp. 474-482, Jul. 1996.

[23] Susan, Seba, and Madasu Hanmandlu. "A non-extensive entropy feature and its application to texture classification." *Neurocomputing* 120 (2013): 214-225.

[24] Kim, Soo Chang, and Tae Jin Kang. "Texture classification and segmentation using wavelet packet frame and Gaussian mixture model." *Pattern Recognition* 40, no. 4 (2007): 1207-1221.

[25] Chetverikov, Dmitry, "Detecting structural defects", http://athos.vision.sztaki.hu:8080/strucdef/strucdef.html

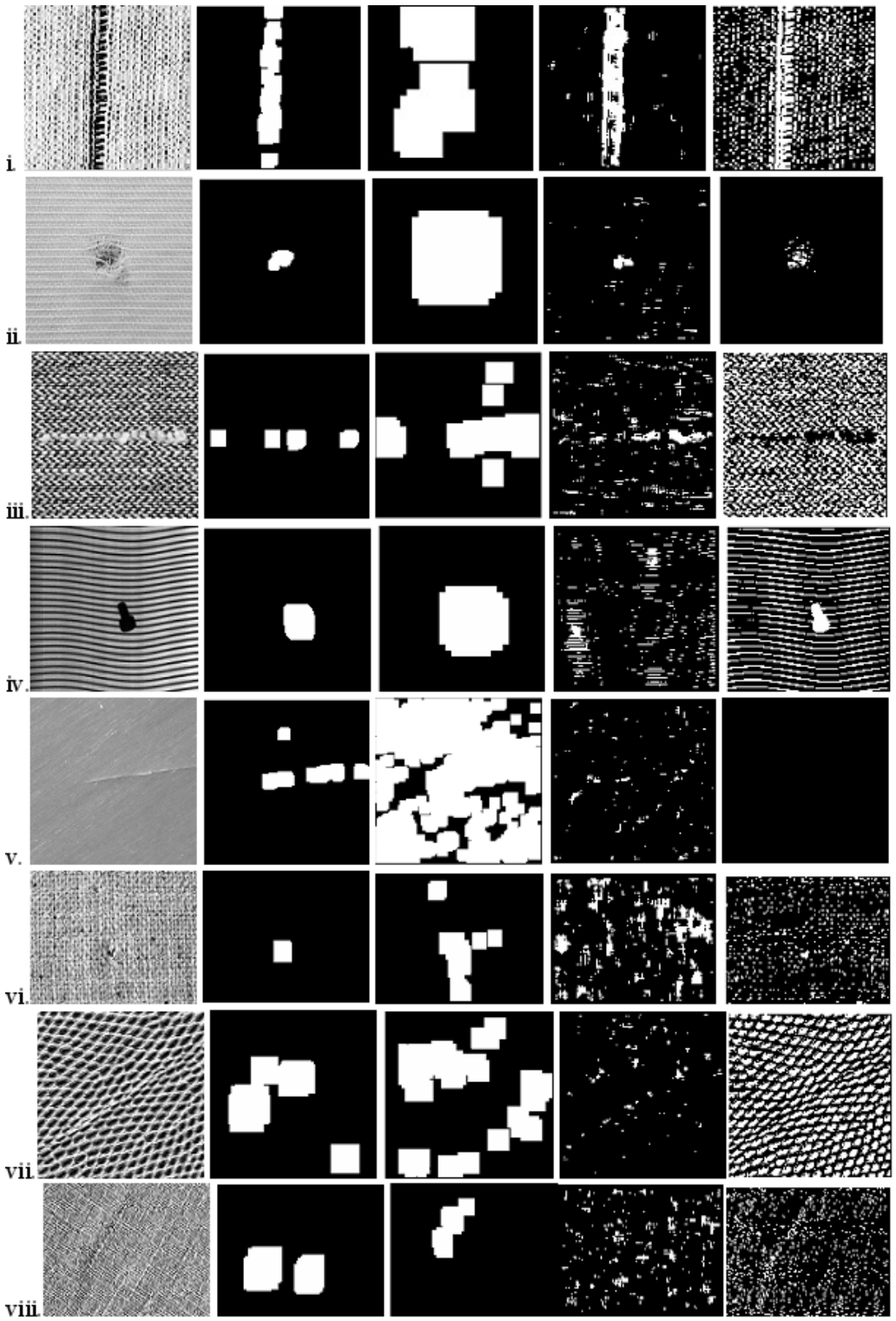
[26] Susan, Seba, and Madasu Hanmandlu, "Unsupervised detection of nonlinearity in motion using weighted average of non-extensive entropies" *Signal Image and Video Processing* 9(3): 511-525 (2015)

[27] F. Pukelsheim, "The three sigma rule", *American Statistician* 48, 88-91, (1994)

[28] Susan, Seba, Shashank Kumar, Rohen Agrawal, and Kartik Yadav. "Statistical Keyword Matching using Automata." *International Journal of Applied Research on Information Technology and Computing* 5, no. 3 (2014): 250-255.

[29] Susan, Seba, and Mayank Dwivedi. "Dynamic Growth of Hidden-Layer Neurons Using the Non-extensive Entropy." In *Communication Systems and Network Technologies (CSNT), 2014 Fourth International Conference on*, pp. 491-495. IEEE, 2014.

ACCEPTED MANUSCRIPT



(a) (b) (c) (d) (e)

Fig.2 : Texture defect segmentation of eight texture samples labeled (i) to (viii) (a) Original images (b) Results of Proposed method (c) Results of Chetverikov and Hanbury's Maximal Regularity method [4] (d) Results of GLCM features [21] (e) Results of Sivabalan and Ghandurai's segmentation technique [8]

ACCEPTED MANUSCRIPT

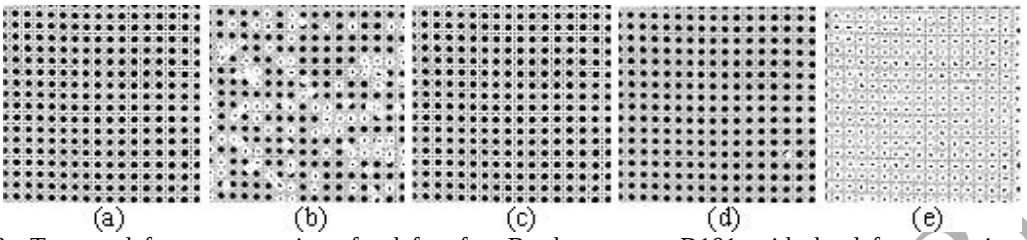


Fig.3 : Texture defect segmentation of a defect-free Brodatz texture *D101* with the defects superimposed on the original image: (a) Original images (b) Results of Proposed method (c) Results of Chetverikov and Hanbury's Maximal Regularity method [4] (d) Results of GLCM features [21] (e) Results of Sivabalan and Ghandurai's segmentation technique [8]

Table 1: The *Ncorr:Nfalse* ratio for texture images containing defects for the proposed method and the comparison methods (best results shown highlighted for each texture sample)

Texture Sample (size of image)	Proposed method (*Ncorr:Nfalse, Optimum window size)*	Chetverikov and Hanbury's Maximal Regularity method [4] *Ncorr:Nfalse*	GLCM features [21] *Ncorr:Nfalse*	Sivabalan and Ghandurai's segmentation technique [8] *Ncorr:Nfalse*
i (128x128)	**(5.612, 9x9)**	0.388	2.86	0.303
ii (128x128)	**(Inf, 5x5)**	0.199	0.636	23.2
iii (128x128)	**(1.882, 8x8)**	0.251	0.469	0.029
iv (128x128)	**(0.650, 13x13)**	0.0988	0.0034	0.0567
v (128x128)	**(0.096, 7x7)**	0.007	0.0639	0
vi (128x85)	**(23.4, 8x8)**	0.137	0.0354	0.099
vii (128x128)	(0.054, 21x21)	0	**0.213**	0.014
viii (128x85)	(0.088, 17x17)	**0.543**	0.053	0.077

ACCEPTED MANUSCRIPT

ACCEPTED MANUSCRIPT

Seba Susan



She received her Ph.D in Image Processing from the Electrical Engineering Department of Indian Institute of Technology (IIT), Delhi in 2014. She is currently Assistant Professor in the Department of Computer Science & Engineering, Delhi Technological University (DTU), Delhi. Her research areas are statistical pattern recognition, image processing and machine learning.

Monika Sharma



She is a postgraduate student of the Department of Computer Science & Engineering, Delhi Technological university, Delhi. Her areas of interest include image processing, machine learning and fuzzy systems.

ACCEPTED MANUSCRIPT

ISSN 1995-0802, Lobachevskii Journal of Mathematics, 2017, Vol. 38, No. 1, pp. 94–100. © Pleiades Publishing, Ltd., 2017.

Better Approximation Results by Bernstein–Kantorovich Operators

M. Dhamija* **and N. Deo****

(Submitted by F. G. Avkhadiev)

Department of Applied Mathematics, Delhi Technological University (Formerly Delhi College of Engineering), Bawana Road, Delhi 110042, India

Received July 7, 2015

Abstract—In this paper, we give a King-type modification of the Bernstein–Kantorovich operators and study the approximation properties of these operators. We prove that the error estimation of these operators is better than the classical Bernstein–Kantorovich operators. We also give some estimations for the rate of convergence of these operators by using the modulus of continuity. Furthermore, we obtain a Voronovskaya-type asymptotic formula for these operators.

DOI: 10.1134/S1995080217010085

Keywords and phrases: *Kantorovich, Voronovskaya, Rate of convergence.*

1. INTRODUCTION AND PRELIMINARIES

Let $C[0,1]$ be the set of continuous functions on $[0,1]$, then the Bernstein operators on $C[0,1]$ are given by

$$(B_n f)(x) = \sum_{k=0}^{n} p_{n,k}(x) f\left(\frac{k}{n}\right), \quad x \in [0,1],$$

$$p_{n,k}(x) = \binom{n}{k} x^k (1-x)^{n-k}, \quad f \in C[0,1],\ n \in N. \tag{1}$$

After a small modification of Bernstein operators due to Kantorovich (see [6]) makes it possible to approximate Lebesgue integrable function in L_1 by the modified operators

$$V_n(f,x) = (n+1)\sum_{k=0}^{n} p_{n,k}(x) \int_{\frac{k}{n+1}}^{\frac{k+1}{n+1}} f(t)dt.$$

Lemma 1.1 [6]. *Let $e_i(x) = x^i,\ i = 0,1,2$, for $x \in [0,1]$ and $n \in N$. The operators V_n verify the following:*

$$(i) \quad V_n(e_0;x) = 1, \quad (ii) \quad V_n(e_1;x) = \frac{1}{2(n+1)} + \frac{n}{(n+1)}x,$$

$$(iii) \quad V_n(e_2;x) = \frac{1}{3(n+1)^2} + \frac{2n}{(n+1)^2}x + \frac{n(n-1)}{(n+1)^2}x^2.$$

*E-mail: minakshidhamija11@gmail.com

**E-mail: dr_naokant_deo@yahoo.com

Lemma 1.2. *For $x \in [0,1]$, $n \in N$ and $\varphi_x(t) = t - x$, we have*

$$(i) \quad V_n(\varphi_x; x) = \frac{1}{2(n+1)} - \frac{x}{(n+1)},$$

$$(ii) \quad V_n(\varphi_x^2; x) = \frac{1}{3(n+1)^2} - \frac{(1-n)}{(n+1)^2}x + \frac{(1-n)}{(n+1)^2}x^2.$$

In the last century, several modifications and generalizations have been given by many mathematicians (see [1, 4, 8, 9]) on Bernstein operators. Deo et al. [3, 4] have given another modification of Bernstein-type operators $\tilde{B}_n$ as

$$\left(\tilde{B}_n f\right)(x) = \sum_{k=0}^{n} v_{n,k}(x) f\left(\frac{k}{n}\right), \tag{2}$$

where

$$v_{n,k}(x) = \left(1 + \frac{1}{n}\right)^n \binom{n}{k} x^k \left(1 - \frac{1}{n+1} - x\right)^{n-k}, \quad n \in N,$$

and $x \in [0, 1 - 1/(n+1)]$ and establish a Voronovskaya-type asymptotic formula and obtain an estimate of error in terms of modulus of continuity in simultaneous approximation by Durrmeyer variant of the operators (2). If n is sufficient large then operators (2) convert into original Bernstein operators (1).

2. CONSTRUCTION OF OPERATORS

King [7] studied an interesting class of Bernstein operators which preserve e_0 and e_2. For $f \in C[0,1]$

$$B_n(f, s_n(x)) = \sum_{k=0}^{n} \binom{n}{k} s_n^k(x) (1 - s_n(x))^{n-k} f\left(\frac{k}{n}\right), \quad x \in [0,1],$$

where $\{s_n(x)\}$ is a sequence of continuous functions on $[0,1]$ with $0 \leqslant s_n(x) \leqslant 1$. For $s_n(x) = x$, $n \in \mathbb{N}$, operators B_n become classical Bernstein operators. Now, let $r_n(x)$ be a sequence of real-valued continuous functions defined on $[0,1]$ with $0 \leq r_n(x) \leq 1$. Then we have

$$\tilde{V}_n(f, r_n(x)) = (n+1) \sum_{k=0}^{n} p_{n,k}(r_n(x)) \int_{\frac{k}{n+1}}^{\frac{k+1}{n+1}} f(t)dt.$$

Now, if we replace $r_n(x)$ by $r_n^*(x)$ defined as

$$r_n^*(x) = \frac{2(n+1)x - 1}{2n}, \quad n \in N, \quad 1/4 \leqslant x \leq 3/4,$$

then we get the King-type modified Bernstein–Kantorovich operators:

$$\tilde{V}_n^*(f,x) = (n+1) \sum_{k=0}^{n} \begin{bmatrix} n \\ k \end{bmatrix} \left(\frac{2(n+1)x - 1}{2n}\right)^k \left[\frac{(2n+1) - 2(n+1)x}{2n}\right]^{n-k} \int_{\frac{k}{n+1}}^{\frac{k+1}{n+1}} f(t)dt$$

$$= (n+1) \sum_{k=0}^{n} p_{n,k}(r_n^*(x)) \int_{\frac{k}{n+1}}^{\frac{k+1}{n+1}} f(t)dt = (n+1) \sum_{k=0}^{n} b_{n,k}(x) \int_{\frac{k}{n+1}}^{\frac{k+1}{n+1}} f(t)dt. \tag{3}$$

For our convenience $p_{n,k}(r_n^*(x))$ is denoted by $b_{n,k}(x)$ in the rest of this paper.

On the other hand, from Lemma 1.1 and Lemma 1.2, respectively, we obtain the following results at once.

Lemma 2.1. *Let $e_i(x) = x^i$, $i = 0, 1, 2$, for $x \in [1/4, 3/4]$ and $n \in N$, then the operators $\tilde{V}_n^*$ verify the following:*

$$(i)\ \tilde{V}_n^*(e_0; x) = 1; \quad (ii)\ \tilde{V}_n^*(e_1; x) = x;$$
$$(iii)\ \tilde{V}_n^*(e_2; x) = \frac{12(n-1)(n+1)^2x^2 + 12(n+1)^2x - (5n+3)}{12n(n+1)^2}.$$

Lemma 2.2. *For $x \in [1/4, 3/4]$ and $\varphi_x(t) = t - x$ we have*

$$(i)\tilde{V}_n^*(\varphi_x; x) = 0; \quad (ii)\tilde{V}_n^*(\varphi_x^2; x) = \frac{x(1-x)}{n} - \frac{(5n+3)}{12n(n+1)^2}.$$

Motive of this paper is to give the error estimation of these operators (3) and our results are better than original classical Bernstein–Kantorovich operators, when $x \in [1/4, 3/4]$. We also obtain the rate of convergence by using the modulus of continuity. Furthermore, we study a Voronovskaya-type asymptotic formula for these operators.

3. MAIN RESULTS

With the help of last two lemmas we give the following Korovkin-type approximation results.

Theorem 3.1. *For $f \in L_1[0, 1]$ the sequence of operators $\left\{\tilde{V}_n^*(f; x)\right\}_{n\in N}$ converges uniformly to $f(x)$ with respect to $x \in [1/4, 3/4]$.*

Definition 3.2. For $\delta > 0$ and $f \in C[0, 1]$, the modulus of continuity $\omega(f; \delta)$ of the function f is defined by $\omega(f; \delta) := \sup_{\substack{x,y\in[0,1]\\ |x-y|\le\delta}} |f(x) - f(y)|$, where $C[0, 1]$ is the space of continuous functions on $[0, 1]$. Then, for any $\delta > 0$ and each $x, y \in [0, 1]$, it is well known that one can write $|f(x) - f(y)| \leqslant \omega(f; \delta)\left(\frac{|x-y|}{\delta} + 1\right)$.

Theorem 3.3. *If $f \in L_1[0, 1]$ and $x \in [1/4, 3/4]$, $n \in N$, then*

$$\left|\tilde{V}_n^*(f; x) - f(x)\right| \leqslant 2\omega(f; \delta_x), \quad \delta_x = \sqrt{\frac{x(1-x)}{n} - \frac{(5n+3)}{12n(n+1)^2}}. \tag{4}$$

Proof. For $f \in L_1[0, 1]$, $x \in [1/4, 3/4]$ and $n \in N$ we have

$$\left|\tilde{V}_n^*(f; x) - f(x)\right| = \left|(n+1)\sum_{k=0}^{n} b_{n,k}(x) \int_{\frac{k}{n+1}}^{\frac{k+1}{n+1}} (f(t) - f(x))dt\right|$$
$$\leqslant (n+1)\sum_{k=0}^{n} b_{n,k}(x) \int_{\frac{k}{n+1}}^{\frac{k+1}{n+1}} |f(t) - f(x)|dt.$$

Then for any $\delta > 0$

$$\left|\tilde{V}_n^*(f; x) - f(x)\right| \leqslant (n+1)\sum_{k=0}^{n} b_{n,k}(x) \int_{\frac{k}{n+1}}^{\frac{k+1}{n+1}} \left(\frac{|t-x|}{\delta} + 1\right)\omega(f; \delta)dt$$

$$\leqslant \left\{ 1+\frac{(n+1)}{\delta}\sum_{k=0}^{n} b_{n,k}(x) \int\limits_{\frac{k}{n+1}}^{\frac{k+1}{n+1}} |t-x|dt \right\} \omega(f;\delta).$$

Using Cauchy−Schwarz inequality for integral, we get

$$\left|\tilde{V}_n^*(f;x)-f(x)\right| \leqslant \left\{ 1+\frac{(n+1)}{\delta}\sum_{k=0}^{n} b_{n,k}(x) \left(\int\limits_{\frac{k}{n+1}}^{\frac{k+1}{n+1}} dt \right)^{1/2} \left(\int\limits_{\frac{k}{n+1}}^{\frac{k+1}{n+1}} (t-x)^2 dt \right)^{1/2} \right\} \omega(f;\delta).$$

Again applying Cauchy−Schwarz inequality for sum, we have

$$\left|\tilde{V}_n^*(f;x)-f(x)\right| \leqslant \left\{ 1+\frac{1}{\delta}\left((n+1)\sum_{k=0}^{n}\binom{n}{k}\left(\frac{2(n+1)x-1}{2n}\right)^k \right.\right.$$

$$\times \left(\frac{(2n+1)-2(n+1)x}{2n} \right)^{n-k} \int\limits_{\frac{k}{n+1}}^{\frac{k+1}{n+1}} dt \Bigg)^{1/2} \times \left((n+1)\sum_{k=0}^{n}\binom{n}{k}\left(\frac{2(n+1)x-1}{2n}\right)^k \right.$$

$$\left.\left. \times \left(\frac{(2n+1)-2(n+1)x}{2n} \right)^{n-k} \int\limits_{\frac{k}{n+1}}^{\frac{k+1}{n+1}} (t-x)^2\, dt \right)^{1/2} \right\} \omega(f;\delta)$$

$$\times \left\{ 1+\frac{1}{\delta}\left(\tilde{V}_n^*\left(1;x\right)\right)^{1/2}\left(\tilde{V}_n^*\left((t-x)^2;x\right)\right)^{1/2} \right\} \omega(f;\delta).$$

Choose $\delta=\delta_x=\left(\tilde{V}_n^*\left((t-x)^2;x\right)\right)^{1/2}$. Using Lemma 2.2, we obtain

$$\left|\tilde{V}_n^*(f;x)-f(x)\right| \leqslant 2\omega(f;\delta_x), \quad \delta_x=\sqrt{\frac{x(1-x)}{n}-\frac{(5n+3)}{12n(n+1)^2}}.$$

□

Remark 3.4. For each $f\in L_1[0,1]$, $x\in[1/4,3/4]$ and $n\in N$, the operator V_n satisfy

$$|V_n(f;x)-f(x)| \leqslant 2\omega(f;\nu_x), \tag{5}$$

where

$$\nu_x=\sqrt{\frac{1}{3(n+1)^2}-\frac{(1-n)}{(n+1)^2}x+\frac{(1-n)}{(n+1)^2}x^2}.$$

Now we claim that the error estimation obtained in (4) is better than (5) for $f\in L_1[0,1]$, $x\in[1/4,3/4]$ and $n\in N$. To prove this claim we must show that $\delta(x)\leq\nu(x)$ for $x\in[1/4,3/4]$. Now

$$\delta(x)\leq\nu(x) \Leftrightarrow \frac{x(1-x)}{n}-\frac{(5n+3)}{12n(n+1)^2} \leq \frac{1}{3(n+1)^2}-\frac{(1-n)}{(n+1)^2}x+\frac{(1-n)}{(n+1)^2}x^2$$

$$\Leftrightarrow -(36n+12)\,x^2+(36n+12)\,x-(9n+3)\leq 0$$

$$\Leftrightarrow (3n+1)\left[-12x^2+12x-3\right]\leq 0 \Leftrightarrow 12x^2-12x+3\geq 0 \Leftrightarrow (2x-1)^2\geq 0.$$

which is always true and hence true for $x\in[1/4,3/4]$.

Let $f \in L_1[0,1]$ be such that f possesses a continuous derivative on the interval $[0,1]$ then we can find rate of convergence for the operators (3) in terms of modulus of continuity of derivative of the function f.

Theorem 3.5. *If $f \in L_1[0,1]$, $x \in [1/4, 3/4]$ and f possesses a continuous derivative on the interval $[0,1]$, then $\left|\tilde{V}_n^*(f;x) - f(x)\right| \leq 2\delta_x \omega_1(f;\delta_x)$, where $\omega_1(\delta)$ is modulus of continuity of f' and*

$$\delta_x = \sqrt{\frac{x(1-x)}{n} - \frac{(5n+3)}{12n(n+1)^2}}.$$

Proof. Since f is differentiable on $[0,1]$ therefore by mean value theorem of differential calculus we have

$$f(t) - f(x) = (t-x) f'(\eta) = (t-x) f'(x) + (t-x)\left(f'(\eta) - f'(x)\right),$$

where $\eta = \eta(x,t)$ belongs to the interval obtained by x and t. Now

$$\tilde{V}_n^*(f;x) - f(x) = (n+1)\sum_{k=0}^{n} b_{n,k}(x) \int_{\frac{k}{n+1}}^{\frac{k+1}{n+1}} (t-x) f'(x)\, dt$$

$$+ (n+1)\sum_{k=0}^{n} b_{n,k}(x) \int_{\frac{k}{n+1}}^{\frac{k+1}{n+1}} (t-x)\left(f'(\eta) - f'(x)\right) dt = f'(x)\, \tilde{V}_n^*\left((t-x);x\right)$$

$$+ (n+1)\sum_{k=0}^{n} b_{n,k}(x) \int_{\frac{k}{n+1}}^{\frac{k+1}{n+1}} (t-x)\left(f'(\eta) - f'(x)\right) dt$$

$$= (n+1)\sum_{k=0}^{n} b_{n,k}(x) \int_{\frac{k}{n+1}}^{\frac{k+1}{n+1}} (t-x)\left(f'(\eta) - f'(x)\right) dt.$$

Therefore,

$$\left|\tilde{V}_n^*(f;x) - f(x)\right| \leq (n+1)\sum_{k=0}^{n} b_{n,k}(x) \int_{\frac{k}{n+1}}^{\frac{k+1}{n+1}} |t-x| \left|f'(\eta) - f'(x)\right| dt.$$

But for a positive number δ, we have

$$\left|f'(\eta) - f'(x)\right| \leq \omega_1(f;|\eta - x|) \leq \left(1 + \frac{1}{\delta}|\eta - x|\right)\omega_1(f;\delta) \leq \left(1 + \frac{1}{\delta}|t-x|\right)\omega_1(f;\delta).$$

Then

$$\left|\tilde{V}_n^*(f;x) - f(x)\right| \leq \left[(n+1)\sum_{k=0}^{n} b_{n,k}(x) \int_{\frac{k}{n+1}}^{\frac{k+1}{n+1}} |t-x|\, dt + \frac{(n+1)}{\delta}\sum_{k=0}^{n} b_{n,k}(x) \int_{\frac{k}{n+1}}^{\frac{k+1}{n+1}} (t-x)^2 dt\right]\omega_1(f;\delta).$$

Applying Cauchy–Schwarz inequality for sum and integration respectively (as in previous theorem), we get

$$\left|\tilde{V}_n^*(f;x) - f(x)\right| \leq \left[\left\{\tilde{V}_n^*(1;x)\right\}^{1/2}\left\{\tilde{V}_n^*\left((t-x)^2;x\right)\right\}^{1/2} + \frac{1}{\delta}\tilde{V}_n^*\left((t-x)^2;x\right)\right]\omega_1(f;\delta)$$

$$\leq 2\delta_x \omega_1 (f;\delta_x).$$

Where δ is chosen so that

$$\delta = \delta_x = \left[\tilde{V}_n^*((t-x)^2;x)\right]^{1/2} = \sqrt{\frac{x(1-x)}{n} - \frac{(5n+3)}{12n(n+1)^2}}.$$

This completes the proof. □

4. VORONOVSKAYA-TYPE FORMULA

In 1955, Lorentz studied that if $\omega(f;\delta)$ is the modulus of continuity of $f(x)$, then

$$|B_n(f;x) - f(x)| \leq \frac{3}{4} n^{-1/2} \omega\left(f; n^{-1/2}\right).$$

In 1932, Voronovskaya proved that

$$\lim_{n\to\infty} n\left[B_n(f;x) - f(x)\right] = -\frac{1}{2}x(1-x)f''(x.)$$

Now we prove a Voronovskaya-type formula for modified Bernstein–Kantorovich operators (3).

Theorem 4.1. *Let f be bounded and integrable function on $[0,1]$, Suppose that the second derivative $f''(x)$ exists at a certain point $x \in [1/4, 3/4]$, then*

$$\lim_{n\to\infty} n\left[\tilde{V}_n^*(f,x) - f(x)\right] = \frac{1}{2}x(1-x)f''(x).$$

Proof. In view of Taylor's expansion of f:

$$f(t) = f(x) + (t-x)f'(x) + \frac{(t-x)^2}{2!}f''(x) + \eta(t-x)(t-x)^2,$$

where $\eta(t-x)(t-x)^2$ is bounded and satisfies $\eta(h) \to 0$ as $h \to 0$. By linearity of modified Bernstein–Kantorovich operators and using Lemma 2.1, we have

$$\tilde{V}_n^*(f;x) - f(x) = f'(x)\tilde{V}_n^*(t-x;x) + \frac{1}{2}f''(x)\tilde{V}_n^*((t-x)^2;x) + \tilde{V}_n^*(\eta(t-x)(t-x)^2;x).$$

From Lemma 2.2, we get

$$\tilde{V}_n^*(f;x) - f(x) = \frac{1}{2}\left(\frac{x(1-x)}{n} - \frac{5n+3}{12n(n+1)^2}\right)f''(x) + \tilde{V}_n^*(\eta(t-x)(t-x)^2;x).$$

The last term on the right hand side can be estimated in the following way. Let $\varepsilon > 0$ and $\delta > 0$ such that $|\eta(h)| < \varepsilon$ for $|h| < \delta$. Now, write $\tilde{V}_n^*(\eta(t-x)(t-x)^2;x) = T_1 + T_2$, where

$$T_1 = (n+1)\sum_{k=0}^{n}\binom{n}{k}\left(\frac{(n+1)x-1}{2n}\right)^k\left(1-\frac{(n+1)x-1}{2n}\right)^{n-k}\int\limits_{|t-x|<\delta}\eta(t-x)(t-x)^2dt$$

and

$$T_2 = (n+1)\sum_{k=0}^{n}\binom{n}{k}\left(\frac{(n+1)x-1}{2n}\right)^k\left(1-\frac{(n+1)x-1}{2n}\right)^{n-k}\int\limits_{|t-x|\geq\delta}\eta(t-x)(t-x)^2dt.$$

The first term can be bounded as follows:

$$|T_1| < \varepsilon(n+1)\sum_{k=0}^{n}\binom{n}{k}\left(\frac{(n+1)x-1}{2n}\right)^k\left(1-\frac{(n+1)x-1}{2n}\right)^{n-k}$$

$$\times \int\limits_{\frac{k}{n+1}}^{\frac{k+1}{n+1}} (t-x)^2 dt = \varepsilon \tilde{V}_n^*((t-x)^2; x),$$

and therefore $\lim\limits_{n\to\infty} n\,|T_1| = 0$. Finally, denote by $K = \sup\{|\eta(h)| : |h| \geq \delta\}$. Thus,

$$|T_2| \leq \frac{K}{\delta^2}(n+1)\sum_{k=0}^{n}\binom{n}{k}\left(\frac{(n+1)x-1}{2n}\right)^k\left(1-\frac{(n+1)x-1}{2n}\right)^{n-k}$$
$$\times \int\limits_{|t-x|\geq\delta} (t-x)^4 dt \leq \frac{K}{\delta^2}\tilde{V}_n^*((t-x)^4; x)$$

By direct calculation we can show that $\tilde{V}_n^*((t-x)^4; x) = O(n^{-2})$, and finally, we obtain $\lim\limits_{n\to\infty} n\,|T_2| = 0$. Hence we get the desired result. □

Remark 4.2. For each bounded and integrable function f, $x \in [0,1]$, $n \in N$ and second derivative $f''(x)$ exists at a certain point $x \in [0,1]$, the operators V_n satisfy

$$\lim_{n\to\infty} n\,[V_n(f,x) - f(x)] = \frac{1-2x}{2}f'(x) - \frac{1}{2}x(1+x)f''(x).$$

ACKNOWLEDGMENTS

The authors are grateful to the referee for valuable suggestions for improvements in the paper.

REFERENCES

1. P. L. Butzer, "On two dimensional Bernstein polynomials," Canad. J. Math. **5**, 107–113 (1953).
2. J. de la Cal, J. Carcamo, and A. M. Valle, "A best constant for bivariate Bernstein and Sz+asz-Mirakyan operators," J. Approx. Theory **123**, 117–124 (2003).
3. N. Deo, N. Bhardwaj, and S. P. Singh, "Simultaneous approximation on generalized Bernstein–Durrmeyer operators," Afrika Mat. **24**, 77–82 (2011).
4. N. Deo, M. A. Noor, and M. A. Siddiqui, "On approximation by a class of new Bernstein type operators," Appl. Math. Comput. **201**, 604–612 (2008).
5. M. M. Derriennic, "Sur l'approximation de fonctions intégrables sur [0, 1] par des polynômes de Bernstein modifies," J. Approx. Theory **31**, 325–343 (1981).
6. L. V. Kantorovitch, "Sur certains développments suivant lés pôynômes dé la forme S. Bernstein I," C. R. Acad. Sci. URSS **20**, 563–568 (1930); "Sur certains développments suivant lés pôynômes dé la forme S. Bernstein II," C. R. Acad. Sci. URSS **20**, 595–600 (1930).
7. J. P. King, "Positive linear operators which preserve x^2," Acta Math. Hungar. **99**, 203–208 (2003).
8. D. D. Stancu, "Approximation of functions by a new class of linear polynomial operators," Rev. Roum. Math. Pures Appl. **13**, 1173–1194 (1968).
9. D. X. Zhou, "Weighted approximation by multidimensional Bernstein operators," J. Approx. Theory **76**, 403–422 (1994).

Applied Materials Today 8 (2017) 18–25

Contents lists available at ScienceDirect

Applied Materials Today

journal homepage: www.elsevier.com/locate/apmt

Charge injection in large area multilayer graphene by ambient Kelvin probe force microscopy

Igor Bdikin[a,b], Dhanajay K. Sharma[a], Gonzalo Otero-Irurueta[a], María J. Hortigüela[a], Pawan K. Tyagi[c], Victor Neto[a], Manoj K. Singh[a,*]

[a] Centre for Mechanical Technology & Automation, Department of Mechanical Engineering, University of Aveiro, 3810-193 Aveiro, Portugal
[b] National Research University of Electronic Technology 'MIET', 124498 Moscow, Russia
[c] Department of Applied & Engineering Physics, Delhi Technological University, New Delhi, India

ARTICLE INFO

Article history:
Received 10 October 2016
Received in revised form
25 November 2016
Accepted 27 November 2016

Keywords:
Graphene
HF-TCVD
Charge injection/relaxation
Charge transport
Surface potential
Kelvin probe force microscopy

ABSTRACT

This study demonstrated an in situ method for quantitative characterization of nanoscale electrostatic properties of as-grown multilayer-graphene (MLG) sheets on nickel by a combination of atomic force microscopy (AFM) and Kelvin probe force microscopy (KPFM). Large area epitaxial MLG sheet were grown on nickel by Hot Filament-Thermal chemical vapor deposition (CVD) technique. The high crystalline MLG sheets on nickel were confirmed by Raman spectroscopy that revealed average G-bandwidths in the range of ~20 cm^{-1}. Herein, for the first time, the charge injection as well as subsequent charge diffusion over time on the MLG/nickel surface was demonstrated. The results unveiled that: (i) MLG surface can be either positively or negatively charged through injection process using Pt coated Si-based AFM probes; (ii) the charges accumulated and eventually reached to saturated concentrations of +4.45 (±0.1) $\mu C/m^2$ and −1.3 (±0.1) $\mu C/m^2$, respectively; (iii) the charge diffusion coefficients on graphene surface were measured to be 1.50 (±0.05) × 10^{-16} m^2/s and 0.64 (±0.05) × 10^{-16} m^2/s for the positive and the negative charges, respectively. The discovery of charge injection in MLG may pave the way for designing a new class of energy harvesting devices. Additionally, our study demonstrated a technique for nano-patterning/charge lithography of surface charges by contact electrification, which could be a promising application to create charged nanostructures for next generation graphene based nanoelectronic devices.

© 2017 Elsevier Ltd. All rights reserved.

1. Introduction

From both scientific and technological point of view, charge injection on insulating films has been of great interest in the development of multiple devices including triboelectric nanogenerators for building self-powered portable electronics, large-scale energy harvesting, and also to develop data storage devices [1]. In particular, a charge injection combined with Kelvin probe force microscopy (KPFM) technique was reported to be a *state-of-the-art* tool to study the electrostatic properties of objects at the nanoscale level [2]. Determination of the interface in carbon nanotubes (CNTs) based devices or distinguishing the metallic and semiconducting nature of CNTs with the same diameters, silicon nanoparticles, and semiconducting quantum nanorods are the major examples of the application of KPFM technique. In addition, KPFM has also been used to study the different charge states of single metal atoms, molecules, atomic point defects, and imaging of the charge percolation pathways in two-dimensional quantum dot arrays [3]. Recently, KPFM was used for imaging the charge distribution in different complex systems such as semiconducting quantum dots, carbon nanotubes, graphene on SiO_2 substrates, organic molecules, and even bacterial protein filaments [4–16].

Besides the KPFM measurements, researchers have also performed nanolithography and manipulation of graphene by using AFM. For example, conductive atomic force microscopy [16] has been used to analyze the local current mapping and patterning of reduced graphene oxide. Sibel et al. used electrostatic force microscopy (EFM) technique for elucidating the charge transport property in reduced graphene oxide [17]. With the given highlighted measurement types it is possible to correlate the detailed morphology of graphene (e.g., wrinkles, multilayer regions, and local defects) with its nanoscale electrical characteristics, reading/writing charges on graphene, and local electronic behavior at graphene–metal interface.

In this particular direction, for the first time the present study demonstrated the charge injection (both positive and negative)

* Corresponding author.
E-mail address: mksingh@ua.pt (M.K. Singh).

http://dx.doi.org/10.1016/j.apmt.2016.11.005
2352-9407/© 2017 Elsevier Ltd. All rights reserved.

and the subsequent visualization of charge distribution, as well as charge diffusion over time on the large area as-grown MLG on nickel. For the set-out experiments, large-area high-quality MLG sheets on nickel were synthesized by using Hot-filament thermal CVD (HF-TCVD), as described elsewhere [18]. Furthermore, HF-TCVD route has the potential to grow large area single and MLG sheets on poly-crystalline metal substrates by controlling the CH_4:H_2 ratio, time of deposition and it is attractive for real *state-of-the-art* graphene-based nanoelectronic device applications [19].

Additionally, the present work also created stable charged nanosized areas, so-called "charge nanolithography", of surface charges by contact electrification by using KPFM at ambient conditions. KPFM exhibits promising potential application for directed self-assembly of charged nanostructures for next generation graphene-based nanoelectronic devices. These findings also provide new insights in understanding the electronic charge behavior in large area MLG on nickel surface at the nanoscale. We assumed that this phenomena arises due to low conductivity, and may be originated from MLG-nickel interface (which often introduce significant defects into the mono and few layer graphene-nickel interface layer so-called "defective region") [20,21], misorientation within the graphene layers, point defects, grain boundary, wrinkles or ripples of the MLG sheets. Indeed it has been already proved that the sensitivity of electronic system directly correlates with the defects and/or deformation in two-dimensional graphene lattice [22].

2. Material and methods

Synthesis of large-area high-quality MLG sheets was grown on high quality nickel (Good Fellow, Cambridge, UK) with thickness 0.025 mm and purity 99.99%. Methane and hydrogen were used as precursor with ratio of CH_4:H_2 (10:50 standard cubic centimeters per minute (sccm)). The deposition time was about 15 min with the pressure of 35 torr. More details have been described in Hawaldar et al. [18] Micro-Raman was performed at room temperature using the 488 nm line of an Ar^+ laser with an incident power ~1.0 mW with an Olympus microscope (×100 objective) of very high numerical aperture, NA = 0.95, and a "super-notch-plus" filter from Kaiser. The scattered light was analyzed with a Jobin-Yvon HR-460 monochromator coupled to a Peltier cooled Synapse CCD. The minimum laser spot size, diffraction limited, for 488 nm and NA = 0.95 is 1.22 λ/NA = 630 nm. Raman spatial resolution is around 0.7 μm.

High resolution X-ray photoelectron spectroscopy (XPS) was acquired in an ultra high vacuum (UHV) system with a base pressure of 2×10^{-10} mbar. The system was equipped with a hemi-spherical electron energy analyser (SPECS Phoibos 150), a delay-line detector and a monochromatic AlKα (1486.74 eV) X-ray source. High resolution spectra were recorded at normal emission take-off angle and with a pass-energy of 20 eV, which provides an overall instrumental peak broadening of around 0.5 eV.

Atomic force microscopy and Kelvin probe force microscopy were performed by Ntegra Prima, NT-MDT in tapping mode with resonance frequency of 50 kHz. The conductive probes used were made up of Pt/Ir coated Si cantilever from nanosensors; with a nominal force constant 15 N/m.

3. Results and discussion

Fig. 1a shows scanning electron microscopy (SEM) image of CVD-grown large-area MLG on nickel foil, which acts as catalyst for graphene growth as well as bottom electrical contact during KPFM measurements. The inset shows some typical graphene wrinkles. To confirm the identity and quality of our as deposited MLG

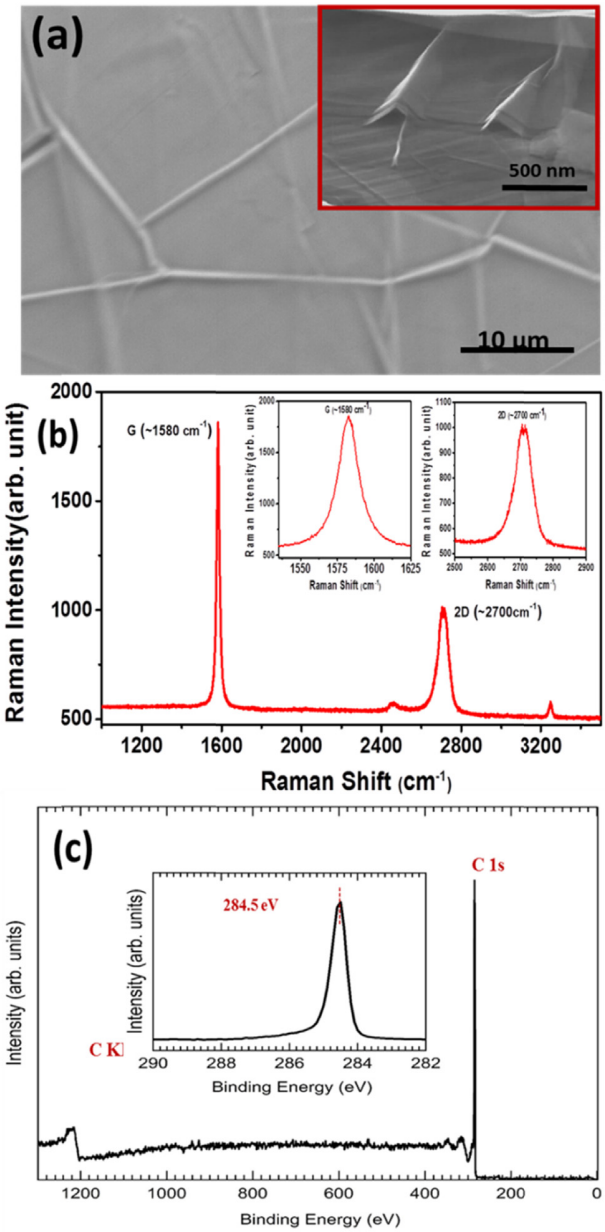


Fig. 1. (a) Scanning electron microscopy (SEM) image of CVD-grown large-area MLG on nickel foil, inset showing a ripple. (b) Raman spectra of as-grown MLG on nickel clearly showing the strong G peak (~1580 cm^{-1}), inset showing zoom-in of the G and 2D peaks. (c) X-ray photoelectron spectroscopy of as-synthesized MLG on nickel, inset showing high-resolution XPS of C 1s core level of MLG on nickel.

sheets on nickel foil, we performed detailed micro-Raman studies (Fig. 1b).

Raman spectroscopy is best suited to envisage graphene owing to the detection of distinct and rich vibrational spectra that reveal key information related to number of layers, strain, edge configuration, electronic properties and defects in graphene structures [18]. Raman mapping over different areas with 1 μm steps (not shown) as well as individual spectra were obtained from MLG-nickel sample. Fig. 1b reveals the Raman spectra clearly showing the strong G peak (~1580 cm^{-1}), which indicates the formation of hexagonal lattice of carbon atoms. The high crystalline quality of MLG sheets on nickel is indicated by Raman spectroscopy revealing average G bandwidths as low as 20 cm^{-1} at 488 nm of excitation. Furthermore, the absence of disorder-induced D peak

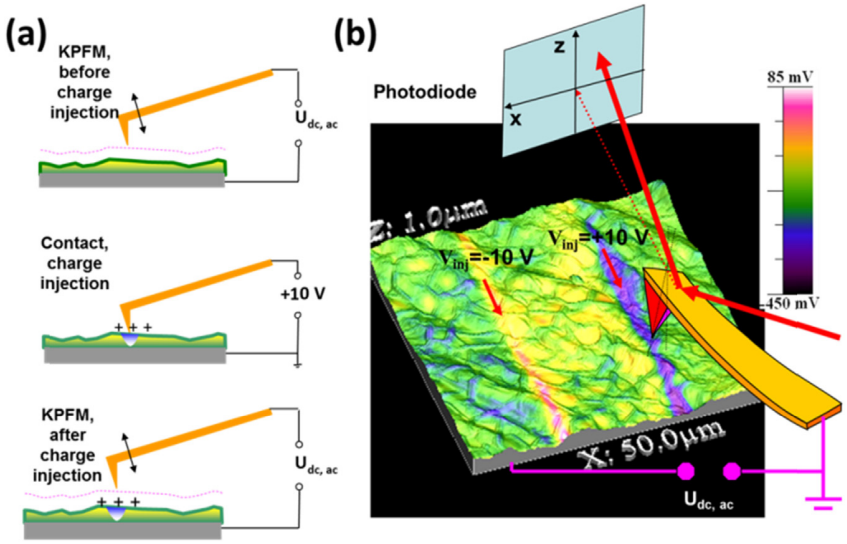


Fig. 2. Charge injection experiments on MLG/nickel surface based on AFM. (a) Schematic illustration of KPFM and contact mode for charge injection process. (b) 3D example of charge injection schematic presentation. The topography is mapped onto the third dimension (*z*-axis) and the recorded surface potential is color coded.

(~1360 cm^{-1}) also indicates extremely low density of defects in as-grown MLG sheets. We note that no D peak has been found in any area of the sample. The 2D peak (~2700 cm^{-1}) is weaker compared to the G peak and has a wide line width of ~60 cm^{-1}, and its position is slightly up shifted compared to monolayer graphene. It is worth to mention that the Raman data presents the information about the top graphene layers away from MLG/nickel interface due to the penetration depth of Raman laser into sample. Thus, the top graphene layers (several nanometers) are free from any crystal defect as evidenced by the absence of Raman D peak mentioned above. Furthermore, XPS was performed to re-confirm the quality of MLG-nickel sample and also for detecting any strange contaminant. XPS is a well-established technique used for revealing the elemental composition and the chemical environment of the detected elements. Fig. 1c shows the overview spectrum of as grown MLG, in which only carbon is detected, while the inset shows the C 1s core level. C 1s spectrum presents a quite sharp peak centered at a binding energy (BE) of 284.5 eV which can be related with high quality of sp^2 carbon [8]. Moreover, its full width at half maximum (FWHM) is 0.5 eV which clearly indicates a high quality sample.

Furthermore, an extra proof of the quality of the graphene sample is the lack of XPS peaks that could be ascribed to contaminants such as oxygen species (C–O or C = O) [8]. Finally, we notice that XPS did not detect any signature of the nickel substrate, indicating that several graphene layers grew on it.

Thus, the full set of characterization techniques (SEM, Raman spectroscopy and XPS) confirmed the high quality, defects free MLG on nickel sample, without impurities. Additionally, the thickness of the MLG sheet was estimated by analyzing the atomic force microscopy (AFM) images of transferred samples (not shown) and was found to be ~150 nm.

KPFM was used to visualize the surface charge potential (SP) and injecting charge on as-grown large area MLG. By combining KPFM with AFM (to apply positive and negative voltages) the surface charge potential (SP) after local charge injection and relaxation process was measured. KPFM was done by using the two-pass technique for imaging of the contact potential difference between the sample and the AFM tip (Fig. 2). The principle of the KPFM is to match the probe bias V_{dc} with the contact potential difference between the sample and the probe V_{cpd} by nullifying the vibration of the probe, which is initially driven (with frequency w) by the electrostatic force (F_{es}) induced on the AFM probe, as described in Eq. (1) [23].

$$F_{es} = -\frac{dC}{dz}\left\{\frac{1}{2}\left[(V_{dc}-V_{cpd})^2+\frac{1}{2}V_{ac}^2\right] +(V_{dc}-V_{cpd})V_{ac}\sin(wt)-\frac{1}{2}V_{ac}^2\cos(2wt)\right\} \quad (1)$$

where C, z, V_{ac}, and t are the equivalent capacitance between the tip and sample, the tip–sample distance, the magnitude of ac voltage applied to the probe, and the time, respectively. V_{dc} is the tip bias voltage and V_{cpd} is the contact potential difference. During the first pass, a topographic image is acquired in tapping mode. In the second pass, the tip follows the topographic profile at a preset lift height. During the second pass, the cantilever is electrically excited by the sum of a variable dc voltage V_{tip} dc, and an ac voltage, V_{tip} ac, with a frequency close to the cantilever resonance. V_{tip} dc is adjusted to nullify the force component at the frequency of V_{tip} ac. The value of V_{tip} dc is then equal to the surface potential. The tip was lifted by just a few nanometers in order to ensure that the tip–sample capacitance was dominant over the cantilever–sample capacitance. In our setup, we grounded the nickel substrate and applied a bias voltage to the tip. To quantify the charge density, the relationship between the surface charge density and the measured potential from KPFM were investigated. The contact potential difference V_{cpd} is generally determined by two components: the effective work function of two materials and the electrostatic potential difference, respectively. The former component depends on the surface properties of the two materials, and the latter one is determined by the bias and surface charges of the sample [23].

Fig. 2 describes shows a schematic illustration of the charge injection experiments on MLG by KPFM. The local charge injection was performed by applying various dc voltages to the conducting tip, and followed by KPFM imaging (Fig. 2a). A representative topographic image with the over-imposed surface charge potential (color coded) of the selected area is shown in Fig. 2b. In the chosen region, the dc biases of V_{inj} = +10 V (on the right) and −10 V (on the left) were applied between the conductive tip and the bottom electrode. The injection time (t_{inj}) was about 10 s, and the time interval between positive and negative applications was about 100 s. Immediately after the charge injection step, the tip was lifted around

20 nm away from the surface and the surface potential image was obtained in the KPFM mode. The KPFM image revealed two stripes with a clear contrast due to the local potential difference and surface charge redistribution (see Fig. 2b). It is worth mentioning that the contact potential difference of the area induced by the applied bias voltage is several times greater than that of the surface potential modulation. Macroscopically, the injection occurs via the local growth area in the situation where the electric field is uniform. The RMS roughness of MLG on nickel, obtained by AFM, is around 3 nm (3 μm × 3 μm scan). Therefore, the injection averaged over the entire region under the electrode. In surface potential experimental conditions, the electric field is strongly localized and inhomogeneous, and therefore the injection starts with the nucleation of a small area just under the AFM tip. Under the applied voltage, this area elongates to the bottom electrode and simultaneously expands in lateral directions until reaching an equilibrium size, which depends on the value of the maximum applied voltage. Saturation of the injection is achieved when the size of the area is much larger than the contact tip-surface area. The threshold voltage describes the voltage at which a stable injected area is formed under the tip.

Fig. 2b shows the effect of the voltage applied to the AFM conducting tip on the surface potential signal. The size and stability of injected area is directly related to macroscopic issues such as conductivity and its anisotropy, effective tip diameter and contact conditions. The calculations of the electric field distribution under AFM tip with effective diameter ~10 nm and applied voltage

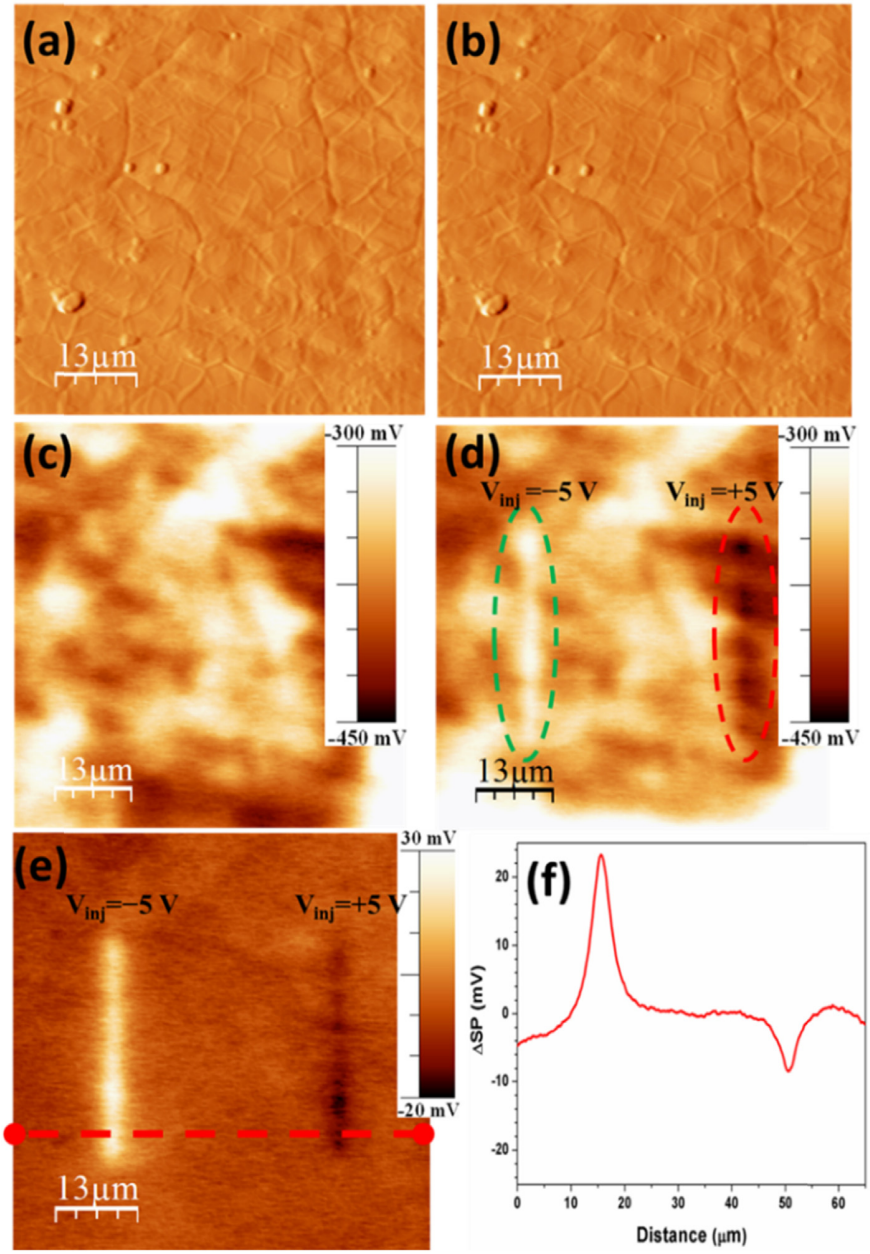


Fig. 3. Charge injection experiments on MLG/nickel. AFM topography image before (a) and after (b) charge injection, performed with the conducting tip (V_{inj} = −5 V, V_{inj} = +5 V; and injection time t_{inj} = 10 s). Surface potential image before (c) and after (d) injection. (e) Represents the difference between images (c) and (d) for more clarity. (e and f) Profile of the surface potential signal across red dotted lines. (For interpretation of the references to color in this legend, the reader is referred to the web version of the article.)

of ±10 V corresponds to an electric field of ~0.006 V/Å at MLG sheet thickness of ~150 nm.

In the present work, the topography of the scanned area was checked each time before and after local charge injection, and no changes were revealed even after the application of dc voltages up to +12 V. Fig. 3a–f show charge injection experiment along linear paths on MLG. Fig. 3 shows the topographic image before (a) and after (b) the charge injection with $V_{inj} = -5$ V and +5 V, injection time (t_{inj}) = 10 s, and scanning tip velocity of 3.5 μm/s. Immediately after the charge injection step the AFM tip was lifted 20 nm to measure the surface potential (see Fig. 3d). For more clarity Fig. 3e represents the difference between the images of Fig. 3c and d. The area in which the charge injection, at +V and −V were done are clearly recognized. Furthermore, the profile presented in Fig. 3f resembles the potential contrast between the charged and non-charged areas.

The difference in SP values (ΔV) was correlated to the surface charge density σ using a parallel capacitor model, as given in Eq. (2), since the scale of the charged area (~4 μm^2) is much larger than the thickness of the MLG sheet.

$$\sigma = \frac{\Delta V \varepsilon_0 \varepsilon_{MLG}}{t_{MLG}} \quad (2)$$

where ε_0 (8.854187817 × 10^{-12} F/m) is the vacuum dielectric constant and ε_{MLG} and t_{MLG} are the relative dielectric constant and thickness of MLG sheets, respectively. Recently, Santos et al. studied the effect of electric field on the effective dielectric constant in N-layer graphene and describes the values of out-of-plane ($\varepsilon_\perp$) and the in-plane ($\varepsilon_\parallel$) dielectric constant are nearly constant (~3 and ~1.8, respectively) at our fields (~0.005 V/Å) [24]. In the case of $\Delta V+ = 0.025$ V, σ is calculated to be (+4.45 ± 0.1) μC/m^2 and $\Delta V- = 0.007$ V, σ is (−1.3 ± 0.1) μC/m^2.

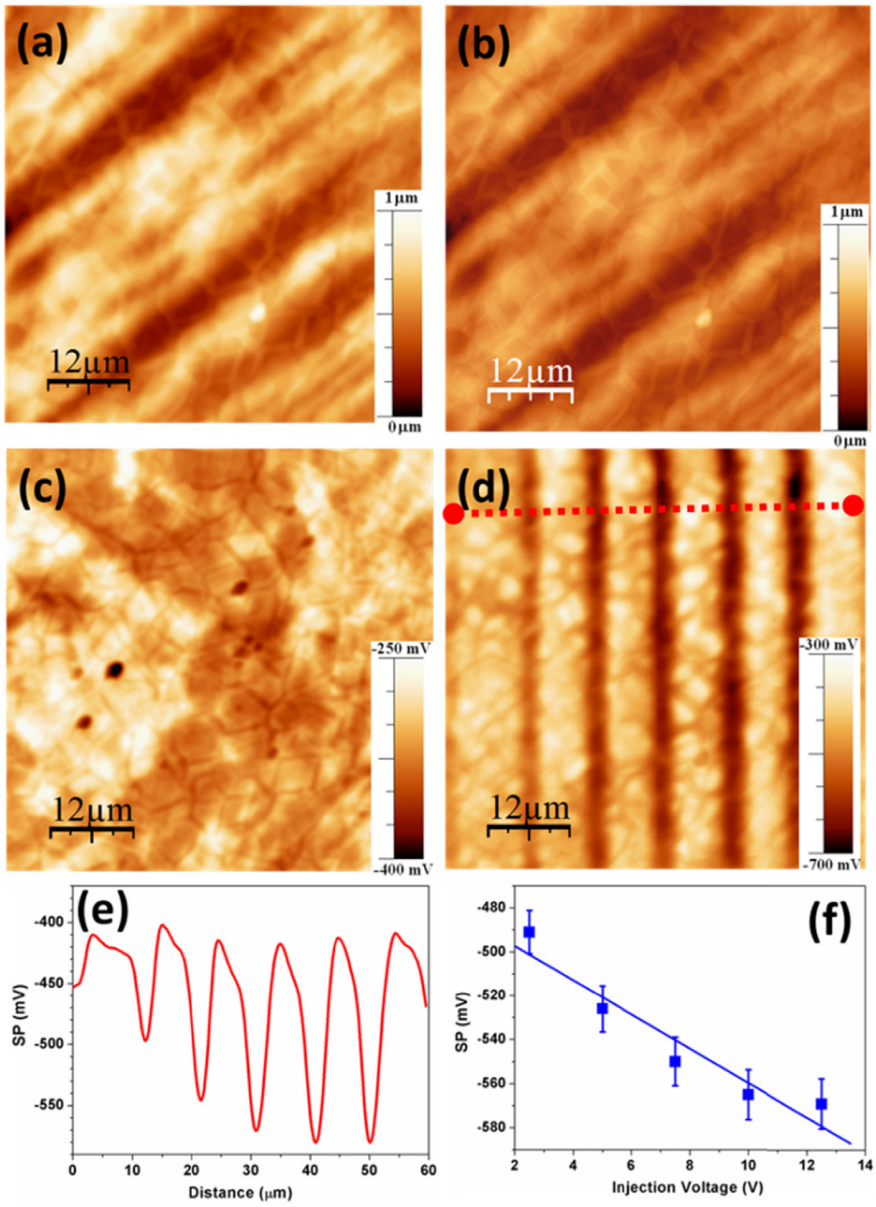


Fig. 4. Surface stability of MLG films under higher voltage injection through the AFM tip. (a) Surface topography of as-grown MLG film before and (b) after injection. (c) Surface potential image before injection and (d) Surface potential images of the electric-field-induced contrast on MLG films obtained after the application of V_{inj} = +2.5, +5.0, +7.5, +10.0, and +12.5 V to the tip (dark lines from left to right). (e) Profile along the red dotted line showed in (d). (f) SP intensity vs applied voltage obtained from (e). (For interpretation of the references to color in this legend, the reader is referred to the web version of the article.)

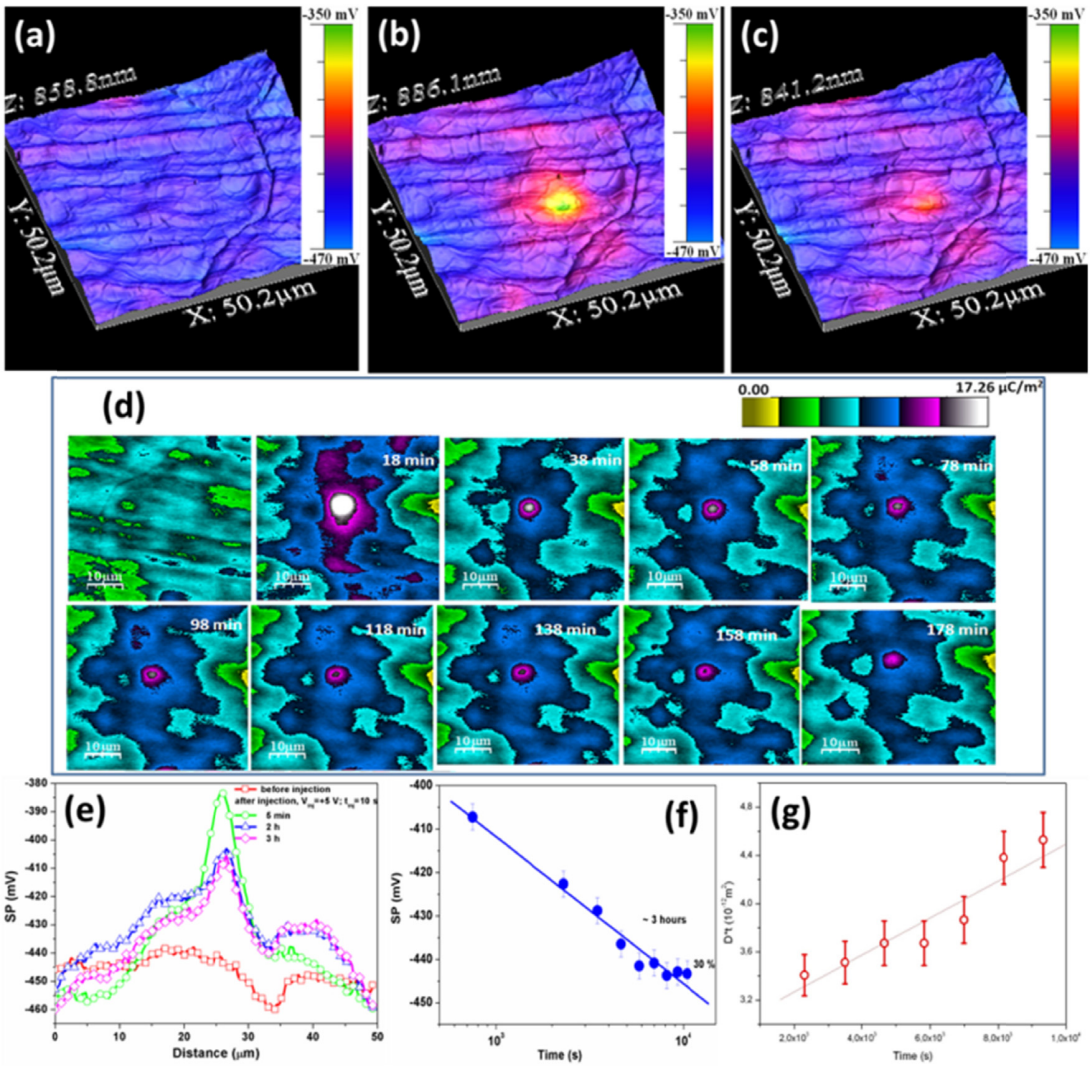


Fig. 5. Topography with KPFM image over-imposed (colored coded) before (a), immediately after (b) poling, +5 V, 10 s, and (c) after prolonged aging 3 h (c). (d) Charge relaxation starting from before injection till 180 min after injection, with the intervals of 20 min. (e) Profile of the images taken before, immediately after poling, and after 2–3 h. (f–g) SP intensity vs time obtained from (e) and (g) D^*t vs time.

Besides this, we study the surface stability of MLG under higher voltage injection through the AFM tip (Fig. 4). Fig. 4a and b show the topography before and after injection, respectively, while (c) shows the surface potential image before injection. In our demonstrating experiment, we created a pattern of dark lines by injecting bias voltages of V_{inj} = +2.5, +5.0, +7.5, +10.0 and +12.5 V, from left to right in Fig. 4d–f, with scanning tip velocity of 3.5 μm/s and injection time of 10 s. Fig. 4e shows the profile along the red line indicated in (d), while (f) shows the surface potential as function of the applied voltage. The difference in the injected charges in the parallel lines leads to variation in contrast, which can be explained by the charge capacitance (polarization). Interestingly, we observe that the MLG surface topography is stable even at the highest tip voltages (Fig. 4b).

Moreover, taking the advantage of the nanometer scale resolution of AFM and KPFM, the method is able to give insight on charge propagation by monitoring the surface charge potential distribution on two-dimensional MLG on nickel surface. In our demonstrating experiment (Fig. 5a–g), we examined the evolution of the induced surface potential as a function of time by measuring immediately after charging (Fig. 5b), and after prolonged aging (Fig. 5c). For this particular experiment, the charge was injected (V_{inj} = +5 V, and t_{inj} = 10 s) in a point and the subsequent charge relaxation was followed (Fig. 5d) during nearly 3 h. In Fig. 5e–f it is clearly seen that the initial pattern is not really stable and reduces about 30% of the initial value of surface potential after about 3 h (t = 300 s is the time needed for a single scan). The fitting was done with the Kohlrausch–Williams–Watts formula (Eq. (3)) commonly used to describe relaxation in systems with dipole–dipole interactions, as described below [25].

$$SP = SP_0 \exp\left[-\frac{t}{t_0}b\right] \tag{3}$$

where t is the time, b and t_0 (effective relaxation time) are the parameters. For b = 1 Eq. (3) reduces to simple Debye relaxation formula. For our case we obtained effective relaxation time ~1 h (see Fig. 5e and f). This value is much higher than 10^{-9} s, which is obtained from simple formula (Eq. (4) for Maxwell relaxation time). Moreover, Maxwell's equation actually reproduces Ohm's law for the case when the initial potential difference is given and discharge as the function of relaxation time (τ) is studied. For the case of

constant voltage (time conductivity does not change) relaxation time and conductivity are related as described in Eq. (4) [26].

$$\tau = 4\pi\varepsilon\varepsilon_0\rho \quad (4)$$

where ε_0 is the vacuum dielectric constant and ε the dielectric constant. Based on the conductivity measurement from the recent report published by Adila et al. [27], the Maxwell relaxation time (from Eq. (4)) for this is estimated $\sim 10^{-9}$ s. It means that the locally induced charged states decay with a characteristic time that is many orders of magnitude greater than the expected Maxwell relaxation time of uncharged surface material. Moreover, charges diffuse laterally on the surface in two-dimensions as well as vertically into the bulk [28,29]. In our charge injection experiment, we noticed that the charge migration is mostly in two-dimension and very low in vertical direction; it is due to some charges leaked into the bottom electrode rather than spreading over the surface. Since the characteristic length of the diffusion on the surface ($\sim$5 μm) is much larger than the thickness of the MLG film ($\sim$150 nm) we can employ the model for a two-dimensional diffusion to estimate the surface charge diffusion coefficient on MLG sheet from a point source (x_0, y_0) from time (t_0), as described in Eq. (5) [30,31].

$$\sigma(x, y, t) = \frac{A}{t - t_0} \exp\left[-\frac{(x - x_0)^2 + (y - y_0)^2}{4D(t - t_0)}\right] \quad (5)$$

where $\sigma(x, y, t)$ is the surface charge density of point (x, y) at time (t), A is the magnitude constant and D is the diffusion coefficient on the given surface [31]. This equation represents the modified theoretical distribution of the applied electric field outside the moving tip in the frame of the spherical model and point charge approximation first developed by Mele et al. [32–34]. Furthermore, Fig. 5d represents a series of images of charge distribution as a function of time after positive charge injection. The surface potential/charge distribution was monitored by KPFM every 20 min. By fitting the data at different diffusing time (as illustrated in Fig. 5e–f), we can calculate the slope of the curve "D" Fig. 5g. From the fitting, the positive surface charge diffusion coefficient $D = (1.50 \pm 0.03) \times 10^{-16}$ m^2/s was obtained. Using the same method, the negative surface charge diffusion coefficient on the MLG film was estimated to be $(0.64 \pm 0.05) \times 10^{-16}$ m^2/s. The difference in the surface diffusion coefficients may be related to difference in charge carriers and the structure of the surface. Interestingly, after several hours KPFM signals from locally modified areas were still visible.

We assume that the charge in the locally modified areas is stabilized due to low conductivity, multi-layer graphene nature, and may be originated from MLG–nickel interface (often introduce significant defects [20,21,35].

A complementary reason may be stress on MLG film on nickel, which arises due to the different thermal expansion coefficients for nickel and graphene sheets [$+13 \times 10^{-6}$/°C and -8×10^{-6}/°C, respectively] [36]. We estimated the total stress on multi-layer graphene film after cooling from 1000 °C to room temperature is $\sim$2%. This stress produces high degree of ripples, and boundary conditions (domain-like structures) on the atomically flat surface of the MLG sheets (clearly observe in Fig. 3a). In addition, differences in work functions and charge density under mechanical deformation [37] could be also responsible for stabilization of the injected states in the MLG films. For example contact with metal and doping modifies the work function of single and MLG graphene sheet [38–40]. In the case of nickel, the reported value is 0.125 eV [41]. We also performed this experiment with monolayer graphene samples fabricated in our laboratory, and did not observe these phenomena; we assume that this is due to the high-conducting nature of monolayer graphene sheet (not shown).

Benefitting from the capability of controlled charge injection process; the method as described above can be used to investigate the local charge transfer at the interface. With a precise position control, the AFM tip induced charge injection can also be used for patterning of surface charges at nanoscale. The polarity of the written charges could be controlled during positive and negative charge injection process.

4. Conclusions

In summary, by performing a full set of experiments we demonstrated nanoscale electrostatic properties of as-grown MLG sheets on nickel by a combination of contact mode AFM and KPFM techniques under ambient condition. By using this method, we systematically investigated the charge injection (by applying positive or negative potential to the AFM tip), and subsequent charge diffusion on the large-area MLG-nickel surface. From the above measurements we elucidated that after injection, charge area is quite stable (even after 3 h); which was many order of magnitude greater than the expected Maxwell relaxation time required for the charge equilibration, and remain in the same state. The outcomes of this study could be promising for nano-patterning of surface charges without assistance of external electric field, which has a promising potential application for directed self-assembly of charged nanostructures for nanoelectronic devices such as super-capacitors, and in the field of energy-harvesting devices. From a broader perspective, this experimental approach by using KPFM to determine the effective charge injection and migration for other two-dimensional layered materials such as transition metal dichalogenides, reduced graphene oxide and based composite structures [42,43] will be useful to explore many exotic properties for future electronic applications such as spintronics, Li-ion batteries, photovoltaic cells, supercapacitors, etc. Also the discovery of local charge injection in MLG on nickel system open an avenue for novel nanoelectronic devices; which will combine extraordinary electronic and physical properties such as non-local spin injection, spin Hall Effect, and spin pumping. In addition, it will allow designing a new class of nanoengineered graphene structures for many exotic applications in the field of next generation graphene-based nanoelectronic devices.

Acknowledgements

MKS and PKT would like to thanks Bilateral Cooperação Científica e Tecnológica FCT/INDIA-2015/2017; between University of Aveiro, Portugal and Delhi Technological University, India (INT/PORTUGAL/P-13/2013); PTDC/CTM-NAN/121108/2010. GO-I thanks to Portuguese Foundation for Science and Technology (FCT) for a Post-Doctoral research grant (SFRH/BPD/90562/2012) and FCT-IF program. TEMA/DEM researchers also acknowledge FCT grant UID/EMS/00481/2013. IB thanks to Russian Science Foundation (Grant 16-19-10112).

Appendix A. Supplementary data

Supplementary data associated with this article can be found, in the online version, at doi:10.1016/j.apmt.2016.11.005.

References

[1] E. Silva-Pinto, B.R.A. Neves, Charge injection on insulators via scanning probe microscopy techniques: towards data storage devices, J. Nanosci. Nanotechnol. 10 (2010) 4204–4212.
[2] V. Panchal, R. Pearce, R. Yakimova, A. Tzalenchuk, O. Kazakova, Standardization of surface potential measurements of graphene domains, Sci. Rep. 3 (2013) 2597.

[3] Y. Zhang, D. Zherebetskyy, N.D. Bronstein, S. Barja, L. Lichtenstein, D. Schuppisser, L.-W. Wang, A.P. Alivisatos, M. Salmeron, Charge percolation pathways guided by defects in quantum dot solids, Nano Lett. 15 (2015) 3249–3253.
[4] L. Gross, F. Mohn, P. Liljeroth, J. Repp, F.J. Giessibl, G. Meyer, Measuring the charge state of an adatom with noncontact atomic force microscopy, Science 324 (2009) 1428–1431.
[5] T. Leoni, O. Guillermet, H. Walch, V. Langlais, A. Scheuermann, J. Bonvoisin, S. Gauthier, Controlling the charge state of a single redox molecular switch, Phys. Rev. Lett. 106 (2011) 216103.
[6] D. Ziegler, P. Gava, J. Güttinger, F. Molitor, L. Wirtz, M. Lazzeri, A.M. Saitta, A. Stemmer, F. Mauri, C. Stampfer, Variations in the work function of doped single- and few-layer graphene assessed by Kelvin probe force microscopy and density functional theory, Phys. Rev. B 83 (2011) 235434.
[7] D.D. Kulkarni, S. Kim, M. Chyasnavichyus, K. Hu, A.G. Fedorov, V.V. Tsukruk, Chemical reduction of individual graphene oxide sheets as revealed by electrostatic force microscopy, J. Am. Chem. Soc. 136 (2014) 6546–6549.
[8] G. Venugopal, K. Krishnamoorthy, R. Mohan, S.-J. Kim, An investigation of the electrical transport properties of graphene–oxide thin films, Mater. Chem. Phys. 132 (2012) 29–33.
[9] D. Esteban-Ferrer, M.A. Edwards, L. Fumagalli, A. Juárez, G. Gomila, Electric polarization properties of single bacteria measured with electrostatic force microscopy, ACS Nano 8 (2014) 9843–9849.
[10] N. Kurra, R.G. Reifenberger, G.U. Kulkarni, Nanocarbon-scanning probe microscopy synergy: fundamental aspects to nanoscale devices, ACS Appl. Mater. Interfaces 6 (2014) 6147–6163.
[11] N.S. Malvankar, S.E. Yalcin, M.T. Tuominen, D.R. Lovley, Visualization of charge propagation along individual pili proteins using ambient electrostatic force microscopy, Nat. Nanotechnol. 9 (2014) 1012–1017.
[12] T. Mélin, H. Diesinger, D. Deresmes, D. Stiévenard, Probing nanoscale dipole–dipole interactions by electric force microscopy, Phys. Rev. Lett. 92 (2004) 166101.
[13] T. Mélin, M. Zdrojek, D. Brunel, Electrostatic force microscopy and Kelvin force microscopy as a probe of the electrostatic and electronic properties of carbon nanotubes, in: B. Bhushan (Ed.), Scanning Probe Microscopy in Nanoscience and Nanotechnology, Springer Berlin Heidelberg, 2010, pp. 89–128.
[14] N. Plumere, Single molecules: a protein in the spotlight, Nat. Nanotechnol. 7 (2012) 616–617.
[15] S.E. Yalcin, J.A. Labastide, D.L. Sowle, M.D. Barnes, Spectral properties of multiply charged semiconductor quantum dots, Nano Lett. 11 (2011) 4425–4430.
[16] J.M. Mativetsky, E. Treossi, E. Orgiu, M. Melucci, G.P. Veronese, P. Samorì, V. Palermo, Local current mapping and patterning of reduced graphene oxide, J. Am. Chem. Soc. 132 (2010) 14130–14136.
[17] S.E. Yalcin, C. Galande, R. Kappera, H. Yamaguchi, U. Martinez, K.A. Velizhanin, S.K. Doorn, A.M. Dattelbaum, M. Chhowalla, P.M. Ajayan, G. Gupta, A.D. Mohite, Direct imaging of charge transport in progressively reduced graphene oxide using electrostatic force microscopy, ACS Nano 9 (2015) 2981–2988.
[18] R. Hawaldar, P. Merino, M.R. Correia, I. Bdikin, J. Grácio, J. Méndez, J.A. Martín-Gago, M.K. Singh, Large-area high-throughput synthesis of monolayer graphene sheet by hot filament thermal chemical vapor deposition, Sci. Rep. 2 (2012) 682.
[19] J.-H. Lee, P.E. Loya, J. Lou, E.L. Thomas, Dynamic mechanical behavior of multilayer graphene via supersonic projectile penetration, Science 346 (2014) 1092–1096.
[20] Y. Ma, Y. Dai, M. Guo, B. Huang, Graphene–diamond interface: gap opening and electronic spin injection, Phys. Rev. B 85 (2012) 235448.
[21] L. Liao, Y.-C. Lin, M. Bao, R. Cheng, J. Bai, Y. Liu, Y. Qu, K.L. Wang, Y. Huang, X. Duan, High-speed graphene transistors with a self-aligned nanowire gate, Nature 467 (2010) 305–308.
[22] J. Lahiri, Y. Lin, P. Bozkurt, I.I. Oleynik, M. Batzill, An extended defect in graphene as a metallic wire, Nat. Nanotechnol. 5 (2010) 326–329.
[23] W. Melitz, J. Shen, A.C. Kummel, S. Lee, Kelvin probe force microscopy and its application, Surf. Sci. Rep. 66 (2011) 1–27.
[24] E.J.G. Santos, E. Kaxiras, Electric-field dependence of the effective dielectric constant in graphene, Nano Lett. 13 (2013) 898–902.
[25] H. Kliem, Kohlrausch relaxations: new aspects about the everlasting story, IEEE Trans. Dielectr. Electr. Insul. 12 (2005) 709–718.
[26] J.A. Stratton, Electromagnetic Theory, John Wiley & Sons, 2007.
[27] A. Rani, S. Nam, K.A. Oh, M. Park, Electrical conductivity of chemically reduced graphene powders under compression, Carbon lett. 11 (2010) 90–95.
[28] N. Knorr, S. Rosselli, G. Nelles, Surface-potential decay of biased-probe contact-charged amorphous polymer films, J. Appl. Phys. 107 (2010) 054106.
[29] A. Crisci, B. Gosse, J.-P. Gosse, V. Ollier-Duréault, Surface-potential decay due to surface conduction, Eur. Phys. J. AP 4 (1998) 107–116.
[30] Y.S. Zhou, Y. Liu, G. Zhu, Z.-H. Lin, C. Pan, Q. Jing, Z.L. Wang, In situ quantitative study of nanoscale triboelectrification and patterning, Nano Lett. 13 (2013) 2771–2776.
[31] R.B. Guenther, J.W. Lee, Partial Differential Equations of Mathematical Physics and Integral Equations, Courier Corporation, 1988.
[32] S.V. Kalinin, D.A. Bonnell, Imaging mechanism of piezoresponse force microscopy of ferroelectric surfaces, Phys. Rev. B 65 (2002) 125408.
[33] E.J. Mele, Screening of a point charge by an anisotropic medium: anamorphoses in the method of images, Am. J. Phys. 69 (2001) 557–562.
[34] S.S. Datta, D.R. Strachan, E.J. Mele, A.T.C. Johnson, Surface potentials and layer charge distributions in few-layer graphene films, Nano Lett. 9 (2009) 7–11.
[35] S.C. Bodepudi, A.P. Singh, S. Pramanik, Giant current-perpendicular-to-plane magnetoresistance in multilayer graphene as grown on nickel, Nano Lett. 14 (2014) 2233–2241.
[36] D. Yoon, Y.-W. Son, H. Cheong, Negative thermal expansion coefficient of graphene measured by Raman spectroscopy, Nano Lett. 11 (2011) 3227–3231.
[37] J. Gunho, C. Minhyeok, L. Sangchul, P. Woojin, K. Yung Ho, L. Takhee, The application of graphene as electrodes in electrical and optical devices, Nanotechnology 13 (2012) 112001.
[38] A. Kyas, J. Fleischhauer, E. Steinmetz, H. Wilhelmi, Investigations concerning the work function of doped graphite, Plasma Chem. Plasma Process 13 (1993) 223–235.
[39] K.C. Kwon, K.S. Choi, S.Y. Kim, Increased work function in few-layer graphene sheets via metal chloride doping, Adv. Funct. Mater. 22 (2012) 4724–4731.
[40] J. Park, W.H. Lee, S. Huh, S.H. Sim, S.B. Kim, K. Cho, B.H. Hong, K.S. Kim, Work-function engineering of graphene electrodes by self-assembled monolayers for high-performance organic field-effect transistors, J. Phys. Chem. Lett. 2 (2011) 841–845.
[41] G. Giovannetti, P.A. Khomyakov, G. Brocks, V.M. Karpan, J. van den Brink, P.J. Kelly, Doping graphene with metal contacts, Phys. Rev. Lett. 101 (2008) 026803.
[42] E. Otyepková, P. Lazar, K. Čépe, O. Tomanec, M. Otyepka, Organic adsorbates have higher affinities to fluorographene than to graphene, Appl. Mater. Today 5 (2016) 142–149.
[43] R.K. Joshia, S. Alwarappan, M. Yoshimura, V. Sahajwalla, Y. Nishina, Graphene oxide: the new membrane material, Appl. Mater. Today 1 (2015) 1–12.

This article has been accepted for inclusion in a future issue of this journal. Content is final as presented, with the exception of pagination.

Compact Model for Ferroelectric Negative Capacitance Transistor With MFIS Structure

Girish Pahwa, *Student Member, IEEE*, Tapas Dutta, *Member, IEEE*, Amit Agarwal, and Yogesh Singh Chauhan, *Senior Member, IEEE*

***Abstract*— We present a physics-based compact model for a ferroelectric negative capacitance FET (NCFET) with a metal–ferroelectric–insulator–semiconductor (MFIS) structure. The model is computationally efficient, and it accurately calculates the gate charge density as a function of the applied voltages. For the first time, an explicit expression for the channel current in bulk NCFET is also deduced taking into account the spatial variation of ferroelectric polarization in the longitudinal direction. Using current continuity condition in the channel, we find that different regions of the ferroelectric may operate in a positive or a negative capacitance state depending on the external biases. The model captures the impact of ferroelectric thickness scaling and variation in the ferroelectric material parameters, and has been validated against the implicit approach involving full numerical computations as well as experimental data. We also compare the device characteristics of the MFIS structure with those of the metal–ferroelectric–metal–insulator–semiconductor structure.**

***Index Terms*— Compact model, ferroelectric, negative capacitance FET (NCFET), negative capacitance.**

I. Introduction

TWO classes of negative capacitance FET (NCFET) structures have been reported in the literature, as shown in Fig. 1. The metal–ferroelectric–metal–insulator–semiconductor (MFMIS) structure has a metal layer between the ferroelectric and the gate insulator and has been primarily used for experimental demonstrations [1]–[4]. The other one is a metal–ferroelectric–insulator–semiconductor (MFIS) structure, in which the intermediate metal layer is not included [5]–[9]. In the MFMIS structure, the metal layer between the ferroelectric and the gate insulator provides an equipotential surface at the internal gate, thus enabling the treatment of the ferroelectric and the underlying MOSFET as two separate circuit entities connected by a wire [1], [10]. In contrast, the ferroelectric polarization and the internal gate voltage, V_{int} (see Fig. 1) in an MFIS device vary spatially in the longitudinal direction at a nonzero drain bias. Recently, it was reported in [11] that in steady state the negative capacitance effect is unstable in any practical MFMIS structure that has gate leakage. In contrast, in the MFIS structure, gate leakage does not affect the stabilization of the ferroelectric, and the internal MOSFET gate oxide and the ferroelectric material can always be properly chosen so as to ensure the stability of the negative capacitance effect in steady state thereby making this structure more promising for the transistor applications. Moreover, our analysis shows that the MFIS device exhibits a higher ON current and a steeper subthreshold swing compared with the MFMIS device for a higher drain bias.

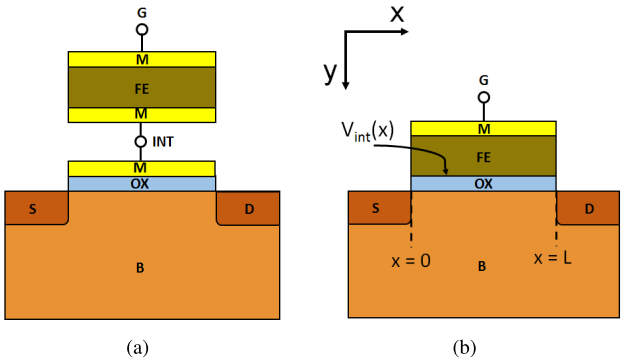


Fig. 1. Two types of NCFET structures (a) MFMIS-FET (b) MFIS-FET. $V_{\text{int}}(x)$ is the potential at the ferroelectric-oxide interface at any position x.

Models for the MFIS-NCFET with bulk and double gate MOSFET as the baseline FET have earlier been proposed in [12] and [13], respectively. However, their modeling approaches involve implicit equations which can only be solved using numerical methods involving several iterations and hence turn out to be tedious and time consuming for real circuit design. Therefore, there is a strong need for an explicit and compact model that is able to capture the physics of these devices, and at the same time, is computationally efficient so

Manuscript received October 8, 2016; revised December 18, 2016, January 7, 2017, and January 11, 2017; accepted January 11, 2017. This work was supported in part by the Council of Scientific and Industrial Research, in part by the Department of Science and Technology, in part by the Science and Engineering Research Board, and in part by the Semiconductor Research Corporation. The review of this paper was arranged by Editor B. Kaczer.

G. Pahwa, T. Dutta, and Y. S. Chauhan are with the Nanolab, Department of Electrical Engineering, IIT Kanpur, Kanpur 208016, India (e-mail: girish@iitk.ac.in; chauhan@iitk.ac.in).

A. Agarwal is with the Department of Physics, IIT Kanpur, Kanpur 208016, India.

Color versions of one or more of the figures in this paper are available online at http://ieeexplore.ieee.org.

Digital Object Identifier 10.1109/TED.2017.2654066

0018-9383 © 2017 IEEE. Personal use is permitted, but republication/redistribution requires IEEE permission.
See http://www.ieee.org/publications_standards/publications/rights/index.html for more information.

as to enable fast circuit simulations. In this paper, we propose a compact model for MFIS-NCFET taking the spatial variation of ferroelectric polarization and V_{int} into account. We have deliberately ignored the short channel effects to exclusively focus on the negative capacitance effect of the ferroelectric. We have only focused on the nonhysteretic NCFET operation primarily desirable for low power logic applications and the explicit modeling approach presented in Section II for gate charge calculation is valid in this regime only.

II. Model Description

In the steady state, the relation between the voltage across ferroelectric V_{fe} and the gate charge density Q_G ($\approx$ polarization) is given by the Landau–Devonshire theory as [10], [14]

$$V_{\text{fe}} = Et_{\text{fe}} = aQ_G + bQ_G{}^3 \tag{1}$$

where t_{fe} denotes the ferroelectric thickness and $a = 2\alpha t_{\text{fe}}$ and $b = 4\beta t_{\text{fe}}$, where α and β are the ferroelectric material dependent Landau parameters. a and b can further be related to the ferroelectric properties, remnant polarization P_r, and coercive field E_c as [15]

$$a = -\frac{3\sqrt{3}}{2}\frac{E_c t_{\text{fe}}}{P_r} \text{ and } b = \frac{3\sqrt{3}}{2}\frac{E_c t_{\text{fe}}}{P_r{}^3}. \tag{2}$$

From the voltage balance condition, we get

$$V_G - V_{\text{FB}} = V_{\text{fe}} + \frac{Q_G}{C_{\text{ox}}} + \psi_S = a_{\text{eff}} Q_G + bQ_G{}^3 + \psi_S \tag{3}$$

where V_{FB} is the flat band voltage, ψ_S is the surface potential, C_{ox} is the oxide capacitance, and $a_{\text{eff}} = a + (1/C_{\text{ox}})$ can be considered as an effective value of the parameter a for the ferroelectric and oxide stack. Q_G as a function of ψ_S can be expressed as [16]

$$Q_G = \text{sign}(\psi_S)\gamma\, C_{\text{ox}}[\psi_S + V_t(e^{-\psi_S/V_t} - 1) + e^{-(2\phi_F+V_C)/V_t}(V_t e^{\psi_S/V_t} - \psi_S - V_t)]^{1/2} \tag{4}$$

where ϵ_s is the permittivity of the semiconductor, N_A is the body doping concentration, $\gamma = (2q\epsilon_s N_A)^{1/2}/C_{\text{ox}}$ is the body coefficient, V_C is the difference between the electron and hole quasi-Fermi levels, ϕ_F is the Fermi potential, and $V_t = kT/q$ is the thermal voltage, where T and q denote the temperature and the electronic charge, respectively. sign(ψ_S) denotes the signum function which is $+1$ for $\psi_S > 0$, 0 for $\psi_S = 0$, and -1 for $\psi_S < 0$.

Substituting ψ_S from (3) into (4) results in an implicit equation in terms of Q_G. Numerical approach without a good initial guess to this equation may require several iterations which is against the incentive of compact modeling for circuit design purpose. Here, we develop a computationally efficient methodology to solve this implicit equation where we derive a competent initial guess for Q_G, separately for weak inversion, strong inversion, and the transition region joining them as described in the following.

A. Weak Inversion Approximation

In depletion and weak inversion regions, Q_G can be approximated as [16]

$$Q_G \approx \gamma\, C_{\text{ox}}\sqrt{\psi_S + V_t(e^{-\psi_S/V_t} - 1)}. \tag{5}$$

Substituting (5) into (3), we get an implicit equation in ψ_S as

$$V_G = V_{\text{FB}} + \psi_S + w_1\sqrt{V_t(e^{-\psi_S/V_t} - 1) + \psi_S} + w_2\left(\sqrt{V_t(e^{-\psi_S/V_t} - 1) + \psi_S}\right)^3 \tag{6}$$

where $w_1 = a_{\text{eff}}\gamma\, C_{\text{ox}}$ and $w_2 = b\gamma^3 C_{\text{ox}}{}^3$.

Now ψ_S is explicitly calculated from the above-mentioned equation using the following two-step procedure:

1) A first-order value of $\psi_S = \psi_{\text{wi0}}$ ("wi" denotes weak inversion) is calculated by approximating the exponential terms in (6) by the second-order Taylor expansion as

$$e^{-\psi_{\text{wi0}}/V_t} = 1 - \frac{\psi_{\text{wi0}}}{V_t} + \frac{1}{2}\left(\frac{\psi_{\text{wi0}}}{V_t}\right)^2. \tag{7}$$

After rearrangement of terms, we get a cubic equation in ψ_{wi0} as

$$\psi_{\text{wi0}}{}^3 + \frac{(2V_t)^{\frac{3}{2}}}{w_2}\left[\left(1 + \frac{w_1}{\sqrt{2V_t}}\right)\psi_{\text{wi0}} - V_G + V_{\text{FB}}\right] = 0. \tag{8}$$

The above-mentioned cubic equation can be solved analytically by the procedure given in the Appendix.

2) This step is used to further improve the accuracy of the solution. Using $\psi_S = \psi_{\text{wi0}}$ obtained in step-1, in the exponential terms of (6) and assuming $[V_t(e^{-\psi_{\text{wi0}}/V_t} - 1) + \psi_S)]^{1/2} = \varphi$, we get a cubic equation in φ as

$$w_2\varphi^3 + \varphi^2 + w_1\varphi - V_t(e^{-\psi_{\text{wi0}}/V_t} - 1) - (V_G - V_{\text{FB}}) = 0. \tag{9}$$

Analytical solution of the above-mentioned equation is again obtained using the procedure given in the Appendix. Finally, the value of $\psi_S = \psi_{\text{wi}}$ in weak inversion is obtained as

$$\psi_{\text{wi}} = \varphi^2 + V_t(1 - e^{-\psi_{\text{wi0}}/V_t}). \tag{10}$$

Gate charge density is now calculated with the substitution of ψ_{wi} in (4).

B. Strong Inversion Approximation

Q_G calculation in this region is also done in two steps as follows:

1) ψ_S in the strong inversion can be approximated to the first order as $\psi_S = \psi_{\text{si0}} = 2\phi_F + \phi_0 + V_C$ ("si" denotes strong inversion), where ϕ_0 is an empirical parameter [16]. ψ_{si0} can be used to obtain the corresponding gate charge density $Q_G = Q_{\text{si0}}$ as a function of gate voltage using (3).

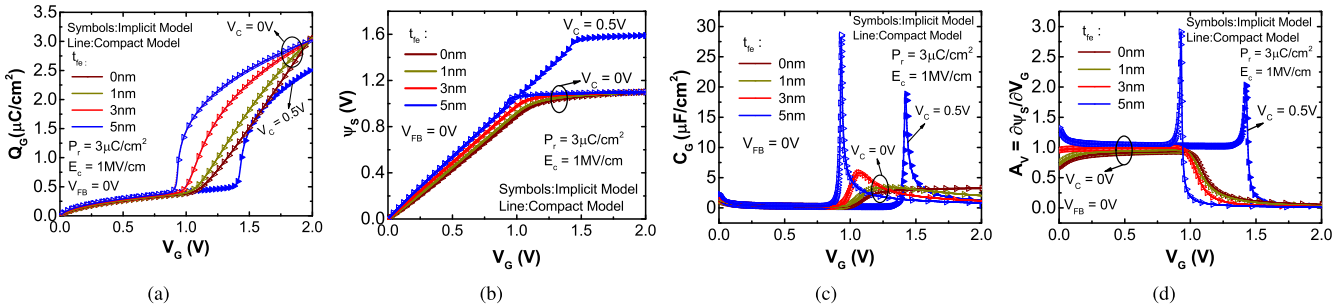


Fig. 2. (a) Comparison of the gate charge density computed from our compact model with the full numerical solution of the implicit equation. (b) Surface potential as a function of V_G for different t_{fe} values. (c) Gate capacitance as a function of V_G for different t_{fe} values. (d) Voltage amplification due the negative capacitance effect of the ferroelectric as a function of V_G for different t_{fe} values. Note that $t_{fe} = 0$ nm corresponds to the baseline FET. Sharp increase in C_G and A_V occurs due to an improved matching between ferroelectric and internal MOSFET capacitances. Impact of a nonzero V_C (= 0.5 V) is also shown for $t_{fe} = 5$ nm, in (a)–(d).

2) In the strong inversion, Q_G in (4) after ignoring the negligible terms can be written as [16]

$$Q_G = \gamma C_{\rm ox}\sqrt{\psi_S + V_t e^{(\psi_S - 2\phi_F - V_C)/V_t}}. \tag{11}$$

Substitution of ψ_S from (3) in the exponential term of (11) and some rearrangements of terms give an implicit equation in Q_G as

$$V_t \log\left[\left(\frac{Q_G}{\gamma C_{\rm ox}\sqrt{V_t}}\right)^2 - \frac{\psi_S}{V_t}\right] = V_G - V_{\rm FB} - (a_{\rm eff} Q_G + b {Q_G}^3) - 2\phi_F - V_C. \tag{12}$$

As Q_G is large in this region, the linear and cubic terms in Q_G become dominant compared with the log term. The log term is, therefore, approximated by assuming $\psi_S = \psi_{\rm si0}$ and $Q_G = Q_{\rm si0}$ in it. We analytically solve the resulting cubic equation in Q_G using the technique given in the Appendix.

C. Transition From Weak Inversion to Strong Inversion

A smooth transition from weak inversion to strong inversion is ensured by employing a polynomial smoothing technique. Q_G in the transition region is assumed to be a cubic polynomial in V_G as

$$Q_G = c_0 {V_G}^3 + c_1 {V_G}^2 + c_2 V_G + c_3 \tag{13}$$

where the polynomial coefficients are determined from a set of four boundary conditions at the two (Q_G, V_G) transition points, one defined corresponding to some $\psi_S = \psi_{\rm wit}$ in the weak inversion and the other corresponding to $\psi_S = \psi_{\rm sit}$ in the strong inversion. In this paper, these values have been taken as, $\psi_{\rm wit} = 2\phi_F + V_C$ and $\psi_{\rm sit} = 2\phi_F + 6V_t + V_C$. $\psi_{\rm wit}$ and $\psi_{\rm sit}$ are used to calculate (Q_G, V_G) pairs from (4) and (3) which constitute the two out of the total four boundary conditions. The continuity of the first-order derivatives at these transition points constitute the other two boundary conditions.

After getting a robust initial guess in either of the three regions (weak inversion, strong inversion, or the transition regions) using the above-mentioned formulation, the final value of Q_G is obtained by solving the complete gate charge implicit equation [(3) and (4)] using the approach presented in [17] as

$$Q_G = Q_{G0} - \frac{g}{g'}\left(1 + \frac{g g''}{2 g'^2}\right) \tag{14}$$

where Q_{G0} denotes the initial guess. Other quantities are defined as

$$g = \left(\frac{Q_{G0}}{\gamma C_{\rm ox}}\right)^2 - \psi_{S0}(1 - \xi_2) - V_t(\xi_1 - \xi_2 + \xi_3) \tag{15}$$

where

$$\xi_1 = e^{-\psi_{S0}/V_t} - 1, \quad \xi_2 = e^{-(2\phi_F + V_C)/V_t}, \quad \xi_3 = \xi_2 e^{\psi_{S0}/V_t} \tag{16}$$

and $\psi_{S0} = \psi_S(Q_{G0})$ is calculated using (3)

$$g' = \frac{2Q_{G0}}{(\gamma C_{\rm ox})^2} + (a_{\rm eff} + 3b{Q_{G0}}^2)(\xi_3 - \xi_1 - \xi_2) \tag{17}$$

$$g'' = \frac{2}{(\gamma C_{\rm ox})^2} + 6bQ_{G0}(\xi_3 - \xi_1 - \xi_2) - \frac{(a_{\rm eff} + 3b{Q_{G0}}^2)^2}{V_t}(\xi_3 + \xi_1 + 1). \tag{18}$$

Fig. 2(a) and (b) shows, respectively, the gate charge density, Q_G and the surface potential, ψ_S calculated using our compact model for different ferroelectric thicknesses (corresponding to $V_C = 0$ V at the source end) and compare it with the exact solution of the complete gate charge implicit equation. Impact of a nonzero V_C (at a different channel location) is also shown for $t_{\rm fe} = 5$ nm. The corresponding derivatives, gate capacitance (per unit area), C_G, and voltage amplification due to negative capacitance, $A_V = \partial\psi_S/\partial V_G$ are shown in Fig. 2(c) and (d). To test the robustness of the model, we have intentionally used a low $P_r = 3$ μC/cm^2 and a high $E_c = 1$ MV/cm which increases the coefficient b of the cubic term in (1) and makes the $Q_G - V_G$ relationship strongly nonlinear. As shown in Fig. 2, our model shows excellent match with the implicit model and precisely captures the nonlinearities involved in Q_G at larger $t_{\rm fe}$ values. For $V_C = 0$ V, increase in Q_G and ψ_S with $t_{\rm fe}$ occurs due to a better capacitance matching of the ferroelectric and internal

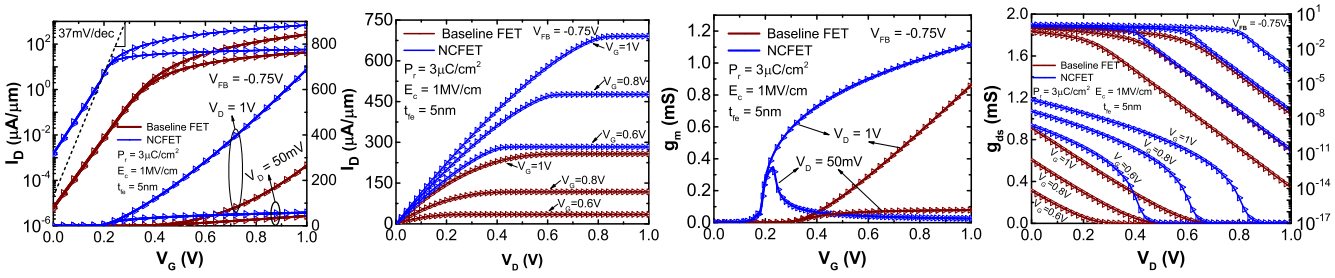


Fig. 3. (a) I_D–V_G characteristics of NCFET and baseline MOSFET. NCFET exhibits a lower subthreshold swing (minimum value is ≈ 37 mV/decade), a higher ON-current, a lower V_{th} and a higher OFF current compared with the baseline MOSFET. (b) I_D–V_D characteristics of NCFET and baseline MOSFET. (c) Transconductance (g_m) variation with V_G. (d) Drain conductance (g_{ds}) variation with V_D. In all the plots, symbols and lines represent the results from the implicit model and our compact model, respectively.

MOSFET capacitances (C_{fe} and C_{int}) [18], [19]. A nonzero V_C postpones the formation of inversion charge density to a higher V_G bias, and hence, all the $V_C = 0.5$ V curves get shifted right. It also reduces C_{int} compared with $V_C = 0$ V case for the same applied V_G. This in turn reduces the matching between C_{fe} and C_{int} and, therefore, reduces the peak values of C_G and A_V compared with $V_C = 0$ V case. Impact of V_C is shown only for one nonzero value of $V_C = 0.5$ V to prevent overcrowding of curves. For still higher values of V_C, surface potential curves in Fig. 2(b) move upward similar to the case of a regular MOSFET [16].

III. Current Modeling

Current at any position in the channel comprising of drift and diffusion components is given by [16], [20]

$$I = -\mu W Q_I \frac{d\psi_S}{dx} + \mu W V_t \frac{dQ_I}{dx} \tag{19}$$

where Q_I is the inversion charge density, W is the width of the internal MOSFET, μ is the mobility of the mobile charge carriers in the channel, and x is the position variable along the channel. Substituting $d\psi_S/dx$ calculated using (3) and integrating both sides with respect to x from the source end to the drain end, we obtain

$$\int_0^L I dx = \mu W \int_{Q_{GS}}^{Q_{GD}} Q_I(a_{eff} + 3bQ_G{}^2) dQ_G + \mu W V_t \int_{Q_{IS}}^{Q_{ID}} dQ_I \tag{20}$$

where L represent the channel length and $Q_{GS(D)}$ and $Q_{IS(D)}$, respectively, denote the gate charge and the inversion charge densities at the source (drain) end. Using the fact that current is continuous in the channel, I in the integration can be taken out and written as

$$I = \bar{I}_{drift} + \bar{I}_{diff} \tag{21}$$

where

$$\bar{I}_{drift} = \mu \frac{W}{L} \int_{Q_{GS}}^{Q_{GD}} Q_I(a_{eff} + 3bQ_G{}^2) dQ_G \tag{22}$$

and

$$\bar{I}_{diff} = \mu \frac{W}{L} V_t \int_{Q_{IS}}^{Q_{ID}} dQ_I = \mu \frac{W}{L} V_t (Q_{ID} - Q_{IS}) \tag{23}$$

represent the average values of drift and diffusion currents over the channel length L, respectively.

From the charge conservation condition, we have $Q_I = -Q_G - Q_B$, where Q_B is the bulk charge density. Using the charge sheet approximation for inversion layer, i.e., $Q_B \approx -\gamma C_{ox}\sqrt{\psi_S}$ [16] and (3), we obtain Q_I entirely in terms of Q_G as

$$Q_I = -Q_G + \gamma C_{ox}\sqrt{V_G - V_{FB} - a_{eff} Q_G - bQ_G{}^3}. \tag{24}$$

The above-mentioned expression can be used to evaluate the diffusion current in (23) in terms of Q_{GS} and Q_{GD}.

Substituting (24) into (22) and after integrating, a closed-form expression of $\bar{I}_{drift}$ is obtained as

$$\bar{I}_{drift} = \frac{\mu W}{L}(f(Q_{GS}) - f(Q_{GD})) \tag{25}$$

where

$$f(Q_G) = \frac{3}{4} bQ_G{}^4 + \frac{1}{2} a_{eff} Q_G{}^2 + \frac{2}{3}\gamma C_{ox}\left(\sqrt{V_G - V_{FB} - a_{eff} Q_G - bQ_G{}^3}\right)^3. \tag{26}$$

IV. Model Validation and Discussion

For validation with the implicit model, we calculate Q_{GS} and Q_{GD} in two ways: our compact modeling approach and the full numerical solution of the implicit gate charge model. We then validate our model by comparing the I_D–V_G and I_D–V_D characteristics obtained using these two approaches. The comparison results for the cases of ferroelectric thickness (t_{fe}) scaling and the material parameters [remnant polarization (P_r) and coercive field (E_c)] variation are demonstrated. For comparison with the implicit model, a long channel baseline MOSFET is used with $L = W = 1$ μm, $N_a = 5\times10^{17}$ cm^{-3}, EOT = 1 nm, and $\mu = 500$ cm^2/Vs without considering mobility degradation in order to emphasize the effect of the ferroelectric only. Validation with experimental data is given in this section.

A. I_D–V_G and I_D–V_D Characteristics

Fig. 3(a) compares the I_D–V_G characteristics of the NCFET ($t_{fe} = 5$ nm) with the baseline MOSFET ($t_{fe} = 0$) for a low $V_D = 50$ mV and a high $V_D = 1$ V. The

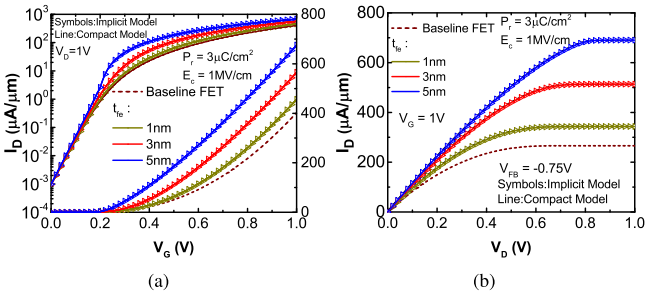


Fig. 4. (a) Impact of variation of the ferroelectric thickness on I_D–V_G characteristics of NCFET. I_{OFF} has been set to 1 nA/μm by V_{FB} tunning for comparison purpose. (b) Impact of variation of the ferroelectric thickness on I_D–V_D characteristics of NCFET.

NCFET shows a lower subthreshold swing (minimum value is $\approx$ 37 mV/decade) compared with the baseline MOSFET. It also exhibits a higher ON and a lower threshold voltage (V_{th}) compared with the baseline MOSFET on account of surface potential amplification due to negative capacitance effect [see Fig. 2(b) and (d)]. A lower V_{th} value also increases its OFF current. Note that the amount of V_{th} shift will depend on the ferroelectric material parameters and thickness and also on the geometry of the baseline MOSFET. In fact, an increase in V_{th} has also been observed in the simulations of short channel NCFET devices which mainly occurs due to an increased drain to channel coupling [21], [22]. We have not covered the short channel aspects of NCFET in this paper.

Fig. 3(b) shows the I_D–V_D characteristics of NCFET and baseline MOSFET. As expected, I_D is higher for NCFET for all the V_G values and it also saturates at a larger V_D value due to a lower threshold voltage [see Fig. 3(a)]. The transconductance and drain conductance are shown in Fig. 3(c) and (d), respectively, and it can be seen that our model fits the numerical simulation very well.

B. Ferroelectric Thickness Scaling

Fig. 4(a) and (b) shows the I_D–V_G and I_D–V_D characteristics of NCFET for different t_{fe} values. In Fig. 4(a), we have set the I_{OFF} value to 1 nA/μm by V_{FB} tunning for comparison purpose. NCFET characteristics still show a higher ON current compared with the baseline MOSFET which increases with increase in t_{fe}. Thus, V_{DD} can be lowered to achieve the same ON current with NCFET as has been reported in the literature [13], [18].

However, benefits of negative capacitance by increasing t_{fe} beyond a critical thickness (t_c) are also accompanied with a hysteresis in the electrical characteristics [18], [19], which is undesirable for logic applications [23]. An approximate value of t_c is calculated using the approach given in [12], but including the effect of the intermediate oxide layer. For a nonhysteretic operation, $\partial V_G/\partial \psi_S \geq 0$ in (3), which implies

$$t_{fe} \leq \frac{2V_t C_{ox} + Q_G}{C_{ox}(2|\alpha| Q_G - 12\beta {Q_G}^3)} \tag{27}$$

where we have approximated $\partial Q_G/\partial \psi_S \approx Q_G/2V_t$ in the inversion region of MOSFET [12]. For the worst case, maximum allowed value of t_{fe} should be less than the minimum value of the right-hand side (RHS) expression in (27) which occurs at a $Q_G = Q_c$. Q_c is obtained by making derivative of RHS in (27) equal to zero which results in the following cubic equation:

$${Q_c}^3 + 3V_t C_{ox} {Q_c}^2 - \frac{1}{6} V_t C_{ox} \frac{|\alpha|}{\beta} = 0. \tag{28}$$

Now, t_c can be calculated by substituting the positive root of the above-mentioned equation in RHS of (27). t_c also puts an upper limit on t_{fe} to be used for Q_G calculation using the explicit approach presented in Section II.

C. Ferroelectric Material Parameter Variation

Ferroelectric material parameters, the remnant polarization (P_r) and the coercive field (E_c) both significantly affect the electrical characteristics of NCFET [22], [24]. We have tested the capability of our model to handle the variation of these parameters in a wide range.

Fig. 5(a) and (b), respectively, shows the I_D–V_G and I_D–V_D characteristics for a wide range of remnant polarization values from 3 to 50 μC/cm^2. A higher P_r of 50 μC/cm^2 results in a lowering of the magnitude of the Landau coefficient a [see (2)] which reduces the step-up conversion capability of the ferroelectric and only a slight improvement in the ON current over the baseline MOSFET is achieved [24]. As P_r is reduced, I_D increases in general but for lower P_r values of 4 and 3 μC/cm^2, I_D of former transcends the I_D of latter at higher gate voltages. In this case, it can be inferred that $P_r = 3$ μC/cm^2 is suitable for low V_{DD} values and $P_r = 4$ μC/cm^2 is suitable for high V_{DD} values. This reverse trend in I_D–V_G for lower P_r values has also been reported earlier in [25]. The criss-crossing in I_D–V_G can be related to the variation of gate charge density with P_r which follows a similar trend, as shown in Fig. 5(c) for the gate charge density at the source end (Q_{GS}). The gate charge saturates earlier at lower P_r values than higher P_r values resulting in a criss-crossing of curves which can be more clearly explained through the loadline analysis, as shown in Fig. 5(d). Operating point of the device at a particular V_G is given by the intersection of Landau curve (1) with the loadline curve obtained by substituting ψ_S in terms of V_{fe} from (3) into (4). Landau curves (solid lines) are shown for low and high values of P_r. Loadline for a low V_G of 0.2 V intersects all the three Landau curves in their respective linear negative capacitance regions. Gate charge at these operating points increases with a decrease in P_r (see the inset for a zoomed-in view), which is in accordance with the $Q_{GS} - V_G$ behavior observed in Fig. 5(c). On the other hand, loadline for a higher V_G of 1 V intersects the Landau curve of $P_r = 10$ μC/cm^2 case in the linear region but those of $P_r = 3$ and 4 μC/cm^2 cases in the saturation regions. It can be clearly seen that the operating point charge, Q_{GS} now increases with P_r following a trend opposite to what is observed at lower gate voltages. Note that the source-end gate charge density is just used for an illustration purpose, and the criss-crossings in $Q_{GS} - V_G$ occur at different (lower) gate voltages than the criss-crossings in the I_D–V_G characteristics [Fig. 5(a)], as I_D also depends on the factors other than Q_{GS} (see Section III). Criss-crossings in I_D–V_G for

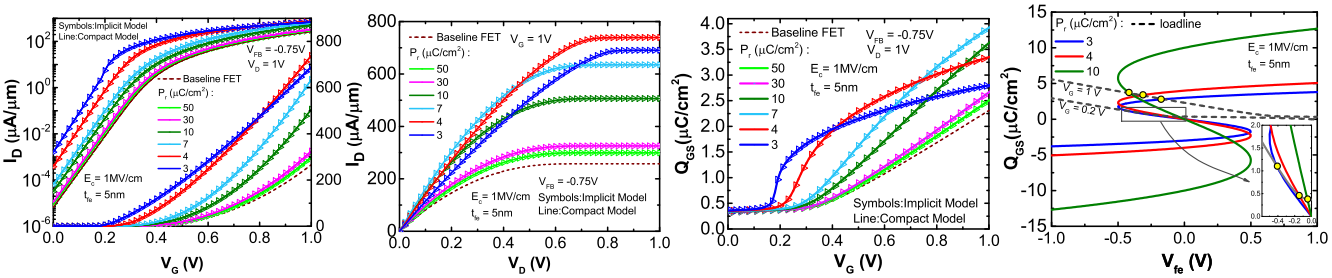


Fig. 5. Impact of variation of remnant polarization on (a) I_D–V_G, (b) I_D–V_D, and (c) Q_{GS}–V_G characteristics of NCFET. Note the crossover in characteristics in the low P_r regime. At low P_r values, the Landau coefficient b becomes very high [see (2)], which causes the gate charge to saturate at high gate bias resulting in a lower current. (d) Loadline analysis to demonstrate how the interplay of gate bias and P_r values can move the operating point to different regions of polarization (see text for details).

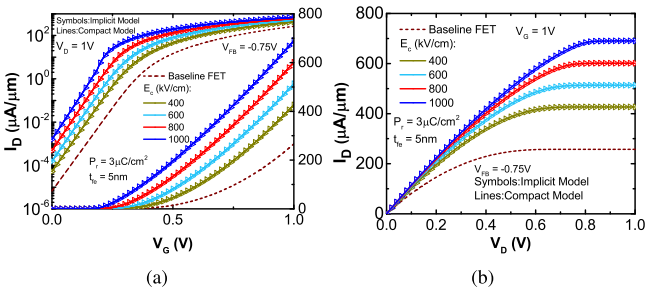


Fig. 6. Impact of variation of coercive field on (a) I_D–V_G and (b) I_D–V_D characteristics of NCFET. Unlike the low P_r case, here, we do not observe the criss-cross in the current–voltage characterisitcs because of the linear dependence of Landau coefficients, a and b on E_c.

higher P_r values will also be observed similar to $Q_{GS} - V_G$ (for, e.g., $P_r = 4$ and 7 μC/cm^2), though at higher gate voltages (>1 V) which has not been shown in Fig. 5(a).

Fig. 6 shows the I_D–V_G and I_D–V_D characteristics for coercive field (E_c) variation from 400 kV/cm to 1 MV/cm. A higher E_c increases the value of Landau coefficient a [see (2)] which results in a greater amplification of the surface potential which in turn yields a higher current [24]. Unlike the case of P_r variation, no criss-cross in I_D–V_G characteristics appears due to a linear dependence of a and b on E_c.

It is clear from Figs. 5 and 6 that our model is accurate and robust in its ability to capture the effect of different ferroelectric material parameter variations.

D. Validation With Experimental Results

Fig. 7 compares the compact model with recent experimental data from [7] and [9]. It can be seen that our model is able to capture sub-60 mV/decade experimental I_D–V_G characteristics quite accurately. Mismatches between the model and experimental data at low V_G are due to the core nature of the model at present without any second order effects added.

E. Comparison With MFMIS NCFET

We compare the I_D–V_G characteristics of MFIS NCFET with that of MFMIS NCFET in Fig. 8(a) and (b) for low and high drain biases, respectively. The MFMIS NCFET has been modeled by coupling the L-K equation with the existing

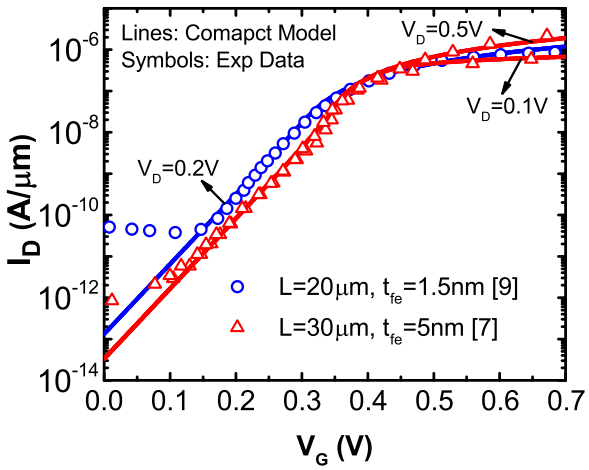


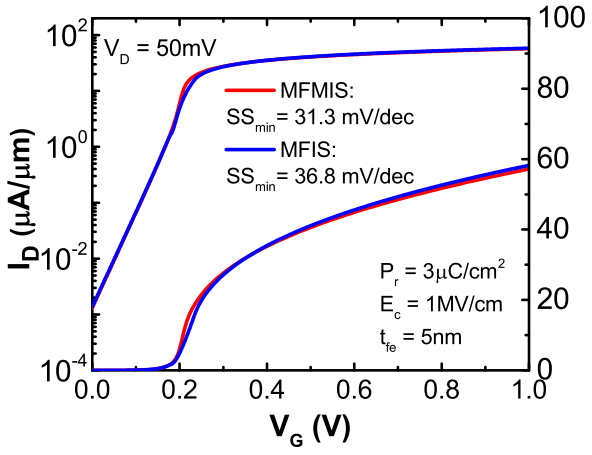
Fig. 7. Comparison of the compact model with the experimental data from [7] and [9]. Differences between the model and experimental data at low V_G are due to the core nature of the model.

standard compact model BSIM6 for bulk MOSFETs [10], [19]. For a low V_D, no appreciable difference is observed between their I_D–V_G characteristics. However, for a high V_D, MFIS device shows a superiority over MFMIS both in terms of ON current and subthreshold swing. A similar result for a high V_D has also been reported very recently in [26] using a different modeling approach for NC-FinFETs. Thus, the MFIS NCFET is much less sensitive to the internal gain reduction caused by mismatching of C_{fe} and C_{int} at higher drain voltages compared with the MFMIS device.

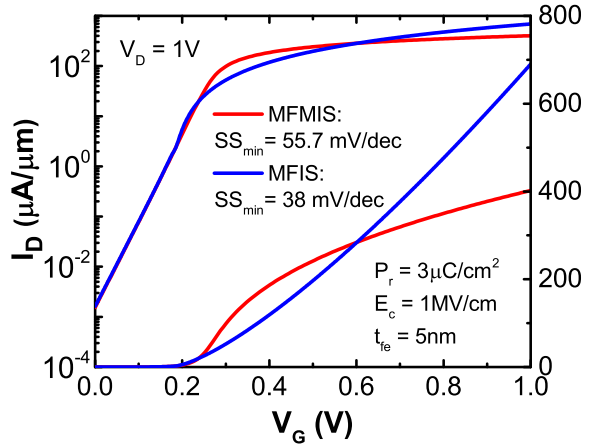
V. Spatial Variation of the Internal Voltage

The main distinction between MFIS and MFMIS structures of NCFET is that the internal gate voltage, V_{int} varies spatially in the longitudinal direction in the former, while it remains constant in the latter. Fig. 9 shows the profiles of $Q_G(x)$ ($\approx$ polarization) and $V_{int}(x)$ obtained by applying the condition of current continuity at every point in the channel as: $I(x) = I(L)$. Here, $I(x)$ denotes the current of a transistor of length x, with x end acting as drain terminal and is of the form

$$I(x) = \frac{\mu W}{x}[F(Q_{GS}) - F(Q_G(x))] \tag{29}$$



(a)



(b)

Fig. 8. Comparison of I_D–V_G characteristics of NCFETs with MFIS and MFMIS architectures at (a) $V_D = 50$ mV and (b) $V_D = 1$ V.

where

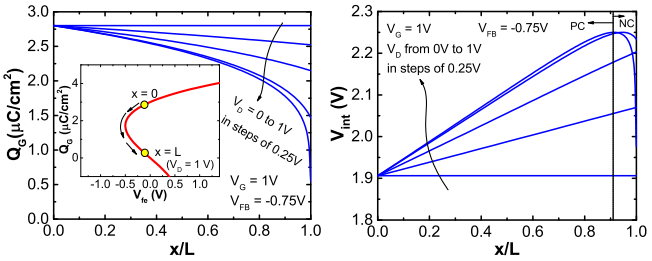
$$F(Q_G(x)) = \frac{3}{4}bQ_G{}^4 + \frac{1}{2}a_{\text{eff}}Q_G{}^2 + V_t Q_G - \gamma C_{\text{ox}}V_t\sqrt{V_G - V_{\text{FB}} - a_{\text{eff}}Q_G - bQ_G{}^3} + \frac{2}{3}\gamma C_{\text{ox}}\left(\sqrt{V_G - V_{\text{FB}} - a_{\text{eff}}Q_G - bQ_G{}^3}\right)^3 \tag{30}$$

is obtained using (21) and (23)–(26). Current continuity now provides a relation between $Q_G(x)$ and x as

$$\frac{x}{L} = \frac{[F(Q_{\text{GS}}) - F(Q_G(x))]}{[F(Q_{\text{GS}}) - F(Q_{\text{GD}})]}. \tag{31}$$

Once, $Q_G(x)$ is obtained, $V_{\text{int}}(x) = V_G - V_{\text{fe}}(Q_G)$ can be obtained using (3).

As shown in Fig. 9(a), Q_G decreases along the channel because of the drain to channel coupling which gets more pronounced at higher V_D values. It can be seen in Fig. 9(a) (inset) that Q_G along the channel rolls off from a positive capacitance region at $x = 0$ and may land in a positive or a negative capacitance zone at any position in the channel depending on the drain bias. Also note that Q_G versus x profiles in Fig. 9(a)



(a) (b)

Fig. 9. (a) Gate charge density profiles along the longitudinal direction for different values of V_D. (b) Internal voltage V_{int} profiles along the longitudinal direction for different values of V_D. NC and PC denote negative and positive capacitance regions, respectively.

are shown only for a high $V_G = 1$ V, but in general, the location of Q_G at the initial point $x = 0$ is V_G dependent, and it may already reside in a negative capacitance zone for low V_G values. Thus, depending upon the gate and drain biases, different regions of the ferroelectric along the longitudinal direction may operate in a positive or a negative capacitance regime. As $V_{\text{int}} = V_G - V_{\text{fe}}$, it increases with x in the positive capacitance regime (as V_{fe} decreases) and decreases with x in the negative capacitance regime (as V_{fe} increases) as shown in Fig. 9(b) for higher V_D values. The negative and the positive capacitance zones are clearly visible around the maxima.

VI. Conclusion

In this paper, we have developed an explicit physics-based core compact model of MFIS type NCFET. While avoiding iterative self-consistent calculations, the model shows excellent agreement with numerical simulations and experimental data. It captures the impact of the ferroelectric thickness scaling and variation in the ferroelectric material parameters. Furthermore, we have demonstrated that due to a spatial variation of the gate charge density, different regions of the ferroelectric can be either in a positive or a negative capacitance state depending on the applied biases. We also compared the I_D–V_G characteristics of the MFIS and MFMIS configurations of NCFET and found that at low drain bias both have similar behavior but at high drain bias, the MFIS structure offers higher drive current as well as better subthreshold swing.

Appendix

A general cubic equation in a variable u is given by

$$r_0u^3 + r_1u^2 + r_2u + r_3 = 0. \tag{32}$$

Dividing the above-mentioned equation by r_0 and substituting $v - (r_1/3r_0)$ for u gives a reduced cubic equation in v as

$$v^3 + s_0v + s_1 = 0 \tag{33}$$

where

$$s_0 = \frac{3r_0r_2 - r_1{}^2}{3r_0{}^2} \tag{34}$$

and

$$s_1 = \frac{2r_1{}^3 - 9r_0r_1r_2 + 27r_0{}^2r_3}{27r_0{}^3}. \tag{35}$$

Analytical solution of a cubic equation in the above-mentioned form can be obtained using the following procedure from [27] and [28]:

1) If $s_0 < 0$ and $4{s_0}^3 + 27{s_1}^2 \leq 0$, (33) has three roots in this case, given by

$$v_n = 2\sqrt{\frac{-s_0}{3}}\cos\left(\frac{1}{3}\left(\cos^{-1}\left(\frac{3s_1}{2s_0}\sqrt{\frac{3}{-s_0}}\right) - \frac{2\pi n}{3}\right)\right) \tag{36}$$

where $n = 0, 1, 2$. Out of the three, we choose the root for which $u_n = v_n - (r_1/3r_0) \geq 0$.

2) If $s_0 < 0$ and $4{s_0}^3 + 27{s_1}^2 > 0$, (33) has only one real root in this case, given by

$$v = -2\frac{|s_1|}{s_1}\sqrt{\frac{-s_0}{3}}\cosh\left(\frac{1}{3}\cosh^{-1}\left(\frac{-3|s_1|}{2s_0}\sqrt{\frac{3}{-s_0}}\right)\right). \tag{37}$$

3) If $s_0 > 0$, (33) has only one real root in this case, given by

$$v = -2\sqrt{\frac{s_0}{3}}\sinh\left(\frac{1}{3}\sinh^{-1}\left(\frac{3s_1}{2s_0}\sqrt{\frac{3}{s_0}}\right)\right). \tag{38}$$

REFERENCES

[1] A. Rusu, G. A. Salvatore, D. Jiménez, and A. M. Ionescu, "Metal-ferroelectric-meta-oxide-semiconductor field effect transistor with sub-60mV/decade subthreshold swing and internal voltage amplification," in *IEDM Tech. Dig.*, Dec. 2010, pp. 16.3.1–16.3.4.

[2] J. Jo and C. Shin, "Experimental observation of voltage amplification using negative capacitance for sub-60 mV/decade CMOS devices," *Current Appl. Phys.*, vol. 15, no. 3, pp. 352–355, 2015.

[3] J. Jo, W. Y. Choi, J.-D. Park, J. W. Shim, H.-Y. Yu, and C. Shin, "Negative capacitance in organic/ferroelectric capacitor to implement steep switching MOS devices," *Nano Lett.*, vol. 15, no. 7, pp. 4553–4556, 2015.

[4] A. I. Khan *et al.*, "Negative capacitance in short-channel FinFETs externally connected to an epitaxial ferroelectric capacitor," *IEEE Electron Device Lett.*, vol. 37, no. 1, pp. 111–114, Jan. 2016.

[5] G. A. Salvatore, D. Bouvet, and A. M. Ionescu, "Demonstration of subthrehold swing smaller than 60mV/decade in Fe-FET with P(VDF-TrFE)/SiO_2 gate stack," in *IEDM Tech. Dig.*, Dec. 2008, pp. 1–4.

[6] S. Dasgupta *et al.*, "Sub-kT/q switching in strong inversion in $PbZr_{0.52}Ti_{0.48}O_3$ gated negative capacitance FETs," *IEEE J. Exploratory Solid-State Comput. Device Circuits*, vol. 1, pp. 43–48, Dec. 2015.

[7] M. H. Lee *et al.*, "Prospects for ferroelectric $HfZrO_x$ FETs with experimentally CET = 0.98nm, SS_{for} = 42mV/dec, SS_{rev} = 28mV/dec, switch-off <0.2V, and hysteresis-free strategies," in *IEDM Tech. Dig.*, Dec. 2015, pp. 22.5.1–22.5.4.

[8] J. H. Park and S. K. Joo, "Sub-kT/q subthreshold slope p-metal-oxide-semiconductor field-effect transistors with single-grained $Pb(Zr,Ti)O_3$ featuring a highly reliable negative capacitance," *Appl. Phys. Lett.*, vol. 108, no. 10, p. 103504, 2016.

[9] M. H. Lee *et al.*, "Physical thickness 1.x nm ferroelectric $HfZrO_x$ negative capacitance FETs," in *IEDM Tech. Dig.*, Dec. 2016, pp. 12.1.1–12.1.4.

[10] G. Pahwa *et al.*, "Analysis and compact modeling of negative capacitance transistor with high ON-current and negative output differential resistance—Part I: Model description," *IEEE Trans. Electron Devices*, vol. 63, no. 12, pp. 4981–4985, Dec. 2016.

[11] A. I. Khan, U. Radhakrishna, K. Chatterjee, S. Salahuddin, and D. A. Antoniadis, "Negative capacitance behavior in a leaky ferroelectric," *IEEE Trans. Electron Devices*, vol. 63, no. 11, pp. 4416–4422, Nov. 2016.

[12] H.-P. Chen, V. C. Lee, A. Ohoka, J. Xiang, and Y. Taur, "Modeling and design of ferroelectric MOSFETs," *IEEE Trans. Electron Devices*, vol. 58, no. 8, pp. 2401–2405, Aug. 2011.

[13] D. Jiménez, E. Miranda, and A. Godoy, "Analytic model for the surface potential and drain current in negative capacitance field-effect transistors," *IEEE Trans. Electron Devices*, vol. 57, no. 10, pp. 2405–2409, Oct. 2010.

[14] A. F. Devonshire, "Theory of barium titanate: Part I," *London, Edinburgh, Dublin Philos. Mag. J. Sci.*, vol. 40, no. 309, pp. 1040–1063, 1949.

[15] D. Ricinschi, C. Harnagea, C. Papusoi, L. Mitoseriu, V. Tura, and M. Okuyama, "Analysis of ferroelectric switching in finite media as a Landau-type phase transition," *J. Phys., Condens. Matter*, vol. 10, no. 2, p. 477, 1998.

[16] Y. Tsividis and C. McAndrew, *Operation and Modeling of the MOS Transitor*. New York, NY, USA: Oxford Univ. Press, 2011.

[17] B. Yu, H. Lu, M. Liu, and Y. Taur, "Explicit continuous models for double-gate and surrounding-gate MOSFETs," *IEEE Trans. Electron Devices*, vol. 54, no. 10, pp. 2715–2722, Oct. 2007.

[18] A. I. Khan, C. W. Yeung, C. Hu, and S. Salahuddin, "Ferroelectric negative capacitance MOSFET: Capacitance tuning & antiferroelectric operation," in *IEDM Tech. Dig.*, Dec. 2011, pp. 11.3.1–11.3.4.

[19] G. Pahwa *et al.*, "Analysis and compact modeling of negative capacitance transistor with high ON-current and negative output differential resistance—Part II: Model validation," *IEEE Trans. Electron Devices*, vol. 63, no. 63, no. 12, pp. 4986–4992, Dec. 2016.

[20] Y. S. Chauhan *et al.*, "BSIM6: Analog and RF compact model for bulk MOSFET," *IEEE Trans. Electron Devices*, vol. 61, no. 2, pp. 234–244, Feb. 2014.

[21] Y. Li, Y. Lian, K. Yao, and G. S. Samudra, "Evaluation and optimization of short channel ferroelectric MOSFET for low power circuit application with BSIM4 and Landau theory," *Solid-State Electron.*, vol. 114, pp. 17–22, Dec. 2015.

[22] G. Pahwa, T. Dutta, A. Agarwal, and Y. S. Chauhan, "Designing energy efficient and hysteresis free negative capacitance FinFET with negative DIBL and 3.5X I_{ON} using compact modeling approach," in *Proc. IEEE Eur. Solid-State Device Res. Conf. (ESSDERC)*, Sep. 2016, pp. 41–46.

[23] J. Jo and C. Shin, "Negative capacitance field effect transistor with hysteresis-free sub-60-mV/decade switching," *IEEE Electron Device Lett.*, vol. 37, no. 3, pp. 245–248, Mar. 2016.

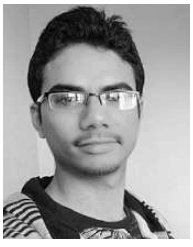
[24] C.-I. Lin, A. I. Khan, S. Salahuddin, and C. Hu, "Effects of the variation of ferroelectric properties on negative capacitance FET characteristics," *IEEE Trans. Electron Devices*, vol. 63, no. 5, pp. 2197–2199, May 2016.

[25] C. Hu, S. Salahuddin, C.-I. Lin, and A. Khan, " 0.2V adiabatic NC-FinFET with 0.6mA/μm I_{ON} and 0.1nA/μm IOFF," in *Proc. 73rd Annu. Device Res. Conf. (DRC)*, Jun. 2015, pp. 39–40.

[26] J. Duarte *et al.*, "Compact models of negative-capacitance FinFETs: Lumped and distributed charge models," in *IEDM Tech. Dig.*, Dec. 2016, pp. 30.5.1–30.5.4.

[27] R. W. D. Nickalls, "A new approach to solving the cubic: Cardan's solution revealed," *Math. Gazette*, vol. 77, no. 480, pp. 354–359, Nov. 1993.

[28] G. C. Holmes, "The use of hyperbolic cosines in solving cubic polynomials," *Math. Gazette*, vol. 86, no. 507, pp. 473–477, Nov. 2002.



Girish Pahwa (S'16) received the B.Tech. degree in electronics and communication engineering from Delhi Technological University, New Delhi, India, in 2014. He is currently pursuing the Ph.D. degree with IIT Kanpur, Kanpur, India.

His current research interests include physics and modeling of negative capacitance transistors.



Tapas Dutta (M'16) received the M.Tech. degree in electronics and communication engineering from IIT Roorkee, Roorkee, India, in 2009, and the Ph.D. degree in nanoelectronics and nanotechnology from the Institut National Polytechnique de Grenoble, Grenoble, France, in 2014.

He is currently a Post-Doctoral Researcher with IIT Kanpur, Kanpur, India. His current research interests include atomistic simulations and compact modeling of emerging electronic devices.

This article has been accepted for inclusion in a future issue of this journal. Content is final as presented, with the exception of pagination.



Amit Agarwal received the M.Sc. and Ph.D. degrees in theoretical physics from the Indian Institute of Science, Bengaluru, India, in 2005 and 2009, respectively.

From 2009 to 2012, he was the Marie Curie Post-Doctoral Researcher with Scuola Normale Superiore-Pisa, Pisa, Italy. He joined IIT Kanpur, Kanpur, India, as an Assistant Professor, in 2012. His current research interests include theoretical condensed matter theory, particularly low-dimensional systems, and nanoscale device modeling.



Yogesh Singh Chauhan (SM'12) was with IBM, Bangalore, India from 2007 to 2010 and the University of California at Berkeley, Berkeley, CA, USA, from 2010 to 2012. He is currently an Associate Professor with IIT Kanpur, Kanpur, India. He is also the Lead Developer of BSIM6 model and a Co-Developer of ASM-HEMT model for GaN HEMTs, which is under industry standardization at the Si2-Compact Model Coalition, Austin, TX, USA.

Design and Pitch Angle Optimisation of Horizontal Axis Hydrokinetic Turbine with Constant Tip Speed Ratio

Suyash Nigam[a], Shubham Bansal, Tanmay Nema, Vansh Sharma and Raj Kumar Singh

Department of Mechanical, Automotive and Production Engineering, Delhi Technological University, Delhi, India

Abstract. Booming population and associated energy demands, looming threat of exhaustion of conventional sources of energy and the severe environmental repercussions of the same call for alternate sources of clean energy. Hydrokinetic turbine is one such developing technology which harnesses zero-head free flow of water and affects hydrological ecology minimally. This paper discusses the optimisation of Horizontal Axis Hydrokinetic Turbine (HAHkT) blade chord length and twist angle using blade element momentum (BEM) theory to achieve a constant optimal angle of attack (AoA), thus maximising the power output. To achieve this while maintaining robustness at the hub end and eliminate cavitation, two different hydrofoils (S832 and E817) are selected. S832 is simulated using ANSYS 14.0 at low (0^0) and high (15^0) angles of attack and compared against more widely used NACA 4412 to study flow separation characteristics. This is followed by calculating angles of relative flow, ratios of chord length and subsequently twist angles for each blade element using MATLAB simulations. A blade model is thus developed for visualisation using computer aided designing after obtaining optimal chord lengths and pitch angles.

1 Introduction

Today's world sees an unprecedented demand for clean and economic sources of energy. Globally, 1.6 billion do not have access to electricity. [1] This calls for a greater shift in focus towards the renewable sources of energy for an energy-secure future.

According to IEA report in 2014, hydropower constitutes about 16.2% of our total energy demands and thus presents a great alternative. [2] However there are several problems associated with the creation of dams and embankments on water bodies to create power, such as sedimentation in the water bodies, significant damage to the aquatic ecosystem and socio-political concerns over displacement of multitudes of people.

Hydrokinetic turbine is a technology which harnesses zero-head free flow of water and presents a low emission way to satisfy the increasing energy demand while minimally affecting the hydrological ecology. This makes these turbines a lucrative alternative in a developing country like India which has a high hydropower potential.

These hydrokinetic turbines are advantageous as compared to wind power because of more predictability of the medium of flow, higher level of energy extraction due to near surface placement, minimal infrastructural investment, reduced environmental hazards and lower noise problems.

The primary classification of these turbines is done on the basis of axis of rotation relative to the flow- horizontal and vertical hydrokinetic turbines. Vertical axis hydrokinetic turbines are subject to some inherent disadvantages such as high starting torque requirements, lower power output at same flow velocity and higher vibrational losses. However Horizontal Axis Hydrokinetic Turbines (HAHkTs) improve upon these problems.

2 Literature review

Hydrokinetic turbines have seen a lot of research work over the past 2 decades. Ducted horizontal hydrokinetic turbines such as two-bladed SeaGen project turbines in the UK manufactured by Marine Current Turbines Limited are axial flow rotors whose mechanism is similar to that of a wind turbine with a capacity of 300kW-1.2MW. [3-5] Three-bladed Hammerfest Strom turbine (Norway) incorporates arrays of multi rotor underwater turbines whose energy is transported using subsea cables running on a maximum capacity of 300kW. Verdant Power has developed two projects- Roosevelt Island Tidal Project (RITE, New York East River, US) [6-8] and Cornwall Ontario River Energy Project (CORE, St. Lawrence River, Canada) [9] projects. It installs turbines which self-rotate from prevailing currents with optimally designed blades. These operate at 35kW-1MW capacity. Un-ducted hydrokinetic turbines comprise those such as multi-bladed Lunar Energy Rotate Tidal Turbine, housed in a converging-diverging duct so as to create a venturi action, and multi-bladed Underwater Electric Kite (UEK) Corp. [10] who now operate a fully functional plant at Eagle, Alaska.

[a] Corresponding author: suyashnigam@dtu.ac.in

© The Authors, published by EDP Sciences. This is an open access article distributed under the terms of the Creative Commons Attribution License 4.0 (http://creativecommons.org/licenses/by/4.0/).

From studying the functional projects, potency and viability of these hydrokinetic turbines can be established. Since HAHkT offer various advantages over the vertical ones, the design optimisation of the same will be the primary objective of this research.

2.1 Selection of hydrofoil geometry

A hydrofoil is a two dimensional surface which operates in water, producing lift force. The following parameters were found to be desirable:

- Glide ratio: This is a measure of the force of lift vs drag. It is important because lift is the primary source of power generation in horizontal axis turbines.
- Stall angle: The foil must produce lift until a high AoA as the velocity of flow varies greatly. Foils with high stall angles must be used towards the tip of the rotor, where the linear velocity is maximum.
- Leading edge area: The leading edge surface area must be small so as to reduce skin friction drag.
- Aft-loading: The trailing edge geometry must permit high values of aft-loading to counter cavitation.

2.2 Series of hydrofoils studied

Many organisations have worked in developing novel foils and studying the viability of already popular foils which are employed for wind turbines and commercial aeronautics.

a) NACA 4 series profiles: The NACA 4412 foil was used extensively for horizontal axis wind turbines (HAWT) purposes owing to large glide ratio values.
b) NREL S Series: National Renewable Energy Laboratory designed several geometries specifically for HAWT. Although they produce lesser coefficient of power than the NACA 4 series, they can be designed to operate at various tip speed ratios. [11]
c) NACA 5 Series: They have a high value of maximum coefficient of lift and can be used at operation near stall angle and off design conditions.
d) Eppler foils: Eppler E817 foil produces close to zero cavitation till 700 pounds per square inch aft loading. [12] This is achieved by using under cambered trailing edges.
e) Delft University Foils: These foils have a specific S-curve in trailing edge [13] to increase permissible aft-loading and a small upper surface area to decrease skin friction.

Several parameters were discussed upon for the optimisation process, namely solidity, chord length, pitch angle, hub design, number of blades, etc. Among these the optimisation of chord length and pitch angle was chosen as the objective of our work because the angle of relative velocity changes at every blade element. To maintain a high coefficient of lift, an optimal AoA is desirable and hence the pitch angles at every blade element have to be optimised accordingly.

3 Methodology

The methodology selected for developing a computational model of the HAHkT involves the selection of hydrofoil using k-ω turbulence model using Ansys Fluent, optimisation of pitch angle and chord length using MATLAB simulations and development of the optimised blade profile using computer-aided modelling for visual representation through Solidworks.

3.1 Procedure for ANSYS simulation

We decided to do a computational analysis of NACA 4412 foil and the NREL S832.

ANSYS Fluent was deployed to index the performance of hydrofoil under various spatial arrangements. For the 2 dimensional computational analysis a standard foil geometry was modeled using ANSYS design modeler and a C-mesh was constructed by employing ANSYS mesh module.

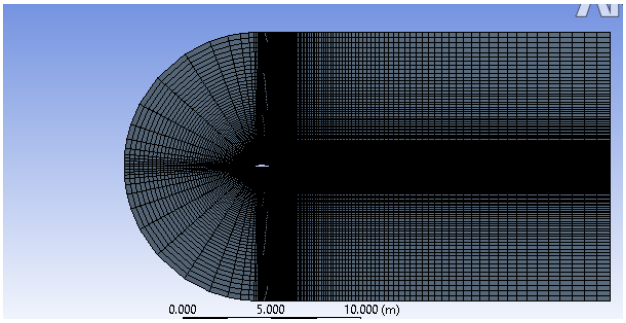


Figure 1. C-Mesh of control volume.

The number of nodes are in the 20,000 range with detailed meshing near the foil boundary so as to accurately capture the physics of boundary-layer flow. Mapped meshing operation was selected and the resultant mesh is displayed in Figure 1.

Simulation parameters:-
Inlet: Velocity inlet
Outlet: Pressure Outlet
Fluid density: 999.7 kg/m^3
Inlet velocity (U): 2m/s
Number of iterations: 500

Turbulence model: The k-ω [14] model was chosen by the virtue of its proven robustness in accurately predicting turbulent flow without high computational requirements.

It's a 2 equation model where 'k' stands for turbulent kinetic energy and 'ω' the specific dissipation rate. 'k' and 'ω' are computed by empirical relations [15]:

$$k = \frac{3}{2}(U * I)^2 \quad (1)$$

$$\omega = C\mu^{\frac{-1}{4}} * \frac{\sqrt{k}}{l} \quad (2)$$

where 'l' is 0.02 meters and denotes average Prandtl-mixing length typically 10% of chord length of 0.2m. 'I'

is the ratio of fluctuation component of velocity to the root mean square velocity of the flow, called turbulence intensity. The value of 'I' for a rotating turbomachinery component is around 10%. 'μ' is the viscosity of flow.

3.1.1 Simulation results

The computation was carried out for NREL S832 and NACA 4412 at 0 degree AoA and a high AoA of 15 degrees to gain insight in flow phenomenon at varying conditions.

At higher AoA the flow separates in case of NACA 4412 while the flow is largely attached in the case of NREL S832. This implies S832 is more robust against varying angular positions.

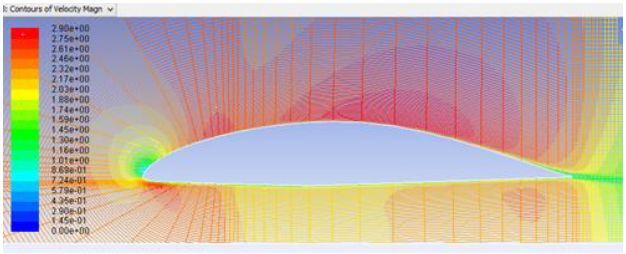


Figure 2. S832 at 0 degree AoA.

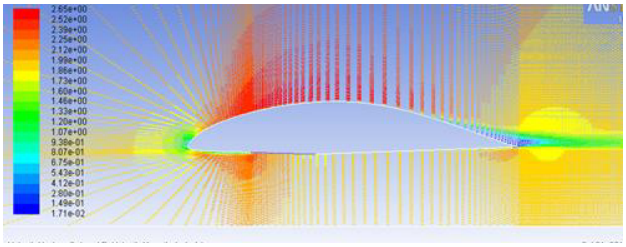


Figure 3. S832 at 15 degree AoA.

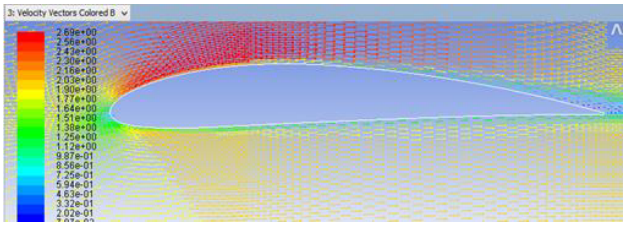


Figure 4. NACA 4412 at 0 degree AoA.

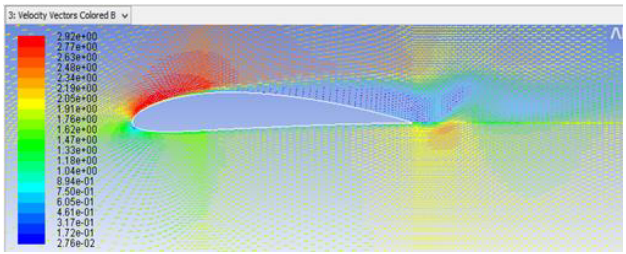


Figure 5. NACA 4412 at 15 degree AoA.

3.2 Optimisation of blade chord length and pitch angle

Two of the most important parameters in deciding the hydrofoil profile and orientation for the turbine blade so as to achieve maximum power output are: ratio of the area occupied by blade with respect to the total area covered by the blade (solidity) and the angle of relative velocity.

Simulation of blade profile data to optimise the chord length and the element twist angle along the length of the blade are done to achieve maximum power output. The variable pitch is important so as to operate at fixed optimal AoA for the respective hydrofoil geometry.

The following assumptions were made for calculations:

- The blade is considered to be a combination of discrete elements of equal length instead of a long single unit.
- The tip speed ratio (TSR) at each element varies linearly along the length of the blade.
- The induced velocity at each element is determined by performing the momentum balance for an annular control volume containing the blade element.
- Tip losses and hub losses and vortices are ignored.

For a specific AoA lift coefficient must be maximum, drag should be minimum while neither flow separation nor cavitation should occur. Optimal pitch angle enables the system to operate at higher relative water velocities. Hydrokinetic turbines are subjected to high thrust and torsional loads due to high density of water which causes high bending moment at the blade root. So, thicker blade sections are preferred near the hub.

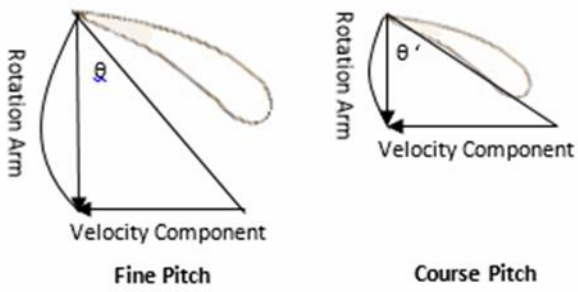


Figure 6. Variation of Relative Velocity Angle with pitch.

At a given water speed, the speed of different blade sections differ depending upon the distance of the section from the hub i.e the rotation arm. We observe that this results in a very low AoA for the sections closer to hub. This needs to be rectified. This is achieved by going for a coarse pitch for the closer section and a fine pitch for sections as we move away from hub.

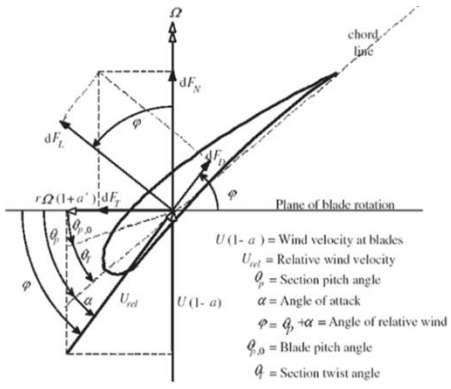


Figure 7. Blade Element Momentum Theory Parameters.

3.2.1 MATLAB simulation

The following parameter values are used:

Number of blades = B = 3
Tip Speed Ratio = TSR = 3
Rated Water Speed (m/s) = 2
Estimated efficiency of system = 0.45
Rotor diameter (m) = (d) = 2.2
Number of blade elements = (ne) = 10
AoA for max L/D ratio for S832 (α1) = 9.75
AoA for max L/D ratio for E817 (α2) = 7.5
Lift coefficient for S832 (Cl1) = 1.1207
Lift coefficient for E817 (Cl2) = 0.9083
Drag coefficient for S832 (Cd1) = 0.0622
Drag coefficient for E817 (Cd2) = 0.04476

An element data matrix is prepared in MATLAB after successive iterations of the calculations on initial data. The hydrofoils E817 and S832 are used in the ratio of length as 1:3.

Length of each element = (L) = (d/2) / ne
Distance from hub = (R) = L/2 + (i-1)*L
Tip Speed Ratio = (TSR) = ΩR/V
Local Tip Speed Ratio = (LSR) = TSR * (R/ (d/2))
Angle of relative velocity = $\varphi = (2/3) * \tan^{-1}(1 / LSR)$
Chord Length for S832 = (8*π*L*(1-φ) / (B*Cl1)
Chord Length for E817 = (8*π*L*(1-φ) / (B*Cl2)
Pitch angle (in radians) = θ = (φ – α)
Solidity Ratio = σ = B*c/ (2πr)

3.2.2 Results and inference

The twist angle/pitch angle output obtained from the optimisation code is mentioned in Table 1. This is obtained by using the following relation: θ = (φ – α)

The first blade element is considered at the hub end and the successive blades are positioned radially outwards.

Table 1: Element Data Parameters from MATLAB Code.

Element No.	Radial Distance Ratio (R/ (d/2))	LSR	Angle of Relative Velocity (^{0})	Ratio of Chord with radial distance	Pitch Angle (^{0})
1	0.05	0.15	54.313	0.192	46.813
2	0.15	0.45	43.848	0.386	36.348
3	0.25	0.75	35.420	0.346	25.670
4	0.35	1.05	29.069	0.330	19.319
5	0.45	1.35	24.353	0.299	14.603
6	0.55	1.65	20.812	0.268	11.062
7	0.65	1.95	18.100	0.240	8.350
8	0.75	2.25	15.975	0.217	6.225
9	0.85	2.55	14.275	0.196	4.525
10	0.95	2.85	12.890	0.179	3.140

For blade elements upto one-fourth of the length of the blade, the AoA is chosen for S832 blade profile i.e. α1 and for the remaining three-fourth length, that of E817, i.e. α2.

a) Chord Length vs Ratio of Radial Distance: Figure 8 shows the graph. The maxima of the chord length is at a value of ratio of radial distance close to 0.15, i.e. between the first and second element. Beyond that, it gradually decreases, narrowing upto the tip. This is in line with the aim to model blades with thicker sections towards the hub so as to bear the high bending moment at the blade root.
b) Angle φ vs Ratio of Radial Distance: Figure 9 shows the graph. It shows a continuous decreasing trend of angle of relative velocity with respect to the radial distance. Decreasing angle of relative velocity result in a lesser lift force and thus a lower TSR towards the root of the blade i.e. the inner elements. Higher relative velocity angles also indicate a higher value of twist angles towards the root of the blade because of the constant AoA for a given blade profile.

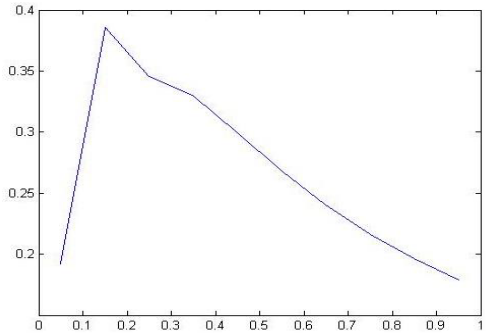


Figure 8. Graphical representation of Chord Length vs Ratio of Radial Distance.

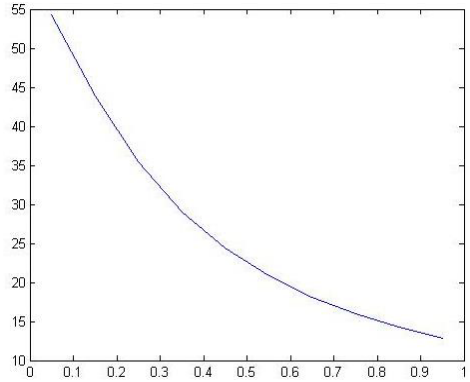


Figure 9. Graphical representation of Angle φ vs Ratio of Radial Distance.

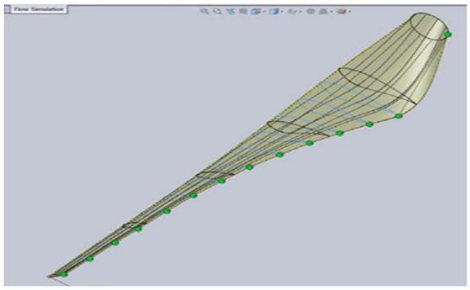


Figure 10. Optimised blade model.

3.3 Computer aided design of blade model

The different profiles are generated by the obtained phase angle and chord length values. Higher the number of blade elements, more accurate blade geometry results will be obtained.

The Fig. 10 depicts the development stages of the blade model.

The primary function of the hub body is to transfer the load from the blades to the low speed shaft. The hub diameter of the turbine is kept 40% of the blade length. The hub design is in accordance with the work of J. Cotrell. [17]

4 Conclusion

The HAHkT blade is formed of two hydrofoil geometries which are twisted about an axis so as to maintain the optimum AoA. The blade uses a combination of E817 and S832 foils. The distribution of the profiles is as follows: E817 constitutes of 25% of the total blade length on the hub end to reduce stresses and avoid cavitation, and the remaining 75% is S832 for no-flow separation even at higher AoA. The hydrofoils are arranged along a common axis to form a blade model which consists of three uniformly distributed blades as shown in Fig. 11.

This HAHkT blade model improves upon the structural stability and power output characteristics of traditional single hydrofoil constant twist angle profiles and thus holds promise as an efficient model.

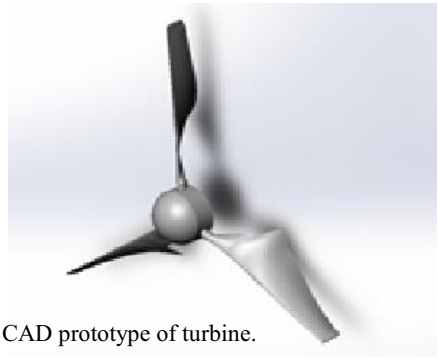


Figure 11. CAD prototype of turbine.

References

1. *BP: Statistical Review of World Energy*, Workbook (xlsx), London, (2013)
2. http://www.iea.org/publications/freepublications/
3. SeaGen Environmental Monitoring Programme Final Report, as available on http://seageneration.co.uk/files/SeaGen-Environmental-Monitoring-Programme-Final-Report.pdf, accessed on October 24, 2015
4. C.A. Douglas, G.P. Harrison, J.P. Chick, Life cycle assessment of the Seagen marine current turbine. *Proceedings of the Institution of Mechanical Engineers*
5. A. Røkke, R. Nilssen, Marine Current Turbines and Generator preference. A technology review, *International Conference on Renewable Energies and Power Quality (ICREPQ'13)* Bilbao (Spain)(2013)
6. J. Colby. Multi-scale Hydrodynamic analysis of kinetic hydropower arrays. *NortekUSA Technical Symposium* (2011)
7. Verdant Power, Inc, Final Report - GO18168 Improved Structure and Fabrication of Large, High-Power KHPS Rotors, Award No. DE-FG36-08GO18168
8. D. Sale, J. Jonkman, W. Musial, A Hydrodynamic Optimization Method and Design Code for Stall-Regulated Hydrokinetic Turbine Rotors (2009)
9. http://www.power-technology.com/projects/cornwall-ontario-river-energy-project/, as accessed on October 27, 2015.
10. P. Vauthier. The underwater electric kite. East river deployment, UEK Corporation.
11. http://www.nrel.gov/docs/legosti/old/7109.pdf
12. http://www.foils.org/hysecdes.pdf
13. https://gcep.stanford.edu/pdfs/energy_workshops_04_04/wind_van_rooij.pdf
14. http://www.cfd-online.com/Wiki/K-omega_models
15. http://www.cfd-online.com/W/index.php?title=Turbulence_free-stream_boundary_conditions&oldid=22693
16. J. Cotrell, The Mechanical Design, Analysis, and Testing of a Two-Bladed Wind Turbine Hub (1995)

This article has been accepted for publication in a future issue of this journal, but has not been fully edited. Content may change prior to final publication. Citation information: DOI 10.1109/JSEN.2017.2655086, IEEE Sensors Journal

Detection of Ultrasonic Waves using Resonant Cylindrical Cavity for Defence Application

Ramesh C. Sharma*, Subodh Kumar, Surya K. Gautam

Abstract: A novel resonant standoff Quantum cascade laser spectroscopy based technique has been demonstrated for the detection of hazardous molecules (chemicals and explosives) on adsorbed surfaces such as plastics and cloths, vapors and in aerosols form in open air. Laser photoacoustic spectra of various trace molecules in the mid-infrared spectral band 7-9 micrometer have been recorded. Cylindrical tube coupled with microphone detector has been developed for the detection in trace amounts. The cylindrical tube has been developed for a compatible microphone detector working at resonant frequency of 40 kHz. The devised quantum cascade laser based acoustic detection set up has high selectivity and sensitivity. The present technique has been developed for screening of suspicious objects for security applications. It has the potential to be converted in to a handy product.

***Index Terms*—Ultrasonic sensor, Laser spectroscopy, Mid IR spectroscopy, Hazardous chemicals, Biological agents, Explosive molecules, Trace detection.**

I. Introduction

Laser photoacoustic spectroscopy has been used by the researchers for standoff detection of hazardous molecules using the so called quartz enhanced laser photoacoustic spectroscopy (QE-LPAS) for at least a decade [1-3]. In this technique diffused reflection of incident light from the target (contaminated with chemicals/hazardous molecules) is collected by an optical receiver after being absorbed by the contaminant to focus on the Quartz tuning fork detector. By observing the characteristic absorption in the acquired spectrum, detection and identification of the absorbing species is done. The QE-LPAS technique is totally dependent on the target reflection. Another type of standoff sensors are based on microphone detector. This type of sensors does not depend on the target reflection. In this case, the generated non-radative transitions in sample are the key which depends on the incident laser intensity, absorption coefficient of the sample and interaction of incident laser with the sample. Standoff liquid chemical has been detected using CO_2 laser Photoacoustic spectroscopy of liquid contamination on surface. The detection setup consists of 60 cm aperture parabolic acoustic receiver [4]. Detection of hazardous chemicals has also been demonstrated using quantum cascade laser photoacoustic spectroscopy with 45 cm aperture acoustic receiver [5]. Xing Chen *et al*. have demonstrated standoff detection of trinitrotoluene (TNT) from a distance of nearly 2.5 meters using an acoustic receiver coupled with a microphone [6]. LED based photoacoustic sensor has also been demonstrated for the applications where very high precisions are not required viz. the detection and continuous monitoring of indoor gas pollutants such as anaesthetic gas in hospitals [7].

The aim of the present work is to develop an ultrasonic standoff sensor based on laser photoacoustic spectroscopy employing a microphone detector coupled with resonant cylindrical tube. We have developed an ultrasonic sensor with resonator attachment having peak sensitivity at 40 kHz. The sensor employs a microphone working at 40 kHz. The ambient noise in ultrasonic band is typically lower than that in audio frequency range. With the developed sensor, we have detected and identified hazardous chemicals, explosives in various forms for the security screening, forensic application and other applications for homeland security and defence.

II. Design of Cylindrical Tube For Acoustic Resonator

The resonant acoustic resonator was designed to amplify the acoustic signal which is received by microphone detector in standoff detection experiments. The pressure waves simulations for one side open ended cylindrical geometry has been carried out to optimize the ultrasonic Eigen frequency centered at ~40 kHz. A stainless steel cylindrical tube was fabricated as per the design. The length and inner diameter of the tube were 2.40 cm and 1.80 cm respectively. The ultrasonic piezo microphone detector was fixed at one open end of cylindrical tube and the other side was kept open. The acoustic resonant Eigen frequencies of an open cylinder can be calculated analytically, using the relation f = n.c/4L, where ‘n’ is an odd number, ‘c’ is speed of sound in air and L is the length of cylinder. Finite-element based, COMSOL Multi-physics software was used to simulate the Eigen frequencies of the resonator.

The Eigen frequency and Eigen-modes are obtained by solving the following differential equation,

*Corresponding author: Dr Ramesh C Sharma, Laser Science and Technology Centre, DRDO, Delhi- 110054. (E-mail: RameshSharma@lastec.drdo.in) Phone: +91 11 23907 539

1530-437X (c) 2016 IEEE. Personal use is permitted, but republication/redistribution requires IEEE permission. See http://www.ieee.org/publications_standards/publications/rights/index.html for more information.

This article has been accepted for publication in a future issue of this journal, but has not been fully edited. Content may change prior to final publication. Citation information: DOI 10.1109/JSEN.2017.2655086, IEEE Sensors Journal

$$\frac{P(r)}{\rho}+\left(\frac{\omega}{2}\right)^2\left(\frac{P(r)}{\rho}\right)=0\,, \qquad (1)$$

where $P(r)$ is the acoustic pressure given by,

$$P(r)=P_0\exp(i\omega t)\,. \qquad (2)$$

Here, P_0 is a harmonic quantity for the pressure acoustics frequency domain study. ω is the angular frequency, ρ is the density of air (1.2 kg/m^3) and c is the speed of sound in air (343) m/s at STP. The pressure inside the cell is taken as 1 Pascal and all the boundaries are taken as sound hard boundaries except one of the surface of the open cylinder. Five quadratic elements should be used to resolve each wavelength. Therefore, the maximum mesh element size is set to 1/5 of the shortest wavelengths present, i.e. mesh size is taken $c/5.f_{max}$ and f_{max} is the maximum frequency for which solutions are to be evaluated. Finite Element Mesh (FEM) simulations provide the results of pressure acoustics frequency domain study. Figure 1 shows the response of photoacoustic cell (PA cell) i.e. average acoustic pressure integrated over the volume with frequency up to 50 kHz for open cylindrical geometry. Eigen frequencies were found to have values ~3.640 kHz, ~10.890 kHz, ~18.140 kHz, ~25.380 kHz, ~32.750 kHz and ~40 kHz, which are in agreement with analytical values.

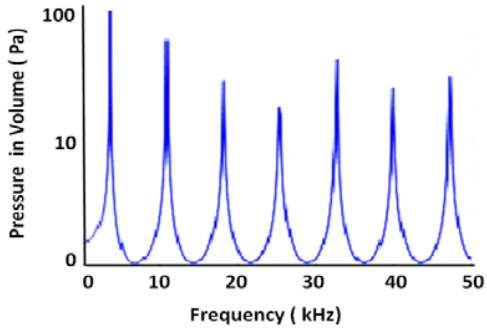


Fig.1: The pressure waves simulations for one side open ended cylindrical geometry to optimize the resonance frequency, using COMSOL Multi physics software.

Figure 2 shows simulated pressure waves field variation for required resonant frequency i.e. 40 kHz showing the pressure variation in color scale for the cylinder. The color pattern shows a standing wave distribution of pressure inside the resonator.

III. Experimental

The schematic of experimental setup for standoff laser photoacoustic spectroscopy is shown in Fig. 3a. For the resonant standoff detection microphone is fitted with cylindrical tube. The tunable quantum cascade laser (QCL) sourced from M/s. Daylight Solutions having tuning range of 7- 9 µm was used in the experiment. The laser is having wavenumber accuracy of 1 cm^{-1} and a line width of ~ 0.5 cm^{-1}. The QCL laser beam was modulated at a frequency of 40 kHz. A function generator card was used to modulate the laser and to give the reference signal to lock-in-amplifier card. The laser is allowed to fall on the target having traces of chemical/explosive species. The absorption of tunable laser radiation by the target is followed by non-radiative decay resulting in pressure fluctuations at the modulation frequency which are detected by a sensitive microphone fixed at the end

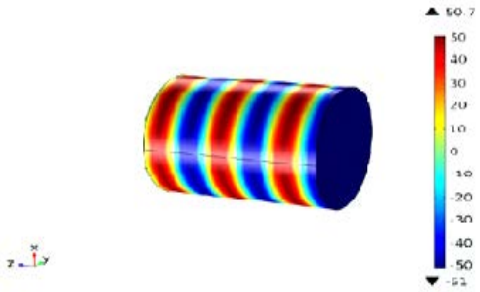


Fig.2: simulated pressure waves field variation for required resonant frequency i.e. 40 kHz, using COMSOL Multi-physics Software.

of cylindrical shape acoustic resonator. The detector is having a resonant frequency response centered at 40 kHz.

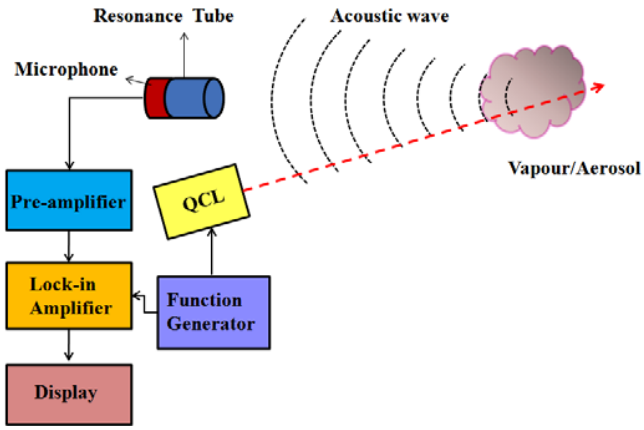


Fig.3a: Schematic representation of Standoff Photoacoustic Sensor for the trace detection based on resonant cylindrical tube attached with microphone.

The block diagram of the electronic processing unit is shown in Fig. 3b. Electrical signal (PA signal) coming from the Microphone is fed to the pre-amplifier (Femto, DLPCA-200). The amplified signal is then processed through the lock-in amplifier card. A function Generator card is used to modulate the laser beam at 40 kHz, and another reference signal (at 40 kHz) from the function generator is sent to the lock-in amplifier card. Sensitivity and time constant settings are remotely controlled by the Lab-view based software through DO card. The sensitivity of Lock-in-amplifier card was set at 3 mV scale all through the measurements. The output of the lock-in card is fed to the computer through a multifunction card. The signal is displayed as amplitude/intensity versus

1530-437X (c) 2016 IEEE. Personal use is permitted, but republication/redistribution requires IEEE permission. See http://www.ieee.org/publications_standards/publications/rights/index.html for more information.

This article has been accepted for publication in a future issue of this journal, but has not been fully edited. Content may change prior to final publication. Citation information: DOI 10.1109/JSEN.2017.2655086, IEEE Sensors Journal

wavenumber in Labview based GUI. Experiments have been carried out by placing the cylindrical resonator (fitted with the microphone) at varying distance up to 30 cm away from the target. The analog signal from lock-in amplifier card was digitized using a multifunction data acquisition card (Advantech USB 4716) and recorded on a computer having a Labview based graphical user interface.

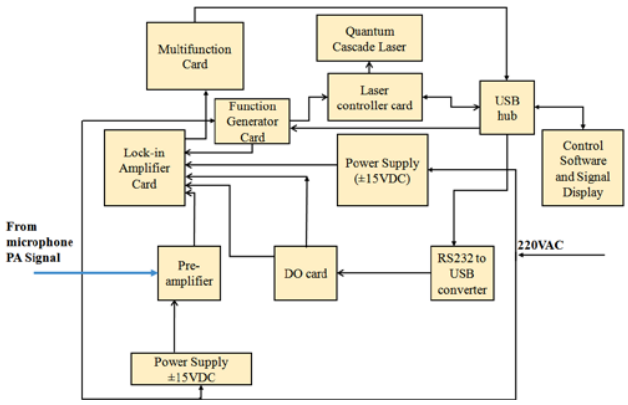


Fig. 3b: Detailed schematic diagram of the processing unit.

All the spectra were recorded by forward scanning mode of Quantum Cascade Laser (QCL) which limits the wavelength accuracy of ±2 cm^{-1}. The samples were prepared by dissolving the hazardous material in Acetone/alcohol and allowing them to dry on the target to form a uniform layer. The solutions were prepared to deposit 5-50 $\mu g/cm^2$ level quantity of analyte under examination, on the target. The targets materials in our case were plastics and cloths. The experiments were conducted with the sensor attached to the cylindrical resonator. Standoff Photo-acoustic spectra were also recorded for the samples in aerosols/vapors forms in open air as well as for samples adsorbed on surfaces from a distance of 30 cm. The employed ultrasonic microphone in our case being piezoelectric, has a narrow frequency response centered at 40 kHz (±1 kHz) that allows less interference from ambient as compared to other microphones (electrets/condenser microphone) having wide acoustic responses. Matching of the Eigen frequency of the cylindrical resonator with modulation frequency of laser ensure a high quality- factor 'Q value', as the energy from many modulation cycles is accumulated in a standing wave and the system works as an acoustic amplifier [8].

IV. Results and Discussion

Photoacoustic spectra of hazardous chemicals such as acetone, acetic acid, ethanol, and propanol in liquid form (adsorbed on cloth surface) were recorded. The size of the surface area of the contaminated cloths was (1.0 cm x 1.0 cm). The used concentration of acetone, propanol, ethanol and acetic acid were in the range between 100 µl to 30 µl. The photoacoustic signal of acetone vapour and acetic acid in aerosol form in open air were recorded. The photoacoustic spectra of analyte molecules adsorbed on surfaces (cloths and plastics) were recorded from a distance of 30 cm and are shown in Fig.4. Concentrations of these molecules were in the range of 50 µl to 5 µl. The photoacoustic spectra of different molecules are shown in different colours. Green, black, red and blue colours correspond to Acetone, Propanol, Acetic acid and Ethanol respectively. In Fig.4, (a), (b) and (c) indicate spectra corresponding to 50 µl, 20 µl and 5 µl concentrations respectively. The orange colour line shows the baseline. Acetone is a precursor of explosive TATP. TATP is largely used as homemade IEDs (Improvised Explosive Devices). Therefore, its detection and identification in trace amounts is important to take counter measures against these threats. The present work shows the potential of Photoaoustic spectroscopy technique from the short distance for scanning suspicious objects.

Laser photoacoustic spectrum of mixture of explosives PETN and RDX adsorbed on plastic surface were recorded from a distance of 30 cm (shown in Fig.5). The characteristic peaks of explosive materials are clearly resolved. In the Fig.5; (a) shows five clearly resolved peaks. Among these, four peaks (1237cm^{-1}, 1264 cm^{-1}, 1314 cm^{-1}, and 1338 cm^{-1}) belong to RDX and one (1276 cm^{-1}) to PETN. The quantity of mixture was 25 µg /cm^2. The photoacoustic spectrum shown in blue colour (b) was recorded without explosive sample. Detection and identification of particular explosive from mixture of explosives is a challenging task. The present set up has the potential to do that. Distinguishable spectra of mixture of molecules (RDX, PETN) having an appreciable signal to noise ratio, were obtained for distance up to 30 cm.

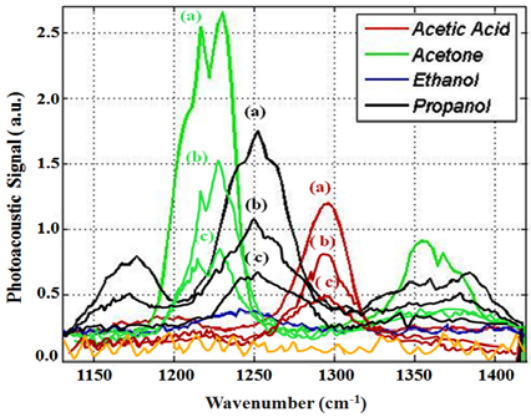


Fig. 4: Standoff Photoacoustic Spectra of Acetone (shown in Green colour), Propanol (black colour), Ethanol (blue colour) and Acetic acid (red colour) adsorbed on cloths surfaces from distance 30 cm for corresponding quantity of (a) 50 µl (b) 20 µl (c) 5 µl. Yellow colour spectrum correspond to the cloth surface without sample.

All the photoacoustic spectra are in reasonable agreement with the available infrared spectroscopy information [1-3]. In Fig. 5 the strong peak of RDX at 1264 cm^{-1} is observed due to C–N stretch vibrational mode. Strong overlapping peaks at 1221 and 1237 cm^{-1} are distinctively resolved in our experimental measurements. Spectral positions of photoacoustic spectrum,

1530-437X (c) 2016 IEEE. Personal use is permitted, but republication/redistribution requires IEEE permission. See http://www.ieee.org/publications_standards/publications/rights/index.html for more information.

This article has been accepted for publication in a future issue of this journal, but has not been fully edited. Content may change prior to final publication. Citation information: DOI 10.1109/JSEN.2017.2655086, IEEE Sensors Journal

as well as relative peaks absorption magnitudes are in agreement with FTIR spectra reported [9, 10].

Figure 6 depicts (a) the Photoacoustic spectrum of DPA (a biological agent) and (b) the base line (spectra of cloth surface without sample). The prominent peak of DPA appears at around 1305 cm^{-1}.

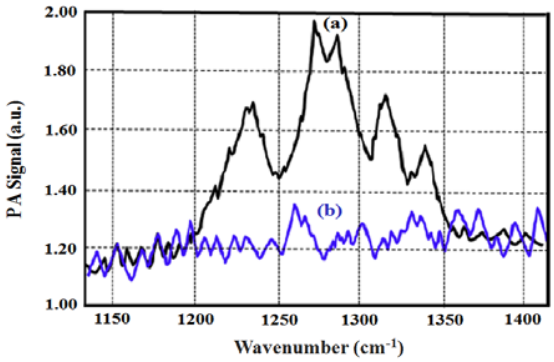


Fig. 5: Standoff photoacoustic spectra of mixture of explosive from 30 cm distance adsorbed on plastic suitcase surface (a) Black colour spectrum correspond to the mixture of RDX and PETN (25 microgram / cm^2 each), (b) Blue colour spectrum correspond to the plastic surface without sample.

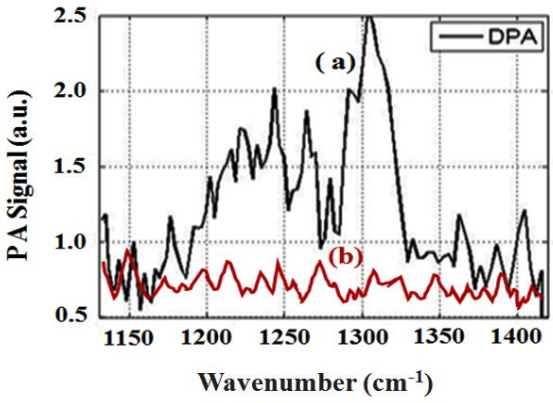


Fig. 6: Standoff photoacoustic spectra of DPA (1.0 ppm) simulant of Bacillus Anthrax (a Biological agent) from 30 cm distance in open air. Spectrum (a) corresponds to DPA and (b) to the back ground without sample.

V. CONCLUSION

The demonstrated ultrasonic photoacoustic spectroscopy methodology using pulsed quantum cascade laser and sensitive microphone detector coupled with resonant cylindrical tube has the potential to detect and identify explosives in trace amounts. The technique is non-invasive, selective and fast as the molecular species were detected in the time taken by the laser to scan the entire tuning range (~ 6 second). This methodology is capable of detecting explosive agents, chemical warfare agents from a distance of up to 30 cm. Microphone based standoff sensor has dependence on the generated non-radative transitions/ acoustic waves, optical intensity of the interacting laser, absorption coefficient of the sample and does not have any dependence on the reflection from the target. The ultrasonic waves propagate towards the detector and detected by the sensitive microphone. The technique can be used to detect samples in powder, liquid, vapour form and also in the form of samples adsorbed on surfaces. It is also capable to detect and identify the traces of explosives from post blast materials and hence can be very useful in forensic applications. Further, the technique can be extended for the detection of biological warfare agents and drugs.

ACKNOWLEDGMENT

Authors are thankful to Professor S N Thakur, BHU Varanasi, Professor J P Singh, ICET, Mississippi State University, USA, and Professor Thomas Thundat, Ulbeta University, Canada for the fruitful discussion. Authors are also thankful to Mrs. Usha Kumari and Mr. Umesh Sah for their assistance during the experiments.

REFERENCES

[1] C. W. Van Neste, L. R. Senesac, and T. Thundat, “Standoff Spectroscopy of Surface Adsorbed Chemicals”, Anal. Chem., vol. 81, no. 5, pp. 1952-1956, Feb. 2009.

[2] C. W. Van Neste, L. R. Senesac, and T. Thundat, Standoff photoacoustic spectroscopy, Appl. Phys. Lett., vol. 92, pp. 234102, Jun 2008.

[3] R. C. Sharma, D. Kumar, N. Bhardwaj, S. Gupta, H. Chandra, A. K. Maini, “Portable detection system for standoff sensing of explosives and hazardous materials”, Opt. Comm., vol. 309, pp. 44-49, Nov. 2013.

[4] B. Perrett, M. Harris, G. N. Pearson, D. V. Willetts, and M. C. Pitter, “Remote photoacoustic detection of liquid contamination of a surface”, Appl. Opt., vol. 42, no.24, pp. 4901-4908, Aug. 2003.

[5] X. Chen, L. Cheng, D. Guo, Y. Kostov, and F. –S. Choa, “Quantum cascade laser based standoff photoacoustic chemical detection”, Optics Express, vol. 19, no. 21, pp.20251-20257, September 2011.

[6] X. Chen, Guo D, F. –S. Choa, C. C. Wang, S. Trivedi, A. P. Snyder, G. Ru, J. Fan, “Standoff photoacoustic detection of explosives using quantum cascade laser and an ultrasensitive microphone,” Appl. Opt., vol. 52, no.12, pp. 2626-32, Apr. 2013.

[7] A. Lay-Ekuakille, G. Vendramin, and A. Trotta, “LED-based sensing system for biological gas monitoring: Design and experimentation of a photoacoustic chamber”, Sensors and Actuators B: Chemical, vol. 135, no. 2, pp. 411-419, Jan. 2009.

[8] A. Miklós, P. Hess and Z. Bozóki, “Application of acoustic resonators in photoacoustic trace gas analysis and metrology”, Rev. of Sci. Instruments, vol.72, pp.1937-1955, Jan. 2001.

[9] F. Pristera, M. Halik, A. Castelli, W. Fredericks, “Analysis of explosives using infrared spectroscopy”, Anal. Chem., vol. 32, no. 4, pp. 495-508, Apr. 1960.

[10] A. Banas , K. Banas , M. Bahou , H.O. Moser , L. Wen , P. Yang , Z.J. Li , M. Cholewa, S.K. Lim , Ch.H. Lim , “Post-blast detection of traces of explosives by means of Fourier transform infrared spectroscopy”, Vibrational Spectroscopy, vol. 51, no. 2, pp.168–176, Nov. 2009.



Ramesh C. Sharma is currently a Senior Scientist with the Laser Science and Technology Centre, Defense Research and Development Organization, Delhi,

1530-437X (c) 2016 IEEE. Personal use is permitted, but republication/redistribution requires IEEE permission. See http://www.ieee.org/publications_standards/publications/rights/index.html for more information.

This article has been accepted for publication in a future issue of this journal, but has not been fully edited. Content may change prior to final publication. Citation information: DOI 10.1109/JSEN.2017.2655086, IEEE Sensors Journal

India. He received the Ph.D. degree in experimental laser spectroscopy from Banaras Hindu University, Varanasi, India, in 1995. He was a Postdoctoral Fellow with Indian Institute of Technology, Kanpur, India, University of California, San Diego, USA, and Mississippi State University; Starkville, MS, USA. He has worked several years as a Project Scientist /Research Fellow/Research Scientist /Senior Scientist with the IAMS Academia Sinica Taipei, Taiwan, University of Tokyo, Japan, The University of Leeds, Leeds, and The University of Manchester, England. He has worked in the fields of laser technology, laser spectroscopy, THz Imaging, bio-photonics imaging, nonlinear optics, nanotechnology, chemical dynamics, laser plasma physics, and laser remote sensing technologies.

Dr. Sharma is the Group Leader and working on remote sensing of biological, explosive and hazardous chemicals using LIDAR and laser spectroscopy. He has more than 50 publications in reputed peer reviewed international journals to his credit.

He is a Life Member of the Indian Laser Association and the Laser and Spectroscopy Society of India.



Subodh Kumar received the M.Sc. degree in physics from Patna University, Patna, India, in 1998. He is currently pursuing the Ph.D. degree in physics with the Indian Institute of Technology Delhi, Delhi. He joined the Laser Science and Technology Centre, Defense Research and Development Organization, Delhi, India, in 2001, as a Scientist.

He is involved in, laser Photoacoustic spectroscopy of explosive and other hazardous materials after having brief experience in the synthesis and characterization of laser materials (glasses). His research interests also include remote sensing of bio-molecules using ultraviolet laser-induced fluorescence technique and terahertz generation by laser plasma interaction.

Mr. Kumar is a Life Member of the Indian Laser Association.



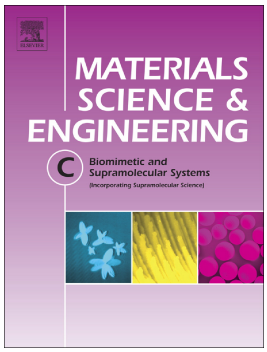
Surya Kumar Gautam received the B.E degree in Electronics and Communication engineering from Delhi Technological University, India, in 2012, and M. Tech. degree in Applied Optics from Indian Institute of Technological Delhi, India, in 2015.

He is currently a Junior Research Fellow in Laser Science and Technology Centre with the Defense Research and Development Organization (DRDO), Delhi, India. He is having research interest in several field of optics like laser spectroscopy, imaging and quantum optics.

Mr. is currently involved in, laser photoacoustic spectroscopy techniques.

1530-437X (c) 2016 IEEE. Personal use is permitted, but republication/redistribution requires IEEE permission. See http://www.ieee.org/publications_standards/publications/rights/index.html for more information.

Accepted Manuscript



Dextrose modified flexible tasar and muga fibroin films for wound healing applications

Chandra Mohan Srivastava, Roli Purwar, Anuradha Gupta, Deepak Sharma

PII: S0928-4931(16)31342-X
DOI: doi: 10.1016/j.msec.2017.02.021
Reference: MSC 7352

To appear in: *Materials Science & Engineering C*

Received date: 15 September 2016
Revised date: 29 November 2016
Accepted date: 6 February 2017

Please cite this article as: Chandra Mohan Srivastava, Roli Purwar, Anuradha Gupta, Deepak Sharma , Dextrose modified flexible tasar and muga fibroin films for wound healing applications. The address for the corresponding author was captured as affiliation for all authors. Please check if appropriate. Msc(2017), doi: 10.1016/j.msec.2017.02.021

This is a PDF file of an unedited manuscript that has been accepted for publication. As a service to our customers we are providing this early version of the manuscript. The manuscript will undergo copyediting, typesetting, and review of the resulting proof before it is published in its final form. Please note that during the production process errors may be discovered which could affect the content, and all legal disclaimers that apply to the journal pertain.

ACCEPTED MANUSCRIPT

Dextrose modified flexible tasar and muga fibroin films for wound healing applications

Chandra Mohan Srivastava[1], Roli Purwar[1*], Anuradha Gupta[2] and Deepak Sharma[2]

Department of Applied Chemistry and Polymer Technology
[1]Delhi Technological University, Shahbad Daulatpur Bawana Road, Delhi-110042, India
[2]Department of Pharmaceutics, Central Drug Research Institute, Lucknow 226031, India
[*]Corresponding author E-mail address: roli.purwar@dce.edu

ACCEPTED MANUSCRIPT

ABSTRACT

This paper is focused on preparation and characterization of regenerated muga and tasar fibroin flexible films from cocoon using ionic liquid. These flexible muga and tasar fibroin films were prepared by incorporating dextrose (5 to 15% w/w) as plasticizer. The mechanical, thermal, physical, morphological and biological properties of dextrose plasticized muga and tasar fibroin films were characterized. These plasticized films showed higher elongation at break as well as water holding capacity as compared to the un-plasticized films. The surface roughness and water absorbance capacity of the dextrose plasticized films were higher than un-plasticized films, which results in improved adherence and proliferation of L929 fibroblast cells. Gentamicin loaded plasticized muga and tasar fibroin films showed slightly higher rate of release as compared to un-plasticized films. The biodegradability of dextrose plasticized films was significantly higher as compared to their respective counterpart. The regeneration of flexible muga and tasar silk fibroin films pave the way to expand potential use of non-mulberry in the field of biomedical such as wound dressing.

Keywords: Flexible; muga; tasar; biocompatibility; biodegradability; wound dressing

1. Introduction

Non-mulberry silk fibroin such as muga (*Antheraea assama*) and tasar (*Antheraea mylitta*) are produced from organism belonging to class saturniidae of the order Lepidoptera [1-2]. Tasar and

ACCEPTED MANUSCRIPT

muga fibroin have been engineered in the form of films [1], nanofibers [3], cryogels [4], aerogels [5], freeze dried scaffolds [6] and have shown promising materials in the field of tissue engineering due to their excellent biocompatibility, controlled biodegradability and higher mechanical property. It is reported that non-mulberry fibroin proteins contain tripeptide Arg(R)–Gly(G)–Asp(D) (AY136274), which is responsible for adherence of cells [1,7].

Recently, various researchers have utilized muga fibroin gland protein to prepare the films, nanofibers, cryogel and 3D scaffolds for tissue engineering and biomedical applications [8-11]. Dutta *et* al. [8] prepared 2D muga silk fibroin film and characterized their physicochemical properties. Kasoju *et* al. [9] prepared muga fibroin based micro-nano fibrous nonwoven scaffolds. These micro-nano architecture based porous scaffolds are highly biocompatible and non hemolytic. Kar *et* al. [10] have found that muga silk fibroin protein extracted from gland of silkworm is more compatible than mulberry fibroin. Highly porous muga fibroin based cryogels are able to absorb large amount of water, withstand high mechanical stress without deformation and showed very good viability of human hepatocarcinoma cells [4].

Tasar silk fibroin obtained from silkworm gland have been successfully utilized for cornea [12], cardiac [13], skin [1,14] and cartilage [15] tissue engineering. Mandal *et* al. [6] have regenerated tasar silk fibroin in the form of highly porous 3D scaffold by using freeze drying technique. They reported that freeze dried 3D scaffolds are highly biocompatible and showed good biodegradability over the time. Andiappan *et* al. [16] have prepared electrospun eri and tasar silk fibroin blend mats for biomedical application and found that these electrospun mats showed good biocompatibility and hemocompatibility. Hydroxyapatite coated eri-tasar silk fibroin nanofibrous mats showed good physiological characteristics [17].

ACCEPTED MANUSCRIPT

Although a good amount of work have been carried out on the muga and tasar silk fibroin protein extracted from silkworm gland, but only little work has been carried out on the muga & tasar silk fibroin extracted from cocoon due to its insolubility in most of the catastrophic solvents [11-12]. Recently, it is reported that muga and tasar cocoon fibroins can be dissolved in ionic liquids and be regenerated in the form of films using alcohol as coagulating agent [11,12,18]. These regenerated fibroin films are highly brittle in nature so it becomes unsuitable for wound dressing & regenerative medicine [19]. It is also observed that mechanical properties of different non-mulberry silk fibroin proteins regenerated from the cocoon have not been reported, which is very important for a material to be used as wound dressing. In our previous research, we have successfully regenerated cocoon extracted muga fibroin protein in the form of electrospun nanofibrous mat. These nanofibers mats showed higher strength & biocompatibility as compared to muga cast film [11]. Regenerated silk fibroin films require flexibility to be used as wound dressing especially when they are used in load bearing area such as knee joints & elbow joints. Beside this, to promote healing these films should provide good biocompatibility, moist environment & protection against pathogens [20–22].

Flexibility of biomaterial films can be improved by incorporating dextrose [19,23], sorbitol and mannitol [24]. Lu *et* al. [25] have developed flexible mulberry silk fibroin films using glycerol. Dextrose is a simple polyhydroxy carbohydrate which increases water absorbance ability of fibroin proteins. In our previous study, we have used dextrose to plasticize the mulberry silk fibroin films [19].

To the best of our knowledge, regenerated silk fibroin films extracted from muga and tasar cocoon have not been exploited for wound dressing applications. In the present study, we have prepared regenerated muga and tasar fibroin flexible films by incorporating dextrose. These

ACCEPTED MANUSCRIPT

plasticized muga and tasar fibroin films are characterized for their physical, mechanical and structural properties. The cytocompatibility and *in vitro* biodegradation of different plasticized and un-plasticized films are also determined. In order to protect the wound against pathogens, gentamicin is further incorporated in these films. The release kinetics of gentamicin from different films was also carried out.

2. Experimental Section

2.1 Materials

Muga and tasar cocoon were purchased from Estofa International Delhi, and Research Extension Center, Silk Research Board, Sonbhadra, Uttar Pradesh, India, respectively. All other chemicals used in the proposed study were purchased from Sigma-Aldrich, India until specified. Distilled water was used throughout the study.

2.2 Extraction of silk fibroin fibers from cocoon

Silk fibroin fibers were extracted from muga and tasar cocoon by the protocol described earlier [1]. Muga and tasar cocoon were cut in small pieces and then washed with distilled water to remove any dust and impurities. Raw silk cocoon pieces were degummed twice with 0.02 M $NaHCO_3$ at 100 ^oC for 30 minutes and then rinsed with distilled water to remove sericin protein. The degummed muga and tasar fibroin fibers were dried in oven at 60 ^oC.

2.3 Preparation of dextrose incorporated muga and tasar silk fibroin films

Degummed muga and tasar fibroin fibers were dissolved in the 1-butyl 3-methyl imidazolium acetate (BMIMAc) ionic liquid (10% w/v) at 90 ^oC for 2h under nitrogen atmosphere with constant stirring. The molecular weight of tasar and muga fibroin proteins after dissolution in

ACCEPTED MANUSCRIPT

ionic liquid was measured with Sodium Dodecyl Sulphate Polyacrylamide Gel Electrophoresis (SDS-PAGE). The molecular weight of tasar and muga proteins was found to be 195 and 230 kDa. Different concentration of dextrose (5 to15% w/w) were mixed with muga and tasar ionic liquid solution separately and then poured into petriplates under laminar air flow to prepare the films of thickness 0.5±0.1 mm. After 2 h, methanol was added to each petriplates in order to crystallize them for 5 h. The residual ionic liquid trapped in the cast films was extracted by the protocol described earlier [11-15]. Briefly, aliquots were replaced continuously with fresh methanol at each 12 h in order to extract the residual ionic liquid from muga and tasar cast films. Residual ionic liquid was checked by measuring the conductivity of the aliquots at different time interval. Conductivity of the pure methanol and ionic liquid was 4 μS/cm and 1500 μS/cm, respectively. Initially, large amount of ionic liquid was released from cast films so conductivity of the aliquots was found to be higher, which was nearly close to the conductivity of pure ionic liquid. With time as the aliquots were replaced with fresh methanol the amount of ionic liquid released from the films reduced, finally after 96 h the conductivity of the aliquots became equal to pure methanol which indicated that there was no trace of ionic liquid released from the films. Ionic liquid was recovered back from aliquots by evaporation of methanol at 60 ^{o}C and 150 mb pressure by using rotatory evaporator. Regenerated muga and tasar films are designated as MF and TF. Dextrose modified muga and tasar films are designated as DMMF and DMTF, respectively. Amount of dextrose (in w/w) is written before the abbreviation. For example 5% dextrose incorporated muga regenerated film is designated as 5% DMMF.

3. Characterization

3.1 Mechanical properties

ACCEPTED MANUSCRIPT

Mechanical properties of different films were characterized by using Universal Testing Machine as per ASTM D 882. The samples of specific size (70x10x0.5 mm) were preconditioned and mount between the grips of the machine with span length of 50 mm and pulled at the speed of 50 mm/min. Average mechanical properties of at least five samples were measured.

Plasticization effect of dextrose was further studied by dynamic mechanical thermal analyzer (Perkin Elmer DM 8000) in tension mode using film testing fixture. The tan δ curve values of different samples (40 x 10 mm) was determined at the series of temperature from 25 to 250 ^{o}C at the frequency of 1Hz with 0.125% of strain & 3 ^{o}C/min temperature rate.

3.2. Surface morphology

Surface morphology of dextrose plasticized and un-plasticized samples were analyzed using scanning electron microscope (Hitachi S3700N) at voltage of 15 KV. Samples were sputtered coated with gold before mounting in SEM machine.

The surface topography and roughness of the films were further analyzed by using atomic force microscopy (AFM-Park 100) in non-contact mode using a tip fixed on V shape silicon nitride cantilever with a spring constant 40 N/m. The samples were analyzed by atomic force microscope at the room temperature with scan area of 2x2 μm. Surface roughness of the different films was measured as root mean square (rms) and arithmetic average height (Ra).

3.3. Structural Characterization

Secondary conformation of silk fibroin films was accessed by acquiring the infrared spectra with Thermo Scientific Nicolet 380 Spectrometer in attenuated total reflection mode in the spectral region of 1800 to 600 cm^{-1}. FTIR spectra were recorded after 64 scan at a resolution of 4 cm^{-1}.

ACCEPTED MANUSCRIPT

3.4. Water uptake

The swelling studies of different silk fibroin films were performed at 37 ^{o}C as per protocol described earlier [26]. First, the film samples (10 x 10 mm) were immersed in 1X PBS at 37 ^{o}C. At predetermined time, the swollen film samples were taken out and wiped with tissue paper to remove excess PBS adhered at the surface, till equilibrium has reached. The wet and dry weights of samples were measured to calculate the water uptake capacity of different samples using equation 1:

$$\text{Water uptake (\%)} = [(W_t - W_d)/ W_d] \times 100 \ldots\ldots\ldots (1)$$

where W_t is the weight of wet samples and W_d is the weight of the dry samples.

3.5. Thermal characterization

Differential scanning calorimetry (DSC) instrument was utilized to determine the thermal behavior of the muga and tasar films. The samples (5 mg) were encapsulated in aluminium pans and heated at the rate of 10 ^{o}C/min from 50 to 500 ^{o}C under nitrogen atmosphere.

3.6. Biocompatibility test

3.6.1 Cell culture

L929 mouse skin fibroblast cells were purchased from National Centre for Cell Science, Pune, India. L929 skin fibroblasts cells were cultured in Dulbecco's Modified Eagle Medium (Sigma Aldrich), supplemented with 10% fetal bovine serum, 100 U/ml penicillin and 100 microgram/mL at 37 ˚C in the atmosphere of 5% CO_2. At confluence stage cells were trypsinized using 0.25% trypsin (sigma), washed with DMEM and centrifuged, after that resuspended these cells using fresh DMEM to the concentration of $1x10^5$ cells/mL with FBS and antibiotic. The

ACCEPTED MANUSCRIPT

different muga and tasar silk fibroin films were seeded with approx $1x10^5$ cells in 98 well plate and incubated at 37 °C in 5% CO_2 for 1 to 5 days.

3.6.2. Adherence, growth and proliferation of L929 cells seeded on different films

In vitro cytocompatibility of different muga and tasar silk fibroin films with L929 fibroblast cells were determined using MTT assay. MTT is a calorimetric technique based on the fact that yellow MTT is reduced to violet formazan by the action of mitochondrial dehydrogenase inside the cells. Briefly, after definite time point (1, 3 and 5 days of incubation) cells seeded samples were removed from tissue culture plate, washed with PBS and incubated with 150 µL of MTT solution (0.50 mg/mL in PBS) for 3 h at 37 °C in CO_2 incubator. After 3 h, exhausted MTT solutions were replaced with dimethyl sulphoxide (Sigma-Aldrich) to dissolve the formazan crystal. The absorbance of formazan solutions was measured using ElX-800 Microelisa reader (BioTek Inc., USA) at the wavelength of 595 nm. Pure DMSO was used as blank.

The number of viable cells seeded on different muga and tasar silk fibroin films were determined by using Trypan blue exclusion assay, which is based on the fact that viable cells have a clear cytoplasm whereas a nonviable cells absorb the dye and have a blue cytoplasm.

The spreading and morphology of L929 fibroblast cells seeded on different muga and tasar silk fibroin were observed under phase contrast microscope (Nikon ECLIPSE TS 100) after 1, 3 and 5 days of incubation.

3.7. *In vitro* biodegradation

ACCEPTED MANUSCRIPT

In vitro biodegradation of flexible muga and tasar fibroin films were assessed through the protocol reported earlier [1,11]. Briefly, the sterile samples were cut in specific size and weighed. Samples were incubated in 48 well tissue culture plate in PBS with and without protease XIV (1 mg/mL). These culture plates were placed in incubator at 37 ^{o}C. The exhausted enzyme solutions were replaced with fresh enzyme solution every day in order to maintain the optimum activity of enzyme. At different time interval of 1, 2, 3 and 4 weeks, the samples were removed, washed with distilled water, dried in oven under vacuum and weighed. The percent mass loss was calculated using following equation:

$$\text{Mass loss (\%)} = W_o - W_t/W_o \times 100 \quad \text{.....(2)}$$

Where, W_o is the initial dried mass and W_t is the vacuum dried mass measured after incubation.

3.8. Antimicrobial activity

Antimicrobial activity of gentamicin sulphate loaded muga and tasar fibroin films were studied by disc diffusion assay (AATCC 30) against gram +ve (*S. aureus*) and gram -ve (*E. coli*) bacteria [27]. Gentamicin sulphate drug was loaded in different film samples by using protocol described by Sampath *et* al. [28]. Briefly, samples were cut in the shape of disc and weighed. These film discs were put in the drug solution (25 mg/mL) for 48 h. These film samples were removed from the drug solution and amount of drug loaded in the different films were determined by measuring the absorbance values of aliquot by UV-Vis spectrophotometer at 333 nm. The drug loaded film samples were sterilized by UV radiation under laminar air flow for 24 h. The *E. coli* and *S. aureus* strains were spread on the agar plates separately. The drug loaded film samples were put on these bacterial cultured agar plates and pressed slightly to ensure close contact between gel and film. These plates were incubated at 37 ^{o}C for 24 h. The zone of inhibition formed around

ACCEPTED MANUSCRIPT

the films was measured carefully using scale to access the antimicrobial activity of drug loaded samples.

3.9. Drug release kinetics

Plasticized and un-plasticized muga and tasar fibroin films were dipped in 50 mL of gentamicin sulphate solution (5 mg/mL) for 48 h at 37 °C. The amount of drug loaded into different film samples was determined by UV-Vis spectrophotometer at the wavelength of 333 nm. Herein, absorbance of gentamicin solution before and after immersion of film samples was measured with the help of standard curve of gentamicin solution obtained through o-phthaldehyde derivatization method [28]. The amount of drug released by these films was determined by dipping these samples into 50 mL of PBS solution for 10 days at 37 °C. At pre-determined time point, amount of drug released by these samples was analyzed by taking 200 μL of aliquots and subjected to o-phthaldehyde derivatization method at the wavelength of 333 nm [29,22]. After each measurement same amount of fresh PBS was added back to experimental stock solution in order to maintain equilibrium condition. Amount of drug released by each sample was measured by standard curve of gentamicin. Drug release experiment was carried out for 10 days. The release mechanism of drug from different samples were determined by fitting the data to Ritger-Peppas, a semi empirical power law method [30].

Statistical Analysis

All the data are presented as mean±SD deviation. The experimental data were analyzed using standard analysis of variance (ANOVA) at the significance level of $p<0.05$. All the experiments were carried out in triplicate.

4. Results and discussion

ACCEPTED MANUSCRIPT

4.1. Mechanical properties

Strength and elasticity of different plasticized and un-plasticized silk fibroin films were determined in terms of tensile strength, elongation at break and Young's modulus, which are depicted in Table 1. Stress-strain curves (Fig. 1) revealed that with increase in the dextrose content from 5 to 15%, the elongation at break of muga and tasar silk fibroin increased. Further it is evident from Table 1 that with increase in dextrose content, tensile strength & modulus values decreased significantly, where as elongation at break values of plasticized silk films increased sharply as compared to un-plasticized films. Highly brittle and hard films showed higher tensile strength, modulus and low elongation at break while flexible films show lower tensile strength, modulus and higher elongation. Many studies revealed that flexibility of protein and polysaccharide films can be increased by the incorporation of hydrophilic molecules [24,25]. These hydrophilic molecules break the inter-chain interactions and establish new interaction with the polymer chains. Being hydrophilic in nature, dextrose attracts the water molecules from surrounding environment that increase the inter-chain space between polymer molecules. Similar observation were reported for dextrose plasticized mulberry silk fibroin films where elasticity of mulberry fibroin films were increased by increasing dextrose content [19]. Lu *et* al. [25] have prepared glycerol blended mulberry silk fibroin films and found that glycerol is very effective to act as plasticizer that increase the flexibility of mulberry fibroin films. Kawahara *et* al. [31] studied the effect of water plasticization on the flexibility of mulberry silk fibroin films.

Plasticization effect of dextrose on the muga and tasar fibroin films were further confirmed by measuring the tan δ peak at different temperature using dynamic mechanical thermal analyzer. The results are shown in Fig. 2. tan δ peaks for TF and MF were found at the temperature of 228 and 224 ^{o}C respectively. As we incorporated dextrose, the peak shifted towards lower

ACCEPTED MANUSCRIPT

temperature region and was observed at 218 and 210 ^{o}C, for 15% DMTF and 15% DMMF, respectively. This behavior was observed due to increase in segmental mobility of muga and tasar fibroin molecules as the amount of bound water increased by dextrose plasticization. As shown in the schematic representation (Fig. 3), dextrose molecules absorb the water molecules from the environment that increases interchain space which results in increased segmental mobility of fibroin molecules. The higher glass transition temperature of the un-plasticized muga and tasar fibroin was associated with limited polymer chain mobility due to the presence of strong secondary forces such as hydrogen bonds in amorphous motifs. These findings are concurred with results reported by Yuon *et* al. [32]. They found that Tan δ peak of mulberry silk fibroin films shifted from 195 to 162 ℃ as the initial water content increased from 6 to 13 wt%.

4.2. Morphological characterization

Surface morphology of different plasticized and un-plasticized muga and tasar silk fibroin films was analyzed by scanning electron microscope. The SEM micrographs of different films are shown in Fig. 4. Regenerated muga (MF) and tasar (TF) films showed comparatively smooth surface morphology (Fig. 4 a & e) as compared to dextrose incorporated films. The surface roughness of muga and tasar fibroin films increased with increase in dextrose content from 5 to 15% (w/w).

For the quantitative analysis, surface roughness and nano-featured topographies of different plasticized and un-plasticized silk fibroin films were further determined by atomic force microscope (Park-100). Results are depicted in the Fig. 5. The average roughness values of different films are shown in Table 2. The root mean square (Rq) and average roughness (Ra) of dextrose (15% w/w) incorporated muga (15% DMMF) and tasar silk fibroin films (15% DMTF)

ACCEPTED MANUSCRIPT

were significantly higher as compared to that of un-plasticized tasar (TF) and muga (MF) film. It was observed that tasar fibroin film had higher surface roughness (Rq & Ra) as compared to muga fibroin film. The surface roughness of 15% DMTF was significantly higher ($p<0.05$) as compared to 15% DMMF.

The higher surface roughness of dextrose incorporated films may be due to some phase separation and leaching off dextrose from surface during the crystallization of films as well as extraction of ionic liquid from plasticized films. It may also be possible that in the presence of dextrose the interactions between fibroin molecules disrupt which lead to higher aggregation at molecular level and caused higher roughness.

4.3. Water uptake

Water uptake ability is an indicator of the hydrophilicity of the material, which is essential requirement of any material to be used as wound dressing. The material to be used as wound dressing should be efficient to absorb fluid for preventing the accumulation of exudates that can cause infection by the bacteria. Water uptake ability of different plasticized and un-plasticized muga and tasar fibroin films were determined and are shown in Fig. 6. Water uptake for 5% DMTF was found to be 37% , which was significantly higher ($p<0.05$) than that of pure tasar fibroin (17%), while for 5% DMMF the value of water uptake was 39% as compared to pure muga fibroin (19%). The water uptake ability of tasar and muga fibroin films increased with an increase in dextrose content from 5 to 15% (w/w) and was found to saturate after 48 h. This difference in water absorbance was due to the difference in amount of dextrose present in the films [19]. The percentage water uptake by unplasticized muga and tasar fibroin films was nearly same, which may be due to the fact that hydrophilic to hydrophobic amino acid ratio for both fibroin proteins is nearly same. The maximum water uptake for TF and 15% (w/w) DMTF was

ACCEPTED MANUSCRIPT

17 and 64%, respectively, which is not significantly ($p>0.05$) different from the water uptake value of MF (19%) and 15% (w/w) DMMF (65%). This is due to no significant difference in hydrophilic to hydrophobic amino acid ratio for the tasar and muga fibroin [33].

Based on the improvement in flexibility, surface roughness and water uptake by incorporating 15% dextrose in both muga and tasar films, further studies were focused only on 15% dextrose plasticized tasar and muga films.

4.4. Structural properties

ATR-FTIR measurements were carried out to access the conformational changes of plasticized and un-plasticized muga and tasar fibroin films. The infrared region between 1700-1600, 1600-1500 to 1300-1200 cm^{-1}, corresponds to amide I, amide II and amide III, used for the study of secondary structure of fibroin proteins. The peaks positioned at 1630-1610, 1520-1510 and 1230-1220 cm^{-1} were characteristic of silk II (β-sheet) conformation. From the Fig. 7 it was evident that bands appeared at 1635 & 1521 cm^{-1}, 1633 & 1527 cm^{-1}, 1625 & 1515 cm^{-1} and 1635 & 1525 cm^{-1} for 15% DMMF, 15% DMTF, MF and TF, respectively, were characteristic of β-sheet conformation. These results showed that dextrose incorporation did not affect the β-sheet conformation of fibroin proteins after coagulation with methanol. Kaplan *et* al. [25] also observed that incorporation of glycerol does not affect silk II structure of regenerated mulberry silk fibroin.

4.5. Thermal properties

Differential scanning calorimetric (DSC) thermograms of different plasticized and un-plasticized muga and tasar silk fibroin films are shown in Fig. 8. The endothermic transitions found in the temperature range below 120 °C associate to evaporative water loss during heating. The bound

ACCEPTED MANUSCRIPT

water evaporation peaks of 15% DMTF and 15% DMMF were larger compared to TF and MF due to higher water absorption tendency of dextrose incorporated silk films. The other endothermic peaks above the temperature boundary of 390 °C were associated to thermal degradation of high ordered fraction of TF and 15% DMTF, while major endothermic peak for the degradation of MF and 15% DMMF was found at 295 °C. This further signifies that addition of dextrose does not affect crystalline structure of muga and tasar fibroin proteins. It has been reported that T_g in lower temperature region (bound water evaporation peak) indicates the interaction between fibroin protein and bound water. High heat capacity of endothermic peaks below 150 °C indicate strong interaction between bound water and silk fibroin macromolecules [34,35].

4.6. Biocompatibility

4.6.1. Cells growth and viability of L929 cells seeded on different silk films by Trypan blue assay

The viability of L929 cells seeded on different plasticized and un-plasticized muga and tasar fibroin films can be determined by counting total number of viable cells by Trypan blue staining using hemocytometer. The number of viable cells seeded on different films is shown in the Fig. 9 (a). After one day of incubation number of viable cells seeded on 15% DMMF and 15% DMTF was significantly higher than the un-plasticized TF and MF, but there was not any significant difference found between the cells seeded on TF and MF as well as 15% DMMF and 15% DMTF, respectively. Similarly, after 3 and 5 day of incubation, number of cells increased for both plasticized and un-plasticized films, but cell proliferation was more significant for plasticized (15% DMMF and 15% DMTF) films as compared to un-plasticized TF and MF.

4.6.2. Growth and viability of L929 cells seeded on different silk films by MTT assay

ACCEPTED MANUSCRIPT

The cellular metabolic activity of L929 cells seeded on different plasticized and un-plasticized films after 1, 3 and 5 days of incubation were determined by MTT assay. MTT assay determine the cellular metabolic activity, which is based on the fact that MTT is reduced to violet color formazan by the mitochondrial dehydrogenase. The optical density (OD) value of MTT formazan solution is directly related to cell population, so by measuring the OD value we can be able to evaluate the relative cells proliferation. For all the samples, cell proliferation was increased with incubation time. From the Fig. 9 (b) it is evident that absorbance value for 15% DMMF and 15% DMTF was significantly higher as compared to MF and TF, but there was no significant difference found between MF & TF as well as 15% DMMF and 15% DMTF after 5 day of incubation.

4.6.3. Spreading and proliferation of L929 cells seeded on different silk films by phase contrast microscopy

The spreading and morphology of L929 cells seeded on plasticized and un-plasticized muga and tasar fibroin films after 1, 3 and 5 days of incubation were determined by phase contrast microscopy.

From the Fig. 9 (c) it is clear that the cells attain their normal morphology after 1 day of incubation with all types of films. The spreading of cells increased with time and reached to confluence stage after 5 days of incubation for 15% DMMF and 15% DMTF, but cells did not reach to confluence state for un-plasticized muga and tasar films. So it is clear that cells spreading and proliferation was significantly higher in the case of plasticized muga and tasar fibroin as compared to un-plasticized muga and tasar fibroin films. However, no significant difference was observed for adherence and proliferation of L929 fibroblast cells seeded on 15% DMMF and 15% DMTF.

ACCEPTED MANUSCRIPT

Tripeptide Arg(R)-Gly(G)-Asp(D) motif of nonmulberry silk fibroin proteins is responsible for higher attachment of cells [36]. A research group of Kundu *et* al. [1,2,8,12,37–41] extensively studied biocompatibility of mulberry and nonmulberry silk fibroin proteins. They have reported that tasar and muga fibroin gland protein showed higher adherence and proliferation as compared to mulberry silk fibroin protein [1].

Cells adherence and proliferation was further increased by incorporating dextrose content. The higher adherence and proliferation of the cells seeded on dextrose plasticized muga and tasar fibroin films over the un-plasticized muga and tasar film was mainly due to increased hydrophilicity and nanophase surface roughness. The dextrose being a hydrophilic molecule has tendency to increase the water absorbance capacity of fibroin films. Zeynep Karahaliloğlu *et* al. [42] have found that mulberry silk fibroin films having nanophase surface roughness shows higher adherence and proliferation of dermal fibroblast cells as compared to films having smooth morphology.

4.7. *In vitro* biodegradation

The stability of these muga and tasar fibroin films in physiological environment was studied by *in vitro* biodegradation assay. *In vitro* biodegradation was performed by incubating different plasticized and un-plasticized silk fibroin films in PBS with and without protease XIV enzyme. The mass change in plasticized and un-plasticized muga and tasar fibroin films after incubation in pure PBS and PBS-protease XIV solution is shown in Fig. 10. It was observed that notable mass loss occurred for each type of films after 50 days of incubation in protease XIV enzyme. The 15% DMTF and 15% DMMF showed significantly higher mass loss as compared to TF and MF after 50 days of incubation. The higher biodegradation of dextrose incorporated fibroin films over pure fibroin films was mainly related to the swelling characteristics of

ACCEPTED MANUSCRIPT

proteins. The crystalline portion of fibroin is highly resisted to degradation because enzyme cannot easily permeate β-sheet region. But with dextrose the swelling ability of fibroin increased which facilitated the permeation of enzyme to the inner extremes of β-sheet crystal that lead to significant mass loss. There was not any significant difference ($p>0.05$) between mass loss of TF and MF over 50 days of incubation. This may be due to nearly same hydrophilic to hydrophobic amino acid ratio of tasar and muga fibroin proteins [43]. The mass loss of TF, MF, 15% DMTF and 15% DMMF was found to be 52, 47, 67 and 60%, respectively which consistently followed second order trend line. No significant differences in mass loss were observed in PBS incubated samples for the same time.

4.8. Antimicrobial activity and Drug Release

4.8.1. Antimicrobial activity

Antimicrobial activity of gentamicin loaded plasticized and un-plasticized muga and tasar fibroin films were analyzed by agar disc diffusion assay. Amount of drug loaded in the dextrose plasticized films was significantly higher as compared to the un-plasticized films, which was found to be 15 and 12 mg for muga and tasar fibroin films and was 25 and 20 mg for 15% DMMF and 15% DMTF, respectively. Fig. 11 shows the antimicrobial activity of different samples in the form of zone of inhibition. Antimicrobial results show that there was no zone of inhibition formed for plasticized and un-plasticized muga and tasar fibroin films without drug. The zone of inhibition for TF, MF, 15% DMMF and 15% DMTF against *E. coli* was found to be 10, 11, 16 and 18 mm, respectively. The zone of inhibition for TF, MF, 15% DMMF and 15% DMTF against *S. aureus* was found to be 11, 13, 19 and 21 mm, respectively. Antimicrobial activity of dextrose plasticized muga and tasar fibroin films were higher as compared to un-plasticized films. This behavior was related to amount of drug loaded and swelling behavior of

ACCEPTED MANUSCRIPT

films. The high swelling ability of dextrose plasticized films caused fast and high drug release as compared to un-plasticized films.

4.8.2. Drug release

Gentamicin is very effective antibiotic that has potential to kill the gram +ve and gram -ve bacterial stain which reduces the infection at wound site and aids in normal wound healing profile. The cumulative release of gentamicin at physiological pH from loaded samples is shown in Fig. 12. Initial burst release of gentamicin was found for all the samples within 24 h due to more drug absorbed at the surface, which was followed by normal release for the rest of the period of study time. Release of drug from any wound dressing depends upon the degree of porosity, pore size, nature of drug. It was found that initial burst release was 20 and 22% for MF and TF, respectively, while it was found to be 28 and 30% for 15% DMMF and 15% DMTF, respectively. The maximum drug released from TF and MF was 45 and 40%, while it was 55 and 50% for 15% DMTF and 15% DMMF, respectively and reached to saturation within 10 day of analysis. The amount of drug released from dextrose plasticized samples was significantly higher than that of un-plasticized films. This behavior may be related to surface roughness and water absorbance ability of films. Due to higher surface roughness as revealed by AFM as well as water absorbance capacity of dextrose plasticized films, amount of drug loaded in the dextrose plasticized films was significantly higher compared to the un-plasticized films. The higher burst release could be the results of high amount of drug adsorbed at the rough surface of dextrose plasticized films as compared to un-plasticized films, similarly gradual release of drug up to 6 days was due to the presence of higher amount of drug in the reservoirs of the films. The release mechanism of gentamicin from different muga and tasar fibroin films were determined by putting the data to semi empirical model known as Ritger-Peppas model to determine value of

ACCEPTED MANUSCRIPT

'n' exponent [20]. The release data are shown in the Table 3. Vasconales *et* al. [44] have also found that value of exponent 'n' depend upon release mechanism and architecture of matrix. To determine the value of exponent 'n' we should consider the portion of curve for which value of M_t/M_o should be less than 0.6. The value of exponent 'n' for Fickian diffusion must be $0.45 \leq n$, for non Fickian diffusion it is $0.45 < n < 0.89$, while $n > 0.89$ corresponds to super case II transport and $n = 0.89$ corresponds to Case II (relaxation) transport [30].

The value of 'n' for muga, tasar, 15% DMMF and 15% DMTF was found to be 0.68, 0.65, 0.51, and 0.52, which depicted anomalous release behavior of drug for all type of films. Additionally, lower 'n' value of dextrose plasticized muga and tasar films as compared to the un-plasticized films further supported higher diffusion of dextrose plasticized films as compared to un-plasticized films. Similarly the higher 'k' value of dextrose plasticized muga and tasar films over the un-plasticized films was responsible for higher release of gentamicin. This phenomena was related to higher surface roughness and swelling capacity of dextrose plasticized films over un-plasticized.

5. Conclusion

Flexible and biocompatible muga and tasar fibroin films were prepared by using ionic liquid. Increase in elongation at break value and lowering of Tan δ value of dextrose plasticized tasar and muga fibroin films indicates that flexibility of films increased by the addition of dextrose. Dextrose content does not affect the secondary structure of silk fibroin protein. Higher water absorption and increased nanophase surface roughness was responsible for significantly improved cellular compatibility. These flexible muga and tasar silk fibroin films would be potential materials for wound dressing, advanced therapeutic devices, scaffolds and drug

ACCEPTED MANUSCRIPT

delivery vehicles, but still there is a need to further explore *in vivo* response of these materials so that we would be able to fully exploit them in the field of wound dressing.

Acknowledgement

Authors are thankful to Council of Scientific and Industrial Research (CSIR-HRDG) for providing SRF grant ((08/133(0009)/2014-EMR-I)). Authors acknowledge Dr. Amit Misra for providing lab facilities for carrying out cytocompatibility tests, Mr. Aman Verma of DTU for the mechanical measurements; Dr. Amrish Panwar and Mr. Sandeep Mishra for XRD and SEM recording and Dr. P. Tyagi, DTU for the AFM recordings.

References

[1] C. Acharya, S.K. Ghosh, S.C. Kundu, Silk fibroin film from non-mulberry tropical tasar silkworms: A novel substrate for in vitro fibroblast culture., Acta Biomater. 5 (2009) 429–37.

[2] S.C. Kundu, B. Kundu, S. Talukdar, S. Bano, S. Nayak, J. Kundu, et al., Nonmulberry silk biopolymers, Biopolymers. 97 (2012) 455–467.

[3] N.N. Panda, A. Biswas, K. Pramanik, S. Jonnalagadda, Enhanced osteogenic potential of human mesenchymal stem cells on electrospun nanofibrous scaffolds prepared from eri-tasar silk fibroin., J. Biomed. Mater. Res. B. Appl. Biomater. 103 (2015) 971–82.

[4] B. Kundu, S.C. Kundu, Bio-inspired fabrication of fibroin cryogels from the muga silkworm Antheraea assamensis for liver tissue engineering., Biomed. Mater. 8 (2013) 055003.

[5] R.R. Mallepally, M.A. Marin, V. Surampudi, B. Subia, R.R. Rao, S.C. Kundu, et al., Silk fibroin aerogels: potential scaffolds for tissue engineering applications., Biomed. Mater. 10 (2015) 035002.

[6] B.B. Mandal, S.C. Kundu, Cell proliferation and migration in silk fibroin 3D scaffolds, Biomaterials. 30 (2009) 2956–2965.

[7] E. Ruoslahti, M.D. Pierschbacher, New perspectives in cell adhesion: RGD and integrins., Science. 238 (1987) 491–7.

[8] S. Dutta, B. Talukdar, R. Bharali, R. Rajkhowa, D. Devi, Fabrication and characterization of biomaterial film from gland silk of muga and eri silkworms., Biopolymers. 99 (2013) 326–33.

ACCEPTED MANUSCRIPT

[9] N. Kasoju, R.R. Bhonde, U. Bora, Fabrication of a novel micro–nano fibrous nonwoven scaffold with Antheraea assama silk fibroin for use in tissue engineering, Mater. Lett. 63 (2009) 2466–2469.

[10] S. Kar, S. Talukdar, S. Pal, S. Nayak, P. Paranjape, S.C. Kundu, Silk gland fibroin from indian muga silkworm Antheraea assama as potential biomaterial, Tissue Eng. Regen. Med. 10 (2013) 200–210.

[11] C.M. Srivastava, R. Purwar, Fabrication of robust Antheraea assama fibroin nanofibrous mat using ionic liquid for skin tissue engineering, Mater. Sci. Eng. C 68 (2016) 276–290.

[12] S. Hazra, S. Nandi, D. Naskar, R. Guha, S. Chowdhury, N. Pradhan, et al., Non-mulberry Silk Fibroin Biomaterial for Corneal Regeneration, Sci. Rep. Nat. Publ. Gr. 6 (2016) 1-13.

[13] C. Patra, S. Talukdar, T. Novoyatleva, S.R. Velagala, C. Mühlfeld, B. Kundu, et al., Silk protein fibroin from Antheraea mylitta for cardiac tissue engineering, Biomaterials. 33 (2012) 2673–2680.

[14] J. Samal, S. Weinandy, A. Weinandy, M. Helmedag, L. Rongen, B. Hermanns-Sachweh, et al., Co-Culture of Human Endothelial Cells and Foreskin Fibroblasts on 3D Silk-Fibrin Scaffolds Supports Vascularization, Macromol. Biosci. 15 (2015) 1433–1446.

[15] S. Talukdar, Q.T. Nguyen, A.C. Chen, R.L. Sah, S.C. Kundu, Effect of initial cell seeding density on 3D-engineered silk fibroin scaffolds for articular cartilage tissue engineering, Biomaterials. 32 (2011) 8927–8937.

[16] M. Andiappan, T. Kumari, S. Sundaramoorthy, G. Meiyazhagan, P. Manoharan, G. Venkataraman, Comparison of eri and tasar silk fibroin scaffolds for biomedical applications, Prog. Biomater. 5 (2016) 81-91.

[17] M. Andiappan, S. Sundaramoorthy, N. Panda, G. Meiyazhaban, S.B. Winfred, G. Venkataraman, et al., Electrospun eri silk fibroin scaffold coated with hydroxyapatite for bone tissue engineering applications, Prog. Biomater. 2 (2013) 1-6.

[18] N. Goujon, R. Rajkhowa, X. Wang, N. Byrne, Effect of solvent on ionic liquid dissolved regenerated *antheraea assamensis* silk fibroin, J. Appl. Polym. Sci. 128 (2013) 4411–4416.

[19] C.M. Srivastava, R. Purwar, R. Kannaujia, D. Sharma, Flexible Silk Fibroin Films for Wound Dressing, Fibers Polym. 16 (2015) 1020–1030.

[20] K.A. Rieger, N.P. Birch, J.D. Schiffman, G.A. James, E. Swogger, R. Wolcott, et al., Designing electrospun nanofiber mats to promote wound healing – a review, J. Mater. Chem. B. 1 (2013) 4531.

[21] G.S. Lazarus, D.M. Cooper, D.R. Knighton, D.J. Margolis, R.E. Percoraro, G. Rodeheaver, et al., Definitions and guidelines for assessment of wounds and evaluation of healing, Wound Repair Regen. 2 (1994) 165–170.

[22] A. Vasconcelos, A.C. Gomes, A. Cavaco-Paulo, Novel silk fibroin/elastin wound

ACCEPTED MANUSCRIPT

dressings, Acta Biomater. 8 (2012) 3049–3060.

[23] Y. Baimark, P. Srihanam, Y. Srisuwan, Preparation of Flexible Silk Fibroin Films Plasticized with Glucose, Asian J. Mater. Sci. 1 (2009) 29–35.

[24] M.J. Franco, A.A. Martin, L.F.B. Jr, J. Caetano, G.A. Linde, D.C. Dragunski, Effect of plasticizer and modified starch on biodegradable films for strawberry protection, J. Food. Process. Preserv. 00 (2016) 1–9.

[25] S. Lu, X. Wang, Q. Lu, X. Zhang, J.A. Kluge, N. Uppal, F. Omenetto, D. L. Kaplan, Insoluble and Flexible Silk Films Containing Glycerol, Biomacromolecules, 11 (2010) 143–150.

[26] S.E. Wharram, X. Zhang, D.L. Kaplan, S.P. McCarthy, Electrospun silk material systems for wound healing, Macromol. Biosci. 10 (2010) 246–257.

[27] R. Purwar, M. Joshi, Recent Developments in Antimicrobial Finishing of Textiles--A Review, AATCC Review, 4 (2004) 22-26.

[28] S.S. Sampath, D.H. Robinson, Comparison of New and Existing Spectrophotometric Methods for the Analysis of Tobramycin and Other Aminoglycosides, J. Pharm. Sci. 79 (1990) 428–431.

[29] S.S. Sampath, D.H. Robinson, Comparison of new and existing spectrophotometric methods for the analysis of tobramycin and other aminoglycosides., J. Pharm. Sci. 79 (1990) 428–31.

[30] P.L. Ritger, N.A. Peppas, A simple equation for description of solute release II. Fickian and anomalous release from swellable devices, J. Control. Release. 5 (1987) 37–42.

[31] Y. Kawahara, K. Furukawa, T. Yamamoto, Self-Expansion Behavior of Silk Fibroin Film, Macromol. Mater. Eng. 291 (2006) 458–462.

[32] Q. Yuan, J. Yao, L. Huang, X. Chen, Z. Shao, Correlation between structural and dynamic mechanical transitions of regenerated silk fibroin, Polymer, 51 (2010) 6278–6283.

[33] K. Sen, M. Babu K, Studies on Indian silk. I. Macrocharacterization and analysis of amino acid composition, J. Appl. Polym. Sci. 92 (2004) 1080–1097.

[34] Q. Lu, X. Hu, X. Wang, J.A. Kluge, S. Lu, P. Cebe, et al., Water-insoluble silk films with silk I structure, Acta Biomater. 6 (2009) 1380–1387.

[35] A. Motta, L. Fambri, C. Migliaresi, Regenerated silk fibroin films: Thermal and dynamic mechanical analysis, Macromol. Chem. Phys. 203 (2002) 1658–1665.

[36] A. Gupta K, K. Mita, K.P. Arunkumar, J. Nagaraju, Molecular architecture of silk fibroin of Indian golden silkmoth, Antheraea assama, Sci. Rep. 5 (2015) 1-17.

[37] C. Acharya, S.K. Ghosh, S.C. Kundu, Silk fibroin film from non-mulberry tropical tasar silkworms: A novel substrate for in vitro fibroblast culture., Acta Biomater. 5 (2009) 429–37.

ACCEPTED MANUSCRIPT

[38] B. Kundu, S.C. Kundu, Bio-inspired fabrication of fibroin cryogels from the muga silkworm Antheraea assamensis for liver tissue engineering., Biomed. Mater. 8 (2013) 1–17.

[39] J. Kundu, R. Mohapatra, S.C. Kundu, Silk fibroin/sodium carboxymethylcellulose blended films for biotechnological applications., J. Biomater. Sci. Polym. Ed. 22 (2011) 519–39.

[40] S.C. Kundu, B. Kundu, S. Talukdar, S. Bano, S. Nayak, J. Kundu, et al., Invited review nonmulberry silk biopolymers., Biopolymers. 97 (2012) 455–67.

[41] J. Kundu, R. Mohapatra, S.C. Kundu, Silk fibroin/sodium carboxymethylcellulose blended films for biotechnological applications., J. Biomater. Sci. Polym. Ed. 22 (2011) 519–39.

[42] Z. Karahaliloğlu, B. Ercan, E.B. Denkbaş, T.J. Webster, Nanofeatured silk fibroin membranes for dermal wound healing applications., J. Biomed. Mater. Res. A. 103 (2015) 135–44.

[43] K. Sen, M. Babu K, Studies on Indian silk. II. Structure–property correlations, J. Appl. Polym. Sci. 92 (2004) 1098–1115.

[44] A. Vasconcelos, A.C. Gomes, A. Cavaco-Paulo, Novel silk fibroin/elastin wound dressings, Acta Biomater. 8 (2012) 3049–3060.

ACCEPTED MANUSCRIPT

ACCEPTED MANUSCRIPT

Figure Captions

Figure 1: Stress-strain curves of different (a): tasar and (b) muga fibroin films

Figure 2: Tan δ curves of different muga and tasar fibroin films

Figure 3: Schematic representation for dextrose plasticized and un-plasticized silk fibroin films

Figure 4: SEM micrographs of different muga and tasar fibroin films (a): MF, (b) 5% DMMF, (c) 10% DMMF & (d) 15% DMMF and (e) TF, (f) 5% DMTF, (g) 10% DMTF & (h) 15% DMTF

Figure 5: AFM micrographs of different muga and tasar fibroin films (a) MF, (b) 15% DMMF, (c) TF & (d) 15% DMTF

Figure 6: Water uptake behavior of different muga and tasar silk fibroin films

Figure 7: FTIR spectra of different muga and tasar fibroin films

Figure 8: DSC thermogram of different muga and tasar fibroin films

Figure 9: (a) Trypan blue assay (b) MTT assay and (c) Phase contrast microscopy of L929 cells seeded on different muga and tasar fibroin films

Figure 10: Protease XIV mediated *In vitro* biodegradation of different muga and tasar silk fibroin

Fig. 11: Disc diffusion assay of gentamicin loaded plasticized and un-plasticized muga and tasar silk fibroin films

Fig. 12: Cumulative release of gentamicin from different plasticized and un-plasticized muga and tasar fibroin films

ACCEPTED MANUSCRIPT

ACCEPTED MANUSCRIPT

Table Captions:

Table 1: Mechanical properties of dextrose modified muga and tasar fibroin films, Data were represented as mean±SD for n=3

Table 2: Surface roughness of dextrose modified muga and tasar fibroin films

Table 3: Kinetic data obtained by fitting the drug release data

ACCEPTED MANUSCRIPT

ACCEPTED MANUSCRIPT

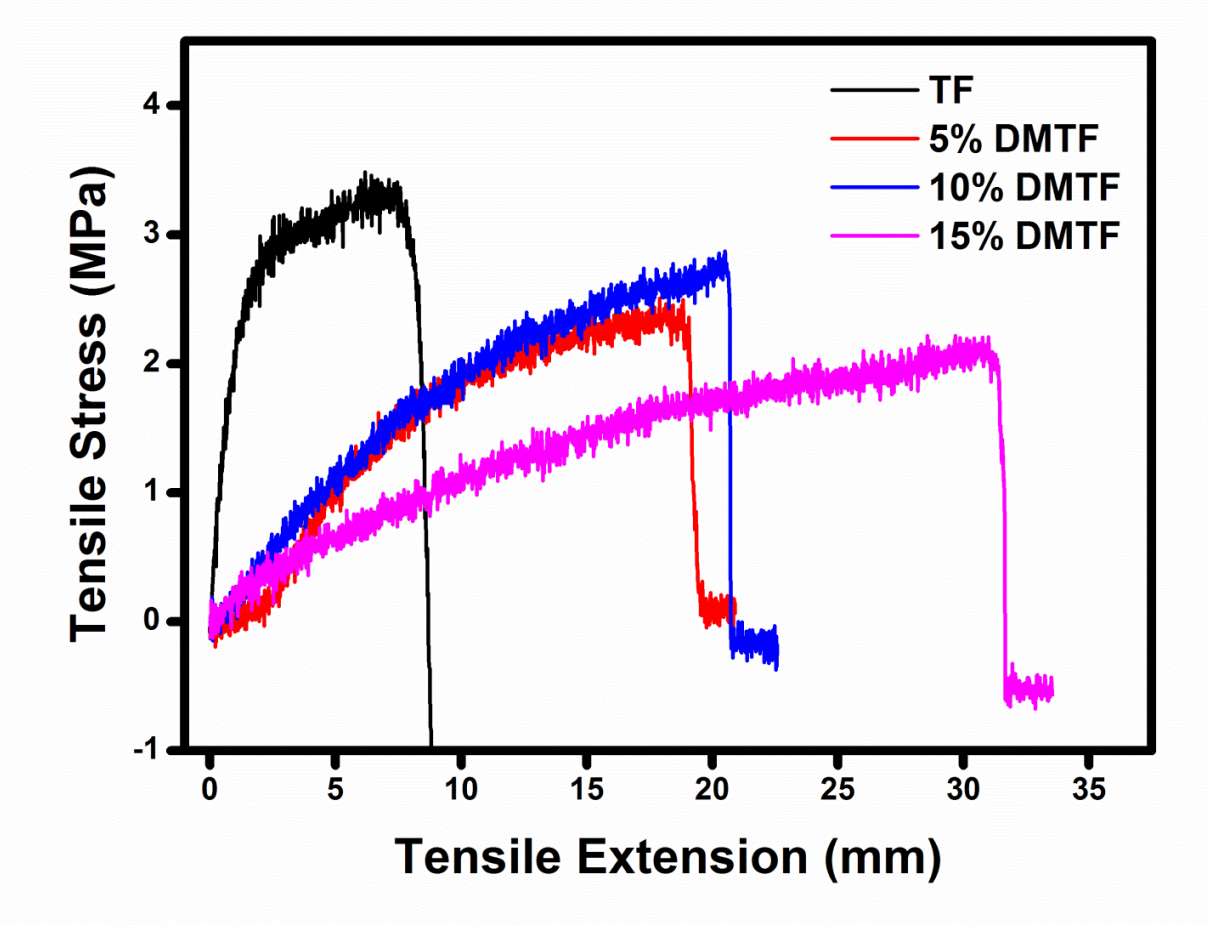


Fig. 1a

ACCEPTED

ACCEPTED MANUSCRIPT

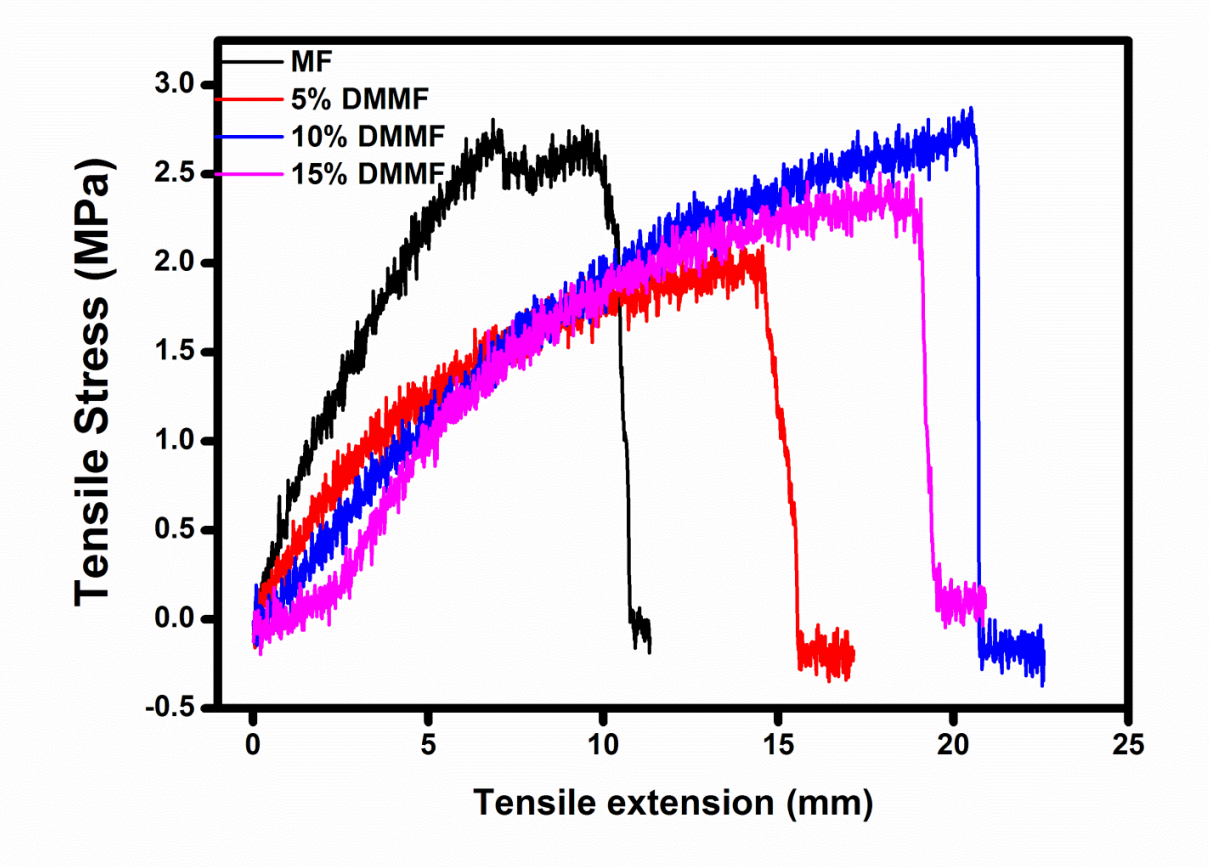


Fig. 1b

ACCEPTED

ACCEPTED MANUSCRIPT

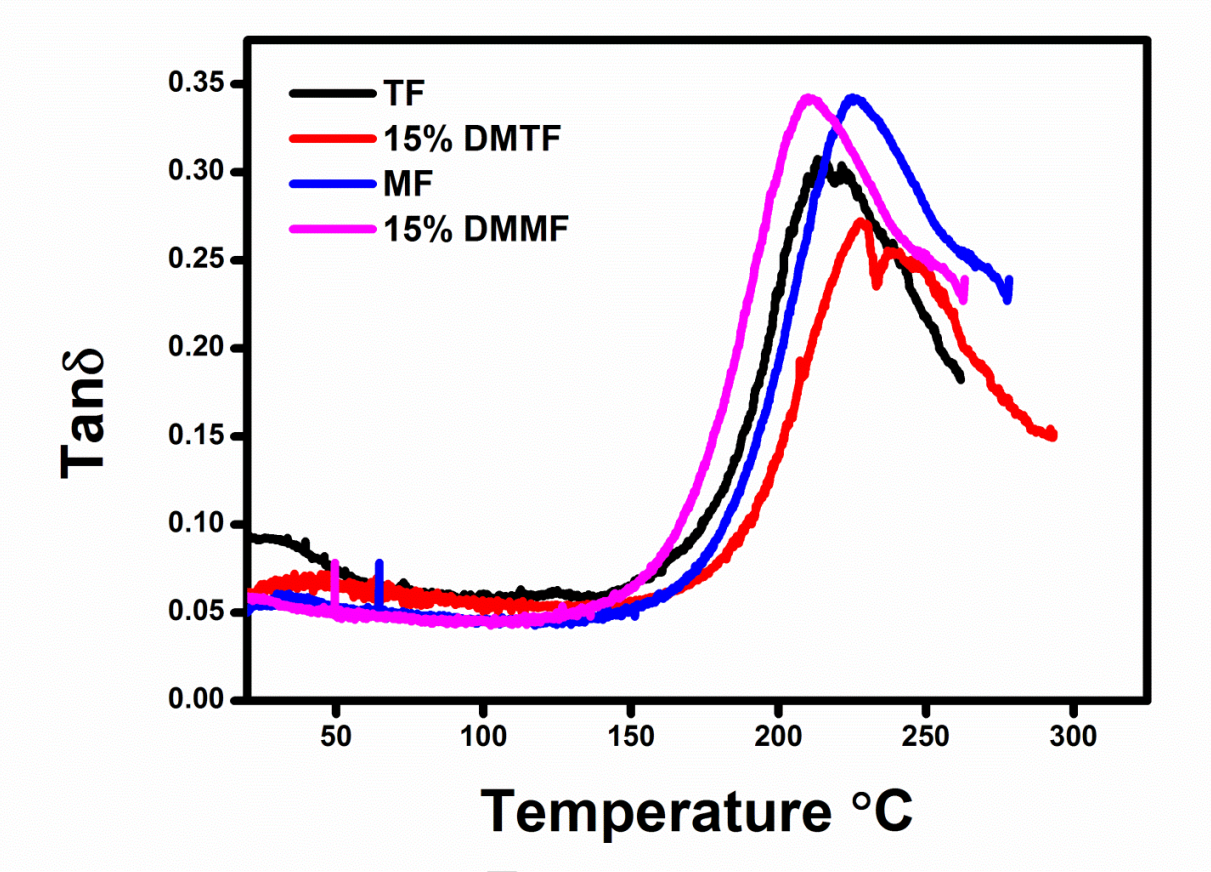


Fig. 2

ACCEPTED

ACCEPTED MANUSCRIPT

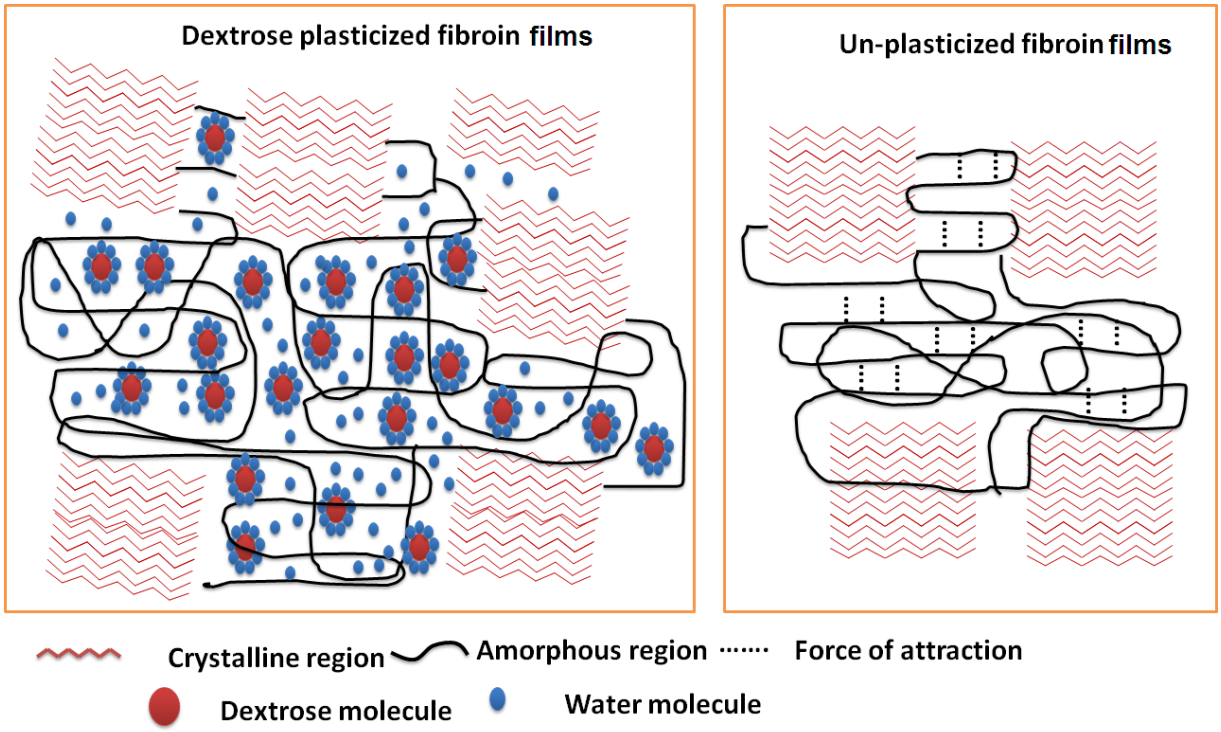


Fig. 3

ACCEPTED MANUSCRIPT

ACCEPTED MANUSCRIPT

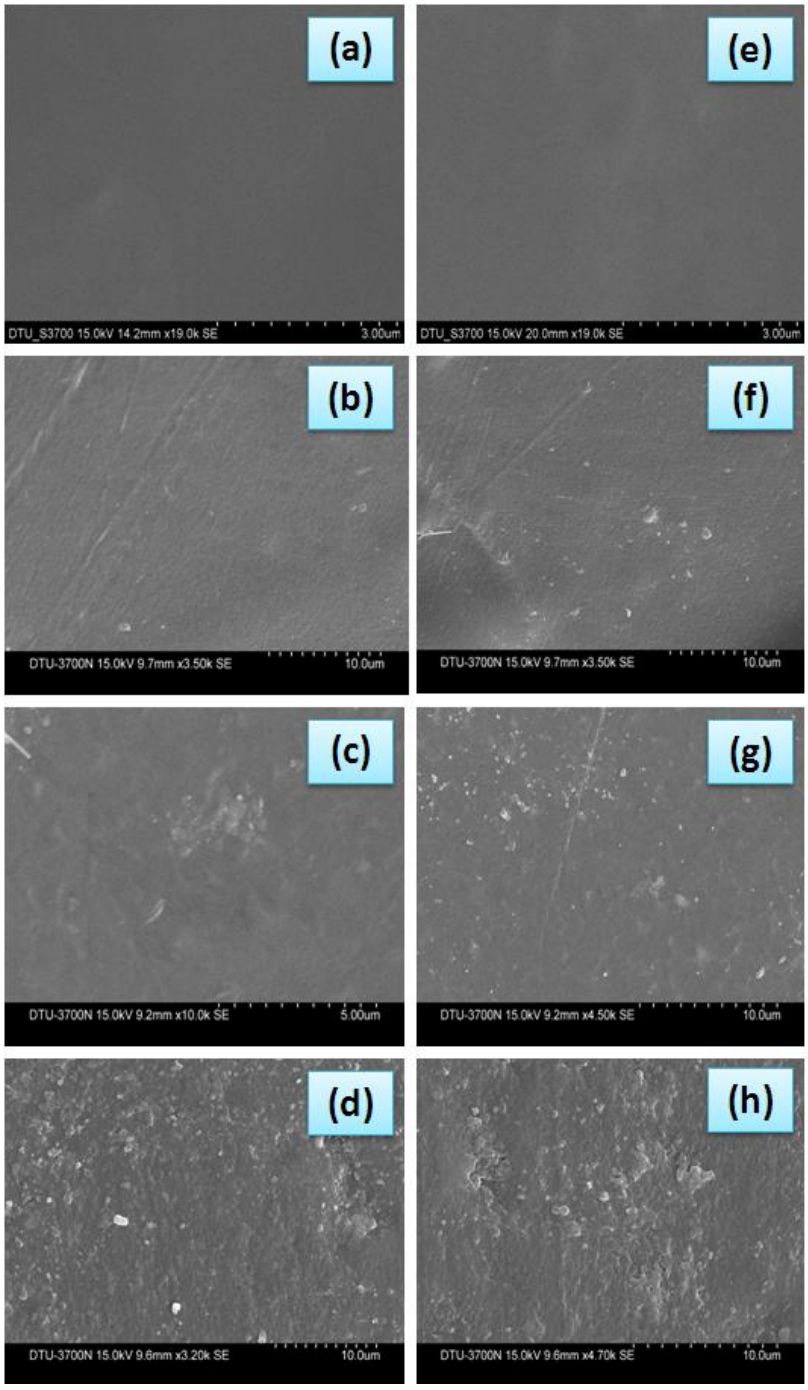


Fig. 4

ACCEPTED MANUSCRIPT

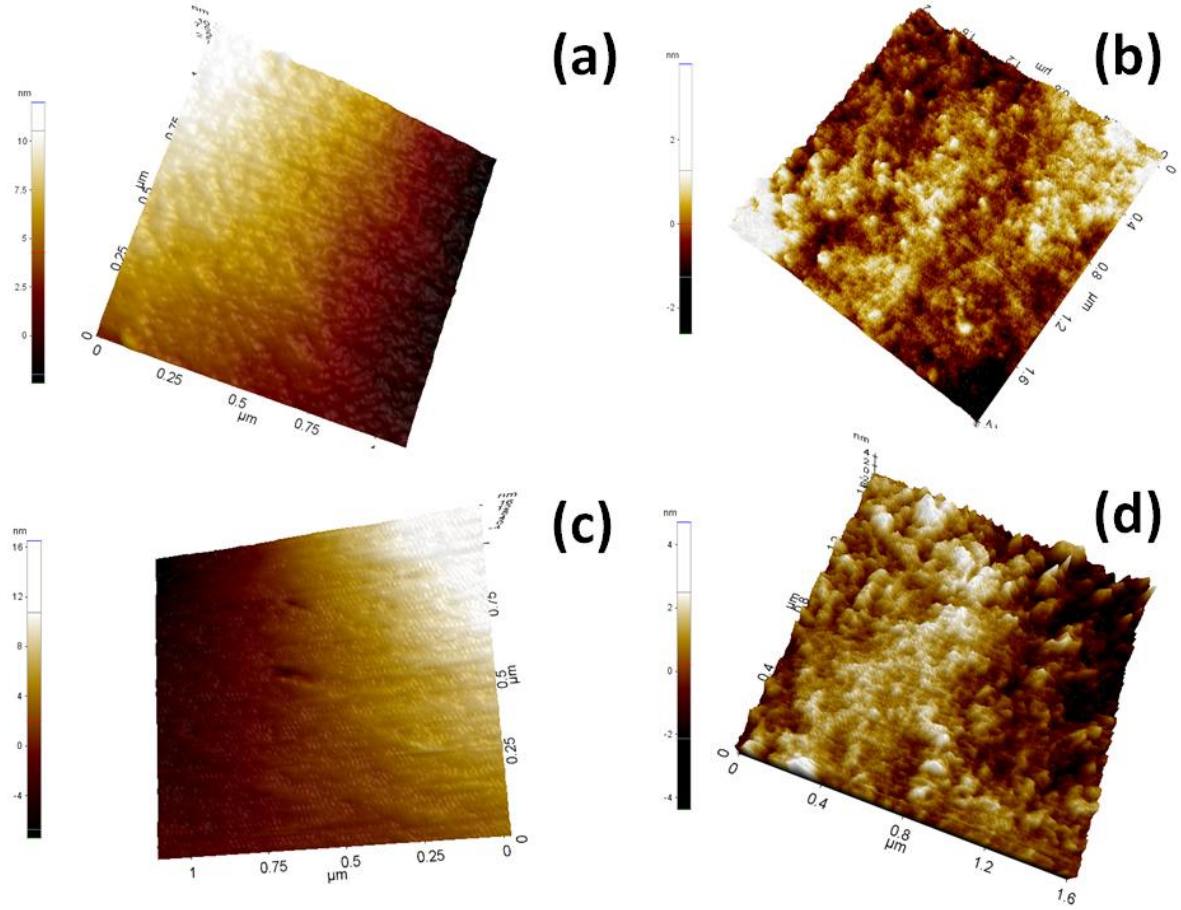


Fig. 5

ACCEPTED

ACCEPTED MANUSCRIPT

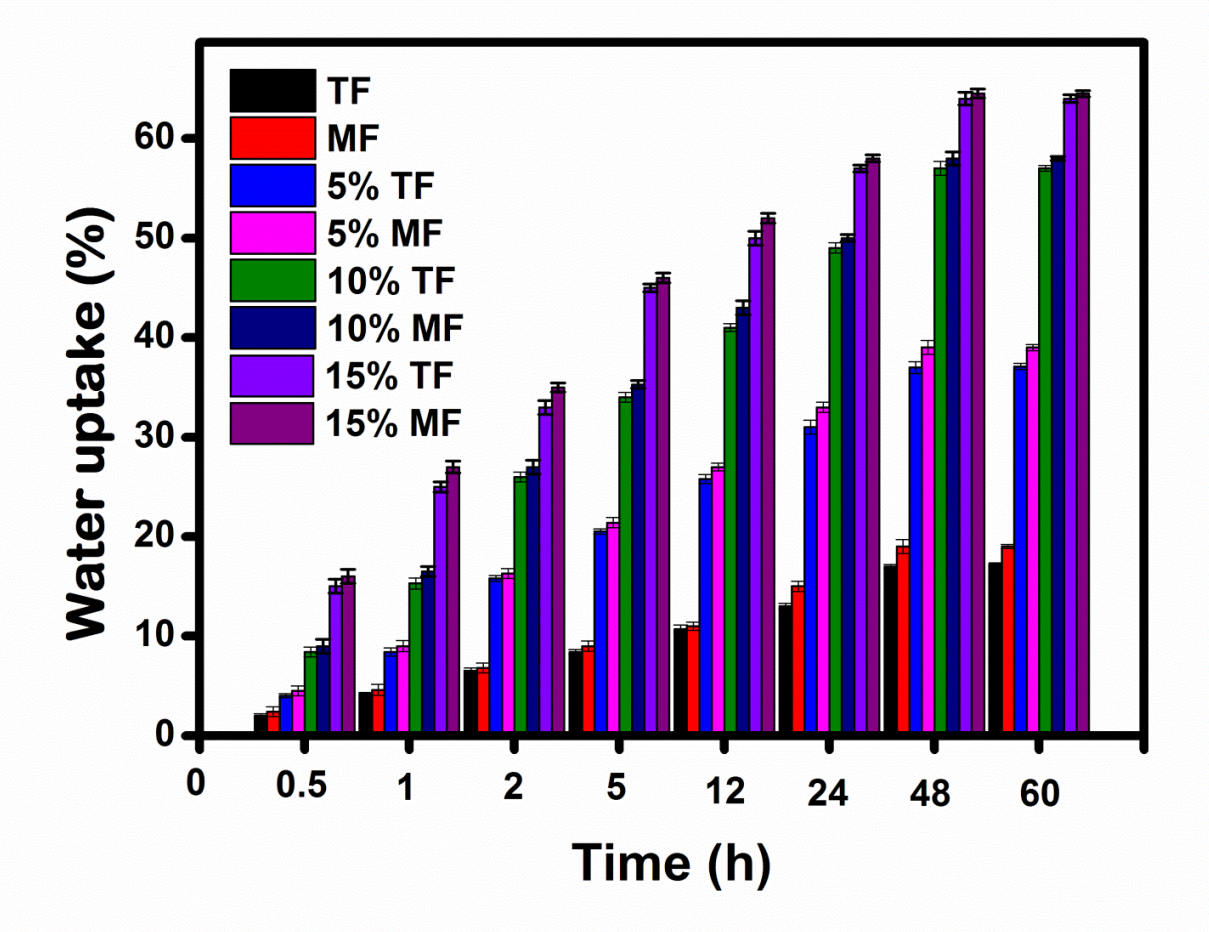


Fig. 6

ACCEPTED

ACCEPTED MANUSCRIPT

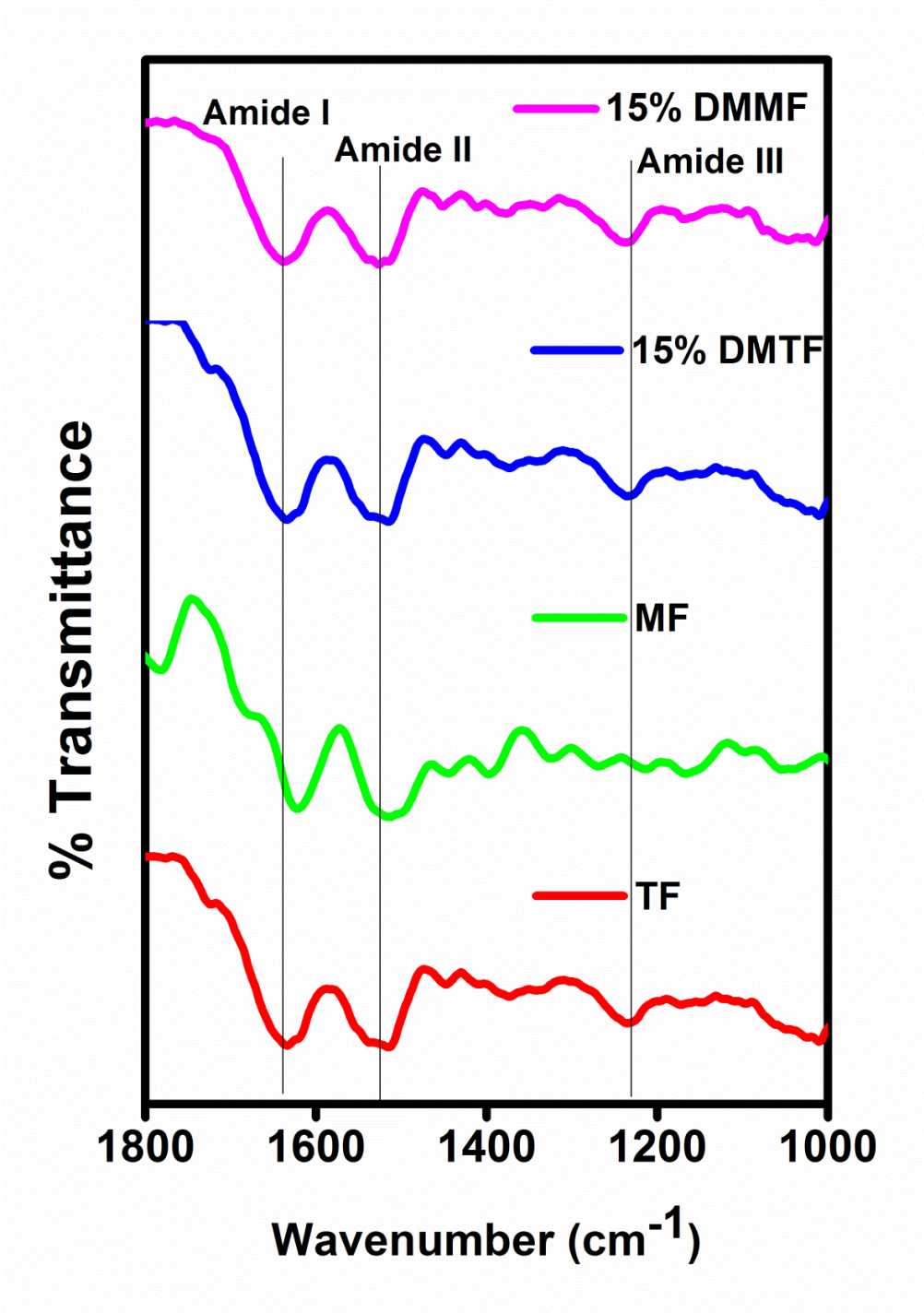


Fig. 7

ACCEPTED MANUSCRIPT

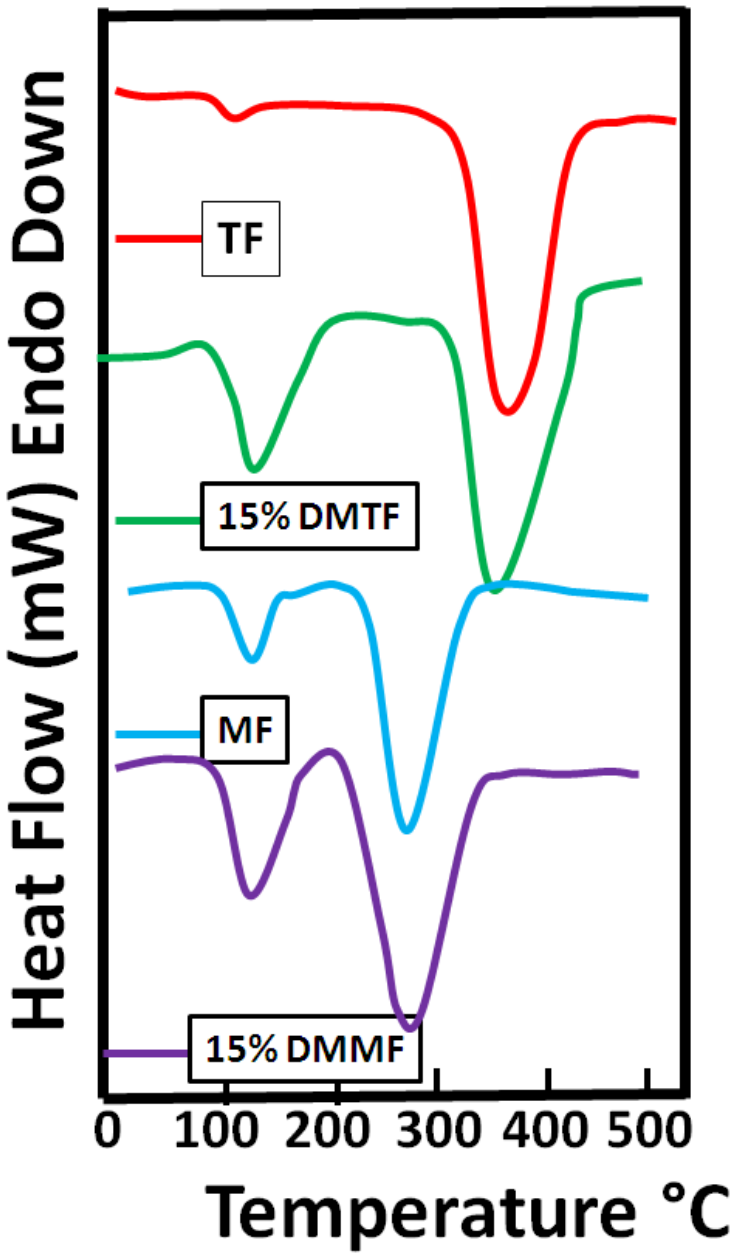


Fig. 8

ACCEPTED MANUSCRIPT

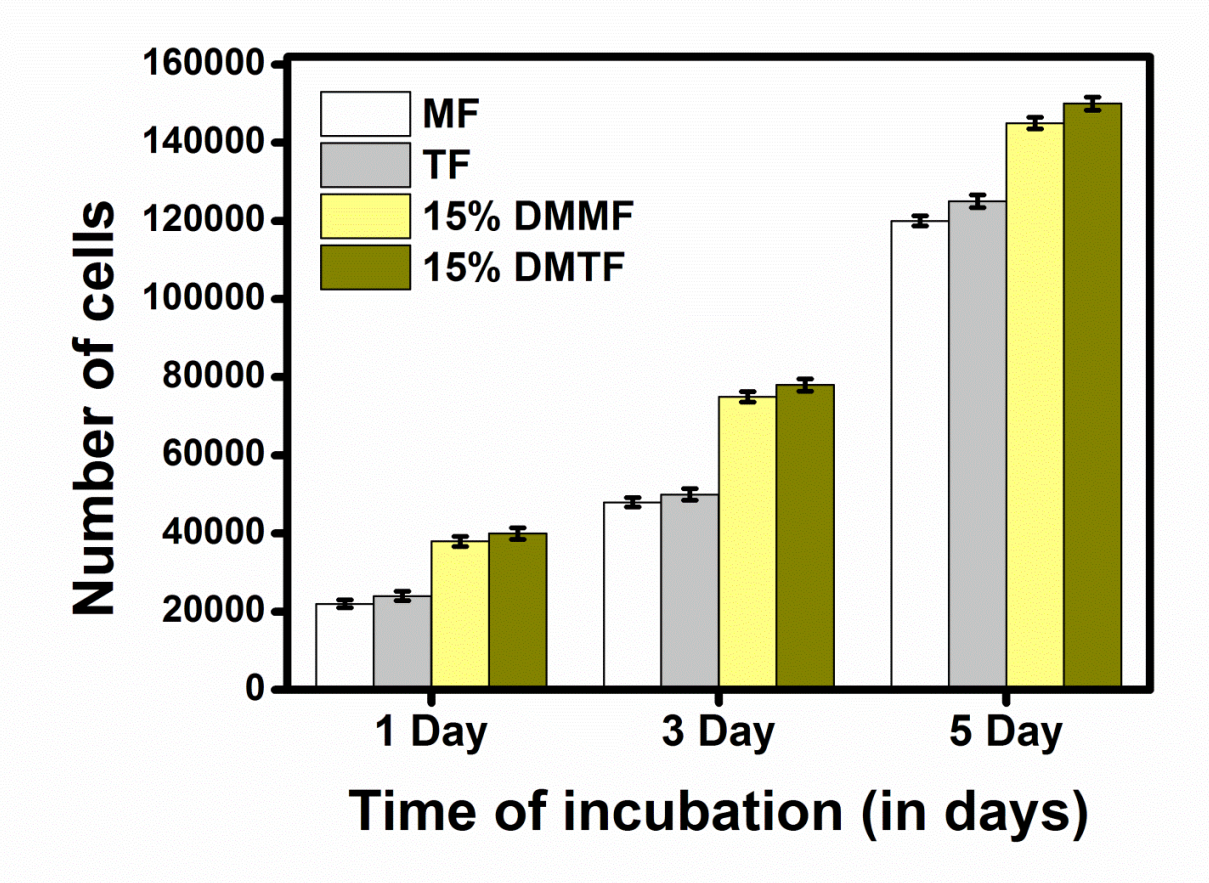


Fig. 9a

ACCEPTED

ACCEPTED MANUSCRIPT

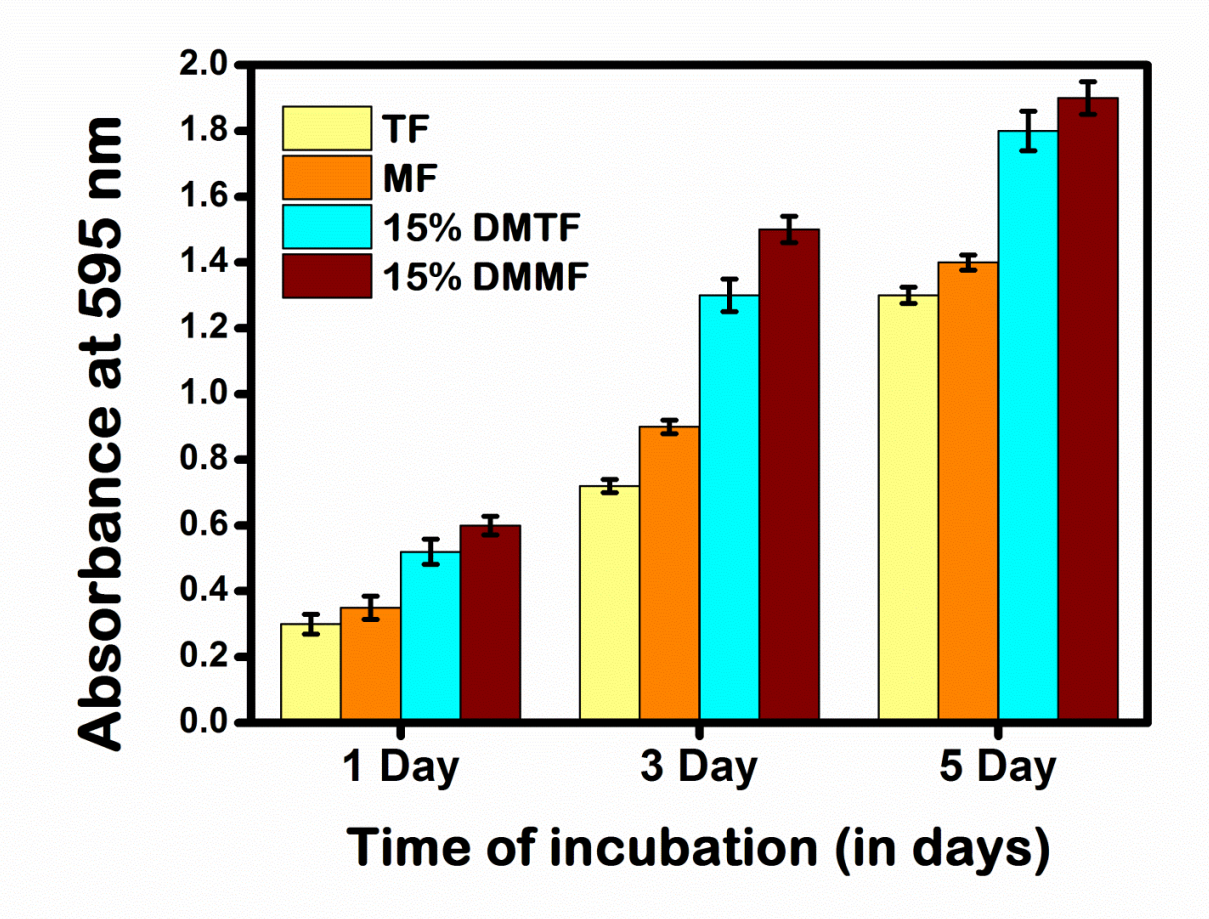


Fig. 9b

ACCEPTED

ACCEPTED MANUSCRIPT

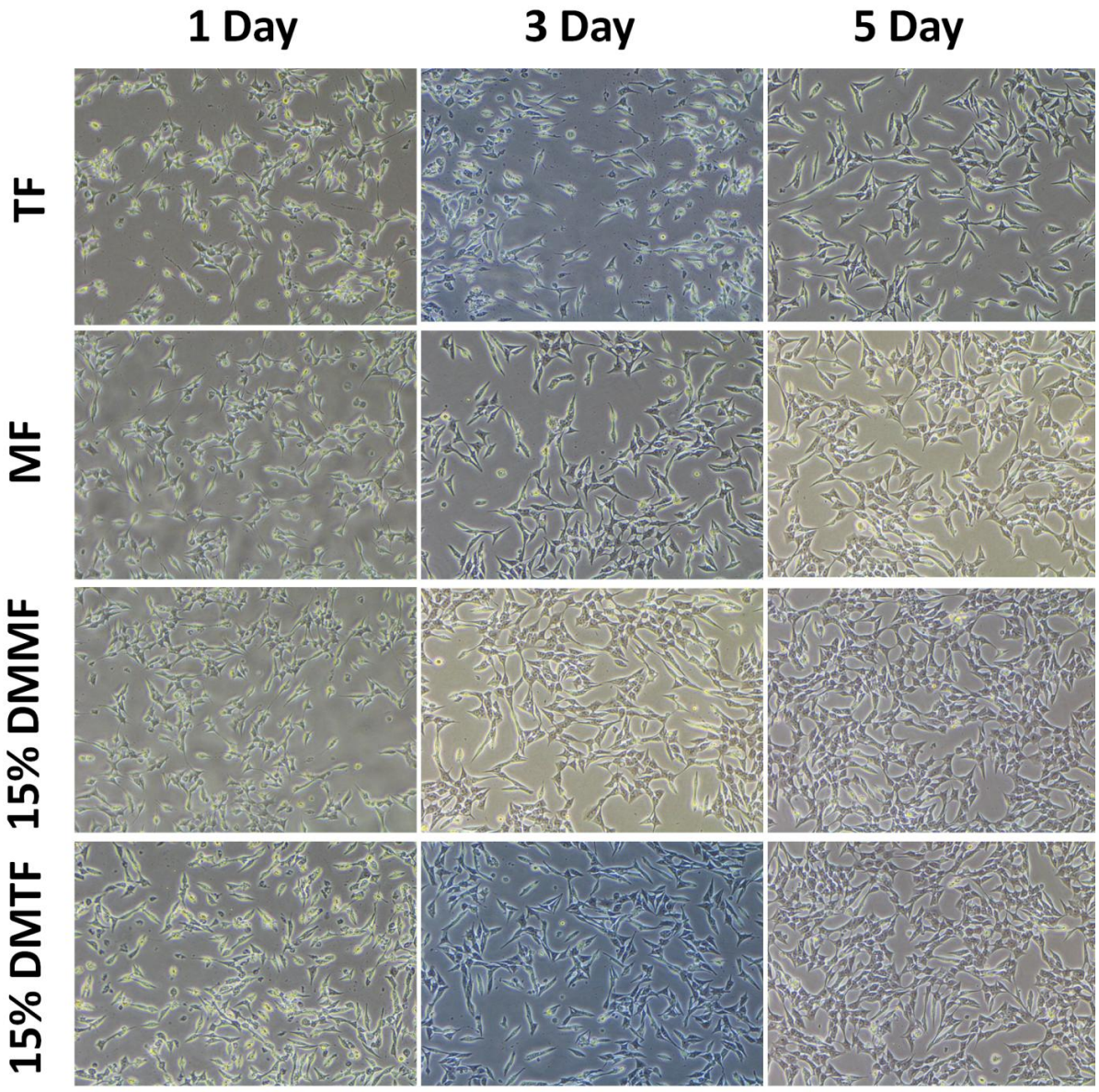


Fig. 9c

ACCEPTED MANUSCRIPT

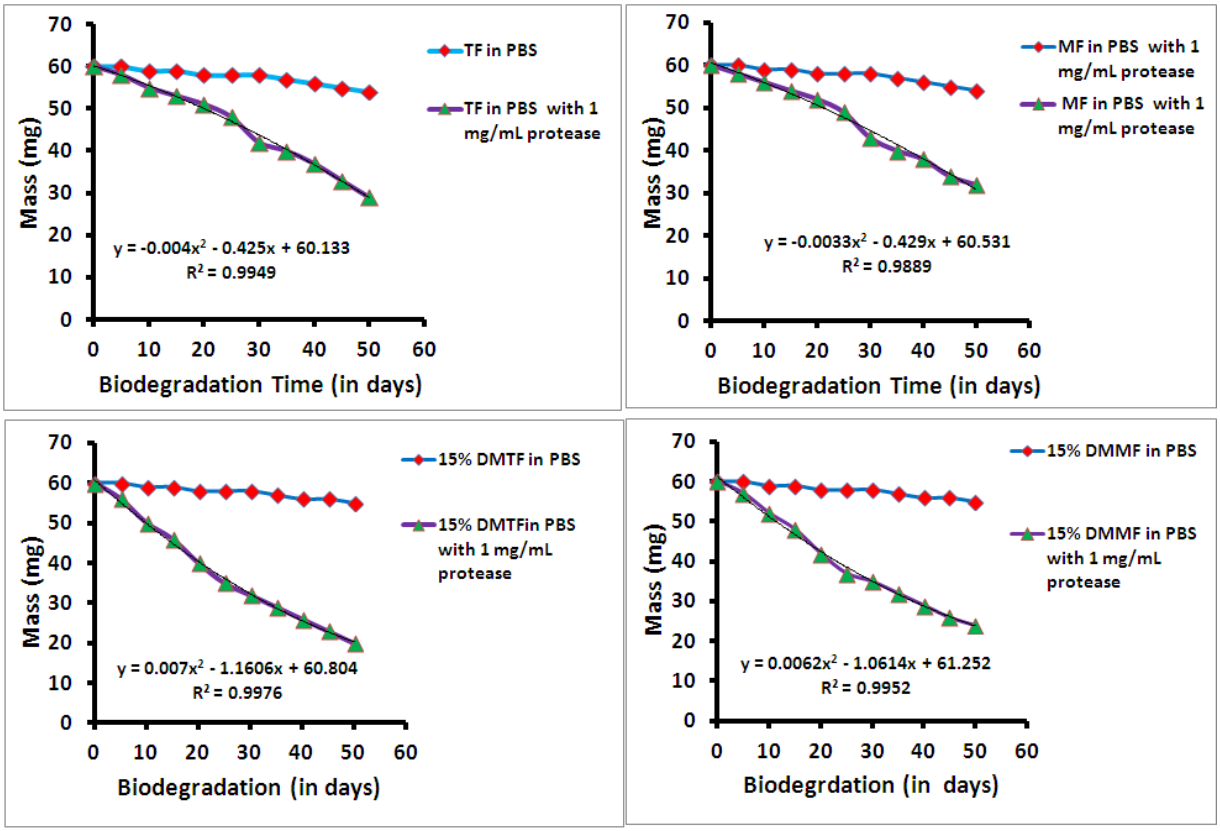


Fig. 10

ACCEPTED MANUSCRIPT

ACCEPTED MANUSCRIPT

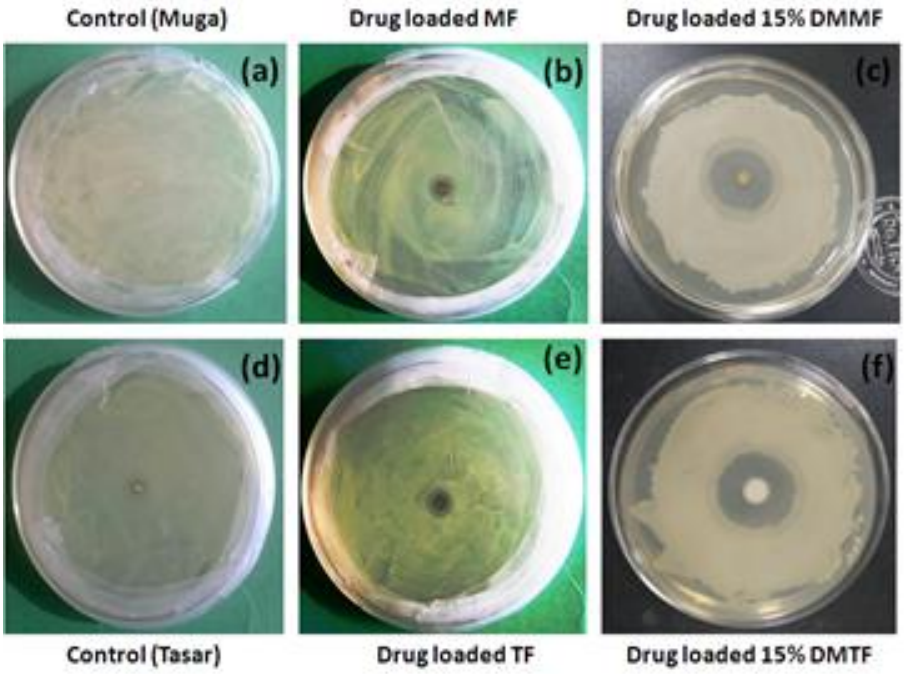


Fig. 11

ACCEPTED MANUSCRIPT

ACCEPTED MANUSCRIPT

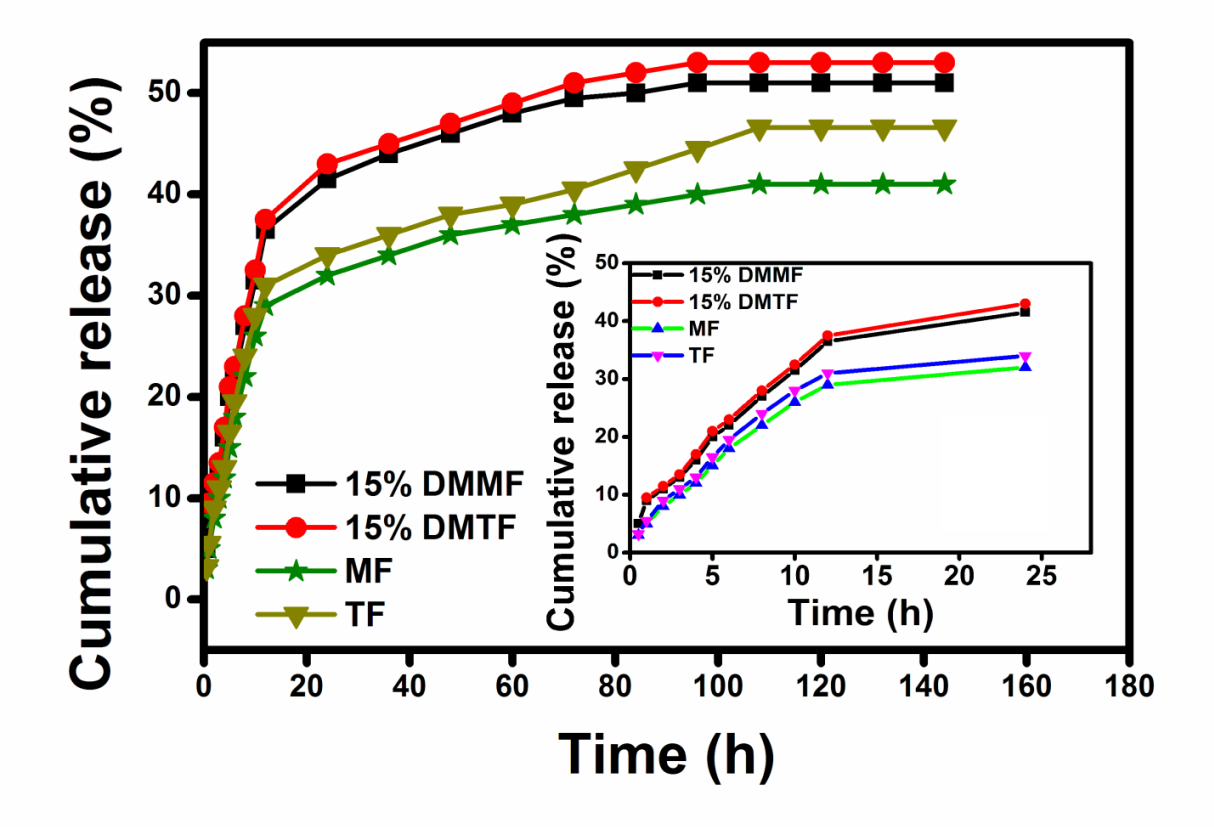


Fig. 12

ACCEPTED MANUSCRIPT

ACCEPTED MANUSCRIPT

Table 1: Mechanical properties of dextrose modified muga and tasar fibroin films, Data were represented as mean±SD for n=3

	Tensile Strength (MPa)	**Tensile Modulus (MPa)**	**Extension at Break (%)**
MF	2.8±0.3	24±2	12±1.7
5% DMMF	2±0.4	15±2.5	18±1.6
10% DMMF	2.5±0.25	13±1.5	21±1.5
15% DMMF	2.3±0.3	11±1.2	23±2.1
TF	3.2±0.32	30±1.6	7±2.4
5% DMTF	2.3±0.26	18±1.8	19±1.5
10% DMTF	2.7±0.28	14±2	25±2
15% DMTF	2±0.27	12±1	32±2.5

ACCEPTED MANUSCRIPT

ACCEPTED MANUSCRIPT

Table 2: Surface Roughness (Root Mean Square and Arithmetic Average) of dextrose plasticized and un-plasticized muga and tasar fibroin films

Samples	Rq (nm)	Ra(nm)
MF	1.08	0.83
15% DMMF	2.5	2.2
TF	1.19	1.2
15% DMTF	3.0	2.5

ACCEPTED MANUSCRIPT

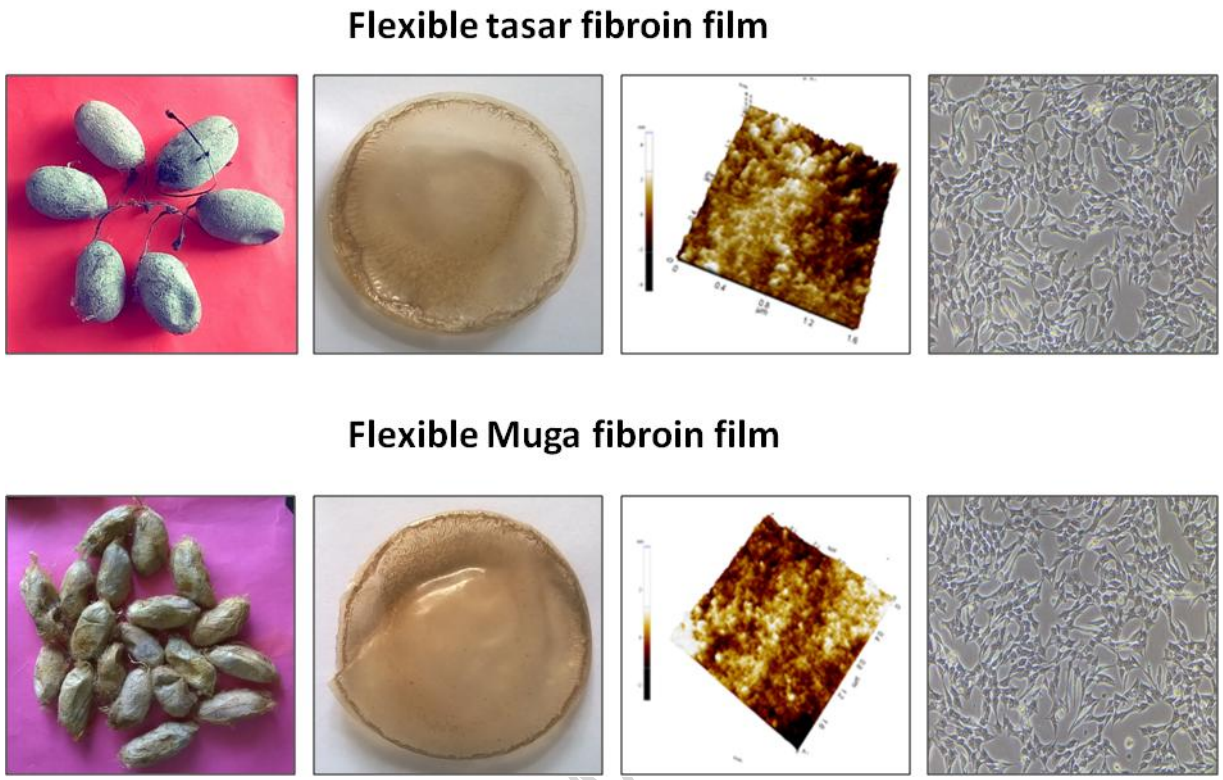
ACCEPTED MANUSCRIPT

Table 3: Kinetic data obtained by fitting the drug release data

	k	n	R^2
MF	0.19	0.68	0.98
TF	0.18	0.65	0.95
15% DMMF	30	0.51	0.97
15% DMTF	29	0.52	0.98

ACCEPTED MANUSCRIPT

ACCEPTED MANUSCRIPT



Graphical abstract

ACCEPTED MANUSCRIPT

ACCEPTED MANUSCRIPT

Highlights (for review):

- Cocoon extracted nonmulberry muga and tasar fibroin have successfully regenerated as flexible films using ionic liquid.
- Dextrose acts as plasticizer to generate flexibility in muga and tasar fibroin films.
- Flexible films show good mechanical integrity, water absorption, biocompatibility, antimicrobial activity and drug release over the un-plasticized films.
- These flexible films are found to be promising candidates for wound dressing.

ACCEPTED MANUSCRIPT

ResearchGate

See discussions, stats, and author profiles for this publication at: https://www.researchgate.net/publication/303684125

Effect of Different Carbon Sources and Elicitors on Shoot Multiplication in Accessions of Centella asiatica

Article · May 2016

DOI: 10.4172/2167-0412.1000251

CITATIONS
0

READS
9

5 authors, including:



Arpita Roy
Delhi Technological University
14 PUBLICATIONS **1** CITATION

SEE PROFILE

Some of the authors of this publication are also working on these related projects:



Estimation of phytosterols using gas chromatography and green synthesis of silver nano particles in Centell asiatica View project

All content following this page was uploaded by Arpita Roy on 29 August 2016.

The user has requested enhancement of the downloaded file. All in-text references underlined in blue are added to the original document and are linked to publications on ResearchGate, letting you access and read them immediately.

Medicinal & Aromatic Plants

Kundu et al., Med Aromat Plants 2016, 5:4
http://dx.doi.org/10.4172/2167-0412.1000251

Research Article Open Access

Effect of Different Carbon Sources and Elicitors on Shoot Multiplication in Accessions of *Centella asiatica*

Koyel Kundu, Arpita Roy, Gaurav Saxena, Lakhan Kumar and Navneeta Bharadvaja*

Plant Biotechnology Laboratory, Department of Biotechnology, Delhi Technological University, New Delhi, India

Abstract

Centella asiatica is a medicinal herb which has been extensively used in the treatment of nervous disorders and skin diseases. It is distributed throughout the tropical and sub-tropical region of the world. This plant contains various bioactive constituents such as asiaticoside, madecassic acid, flavonoids etc. *Centella* is in huge demand in International market for the preparation of pharmaceuticals and cosmetics which has resulted in its overexploitation. This situation demands the use of biotechnological methods to conserve as well as increase the production of biomass and bioactive compounds. The present study focused the use of different carbon sources (sucrose and fructose) and elicitors (Malt extract, Salicylic acid and Jasmonic acid) for the enhancement of biomass in five accessions of *Centella asiatica*. It was concluded that Murashige and Skoog (MS) medium supplemented with 1 mg/L concentration of Malt extract and 1.5 mg/L concentration of 6-Benzyl amino purine (BAP) showed highest biomass production among all elicitors. Among two carbon sources, MS media supplemented with Sucrose (3 mg/L) along with BAP (1.5 mg/L) showed better result than fructose.

Keywords: *Centella asiatica*; Carbon sources; Elicitors; Sucrose; Fructose; Malt extract; Salicylic acid; Jasmonic acid

Introduction

Centella asiatica is a perennial herb belonging to the family Apiaceae and found throughout tropical and sub-tropical regions of India. This plant is known by different names in different regions of India, Manimunni in Assam, Thankuni in Bengali, Vallari in Decan, Mandookaparni in Hindi and Gotukola in Sinhali [1]. It is a softly perfumed, creeping plant that attains height up to 15 cm. Stem is smooth and rooting occurs at the nodes. It grows extensively in marshy, damp and wet places and flowering occurs during April to June with white to purple or pink flowers. Fruits are approximately 2 inches long, globular in shape and strongly thickened pericarp [2]. This plant has been used since ancient days in Ayurvedic medicines. Use of this plant has been described in the ancient literature Charaka Chikitsa [3]. Whole plant is used for the preparation of drug and these drugs can be used internally or externally. Paste from fresh herbs can be used externally for the treatment of rheumatism and elephantitis. Leaf juice can be applied on forehead in case of headache. An ointment prepared from this plant can be used for the treatment of leprosy or any skin disorder [3]. One of the bioactive compound i.e., asiaticoside helps in collagen I synthesis in human [4]. Asiaticoside shows antitumor activity by apoptosis of cancer cells. This plant can also be used for the treatment of eczema. Internally, it can also be used for the treatment of various diseases such as bronchitis, asthma, gastric, leucorrhea, kidney disease, urethritis and dropsy [5]. *Centella asiatica* contain various types of bioactive compounds like Asiaticoside, Medacassoside, Brahmoside, Alkaloids (Hydrocotylin), triterpene glycoside, Triterpene acid, Anthrone of Asiaticoside, Asiatic acid, Madegascaric or madecassic acid Isothankuniside, Brahmic acid, Centelloside, Centic acid, Indocentoic acid, Indocentelloside, Oligosaccharide, etc. [6,7]. The plant also contains volatile and fatty oils. Glycosides of palmitic, stearic, oleic and linolenic acids are present in fatty oils.

Due to great medicinal importance of *Centella asiatica* in the preparation of different pharmaceutical compounds, this plant has been overexploited and marked as threatened plant species by the International Union for Conservation of Nature and Natural Resources (IUCN), and also as an endangered plant species [8,9]. Thus conservation of this plant is need of the hour. Biotechnological methods not only help in the conservation of endangered plants but also help in the enhancement of biomass and commercially important plant products.

Mass propagation of plants through *in vitro* micro propagation is the most successful commercial application of plant tissue culture technique. *In vitro* propagation may provide a potential solution for cloning of plant and secondary metabolite production. Application of elicitors is one of the most important method to increase the production of secondary metabolites in plants. Elicitors are the molecule that enhances the secondary metabolite production under stress [10]. In plant tissue culture, plants are grown under stress condition but the plant genome has the defense mechanism to protect the plant via some secondary metabolite production. Elicitors are the signal compound of plant defense mechanism [11]. It was reported that elicitors enhance bioaccumulation of asiaticoside in *C. asiatica* [12]. Sugars also have important role in metabolic activity [13] as they enhance the formation of auxiliary buds and branching of adventitious roots [14]. But the above mentioned effects are not universal and depend on the geographical conditions of plant to a great extent. Plant of same species is collected from different locations and is assigned an accession number. Accessions differ in their growth pattern and secondary metabolite content. Therefore the present study was undertaken to determine the effect of different carbon sources like sucrose and fructose and different elicitors, like Malt extract (ME), Salicylic acid (SA), Jasmonic acid (JA) on growth of five different accession of *Centella asiatica* and to assess the response of different accession to variable conditions of carbon sources and elicitors.

***Corresponding author:** Navneeta Bharadvaja, Plant Biotechnology Laboratory, Department of Biotechnology, Delhi Technological University, New Delhi-110 042, India, Tel: 9198684466137; E-mail: navneetab@dtu.co.in

Received April 19, 2016; **Accepted** May 20, 2016; **Published** May 23, 2016

Citation: Kundu K, Roy A, Saxena G, Kumar L, Bharadvaja N (2016) Effect of Different Carbon Sources and Elicitors on Shoot Multiplication in Accessions of *Centella asiatica*. Med Aromat Plants 5: 251. doi:10.4172/2167-0412.1000251

Copyright: © 2016 Kundu K, et al. This is an open-access article distributed under the terms of the Creative Commons Attribution License, which permits unrestricted use, distribution, and reproduction in any medium, provided the original author and source are credited.

Materials and Methods

Cultures of five different accessions i.e., 281374, 383913, 342109, 347492, 331514 of *C. asiatica* were collected from NBPGR New Delhi, India. To study the effect of carbon source and elicitors on shoot multiplication MS media was used. Murashige and Skoog (MS) [15] media was prepared and pH was adjusted to 5.8 using 1 N HCl or 1 N NaOH solution. 0.8% plant agar was used to solidify the media. Sterilization of the media was done by autoclaving for 20 min at 121°C and 15 lb pressure. For experiment on elicitors and carbon sources, MS media was supplemented with 1.5 mg/L 6- Benzyl amino purine along with different elicitors {Malt extract (1 mg/L), Salicylic acid (1 mg/L), Jasmonic acid (1 mg/L)} and different carbon sources {Sucrose (3%) and fructose (3%)} separately. After the solidification of media, sterile shoot nodes from each accession were inoculated in culture tubes (25 × 150 mm) separately. The cultures were incubated at 26 ± 2°C under 16 h photoperiod and light intensity of 3000 lux for four weeks. Each and every experiment was done in triplicates. Visual data was recorded after 4th week of inoculation in terms of number of shoots and length of shoots for *in vitro* growth measurement.

Data analysis

Observations were recorded and are presented as means ± standard deviation of 3 biological replicates to estimate the variability between the accessions.

Results and Discussion

Effect of carbon source and elicitors on shoot regeneration was observed in five accessions of *Centella asiatica*. Observation was recorded as mean value of triplicate samples after four weeks of inoculation (Tables 1 and 2). Among the elicitors used, MS media supplemented with malt extract (1 mg/ltr) showed maximum number and maximum length of shoots (Figure 1). Maximum effect of malt extract was found on accession no. 281374 as maximum number of shoots i.e., 25 were reported in this accession followed by 342109 (16), 331514 (15), 347492 (14) and 383913 (10). Maximum average length was reported in accession number 347492 (3.07) followed by 281374 (2.35), 342109 (1.69), 331514 (1.75), 383913 (1.5).

Two different carbohydrate sources i.e., sucrose and fructose were tested for their potential on shoot regeneration in five different accession of *Centella asiatica* and it was found that sucrose showed better shoot growth than fructose in different accession of *Centella asiatica* (Figure 2). Maximum number of shoots generation was recorded in MS media supplemented with Sucrose (3%). In case of sucrose as carbon source, maximum number of shoots was reported in accession number 347492 (16) followed by 331514 (10), 281374 (8), 342109 (5) and 383913 (3). Maximum average length was reported in accession number 347492 (1.66).

Order of other accession's average length of shoots in sucrose experiment is 281374 (1.5) and 331514 (1.5), 342109 (0.75),

S No	Accession Number	Treatment	No. of shoots (M ± SE)	Length of shoot (cm.) (M ± SE)
1	Accession No. 281374	MS+BAP (1.5 mg/ltr)+ME (1 mg/ltr)	25 ± 1.52	2.35 ± 0.12
		MS+BAP (1.5 mg/ltr)+SA (1 mg/ltr)	4 ± 1.15	1 ± 0.08
		MS+BAP (1.5 mg/ltr)+JA (1 mg/ltr)	2 ± 1	0.75 ± 0.12
2	Accession No. 383913	MS+BAP (1.5 mg/ltr)+ME (1 mg/ltr)	10 ± 0.57	1.3 ± 0.05
		MS+BAP (1.5 mg/ltr)+SA (1 mg/ltr)	1 ± 0.33	1.5 ± 0.12
		MS+BAP (1.5 mg/ltr)+JA (1 mg/ltr)	1 ± 0	0.5 ± 0.05
3	Accession No. 342109	MS+BAP (1.5 mg/ltr)+ME (1 mg/ltr)	16 ± 3.46	1.69 ± 0.09
		MS+BAP (1.5 mg/ltr)+SA (1 mg/ltr)	1 ± 0	2.5 ± 0.28
		MS+BAP (1.5 mg/ltr)+JA (1 mg/ltr)	2 ± 0.57	0.75 ± 0.07
4	Accession No. 347492	MS+BAP (1.5 mg/ltr)+ME (1 mg/ltr)	14 ± 1.15	3.07 ± 0.12
		MS+BAP (1.5 mg/ltr)+SA (1 mg/ltr)	5 ± 1.15	0.9 ± 0.10
		MS+BAP (1.5 mg/ltr)+JA (1 mg/ltr)	5 ± 1.52	0.52 ± 0.03
5	Accession No. 331514	MS+BAP (1.5 mg/ltr)+ME (1 mg/ltr)	15 ± 1.15	1.43 ± 0.07
		MS+BAP (1.5 mg/ltr)+SA (1 mg/ltr)	8 ± 2	1.75 ± 0.07
		MS+BAP (1.5 mg/ltr)+JA (1 mg/ltr)	12 ± 2.88	1.66 ± 0.07

Table 1: Effect of different elicitors on number and length of regenerated shoots in five different accession of *Centella asiatica* after four weeks of inoculation. Values are expressed as mean ± Standard Error (M ± SE). MS: Murashige and Skoog medium; BAP: 6-Benzyl amino purine; ME: Malt Extract; SA: Salicylic acid; JA: Jasmonic acid.

S No	Accession Number	Treatment	No. of shoots (M ± SE)	Length of shoot (cm) (M ± SE)
1	Accession No. 281374	MS+Sucrose+BAP (1.5 mg/ltr)	8 ± 1.15	1 ± 0.06
		MS+Fructose+BAP (1.5 mg/ltr)	2 ± 0.57	1.5 ± 0.16
2	Accession No. 383913	MS+Sucrose+BAP (1.5 mg/ltr)	3 ± 0.57	0.27 ± 0.04
		MS+Fructose+BAP (1.5 mg/ltr)	2 ± 0.57	0.75 ± 0.08
3	Accession No. 342109	MS+Sucrose+BAP (1.5 mg/ltr)	5 ± 1.2	0.52 ± 0.02
		MS+Fructose+BAP (1.5 mg/ltr)	2 ± 0.57	0.75 ± 0.10
4	Accession No. 347492	MS+Sucrose+BAP (1.5 mg/ltr)	16 ± 3.05	1.66 ± 0.15
		MS+Fructose+BAP (1.5 mg/ltr)	5 ± 0.57	0.7 ± 0.05
5	Accession No. 331514	MS+Sucrose+BAP (1.5 mg/ltr)	10 ± 1.15	1.5 ± 0.08
		MS+Fructose+BAP (1.5 mg/ltr)	3 ± 0.57	1 ± 0.09

Table 2: Effect of different carbon sources on number and length of regenerated shoots in five different accession of *Centella asiatica* after four weeks of inoculation. Values are expressed as mean ± Standard Error (M ± SE). MS: Murashige and Skoog medium; BAP: 6-Benzyl amino purine.

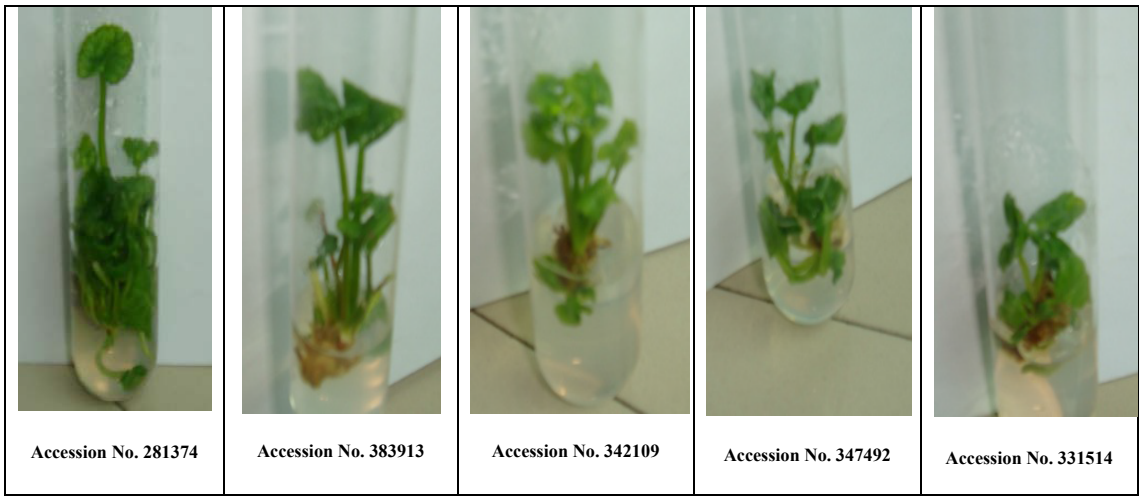


Figure 1: *In vitro* culture of five different accession of *Centella asiatica* in malt extract (After four weeks of inoculation).

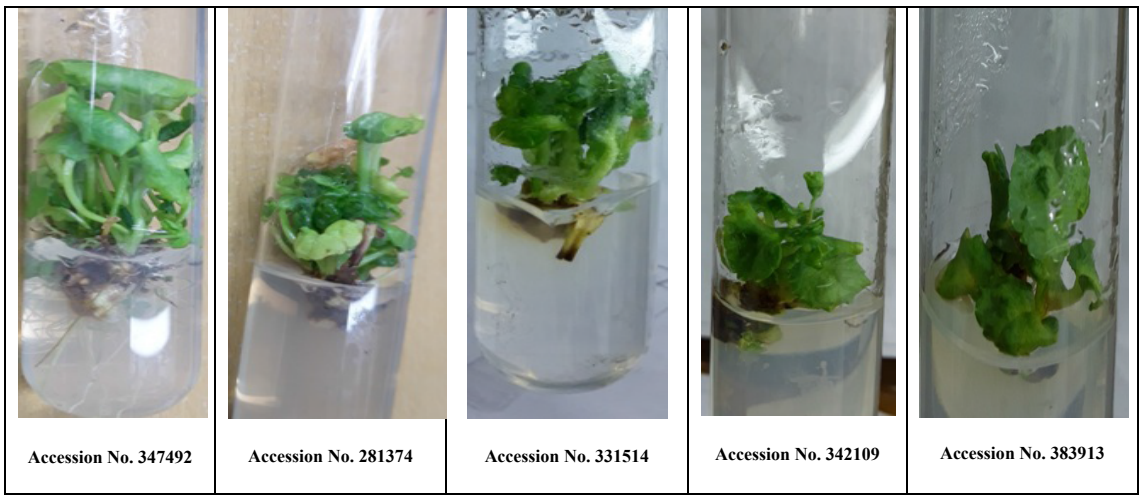


Figure 2: *In vitro* culture of five different accession of *Centella asiatica* in sucrose (After four weeks of inoculation).

383913(0.75). These parameters can be used for maximum production of biomass and bioactive compounds. Focus can be drawn on high yielding accessions for secondary metabolite production. Hossain et al. [16] also reported similar results in *C. asiatica*. They concluded that sucrose showed best results as it helped in the production of maximum shoot length in presence of BA and Kinetin.

Conclusion

From the above study, it can be concluded that different carbon sources and elicitors have significant effect on the shoot formation of *Centella asiatica* as they have the capacity to enhance shoot multiplication as well as shoot length which ultimately increases the growth of the plant. Among the carbon source, sucrose showed better capability to enhance the growth of *Centella asiatica* than fructose. Accession no. 347492 showed maximum number of shoots in MS media containing sucrose. Malt extract showed the highest number of shoots generation among the other elicitors used. Accession no. 281374 showed maximum number of shoots regeneration in MS media containing Malt extract. Shoot proliferation can be used for production of important bioactive compound of this plant i.e., asiaticoside. This study not only finalized the appropriate elicitors and carbon source but also the high yielding accession of *Centella asiatica*. Further study will include the quantitative and qualitative analysis of various secondary metabolites like saponins, terpenoids, and alkaloids extracted from *Centella asiatica*.

Acknowledgements

The authors are grateful to the Department of Biotechnology, Delhi Technological University, Delhi for extending all the laboratory facilities towards successful completion of this investigation and National Bureau of Plant Genetic Resources for providing the plant materials.

References

1. Jamil SS, Nizami Q, Salam M (2007) *Centella asiatica* (Linn.) Urban A Review. Natural Product Radiance 6: 58-170.
2. Tripathi G, Mishra S, Upadhyay P, Purohit S, Dubey GP (2015) Ethno pharmacological importance of *Centella asiatica* with special reference to neuroprotective activity. Asian Journal of Pharmacology and Toxicology 3: 49-53.
3. Bhavna D, Jyoti K (2011) *Centella asiatica*: The elixir of life. International Journal of Research in Ayurveda & Pharmacy 2: 431-438.

4. Bonte F, Dumas M, Chaudagne C, Maybeck A (1994) Influence of asiatic acid, madecassic acid and asiaticoside on human collagen I synthesis. Planta Med 60: 133-135.
5. Evans WC (2002) Saponin, cardioactive drugs and other sterols. Pharmacognosy, Saunders 15: 303-304.
6. Gohil KJ, Patel JA, Gajjar AK (2010) Pharmacological review on *Centella asiatica*: A potential herbal cure-all. Indian J Pharm Sci 72: 546-556.
7. Das KM, Kumar B (2012) Ancient and pharmacological review on *Centella asiatica* (Mandukparni): A potential herbal panacea. International Journal of Research and Reviews in Pharmacy & Applied Science 2: 1062-1072.
8. Singh HG (1989) Himalayan herbs and drugs, importance and extinction threat. Journal of Medicinal Plants Research 10: 47-52.
9. Pandey NK, Tewari KC, Tewari RN, Joshi GC, Pande VN, et al. (1993) Medicinal plants of kumaon Himalaya. In: Dhar U (ed). Strategies for conservation of Himalayas, Himavikas Publication, Nanital, India 3: 293-302.
10. Zhao J, Davis LC, Verpoorte R (2005) Elicitor signal transduction leading to production of plant secondary metabolites. Biotechnol Adv 23: 283-333.
11. Patel H, Krishnamurthy R (2013) Elicitors in plant tissue culture. Journal of Pharmacognosy and Phytochemistry 2: 60-65.
12. Loc NH, Giang NT (2012) Effects of elicitors on the enhancement of asiaticoside biosynthesis in cell cultures of Centella (*Centella asiatica* L. Urban). Chemical papers 66: 642-648.
13. Panathula CS, Mahadev MD, Naidu CV (2014) Effect of different carbohydrates on *in vitro* plant regeneration of *Centella asiatica* (L.), an important antijaundice medicinal plant. International Journal of Medicinal and Aeromatic Plants 4: 41-47.
14. Saad AIM, Elshahed AM (2012) Plant tissue culture media, Recent advances in plant *in vitro* culture. Chapter 2. In Tech Publisher (Online book).
15. Murashige T, Skoog F (1962) A revised medium for rapid growth and bioassays with tobacco tissue cultures. Physiologia Plantarum 15: 473-497.
16. Hossain A, Hossain T, Ali R, Rahman M (2005) Effect of different carbon sources on in vitro regeneration of Indian Pennywort (*Centella asiatica* L.). Pakistan Journal of Biological Science 8: 963-965.

Citation: Kundu K, Roy A, Saxena G, Kumar L, Bharadvaja N (2016) Effect of Different Carbon Sources and Elicitors on Shoot Multiplication in Accessions of *Centella asiatica*. Med Aromat Plants 5: 251. doi:10.4172/2167-0412.1000251

OMICS International: Publication Benefits & Features

Unique features:

- Increased global visibility of articles through worldwide distribution and indexing
- Showcasing recent research output in a timely and updated manner
- Special issues on the current trends of scientific research

Special features:

- 700+ Open Access Journals
- 50,000+ Editorial team
- Rapid review process
- Quality and quick editorial, review and publication processing
- Indexing at major indexing services
- Sharing Option: Social Networking Enabled
- Authors, Reviewers and Editors rewarded with online Scientific Credits
- Better discount for your subsequent articles

Submit your manuscript at: http://www.omicsonline.org/submission

View publication stats

International Conference on Advanced Material Technologies (ICAMT)-2016

27th and 28th December 2016

Dadi Institute of Engineering and Technology (DIET), Visakhapatnam, Andhra Pradesh, India.

Effect of Ratio of Visco-Elastic Material Viscosity to Fluid Viscosity on Stability of Flexible Pipe Flow

S. ANBUKUMAR[1] AND MUNENDRA KUMAR[2]

[1] and [2] Assistant Professor, Civil Engineering Department, Delhi Technological University (DTU), Delhi -110042,

Email: anbukumars@yahoo.com

Abstract: In the present study, a flexible pipe has been considered to study the effect of ratio of visco-elastic material viscosity to fluid viscosity on the stability of flexible laminar pipe flow with axi-symmetric disturbances. The effect of thickness of visco-elastic material on the stability of flexible pipe flow with outer rigid shroud has also been studied. The stability curves are drawn for various values of the ratio of visco-elastic material viscosity to fluid viscosity. It is observed that stability of flow is increasing by decreasing the ratio of visco-elastic material viscosity to fluid viscosity.

Keywords: Viscosity, stability, flexible pipe flow, laminar flow, rigid shroud.

1. INTRODUCTION

Flexible pipe flow is normally seen in nature such as human body, industrial applications for reactors and membranes. Two types of flexible pipe flow are found in nature. First type is one in which shape and size of pipe is changed due to internal pressure of the fluid. Second type is the one in which shape and size are not deforming, which means pressure gradient is constant along the direction of flow.

Kramer's [1] - [4] studied the flow over flexible surface on a flat plate and it was found that flexibility of flat surface delay the transition and drag is reduced that means flow remains laminar for a longer period. Carpenter [5], [6], Davies, Carpenter and Lucey [7], [8] also obtained the same result.

Reynolds [9] performed the experiment in rigid circular pipe and classified the flow as laminar, transition and turbulent based on the Reynolds number. Davey and Drazin [10] shown by numerical analysis that flow is stable to very small disturbances at all Reynolds number R and axial wavenumbers α. Rouleau and Garg [11] and Grosch and Salwen [12] have also confirmed this result by numerical studies. Salwen and Grosch [12] showed that center line modes (waves) are more unstable as compared to wall modes. Venkateswarlu et.al [13] have studied that non-linear terms increased the instability of pipe flow.

Hamadiche and Gad-el-Hak [14] also studied the flexible tube flow with 2-Dimension and 3-Dimemnsion disturbances problems. They found that flexible tube is unstable at all Reynolds number R and all axial wavenumbers α.which indicates flexible tube is unstable at very small, medium and higher Reynolds number R and all axial wavenumbers α. In the present study considered a non-collapsible pipe flow problem. The flows have been chosen in such a way that the interface of the visco-elastic material and the fluid is getting deformed in the normal (N) as well as on the tangential (T) direction to flow and hence such a flow is defined by (N+T).

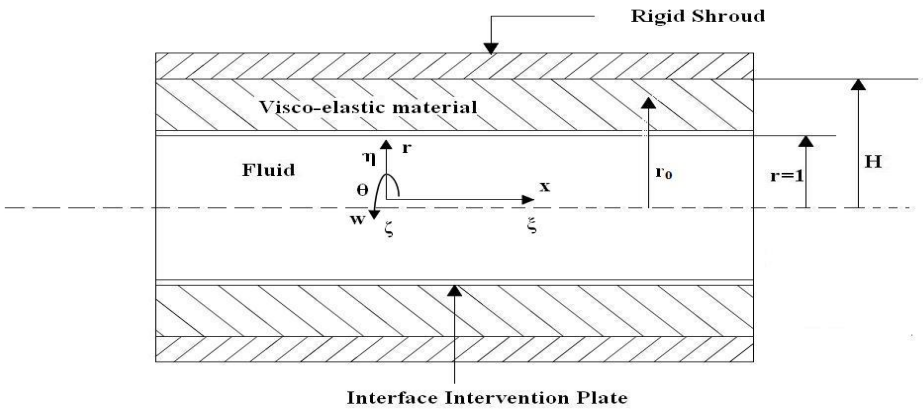


Figure 1: *Model of the visco-elastic pipe problem.*

2. FORMULATION

2.1 The fluid-side disturbance equations

Here, the laminar flow through circular flexible pipe for linear stability is considered as given in figure-1. The outer side of the pipe is considered as rigid surface. Figure 1 shows the two dimensional flexible pipe flow. The u and v are the velocity along axial x-axis and radial r-axis. The laminar average velocity can be written as $\bar{u} = 1 - r^2$. Reynolds number $R = Vr_o^*/\nu$, where V is maximum center line velocity and ν is the kinematic fluid viscosity.

The $\hat{\eta}$ and $\hat{\xi}$ are the deformation of flexible material along *r*-direction and x -direction and $\hat{p}_s$ is the pressure in the visco-elastic material. All details of mathematical terms are given in figure-1.

In this paper, the stability is studied for flexible laminar pipe flow and outer surface of pipe is considered as rigid. The Fourier waves (modes) are inserted into pipe as a disturbance as given below:

$$(\hat{u}, \hat{v}, \hat{p}) = [u(r), v(r), p(r)]\, e^{i\alpha(x-ct)} \tag{1}$$

Here the disturbance velocity is given by $c = c_r + ic_i$

The Navier Stokes and continuity equations may be expressed as follows:

x-momentum:

$$i\alpha(\bar{u} - c)u + \bar{u}'v = -i\alpha\, p + \frac{1}{R}\left[u'' + \frac{u'}{r} - (\alpha^2)u\right], \tag{2}$$

y-momentum:

$$i\alpha(\bar{u} - c)v = -p' + \frac{1}{R}\left[v'' + \frac{v'}{r} - \left(\alpha^2 + \frac{1}{r^2}\right)v\right], \tag{3}$$

*Continuity***:**

$$i\alpha u + v' + \frac{v}{r} = 0. \tag{4}$$

Here prime $(')$ represent the differentiation with r.

The Fourier waves are inserted into the linearized Navier-Stokes and continuity equations (2-4). After doing some mathematical exercise, the 4th order differential equation in terms of *v* for axi-symmetric disturbances (2-D waves) in the fluid-side is obtained as follows:

$$v'''' + \frac{2}{r}v''' - [\frac{3}{r^2} + 2\alpha^2 + i\alpha R(\bar{u} - c)]v'' + [\frac{3}{r^3} - \frac{2\alpha^2}{r} - \frac{i\alpha R}{r}(\bar{u} - c)]v' + [-\frac{3}{r^4} + \frac{2\alpha^2}{r^2} + \alpha^4 + (\alpha^2 + \frac{1}{r^2})i\alpha R(\bar{u} - c)]v = 0.$$

(5)

2.2 The flexible material equations

The Navier and continuity equations for displacements in the flexible materials may be expressed as follows:

ξ - Displacement:

$$\frac{\partial^2\hat{\xi}}{\partial t^2} = -\frac{\partial \hat{p}_s}{\partial x} + \frac{\hat{K}}{R}\left[\frac{\partial^2\hat{\xi}}{\partial x^2} + \frac{\partial^2\hat{\xi}}{\partial r^2} + \frac{1}{r}\frac{\partial\hat{\xi}}{\partial r} + \frac{1}{r^2}\frac{\partial^2\hat{\xi}}{\partial\theta^2}\right], \tag{6}$$

η - Displacement:

$$\frac{\partial^2\hat{\eta}}{\partial t^2} = -\frac{\partial \hat{p}_s}{\partial r} + \frac{\hat{K}}{R}\left[\frac{\partial^2\hat{\eta}}{\partial x^2} + \frac{\partial^2\hat{\eta}}{\partial r^2} + \frac{1}{r}\frac{\partial\hat{\eta}}{\partial r} + \frac{1}{r^2}\frac{\partial^2\hat{\eta}}{\partial\theta^2} - \frac{\hat{\eta}}{r^2}\right], \tag{7}$$

Continuity:

$$\frac{\partial\hat{\xi}}{\partial x} + \frac{\partial\hat{\eta}}{\partial r} + \frac{\hat{\eta}}{r} = 0 \tag{8}$$

Where, $\hat{K}$ is the flexible term and is given as $\hat{K} = \hat{K}_r + i\hat{K}_i$

$\hat{K} = \tilde{K} + \mu_r \frac{\partial}{\partial t}$ or (9)

$$\frac{\hat{K}}{R} = \frac{\tilde{K}}{R} + \frac{\mu_r}{R}\frac{\partial}{\partial t}\,. \tag{10}$$

Kumaran (1995) gave a flexible parameter Γ as $\Gamma = \sqrt{\rho V^2/G}$, where G is shear modulus of flexible material. The $\hat{K}$ is given by Kumaran as

$$\frac{\hat{K}}{R} = \frac{1}{\Gamma^2} + \frac{\mu_r}{R}\frac{\partial}{\partial t} \quad \text{and} \quad \frac{\tilde{K}}{R} = \frac{1}{\Gamma^2}. \tag{11}$$

For the visco-elastic material and fluid sides. Introducing $\frac{\partial}{\partial t} \to -i\alpha c$, we have $\hat{K} \to K$, where

$K = K_r + iK_i$ as follows: (12a)

$$K_r = \frac{R}{\Gamma^2} + \alpha\mu_r c_i = \tilde{K} + \alpha\mu_r c_i \;; \quad K_i = -\alpha\mu_r c_r \tag{12 b}$$

The flexible material deformations may written as follows: $(\hat{\xi}, \hat{\eta}, \hat{p}_s) = [\xi(r), \eta(r), p_s]\ \exp[i\{\alpha(x - ct)\}]$ (13)

The following differential equation for the visco-elastic material can be obtained in terms of η displacement as follows:

$$\eta''' + \frac{2}{r}\eta'' - \left[\frac{3}{r^2} + 2\alpha^2 - \alpha^2c^2\frac{R}{K}\right]\eta'' + \left[\frac{3}{r^3} - \frac{2\alpha^2}{r} + \frac{1}{r}\alpha^2c^2\frac{R}{K}\right]\eta' + \left[-\frac{3}{r^4} + \frac{2\alpha^2}{r^2} + \alpha^4 - (\alpha^2 + \frac{1}{r^2})\alpha^2c^2\frac{R}{K}\right]\eta = 0. \tag{14}$$

2.3 Boundary conditions for visco-elastic and fluid sides

The boundary conditions for combined fluid-solid problem for axisymmetric case, *n* = 0, are given as below:

Pipe center at, $r = 0$:

$$u'(0) = 0, \quad v(0) = 0. \tag{15}$$

Surface of the pipe

At the surface of the visco-elastic pipe, viz. at r = *H*:

$$\xi(H) = 0, \quad \eta(H) = 0\,. \tag{16}$$

2.4 Interface between the fluid and the visco-elastic material

The boundary conditions at the interface between the solid and the fluid-sides may be written as below: The continuity of velocities, linearised with respect to *r* = 1, is given as follows:

$$\frac{\partial \hat{\xi}}{\partial t} = \hat{u} + \hat{\eta}_w \bar{u}'_w, \quad \frac{\partial \hat{\eta}}{\partial t} = \hat{v}; \tag{17a, b}$$

Particularly, eq. (22a) is the tangential no-slip boundary condition. The above interface velocities can also be written as follows:

$$-i\alpha c\xi_w = u_w + \eta_w \bar{u}'_w, \qquad -i\alpha c\eta_w = v_w \tag{18a, b}$$

The expressions for the stresses from the fluid-side and solid-side are given as below, where generically τ represents to the fluid-side stresses and σ represents to the *visco-elastic material* -side stresses.

Fluid-side:

$$\hat{\tau}_{rr} = -\hat{p} + \frac{2}{R}\left[\frac{\partial \hat{v}}{\partial r}\right] \quad \text{or} \quad \tau_{rr} = -p + \frac{2}{R}[v'], \tag{19a, b}$$

$$\hat{\tau}_{rx} = \frac{1}{R}\left[\frac{\partial \hat{v}}{\partial x} + \frac{\partial \hat{u}}{\partial r}\right] \quad \text{or} \quad \tau_{rx} = \frac{1}{R}[i\alpha v + u'], \tag{20a, b}$$

Solid-side:

$$\hat{\sigma}_{rr} = -\hat{p}_s + \frac{2\hat{K}}{R}\left[\frac{\partial \hat{\eta}}{\partial r}\right] \quad \text{or} \quad \sigma_{rr} = -p_s + \frac{2K}{R}[\eta'], \tag{21a, b}$$

$$\hat{\sigma}_{rx} = \frac{\hat{K}}{R}\left[\frac{\partial \hat{\eta}}{\partial x} + \frac{\partial \hat{\xi}}{\partial r}\right] \quad \text{or} \quad \sigma_{rx} = \frac{K}{R}[i\alpha\eta + \xi'], \tag{22a, b}$$

The stress matching conditions respectively for the normal and axial directions, are given as $\sigma_{rr} = \tau_{rr}$ and $\sigma_{rx} = \tau_{rx}$

3. NUMERICAL METHODS

The above differential equations can be solved by using the basic concept of the finite difference techniques. The differential equations can be written for the Fourier modes in the matrix forms as follows:

$$[A_{IJ}][\Gamma_J] = [P_I], I, J = 1, 2, 3, 4, ..(2N+2),$$

Here, N is the number of intervals for above matrix. The above matrix can be solved for visco-elastic material side and fluid-side by using the finite difference method. The numerical equation for the fluid side and visco-elastic side are solved by using the FORTRAN programming and these programs are compiled by the Fortran Lahey Fitjtsu.

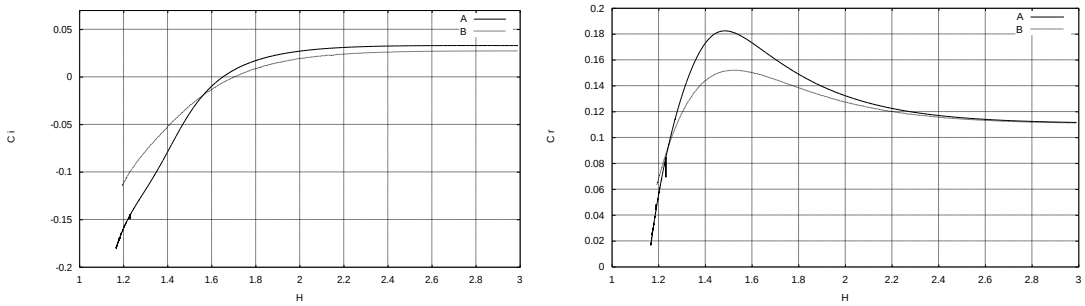
4. RESULTS

In present paper, stability curves are drawn for the effect of ratio of visco-elastic material viscosity to fluid viscosity ($\mu_r = \mu_s / \mu_f$) for normal plus tangential (N+T) motion of interface of the fluid and visco-elastic material. Here, it has been considered two types of modes (waves) for the analysis of stability problem. One mode is unstable at very low Reynolds numbers and defined it as M1 types modes. Other mode is unstable at intermediate and higher Reynolds numbers and referred it as M2 types of modes. Further discussion, it has been referred these modes as M1 and M2 modes. The effect of ratio of visco-elastic material viscosity to fluid viscosity on the thickness of visco-elastic wall has also observed. Stability of flexible pipe flow depends upon the damping of the modes. i.e. Whether Fourier waves (modes) are damped or amplified. The modes are unstable for $c_i > 0$, stable for $c_i < 0$ and neutral for $c_i = 0$.

4.1 Effect *of* μ_r on *visco-elastic wall thickness (H)*

The figures 2(a) and 2(b) show the effect of different values of μ_r for the axi-symmetric disturbances of M1 types of modes. From these figures, it is seen that the higher values of μ_r decreases the imaginary values of wave speed ($c = c_r + ic_i$) because it is seen that the lower positive values of c_i is

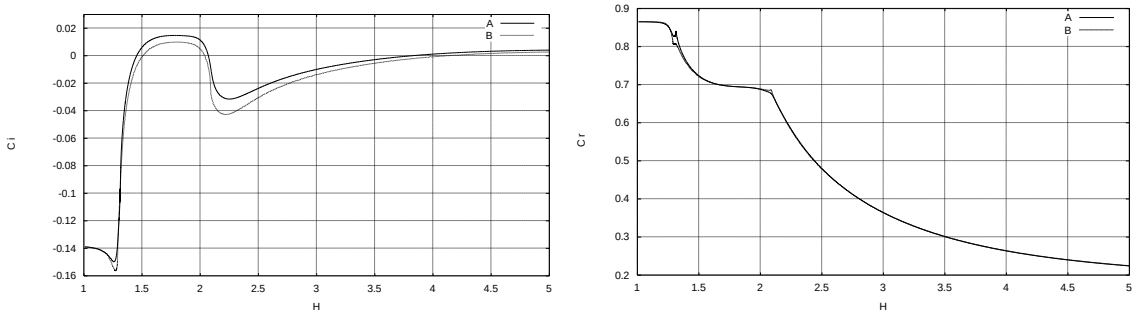
more stable as compare to higher positive values of ci. So, the lower value of c_i makes the modes more stable. The real part of wave speed (c_r) has no effect on the μ_r values. It is also found that higher value of wall thickness (*H*) makes the modes more unstable as compare to lower *H*.



(a) (b)

Figure 2: *(a) Curve for variation of H and c_i for modes M1, $\Gamma = 6$. 'A' is for $\mu_r = 0.0$ 'B' is for $\mu_r = 0.5$.(b) Curve for Variation of H and c_r for modes M1, $\Gamma = 6$. 'A' is for $\mu_r = 0.0$ 'B' is for $\mu_r = 0.5$.*

The figures 3(a) and 3(b) show the variation of visco-elastic wall thickness (*H*) versus c_r and c_i for M2 types of modes for different values of μ_r. From these figures, we found the same observations and behavior of effect of μ_r as discussed above for M1 types of modes on the stability of flexible pipe flow i.e. flexible pipe surface becomes more rigid for higher values of μ_r. So, we can conclude that higher μ_r value makes the all types of modes more stable.



(a) (b)

Figure 3 :*(a) Curve for variation of H and c_i for modes M2, $\Gamma = 6$. 'A' is for $\mu_r = 0.0$ 'B' is for $\mu_r = 0.8$. (b) Curve for variation of H and c_i for modes M2, $\Gamma = 6$. 'A' is for $\mu_r = 0.0$ 'B' is for $\mu_r = 0.8$.*

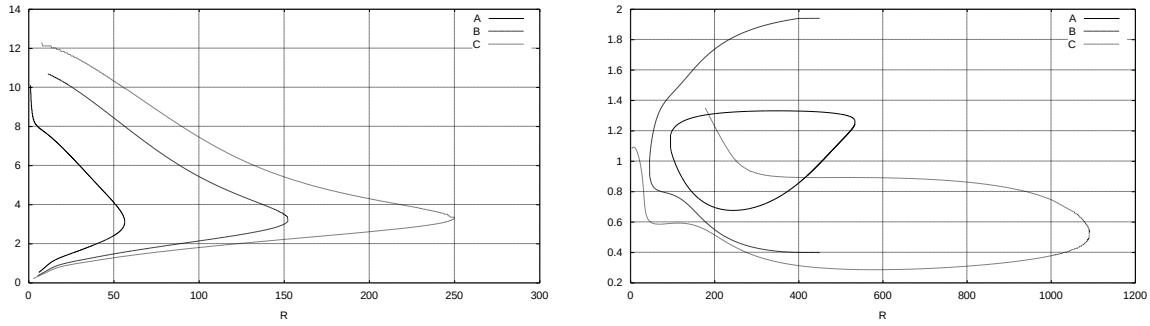
4.2 Effect of wall compliance Γ

Figures 4 (a) shows the neutral stability curves in α-R plane for different values of Γ for M1 types of modes. Here, we have taken the $\mu_r = 0$ and $H = 2$. From this figure 4, we observed that higher values of wall compliance Γ increases the instability of the modes. i.e. area under curves are increased by higher values Γ. It is also seen from figure 4 that M1 types of modes are more unstable for very lower values of Reynolds number R. Modes are unstable inside the curve, neutral on the curve and stable outside the curves. Figure 4.(b) shows variation of the neutral stability curves in α-R plane for different values of Γ for M2 types of modes and these modes are unstable for medium and higher Reynolds number R. We found that the higher value increases the instability of modes. So, we can conclude that all types of modes increases the instability for higher values of Γ.

4.3 *Effect of wall damping* μ_r

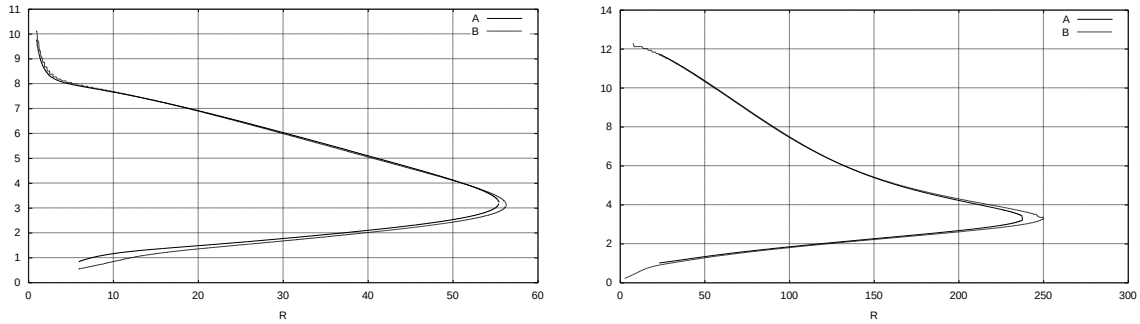
The figures 5 (a) and 5 (b) show the effect of visco-elastic viscosity to fluid viscosity (μ_r) for M1 types of modes. Here, we considered $H = 2$ and different values of μ_r. From these figures, it is observed that the higher value of μ_r decrease the instability of visco-elastic pipe flow. Higher values of μ_r means the more rigidity i.e. less visco-elasticity. It is found that even with a large value of $\mu_r = 0.2$,

there is little influence of μ_r on the upper limb of the neutral curve, and modest influence on the lower limb of the neutral curve. We may conclude that higher values of wall damping μ_r increases the stability of visco-elastic pipe flow.



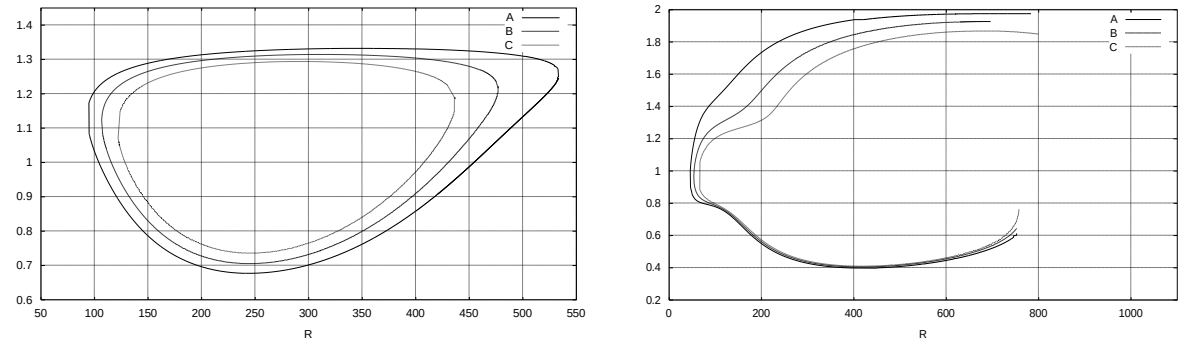
(a) (b)

Figure 4: *(a) Stability Curves in α - R plane various Γ for modes M1, H=2.0. 'A' is for $\Gamma = 6$, $\mu_r = 0$, 'B' is for $\Gamma = 8$, $\mu_r = 0$, 'B' is for $\Gamma = 9$, $\mu_r = 0$, (b) Stability curves in α - R plane various Γ for modes M2, H=2.0. 'A' is for $\Gamma = 4$, $\mu_r = 0$, 'B' is for $\Gamma = 6$, $\mu_r = 0$, 'B' is for $\Gamma = 8$, $\mu_r = 0$*



(a) (b)

Figure 5: *(a) Neutral stability curves in α - R plane various μ_r for modes, M1, H=2.0. 'A' is for $\Gamma = 6$, $\mu_r = 0$, 'B' is for $\Gamma = 6$, $\mu_r = 0.2$, (b) Stability curves in α - R plane for various μ_r for modes, M1. 'A' is for $\Gamma = 9$, $\mu_r = 0$, 'B' is for $\Gamma = 9$, $\mu_r = 0.1$.*



(a) (b)

Figure 6: *(a) Stability curves in α - R plane for various μ_r for modes, M2. 'A' is for $\Gamma = 4$, $\mu_r = 0$, 'B' is for $\Gamma = 4$, $\mu_r = 0.2$ and 'C' is for $\Gamma = 4$, $\mu_r = 0.4$. (b) Stability curves in α - R plane for different values of μ_r for modes, M2. 'A' is for $\Gamma = 6$, $\mu_r = 0$, 'B' is for $\Gamma = 6$, $\mu_r = 0.1$ and 'C' is for $\Gamma = 1$, $\mu_r = 0.2$.*

Figure 6 (a) shows the effect of μ_r in α - *R* on the stability of flexible pipe flow for M2 type of modes. Here, we have considered $H = 2$, Γ=4 and different values of μ_r. From figure 8, it found that the

higher values of μ_r increases the stability. It is seen that effect of μ_r is moderate on the neutral stability curve. Figure 6 (b) represent the effect of μ_r on the neutral stability curve of M2 typed of modes on the flexible pipe flow for axi-symmetric disturbances. In this figure, we considered $H = 2$, Γ=6 and different values of μ_r .It is observed that there is little influence of μ_r on the lower limb of the neutral curve, and modest influence on the upper limb of the neutral curve.

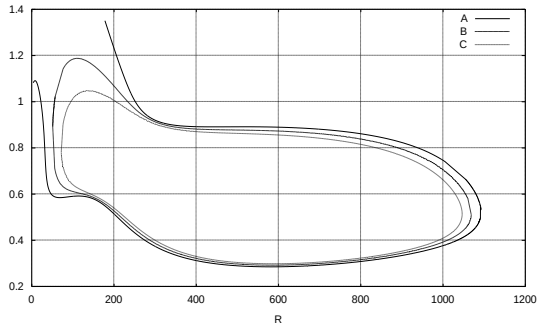


Figure 7. *Stability curves in α - R plane for different values of μ_r for modes, M2. 'A' is for $\Gamma = 8$, $\mu_r = 0$, 'B' is for $\Gamma = 8$, $\mu_r = 0.2$ and 'C' is for $\Gamma = 8$, $\mu_r = 0.4$.*

Figure 7. Shows the variation of neutral stability curve in α - *R* for different values of μ_r for M2 typed of modes. It is observed that there is little influence of μ_r on the higher Reynolds number R on the neutral curve, and large influence on the lower values Reynolds number R on the neutral stability curve. From the above discussions of effect of wall damping μ_r , we may conclude that the higher wall damping damps the modes. i.e higher values of μ_r increases the stability of flexible pipe flow. The higher values of μ_r ($\mu_r = \mu_s / \mu_f$) means the higher viscosity of visco-elastic material as per the definition of μ_r . The higher values of μ_r makes the flexible pipe more rigid. As we know that the rigid pipe flow is more stable than the flexible pipe flow. Hence, final conclusion can be drawn that the more viscosity of visco-elastic material makes the flow more stable.

5 CONCLUSION

The following conclusions have been drawn on the basis of the results given above.

(1) It is found that the flexible pipe is unstable for all ranges of Reynolds number (R) and azimuthal wave number (α).

(2) The increase in the visco-elastic material thickness (H) increases the instability of flexible pipe flow, which means higher visco-elastic material thickness makes the pipe more flexible and hence more flexibility of pipe increases the instability. As it is know that the rigid pipe is more stable as compare to flexible pipe.

(3) The higher values of visco-elastic parameter (Γ) increases the instability of flexible pipe flow because more Γ makes the pipe more flexible. So flexible pipes flow becomes more unstable with higher Γ.

(4) Instability of flexible pipe flow decreases with the larger values of μ_r. i.e. the larger values μ_r makes the flexible pipe flow more rigid. It means that rigidity of visco-elastic material pipe is increased by increasing the values of μ_r.

REFERENCES

[1] Kramer, M. O, "Boundary layer stabilization by distributed damping", J. Aeronaut Science, 24, PP. 459 – 460, 1957.

[2] Kramer, M. O, "Boundary layer stabilization by distributed damping". J. Aero/Space Science, 27, 69, 1960.
[3] Kramer, M. O, "Boundary layer stabilization by distributed damping". J. Am. Soc. Naval Engineers, 74, PP. 341 – 348, 1960.
[4] Kramer, M. O, "Hydrodynamics of dolphin, in advance Hydro-science", ed. V. T. Chow, 2, PP. 110 – 130, Academic press, New York. 1965.
[5] Carpenter, P. W, " Status of transition delay using compliant walls, in viscous drag reduction in boundary layers", eds. D. M. Bushell and J. N. Hefner, PP. 79-113, AIAA, Washington, D.C, 1990.
[6] Carpenter, P. W, "Current status of the wall compliance for Laminar flow control", Exp. Thermal & fluid Science., 16, PP. 133-140, 1998.
[7] Carpenter, P. W**.,** Davies, C. and Lucey, A. D, "Hydrodynamics and compliant walls: Does the Dolphin have a secret?" Current Science 79, PP. 758-765, 2000.
[8] Carpenter, P. W**.,** Lucey, A. D. and Davies C, "Progress on the use of compliant walls for Laminar flow control", J. Aircraft 38, PP. 504-512, 2001.
[9] Reynolds, O, "An experiment investigation of the circumstances which determines the motion of water in pipe", Phill. Trans. Roy. Soc. 174, PP. 953-982, 1883.
[10] Davey, A. and Drazin, P. G, "**Stability** of Poiseuille flow in a pipe", J. Fluid Mech., 36, PP. 209-218, 1969.
[11] Garg, V. K. and Rouleau, W. T, "**Linear** spatial problem of the pipe-Poiseuille flow", J. Fluid Mech., 54, PP. 113-127, 1972.
[12] Salwen, H. and Grosch, C. E, "The stability of Poiseuille flow in a pipe of circular –section", J. Fluid Mech., 54, PP. 93-112, 1972
[13] Sen, P. K., Venkateswarlu, D. and Maji S, "On the stability of plane-Poiseuille flow to finite-amplitude disturbances considering the higher order Landau coefficients", J. Fluid Mech., 68, PP. 345-351, 1985
[14] Hamadiche, M. and Gad-el-hak, M, "Temporal Stability of flow through a visco-elastic tubes", J. Fluid Structure, 16, no. 3, PP. 331-359, 2002



S. Anbukumar is an Assistant Professor in the Department of Civil Engineering at Delhi Technological University, since 1999. He has done B.E. in Civil Engineering from Bharathidasan University, Trichy, and M.Tech. in Ocean Engineering from Indian Institute of Technology, Madras. Currently, he is pursuing Ph.D. in Civil Engineering from Delhi Technological University. He has published a number of technical papers in various national and international conferences and reputed journals.



Dr. Munendra Kumar graduated from the Aligarh Muslim University. Aligarh with B.E. and M.E. degrees and from IIT, Delhi with Ph. D degree in the area of Hydrodynamic stability of compliant pipe flow. He has 20 years of teaching experience in technical institutions. Presently, he is working as a senior lecturer in Delhi Technological University, Bawana road, Delhi – 110042. He has published 14 research papers in various National and international journals and conference proceedings.

Multimed Tools Appl
DOI 10.1007/s11042-017-4447-x

Efficient music recommender system using context graph and particle swarm

Rahul Katarya [1] · **Om Prakash Verma** [1]

Received: 17 June 2016 / Revised: 3 January 2017 / Accepted: 27 January 2017
© Springer Science+Business Media New York 2017

Abstract Music recommender systems is an important field of research because of easy availability and use of online music. The most existing models only focus on explicit data like ratings and other user-item dimensions. A challenging problem in music recommendation is to model a variety of contextual information, such as feedback, time and location. In this article, we proposed a competent hybrid music recommender system (HMRS), which works on context and collaborative approaches. The timestamp is extracted from users listening log to construct a decision context behavior that extracted various temporal features like a week, sessions(as morning, evening or night). We used depth-first-search (DFS) algorithm which traverses the whole graph through the paths in different contexts. Bellman-Ford algorithm provides ranked list of recommended items with multi-layer context graph. We enhanced the process using particle swarm optimization (PSO) which produced highly optimized results. The dataset is used from Last.fm which contains 19,150,868 music listening logs of 992 users (till May, 4th 2009). We extract the properties of music from user's listening history and evaluate the efficient system to recommend music based on user's contextual preferences. Our system noticeably delivers the best recommendations regarding recall results when compared to existing methods.

Keywords Recommender system · Collaborative filtering · Hybrid · Particle swarm optimization · Music

✉ Rahul Katarya
rahulkatarya@dtu.ac.in; http://www.dtu.ac.in/Web/Departments/CSE/faculty/

Om Prakash Verma
http://www.dtu.ac.in/Web/Departments/CSE/faculty/

[1] Department of Computer Science & Engineering, Delhi Technological University (Formerly Delhi College of Engineering), Shabad Daulatpur, Main, Main Bawana Road, Delhi 110042, India

Published online: 10 February 2017

1 Introduction

Recommender systems are information delivery and knowledge management tools which are delivering accurate online recommendations to the web users [4, 18–22]. Most of the existing recommender models are based on explicit feedback data like ratings and votes. However, the explicit feedback data is not always available in real-life scenarios. Thus, the model that uses only explicit data for recommendation seems to be ineffective. On the contrary, implicit data is always available since most of the data produced by the user is implicit [14, 28]. The implicit data are automatically recorded by the system and can be in the form of music listening logs of users or purchase histories. Hence, the system using implicit feedback data tends to provide more accurate recommendations of users interests [43]. There is a need to incorporate contextual information, such as time, location, mood, genre and social tagging with the conventional recommender systems. Contextual information helps the user to recommend an item on his interest by considering the context of the particular user [17, 35, 39]. Recommender systems frequently produce a list of recommendations by building models from a user"s historical performance such as items previously purchased, selected or numerical ratings [13, 36, 44]. In our methodology, we considered various types of contexts in recommender system with implicit feedback [43]. User context describes user's personal information such as gender, age, country, education, and some other social attributes. Item context describes various attributes of the item. In the case of music recommender system, the song is treated as an item, and different contexts for the song can be like as artist, genre, pitch, loudness, intensity and frequency. Decision context is the another type of contextual information which involves the context where the decision is to be made with various factors such as time, location, and mood. The users with different decision context show different tastes and preferences. Moreover, this is the main reason decision context is taken into consideration in our model. We adopted collaborative filtering that is used to predict items or ratings for items that the user may have an interest in and can find similar users and items [1, 34]. We also used graph based approach to capture user preferences [43]. We used a depth-first-search algorithm which traverses the whole graph through the paths in different contexts. Bellman-Ford algorithm delivered a ranked list of recommended items [9]. Finally, Particle Swarm Optimization (PSO) produced highly optimized results.

The major contributions of this article are:

- A hybrid music recommender system (HMRS) is proposed with context-collaborative features.
- We found similarity score for items using Pearson Correlation coefficient.
- Depth-first search & Bellman-Ford algorithms were employed with multi-layer context graph.
- Particle swarm optimization (PSO) was applied to get highly optimized results.
- We compared our proposed system with the already existing systems such as CORLP, MGW, CF, UIG, and PG.
- Best recommendations recall results were retrieved when compared with other existing systems.

The rest of the article is structured as in section 2 background, and related work is explained. Necessary concepts with their applications are highlighted in Section 3. Our proposed work is demonstrated with suitable examples in section 4. Improved results and comparisons are shown in section 5, and conclusion with future work is discussed in section 6.

2 Background and related work

Nowadays music recommender systems have grown exponentially especially for mobile users in which users can choose their songs according to their past searches and likes. Some researchers employed the user rating information, without taking into account valuable social media information. There are numerous kinds of social media resources which include different type of music objects and relations among these objects such as Last.fm and Pandora. There can be several types of recommender systems such as in rank-based recommendation in which the primary purpose is to compute a score for each item, and order items from it. Examples of these techniques are matrix factorization and pagerank [8, 24, 27]. In the content-based recommender systems similar items or products are recommended which are liked by the users or people in the past [29, 37]. User-based recommendation uses other friends or related users to learn about the existing users and get their suggestions for a practical recommendation [44, 45]. Traditional recommender systems use techniques such as collaborative filtering (CF), which only apply user-item feedback matrix. Collaborative filtering is a class of method for recommending appropriate items to users who are based on the likings of other users [15, 33]. Collaborative filtering is the most popular technique which is used to recommend the items to the users. As a kind of user collective action, feedback data or the user item interaction presents shared information among users. The neighborhood-based algorithm computes the resemblance among users or items and delivers predictions by using a weighted average of all the ratings [2, 52]. If we want to make appropriate recommendations for a new user, we require a system first to learn the user"s preferences that are possible only when the system can analyze past voting or rating activities or any other kind of user's contextual activity. Some researchers performed their work related to recommendations and learning in the multimedia domain which included music, image, and video. An optimized multigraph-based semi-supervised learning (OMG-SSL) method was presented in which various factors such as video annotation, multiple modalities, multiple distance functions, and temporal consistency were included [40]. For facial expression recognition, a method was proposed in which spatio–temporal features were included with improved AdaBoost algorithm [46] and visual features were extracted to identify image emotion [47]. For a view-based 3D object, a feature fusion scheme was offered on multi-modal graph learning [48]. Recent research works employed simple graphs to model user-item constructive feedback interaction for recommendation problems [23, 49]. Some works used a page-ranking algorithm for ranking the nodes in the graph. With the recent advances in social media communities (e.g., Last.fm, YouTube), there is an emerging presence of implicit social information, e.g., a user listening logs and another user, item, and decision contexts. Implicit information is important sources of information for recommender systems [5, 11, 51]. We proposed our context graph approach for modeling the user-item implicit relations.

3 Methods

We have employed four different methods in hybrid music recommender system (HMRS), such as collaborative based model, depth-first search algorithm, Bellman-

ford Algorithm and Particle swarming optimization to build an efficient recommendation system.

3.1 Collaborative based model

Collaborative filtering approaches typically work by searching a large group of people and finding a smaller set of similar tastes [42]. Collaborative filtering is an important technique for recommender system which makes predictions based on some similarity measures between users and between items. They can be classified into user-based and item-based models. In the item-based model, it is expected that songs that are frequently listened together by some users tend to be alike and are more likely to be heard together in future also by some other user [32, 41]. According to user based similarity model users who have similar listening histories, i.e., have listened to the similar songs in the past and will probably listen to the same songs in future too. We need nearly similarity measure to compare between two songs or between two users for each timestamp [6, 30]. We employed Pearson correlation to compute the similarity between users and items for given timestamp [7]. The Pearson correlation similarity of two users x, y is defined as [16, 25]

$$\text{Pearson similarity(r)} = \frac{\sum_{a=1}^{n}\left(x_a-\overline{x}\right)\left(y_a-\overline{y}\right)}{\sqrt{\sum_{a=1}^{n}\left(x_a-\overline{x}\right)\left(x_a-\overline{x}\right)}\sqrt{\sum_{a=1}^{n}\left(y_a-\overline{y}\right)\left(y_a-\overline{y}\right)}} \tag{1}$$

Where, I_{xy} is the group of items rated by both user x and user y. As stated in Eq. 1, we calculated the similarity score using the Pearson correlation using Eq. 1. The Pearson correlation coefficient is an amount of correlation between two variables (in this particular case the correlation between two song listeners). It ranges between −1 and 1 inclusive. 1 indicates perfect agreement. -1 means complete disagreement. The problem with the Eq. 2 is that the algorithm would require multiple passes through the data.

$$\mathrm{r} = \frac{\sum_{a=1}^{n} x_a y_a - \frac{\sum_{a=1}^{n} x_a \sum_{a=1}^{n} y_a}{n}}{\sqrt{\sum_{a=1}^{n} {x_a}^2 - \frac{\left(\sum x_a\right)^2}{n}}\sqrt{\sum_{a=1}^{n} {y_a}^2 - \frac{\left(\sum y_a\right)^2}{n}}} \tag{2}$$

Equation 2 is an amendment of Eq. 1. The similarity of the individual tracks and genre-based similarity was calculated between every music track. Each playlist and every music track were embedded in a list (for example metallic, rock, pop) and this list was also assigned to each user. We finally computed the similarity of each and every track with every user and recommended the top songs.

3.2 Depth-first search (DFS)

Depth-first search searches “deeper” in the graph whenever possible. Depth-first search discovers outgoing edges of the most freshly created vertex *v* that still has unexplored edges [9].

Once all of the *v*'s edges have been explored, the search "backtracks" and explore outgoing edges in which vertex from which *v* were discovered. This process lasts until we found all the vertices that are reachable from the source vertex. If any unnoticed vertices remain, then depth-first search selects one of them as a new source, and it replicates the search from that source. The algorithm repeats this entire process until it has discovered every vertex. In a depth-first search, the frontier acts like a last-in-first-out stack. The elements are added to the stack one at a time. We use a depth-first search algorithm to search the music network to compute a relevant set of users to whom the item can be recommended.

3.3 Bellman-ford algorithm

Bellman and Ford proposed a method for finding single source shortest or longest path [3, 9, 12]. The algorithm executes in O(nm) time on a graph with "n" nodes and "m" arcs. This is the currently recognized strongly polynomial bound for the problem. Although it does not find paths from source vertex, it is possible to find out if paths exist beyond immediate neighbors. It can be used as a step before to decide if it is required to explore graph further. The method proposed by Bellman-Ford is optimally suited for the recommendation in our work for the scenario of music recommender system. Bellman-Ford algorithm considers all edges (u, v) ∈ E in turn. Once an edge leading to the shortest path is discovered, in our case it is possible to consider inverse of similarity then path distance is updated. The algorithm is repeated until distances converge; that is until there are no more distance updates.

$$D_i(v) = \min(D_{i-1}(v), d + D_{i-1}(u)); \quad \text{Where}, u = v, (u, v) \in E \tag{3}$$

The algorithm is based on the standard of reduction; that is the shortest path connecting vertices u and v is an overestimate. The existence of shortest path is guaranteed if there are no negative cycles. The algorithm assigns each vertex v in V.

3.4 Particle swarm optimization

We employed the item based prediction task of recommender systems and presented swarm rank collaborative filtering that is responsible for optimizing the performance quality of recommender systems [10, 31, 38]. PSO is an evolutionary computation optimization method inspired by social behavior of bird flocking or fish schooling. In PSO, the potential answers, called particles, fly through the problem space by following the current optimum particles. Each particle checks the coordinates in the problem space that are associated with the best answer (fitness). The fitness value is also stored. This value is called *pbest*. Another "best" value that is searched by the particle swarm optimizer is the best value, obtained by any particle in the nearby of the particle. This location is called *lbest*. When a particle profits all the population as its topological neighbors, then the best value is a global best and is called *gbest*. In our proposed work, swarming is used to address the task of learning to rank. As an instance of PSO, it enumerates the optimality of a solution using a fitness function, which serves as some criteria to update the particle and global best solutions. As output, the procedure returns a linear ranking function whose coefficients are given by the dimension values equivalent to the

global best solution vector found by the swarm. Fitness function measures the quality of the ranking generated by a given particle. PSO automatically optimizes the performance quality of music recommender systems using a swarm intelligence perspective as it contains the best search efficiency.

4 Proposed work

In this section, we will illustrate the proposed work for our hybrid music recommender system (HMRS). The experiments have been carried on the Last.fm dataset.

4.1 System architecture

In this section, we will explain the strategy of our graph-based recommender system. The architecture is shown in Fig. 1. It displays the overall structure of the proposed music recommendation system. This system provides personalized ranked list of results by using collaborative filtering and another method that includes backtracking through depth first search algorithm and bellman-ford algorithm. Our system has the following eight major components: a User-Context layer, an Item-context layer, a Decision-context layer, user's listening logs, collaborative filtering, DFS, Bellman-Ford Algorithm and Particle Swarm Optimization. Decision-context layer extracts accurate data from user's listening log, i.e., from user's history database. Two methods were employed in our proposed work that includes collaborative filtering and graph algorithms. In collaborative filtering, we found similarity score for items using Pearson correlation coefficient. It helps us in the search for the songs that are similar to other songs. Then a ranked list of songs is produced for a given user, and thus, songs of similar preferences are being recommended to the user. The next method that is purely graph based method is also employed in our proposed work. We use two graph algorithms, Depth-First-Search (DFS) algorithm for backtracking and Bellman-Ford algorithm. The intelligent optimization algorithm is implemented at last to produces optimized ranked list of recommended results with PSO.

Figure 1 shows the system architecture of the proposed system constructed using multi-layer. The system consists of eight main components. The very first component has Multi-layer graph, which includes three different context layers, user-context layer, item-context-layer and decision context layer. The context decision layer is connected with the user's listening logs. Thus, it extracts past useful information of a user. There are two other components of the system. One includes collaborative filtering that computes similarity score using Pearson coefficient and connected to the final element of recommended items. Particle swarm optimizer follows this component and then leads to recommended items.

4.2 Constructing multi-layer context graph

We build multi-layer context graph with implicit feedback data for our music recommendation system. A graph consists of three layers viz., user-context layer, item-context layer and decision context layer. Context graph stresses the interrelationship and real-time condition of the user-item collaborations. We consider all of the three types of contexts into recommender systems and model the interactions between users and items in the corresponding decision context. It shows three different with its context. Thus, we have user

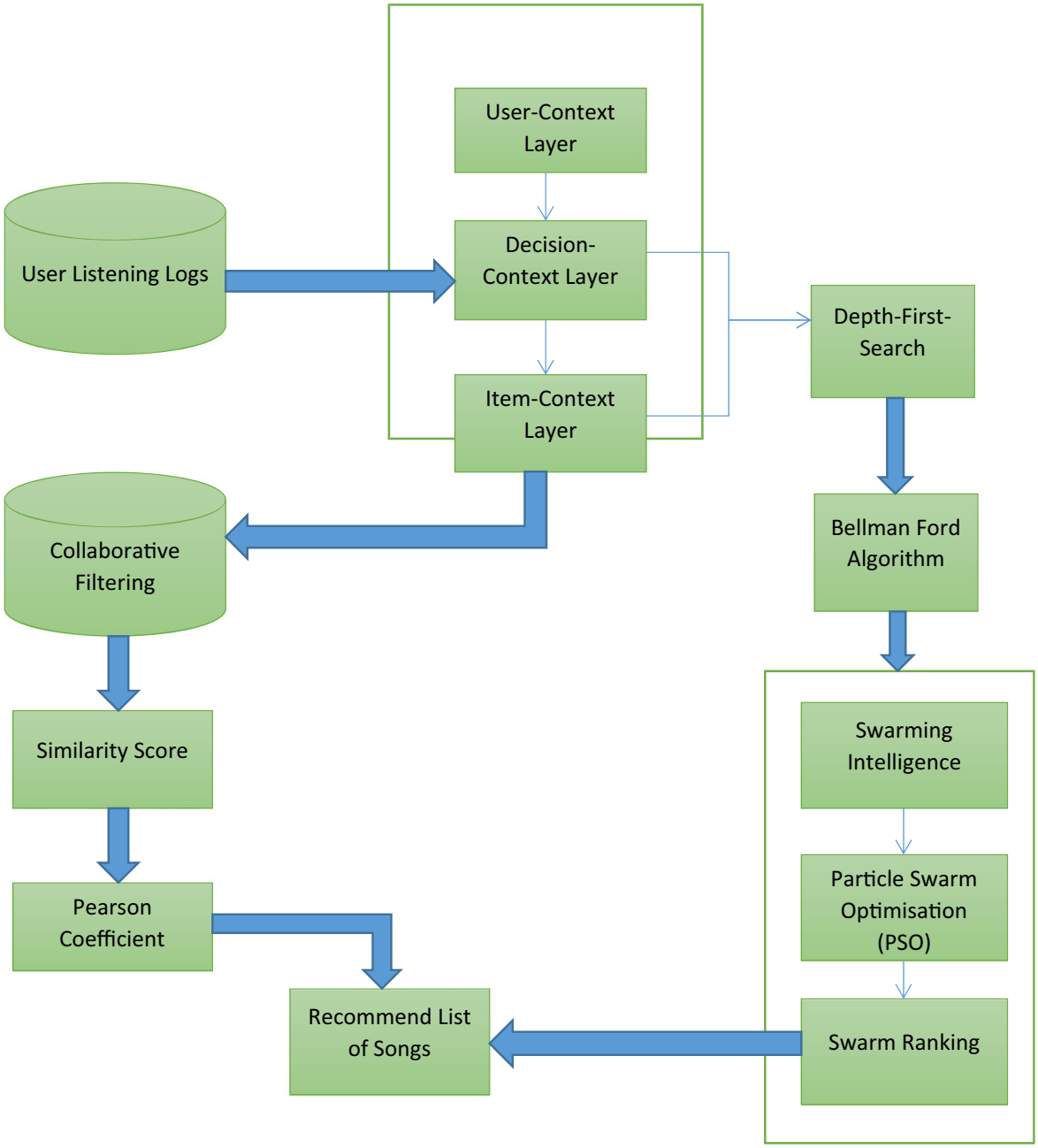


Fig. 1 System architecture of hybrid music recommendation system (HMRS)

context C_u, item context C_i and decision context C_d corresponding to user, item and decision layer respectively. In order to construct a user-context layer, let U be the set of users such that U = $\{u_k|k=1,2,\ldots\ldots.|U|\}$ and C_u be the user context for each user. Similar to user-context, we have item-context, where I is the set of all items. In this case we consider, songs as the item. Hence, I = $\{i_k|k=1,2,\ldots\ldots..|I|\}$ be the set of items with i_k as the item-context. Item-context can be like artist, genre, frequency, pitch and intensity. Decision-context layer is constructed with the help of user's history or the listening logs of user. Timestamp can be extracted in order to get various temporal features such as find day of the week or the session of the day like morning, evening or night. When timestamp is extracted into such temporal features, we then incorporate such information with user and item contexts to provide user with the recommendation of items based on implicit

feedback data. The interaction between user, item and decision context can be seen by directly creating edges between two nodes and pseudocode is given in Algorithm 1.

Algorithm 1. Pseudocode of the hybrid music recommender system (HMRS)

```
Input: Set of users U for which we want to generate recommendations.
Output: Recommended songs for user
1. Construct Multi-layered context graph
2.      Initialize a directed graph G with User-Layer, Song-Layer and Decision layer
3.      Extract and add "user" nodes in graph
4.      for row in file f1:
5.              G.add_nodes_from (row, color = 'red')
6.      Extract and add "song" nodes in graph
7.      for row in file f2:
8.              G.add_nodes_from (row, color = 'blue')
9.      Extract and add "artist" nodes in graph
10.     for row in file f3:
11.             G.add_nodes_from (row, color = 'blue')
12.     Extract and add "weekday" nodes in graph
13.     for row in file f4:
14.             G.add_nodes_from (row, color = 'blue')
15. Perform a DFS search at each user node to find weekdays
16. def dfs_user (g2, start, path1 = []):
17. DFS at each weekday corresponding to given user to find artists.
18. for i, val in enumerate (days):
19.     def dfs_day (g1, start, path2 = []):
20. Bellmanford with negated edges to recommend favorite artist
21. def longest_path (g1):
22.     dist = {} # stores [node, distance] pair
23. Perform swarming to rank to evaluate results
24.     Extract k collaborative features (i.e., latent factors) I by factorizing matrix R.
25.     Apply Swarm Rank to learn a ranking function f (u; i), by optimizing
26.      return f (u; i)
24.     Extract k collaborative features (i.e., latent factors) I by factorizing matrix R.
25.     Apply Swarm Rank to learn a ranking function f (u; i), by optimizing
26.      return (u; i)
```

In Algorithm 1, we have set of users for whom songs will be recommended. Initially, Multi-layered context graph is constructed. The graph has three layers such as User-Layer, Song-Layer, and Decision layer in which Depth first search was applied to each user node. Bellman-Ford recommends the favorite artist and finally Particle swarm optimization was applied to get optimized rank results.

We constructed multi-layer context graph with implicit feedback data for our music recommendation system. A graph consists of three layers viz., User-context layer, Item-context layer, and Decision-context layer. We considered all of the three types of contexts into recommender systems, and model the interactions between users and items in the corresponding decision context. Thus we have user context C_u, item context C_i and decision context C_d corresponding to user, item and decision layer respectively. Decision-context layer extracts implicit data from user's listening log i.e., from user's history database. Various features are extracted from that information. Two methods are employed in our proposed work which includes Collaborative filtering and using graph algorithms. In collaborative filtering, we find similarity score for items using Pearson Correlation coefficient. Figure 2

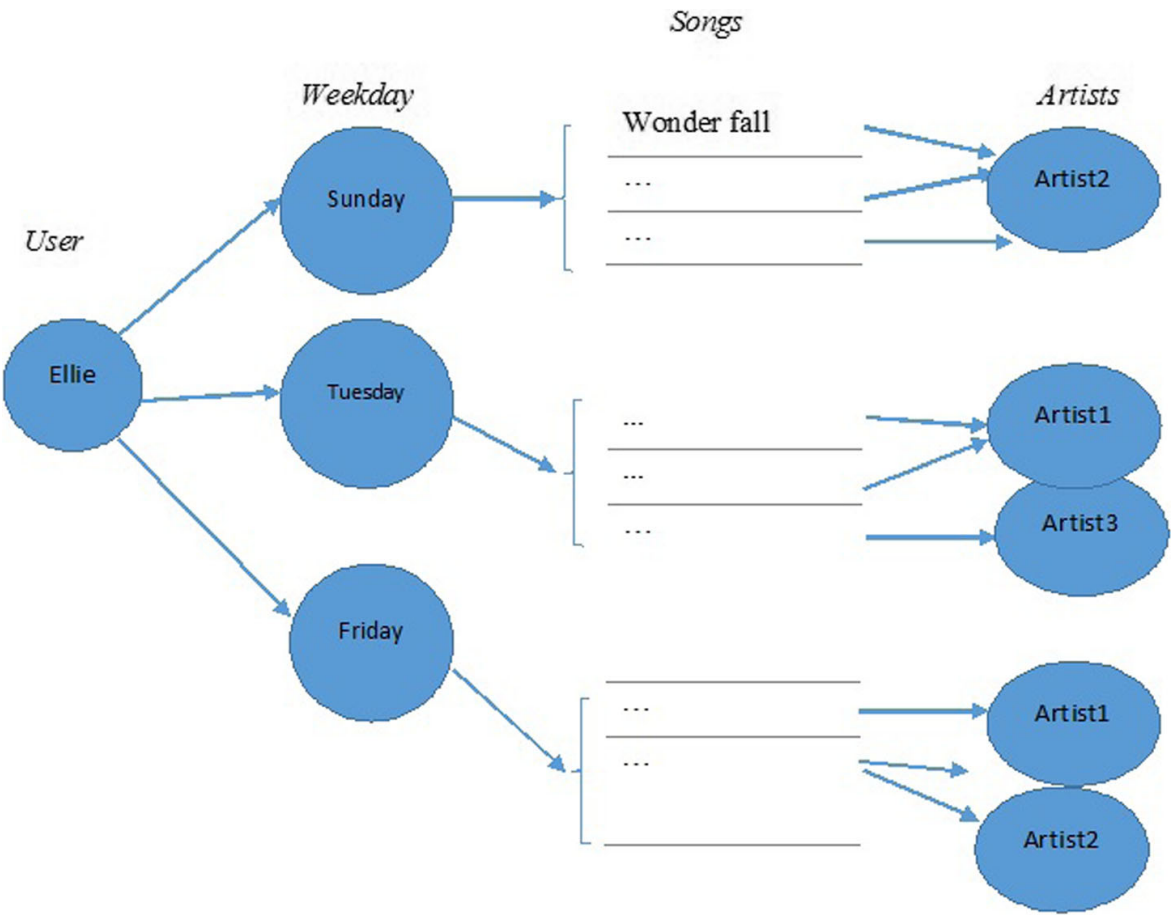


Fig. 2 An example of representation internal structure of proposed system

shows an example of illustration of internal structure of the proposed system for one user. Ellie must have listened to various songs of from various artist on a single day. For the purpose of illustrating the music network worked out in the system we lay out this simple graph that easily illustrates how we laid out the network for the purpose of building framework of recommender system. Here, we learn that user named Ellie listens to songs on Sunday, Tuesday and Friday. The songs that she ever listened belonged to Artist1, Artist2 and Artist3. So, it is quite obvious that if she is more preferred to like other songs of these artists in the given context comprising inherent time slice of the day and season too.

5 Experiment and result

In this section, an experimental study is conducted on real-world datasets to demonstrate the effectiveness of hybrid music recommender system (HMRS). The dataset used is Last.fm which contains 19,150,868 music listening logs of 992 users (till May, 4th 2009). We extract the logs from April to May and remove these songs that listened to less than 10 times; then the final dataset contains 992 users, 12,286 songs, and 264,446 logs. Finally, we use logs in April as a training set, and randomly choose 1000 logs from 1st to 4th May 2009 as a test set. For Last.fm dataset, our experiments provide a ranked list of songs, which might have been listened to before by the given user, since users listen to the same song more than once. Last.fm dataset is available from *http://www.dtic.upf.edu/~ocelma/MusicRecommendationDataset/,* or we can

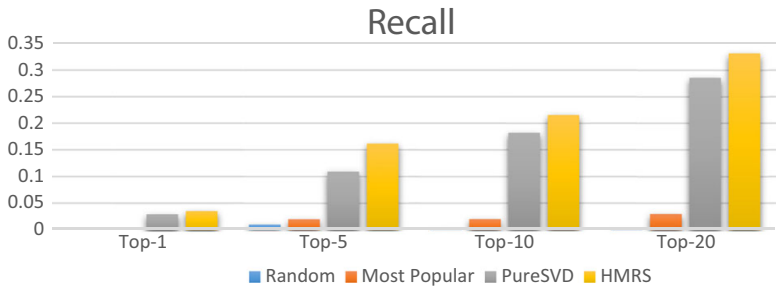


Fig. 3 Ranking results based on recall estimation

also obtain desired particular dataset using last.fm API requests but data obtained from APIs is not clean or unfit for using directly for work research purposes. So, we used the bundled dataset readily available from the URL. On last.fm dataset, we first carried out necessary pre-experimental processing to avoid possible errors when we use the dataset as an input in the established algorithms utilized in the later stages. Timestamp column in the dataset is available in the format: YYYY-MM-DD*; hh-mm-ss;* First part of the timestamp contains the inhibit information about the date and second contains the information about the time of the day. First part reveals various key information such as day of the week, month, season, etc. and similarly second part shows information related to the time of day or time slice when the user prefers to listen to music. These are the key information that we have used in the recommender system. More generally, this is all primary user's contextual information. We created directed acyclic graphs using our dataset by splitting user, item and decision contexts into different layers. The paths followed through the whole network graph that never repeats itself and henceforward the efficiency of the system. We split dataset "S" into two sets: a training set and a testing set. To estimate the recommendations we used leave-one-out holdout method. In particular, we followed a similar approach as the one described in the previous sections. Our goal is to estimate the system performance when it suggests Top-N items to a user. The items sorted in descending order of their accumulated frequencies. We accepted one item at random from the top 10 of the aggregated ranking. In total, we have |U| hidden items. Notice that most of those items selected are probably not interesting to user u and generate Top-N recommendations. If the test element i, is in the Top-N, then we have a hit. Otherwise, we have a miss. We measure the superiority by looking at the recall metric. A recall value of 1.0 indicates that the system was able always to recommend the hidden item while a recall of 0.0 shows that the system was not able to recommend any of the hidden items. Recall in this context can also be mentioned too as the true positive rate or sensitivity, and precision is also denoted by as positive predictive value (PPV).

In Fig. 3 and Table 1 we compared the various systems such as Random, Most popular, PureSVD and proposed HMRS. We computed recall value for all systems for Top-1, Top-5, Top-5, and Top-20. HMRS clearly delivers the best recommendations, achieving significantly better results than the other methods (two-sample t-test, $p < 0.025$). As expected, ours and PureSVD widely outperform the non-personalized baselines.

Table 1 Recall ranking results of the proposed system compared with other systems

Method\Top-n	Top-1	Top-5	Top-10	Top-20
Random	0.000	0.010	0.002	0.002
Most Popular	0.000	0.020	0.020	0.030
PureSVD	0.0294	0.1096	0.1824	0.2862
HMRS	0.0355	0.1621	0.2158	0.3321

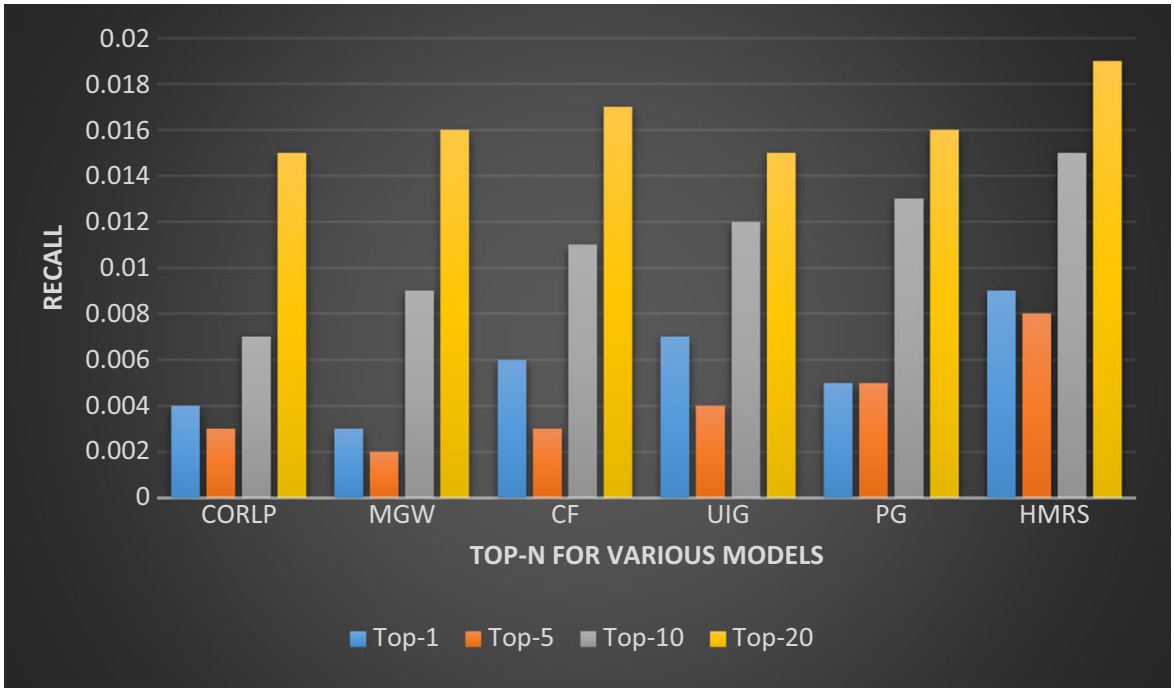


Fig. 4 Ranking results based on recall estimation for various systems

The proposed recommender system HMRS was also compared with already existing systems. In Fig. 4, we have compared the HMRS system with various state of the art systems [26, 50].

We compared proposed recommender system (HMRS) with various other music recommender systems with respect to time (Fig. 5). Ranking results of HMRS were better than other systems such as complex number representation link prediction method (CORLP), music genre weight-based music recommendation model (MGW), Collaborative Filtering (CF), User-Item Graph (UIG) based method and Preference Graph (PG) based method.

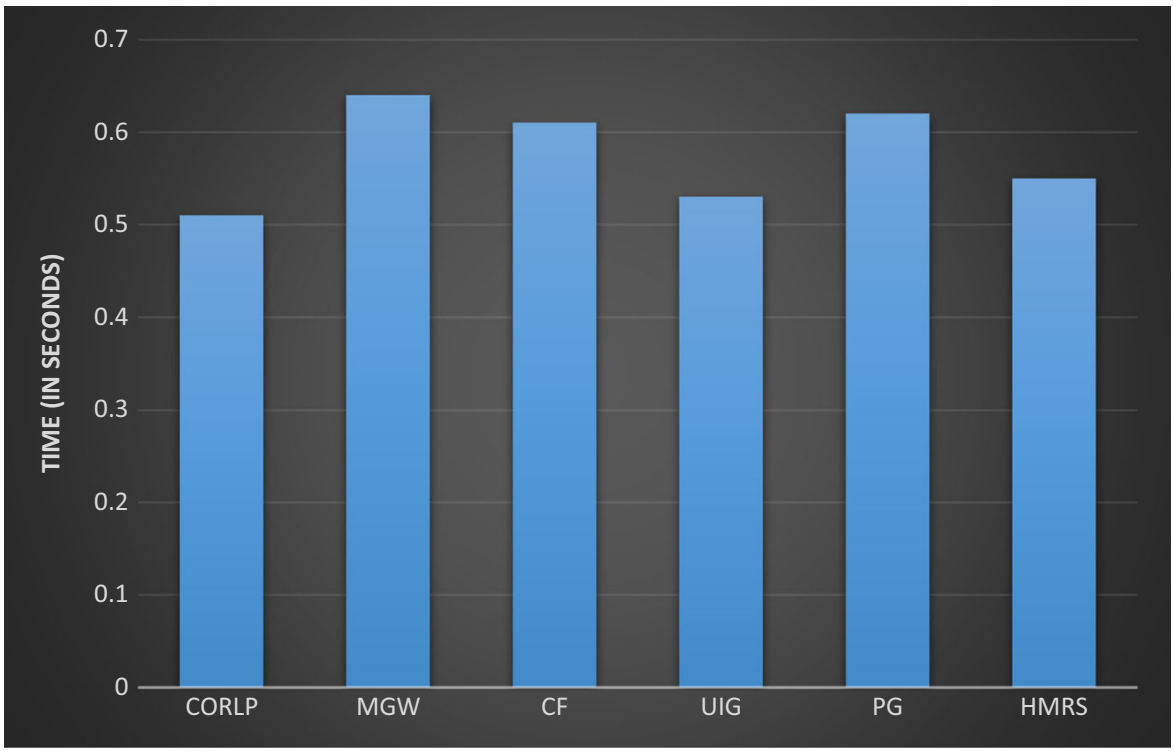


Fig. 5 Performance comparison of various systems

6 Conclusion and future work

With the evolution of the internet, there is a rapid increase in exposure of human with the online music websites like YouTube, Last.fm, Pandora, Sound cloud. In this article, we have suggested a hybrid music recommender system (HMRS), that utilizes graph based algorithms to make recommendations based on implicit feedback data. We created a multi-layer context graph that constructs a layer for each type of contexts respectively. The timestamp is extracted from users listening log to build a decision context. It provides us with temporal features such as day of the week, month, and a session of the day. We then make use of this implicit data to recommend songs based on the user's behavior and preferences in different temporal features. Thus, we were able to recommend pieces of music to the user based on the analysis of contextual information. Using an actual last.fm dataset, we show how our system produces a significant performance improvement compared to the basic collaborative filtering model. We employed two methods for making a contextual recommendation. The first method uses collaborative filtering that is used to predict items that the user may have an interest in and can find similar users and items. We then implemented our second method that uses graph-based approach to capturing user preferences. We use a depth-first-search algorithm to traverse the whole graph through the paths in different contexts and Bellman-Ford algorithm to provide a ranked list of recommended items. We then implemented bioinspired technique particle swarm optimization (PSO) to produce highly optimized results. As the future work is a concern we are planning to design recommender system which should include less runtime with more context factors such as location, mood, and social aspects in our music recommendation system which may provide precise results for observing users temporal and social behavior.

References

1. Adomavicius G, Tuzhilin A (2005) Toward the next generation of recommender systems: a survey of the state-of-the-art and possible extensions. Adapt Web 69:253–260. doi:10.1007/978-3-540-72079-9_9
2. Alqadah F, Reddy CK, Hu J, Alqadah HF (2015) Biclustering neighborhood-based collaborative filtering method for top-n recommender systems. Knowl Inf Syst 44:475–491. doi:10.1007/s10115-014-0771-x
3. Awerbuch B, Noy Bar A (1994) Approximate distributed Bellman-Ford algorithms. IEEE Trans Commun 42:2515–2519. doi:10.1109/26.310604
4. Bobadilla J, Ortega F, Hernando A, Gutiérrez A (2013) Recommender systems survey. Knowledge-Based Syst 46:109–132. doi:10.1016/j.knosys.2013.03.012
5. Chen S, Wang G, Jia W (2015a) κ-FuzzyTrust: efficient trust computation for large-scale mobile social networks using a fuzzy implicit social graph. Inf Sci (Ny) 318:123–143. doi:10.1016/j.ins.2014.09.058
6. Chen L, Chen G, Wang F (2015b) Recommender systems based on user reviews: the state of the art. User Model User-adapt Interact 25:99–154. doi:10.1007/s11257-015-9155-5
7. Chen H, Li Z, Hu W (2015c) An improved collaborative recommendation algorithm based on optimized user similarity. J Supercomput. doi:10.1007/s11227-015-1518-5
8. Christensen I, Schiaffino S (2013) Matrix factorization in social group recommender systems. In: 12th Mexican International Conference on Artificial Intelligence, pp. 10–16
9. Cormen TH, Leiserson CE, Rivest RL, Stein C (2009) Introduction to Algorithms. doi:10.1163/9789004256064_hao_introduction
10. Diaz-Aviles E, Nejdl W, Schmidt-Thieme L (2009) Swarming to rank for information retrieval. Proc 11th Annu Conf Genet Evol Comput 9–16. doi:10.1145/1569901.1569904
11. Elmisery AM, Rho S, Botvich D (2015) Privacy-enhanced middleware for location-based sub-community discovery in implicit social groups. J Supercomput. doi:10.1007/s11227-015-1574-x
12. Goldberg AV, Radzik T (1993) A heuristic improvement of he Bellman-Ford algorithm. Appl Math Lett 6: 3–6. doi:10.1016/0893-9659(93)90022-F

13. Gong Y-J, Chen W-N, Zhan Z-H et al (2015) Distributed evolutionary algorithms and their models: a survey of the state-of-the-art. Appl Soft Comput 34:286–300. doi:10.1016/j.asoc.2015.04.061
14. Guo L, Ma J, Chen Z, Zhong H (2014) Learning to recommend with social contextual information from implicit feedback. Soft Comput 19:1351–1362. doi:10.1007/s00500-014-1347-0
15. Huang Z, Zeng D, Chen H (2007) A comparison of collaborative-filtering algorithms for E-commerce. IEEE Intell Syst 22:68–78. doi:10.1109/MIS.2007.80
16. Hwang W-S, Lee H-J, Kim S-W et al (2015) Efficient recommendation methods using category experts for a large dataset. Inf Fusion 28:75–82. doi:10.1016/j.inffus.2015.07.005
17. Jiang M, Cui P, Wang F et al. (2014) Scalable recommendation with social contextual information. IEEE Trans Knowl Data Eng 26:2789–2802. doi:10.1109/TKDE.2014.2300487
18. Katarya R, Verma OP (2016a) Recent developments in affective recommender systems. Phys A Stat Mech Appl 461:182–190. doi:10.1016/j.physa.2016.05.046
19. Katarya R, Verma OP (2016b) A collaborative recommender system enhanced with particle swarm optimization technique. Multimed Tools Appl 75:1–15. doi:10.1007/s11042-016-3481-4
20. Katarya R, Verma OP (2016c) An effective web page recommender system with fuzzy c-mean clustering. Multimed Tools Appl. doi:10.1007/s11042-016-4078-7
21. Katarya R, Verma OP (2016d) An effective collaborative movie recommender system with cuckoo search. Egypt Informatics J. doi:10.1016/j.eij.2016.10.002
22. Katarya R, Verma OP (2016e) Recommender system with grey wolf optimizer and FCM. Neural Comput & Applic. doi:10.1007/s00521-016-2817-3
23. Kim HN, Bloess M, El Saddik A (2013) Folkommender: a group recommender system based on a graph-based ranking algorithm. Multimedia Systems 19:509–525. doi:10.1007/s00530-012-0298-5
24. Koren Y, Bell R, Volinsky C (2009) Matrix factorization techniques for recommender systems. Computer (Long Beach Calif) 42:30–37
25. Lee W-P, Ma C-Y (2016) Enhancing collaborative recommendation performance by combining user preference and trust-distrust propagation in social networks. Knowledge-Based Syst 106:125–134. doi:10.1016/j.knosys.2016.05.037
26. Mao K, Chen G, Hu Y, Zhang L (2016) Music recommendation using graph based quality model. Signal Process 120:1–8. doi:10.1016/j.sigpro.2015.03.026
27. Maurus S, Plant C (2015) Ternary matrix factorization: problem definitions and algorithms. Knowl Inf Syst. doi:10.1007/s10115-015-0838-3
28. Najafabadi MK, Mahrin MN (2015) A systematic literature review on the state of research and practice of collaborative filtering technique and implicit feedback. Artif Intell Rev. doi:10.1007/s10462-015-9443-9
29. Pazzani MJ, Billsus D (2007) Content-based recommendation systems. Adapt Web 4321:325–341. doi:10.1007/978-3-540-72079-9
30. Pirasteh P, Hwang D, Jung JJ (2015) Exploiting matrix factorization to asymmetric user similarities in recommendation systems. Knowledge-Based Syst 83:51–57. doi:10.1016/j.knosys.2015.03.006
31. Poli R, Kennedy J, Blackwell T (2007) Particle swarm optimization. Swarm Intell 1:33–57. doi:10.1007/s11721-007-0002-0
32. Sarwar B, Karypis G, Konstan J, Riedl J (2001) Item-based collaborative filtering recommendation algorithms. Proc 10th … 1:285–295. doi:10.1145/371920.372071
33. Shi YUE, Larson M, Hanjalic A (2014) Collaborative filtering beyond the user-item matrix : a survey of the state of the art and future challenges. ACM Comput Surv 47:1–45
34. Su X, Khoshgoftaar TM (2009) A survey of collaborative filtering techniques. Adv Artif Intell 2009:1–19
35. Systems C, Wang J, Li H, Zhao H (2013) The contextual group recommendation. 2013 5th International Conference on Intelligent Networking and Collaborative Systems. doi:10.1109/INCoS.2013.27
36. Thakkar S, Bhosale S, Gawade N, Mehta PS (2015) Proposed advance taxi recommender system based on a spatiotemporal factor analysis model. International Journal of Application or Innovation in Engineering & Management (IJAIEM) 4:161–166
37. Tkalčič M, Burnik U, Košir A (2010) Using affective parameters in a content-based recommender system for images. User Model User-Adapted Interact 20:279–311. doi:10.1007/s11257-010-9079-z
38. Ujjin S, Bentley PJ (2003) Particle swarm optimization recommender system. Proc 2003 I.E. Swarm Intell Symp SIS'03 (Cat No03EX706):124–131. doi:10.1109/SIS.2003.1202257
39. Vanattenhoven J, Geerts D (2015) Contextual aspects of typical viewing situations: a new perspective for recommending television and video content. Pers Ubiquit Comput 19:761–779. doi:10.1007/s00779-015-0861-0
40. Wang M, Hua XS, Hong R et al (2009) Unified video annotation via multigraph learning. IEEE Trans Circuits Syst Video Technol 19:733–746. doi:10.1109/TCSVT.2009.2017400
41. Wang J, Vries AP, De Reinders MJT (2006) Unifying user-based and item-based collaborative filtering approaches by similarity fusion categories and subject descriptors. Proceedings of the 29th Annual

International ACM SIGIR Conference on Research and Development in Information Retrieval. doi:10.1145/1148170.1148257
42. Xu Y, Yin J (2015) Collaborative recommendation with user generated content. Eng Appl Artif Intell 45: 281–294. doi:10.1016/j.engappai.2015.07.012
43. Yao W, He J, Huang G et al (2015) A graph-based model for context-aware recommendation using implicit feedback data. World Wide Web 18:1351–1371. doi:10.1007/s11280-014-0307-z
44. Yin H, Cui BIN, Chen L et al. (2015) Modeling location-based user rating profiles for personalized. ACM Trans Knowl Discov Data (TKDD) 9:1–41. doi:10.1145/2663356
45. Yuan T, Cheng J, Zhang X et al (2015) How friends affect user behaviors? An exploration of social relation analysis for recommendation. Knowledge-Based Syst. doi:10.1016/j.knosys.2015.08.005
46. Zhao S, Yao H, Sun X (2013) Video classification and recommendation based on affective analysis of viewers. Neurocomputing 119:101–110. doi:10.1016/j.neucom.2012.04.042
47. Zhao S, Yao H, Wang F et al (2014) Emotion based image musicalization. IEEE Int Conf Multimed Expo Work ICMEW. doi:10.1109/ICMEW.2014.6890565
48. Zhao S, Yao H, Zhang Y et al (2015a) View-based 3D object retrieval via multi-modal graph learning. Signal Process 112:110–118. doi:10.1016/j.sigpro.2014.09.038
49. Zhao W, Guan Z, Liu Z (2015b) Ranking on heterogeneous manifolds for tag recommendation in social tagging services. Neurocomputing 148:521–534. doi:10.1016/j.neucom.2014.07.011
50. Zhao D, Zhang L, Zhao W (2016) Genre-based link prediction in bipartite graph for music recommendation. Procedia Comput Sci 91:959–965. doi:10.1016/j.procs.2016.07.121
51. Zhou W, Duan W, Piramuthu S (2014) AC a social network matrix for implicit and explicit. Decis Support Syst. doi:10.1016/j.dss.2014.09.006
52. Zhu T, Ren Y, Zhou W et al (2014) An effective privacy preserving algorithm for neighborhood-based collaborative filtering. Futur Gener Comput Syst 36:142–155. doi:10.1016/j.future.2013.07.019

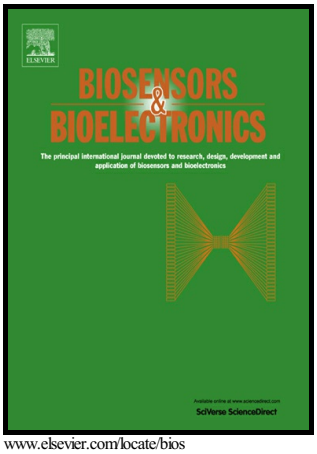


Rahul Katarya is working as an Assistant Professor in Department of Computer Science & Engineering in Delhi Technological University, Delhi India. His research interests include Big Data & prediction, Web Mining, Social Networks, Recommender systems, Personalization, Knowledge discovery, Computational intelligence, Multimedia, Human behaviour, and business intelligence.



Dr. Om Prakash Verma is HOD and Professor in Department of Computer Science & Engineering in Delhi Technological University, Delhi India. His research interests include signal processing, image processing, soft computing, evolutionary computing, nature inspired swarm algorithm.

Author's Accepted Manuscript



www.elsevier.com/locate/bios

Excellent storage stability and sensitive detection of neurotoxin quinolinic acid

Ranjana Singh, Sunayana Kashyap, Suveen kumar, Shiju Abraham, Tejendra K. Gupta, Arvind M. Kayastha, Bansi D. Malhotra, Preeti Suman Saxena, Anchal Srivastava, Ranjan K. Singh

PII: S0956-5663(16)31205-2
DOI: http://dx.doi.org/10.1016/j.bios.2016.11.053
Reference: BIOS9375

To appear in: *Biosensors and Bioelectronic*

Received date: 26 October 2016
Accepted date: 22 November 2016

Cite this article as: Ranjana Singh, Sunayana Kashyap, Suveen kumar, Shiju Abraham, Tejendra K. Gupta, Arvind M. Kayastha, Bansi D. Malhotra, Preeti Suman Saxena, Anchal Srivastava and Ranjan K. Singh, Excellent storage stability and sensitive detection of neurotoxin quinolinic acid, *Biosensors and Bioelectronic,* http://dx.doi.org/10.1016/j.bios.2016.11.053

This is a PDF file of an unedited manuscript that has been accepted for publication. As a service to our customers we are providing this early version of the manuscript. The manuscript will undergo copyediting, typesetting, and review of the resulting galley proof before it is published in its final citable form. Please note that during the production process errors may be discovered which could affect the content, and all legal disclaimers that apply to the journal pertain.

ACCEPTED MANUSCRIPT

Excellent storage stability and sensitive detection of neurotoxin quinolinic acid

Ranjana Singh[a], Sunayana Kashyap[b], Suveen kumar[c], Shiju Abraham[a], Tejendra K. Gupta[a], Arvind M. Kayastha[d], Bansi D. Malhotra[c], Preeti Suman Saxena[b*], Anchal Srivastava[a*], Ranjan K. Singh[a*]

[a]Department of Physics, Institute of Science, Banaras Hindu University, Varanasi-221005, India
[b]Department of Zoology, Institute of Science, Banaras Hindu University, Varanasi-221005, India
[c]Department of Biotechnology, Delhi Technological University, Main Bawana Road, Delhi-110042, India
[d]School of Biotechnology, Institute of Science, Banaras Hindu University, Varanasi 221005, India

pssaxena@rediffmail.com
anchalbhu@gmail.com
ranjanksingh65@rediffmail.com

[*]Corresponding Author. Phone No:+091-9450593210(P. S. Saxena)
[*]Corresponding Author. Phone No:+091-9453203122 (Anchal Srivastava)
[*]Corresponding Author. Phone No:+091-9451272424 (Ranjan K. Singh)

Accepted manuscript

Abstract

Quinolinic acid (QA) is a metabolite of tryptophan degradation obtained through kynurenine pathway, produced naturally in the mammalian brain as well as in the human cerebrospinal fluid. The presence of QA ~10-40 μM is a clear indicator of many neurological disorders as well as deficiency of vitamin B_6 in human being. In the present work; rapid, sensitive and cost-effective bio-electrodes were prepared to detect the trace amount of endogenous neurotoxin (QA). Cyclic voltammetry (CV) and differential pulse voltammetry (DPV) studies were carried out to measure the electrochemical response of the fabricated bio-electrodes as a function of QA concentrations. These devices were found to exhibit desirable sensitivity of ~7.86 mA μM^{-1} cm^{-2} in wide concentration range (6.5 μM-65 mM). The lower detection limit of this device is as low as 6.5 μM and it has excellent storage stability of ~30 days. The capability of the proposed electrochemical bio-sensor was also checked to detect QA in the real samples (human serum). These results reveal that the use of this electrochemical bio-sensor may provide a potential platform for the detection of QA in the real samples for the prior detection of many diseases.

ACCEPTED MANUSCRIPT

Keywords: *Quinolinic Acid, QPRT, Enzyme, Neurotoxin, Bio-electrodes.*

1. Introduction

Quinolinic acid (pyridine 2,3-dicarboxilic acid, hereafter referred as QA) (Heyes et al., 1992) occurs naturally in the mammalian brain in nano-molar as well as in the human cerebrospinal fluid in several nano-molar to micro-molar amounts (Heyes et al., 1992; Chen et al., 2009; Schwarcz and Pellicciari, 2002). The presence of QA is found below 100 nM, whereas the increased level of this molecule (10-40 μM) can be detected in pathological conditions (Guillemin, 2012; Leipnitz et al., 2005). The increased level of this molecule is known to be responsible for many neurological disorders such as Alzheimer, (Guillemin and Brew, 2002) Huntington disease (Schwarcz et al., 2010) and HIV associated dementia (HAD) (Guillemin et al., 2004). The presence of QA also affects the function of neurons by the activation of *N*-methyl-D-aspartate (NMDA) receptors (Birley et al., 1982; Stone and Connick, 1985). Apart from these effects, its elevated level (30-164 μM) has also been recognized as a clear indicator of deficiency of vitamin B_6 in the human being (Brown et al., 1965). All these reports reveal that the elevated level of QA can be used to detect the presence of many diseases (Guillemin, 2012; Leipnitz et al., 2005; Guillemin and Brew, 2002; Schwarcz et al., 2010; Guillemin et al., 2004; Birley et al., 1982; Stone and Connick 1985; Brown et al., 1965). Hence there is urgent need to fabricate; rapid, cost-effective, durable and sensitive sensor that can be used to detect the trace amount of QA for the early detection of many diseases as mentioned above (Guillemin, 2012;

Accepted manuscript

ACCEPTED MANUSCRIPT

Leipnitz et al., 2005; Guillemin and Brew, 2002; Schwarcz et al., 2010; Guillemin et al., 2004; Birley et al., 1982; Stone and Connick 1985; Brown et al., 1965).

Several detection techniques such as gas chromatography, mass spectrometry (During, 1989; Shoemaker and Elliott, 1991) liquid-chromatography (Patterson and Brown, 1980), thin layer chromatography (Taguchi et al., 1983), radio enzymatic assay (Foster et al., 1986) and capillary electrophoresis-mass spectrometry (Wang et al., 2013) can be utilized to determine the trace amount of QA in the biological samples. All these reported methods are time consuming as well as suffer from lack of selectivity, sensitivity and stability. Liquid chromatography with fluorimetric detection (Mawatari et al., 1995) has been reported to determine the trace amount of QA. However, this method suffers from certain limitations such as tedious procedure to handle the sample, to protect it from light and lack of selectivity. Fluorimetric detection of QA, based on catalytic activity of horseradish perioxidase (HRP) (Odo and Inoguchi, 2009) in presence of hydrogen peroxide (H_2O_2) has been available to determine trace amount of QA. In this method; QA acquires fluorescing property but some reducing and oxidizing substances were found to affect the fluorescent derivatization of QA with HRP in presence of H_2O_2. Although sensitivity associated with this method is high but lack of selectivity, stability and time consuming procedure has remained as a challenge. Hence to remove all these short-comings, fabrication of such a sensing device having excellent storage stability and quick response is highly desirable for the early detection of the trace amount of QA.

Electrochemical bio-sensors have become more powerful sensing devices in recent years (Chikkaveeraiah et al., 2009) because of its quick response, sensitivity, simplicity, reproducibility and selectivity. These sensing devices require low reagents consumption, ease of fabrication, miniaturization and continuous monitoring of the analytes (Srivastava et al., 2011).

Accepted manuscript

ACCEPTED MANUSCRIPT

As synthesized reduced graphene oxide (RGO, derivative of graphene) has become a promising material for biosensing applications recently in comparison to the graphene oxide (GO), (Srivastava et al., 2011; Schwierz, 2010; Park et al., 2012; Han et al., 2007; Pumera et al., 2010; Pumera, 2011; Huang et al., 2010; Huang et al., 2011; Wang et al., 2009; Srivastava et al., 2013). Chemically active RGO has large surface area, sufficient functional groups, potential to facilitate electron transfer from enzymes and proteins, cost-effective and easy to handle which are the essential properties of the electrochemical bio-sensors (Pumera et al., 2010; Pumera, 2011; Compton et al., 2011).

We have fabricated the cost-effective bio-sensor to detect the trace amount of QA. Various parameters (reproducibility, selectivity, magnitude of currents, linear coefficient and standard deviation) have been calculated for these devices. These bio-electrodes have good sensitivity of 7.86 mA μM^{-1} cm^{-2} with a wide range (6.5 μM- 65 mM) responses. It has good selectivity and excellent storage stability of ~ 30 days. The observed properties of the present bio-sensor are exciting and it can be useful to develop electrochemical bio-sensor for the early detection of QA. In the present work, we report results of the studies relating to the development of an electrochemical bio-sensing technique differential pulse voltammetry (DPV) to detect the trace amount of endogenous neurotoxin QA in the real samples (serum) also.

2. Experimental Section

2.1. Materials

Quinolinate phosphoribosyl transferase (QPRT) enzyme was procured from Krishgen Biosystems, New Delhi India. Quinolinic acid (QA), 2, 6 pyridine di-carboxylic acid (PD), graphite flakes, acetonitrile, magnesium nitrate, sodium citrate, *N*-hydrooxysuccinimide (NHS), *N*-ethyl-*N*-(3-dimethylaminopropyl) carbodiimide (EDC), bovine serum albumin (BSA)

Accepted manuscript

ACCEPTED MANUSCRIPT

and other analytical grade chemicals used in this work were procured from Sigma-Aldrich, India. All these materials were used without further purification.

2.2. Synthesis of reduced graphene oxide (RGO)

Graphene oxide (GO) was prepared by chemical route using Hummer's method (Marcano et al., 2010) and reduced graphene oxide (RGO) was obtained by reduction of GO with sodium citrate (Zhang et al., 2011). In this method, 100 mg sodium citrate was added into 10 ml aqueous suspension of GO (1mg/ml) and the solution was stirred magnetically at 60 ˚C for ~ 6 h. Change in color from brown to black clearly indicates the reduction of GO to RGO. The RGO was treated in the following sequence; cooled down to room temperature, centrifuged at 10,000 rpm, washed with triple distilled water repeatedly and finally dried in the oven. The dried RGO powder was dispersed into water and acetonitrile for further use.

2.3. Preparation of RGO/ITO electrodes

Electrophoretic deposition (EPD) (Srivastava et al., 2013; Srivastava et al., 2012) technique was employed to fabricate RGO films on indium tin oxide (ITO) coated glass plate with sheet resistance ~ 30 Ω cm^{-1}. In this method, ITO-coated glass substrate acted as cathode and a platinum (Pt) foil (1 cm×2 cm) acted as an anode. These electrodes were kept parallel separated by 1 cm in a colloidal suspension of RGO prepared in acetonitrile (0.5 mg dl^{-1}). The 10^{-4}-10^{-5} M solution of Mg $(NO_3)_2.6H_2O$ was added to the RGO suspension to enhance the deposition rate of RGO sheets on the cathode (ITO) (Wang et al., 2009; Compton et al., 2011). During the EPD process, DC voltage (150 V) was applied for two minutes. All these process involved in the preparation of working electrode has been depicted schematically in Fig. 1(a).

2.4. Immobilization of QPRT enzyme onto the RGO/ITO electrodes surface

Accepted manuscript

ACCEPTED MANUSCRIPT

An enzyme QPRT was covalently attached to RGO/ITO electrode. Prior to covalent attachment of the enzyme, COOH group of RGO was activated using EDC as a coupling agent and NHS as an activator. The COOH groups of RGO activated by following EDC/NHS chemistry (Srivastava et al., 2013; Sarkar and Nicholson, 1996) bind to the NH_2 groups of QPRT which results into the covalent amide bond (CO-NH) formation between RGO and QPRT. During the process of covalent attachment of QPRT to RGO/ITO electrode, 10 µl of QPRT enzyme (concentration 300 µg/ml) was freshly prepared in Tris HCl buffer (PH 8.0) and it was uniformly spread on the EDC/NHS activated RGO/ITO electrode [see Fig.1(b)]. This electrode; immobilized with QPRT was incubated in humid chamber at room temperature for ~ 6 h. Since QPRT consisted of amino acids residues having NH_2 groups hence the formation of covalent immobilization was proposed via interaction between NH_2 functional groups of QPRT and COOH groups of RGO. Non-specific sites of the bio-electrodes were blocked by using bovine serum albumin (BSA). The amide bond formation was experimentally verified by FTIR spectra of QPRT/RGO. Schematic of immobilization of QPRT on working electrode RGO/ITO treated with EDC/NHS and BSA along with sensing of QA via differential pulse voltammetry (DPV) technique has been shown in Fig. 1(b).

3. Characterization

Structural and morphological characterizations were carried out using scanning electron microscopy (SEM, Philips XL 20), transmission electron microscopy (TEM-FEI Tecnai G2 electron microscope) and X-ray diffraction (XRD, Rigakuminiflex II). Raman (In-via Raman spectrometer, Renishaw), FTIR (Spectrum 65 FT-IR spectrometer, Perkin Elmer), UV-Visible (Lambda 25 UV-Visible spectrometer, Perkin Elmer) spectroscopic techniques were employed to characterize the as synthesized RGO. All the electrochemical measurements such as cyclic

Accepted manuscript

ACCEPTED MANUSCRIPT

voltammetry (CV) and differential pulse voltammetry (DPV) were carried on Auto lab Potentiostat/Galvanostat (Eco Chemie, Netherlands) using three electrode cell configurations. Bio-electrode (QPRT/BSA/RGO/ITO), platinum foil and Ag/AgCl electrodes were used as working, counter and reference electrodes, respectively. The mixture of 5 mM $Fe(CN)_6^{4-}$ (Ferrocynide) and 5 mM $Fe(CN)_6^{3-}$ (Ferricynide) was used as the redox probe.

4. Results and discussion

4.1. Microstructural studies of RGO

SEM images of RGO shown in Fig. S1 (a) indicates the uniform and sheet like morphology which is extended to several micrometers. Further, it is clearly visible that the thin layered RGO sheets consist of several wrinkles and folds. These wrinkles and folds might have developed due to defects and functional groups present in the carbon lattice. Fig. S1 (b) shows TEM micrograph of RGO, which reveals a few layers of RGO sheets along with wrinkles and folds. HRTEM images in the inset of Fig. S1 (b) indicates that the average inter-planar spacing of the lattice fringes of RGO is found to be ~3.5Å.

The Raman spectrum of RGO has been shown in Fig. S1 (c) containing four Raman bands observed at 1352, 1595, 2708 and 2930 cm^{-1}. The most prominent Raman band observed at 1352 cm^{-1} is assigned as D band which is attributed to the disorder present in the RGO. This structural disorder may be correlated to the oxygen functional groups as well as point defects present in the system. The Raman band centered at 1595 cm^{-1} is a well-defined; G band which represents the presence of sp^2 bonded carbon atoms. Overtone of D band i.e. 2D band is found at 2708 cm^{-1}. The presence of this overtone is clearly related to the dispersive nature as a function of frequency (Srivastava et al., 2012).

Accepted manuscript

ACCEPTED MANUSCRIPT

The X-ray diffraction (XRD) pattern of RGO which has been used as a working electrode for electrochemical bio-sensing studies recorded in the range of 10°-75° is shown in Fig. S1 (d). In the XRD pattern of RGO, an intense and broad peak with a 2θ value at around 25.28˚ is observed and assigned to the (00.2) (Srivastava et al., 2013) reflection plane corresponding to an inter-planner spacing of 0.352 nm, which is in good agreement with the HRTEM study [discussed in inset of Fig. S1 (b)]. In addition to this, another peak of lower intensity is found at ~43.3˚ which is assigned to the (00.1) reflection plane of RGO (Srivastava et al., 2013). UV-Visible absorption spectrum of chemically synthesized RGO is shown in Fig. S1 (e) where triple distilled water was taken as reference to record UV-Vis spectrum of RGO. The absorption peak at 268 nm can be assigned as π-π* transition of aromatic C=C bonds (Srivastava et al., 2013). Figs. S1 (a), S1 (b), S1 (c), S1 (d) and S1 (e) have been provided in the supplementary material.

4.2. FTIR spectroscopic studies of RGO, QPRT and QPRT/RGO electrodes

The IR spectra of RGO, QPRT and QPRT/RGO have been shown by (A), (B) and (C), respectively in Fig. 2(a). The IR bands observed at 1650 and 1400 cm^{-1} are attributed to stretching and bending mode vibrations of C=O and O-H bonds of carboxyl groups present in the RGO respectively. The C-OH and C=C stretching mode of vibrations are obtained at 1110 cm^{-1}, 1631 cm^{-1}, respectively. A broad band observed at 3453 cm^{-1} is assigned to stretching vibration of O-H group. It is important to note that the IR spectra were taken in aqueous medium. The O-H bonds of water strongly absorb at ~3453 cm^{-1} which overlaps with O-H absorption of RGO. The O-H stretching band of RGO is sharp. The O-H stretching band of water being broad and strong hides the O-H stretching band of RGO. New IR band of QPRT/RGO is obtained 985 cm^{-1} due to O-H bending vibration of carboxylic group. While stretching vibrational mode corresponding to C-N becomes prominent and is observed at 1215 cm^{-1}. The intensity of

Accepted manuscript

ACCEPTED MANUSCRIPT

stretching mode of C=O in QPRT/RGO is found to be enhanced and blue shifted which confirms the amide bond formation between carboxylic and amino group of RGO and QPRT, respectively.

4.3. Electrochemical Studies

The cyclic voltammetry (CV) studies of the fabricated electrodes were conducted in phosphate buffer solution (PBS) of pH 7.0 containing 0.9% NaCl and 5 mM solution of $[Fe(CN)_6]^{3-/4-}$. Fig. 3(b) shows cyclic voltammetry (CV) studies of ITO, RGO/ITO, QPRT/RGO/ITO and BSA/QPRT/RGO/ITO electrodes. It was found from the [Fig. 2(b)] that the magnitude of current for RGO/ITO electrode (Peak current 0.580 mA) is lower than that of bare ITO electrode (Peak current 0.616 mA), which indicated the reduction in electron transfer between solution and RGO/ITO interface. The immobilization of QPRT onto the RGO/ITO electrode further lowers the magnitude of peak current (0.565 mA) as compared to that of the RGO/ITO electrode. Bovine serum albumin (BSA) has been used for blocking of non-specific sites of QPRT/RGO/ITO bio-electrode. It was observed that magnitude of the peak current decreased again to 0.521 mA after coating of BSA on the surface of QPRT/RGO/ITO electrode. This reduction in peak current can be assigned due to adsorption of BSA on RGO/ITO sites of the QPRT/RGO/ITO immunoelectrode. To investigate the interfacial kinetics of the fabricated electrodes and bio-electrodes (RGO/ITO and BSA/QPRT/RGO/ITO) scan rate studies were conducted through CV. Fig. 3 and Fig. 4 show the observed CV response of RGO/ITO and BSA/QPRT/RGO/ITO electrodes respectively as a function of the scan rate (50-150 mV/s). A shift was observed in the redox peaks with increase in scan rate. It was also observed that cathodic (Ipc) and anodic peak (Ipa) currents both vary linearly with square root of the scan rate [insets (a) in Fig. 3 and Fig. 4], which indicated that the electrochemical reaction was a

Accepted manuscript

ACCEPTED MANUSCRIPT

diffusion-controlled process (Kumar et. al., 2015). The slopes and intercepts for the bio-electrodes RGO/ITO, and BSA/QPRT/RGO/ITO can be given by equations (1-4):

$I_{pc(RGO/ITO)}$ = [0.066 mA(s/mV)× (scan rate (mV/s))$^{1/2}$] + 0.119 mA,

R^2 = 0.999, SD = 7.26 × 10^{-3} (1)

$I_{pa(RGO/ITO)}$ = –[0.044 mA(s/mV)× (scan rate (mV/s))$^{1/2}$] – 0.175 mA,

R^2 = 0.999, SD = 5.51 × 10^{-3} (2)

$I_{pc(BSA/QPRT/RGO/ITO)}$ = [0.058 mA(s/mV)× (scan rate (mV/s))$^{1/2}$] + 0.120 mA,

R^2 = 0.999, SD = 5.13 × 10^{-3} (3)

$I_{pa(BSA/QPRT/RGO/ITO)}$ = –[0.039 mA(s/mV)× (scan rate (mV/s))$^{1/2}$] – 0.152 mA,

R^2 = 0.999, SD = 4.45 × 10^{-3} (4)

The difference of cathodic (E_{pc}) and anodic (E_{pa}) peak potentials ($\Delta E_p = E_{pc} - E_{pa}$) and square root of scan rate for RGO/ITO and BSA/QPRT/RGO/ITO electrodes exhibit a linear relationship and follow equations (5) and (6). A good linear relationship indicates the facile electron transfer from medium to the electrodes [inset (b) in Fig. 3 and 4].

$\Delta E_p(V)_{(RGO/ITO)}$ = [0.015 V(s/mV) × (scan rate (mV/s))$^{1/2}$] + 0.11 V,

R^2 = 0.999, SD = 1.31 × 10^{-3}

$\Delta E_p\ (V)_{(BSA/QPRT/RGO/ITO)}$ = [0.016 V(s/mV) × (scan rate (mV/s))$^{1/2}$] + 0.13V, (5)

R^2 = 0.998, SD = 1.78 × 10^{-3} (6)

Where, R is the correlation coefficient and SD is the standard deviation.

The diffusion coefficient (D) of bio-electrode BSA/QPRT/RGO/ITO was calculated using Randle Sevick equation (Kumar et. al., 2016) (Eqn. 7) and found to be 0.31$cm^2\ s^{-1}$.

$I_p = (2.69 \times 10^5)\ n^{3/2}\ A\ D^{1/2}\ C\ \upsilon^{1/2}$ (7)

Accepted manuscript

ACCEPTED MANUSCRIPT

where Ip is the peak current of immunoelectrode, n is the number of electrons (1) transferred, A is the active surface area of the immunoelectrode (0.25 cm^2), D is the diffusion coefficient, C is the concentration of redox species (5 mmol cm^{-2}) and υ is the scan rate (50 mV/s). Surface concentration (γ) of BSA/QPRT/RGO/ITO electrode was determined by using Laviron's theory (Sharma et. al., 2012) given by

$$I_p = n^2F^2\gamma A\upsilon(4RT)^{-1} \quad (8)$$

where I_p represents the peak current of electrode, n is the number of electrons (1) transferred, F is the Faraday constant (96485 C mol^{-1}), γ is the surface concentration of the absorbed electro-active species, A is the surface area of the electrode, ν is the scan rate (V/s), R is the gas constant (8.314 J mol^{-1} K^{-1}) and T is room temperature (25 ˚C or 298 K). The equation 8 yields ϒ to be 4.42×10^{-8} mol.cm^{-2}.

4.4. Differential pulse voltammetry measurements

Differential pulse voltammetery (DPV) studies were carried out to measure the electrochemical response of the fabricated bio-electrodes (BSA/QPRT/RGO/ITO) as a function of QA concentration varying from 6.5 μM to 65 mM in PBS (pH 7.0, 0.9% NaCl) containing 5 mM $[Fe(CN)_6]^{3-/4-}$ [Fig. 5(a)]. It was observed that the magnitude of current increased with increase in concentration of QA which can be attributed to the formation of enzyme-ligand complex at the electrode surface. This process of complex formation leads to electron release at the electrode surface. QPRT; a member of the phosphoribosyl family of enzymes has been recognized to catalyze the formation of nicotinic acid mononuleotide from QA and substrate 5-phosphoribosyl-1-pyrophosphate (Bello and Grubmeyer, 2010). In this process, QA binds first to QPRT which may cause release of electron at the electrode surface. In the present work this process was monitored through differential pulse voltammetry measurements. Furthermore, a

Accepted manuscript

ACCEPTED MANUSCRIPT

linear correlation was obtained in the wide concentration range of 6.5 μM to 65 mM (R^2 = 0.993, SD = 4.71 × 10^{-4}) and follow equation [9]. Linearity between peak current of the bio-electrodes measured by differential pulse voltammetry (DPV) and QA concentration shown on log scale has been depicted in Fig. 5(b). The sensitivity of the electrode is found to be 7.86 mA μM^{-1} cm^{-2}.

I_p (mA) = 7.86 mA μM^{-1} cm^{-2} × log[concentration (μM)] + 0.143 mA,

R^2 = 0.993, SD = 4.71 × 10^{-4} (9)

Several studies on different sensing techniques and sensing characteristic of the proposed electrochemical bio-sensor BSA/QPRT/RGO/ITO discussed above have been compared and summarized in Table 1.

The stability of the BSA/QPRT/RGO/ITO electrode was determined by CV studies at a regular interval of 5 days up to 45 days [Fig. 5(c)] and stored at 4˚C until further use. It was observed that magnitude of the peak current exhibited 95% response upto 30 days and there after the peak current decreased and reached to 80% at the end of 45 days. It indicates that the stability of the fabricated BSA/QPRT/RGO/ITO bio-electrode is upto ~30 days. In order to ensure reproducibility, five different bio-electrodes of constant surface area were prepared under similar conditions and their electrochemical responses were investigated by DPV studies. These bio-electrodes exhibit good reproducibility. Mean value of the current was found equal to ~119 μA. Each measurement was repeated for three times for each electrode and error bar was included accordingly. The relative standard deviation (RSD) for each bio-electrode was less than ~5% which showed the reproducibility of the fabricated bio-electrodes is high [Fig. 5(d)]. DPV measurements have also been carried out for the detection of QA in the real sample (serum) as shown in Fig. S3.

5. Conclusions

Accepted manuscript

ACCEPTED MANUSCRIPT

Early detection of endogenous neurotoxin, quinolinic acid may be helpful to the patients suffering from many neurological disorders such as Alzheimer's, Huntington's and HIV associated dementia (HAD) as well as deficiency of vitamin B_6. In this work selective, stable and reproducible bio-electrodes have been fabricated to detect quinolinic acid. The proposed bio-sensor based on electrochemical sensing may provide potential platform for the sensitive and selective detection of QA which can be used for the early detection of the neurological disorders and other diseases in the real samples in future.

Conflict of Interests

The authors declare no competing financial interest.

Acknowledgements

Ranjana Singh is grateful to UGC, New Delhi, Govt. of India for providing financial support in terms of BHU research fellowship. One of the authors (TKG) is grateful to UGC for providing the research grant under the UGC Dr. D. S. Kothari Post-Doctoral Fellowship Scheme [No. F. 4-2/2006 (BSR)/PH/13-14/0108]. RKS is grateful to AvH Foundation, Germany, DST and CSIR, New Delhi, Govt. of India for support to procure Micro-Raman setup. AS is thankful to DST India (Project Code: DST/TSG/PT2012/68 & DST PURSE SCHEME 5050) and CAS-UGC; Departmental Programme for providing financial assistance.

Accepted manuscript

ACCEPTED MANUSCRIPT

References

Bello, Z., Grubmeyer, C., 2010. Biochemistry, 49, 1388-1395.

Birley, S., Collins, J.F., Perkins, M.N., Stone, T.W., 1982. Br. J. Pharmacol, 77, 7-12.

Brown, R.R., Yess, N., Price, J.M., Linkswiler, H., Sawan, P., Hankes, L.V., 1965. J. Nutrition, 87, 419-422.

Chen, Y., Meininger, V., Guillemin, G.J., 2009. Cent Nerv Syst Agents Med Chem. 9, 32-39.

Chikkaveeraiah, B.V., Liu, H., Mani, V., Papadimitrakopoulos, F., Rusling, J.F., 2009. Electrochem. Commun. 11, 819-822.

Compton, O.C., Jain, B., Dikin, D.A., Abouimrane, A., Amine, K., Nguyen, S.T., 2011. ACS Nano, 5, 4380-4391.

During, M.J., Freese, A., Heyes, M.P., Swartz, K.J., Markey, S.P., Roth, R.H., Martin, J. B.,1989. FEBS Lett. 247, 438-444.

Foster, A.C., Okuno, E., Brougher, D.S., Shwarcz, R., 1986. Anal. Biochem. 158, 98-103.

Guillemin, G.J., 2012. FEBS J. 279, 1356-1365.

Guillemin, G.J., Brew, B.J., 2002. Redox Rep. 7, 199-206.

Guillemin, G.J., Kerr, S.J., Brew, B.J., 2004. Neurotox. Res. 7, 103-123.

Heyes, M.P., Saito, K.J., Crowley, S., Davis, L.E., Demitrack, M., Der, A.M., Dilling, L.A., Elia, J., Kruesi, M.J.P., Lackner, A., Larsen, S.A., Lee, K., Leonard, H.L., Markey, S.P., Martin, A., Milstein, S., Mouradian, M.M., Pranzatelli, M.R., Quearry, B.J., Salazar, A., Smith, M., Strauss, S.E., Sunderland, T., Swedo, S.W., Tourtellotte, W.W., 1992. Brain. 115, 1249-1273.

Huang, Y., Dong, Shi, X., Li, Y., Li, C.M., Chen, L.-J.P., 2010. Nanoscale, 2, 1485-1488.

Han, M.Y., Oezyilmaz, B., Zhang, Y., Kim, P., 2007. Phys. Rev. Lett. 98, 206805-206809.

Huang, X. Yin, Z., Wu, S., Qi, X., He, Q., Zhang, Q., Yan, Q., Boey, F., Zhang, H., 2011. Small, **7**, 1876-1902.

Kumar, S., Kumar, S., Tiwari, S., Srivastava, S., Srivastava, M., Yadav, B.K., Kumar, S., Tran, T.T., Dewan, A.K., Mulchandani, A., Sharma, J.G., Maji S., Malhotra, B.D., 2015. Advanced Science. 2(8), 1500048.

Kumar, S., J.G., Maji S., Malhotra, B.D., 2016. Biosens. Bioelectron. 78, 497-504.

Leipnitz, G., Schumacher, C., Scussiato, K., Dalcin, K.B., Wannacher, C.M.D., Wayse, A.T.D., Dutra, C.S., Wagner, M., Latini, A., 2005. Int. J. Dev. Neurosci. 23, 695-701.

Mawatari, K.-I., Oshida, K., Iinuma, F., Watanabe, M., 1995. Anal. Chim. Acta, 302, 179-183.

Marcano, D.C., Kosynkin, D.V., Berlin, J.M., Sinitsakii, A., Sun, Z., Slesarev, A., Alemany, L. B., Lu, W., Tour, J.M., 2010. ACS Nano. 4, 4806-4814.

Odo, J., Inoguchi, M., Hirai, A., 2009. J. Health. Sci. 55, 242-248.

Pumera, M., Ambrosi, A., Bonanni, A., Chng, E.L.K., Poh, H.L., 2010. Trac-Trend Anal. Chem. 29, 954-965.

Pumera, M., 2011. Mater. Today, 14, 308-315.

Park, S.J., Kwon, O.S., Lee, S.H., Song, H.S., Park, T.H., Janng, J., 2012. Nano Lett. 12, 5082-5090.

Patterson, J.I., Brown, R.R., 1980. J. Chromatogr., 182, 425-429.

Schwarcz, R., Pellicciari, R., 2002. J. Pharmacol Exp. Ther. 303, 1-10.

Accepted manuscript

ACCEPTED MANUSCRIPT

Schwarcz, R., Guidetti, P., Sathyasaikumar, K.V., Muchowski, P.J., 2010. Prog Neurobiol. 90, 230-245.
Stone, T.W., Connick, J.H., 1985. Neuroscience, 15, 597-617.
Shoemaker, J.D., Elliott, W.H., 1991. J. Chromatogr. 562, 125-138.
Srivastava, S., Solanki, P.R., Kaushik, A., Ali, M.A., Srivastav, A., Malhotra, B.D., 2011. Nanoscale 3, 2971-2977.
Schwierz, F., 2010. NNANO, 5, 487-496.
Srivastava, S., Kumar, V., Ali, M.A., Solanki, P.R., Srivastava, A., Sumana, G., Saxena, P.S., Joshi, A. G., Malhotra, B.D., 2013. Nanoscale, **5**, 3043-3051.
Sarkar, P., Nicholson, P.S., 1996. J. Am. Ceram. Soc. 79, 1987-2002.
Srivastava, R.K., Srivastava, S., Narayanan, T.N., Mahlotra, B.D., Vajtai, R., Ajayan, P.M., Srivastava, A., 2012. ACS Nano. 6, 168-175.
Sharma, A., Pandey, C.M., Sumana, G., Soni, U., Sapra, S., Srivastava, A., Chatterjee, T., Malhotra, B.D., 2012. Biosens. Bioelectron. 38(1), 107-113.
Taguchi, H., Koyama, S., Shimabyashi, Y., Iwai, K., 1983. Anal. Biochem. 131, 194-197
Wang, X., Davis, I., Liu, A., Miller, A., Shamsi, S.A., 2013. J. Chromatogr. A, 1316, 147-153.
Zhang, Z., Chen, H., Xing, C., Guo, M., Xu, F., Wang X., Gruber, H.J., Zhang, B., Tang, J., 2011. Nano Res. 4, 599-611.

Accepted manuscript

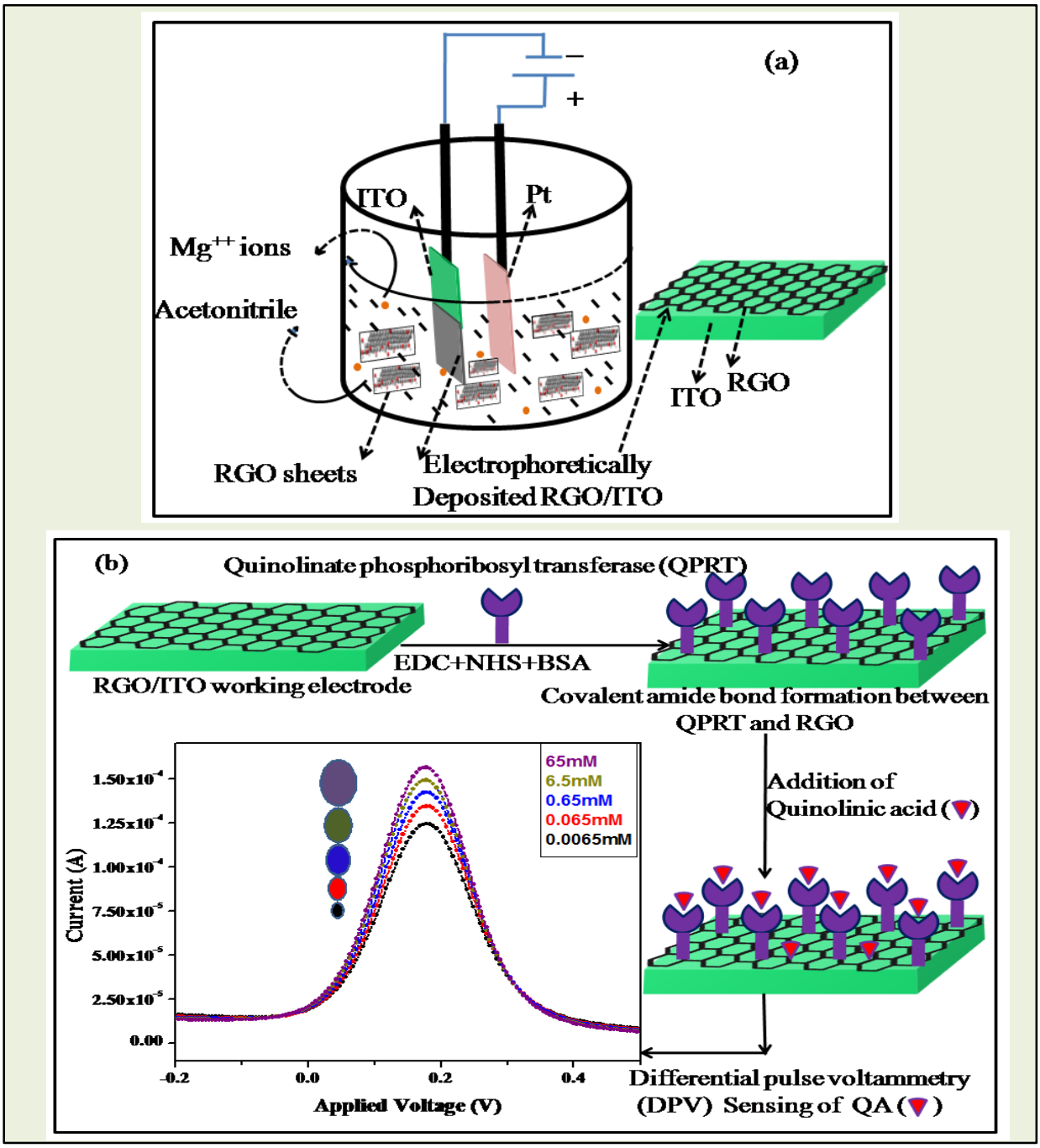


Fig. 1. Schematics for the (a) Fabrication of working electrode RGO/ITO by using electrophoretic deposition (EPD) technique and (b) immobilization of quinolinate phosphoribosyl transferase (QPRT) on working electrode RGO/ITO treated with EDC/NHS and BSA and sensing of QA via differential pulse voltammetry (DPV) technique.

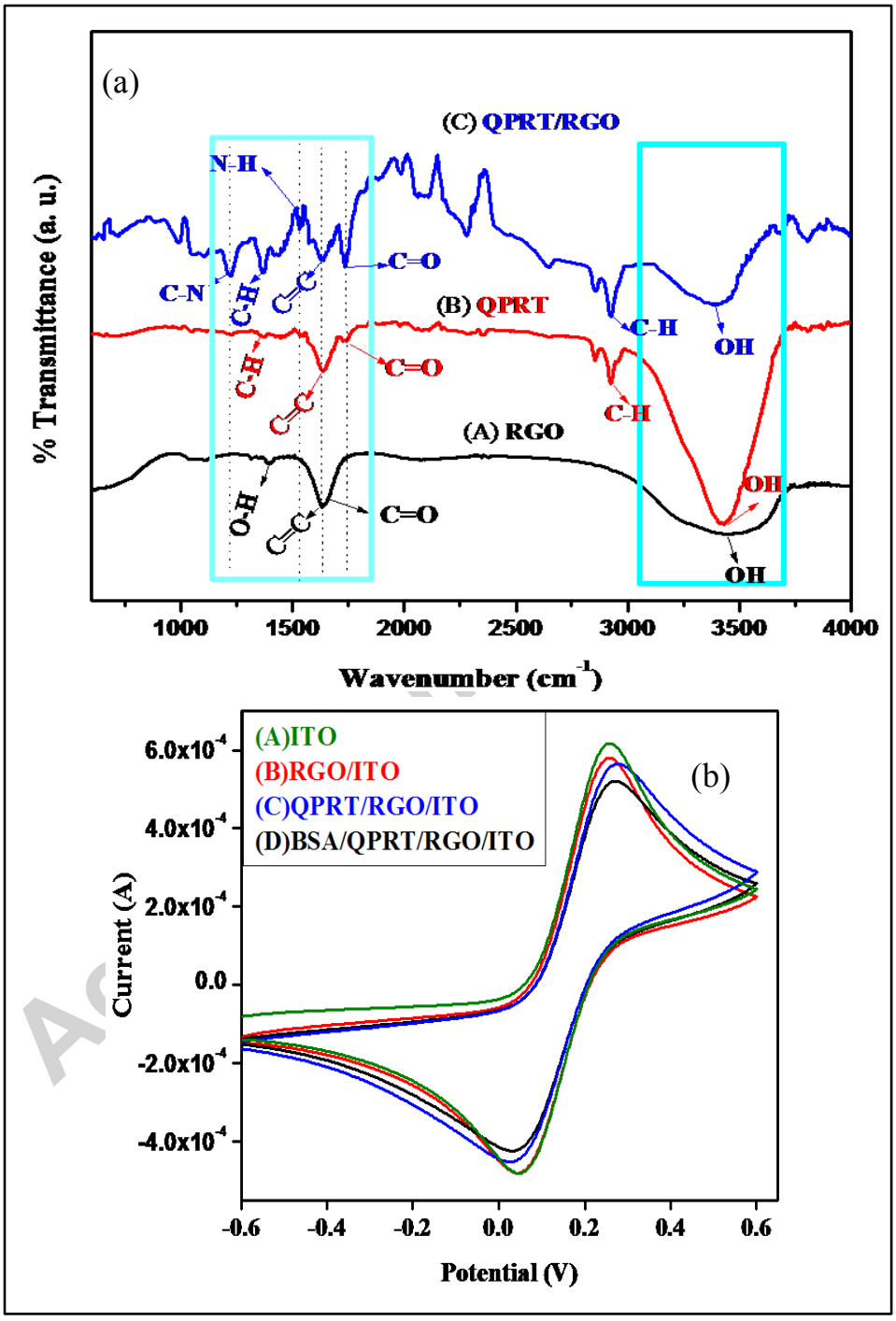


Fig. 2. (a) FT-IR spectrum of (A) RGO (B) QPRT and (C) QPRT/ RGO 3(b) CV curves of (A) ITO (B) RGO/ITO (C) QPRT/RGO/ITO and (D) BSA/QPRT/RGO/ITO electrodes.

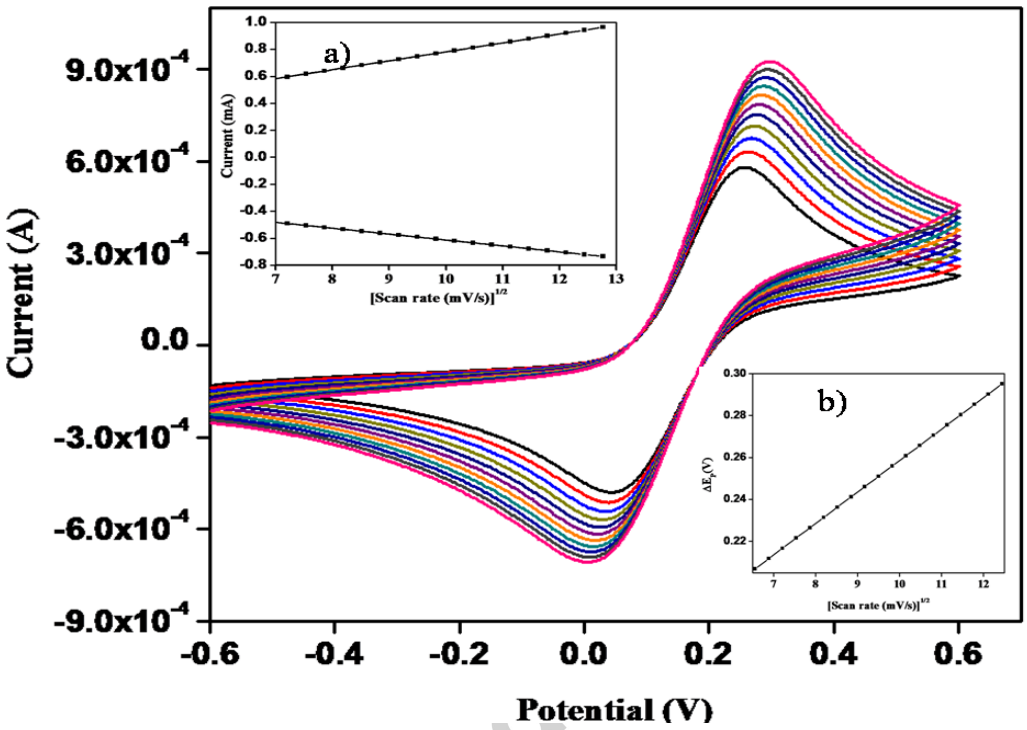


Fig. 3. Scan rate studies of RGO/ITO [Inset (a) magnitude of oxidation and reduction current generated as response of square root of scan rate (mV/s), Inset (b) potential as function of square root of scan rate] electrodes**.**

Accepted

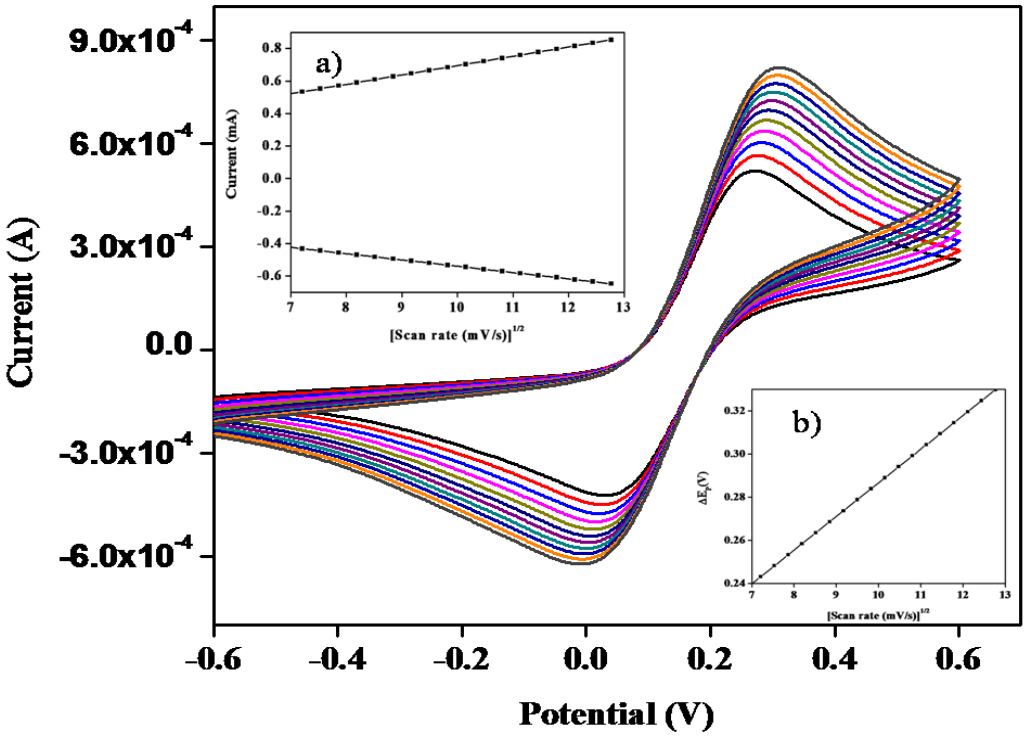


Fig. 4. Scan rate studies of BSA/QPRT/RGO/ITO [Inset (a) magnitude of oxidation and reduction current generated as response of square root of scan rate (mV/s), Inset (b) potential as function of square root of scan rate] electrodes**.**

Accepted manuscript

ACCEPTED MANUSCRIPT

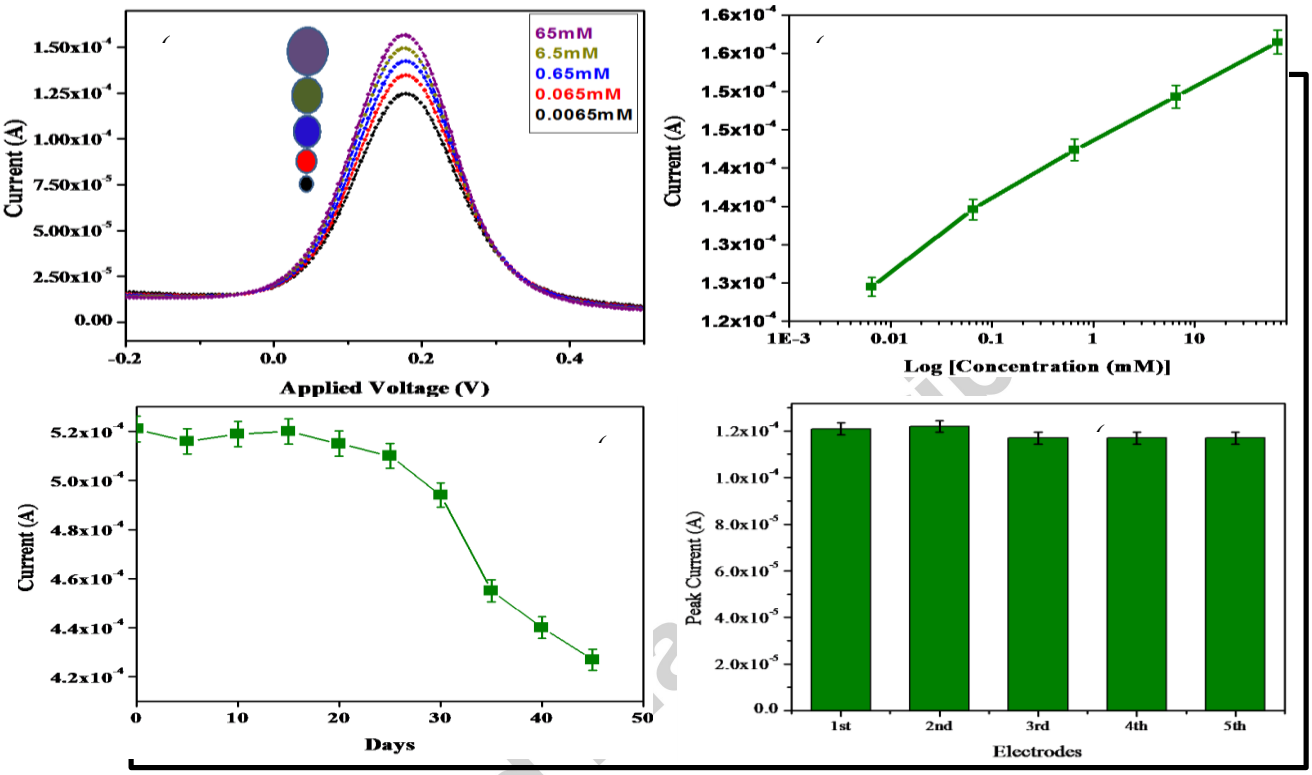


Fig. 5. (a) Electrochemical current response studies (differential pulse voltammetry, DPV) of BSA/QPRT/RGO/ITO electrode as a function of QA concentration [ranging from 6.5 µM to 65 mM] (b) Linearity between peak current of the bio-electrode measured by differential pulse voltammetry (DPV) and QA concentration has been shown on Log scale (c) Electrochemical current response studies (cyclic voltammetry, CV) of BSA/QPRT/RGO/ITO electrode as a function of time (days) and (d) Electrochemical current response studies (differential pulse voltammetry, DPV) of five different bio-electrodes BSA/QPRT/RGO/ITO fabricated via same set of procedure.

ACCEPTED MANUSCRIPT

Table1: Sensing characteristics of the proposed electrochemical bio-sensor BSA/QPRT/RGO/ITO summarized along with some results reported in the literature.

Detection Techniques of Quinolinic Acid (QA)	Detection range	Detection limit	Sensitivity	Stability (days)	References
Radio enzymatic assay for quinolinic acid	-	2.5 pmol	-	-	16
Capillary electrophoresis-mass spectrometry	0.4-40 μM	-	-	-	17
Liquid chromatography with fluorimetric detection	0.36 - 68.8 nmol ml^{-1}	-	-	-	18
Fluorimetric detection of quinolinic acid by catalytic activity of horseradish peroxidase	0.1-5 nmol ml^{-1}	0.04 nmol ml^{-1}	-	-	19
Electrochemical bio-sensor	**6.5 μM - 65 mM**	**6.5 μM**	**7.86 mA μM^{-1} cm^{-2}**	**30**	**Present work**

Accepted manuscript

Highlights

- Sensitive and selective detection of endogenous neurotoxin quinolinic acid (QA) by using electrochemical biosensor.
- Amide bond formation between quinolinate phosphoribosyl transferase (QPRT) enzyme and reduced graphene oxide (RGO)
- Electrophoretically deposited working electrode prepared by reduced graphene oxide.

Available online at www.ijapie.org

International Journal of Advanced
Production and Industrial Engineering

IJAPIE-SI-IDCM 607 (2017) 31–35

Special Issue on

INNOVATIVE DESIGN
&
COMPUTATIONAL
MODELLING

Experimental Investigation of Waste Animal Fat Methyl Ester Blends in Diesel Engine

Sharad Pratap Singh[1], Harveer Singh Pali[1]*, Naveen Kumar[2]

[1] *(Noida Institute of Engineering & Technology, Greater Noida, India)*

[2]*(Delhi Technological University, Delhi, India)*

Email: harvirpali@gmail.com

Abstract : The energy crisis is the concern that the world's demands on the limited natural resources that are used to power industrial society are diminishing as the demand rises. So alternative source is required to meet this requirement. This research work reports the preparation of Waste animal fat methyl ester (WAFME) and exhaustive trials of its blends on single cylinder-four stroke diesel engine for evaluation of performance and emission characteristics. The assessed performance parameters include Brake Thermal Efficiency (BTE) and Brake Specific Energy Consumption (BSEC). In addition, engine emissions like CO, HC, and smoke were found to be significantly reduced except NOx. Conclusions specified that WAFME- diesel blends up to 20% (v/v) could be used in the engine without modification.

Keywords: Diesel engine, Emission, Performance, Waste animal fat methyl ester

I. INTRODUCTION

Energy is essential and plays a pivotal role for growth and development of global economy. Use of fossil fuels as energy sources has become a serious matter of concern primarily because of their limited reserves and environmental problems associated with their use as fuels. The modern world has been confronted with an energy crisis to depletion of finite resources of fossil fuel. The rapidly growing demand for transport fuel and industrialization has caused serious threats to the environment and energy security of the world. Global fossil fuel consumption increased by around 40% in 2011 compared with 2010. Moreover, only half of the usual energy demand can be supplied until 2023 with the current liquid fuel reserve. The consumption of fossil fuel at this fast rate is affecting environment and is leading to ruthless effects. These environmental degradation effects include global warming, air quality deterioration, ozone depletion, eutrophication, photochemical smog, oil spills, and acid rain.

Biofuels have that capacity to replace the markets of conventional fuels to a larger extent. Due to their non-polluting and easily degrading properties, enormous research works are being carried on in this field. Continuous efforts are being made to improve quality of biodiesel. Several blends of the biodiesel along with the diesel are being used. Biodiesel, the non-toxic fuel, is biodegradable and environmentally non-threatening fuel used in diesel engines. Sulphur or aromatic compounds are negligibly present in these fuels so their combustion results in lower emission of carbon monoxides, hydrocarbons and particulates. Biodiesel is produced from biological sources such as vegetable oils, animal fats and microalgae using a biochemical process known as 'transesterification' involving reaction of the reaction of an alkoxy group of an ester (i.e., monoglyceride, diglyceride, or triglyceride) with that of a lower alcohol and a catalyst (potassium hydroxide). Biodiesel is produced through process of transesterification and methanol is the most widely used alcohol owing to its simple geometry, excellent catalyst dissolution and relatively low cost. Various alcohols such as methanol and ethanol are commonly used for trans-esterification, due to their low price, chemical and physical advantages such as polarity of short-chain alcohols. The solubility of catalyst in methanol is faster as compared to other alcohols and it can easily react with triglycerides leading to faster reaction rates. Methanol is non-renewable but ethanol being renewable in nature is now investigated for transesterification. By comparison, the formation of ethyl esters is more difficult than of methyl esters due to the differing reactivity's of alcohols with catalysts in order to produce alkoxide ion (the active moiety in transesterification).

II. MATERIALS AND METHODS

A. Biodiesel Production

Mutton Fat is taken in a beaker and heated to above 120^0 C with the help of a hot plate for 30 minutes. Solid form fat transform into liquid form. Heating of the fat above 120^0 C will reduces moisture level in the fat otherwise, presence of water in the oil will affect the biodiesel preparation as there will be more probability of the formation of soap. After heating the fat, fat is melted and the oil is then cooled to 60^0C.

Methanol is used as an alcohol and KOH is used as a homogenous base catalyst in the trans-esterification reaction. Methanol is added to the sample in the molar ratio of 1:6. KOH (0.25 % wt.) is added to the mixture and the resulting mixture is heated on the Hot plate with the help of magnetic

stirrer at below 65^0 C. After the trans-esterification reaction, the whole mixture is transferred into a separating funnel.

After 24 hours, both biodiesel and glycerol (trans-esterification by-product) separates out. Biodiesel occupies the top layer and glycerol settles down at the bottom of the separating funnel. Glycerol is separated out and Biodiesel is left in the separating Funnel.

Warm water at 50^0 C is taken in the volumetric ratio of 1:1 in the separating funnel and gently mixed with the biodiesel and the mixture is left out in the separating funnel to separate out. Washing removes the un-used KOH from the biodiesel. This process is repeated for 5-6 times. Finally, clear water is visible at the end of washing process in the separating funnel which marks the end of washing process.

Finally, Mutton Fat Methyl Ester is heated over 120^0C in the hot plate for removing the moisture content from it. After following the above processes, pure biodiesel is produced.

B. Experimental Setup and Procedure

A single cylinder, four-stroke, water cooled diesel engine was used in this research. The engine was operated at a constant speed of 1500 rpm. The fuel injection pressure was in the range of 200–205 bars. The loading was provided by an eddy current dynamometer coupled with the engine shaft. Also, an rpm encoder was attached at the end of the dynamometer for rpm measure. Fig. 1 presents the block diagram of the experimental setup.

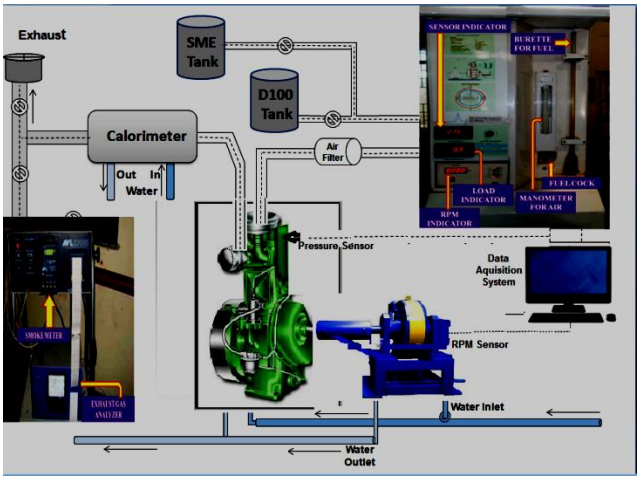


Fig. 1 Schematic diagram of the test setup used for this study

The cyclic variation of combustion pressure and the corresponding crank angle were recorded using a piezoelectric transducer. For exhaust gas temperature measurement; thermocouples (K-Type) were employed. The air flow rate was measured using a mass airflow sensor. A fuel pump measured fuel consumption rate. The fuel and air flow rates, load, rpm, pressure crank angle and temperature data were fed to the centralized data acquisition system. Engine-soft (computer software), was connected to the data acquisition system for automated and manual analyses. Test engine specifications as shown Table 1.

TABLE I
Test Engine specification

Make of the engine	Kirloskar
No. of cylinder	1
Strokes	4
Rated Power	3.5 kW@1500rpm
Cylinder diameter	87.5mm
Stroke length	110mm
Connecting rod length	234mm
Compression ratio	17.5:1
Orifice diameter	20mm
Dynamometer type	Eddy current
Rated power (dynamometer)	7.5 kW@1500rpm
Dynamometer arm length	185mm
Fuel injection timing	23^0BTDC
No. of injector holes	3
Nozzle diameter	0.148 mm
Spray orientation angle	55°CA
Injection duration	18°CA
Full load diesel injection per cycle	32.8 mg

III. RESULTS AND DISCUSSION

A. Physico-chemical characterization of WAFME

The study determines the physico-chemical properties according to standard methods. Table 2 presents the average values of triplicate analyses. The major constituents are: saturated fatty acid methyl esters and unsaturated fatty acid methyl ester (Octadecadienioc acid methyl ester).

TABLE III
PHYSICO CHEMICAL PROPERTIES OF WAFME AND ITS BLENDS

S. No	Property (units)	ASTM D6751	WAFME 100	WAFME 10	WAFME 20	D100
1	Kinematic viscosity (cSt)	D445	5.9	3.23	3.36	3.2
3	Oxidative stability (hours)	D675	<6	<6	<6	--
4	Density (g/cc)	D1298	0.8765	0.8281	0.8333	0.8227
5	Flash Point (°C)	D93	127	67.3	71.5	61
6	CFPP (°C)	D6371	12	0	4	-12
7	Calorific value (MJ/kg)	D4239	39.65	45.16	45.07	45.49

Table 2 presents the physico-chemical properties of WAFME100, diesel, and their corresponding blends. Although, WAFME40 shows 2.1 % higher density than mineral diesel, it was within the standard limit of 0.86-0.89 g/cc according to ASTM standard. The viscosity of the

WAFME100 was higher than diesel but conforms to ASTM D6751 standard. The calorific value of WAFME was comparable to baseline (D100). However, the Cold Filter Plugging Point (CFPP) of WAFME sample is 12°C as compared to -9°C exhibited by the diesel. Despite the inferior CFPP of WAFME it could be suitable to warm climatic conditions like India.

B. Engine Performance

1) Brake Thermal Efficiency (BTE)

The BTE is a vital engine performance parameter that needs to be investigated. It defines the ratio between useful mechanical work obtained at the engine shaft and the energy of the supplied fuel Fig. 2 shows the variation in BTE of various test fuels compared to the baseline data, at all loading conditions. It is significant to note that at 80% load, the BTE exhibited by WAFME10 and WAFME20 were 5.3% and 5.7% respectively, much higher than the baseline diesel operation. This could be attributed to the higher A/F ratio at higher load, coupled with the oxygenated nature of WAFME leads towards improved combustion; even at higher volume fractions. WAFME10 and WAFME20 illustrated similar BTE at all loads compared to the baseline data.

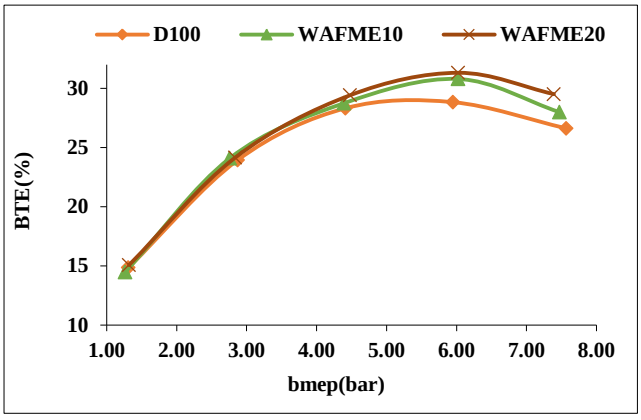


Fig. 1 Effect of brake thermal efficiency of the test fuels

It is concluded that the engine performance in terms of BTE was improved with biodiesel blends up to 20% substitution. Higher volume fraction of WAFME in the fuel, it resulted in a reduction of BTE as compared to the diesel baseline.

2) Brake Specific Energy Consumption (BSEC)

The comparative asses WAFME of volumetric consumption of fuel is an important parameter in explaining the engine performance exhibited by various test fuels. Fig. 3 shows BSEC with increasing load for the test fuels. It is pragmatic that BSEC was reduced with increasing WAFME volume fraction at 20% load. The reductions shown by the test fuels compared to the baseline data are 1.84%, 2.09%, for WAFME10 and WAFME20 respectively at 80% load condition. It was evident that WAFME10 and WAFME20 exhibited reduced BSEC compared to the baseline data. On the contrary, WAFME30 and WAFME40 illustrated higher BSEC than neat diesel data after 80% load.

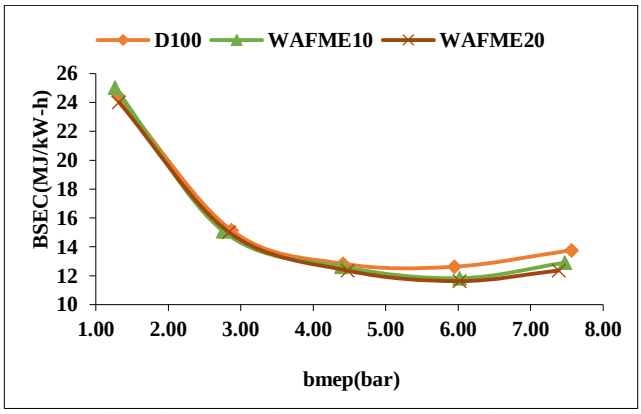


Fig.3- Effect of Brake specific energy consumption of the test fuels

3) - Exhaust temperature (EGT)

Fig. 4 shows the disparity of exhaust gas temperature with the load. It demonstrated that the temperature of the engine exhaust gasses varied linearly with load test fuels. It was evident that WAFME blends revealed reduced exhaust temperature compared to the baseline diesel at higher loads.

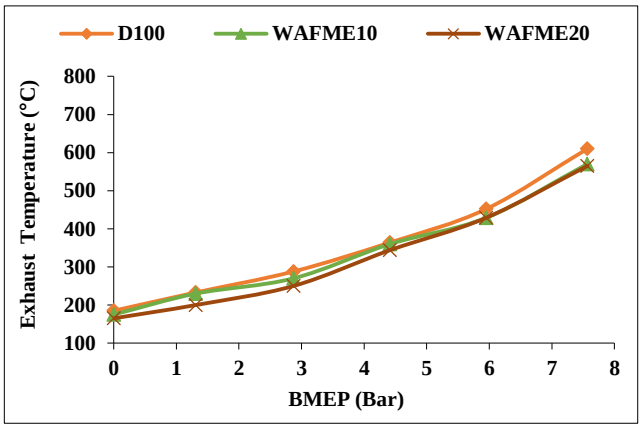


Fig.4- Effect of Exhaust temperature of the test fuels

C. Engine Emission

1) Carbon monoxide (CO)

Initially, the CO emission lower with varying load. Afterward, it records 60% load high CO emission, irrespective of test fuels. Under no-load condition, in-cylinder temperatures were fairly lower leading towards incomplete combustion. However, with increasing load, the temperature increased due to fuel injected in the cylinder. At higher temperature, improved fuel burning reduced the CO emissions. Interestingly, beyond 60% loading, higher fuel injection into the engine led to an incomplete combustion and increased CO emissions. At higher loads, WAFME and its blends revealed lower CO emissions as compared to the baseline data. Fig. 5 compares analysis of CO emissions from different WAFME blends to the baseline data. Theoretically, the air–fuel mixing process handles atomization difficulty of biodiesel, due to its higher viscosity, ensuring locally rich mixtures of biodiesel and higher CO emissions. This explains the premixed lean combustion in the excess air in the loads,

thereby reducing CO emission to almost tangible. The reduced CO emission for WAFME and its blends at higher loads was associated with biodiesel oxygenation than diesel resulting in enhanced combustion.

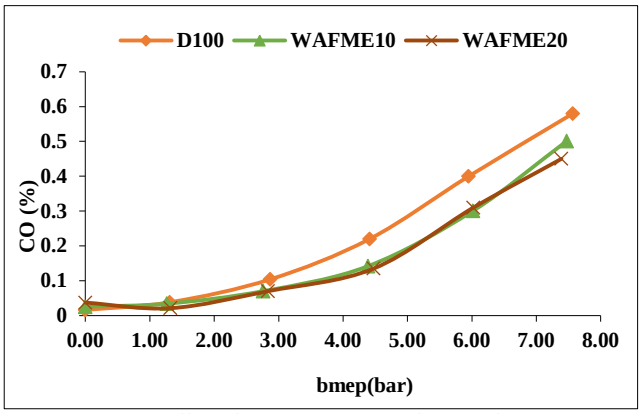


Fig.5- Effect of Carbon monoxide of the test fuels

2) Hydrocarbons (HC)

Fig. 6 presents the total hydrocarbons emission with the load. Test fuels for all loading conditions demonstrated HC reduction as compared to the baseline data. However, two basic explanations proved the description. Firstly, the HC reduction with increased fractions of WAFME in the test fuel was evident. In comparison to the neat diesel operation, it recorded up to 30% blend of WAFME in diesel, higher in-cylinder pressure and the bulk gas temperature. Secondly, WAFME has higher cetane rating and lower ignition delay than diesel.

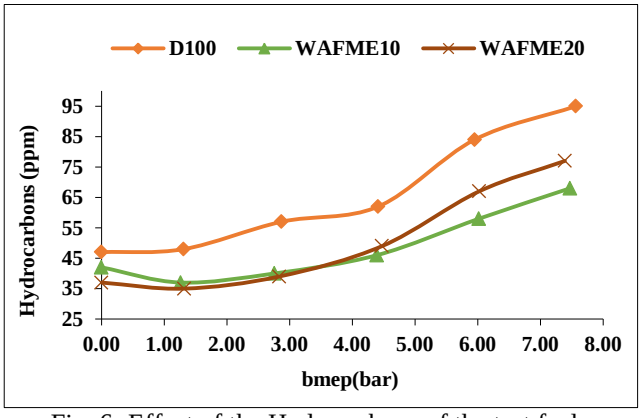


Fig. 6- Effect of the Hydrocarbons of the test fuels

Therefore, the combined effects of higher in-cylinder temperature, cetane rating and reduced ignition delay resulted in reduced emissions of HC for both WAFME and its blends compared to the baseline data of diesel.

3) Oxides of nitrogen (NO_x)

Oxides of nitrogen comprising nitrogen oxide (NO) and nitrogen dioxide (NO_2) are the critical diesel engine emissions of key concern. The "Zeldovich Mechanism" forms NO. Factors including combustion flame temperature, availability of oxygen and time for oxygen-nitrogen reaction, significantly influence NO_x formation in diesel engines [21]. Fig. 7 shows the bar chart of NO_x produced with respect to load. Lower NO_x emission is observable in all samples for WAFME and its blends, specifically at lower loading, compared to the baseline data. However, WAFME and its blends demonstrate higher NO_x emission as compared to the baseline data. The oxygenated fuel and the adiabatic flame temperature are responsible for this improvement. So, higher combustion temperatures are the predominant factor for increased NOx emissions for WAFME blends, whereas excess availability of oxygen is the predominant factor for increased NOx emissions.

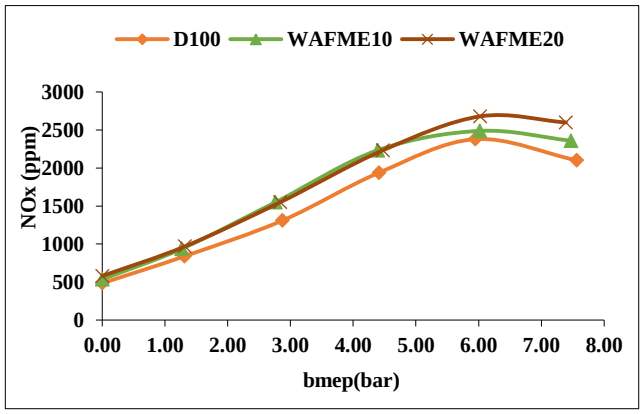


Fig. 7- Effect of the Oxides of the Nitrogen of the test fuels

4) Smoke opacity

Smoke is one of the most objectionable discharges in CI engines. The study observes that at part loads WAFME and its blends exhibit higher smoke opacities than from the baseline. Fig. 8 shows smoke opacities as exhibited by WAFME and its blends with the baseline data of diesel at various loads.

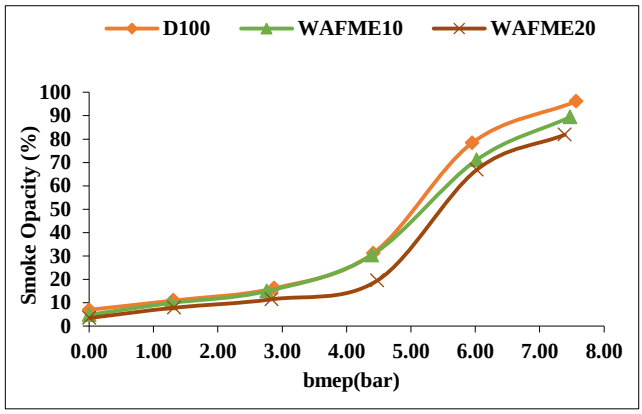


Fig. 8- Effect of the Smoke Opacity of the test fuels

This attributes to higher viscosities of biodiesel and lower in-cylinder temperatures at lower and medium engine loads, leading to poor atomization, locally rich mixtures and higher emissions of smoke [25-26]. However, like previously reported emissions, the smoke opacities at lower and medium loads are less than 50% hence, significantly lower than the 90% engine loading [27]. The researchers also record similar results.

IV. CONCLUSION

The present work evaluated the performance and emission characteristics of different WAFME-diesel blends. Physico-chemical properties of WAFME showed the dominance of saturated and oxygenated compounds, which improves its fuel properties such as its calorific value. During engine operations, lower WAFME blends demonstrated higher BTE at full load, in contrast to lower BSEC was analogous to the baseline diesel. Lower CO, HC and smoke opacity emissions were recorded as well, in contrast to the observed increasing NOx. Therefore, it is concluded that WAFME diesel blend is a potential greener fuel for CI engines.

REFERENCES

1. World development Indicators; http://data.worldbank.org. (Data taken on 07.07.2015.)
2. BP-Statistical Review of world Energy 2015. (BPSR-2015)
3. GTZ report; Liquid biofuels for transportation: India country study on potential and implications for sustainable argicuture and Energy, (2003).
4. K. Murlidharan, D. Vasudevan, K.N. Sheeba, Performance, emission and combustion characteristics of biodiesel fuelled variable compression ratio engine. Energy, 36 (2011) 5385-5393.
5. A.E. Ozcelik, H. Aydogan, M. Acaroglu, Determining the performance, emission and combustion properties of camelina biodiesel blends. Energy conversion and management, 90 (2015) 47-57.
6. A. Dhar , R. Kevin, A. Kumar, Production of biodiesel from high-FFA neem oil and its performance , emission and combustion characterization in a single cylinder DICI engine. Fuel Process. Technol, 97 (2012) 118–129. doi:10.1016/j.fuproc.2012.01.012.
7. J. Hwang, D.Qi, Y. Jung, C. Bae, Effect of injection parameters on the combustion and emission characteristics in a common-rail direct injection diesel engine fueled with waste cooking oil biodiesel. Renew. Energy. 63 (2014) 9–17. doi:10.1016/j.renene.2013.08.051
8. O. Ozener, L. Yüksek,A.T. Ergenç , M. Ozkan, Effects of soybean biodiesel on a DI diesel engine performance, emission and combustion characteristics. Fuel, 115(2012) 875-883.
9. D.H.Qi, , L.M. Geng, H. Chen, Y.Z.H. Bian,J. Liu, ,X.C.H.Ren, Combustion and performance evaluation of a diesel engine fueled with biodiesel produced from soybean crude oil. Renew. Energy, 34 (2009) 2706–2713. doi:10.1016/j.renene.2009.05.004.
10. X.Wang, Y. Ge, L.Yu, X. Feng, , Comparison of combustion characteristics and brake thermal efficiency of a heavy-duty diesel engine fueled with diesel and biodiesel at high altitude. Fuel, 107 (2013) 852–858. doi:10.1016/j.fuel.2013.01.060.
11. M.Gumus, A comprehensive experimental investigation of combustion and heat release characteristics of a biodiesel (hazelnut kernel oil methyl ester) fueled direct injection compression ignition engine. Fuel, 89 (2010) 2802–2814. doi:10.1016/j.fuel.2010.01.035.
12. A.K. Agarwal and A.Dhar, Combustion Characteristics of Rice-Bran Oil and Its Biodiesel in a Transportation Diesel Engine. Journal of Engineering for Gas Turbines and Power. 132 (2010) 2–5. doi:10.1115/1.4000143.
13. M.I. Arbab, M. Varman, H.H. Masjuki, et al., Evaluation of combustion , performance , and emissions of optimum palm – coconut blend in turbocharged and non-turbocharged conditions of a diesel engine, Energy Convers. Manag. 90 (2015) 111–120. doi:10.1016/j.enconman.2014.11.017.
14. K. Purushothaman, G. Nagarajan, Performance , emission and combustion characteristics of a compression ignition engine operating on neat orange oil, 34 (2009) 242–245. doi:10.1016/j.renene.2008.03.012.
15. A.K.Agarwal, A. Dhar, Experimental investigations of performance , emission and combustion characteristics of Karanja oil blends fuelled DICI engine, Renew. Energy. 52 (2013) 283–291. doi:10.1016/j.renene.2012.10.015.
16. T. Ganapathy, R.P. Gakkhar, K. Murugesan, Influence of injection timing on performance, combustion and emission characteristics of Jatropha biodiesel engine. Applied Energy, 88 (2011) 4376–4386.
17. H.S. Pali , N. Kumar, Y. Alhassan, Amardeep, Process Optimization of Biodiesel Production from Sal Seed Oil using Response Surface Methodology [RSM] and Diesel. SAE Technical Paper 2015-01-1297; (2015). doi:10.4271/2015-01-1297.
18. H.S. Pali , N. Kumar, Y. Alhassan, Performance and emission characteristics of an agricultural engine with Sal methyl ester and diesel. Energy Conversion and Management90(2015)146-153. http://dx.doi.org/10.1016/j.econman.2014.10.064.
19. P.K. Sahoo, L.M. Das, Combustion analysis of Jatropha, Karanja and Polanga based biodiesel as fuel in a diesel engine. Fuel, 88 (2009) 994–999.
20. D.H. Qi, H. Chen, L.M. Geng, Y.Z. Bian, Experimental studies on the combustion characteristics and performance of a direct injection engine fuelled with biodiesel/diesel blends. Energy Conversion and Management 51 (2010) 2985–2992.
21. M. Lapuerta, O.A . Jose, R. Ferna´ndez, Effect of biodiesel fuels on diesel engine emissions. Progress in Energy and Combustion Science. 34, (2008) 198–223.
22. H. Raheman and S.V.Ghadge, Performance of compression ignition engine with mahua (Madhuca indica) biodiesel. Fuel, 86 (2007) 2568–2573.
23. S Godiganur, C.H.S Murthy, R.P.Reddy, 6BTA 5.9 G2-1 Cummins engine performance and emission tests using methyl ester mahua (Madhuca indica) oil/diesel blends. Renewable Energy 34 (2009) 2172–2177.
24. R.J. Last, M. Kruger, M. Durnholz. Emissions and performance characteristics of a 4-stroke, direct injected diesel engine fuelled with blends of biodiesel and low sulphur diesel fuel. SAE paper, no. 950054; (1995).
25. E.Buyukkaya, Effects of biodiesel on a DI diesel engine performance, emission and combustion characteristics. Fuel 89 (2010) 3099–3105.
26. A. Monyem, Van Gerpen, M. Canakci, The effect of timing and oxidation on emissions from biodiesel-fueled engines. ASAE , 44, (2001) 35–42.
27. M.R. Chao, T.C. Lin, H.W. Chao, F.S Chang, C.B. Chen, Effects of methanol-containing additive on emission characteristics from a heavy-duty diesel engine. Sci Total Environ. 279 (2001)167–79.

This article has been accepted for publication in a future issue of this journal, but has not been fully edited. Content may change prior to final publication. Citation information: DOI 10.1109/TIP.2017.2665975, IEEE Transactions on Image Processing

Fuzzy-Contextual Contrast Enhancement

Anil Singh Parihar, *Member, IEEE*, Om Prakash Verma, *Member, IEEE* and Chintan Khanna

***Abstract*—This paper presents contrast enhancement algorithms based on fuzzy contextual information of the images. We introduce fuzzy similarity index and fuzzy contrast factor to capture the neighborhood characteristics of a pixel. A new histogram, using fuzzy contrast factor of each pixel is developed, and termed as the fuzzy dissimilarity histogram (FDH). A cumulative distribution function (CDF) is formed with normalized values of FDH and used as a transfer function to obtain the contrast enhanced image. The algorithm gives good contrast enhancement and preserves the natural characteristic of the image. In order to develop a contextual intensity transfer function, we introduce a fuzzy membership function based on fuzzy similarity index and coefficient of variation of the image. The contextual intensity transfer function is designed using the fuzzy membership function to achieve final contrast enhanced image. The overall algorithm is referred as the fuzzy contextual contrast-enhancement (FCCE) algorithm. The proposed algorithms are compared with conventional and state-of-art contrast enhancement algorithms. The quantitative and visual assessment of the results is performed. The results of quantitative measures are statistically analyzed using t-test. The exhaustive experimentation and analysis show the proposed algorithm efficiently enhances contrast and yields in natural visual quality images.**

***Index Terms*— Contrast enhancement, fuzzy logic, histogram equalization, context adaptive.**

I. INTRODUCTION

CONTRAST enhancement improves the visual perception of an image. The details of the image are enhanced by increasing the intensity difference between the objects and background to improve the visual quality. There are several contrast enhancement algorithms in the literature. Histogram equalization (HE) [1] is one of the most popular enhancement techniques. The advantage of HE is its simplicity with reasonably good results. However, HE tends to over-stretch intensity levels. Thus, HE introduces various artifacts such as saturation and halo artifacts.

There have been various attempts to overcome the drawbacks of HE. A family of the algorithms tried to preserve the mean brightness of the original image, while enhancing the contrast. In general, these algorithms divide original histogram into sub-histograms and equalize each division independently. Bi-histogram equalization (BBHE) [2] divides the histogram at the mean intensity. Recursive mean-separated histogram equalization (RMSHE) [3] used BBHE in a recursive manner to preserve the original mean intensity. Kim & Chung [4], proposed a modification to RMSHE, the sub - histograms are modified before equalization. Dynamic histogram equalization (DHE) [5] divides the histogram at local minima, and the dynamic range allotted to each sub-histogram is kept in proportion to the ratio of the original image. In brightness preserving histogram equalization (BPDHE) [6] local maxima are used for sub-histogram divisions, and mean brightness is preserved by brightness normalization. Sengee & Choi [7] used all non-zero bins as initial sub-histograms, then clusters are formed by merging the related bins. Singh *et al.* [8] presented a recursive histogram division based algorithm using image exposure. The mean brightness preserving algorithms have limited applications. These algorithms may fail to give significant contrast enhancement for images with very low (or very high) mean intensity. Moreover, algorithms involving histogram division tend to show sprectrum effect due independent equalization of sub-histograms and limited dynamic range of some of the sub-divisions. However, DHE based algorithms some what reduce these artifacts.

The fuzzy theory has also found many applications in contrast enhancement. Pal & King [9] used a fuzzy property of the image and applied a contrast intensifier. Hanmandlu & Jha [10] proposed a global contrast intensification operator and fuzzy quality measures. The contrast enhancement is achieved by minimizing fuzzy entropy. Hanmandlu *et al.* [11] proposed an algorithm for the enhancement of the under exposed and overexposed images using fuzzy theory. The bacterial foraging algorithm (BFA) is used for parameter optimization. The algorithm performs well, however complexity is high due BFA. Sheet *et al.* [12] used a fuzzy histogram to smoothen the histogram and presented a modified BPDHE algorithm. The algorithm works well for low dynamic range images, but the performance degrades for images with full dynamic range.

Most of the methods discussed so far use global enhancement. However, global enhancement ignores local characteristics of a pixel and may result in artifacts. In the local histogram equalization (LHE) [1, 13], pixels in the small neighborhood are considered for histogram equalization. LHE incorporates local property, but may introduce the checkerboard artifacts. Celik [14, 15] constructed a two-dimensional histogram to consider contextual properties of the pixels. However, the pixels with equal intensity are transformed to the same intensity irrespective of the pixel's

Manuscript received October 19, 2015; revised June 19, 2016, and August 16, 2016; Accepted January 24, 2017.

Anil Singh Parihar[1], Om Prakash Verma[2], and Chintan Khannna[3] are with Department of Computer Science & Engineering, Delhi Technological University, Delhi, India (e-mail: [1]parihar.anil@gmail.com, [2]opverma.dce@gmail.com, [3]mail4chintan@yahoo.com).

This paper has supplementary downloadable material available at http://ieeexplore.ieee.org., provided by the author. The material includes high resolution color version of one or more image used in the paper. Contact parihar.anil@gmail.com for further questions about this work.

1057-7149 (c) 2016 IEEE. Personal use is permitted, but republication/redistribution requires IEEE permission. See http://www.ieee.org/publications_standards/publications/rights/index.html for more information.

This article has been accepted for publication in a future issue of this journal, but has not been fully edited. Content may change prior to final publication. Citation information: DOI 10.1109/TIP.2017.2665975, IEEE Transactions on Image Processing

location. It may degrade the quality of enhanced images. Moreover, creating a 2-D histogram increases the complexity, which makes these methods computationally inefficient. Lee *et. al* [16] proposed a layered representation of 2-D histogram. The contrast enhancement is achieved by optimally increasing the frequently occurring gray level differences. Celik [17] presented another enhancement algorithm referred as spatial entropy-based contrast enhancement in discrete cosine transform (SECEDCT). The algorithm performs local contrast enhancement using the spatial entropy of a 2-D histogram, and global contrast enhancement is achieved by DCT. SECEDCT gives enhanced images with natural visual quality. However, SECEDCT is computationally demanding algorithm as it involves a 2-D histogram.

Huang *et al.* [18] presented a modification to gamma correction technique [1], where gamma is adaptively computed from the weighted histogram of the image. The algorithm requires careful selection of parameters, which may degrade the performance. Abdoli *et al.* [19] used Gaussian mixture model to approximate the histogram and stretched the individual components to utilize entire dynamic range. Wei *et al.* [20] proposed an enhancement algorithm based on entropy maximization by merging non-zero bins. However, reducing the number of gray levels may result in saturation. Fu *et al.* [21] proposed an algorithm to perform both global and local contrast enhancement. The histogram is modified using a sigmoid function for global enhancement and used DCT for local contrast enhancement. Singh *et al.* [22] proposed a histogram equalization approach using a histogram of the textured region. The algorithm may fail to give significant enhancement for smooth regions. Chen and Beghdadi [23] presented a contrast enhancement algorithm based on the multiscale Retinex model. The global mapping is performed using gamma correction, and local enhancement is achieved by modified Retinex filter. Fu *et al.* [24] presented a variational retinex model without using logarithmic transformation. However, this algorithm involves several parameters and a particular set of parameters may not be suitable for all types of images. Liang *et al.* [25] proposed a method to estimate illumination of an image by iteratively solving the nonlinear diffusion equation. The algorithm gives good contrast but may result in faded colors due to an excessive increase in the brightness.

Most of the contrast enhancement methods suffer from either of the following drawbacks:

- The dominant components of the intensity histogram get over-enhanced, and the less-frequent intensity levels are suppressed.
- All pixels of the same intensity are transformed to a single intensity, irrespective of contextual information. It may degrade the visual perception of the images.
- Contrast enhancement using global properties, may not improve the contrast of all the regions of the image.
- Contrast enhancement using local properties may over-enhance some regions while some other regions may not improve. It may result in the checkerboard artifacts.
- Computational complexity may be high, which makes the algorithm inefficient for practical uses.
- The algorithm may involve parameters, which requires careful selection or computationally demanding optimization.

In this paper, we propose a new contrast enhancement algorithm based on the fuzzy contextual information. The proposed algorithm increases the intensity differences according to the local characteristics (contextual information) of the input image. To incorporate the contextual information, a fuzzy dissimilarity histogram (FDH) is introduced. An intensity transfer function is constructed from FDH, and used for contrast enhancement. The algorithm is further extended to incorporate the contextual behavior, in the intensity transfer function. A fuzzy membership function is formulated to characterize the neighborhood property of the pixels. The final enhanced image is obtained by a new intensity transfer function, which depends on pixel's location along with intensity. The exhaustive experimentation shows that the proposed algorithm results in a natural visual perception for contrast enhanced image. The main contributions of this work are as follows:

- The introduction of the fuzzy similarity index φ and fuzzy contrast factor (FCF) to develop the fuzzy measures of dissimilarity of a pixel with its neighborhood.
- The introduction of an FDH, based on FCF, to achieve the global contrast enhancement, involving contextual properties of the image.
- The development of a new fuzzy membership function using the fuzzy similarity index φ, and the coefficient of the covariance (CV).
- The introduction of a new contextual intensity transfer function, which uses the contextual information along with intensity.

The rest of the paper is organized as follows. The proposed algorithm is presented in Section II. The experimental results and analysis are presented in Section III. The conclusion of the work is presented in section IV.

II. The Proposed Approach

We propose a contrast enhancement algorithm based on fuzzy contextual information of the pixels. The framework of the proposed algorithm is shown in Fig. 1. The algorithm consists of two modules. In the first module, an FDH is constructed using the membership values of a fuzzy set "dissimilar". An intensity transformation function, derived from FDH is used to obtain the enhanced image. This module of the algorithm is referred as Fuzzy Dissimilarity Histogram Equalization (FDHE). The second module is referred as Context Adaptive Contrast Enhancement (CACE). The CACE uses contextual information of each pixel to further improve the contrast enhancement and restores the natural characteristics of the image. A contextual intensity transfer function based on the pixel's location and its intensity is formulated in CACE. The overall algorithm is termed as the fuzzy contextual contrast enhancement (FCCE) algorithm.

1057-7149 (c) 2016 IEEE. Personal use is permitted, but republication/redistribution requires IEEE permission. See http://www.ieee.org/publications_standards/publications/rights/index.html for more information.

This article has been accepted for publication in a future issue of this journal, but has not been fully edited. Content may change prior to final publication. Citation information: DOI 10.1109/TIP.2017.2665975, IEEE Transactions on Image Processing

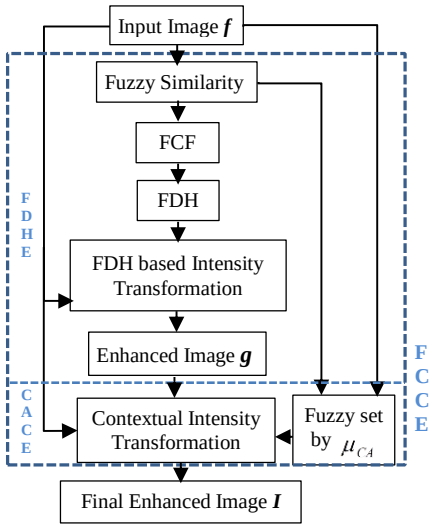


Fig. 1 The framework of the proposed algorithm FCCE

A. Motivation

The contrast of an image can be enhanced by increasing the intensity level differences between neighboring pixels [14]. However, an inappropriate increase in the differences may result in a degraded image. Consider a smooth region of an image, if intensity level differences are increased in the smooth region, the enhanced image would become noisy. On the other hand, the increase in the intensity level differences in a highly detailed region would result in a pleasant visual perception. Thus, the magnitude of difference increment should be according to the local characteristics of the region. A context adaptive algorithm is required to compute the appropriate magnitude of the increase in the intensity level differences for each pixel.

Most of the histogram based algorithms perform intensity transformation based on pixel distribution in the histogram. This may lead to over-enhancement (or under-enhancement) due to dominating (or inferior) components of the histogram. Many algorithms tackle this problem by suppressing the dominating components and enhancing the inferior components. However, this may distort the natural characteristics of the image and may result in degraded images. Moreover, most of the algorithms transform the intensities based on their value only, without considering the neighborhood. This may lead to unpleasant visual perception. For example, consider two pixels of same intensity one located in a smooth region and other on an edge. For better contrast, an edge pixel may require higher change in the intensity than a pixel in the smooth region. Thus, the transfer function should involve the location of the pixel along with its intensity.

On the contrary to other algorithms, we constructed the histogram using FCF of image pixels. FCF gives the degree of dissimilarity (contrast) of a pixel from its neighborhood. Computing such degree of dissimilarity always has some vagueness, which is best dealt by the fuzzy theory. Thus, a fuzzy membership function is devised to measure the degree of similarity of a pixel with its neighborhood, and the complement of which gives FCF. A cumulative distribution function (CDF) is derived from FDH and used as an intensity transformation function. The intensity histogram and FDH for "House" and "nest" images are shown in Fig. 2. In the intensity histogram, the peaks occur at the intensity levels corresponding to smooth regions because of a large number of similar intensity pixels. Thus, the saturation effect is shown in most of the HE based algorithms. However, in FDH the pixels in the smooth region have lower FCF and distributed in the lower end of the FDH. Thus, the magnitude of the change in intensities is almost equal for the pixels in the smooth regions. In other words, the intensity difference among the smooth region pixels in not changed much. Thus, the smooth regions do not get overstretched, while detailed regions are significantly enhanced. Although, the contextual information is used to construct FDH, but pixels with equal intensity in the input image are transformed to the same intensity in the enhanced image, irrespective of characteristics of the pixel's neighborhood. Thus, the local characteristics of the pixels are formulated in terms of another fuzzy membership function and used to control the level contrast enhancement.

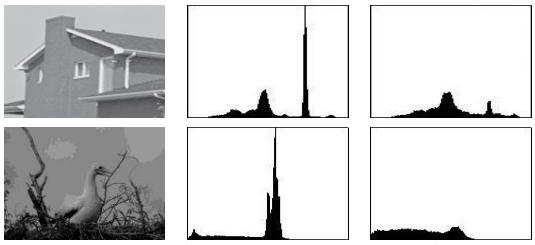


Fig. 2 Image, intensity histogram, Fuzzy Dissimilarity Histogram (FDH)

B. Fuzzy Dissimilarity Histogram Equalization

In this section, the first module of the algorithm i.e. FDHE is described. The FDH is constructed using a fuzzy property (FCF) of the input image. A CDF is derived from FDH and used as an intensity transfer function to achieve contrast-enhancement.

1) Fuzzy Dissimilarity Histogram

Consider an input image $\mathbf{f}$ of size $M \times N$, i.e. $\mathbf{f} = \{ f(x,y) | 0 \le x \le M-1, 0 \le y \le N-1 \}$. A general pixel intensity at location (x,y) is denoted as $f(x,y) = r_k$, where $k \in \{0,1,...,L-1\}$ and L is the number of intensity levels. We calculate fuzzy neighborhood similarity for each pixel in a 3×3 neighborhood. The fuzzy membership function for calculating fuzzy neighborhood similarity of a pixel in 3×3 neighborhood of a pixel at (x,y) is given as:

$$\mu_{ns}(u,v) = \max\left\{1 - \left| f(x,y) - f(u,v) \right| / \sigma, 0\right\} \qquad (1)$$

where $u = x+i, v = y+j; \quad i, j \in \{-1,0,1\}$ and σ is standard deviation of the input image. These membership values of the neighboring pixels are used to construct a fuzzy set "similar", defined by the fuzzy membership function φ. The membership function φ is referred as fuzzy similarity index and defined as:

1057-7149 (c) 2016 IEEE. Personal use is permitted, but republication/redistribution requires IEEE permission. See http://www.ieee.org/publications_standards/publications/rights/index.html for more information.

This article has been accepted for publication in a future issue of this journal, but has not been fully edited. Content may change prior to final publication. Citation information: DOI 10.1109/TIP.2017.2665975, IEEE Transactions on Image Processing

$$\varphi(x,y) = (1/9)\sum_{i=-1}^{1}\sum_{j=-1}^{1}\mu_{ns}(x+i, y+j) \quad (2)$$

A new fuzzy set "dissimilar" is obtained by taking compliment [26] of the fuzzy set "similar". Thus, the membership function of the fuzzy set "dissimilar" is (referred as FCF) given as:

$$\mu_{Cf}(x,y) = \bar{\varphi}(x,y) \quad (3)$$

The FCF gives the degree of the dissimilarity (contrast) of a pixel from its neighborhood. A fuzzy dissimilarity histogram $\mathbf{H}_{fd}$ is constructed using FCF values of each intensity level in the image.

$$\mathbf{H}_{fd} = \{h_{fd}(r_k) \,|\, 0 \le r_k \le L-1\} \quad (4)$$

$$h_{fd}(r_k) = \sum_{x=0}^{M-1}\sum_{y=0}^{N-1}\mu_{r_k}(x,y) \quad (5)$$

$$\mu_{r_k}(x,y) = \begin{cases} \mu_{Cf}(x,y), & if\ f(x,y) = r_k \\ 0, & otherwise \end{cases} \quad (6)$$

The FDH (fuzzy dissimilarity histogram) accounts for the contextual information present in the neighborhood of a pixel. It gives the mean dissimilarity measure of each intensity level present in the image. The comparison of FDH with intensity histogram is shown in Fig. 2.

2) Contrast enhancement using FDH

The contrast enhancement is achieved by equalizing FDH. The FDH is normalized to get probabilistic distribution as:

$$p_{fd}(r_k) = h_{fd}(r_k) \Big/ \sum_{k=0}^{L-1} h_{fd}(r_k) \quad (7)$$

The CDF is obtained from $p_{fd}(r_k)$ as:

$$C_{fd}(r_k) = \sum_{j=0}^{k} p_{fd}(r_j) \quad (8)$$

The image $\mathbf{g} = \{g(x,y) \,|\, 0 \le x \le M-1, 0 \le y \le N-1\}$ is obtained using following intensity transformation.

$$s_k = s_0 + (s_{L-1} - s_0) C_{fd}(r_k) \quad (9)$$

The intensity levels present in the image $\mathbf{g}$ are denoted as $s_k \in \{0,1,...,L-1\}$. For 8-bit image $s_0 = 0$ and $s_{L-1} = 255$. The FDHE achieves the contrast enhancement by spreading the intensity distribution according to the fuzzy dissimilarity of the intensity levels. The height of a bin in FDH depends on the number of pixels of an intensity and the FCF value of each pixel of that intensity. Thus, the bins corresponding to smooth regions would not have a peak, despite the large no of pixels of the same intensity as the pixels have FCF values close to zero. Thus, the smooth regions are not overstretched, and saturation effect does not occur. However, the pixels in the highly detailed regions have high FCF values and the corresponding bins have peaked in FDH. Thus, the intensity level differences in detailed regions are sufficiently increased.

C. Context Adaptive Contrast-enhancement

FDHE gives good contrast enhancement, but pixels with equal intensities are transformed to the same intensity, which may degrade the enhanced image. Thus, to restore the natural characteristics of the image, an intensity transfer function based on the intensity level r_k and the location (x,y) of the pixel is formulated. A new fuzzy set "contextual contrast" is derived from the image, and defined by following membership function.

$$\mu_{CA}(x,y) = \exp\left(-\varphi^2(x,y)\sigma/m_0\right) \quad (10)$$

Where φ is the fuzzy similarity index, defined in (2), σ and m_0 are the standard deviation and the mean intensity of the input image, respectively. The ratio σ/m_0 is called coefficient of variation (CV) [27]. The CV represents the dispersion of intensities. Thus, a high contrast image has high CV value. It is a global property of the input image. It may be observed from (10) that for a higher value of CV, μ_{CA} assigns lower membership values and vice-a-versa (for fixed value of φ). In other words, a high contrast image has lower membership values in the fuzzy set "contextual contrast" and vice-a-versa. For a given image (i.e. fixed CV value), the pixels in the smooth region are assigned lower membership value, and those of detailed region are assigned high membership value. Remember φ has high value for pixels in the smooth region and low value for pixels in the detailed region. A transformation function based on contextual information is defined using fuzzy membership function μ_{CA} as:

$$I(x,y) = \mu_{CA}(x,y)\, g(x,y) + \bar{\mu}_{CA}(x,y)\, f(x,y) \quad (11)$$

where $\mathbf{I} = \{I(x,y) \,|\, 0 \le x \le M-1, 0 \le y \le N-1\}$ is the final contrast-enhanced image. It may be observed from (11) that the final intensity of the pixels in the smooth region approach to the original value, and those of in the highly detailed region the intensity approach to enhanced intensity level obtained by FDHE. Moreover, a higher value of CV represents better contrast image i.e. lesser enhancement is required. Therefore, a good contrast image is not over-enhanced by the proposed approach. Which is again a desired property. Thus, the CACE modulates the contrast-enhancement achieved by FDHE according to contextual properties of the pixel. CACE restores the natural visual appearance of the input image using contextual information.

D. Color Image Contrast-enhancement

We have used HSV color model to represent the color images. The contrast-enhancement of color images can be effectively achieved by using the luminance component (V) [10, 17] only. Component V represents non-chromatic information present in the image. Thus, the proposed algorithm is applied to V component only. The hue (H) and Saturation (S) components are not changed. It helps in preserving the chromatic information of the original image. Alternatively, the proposed algorithm can be applied to each component of the RGB color model, but it increases computation cost. The use of HSV model over RGB model makes the proposed algorithm universally applicable, i.e. for both gray and color images.

III. Experimental Results and Analysis

The proposed algorithm is tested on nearly all kinds of low contrast images. The image databases used in this are: the Berkeley image database [28], USC-SIPI image Database [29], CSIQ image database [30], and TID2013 image database [31]. The performance of the proposed approach is tested on

1057-7149 (c) 2016 IEEE. Personal use is permitted, but republication/redistribution requires IEEE permission. See http://www.ieee.org/publications_standards/publications/rights/index.html for more information.

This article has been accepted for publication in a future issue of this journal, but has not been fully edited. Content may change prior to final publication. Citation information: DOI 10.1109/TIP.2017.2665975, IEEE Transactions on Image Processing

more than 500 images. The proposed approach is compared with conventional and state-of-art approaches: HE [1], CELDR [16], SECEDCT [17], NECI [23], REIA [24], NDFE [25]. The MATLAB codes for CELDR, SECEDCT, RECI, and NDFE are provided by corresponding authors. HE and NECI are implemented with default parameters, as suggested in respective papers. The quantitative and visual assessment of the enhanced images by various methods is carried out to analyze the overall performance.

A. Quantitative Assessment

The quantitative assessment of the contrast enhancement algorithm is a challenging task. There is no particular universally accepted quantitative quality assessment method for enhanced images. All the methods fail to capture visual contrast quality of images in one or other situations. We use two qualitative measures for contrast quality assessment: the normalized discrete entropy (DE_N) [15, 32], and measure of enhancement EME [33]. The contrast measure of the color images is computed using luminance component, as other components are preserved in most of the algorithms.

1) Normalized Discrete Entropy

The entropy is a measure of information present in the image. Higher the entropy greater the information and vice-a-versa. The discrete entropy [32] of the input image $\mathbf{f}$ is given as:

$$DE(\mathbf{f}) = -\sum_{k=0}^{L-1} p_r(r_k)\log(r_k) \quad (11)$$

Similarly, the discrete entropy of enhanced image $\mathbf{I}$ is given as:

$$DE(\mathbf{I}) = -\sum_{k=0}^{L-1} p_z(z_k)\log(z_k) \quad (12)$$

where L is the maximum possible number of levels of intensities present in the image; r_k and z_k are the k^{th} intensity levels present in the input and the enhanced images, respectively; p_r and p_z are the normalized histograms of the input and the enhanced images, respectively.

The normalized discrete entropy [15] between input and enhanced images is defined as:

$$DE_N(\mathbf{f},\mathbf{I}) = 1/\left(1+(\log(L)-DE(\mathbf{I})/\log(L)-DE(\mathbf{f}))\right) \quad (13)$$

The values of $DE_N \in [0,1]$, and the condition $DE_N > 0.5$ reflects the higher discrete entropy of the enhanced image than the input image. The normalized discrete entropy is no-reference quality measure, i.e. it does not require the original undistorted image. The quality measure is taken between input (distorted) image, and contrast-enhanced image. Therefore, higher the DE_N values, better the contrast-enhancement achieved. The DE_N values for the contrast-enhanced images by various algorithms are shown in Table I. The highest and second highest value are highlighted in bold with the highest value underlined. FCCE yields highest DE_N values for most of the images. SECEDCT also gives comparable values, and in few cases highest value. Although, it may be noticed that SECEDCT uses DCT, which enhances noise along with image details. The noise may increase DE_N values. Therefore, DE_N measure shows that FCCE gives better contrast-enhancement in comparison to other algorithms.

2) EME

The measure of contrast EME [33] based on weber contrast. The image $\mathbf{I}$ is divided into $k_1 k_2$ non-overlapping blocks of the block size $w_1 \times w_2$. The EME is computed as:

$$EME(\mathbf{I}) = 1/k_1 k_2 \sum_{k=1}^{k_1}\sum_{l=1}^{k_2} 20\log\left(\max(\mathbf{I}_{k,l})/\min(\mathbf{I}_{k,l})\right) \quad (14)$$

This is no-reference contrast measure, and quality of the image is computed independently. The higher value of EME represents the better contrast, and vice-a-versa. It may be noticed from (14) that sometimes a noisy image may have a higher value than a better contrast image. Table II shows the EME values of enhanced images by various algorithms. The highest and second highest values are highlighted in bold with the highest value underlined. BBHE gives highest EME values followed by HE and FDHE for most of the images. FCCE gives higher EME values than BPDHE, CEDLR, CVC, and SECEDCT, except for few images.

3) Statistical Analysis of quantitative measures

The performance analysis of the proposed algorithm is further evaluated using statistical analysis of quantitative results. We perform statistical analysis of quantitative results, using paired t-test [34]. The t-test is performed between the proposed algorithms and other comparing algorithms. We proposed the null hypothesis (H_0) and alternate hypothesis (H_1) as:

H_0: There is no difference in the performance (contrast measures) of the algorithm A and algorithm B.

H_1: The algorithm A gives better contrast-enhancement than the algorithm B.

We perform hypothesis testing for both measures, i.e. DE_N and EME. The t values are calculated as:

$$t = \bar{d}(\sqrt{n}/s_d), \text{ where } s_d = \sqrt{\sum(d-\bar{d})^2/n-1} \quad (15)$$

Where $\bar{d}$ is the mean of the differences (d) for the paired observations, s_d is the standard deviation of the differences between the paired observations, and n is the number of observations. We perform one tail testing to examine the improvement. The t -statistics is compared against a critical value for a particular level of significance. The level of significance is the probability of rejecting H_0, while it is true. The p -value is the probability of observing a sample value as extreme as, or more extreme than the value observed, provided the null hypothesis is true [34]. In other words, if p -value is very large then H_0 is likely to be true; and if p -value is small enough, we can reject the null hypothesis. The t -values are calculated using (15), and corresponding p -values are obtained using t -distribution table [34]. Table III shows t -statistics and p -values for DE_N and EME measures. Note that the negative value of t -stat reflects that the alternate hypothesis is true in reverse relation i.e. algorithm B performs better than algorithm A. The critical value of t -stat for the level of significance 0.05 and 0.01 are 1.7613 and 2.6245. To reject the null hypothesis, t -stat should be greater than critical value or equivalently, p -value should be less than a level of significance.

1057-7149 (c) 2016 IEEE. Personal use is permitted, but republication/redistribution requires IEEE permission. See http://www.ieee.org/publications_standards/publications/rights/index.html for more information.

This article has been accepted for publication in a future issue of this journal, but has not been fully edited. Content may change prior to final publication. Citation information: DOI 10.1109/TIP.2017.2665975, IEEE Transactions on Image Processing

TABLE I
NORMALIZED DISCRETE ENTROPY VALUES FOR DIFFERENT ALGORITHMS

Image	HE	CELDR	SECEDCT	NECI	REIA	NDFE	FDHE	FCCE
Beans	0.499	0.499	0.809	**0.858**	0.484	**0.876**	0.498	0.659
House	0.472	0.496	0.601	0.600	0.460	**0.660**	0.489	**0.613**
Parrot	0.470	0.498	**0.653**	0.579	0.401	0.631	0.486	**0.676**
Temple	0.472	0.498	0.561	0.586	0.577	**0.601**	0.492	**0.565**
Monument	0.474	0.494	**0.672**	0.566	0.458	**0.703**	0.477	0.649
Roping	0.462	0.493	**0.643**	0.532	0.408	0.555	0.488	**0.687**
Nest	0.466	0.485	**0.579**	0.483	0.481	0.519	0.497	**0.605**
Lake	0.463	0.491	0.704	0.801	0.678	**0.815**	0.470	**0.821**
Trolley	0.455	0.497	**0.718**	0.693	0.479	0.692	0.473	**0.766**
Leopard	0.468	0.493	**0.686**	0.603	0.415	0.621	0.485	**0.805**
Zebra	0.435	0.491	0.580	**0.757**	0.537	**0.752**	0.463	0.710
Bridge	0.446	0.486	0.571	0.699	0.574	**0.733**	0.446	**0.880**
Pillars	0.422	0.405	0.626	0.568	0.378	**0.663**	0.333	**0.644**
Island	0.464	0.498	**0.721**	0.599	0.387	0.646	0.465	**0.739**
Flower	0.475	0.498	0.697	0.654	0.487	**0.738**	0.483	**0.781**

TABLE II
EME VALUES FOR DIFFERENT ALGORITHMS

Image	HE	CEDLR	SECEDCT	NECI	REIA	NDFE	FDHE	FCCE
Beans	13.457	9.863	**20.662**	11.780	1.4857	14.989	**19.858**	19.838
House	**15.854**	8.272	13.140	7.688	2.559	8.566	**14.809**	12.399
Parrot	**12.507**	10.292	10.189	7.103	3.115	7.673	**12.409**	10.930
Temple	16.301	15.816	2.043	13.532	10.099	13.942	**17.182**	**18.174**
Monument	18.156	14.985	14.631	18.334	7.893	15.588	**22.865**	**21.894**
Roping	11.052	16.911	13.385	**30.963**	12.512	20.974	**23.787**	22.512
Nest	**17.578**	15.189	3.101	15.965	14.670	14.111	**16.864**	16.792
Lake	28.855	30.367	9.924	35.801	16.065	**36.995**	35.627	**37.280**
Trolley	**29.010**	21.544	13.819	20.869	9.180	21.291	28.868	**30.479**
Leopard	22.130	21.107	14.941	17.204	7.691	13.751	**25.251**	**25.111**
Zebra	**35.679**	24.898	14.449	22.853	11.497	27.412	**35.541**	31.832
Bridge	40.058	35.059	3.968	29.191	21.504	32.089	**42.514**	**45.562**
Pillars	**29.585**	22.941	6.162	18.582	8.044	22.669	**31.339**	26.379
Island	**19.254**	16.701	9.417	12.500	3.689	12.773	**18.447**	18.314
Flower	**25.255**	**24.293**	10.033	18.457	6.736	19.469	22.882	23.301

TABLE III
THE t -STAT AND p -VALUES OF ONE TAIL PAIRED t -TEST FOR DE_N AND EME MEASURES

Measure	Alg. A	Alg. B	HE	CEDLR	SECEDCT	NECI	REIA	NDFE	FDHE	FCCE
DE_N	FDHE	*t*-stat	6.77	1.43	-3.67	0.05	5.69	-3.04	----	-6.50
		p-value	3.3E-09	8.0E-02	3E-04	4.8E-01	2.1E-07	1.8E-03	----	9.4E-09
	FCCE	*t*-stat	11.32	7.22	2.08	4.41	9.34	0.23	6.50	----
		p-value	1.0E-16	5.7E-10	2.1E-02	2.2E-05	1.5E-13	4.1E-01	9.4E-09	----
EME	FDHE	*t*-stat	3.49	6.33	5.25	6.68	11.47	7.97	----	3.18
		p-value	5E-04	2E-08	1E-06	5E-09	6E-17	3E-11	----	1E-03
	FCCE	*t*-stat	1.32	4.37	4.39	6.17	11.06	7.25	-3.18	----
		p-value	9.5E-02	2.6E-05	2.4E-05	3.4E-08	2.6E-16	5.1E-10	1.2E-03	----

It may be observed from Table III that we are able to reject the null hypothesis with at least 0.01 level of significance, while comparing FCCE with all other algorithms except SECEDCT and NDFE. In the case of SECEDCT and NDFE, we can reject the null hypothesis with 0.05 and 0.5 level of significance, respectively. Therefore, we accept the alternate hypothesis, i.e. FCCE gives better contrast than all other algorithms, except NDFE. The performance of NDFE is comparable to FCCE. The t -test analysis of EME measures shows that FDHE performs better than other algorithms. FCCE performs better than other algorithms except FDHE, while the performance of HE is comparable. The EME measure analysis suggests that HE gives comparable or sometimes better performance than proposed algorithms. However, it should be noted that EME measure is highly sensitive to noise. The visual analysis in next section shows HE yields in degraded images. Thus, in the case of HE, the high values of EME measure is due to noisy image.

B. Visual Assessment

The contrast of the image cannot be judged using a quantitative measure alone. At times, an image with higher quantitative measure may turn out to be of poor quality. Therefore, the visual assessment of the enhanced images by different methods is presented in this section. The sample output images and corresponding histograms of different algorithms are shown in Fig. 3-8.

1057-7149 (c) 2016 IEEE. Personal use is permitted, but republication/redistribution requires IEEE permission. See http://www.ieee.org/publications_standards/publications/rights/index.html for more information.

This article has been accepted for publication in a future issue of this journal, but has not been fully edited. Content may change prior to final publication. Citation information: DOI 10.1109/TIP.2017.2665975, IEEE Transactions on Image Processing

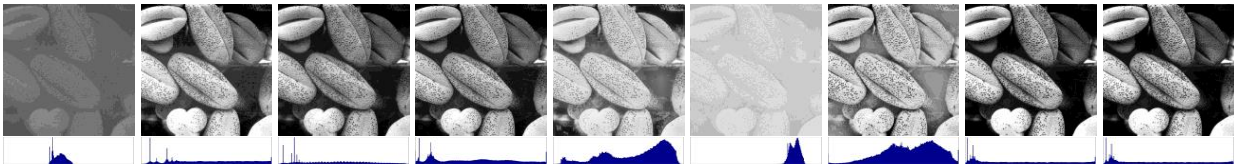


Fig. 3 Beans (a) input, (b)HE, (c)CELDR, (d)SECEDCT, (e)NECI, (f)REIA, (g)NDFE, (h)FDHE, (i)FCCE

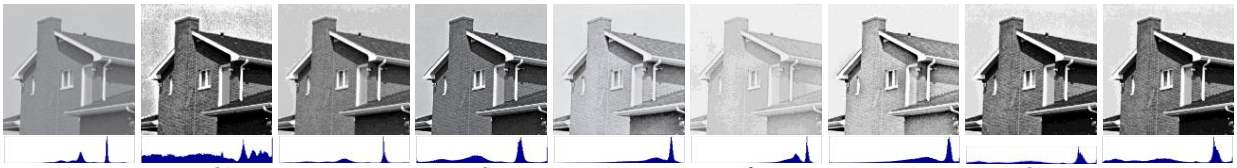


Fig. 4 House (a) input, (b)HE, (c) CELDR, (d)SECEDCT, (e)NECI, (f)REIA, (g)NDFE, (h)FDHE, (i)FCCE

We present the visual analysis for both gray and color images. Fig. 3 shows input and enhanced images of the "Beans" image. The input "Beans" image is a low contrast image, and the same is suggested by its histogram. It may be noticed from Fig. 3(b) that HE over stretches the intensity levels in smooth regions between the beans and produces patches and noisy spots. CELDR gives good contrast output, some checkerboard artifacts may be noticed near boundaries in Fig. 3(c). Fig. 3(d) shows that SECEDCT produces a good contrast image. However, there are few noisy patches in the smooth regions. Moreover, the boundary edges of beans are broken and noisy. NECI gives a low contrast brightened image. Fig. 3(f) shows that REIA gives an excessively brightened image. The corresponding histogram shows that intensity levels are pulled towards higher values and dynamic range is small. Thus, a bright low-contrast image is produced. NDFE also shows washout effects, especially in the dark regions. The histogram in Fig. 3(g) shows that very few pixels are present in lower part of the dynamic range. Fig. 3(h) and (i) shows the enhanced "Beans" images produced by the proposed algorithms: FDHE and FCCE. Both the algorithms produces good contrast images and have almost no artifacts. The input and enhanced "House" images and their histograms are shown in Fig. 4. The input image is a low contrast image. Fig. 4(b) shows HE results in the patchy background of the house. NECI, REIA and NDFE give washout effects similar to "Beans" image. SECEDCT and the proposed algorithms FDHE and FCCE, all result in good contrast images. However, Fig. 4(e) shows that CELDR provides a good quality image with slightly lesser contrast. Moreover, the contrast of the resulting images, in the case of the proposed algorithms is slightly better than SECEDCT. The quantitative and visual analysis shows that HE performs poorly in comparison to other algorithms. Thus, the results for HE are not included in the further visual assessment. The sample outputs for color images are presented in Fig. 5-8. A low contrast "Parrot" image and contrast-enhanced results of various algorithms are shown in Fig. 5. It may be noticed from the histogram of the input image that the majority of the intensities are present in the middle of the dynamic range. REIA shifts pixel values to upper half the dynamic range. Thus, it produces a poor quality image. NECI and NDFE produce "Parrot" images with faded colors. It may be noticed from the Fig. 5(d) and 5(f) that majority of the pixels are shifted towards right part of the histogram. CELDR, SECEDCT, and the proposed algorithms utilize entire dynamic range and produce good quality images. The "Temple" image and the contrast-enhanced images are shown in Fig. 6. The input image is a low-contrast image with a narrow dynamic range. SECEDCT results in good contrast but noise may be noticed in smooth regions. The effect of the noise can also be observed from two peaks at both ends of the histogram. NECI fails to give significant contrast enhancement. REIA gives a brightened image with faded natural colors. FDHE gives good contrast, however, the sky region has some artifacts. NDFE, CELDR, and FCCE produce good contrast images with natural visual quality. However, FCCE gives slightly better contrast than other algorithms. Fig. 7 shows "Monument" image and results of various contrast enhancement algorithms. The input image is a low contrast image as its histogram is mostly spread in the middle part the dynamic range. It is evident from Fig. 7(e) that REIA did not utilize the entire dynamic range and resulted in a degraded image. Fig. 7(d) and 7(f) shows that NECI and NDFE give brighter images but introduced artifacts. The artifacts are clearly visible in green leafs present in the bottom of the images. However, the performance of these algorithms is better in the shadow regions of the image. The histograms of these images show that a large number of pixels are shifted towards extreme right. CELDR, SECEDCT, and FDHE give good contrast images with comparable quality.

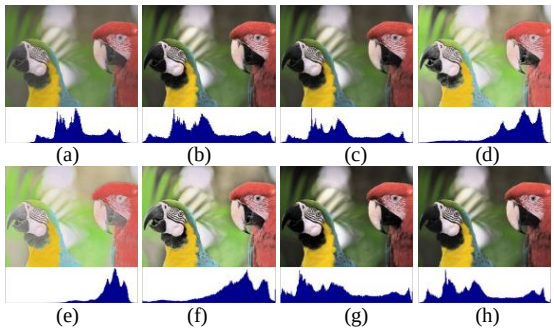


Fig. 5 Parrot (a)input, (b)CELDR, (c)SECEDCT, (d)NECI, (e)REIA, (f)NDFE, (g)FDHE, (h)FCCE

1057-7149 (c) 2016 IEEE. Personal use is permitted, but republication/redistribution requires IEEE permission. See http://www.ieee.org/publications_standards/publications/rights/index.html for more information.

This article has been accepted for publication in a future issue of this journal, but has not been fully edited. Content may change prior to final publication. Citation information: DOI 10.1109/TIP.2017.2665975, IEEE Transactions on Image Processing

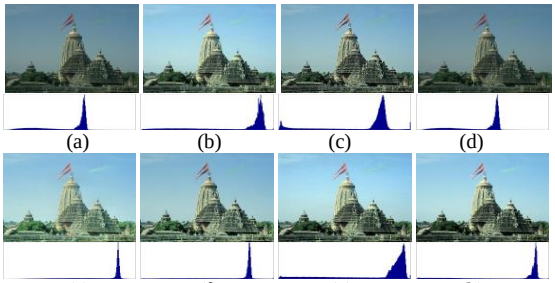


Fig. 6 Temple (a)input, (b)CELDR, (c)SECEDCT, (d)NECI, (e)REIA, (f)NDFE, (g)FDHE, (h)FCCE

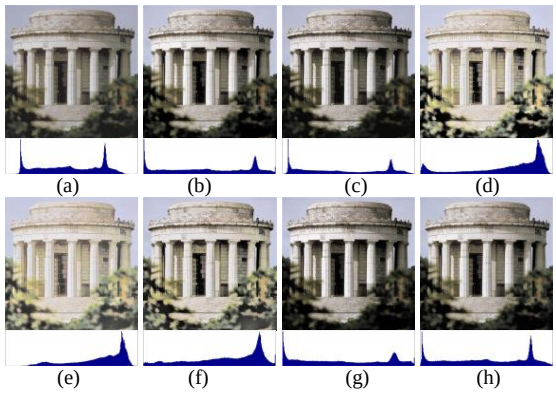


Fig. 7 Monument (a)input, (b)CELDR, (c)SECEDCT, (d)NECI, (e)REIA, (f)NDFE, (g)FDHE, (h)FCCE

However, FCCE utilizes the entire dynamic range in an efficient manner and produce slightly better contrast image. The "Roping" image and the contrast-enhanced images are shown in Fig. 8. The input image is again a low-contrast image with most of the pixels in lower part of the histogram. It may be noticed that input image has some black regions with no information present in it. REIA and NDFE give degraded images. The black regions are blurred with a smoky look and halo artifacts may be noticed around the man. NECI gives slightly better result but the halo artifacts are still noticeable. CELDR, SECEDCT, and FDHE again give comparable results. FCCE gives the best contrast with almost no artifacts. The visual analysis shows that HE over stretches the smooth region intensities and produces a poor visual quality image in many cases. CELDR gives good contrast and shows comparative results in many cases. SECEDCT gives good contrast in most of the cases, but it gives slightly noisy output. NECI, REIA, and NDFE shift pixels towards the right end of the histogram and result in brighter images. Thus, these algorithms perform better in shadow regions, but may lead to fading effect in bright color regions. Moreover, these algorithms chop off around 1% of pixels at both ends of the histogram and use the suppression function with multiple scales. This may lead to a loss of the original details and may result in a degraded image as in Fig. 8. The drawbacks of these algorithms are further analyzed with the help of "Gradient" image shown in the Fig. 9. The input "Gradient" image shows shades of gray intensity levels. NECI and NDFE both reduces the gradient details. However, the proposed algorithm enhances the gradient details. FDHE uses dissimilarity rather than number of pixels.

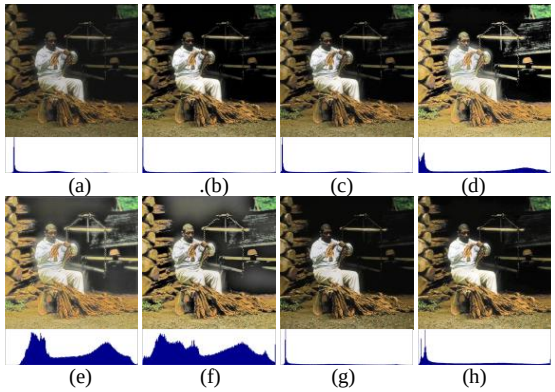


Fig. 8 Roping (a)input, (b)CELDR, (c)SECEDCT, (d)NECI, (e)REIA, (f)NDFE, (g)FDHE, (h)FCCE

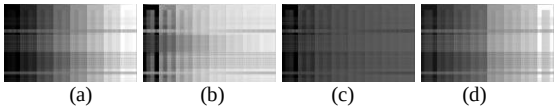


Fig. 9 Gradient (a)Input, (b)NECI, (c)NDFE, (d) FCCE

Thus saturation effects do not surface and FDHE results in good contrast images in most of the cases. However, few artifacts are noted in some images as equal intensity pixels are transformed to same intensity irrespective of its location. The algorithm FCCE uses contextual intensity transformation function i.e. pixels of same intensity may be transformed to different intensities depending on the neighborhood characteristics of the pixels. This preserves the natural characteristics of image and results in good contrast natural looking images with almost no artifacts. The quantitative and visual, both assessments establish the fact that the proposed algorithms outperform most of the conventional and state-of-art contrast enhancement algorithms.

C. Computation Time Analysis

The computation time is an important parameter to evaluate the performance. The lower complexity is always a desirable factor for any algorithm. A slow algorithm with high accuracy becomes practically non-usable for real-time applications. To calculate the computation time, we perform the experimentation with data set of 200 images of the size 321×481. The average computation time per image is recorded in Table IV. We use MATLAB 2012b on Windows10 Pro system with core i5 processor @ 3.10GHz and 3GB RAM. The computation time of the various contrast enhancement algorithms is given in Table IV. HE takes smallest time as it involves simple transformation function using the histogram. NECI is a slow algorithm because of the Cortex Transform, thus useful for off-line applications only. Thus, it is not used in computational time analysis. CELDR computes the 2-D histogram, which requires more computation time than HE. SECEDCT has much higher computation time as it computes 2-D histogram using much larger neighborhood block in comparison to CELDR, and requires computation of spatial entropy to construct transfer function. REIA and NDFE are taking longer time because of the iterative nature of the algorithms. The proposed algorithms FDHE and FCCE take much less time than SECEDCT and CVC.

1057-7149 (c) 2016 IEEE. Personal use is permitted, but republication/redistribution requires IEEE permission. See http://www.ieee.org/publications_standards/publications/rights/index.html for more information.

This article has been accepted for publication in a future issue of this journal, but has not been fully edited. Content may change prior to final publication. Citation information: DOI 10.1109/TIP.2017.2665975, IEEE Transactions on Image Processing

TABLE IV
AVERAGE COMPUTATION TIME PER IMAGE (IN SECONDS)

HE	CEDLR	SECEDCT	REIA	NDFE	FDHE	FCCE
0.031	0.069	0.397	0.328	0.379	0.161	0.174

Although CEDLR takes lesser time than proposed algorithms, as CEDLR considers only 4-adjacent pixels for neighborhood computation. Moreover, CEDLR performs only global contrast enhancement, while FCCE performs both local and global contrast-enhancement.

IV. CONCLUSION

In this paper, we proposed a contrast enhancement algorithm FDHE and its extended version FCCE. We proposed a fuzzy dissimilarity histogram, to effectively capture intensity level differences in the neighborhood of the pixels. FDHE enhances the intensity level differences without losing the natural characteristics of the images. The use of fuzzy theory enables FDHE in retaining continuity in smooth regions, while increasing the contrast. FDHE provides global contrast-enhancement using local characteristics of the pixels. We extended FDHE as FCCE to achieve contextual contrast enhancement. We proposed a contextual intensity transfer function, which transforms an intensity level based on its spatial location in the image and its intensity value. FCCE provides both local and global contrast enhancement based on contextual characteristics of the image. The main advantages of the proposed algorithm are:

- The over-enhancement and the under-enhancement problem do not surface.
- FCCE uses both global and local enhancement; therefore, it results in natural visual quality images.
- Almost, no artifacts in contrast-enhanced images.
- It retains the original shape of the histogram.
- Computationally efficient
- FDHE and FCCE involve no parameters to be selected or optimized i.e. parameter-free algorithms.

An extensive experimentation is done on images from the Berkeley, USC-SIP, CSIQ, and TID2013 image databases. Quantitative and visual analysis of the results shows that proposed algorithms yields contrast enhanced images with natural visual quality. FCCE utilizes full dynamic range and preserves the original shape of the histogram. Thus, the original characteristic of the image is not disturbed. The comparative analysis shows that FDHE and FCCE outperform most of the traditional and state-of-art algorithms. The statistical analysis (t-test) also suggests the supremacy of the proposed algorithms.

REFERENCES

[1] R. C. Gonzalez and R. E. Woods, Digital Image Processing, 3rd ed., Pearson.

[2] Y.-T. Kim, "Contrast enhancement using brightness preserving bi-histogram equalization," *IEEE Trans. Consum. Electron.*, vol. 43, no. 01, pp. 1-8, 1997.

[3] S.-D. Chen and A. R. Ramli, "Contrast Enhancement using Recursive Mean-Separate Histogram Equalization for Scalable Brightness Preservation," *IEEE Trans. Consum. Electron.*, vol. 49, no. 4, pp. 1301-1309, 2003.

[4] M. Kim and M. G. Chung, "Recursively Separated and Weighted Histogram Equalization for Brightness Preservation and Contrast Enhancement," *IEEE Trans. Consum. Electron.*, vol. 54, no. 3, pp. 1389-1397, 2008.

[5] M. Abdullah-Al-Wadud, M. H. Kabir, M. A. A. Dewan and O. Chae, "A Dynamic Histogram Equalization for Image Contrast Enhancement," *IEEE Trans. Consum. Electron.*, vol. 53, no. 2, pp. 593-600, 2007.

[6] H. Ibrahim and N. S. P. Kong, "Brightness Preserving Dynamic Histogram Equalization for Image Contrast Enhancement," *IEEE Trans. Consum. Electron.*, vol. 53, no. 4, pp. 1752-1758, 2007.

[7] N. Sengee and H. K. Choi, "Brightness preserving weight clustering histogram equalization," *IEEE Trans. Consum. Electron.*, vol. 54, no. 3, pp. 1329-1337, 2008.

[8] K. Singh, R. Kapoor and S. K. Sinha, "Enhancement of low exposure images via recursive histogram equaliztion algorithms," *Optik*, vol. 126, no. 20, pp. 2619-2625, 2015.

[9] S. K. Pal and R. A. King, "Image Enhancement Using Smoothing with Fuzzy Sets," *IEEE Trans. Syst., Man, Cybern.*, Vols. SMC-11, no. 7, pp. 494-501, 1981.

[10] M. Hanmandlu and D. Jha, "An Optimal Fuzzy System for Color Image Enhancement," *IEEE Trans. Image Process.*, vol. 15, no. 10, pp. 2956-2966, 2006.

[11] M. Hanmandlu, O. P. Verma, N. K. Kumar and M. Kulkarni, "A Novel Optimal Fuzzy System for Color Image Enhancement Using Bacterial Foraging," *IEEE Trans. Instrum. Mea.*, vol. 58, no. 8, pp. 2867-2879, 2009.

[12] D. Sheet, H. Garud, A. Suveer, M. Mahadevappa and J. Chatterjee, "Brightness Preserving Dynamic Fuzzy Histogram Equalization," *IEEE Trans. Consum. Electron.*, vol. 56, no. 4, pp. 2475-2480, 2010.

[13] T. K. Kim, J. K. Paik and B. S. Kang, "Contrast Enhancement System Using Spatially Adaptive Histogram Equalization with Temporal Filtering," *IEEE Trans. Consum. Electron.*, vol. 44, no. 1, pp. 82-87, 1998.

[14] T. Ceilik and T. Tjahjadi, "Contextual and Variational Contrast Enhancement," *IEEE Trans. Image Process.*, vol. 20, no. 12, pp. 3431-3441, 2011.

[15] T. Celik, "Two-dimensional histogram equalization and contrast enhancement," *Pattern Recognition*, vol. 45, pp. 3810-3824, 2012.

[16] C. Lee, C. Lee and C.-S. Kim, "Contrast Enhancement Based on Layered Difference Representation of 2D Histograms," *IEEE Trans. Image Process.*, vol. 22, no. 12, pp. 5372-5384, 2013.

[17] T. Celik, "Spatial Entropy-Based Global and Local Image Contrast Enhancement," *IEEE Trans. Image Process*, vol.

1057-7149 (c) 2016 IEEE. Personal use is permitted, but republication/redistribution requires IEEE permission. See http://www.ieee.org/publications_standards/publications/rights/index.html for more information.

This article has been accepted for publication in a future issue of this journal, but has not been fully edited. Content may change prior to final publication. Citation information: DOI 10.1109/TIP.2017.2665975, IEEE Transactions on Image Processing

23, no. 12, pp. 5298-5308, 2014.

[18] S.-C. Huang, F.-C. Cheng and Y.-S. Chiu, "Efficient Contrast Enhancement using Adaptive Gamma Correction with Weighting Distribution," *IEEE Trans. Image Process.*, vol. 22, no. 3, pp. 1032-1041, 2013.

[19] M. Abdoli, H. Sarikhani, M. Ghanbari and P. Brault, "Gaussian mixture model-based contrast enhancement," *IET Image Processing*, vol. 9, no. 7, pp. 569-577, 2015.

[20] Z. Wei, H. Lidong, W. Jun and S. Zebin, "Entropy maximisation histogram modification scheme for image enhancement," *IET Image Processing*, vol. 9, no. 3, pp. 226-235, 2015.

[21] X. Fu, J. Wang, D. Zeng, Y. Huang and X. Ding, "Remote Sensing Image Enhancement Using Regularized-Histogram Equalization and DCT," *IEEE Geosci. Remote Sens. Lett.*, vol. 12, no. 11, pp. 2301-2305, 2015.

[22] K. Singh, D. K. Vishwakarma, G. S. Walia and R. Kapoor, "Contrast enhancement via texture region based histogram equalization," *Journal of Modern Optics*, 2016.

[23] S. Chen and A. Beghdadi, "Natural Enhancement of Color Image," *EURASIP Journal and Video Processing*, vol. 2010, pp. 1-19, 2010.

[24] X. Fu, M. LiWang, Y. Huang, X.-P. Zhang and X. Ding, "A Novel Retinex based Approach for Image Enhancement with Illumination Adjustment," in *IEEE International Conference on Acoustic, Speech and Signal Proccessing*, Florence, 2014.

[25] Z. Liang, W. Liu and R. Yao, "Contrast Enhancement by Nonlinear Diffusion Filtering," *IEEE Trans. Image Process.*, vol. 25, no. 2, pp. 673-686, 2016.

[26] L. A. Zadeh, "Fuzzy Sets," *Information and Control*, vol. 8, pp. 338-353, 1965.

[27] K. K. Sharma and H. Krishna, "Asymptotic Sampling Distribution of Inverse Coefficient-of-Variation and Its Applications," *IEEE Trans. Rel.*, vol. 43, no. 4, pp. 630-633, 1994.

[28] P. Arbela´ez, M. Maire, C. Fowlkes and J. Malik, "Contour Detection and Hierarchical Image Segmentation," *IEEE Trans. Pattern Anal. and Mach. Intell.*, vol. 33, no. 5, pp. 898-916, 2011.

[29] "USC-SIPI Database," [Online]. Available: http://sipi.usc.edu/database. [Accessed 2015].

[30] E. C. Larson and D. M. Chandler, "Most apparent distortion: full-reference image quality assessment and the role of strategy," *Journal of Electronic Imaging*, vol. 19, no. 1, pp. 011006-1-011006-21, 2010.

[31] N. Ponomarenko, L. Jin, O. Ieremeiev, V. Lukin, K. Egiazarian, J. Astola, B. Vozel, K. Chehdi, M. Carli, F. Battisti and C.-C. J. Kuo, "Image database TID2013: Peculiarities, results and perspectives," *Signal Processing: Image Communication*, vol. 30, pp. 57-77, 2015.

[32] C. E. Shannon, "A Mathematical Theory of Communication," *Bell System Technical Journal*, vol. 27, pp. 623-656, 1948.

[33] S. S. Agaian, B. Silver and K. A. Panetta, "Transform Coefficient Histogram-Based Image Enhancement Algorithms Using Contrast Entropy," *IEEE trans. Image Process.*, vol. 16, no. 03, pp. 741-758, 2007.

[34] D. A. Lind, W. G. Marchal and S. A. Wathen, Statistical Technics in Business and Economics, 13 ed., Tata McGraw Hill Education Pvt. Ltd.



Anil Singh Parihar (M'12) received his B.Tech Degree in Electronics and Communication Engineering in 2005 from U. P. Technical University, Lucknow, India, M.E. degree in Electronics and Communication Engineering from Delhi College of Engineering, New Delhi, India in 2008, and Ph.D. degree in the area of applications of soft comping in image processing in 2016. He joined the Department of Information Technology at Delhi Technological University, Delhi, India as Assistant Professor in 2010. Currently, he is Assistant Professor in the Department of Computer Science & Engineering at Delhi Technological University, Delhi, India. His research interest includes Image Processing, Pattern Recognition, Soft Computing and Evolutionary Algorithms.



Om Prakash Verma (M'12) received his B.E. degree in Electronics and communication engineering from Malaviya National Institute of Technology, Jaipur, India, M.Tech. degree in Communication and Radar Engineering from Indian Institute of Technology, Delhi, India and PhD in the area of applications of soft and evolutionary computing in image processing from University of Delhi, Delhi, India. From 1992 to 1998 he was assistant professor in Department of ECE at Malaviya National Institute of Technology, Jaipur, India. He joined Department of Electronics & Communication Engineering, Delhi Technological University (formerly Delhi College of Engineering) as Associate Professor in 1998. Currently, he is Head & Professor in Department of Computer Science and Engineering, Delhi Technological University, Delhi, India. His present research interest includes: Applied Soft Computing, Nature Inspired Algorithms, Swarm Intelligent, Evolutionary Computing, and Image Processing.



Chintan Khanna received his B.Tech degree in Information Technology from Indian Institute of Information Technology, Allahabad, India in 2003 and M.Tech degree in Information Systems from Delhi Technological University, New Delhi, India in 2016. His current area of interest include Pattern Recognition, Fuzzy-neural networks, Nature inspired optimization algorithms, and Image Processing.

1057-7149 (c) 2016 IEEE. Personal use is permitted, but republication/redistribution requires IEEE permission. See http://www.ieee.org/publications_standards/publications/rights/index.html for more information.

Composites Communications 3 (2017) 38–41

Contents lists available at ScienceDirect

Composites Communications

journal homepage: www.elsevier.com/locate/coco

Healant release from microcapsules with varied internal microstructure

Manorama Tripathi[a,b], Devendra Kumar[b], Prasun Kumar Roy[a,*]

[a] Centre for Fire, Explosive and Environment Safety, DRDO, Timarpur, Delhi 110054, India
[b] Department of Applied Chemistry and Polymer Technology, Delhi Technological University, Delhi 110042, India

ARTICLE INFO

Keywords:
Analytical model
Microcapsule
Self-healing
Encapsulation

ABSTRACT

One of the most common methodologies of introducing extrinsic healing property to a polymer composite involves inclusion of healant-loaded microcapsules in the formulation prior to curing. In this paper,we discuss an analytical model for predicting the amount of healant released due to microcapsule rupture. Of particular interest is to understand the role of internal microstructure in the context of extrinsic healing. In microcapsules possessing "reservoir" type microstructure, the healant exists as a single droplet, and the entire contents are released upon rupture. On the other hand, in monolithic microcapsules, the healant is dispersed in the form of discrete micro-droplets, and depending upon the micro-droplet dimensions, significantly lower amount of healant is released in comparison to reservoir microcapsules. For the purpose of validation, composites were prepared using epoxy encapsulated microcapsules with varied internal structures. In line with our predictions, the extent of healing was much lower in the case of samples containing monolithic microcapsules. At 20% w/w microcapsule loadings, healing efficiencies close to 60% was observed upon introduction of reservoir type microcapsules, while under similar loadings, only 10% healing could be evidenced in the presence of monolithic microcapsules.

1. Introduction

One of the most common methodologies towards introduction of self-healing functionality to any polymer involves inclusion of healant-loaded microcapsules in the formulation prior to curing [1]. Upon rupture of these microcapsules, the encapsulated healant flows into the crack plane and undergo crosslinking, forming a polymer which bridges the gap thereby arresting the crack growth. Conventionally, the healant is encapsulated in a fragile shell by adopting a dispersion polymerization route, which leads to formation of microcapsules with "reservoir" type microstructure. Typically, during the polymerization process, the shell wall constituents within the aqueous phase form a low molecular weight pre-polymer, which deposit preferentially over the hydrophobic healant at the oil-water interface. Eventually, a spherical solid shell is formed around a droplet of liquid healant forming a microcapsule with healant "reservoir".

Another relatively less complex methodology is that of "solvent evaporation", which is routinely employed for drug encapsulation [2]. The same is lately been explored for encapsulation of healants too [3–6]. The adoption of this route leads to the formation of microcapsules with monolithic structure, where the healant is dispersed as micro-droplets within the polymeric shell. It is obvious that the self-healing efficiency is strongly dependent on the internal morphology of the microcapsule. Numerical models for healant delivery exist for rupture of "reservoir" type microcapsules [7], however, to the best of our knowledge, such models for a monolithic type geometry have not yet been developed, which prompted us to take up this study.

In the present paper, we propose and discuss an analytical model for estimating the amount of healant released in the event of rupture of microcapsule with monolithic morphology and compared with "reservoir" type microcapsules. The predictions have been validated with experimental studies, where epoxy encapsulated microcapsules with varied microstructure were included in the formulation to obtain mendable compositions. The healing efficiency was quantified in terms of the ratio of impact strength and the effect of internal microstructure was evidenced.

2. Experimental

2.1. Materials

Aliphatic Epoxy resin (Ciba Geigy, Araldite CY 230; epoxy equivalent 200eq g^{-1}) and TETA based hardener (HY 951; amine content 24 eq kg^{-1}) was used as received. Urea, formalin (37% formaldehyde in water), sodium hydroxide, resorcinol, ammonium chloride, dichloromethane and polyvinyl alcohol (PVA) (Mw ~14,000) was obtained from

* Corresponding author.
E-mail addresses: pk_roy2000@yahoo.com, pkroy@cfees.drdo.in (P.K. Roy).

http://dx.doi.org/10.1016/j.coco.2017.02.002
Received 19 December 2016; Received in revised form 7 February 2017; Accepted 7 February 2017
2452-2139/ © 2017 Elsevier Ltd. All rights reserved.

CDH. EMA (Sigma Aldrich) and ethyl acetate (E.Merck) was used without any further purification. Polystyrene used for the preparation of monolithic microcapsules was obtained by emulsion polymerization, the procedure of which is presented in the Supplementary section. Double distilled water was used throughout the course of this work.

2.2. Epoxy microencapsulation

Epoxy encapsulating microcapsules with monolithic structure were prepared by solvent evaporation technique [8] for which a solution of epoxy(4 g) and polystyrene (1 g) in dichloromethane (30 ml), was added to 50 ml of aqueous PVA solution (2.5% w/w) followed by agitation. The same was poured into 150 ml aqueous PVA solution, while maintaining a stirring speed of 550 rpm at a temperature of 35 °C. Post-solvent evaporation, epoxy encapsulated PS microcapsules were filtered, washed and dried under vacuum.

The procedure employed for encapsulation of epoxy in Urea-formaldehyde shells to form microcapsules with "reservoir" microstructure has been detailed in our previous paper [9]. In brief, 100 mL distilled water was mixed with 25 ml EMA solution (2.5% w/v) by stirring at room temperature (~ 350 rpm). To this solution, 2.5 g urea, 0.25 g ammonium chloride and 0.25 g resorcinol was added. After complete dissolution, the pH was adjusted to 3.2 ± 0.2. Subsequently, ~ 60 ml of the healing agent solution (epoxy: ethyl acetate: 1:1 w/w) was slowly added over a period of 20 min while maintaining a stirring speed of ~350 rpm. Thereafter, requisite amount (6.33 g) of formalin was introduced and the temperature was increased to 50–55 °C, while maintaining a constant stirring speed of ~350 rpm. The reaction was allowed to proceed for 4 h, followed by filtration of the microcapsules and air drying for 24 h, which resulted in free-flowing powder.

2.3. Preparation of self-healing composites

Self-healing epoxy composites containing varying amounts of microcapsules (5–25% w/w) were prepared by room temperature curing of epoxy with TETA as per the procedure reported previously [10]. Copper imidazolate (1% w/w microcapsule) was included in the formulation to act as the latent hardener, and all the healing studies were performed at 150 °C.Healing efficiency was quantified in terms of the ratio of impact strength both before and after healing [11].

3. Results and discussion

The cross-sectional view of the plane formed as a result of rupture of microcapsules with different internal microstructure is presented in Fig. 1. It is clear that rupturing of microcapsules with "reservoir" type morphology lead to the release of the entire amount of healant into the crack place. Also, if all the microdroplets present within the monolithic microcapsule rupture, the healing efficiency of reservoir and monolithic microcapsules would not vary. However, only the healant released from microdroplets present on the crack plane due to rupture of monolithic microcapsules is available for healing purposes. In view of the same, the healing efficiency for monolithic microcapsules will be lesser than that obtained using reservoir microcapsules.

3.1. Release of healant from microcapsules with "monolithic" microstructure

For the sake of calculation, it is assumed that the healant is homogeneously dispersed inside the microsphere, with each micro-droplet separated from the other by the matrix. A single microcapsule is assumed to be composed of cubic spaces each of length (L) containing a single microdroplet (Fig. 2a) [2]. The micro-droplets are assumed to be perfectly spherical (diameter, D_d) with the distance between each droplet being L_{drop}. The core content ($core_{mic}$%, v/v), is related to the droplet diameter (D_d) and cubic edge length (L) as:

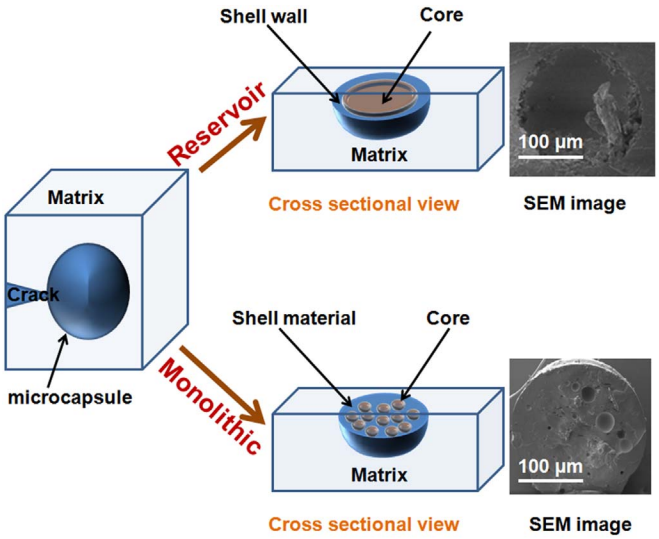


Fig. 1. Pictorial representation of reservoir type and monolith type microcapsule. SEM image of the fractured microcapsules is also included.

$$\text{core}_{\text{mic}} = \frac{(\frac{\pi}{6})D_d^3}{L^3} \quad (1)$$

The distance between two microdroplets($L - D_d$) can hence be expressed as

$$L_{drop} = D_d\left[\left(\frac{\pi}{6\times core_{mic}}\right)^{1/3} - 1\right] \quad (2)$$

The effect of increasing microdroplet dimensions on the distance between drops (L_{drop}) is also presented in Fig. 2b. It can be seen that with increasing droplet size, the distance between two adjacent drops increases. The effect of increasing core content on the distance between two adjacent droplets is also presented in Fig. 2c. As can be seen from the figure, at core content≥ ~50%, irrespective of the dimensions of the dispersed microdroplets, the microcapsules essentially exhibit "reservoir" type morphology, as the distance between two adjacent droplets reduces to zero.

For the purpose of determining the amount of healant released in the event of rupture of microcapsule, a 2D cross-section of both monolithic and reservoir type microcapsule is considered, as shown in Fig. 3.

The number of micro-droplets in a single microcapsule (N) can be estimated as $\frac{\pi r^2}{(L_{drop}+D_d)^2}$.The volume of liquid entrapped in a single micro-droplet (V_d) is $\frac{4}{3}\pi r_d^3$. The total volume of liquid released in the event of rupture of monolithic microcapsule, $V_{monolith}$ is $N \times \frac{4}{3}\pi r_d^3$. For a representative scenario (D = 150 μm) the detailed calculations are presented in supplementary section (Table S1).

In comparison, the total volume of liquid released in the event of rupture of microcapsule with comparable core contents, but possessing "reservoir" type microstructure, is $V_{reservoir} = \frac{4}{3}\pi r_{reservoir}^3$, where the radius of the healant reservoir ($r_{reservoir}$) is related to the diameter of the microcapsule (D) by $r_{reservoir} = \frac{D}{2}(core\ content)^{1/3}$. It is obvious that for lower core contents, $V_{monolith}$ is much lesser than $V_{reservoir}$.

3.2. Healant delivery into the crack plane

Rule et al. [7] has proposed an analytical model for predicting the extent of healant delivery, where it is assumed that the entire amount of healant flows into the crack plane and undergoes curing to aid the healing phenomenon. A pictorial of the model as well as the involved calculations are presented in the supplementary section (Fig. S2). It is obvious that these predictions are restricted to that of microcapsule

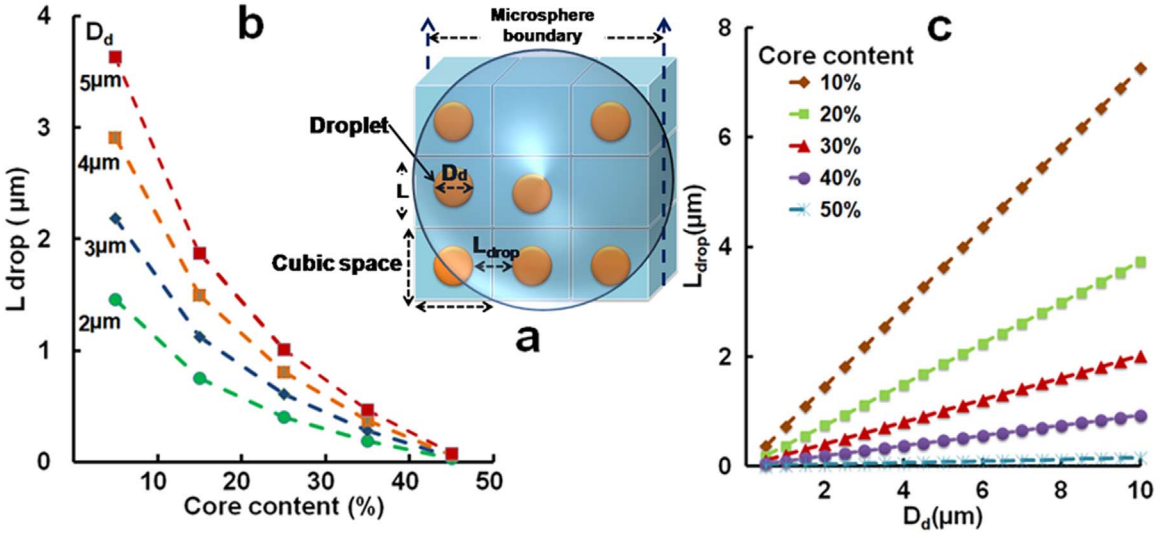


Fig. 2. a) Model for estimating distance between droplets within a microcapsule with monolithic internal microstructure. Variation of distance between microdroplets (L_{drop}) with b) core content and c) microdroplet diameter.

possessing "reservoir" type microstructure. The amount of healant delivered in a unit crack area (m) is found to be directly proportional to both the microcapsule mass fraction (ϕ) as well as microcapsule diameter (D).

$$m = \rho_s . \phi . D \quad (3)$$

The effect of microcapsule loading and size on the healant delivery per unit crack area is presented in Table S2.

3.3. Comparison of "reservoir" and "monolithic"

The effect of increasing microcapsule loading on the amount of healant delivered per unit area of crack plane is presented in Fig. 4a. It is to be noted however, that for the sake of calculations it is assumed that the shell wall around the healant is infinitely thin, i.e. the core content is close to 100%.

For all practical purposes, irrespective of the methodology adopted for preparation, the microcapsules possess relatively lower core contents [12], and the predictions performed on microcapsules with 40% core content (D =150 μm) are presented in Fig. 4b.

As explained in the previous section, for microcapsules with monolithic structure there is a pronounced effect of microdroplet diameter on the healant delivered. The effect of increasing microdroplet diameter is also included in Fig. 4b. It is clear that the difference between reservoir and monolithic morphology is particularly pronounced as the microdroplet diameter reduces. In fact, as the dimensions increase, the monolith type configuration essentially converges to that of a reservoir.

3.4. Self-healing epoxy composites

To experimentally validate the predictions, epoxy resin encapsulated microcapsules with different internal microstructures were prepared and dispersed within a representative epoxy matrix to yield self-healing compositions. The detailed characterization of microcapsules prepared is presented in the Supplementary section. Introduction of either type of microcapsule is expected to endow the polymer with self-healing functionality, however as per the predictions, self healing efficiency should be lesser in samples containing monolithic microcapsules. To demonstrate the same, specimens as per required dimensions (63.5 mm x 12.5 mm x 3 mm) were prepared and the izod impact strength was determined. As previously observed, introduction of microcapsules led to deterioration in the mechanical properties, the extent being much larger in microcapsules with reservoir type structure [13]. The broken faces were duly aligned and placed in an air oven at 150 °C, which led to healing of the samples. The impact strength was re-determined after 24 h, and the results are presented in Fig. 5. In line with our expectations, the self healing efficiency was lower in the case of samples containing monolithic microcapsules.

SEM image of fractured plane of a representative sample, containing monolithic microcapsule (20% w/w loading) is presented in the supplementary section (Fig. S9). The figure is annotated with the dimensions of few microdroplets. For the ease of calculation, the average diameter of the microdroplet was calculated, which was of the order of ~15 μm. With the diameter of a monolithic microcapsule being 130 μm, the healant released is expected to be only 16.4% of the amount released in the event of rupture of an analogous "reservoir"

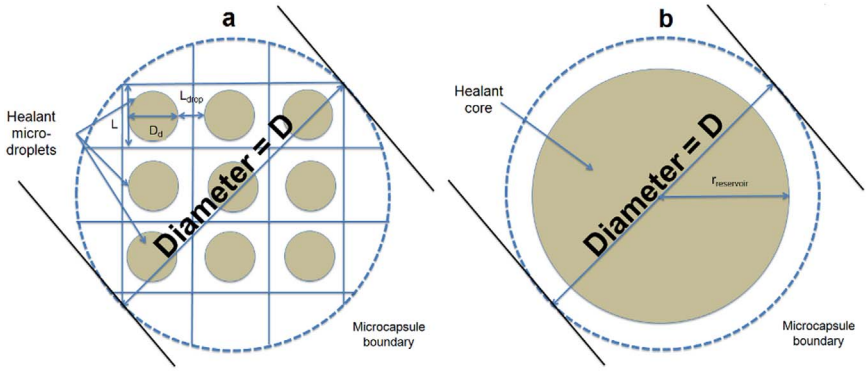


Fig. 3. Cross sectional plane of a) monolithic microcapsule and b) reservoir microcapsule.

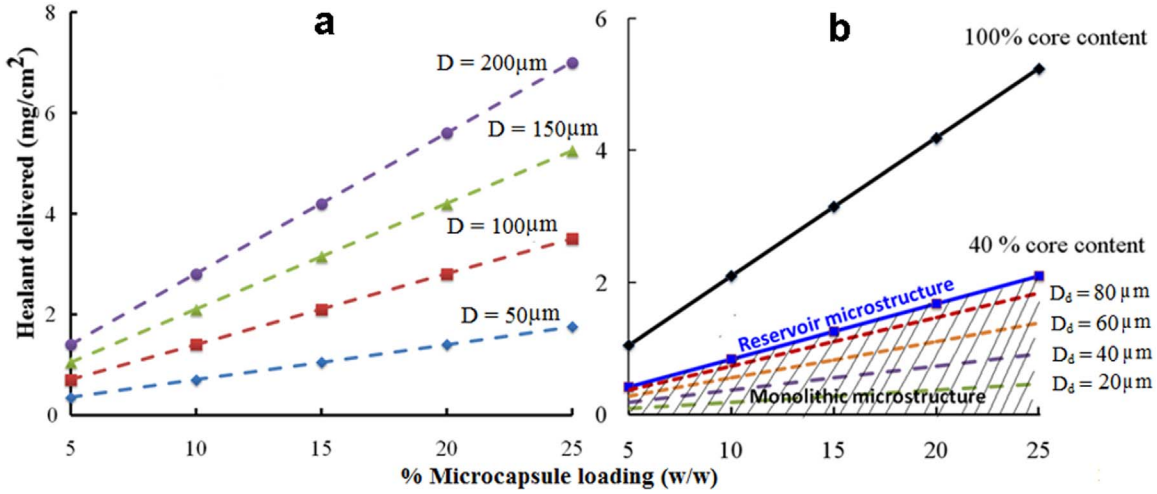


Fig. 4. Effect of increasing microcapsule loading on healant delivery a) reservoir type microcapsule (100% core content), b) comparison of reservoir with monolithic microcapsules (40% core content).

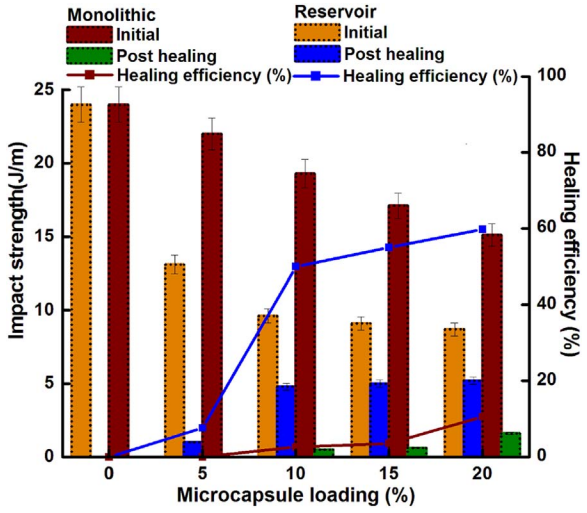


Fig. 5. Effect of internal microstructure and loading of microcapsule on the impact strength (primary axis) and healing efficiency (secondary axis) of epoxy composite.

microcapsule. Experimentally, the healing efficiency was found to be 17.7%, which is well within the range. The detailed calculation is presented in the supplementary section (Table S2).

4. Conclusions

In this paper, a comparative evaluation of the effectiveness of "reservoir" and "monolithic" microcapsules towards release of encapsulated healant is presented in the context of self healing polymers.An analytical model was proposed to predict the amount of healant released for microcapsules with different internal microstructures. In monolithic microcapsules, discrete micro-droplets are dispersed homogenously throughout the shell and calculations reveal that with increasing core content, the monolithic morphology essentially converges to that of a reservoir (core content > 50%). To validate the results, epoxy resin encapsulated microcapsules with different internal microstructures were prepared and dispersed in an epoxy matrix (loadings 5–20% w/w) to yield self-healing compositions. In line with the theoretical predictions, the healing efficiency was significantly higher in composites containing microcapsules with "reservoir" type morphology. Complete healing was observed at higher loadings (> 20% v/v) for reservoir type microcapsule, while under similar loadings, the healing efficiency was significantly lower (~10%) for monolithic microcapsules.

Acknowledgements

The authors gratefully acknowledge Defence Research and Development Organisation (DRDO) for funding this research work through grant ST/14–15/CFE-1311.

Appendix A. Supporting information

Supplementary data associated with this article can be found in the online version at doi:10.1016/j.coco.2017.02.002.

References

[1] S.R. White, N.R. Sottos, P.H. Geubelle, J.S. Moore, M.R. Kessler, S.R. Sriram, et al., Autonomic healing of polymer composites, Nature 409 (6822) (2001) 794–797.
[2] S. Freiberg, X.X. Zhu, Polymer microspheres for controlled drug release, Int. J Pharm. 282 (1–2) (2004) 1–18.
[3] E.N. Brown, M.R. Kessler, N.R. Sottos, S.R. White, In situ poly(urea-formaldehyde) microencapsulation of dicyclopentadiene, J. Microencapsul. 20 (6) (2003) 719–730.
[4] T. Zorba, E. Papadopoulou, A. Hatjiissaak, K.M. Paraskevopoulos, K. Chrissafis, Urea-formaldehyde resins characterized by thermal analysis and FTIR method, J. Therm. Anal. Calorim. 92 (1) (2008) 29–33.
[5] Q. Li, Siddaramaiah, N.H. Kim, D. Hui, J.H. Lee, Effects of dual component microcapsules of resin and curing agent on the self-healing efficiency of epoxy, Compos. Part B: Eng. 55 (0) (2013) 79–85.
[6] P. Sharma, S. Shukla, B. Lochab, D. Kumar, P. Kumar Roy, Microencapsulated cardanol derived benzoxazines for self-healing applications, Mater. Lett. 133 (2014) 266–268.
[7] Joseph D. Rule, Effect of microcapsule size on the performance of self-healing polymers, Polymer 48 (2007) 3520–3529.
[8] Q. Li, Siddaramaiah, N.H. Kim, D. Hui, J.H. Lee, Effects of dual component microcapsules of resin and curing agent on the self-healing efficiency of epoxy, Compos. Part-B Eng. 55 (2013) 79–85.
[9] M. Tripathi, R. Dwivedi, D. Kumar, P.K. Roy, Application of microencapsulated unsaturated polyester toward temperature-triggered healing in epoxy composites, J Intell. Mater. Syst. Struct. (2015).
[10] M. Tripathi, R. Dwivedi, D. Kumar, P.K. Roy, Thermal activation of mendable epoxy through inclusion of microcapsules and imidazole complexes, Polym. Plast. Tech. Eng. 55 (2) (2016) 129–137.
[11] Ce Yuan, M.Q. Zhang, M.Z. Rong, Application of alkoxyamine in self-healing of epoxy, J. Mat. Chem. A 2 (18) (2014) 6558–6566.
[12] S.H. Ikbal Choudhury, Nazrul Islam Khan, Abhinav Mathur, Writuparna Nath, Aniruddha Phukan, Effect of teta microcapsules on self-healing ability of dual component epoxy system, Adv. Mater. Lett. 7 (10) (2016) 836–843.
[13] M. Tripathi, Rahamtullah, D. Kumar, C. Rajagopal, P. Kumar Roy, Influence of microcapsule shell material on the mechanical behavior of epoxy composites for self-healing applications, J Appl. Polym. Sci. 131 (15) (2014) 40572.

arXiv:1702.05308v1 [cs.NE] 17 Feb 2017

Hierarchy Influenced Differential Evolution: A Motor Operation Inspired Approach

Shubham Dokania[1], Ayush Chopra[2], Feroz Ahmad[3], Om Prakash Verma[4]
[1]Department of Applied Mathematics, [234]Department of Computer Science
Delhi Technological University
New Delhi, India 110042
shubham.k.dokania@gmail.com,ayushchopra_2k14@dtu.ac.in
ferozahmad_2k14@dtu.ac.in,opverma.dce@gmail.com

ABSTRACT

Operational maturity of biological control systems have fuelled the inspiration for a large number of mathematical and logical models for control, automation and optimisation. The human brain represents the most sophisticated control architecture known to us and is a central motivation for several research attempts across various domains. In the present work, we introduce an algorithm for mathematical optimisation that derives its intuition from the hierarchical and distributed operations of the human motor system. The system comprises global leaders, local leaders and an effector population that adapt dynamically to attain global optimisation via a feedback mechanism coupled with the structural hierarchy. The hierarchical system operation is distributed into local control for movement and global controllers that facilitate gross motion and decision making. We present our algorithm as a variant of the classical Differential Evolution algorithm, introducing a hierarchical crossover operation. The discussed approach is tested exhaustively on standard test functions from the CEC 2017 benchmark. Our algorithm significantly outperforms various standard algorithms as well as their popular variants as discussed in the results.

KEYWORDS

Differential Evolution, Metaheuristics, Combinatorial Optimization, Hierarchical Influence

ACM Reference format:
Shubham Dokania[1], Ayush Chopra[2], Feroz Ahmad[3], Om Prakash Verma[4]. 2017. Hierarchy Influenced Differential Evolution: A Motor Operation Inspired Approach. In *Proceedings of the Genetic and Evolutionary Computation Conference 2017, Berlin, Germany, July 15–19, 2017 (GECCO '17),* 8 pages.
DOI: 10.475/123_4

1 INTRODUCTION

Evolutionary algorithms are classified as meta-heuristic search algorithms, where possible solution elements span the n-dimensional search space to find the global optimum solution. Over the years, natural phenomena and biological processes have laid the foundation for several algorithms for control and optimization that have highlighted their applicability in solving intricate optimization problems. For instance, at the cellular level in the E.Coli Bacterium, there is sensing and locomotion involved in seeking nourishment and avoiding harmful chemicals. These behavioral characteristics fuelled the inspiration for the Bacterial Foraging Optimization algorithm [8][7]. Ant Colony Optimization [3] deals with behavior of ants and has been a successful model for solving complex problems. Particle Swarm Optimization [5] is a swarm intelligence algorithm based on behavior of birds and fishes that models these particles as they traverse an n-dimensional search space and share information in order to obtain global optimum. From a biological control point, the human brain represents one of the most advanced architectures and several research attempts seek to mimic its functional accuracy, precision and efficiency. The brain function activities can be broadly classified into 2 categories: sensory and motor operations. Sensory cortical functions inspired the concept of neural networks that are being scaled successfully in deep learning to solve vast amount of problems.

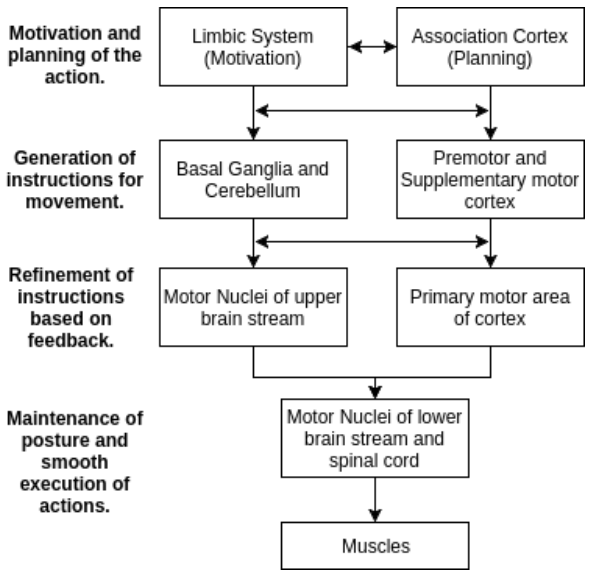


Figure 1: Hierarchy of Motor Control in Humans

The human motor function represents a distributed neural and hierarchical control system. It can be classified as having local control functions for movement as well as higher level controllers for gross motion and decision making. The execution of motor

Permission to make digital or hard copies of part or all of this work for personal or classroom use is granted without fee provided that copies are not made or distributed for profit or commercial advantage and that copies bear this notice and the full citation on the first page. Copyrights for third-party components of this work must be honored. For all other uses, contact the owner/author(s).
GECCO '17, Berlin, Germany
© 2017 Copyright held by the owner/author(s). 123-4567-24-567/08/06…$15.00
DOI: 10.475/123_4

operation involves distributed brain structures at different levels of hierarchy. These include the pre-frontal cortex, motor cortex, spinal cord, anterior horn cells etc [10]. For executing an action sequence, a sequence of actions is implemented by a string of subsequences of actions each implemented in a different part of the body. The operational structure has been depicted in Figure 1[9]. For optimality of actions, neurons act in unison. The neurons in the motor cortex act like global leaders and send inhibitory or facilitatory influence over anterior horn cells, the local leaders, located in the spinal cord[10]. These local leaders are connected to muscle fibers, the effectors, through a peripheral nerve and neuromuscular junction. Efficient execution of task requires feedback based facilitation and inhibition of the effectors over the anterior horn cells. These sequence of operations realise the optimal convergence of the system leading to smooth motor execution.

The present work introduces an algorithm modelled intuitively on the distributed and hierarchical operation of the brain motor function.

The Classical DE Algorithm [11], proposed by Storn and Price has been hailed as one of the premier evolutionary algorithms, owing to its simple yet effective structure[2]. However, in recent times, it has been criticized for its slow convergence rate and inability to effectively optimize multimodal composite functions[2]. This work focusses on supplementing the algorithm's performance through the introduction of hierarchical influence in the pipeline. The architecture enables the algorithm to control the flow of agents through the cummulative effect of global and local leaders in the hierarchy.

The proposed approach, Hierarchy Influenced Differential Evolution (HIDE), has been subjected to exhaustive analysis on the hybrid and composite objective functions of the CEC 2017 benchmark[1]. Comparison with the classical DE algorithm and its other popular variants including JADE and PSODE [13] highlights the particular viability of the schemed approach in solving complex optimization tasks. We show that even with fixed parameters, HIDE is able to outperform adaptive architectures such as JADE by a respectable margin, as discussed in the result sections.

2 CLASSICAL DIFFERENTIAL EVOLUTION

The classical Differential Evolution (DE) algorithm is a population-based global optimization algorithm, utilizing a crossover and mutation approach to generate new individuals in the population for achieving optimum solutions[2]. For each individual x_i that belongs to the population for generation G, DE randomly samples three individuals from the population namely $x_{r1,G}$, $x_{r2,G}$ and $x_{r3,G}$. Employing these randomly chosen points, a new individual trial vector, v_i, is generated using equation (1):

$$v_i = x_{r1,G} + F(x_{r2,G} - x_{r3,G}) \tag{1}$$

Where, F is called the differential weight (Usually lies between $[0, 1]$).

To obtain the updated position of the individual, a crossover operation is implemented between $x_{i,G}$ and v_i, controlled by the parameter CR called the crossover probability. The value for CR always lies between $[0, 1]$.

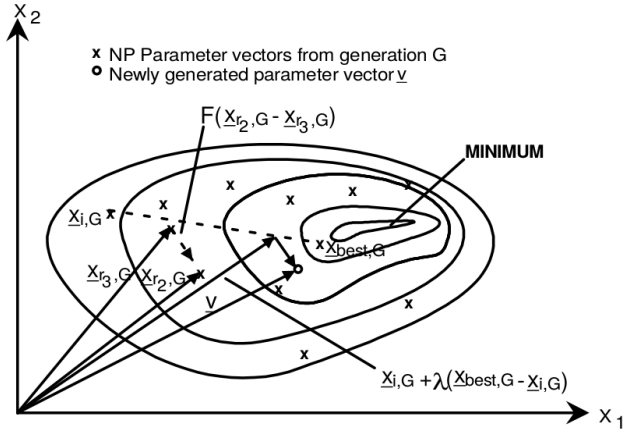


Figure 2: Motion planning of individuals in DE on two dimensional example of objective function.

3 HIERARCHY INFLUENCED DIFFERENTIAL EVOLUTION

Taking inspiration from the human motor system, we model the hierarchical motor operations in our optimization agents, where we define a global leader which influences the action of several distributed local leaders and the particle agents which act as the effectors. The global leader is analogous to the decision making and planning section in the motor system hierarchy whilst, the local leaders correspond to motion generators acting under the influence of the global leader.

The position of each particle in the population is affected by the influence of global leader and local leaders, while also being affected by a randomly chosen particle from the population to induce some stochasticity in the optimization pipeline. We first model the influence of the global leader on the local leaders and the influences of the local leaders on each population element using equation (3) and (4). We introduce a hierarchical crossover between the two influencing equations governed by a hierarchical crossover parameter HC.

Analogously to the brain motor operation as depicted in Figure 1, the updation of particle positions requires generating feedback for the leaders as a part of the optimization procedure, and hence the local leaders and the global leader are updated based on their objective function value generated from the perturbations in population particles. This series of events comprise of one optimization pass (one generation step). On execution of several optimization passes as described, the system is able to converge to an optimal configuration, analogous to the successful execution of the required task as shown in the final steps of Figure 1.

For each particle $x_{i,G}$, $i = 0, 1, 2, ...NP - 1$ for generation G, the trial vector x'_i of the particle, is governed by the hierarchical crossover operation and a mutation operation as follows :

$$u_i = \begin{cases} E_g, & if\ G < HC * G_t \\ E_l, & otherwise \end{cases} \tag{2}$$

$$E_g = g_L + F(x_{L_i,G} - x_{r,G}) \tag{3}$$

$$E_l = x_{L_i,G} + F(x_{i,G} - x_{r,G}) \tag{4}$$

for each dimension j of $x_{j,i,G}$:

$$x'_{j,i} = \begin{cases} x_{j,i,G} & if\ rand(0,1) < HC \\ u_{j,i} & otherwise \end{cases} \tag{5}$$

where,
G_t is the total number of generations,
F is factor responsible for amplification of differential variation,
f is the objective function,
$x_{i,G}$ is the current position of the individual for generation G,
u_i is the intermediate trial vector of the current individual,
E_g represents the global and local leader interaction,
E_l represents the local leader and effector interaction,
g_L is the global leader for generation G,
$x_{L_i,G}$ is the position of the local leader for current individual,
$x_{r,G} \epsilon P$; $r \epsilon [0, 1, ..NP - 1]$
$x'_{j,i}$ is the trial vector

Algorithm 1 Hierarchy Influenced Differential Evolution

procedure START
  Initialize parameters (HC, F, P, N_l, NP).
  Generate initial global leader g_L as a random point.
  Generate N_l local leader points around g_L global leader.
  Using a Normal distribution, generate NP points for population P around the local leaders.
  while termination criteria is not met **do**
    for each individual $x_{i,G}$ in P **do**
      Determine the corresponding local leader $x_{L_i,G}$ from the set of all local leader based on nearest position.
      Let $u = 0$ be an empty vector.
      Let G and G_t be the current generation and total generations of the procedure.
      if G<$(HC * G_t)$ **then**
        $u_i = E_g$ from (3).
      else
        $u_i = E_l$ from (4).
      end if
      for each dimension j **do**
        if $random(0,1)$<HC **then**
          Set $x'_{j,i} = x_{j,i,G}$.
        else
          Set $x'_{j,i} = u_{j,i}$
        end if
      end for
      if $f(x'_i)$<$f(x_{i,G})$ **then**
        Replace $x_{i,G}$ with x'_i in the next generation.
      end if
    end for
    Alter local leaders in each population cluster based on objective function value.
    Compute updated global leader g_L.
  end while
end procedure

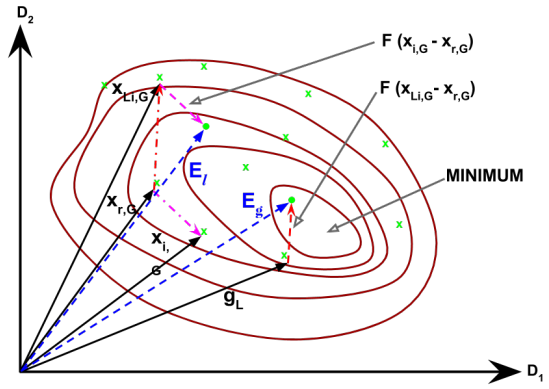


Figure 3: Hierarchical Decisive Motion planning of individuals in HIDE on two dimensional example of objective function. The position vectors resulting from the influence of global leader and local leaders are both represented as E_g and E_l on the contour of a two dimensional objective function.

$x_{r,G}$ is randomly chosen particle from the population to induce stochasticity. The hierarchical operation is affected by the global leader g_L and the local leader $x_{L_i,G}$ through the parametric equations (3) and (4). Switching between the two is governed by the hierarchical crossover parameter HC.

$$x_{i,G+1} = \begin{cases} x'_{i,G}, & if\ f(x'_{i,G}) < f(x_{i,G}) \\ x_{i,G}, & otherwise \end{cases} \tag{6}$$

where $x_{i,G+1}$ is the vector position of $x_{i,G}$ for next generation

3.1 Hierarchical Crossover

Convergence trend in HIDE is largely pivoted about (3) and (4), which in unison, lend a hierarchical structure to the algorithm. A successful optimization algorithm involves establishing a trade-off between fast convergence and robust optimization [11]. Achieving global optimization can be visualized as collaboration of two forces, greedy exploration over a larger subspace followed by intensive exploration over the resulting restricted search space. Phase 1, involving (3) is marked by the interaction between the global and local leaders representing decision planning and facilitation of gross motion. This is followed by phase 2, involving (4) wherein the local leaders interact with and guide their effector population to control intricate motion over the constraint subspace to achieve smooth convergence. Robust covergence necessitates an optimal transition from phase 1 to phase 2 in the hierarchy. This hierarchical transition is characterized by our proposed parameter, HC. The value of HC belongs to [0,1]. An optimal value for HC was observed experimentally to lie about one-quarter. For the purpose of our results, we have fixed HC to be 0.27. The differential influence of the global leader and distributed local leaders at the higher levels of hierarchy balances the greediness of mutation. Running these

vector configurations concurrently has enabled our algorithm to largely avoid local minima in quest to attain global minimum. Our proposition is complemented by the observations in our results section wherein we significantly outperform several popular algorithms on involved multimodal hybrid and composite functions on higher dimensions.

Table 1: CEC 2017 Test Functions

F_{id}	Problem Function	F*
f_1	Shifted and Rotated Bent Cigar Function	100
f_2	Shifted and Rotated Sum of Different Power Function	200
f_3	Shifted and Rotated Zakharov Function	300
f_4	Shifted and Rotated Rosenbrock's Function	400
f_5	Shifted and Rotated Rastrigin's Function	500
f_6	Shifted and Rotated Expanded Scaffer's F6 Function	600
f_7	Shifted and Rotated Lunacek Bi_Rastrigin Function	700
f_8	Shifted and Rotated Non-Continuous Rastrigin's Function	800
f_9	Shifted and Rotated Levy Function	900
f_{10}	Shifted and Rotated Schwefel's Function	1000
f_{11}	Hybrid Function 1 (N=3)	1100
f_{12}	Hybrid Function 2 (N=3)	1200
f_{13}	Hybrid Function 3 (N=3)	1300
f_{14}	Hybrid Function 4 (N=4)	1400
f_{15}	Hybrid Function 5 (N=4)	1500
f_{16}	Hybrid Function 6 (N=4)	1600
f_{17}	Hybrid Function 7 (N=5)	1700
f_{18}	Hybrid Function 8 (N=5)	1800
f_{19}	Hybrid Function 9 (N=5)	1900
f_{20}	Hybrid Function 10 (N=6)	2000
f_{21}	Composition Function 1 (N=3)	2100
f_{22}	Composition Function 2 (N=3)	2200
f_{23}	Composition Function 3 (N=4)	2300
f_{24}	Composition Function 4 (N=4)	2400
f_{25}	Composition Function 5 (N=5)	2500
f_{26}	Composition Function 6 (N=5)	2600
f_{27}	Composition Function 7 (N=6)	2700
f_{28}	Composition Function 8 (N=6)	2800
f_{29}	Composition Function 9 (N=3)	2900
f_{30}	Composition Function 10 (N=3)	3000
Search Range: $[-100,100]^D$		

4 RESULTS AND DISCUSSIONS

All evaluations were performed using Python 2.7.12 with Scipy[6] and Numpy[12] for numerical computations and Matplotlib [4] package for graphical representation of the result data. This section is divided into two sub-sections: Section A provides description about the problem set used for analysis of algorithmic efficiency and accuracy, and section B comprises of tabular and graphical data to reinforce the claim of superiority of the proposed approach.

4.1 Problem Set Description

The set of objective functions considered for testing the proposed algorithm and compare its performance against classical DE and its variants PSODE and JADE have been taken from the CEC 2017 set of benchmark functions. Exhaustive comparisons and analysis have been depicted on dimensions D = 10, 30, 50 and 100 for a clear understanding of the strengths of the proposed algorithm. Objective functions $f_1 - f_3$ are simple unimodal functions and $f_4 - f_{10}$ are multimodal functions with a high number of local optima values. Functions $f_{11} - f_{20}$ are all hybrid functions using a combination of functions from $f_1 - f_{10}$. The set of composite function range from $f_{21} - f_{30}$ and merges the properties of the sub-functions better while incorporating the basic functions as well as hybrid functions to increase complexity while maintaining continuity around the global optima.

Summarized in Table 1 are the 30 objective functions from the CEC 2017 dataset and the global optimum value for each fiction denoted by $F*$. In all simulation runs, we set the population size NP to a fixed value of 40, and the results are shown in a tabular structure depicting the best and average values of the population individuals for the simulations. Additionally, several graphical results have been discussed to observe the convergence rate and efficiency of the algorithms used in the simulation. These graphs were plotted based on the numerical results obtained from the simulation runs used to build the tables.

4.2 Parameter Settings

For fair comparisons, the parameters for all algorithms are fixed to the values depicted in table 2. As clear from the table, we set the parameters F and CR as 0.42 and 0.48 for DE across all experiments. The parameters for JADE were selected as suggested in the original work. These parameter settiings allow transparency in results and a base for fair and clear comparisons in the analysis of the algorithms.

4.3 Numerical and Graphical Results

In tables 3-6, the best and mean values obtained for the population agents in the simulation runs have been reported, and the optimum values for each objective function have been highlighted in **bold**. For the sake of clarity, the comparison results in each table

Table 2: Algorithm Parameter Settings used for comparision

Algorithm	Parameter	Value
DE	F	0.42
	Cr	0.48
PSODE	w	0.7
	Cp	2.0
	Cg	2.0
	F	0.48
	Cr	0.5
JADE	μ_{CR}	0.5
	μ_F	0.5
HIDE	HC	0.27
	F	0.48
	N_l	5

Table 3: Objective Function Value for Dimension: 10

ID	DE		JADE		PSO-DE		HIDE	
	best	mean	best	mean	best	mean	best	mean
f_1	100.000051	100.011085	**100.0**	**100.0**	100.000712	185.975885	**100.0**	**100.0**
f_2	**200.0**	200.1	**200.0**	**200.0**	**200.0**	**200.0**	**200.0**	**200.0**
f_3	300.00134	300.214502	**300.0**	**300.0**	300.000006	300.000985	**300.0**	**300.0**
f_4	400.042617	403.674837	**400.0**	400.409399	400.064644	404.307763	**400.0**	**400.000003**
f_5	566.661791	604.867489	**523.908977**	**541.521084**	525.868824	575.61616	533.803201	579.483815
f_6	621.914237	634.807962	620.878276	636.034759	**603.187964**	635.865001	613.730565	**629.293758**
f_7	724.831278	739.129935	**717.016542**	**723.983312**	725.44788	733.15638	720.345706	725.233785
f_8	**818.904202**	829.749207	821.914433	**826.321588**	820.8941	830.246691	821.064763	828.160987
f_9	**900.0**	908.104383	**900.0**	1084.478253	**900.0**	1124.102561	**900.0**	**903.454324**
f_{10}	1911.510092	2447.443751	1760.956867	2162.648588	2049.644727	2518.241095	**1694.437597**	**2049.074266**
f_{11}	1102.985708	1113.423105	1105.661676	1117.509748	1105.97013	1120.192974	**1101.769749**	**1108.863598**
f_{12}	2531.746305	6509.743078	1438.605713	5430.674683	4089.006352	10810.387667	**1308.438341**	**1327.405881**
f_{13}	1313.130226	1404.903601	**1304.681558**	**1328.755262**	1319.839199	1453.340785	1306.682039	1344.282241
f_{14}	1409.949612	1426.571937	1412.934432	1428.169439	1420.91065	1434.112884	**1404.928993**	**1410.000769**
f_{15}	1504.131392	1521.446614	1502.496189	1508.31154	1501.389515	1518.310358	**1500.08137**	**1503.169264**
f_{16}	1958.42062	2104.555728	1958.857997	2094.630816	**1958.411527**	**2048.156879**	1958.433511	2062.385949
f_{17}	1728.194973	**1743.155244**	1730.715318	1748.129878	1727.80039	1791.607742	**1723.853972**	1747.589077
f_{18}	1801.586012	1838.840555	1804.298538	1825.091639	1817.154641	1840.546923	**1800.235516**	**1804.014301**
f_{19}	1901.195482	1903.604767	1900.399786	1902.152965	1902.71174	1906.252333	**1900.005632**	**1901.014116**
f_{20}	2204.55412	2289.226577	2148.538938	2178.313173	2140.561308	2261.038768	**2139.915527**	**2172.816519**
f_{21}	2337.772994	2387.230357	**2314.421135**	**2338.688719**	2337.207339	2351.898856	2320.496212	2344.61612
f_{22}	2300.805852	2304.132879	**2300.0**	**2300.093485**	2300.684181	2301.710478	2300.000015	2301.095975
f_{23}	3070.177083	3145.772296	3003.678563	3091.22041	**2773.372859**	3060.022519	2867.020036	**3047.982305**
f_{24}	**2500.0**	**2500.0**	**2500.0**	**2500.0**	**2500.0**	**2500.0**	**2500.0**	**2500.0**
f_{25}	2899.584968	2933.249812	2899.584968	2930.266506	**2897.742869**	**2921.27479**	2897.833388	2927.976511
f_{26}	**2800.0**	4117.597033	**2800.0**	**2956.064173**	**2800.0**	3367.60765	**2800.0**	3161.548079
f_{27}	3113.157656	3358.806434	3072.439023	3178.509645	3078.873134	3240.501812	**3071.203569**	**3107.268539**
f_{28}	3184.75565	3230.921422	3184.75565	**3195.113042**	3184.755652	3198.370691	**3100.0**	3195.411961
f_{29}	**3148.587115**	3266.979786	3172.400194	**3233.707677**	3191.348193	3244.892638	3189.211417	3292.420474
f_{30}	3442.555095	11927.404685	3207.766942	4615.591316	4573.358512	16415.162901	**3205.740954**	**3249.710975**
$w/t/l$	2/4/24	1/1/28	5/7/18	9/4/17	4/4/22	2/2/26	12/7/11	14/4/12

Table 4: Objective Function Value for Dimension: 30

f_{id}	DE		JADE		PSO-DE		HIDE	
	best	mean	best	mean	best	mean	best	mean
f_1	100.001508	4334.438478	100.001338	100.056201	364.295574	4236.363207	**100.0**	**100.0**
f_2	40412441.0	5.129601e+19	**200.0**	1535352368.6	332899.0	9.590679e+11	**200.0**	**159855.5**
f_3	17926.872873	22131.542719	69304.926091	74080.700372	15792.547575	21683.209092	**3679.811599**	**8999.947269**
f_4	481.255055	519.422652	403.633939	**442.206911**	468.341175	479.341966	**400.004163**	443.016156
f_5	689.041352	737.79326	**667.50756**	**735.204027**	715.904429	746.548906	685.40454	738.842184
f_6	**643.626307**	652.582714	651.39169	655.142819	642.724237	655.106996	644.701241	**652.002395**
f_7	883.347367	962.591129	**779.907693**	**818.344111**	790.014281	854.285524	812.923573	856.90477
f_8	923.37426	967.251501	931.500175	**957.362003**	**915.414882**	960.486239	930.288539	964.11663
f_9	5652.483961	7878.781444	4953.05469	5146.600953	6018.417197	9042.410178	**4003.118072**	**4734.984364**
f_{10}	**3596.63104**	4536.989761	4012.723292	**4204.18969**	3934.606704	4863.741107	3793.781776	4346.741344
f_{11}	1162.405965	1184.634006	1152.748529	1174.58813	1165.144993	1189.171787	**1149.748499**	**1171.130409**
f_{12}	56679.435092	317650.61349	24821.171765	58930.090242	10221.077465	161046.05540	**9208.289246**	**41947.22269**
f_{13}	3002.029489	18794.835991	4276.907742	13775.816239	3871.279833	10612.26359	**1664.06241**	**2453.606969**
f_{14}	1773.180798	5502.160382	1496.219858	42868.9158	1555.452763	4029.808535	**1462.926848**	**1504.191515**
f_{15}	1860.435669	2484.689969	1688.05046	2222.674323	1651.747476	2223.060542	**1611.074402**	**1852.66177**
f_{16}	2517.439623	2827.004968	2344.19818	2621.618684	**2239.242719**	**2664.114667**	2298.041965	2691.674809
f_{17}	2321.175936	2604.529778	2062.898023	2546.995596	2107.43677	2457.34021	**1820.806639**	**2418.723829**
f_{18}	38987.282456	94156.328505	**11841.60813**	184888.162181	62294.853257	118430.28912	12578.003784	**23024.11193**
f_{19}	2043.469888	3010.235379	1959.71819	2156.957875	3049.52231	6840.408394	**1949.271714**	**1987.866761**
f_{20}	2625.539158	2864.832611	**2706.314441**	**2805.600064**	2619.996493	2895.107238	2753.806213	2966.035793
f_{21}	2412.081757	2504.777775	2414.52134	2456.718982	2431.740293	2478.841357	**2200.0**	**2442.734316**
f_{22}	2300.481796	5655.569322	**2300.0**	**4157.698784**	2307.721358	6811.069162	2300.009985	6795.24842
f_{23}	3050.654508	3572.965066	**2772.002023**	**2946.749322**	2764.922461	3199.874364	2883.276891	3543.839343
f_{24}	3104.623692	3290.698756	2891.557648	2965.225566	**2911.63347**	2983.772932	**2500.0**	2940.75997
f_{25}	2916.180657	2946.711753	2875.106846	2881.091389	2875.498843	2889.943671	**2874.171109**	**2877.484904**
f_{26}	4043.691403	6756.3724	2900.0	**3266.510982**	**2800.007809**	3273.128769	2900.0	3298.490539
f_{27}	3200.005857	3998.876498	3145.810354	**3189.82261**	3145.425231	3639.634132	**3132.816283**	3284.28897
f_{28}	3290.744025	3326.263983	**3100.0**	3131.027315	3195.486838	3225.594053	**3100.0**	**3115.505829**
f_{29}	3720.314598	4115.185803	**3305.310139**	**3626.887552**	3535.952295	3867.593068	3352.845055	3709.102375
f_{30}	3359.030768	3900.826662	**3263.496536**	3749.610722	3312.635025	3524.714477	3298.704645	**3421.715322**
$w/t/l$	2/0/28	0/0/30	8/2/20	11/0/19	4/0/26	1/0/29	15/2/13	17/0/13

Table 5: Objective Function Value for Dimension: 50

f_{id}	DE		JADE		PSO-DE		HIDE	
	best	mean	best	mean	best	mean	best	mean
f_1	5884574.87314	367294248.521	136.072384	3708.75086	5811.218992	154233.646744	**106.072862**	**3665.419272**
f_2	4.718137e+24	3.364977e+44	**2635725.0**	**5.02374e+26**	2.212101e+19	2.544543e+23	2.279950e+17	1.00729e+31
f_3	45520.966376	62237.296819	143481.793147	156166.762356	52308.42743	64435.24063	**44613.29993**	**58182.83733**
f_4	574.400328	801.384952	418.580378	470.113207	477.080964	574.528479	**400.005049**	**447.775413**
f_5	816.394775	843.258843	809.899483	834.131266	**778.59312**	831.066954	791.405194	**830.218472**
f_6	652.541914	655.794152	**633.217881**	**654.893828**	653.291336	658.183613	645.25633	656.060597
f_7	1109.02123	1263.038487	**889.036574**	**944.90319**	915.153525	1047.43879	989.957862	1186.248741
f_8	1139.278925	1175.893113	1118.339103	**1144.604745**	**1092.62639**	1159.032351	1100.476077	1168.529946
f_9	22196.387817	29218.775982	11958.280061	**13174.66236**	24753.040541	32233.95451	**10251.47631**	14752.7168
f_{10}	6228.49289	7289.183679	6054.707691	6833.306317	6207.795302	7055.595231	**6050.434374**	**6609.804567**
f_{11}	1170.858603	1258.517635	1202.694857	1232.204268	1206.154564	1252.939541	**1156.439606**	**1205.254497**
f_{12}	677263.0799	16987989.981	**74784.6159**	530814.6481	584300.6983	3448448.7906	126908.2157	**494471.0756**
f_{13}	6005.535308	16893.949921	2041.488125	4332.5945	1572.252973	**4301.829606**	**1484.761799**	7760.056137
f_{14}	38490.532315	174367.45065	**2466.047056**	238838.470051	16327.42317	67939.000264	2967.818485	**26290.31618**
f_{15}	2278.141229	26989.255509	13553.041864	25636.769611	3443.587343	**9167.267098**	**1938.200405**	14976.72189
f_{16}	2722.026011	3176.916902	**2345.400708**	**2916.561016**	2521.93881	3146.04527	2436.449338	2978.37746
f_{17}	2799.949776	3289.61565	2568.383575	2907.869272	2887.281107	3236.957928	**2561.370306**	**2874.965038**
f_{18}	264037.12570	872072.47739	36176.58677	**113941.3176**	**26965.28512**	114846.121366	260540.781819	536454.326476
f_{19}	10051.912407	20380.25713	2089.172253	7763.17234	9905.850822	16555.756926	**2013.126904**	**3609.258962**
f_{20}	2950.923195	3274.334015	3041.81309	3113.289461	2991.589293	3361.823946	**2495.031774**	**3080.137478**
f_{21}	2596.725663	2689.688363	2526.190898	2597.677199	2555.8788	2642.381597	**2447.758274**	**2570.911014**
f_{22}	9713.993241	10803.653732	10759.59674	11032.880953	8918.436264	10465.022457	**8181.446081**	**9755.070369**
f_{23}	3451.104943	4200.174424	2971.160647	3237.778662	2977.554961	3490.639751	**2851.650254**	**3162.313622**
f_{24}	3434.465028	3682.846708	3103.955173	3185.382676	**3036.799607**	**3158.330504**	3136.927747	3284.656095
f_{25}	3141.144886	3292.303449	2931.162959	2962.471758	2931.926959	3008.895353	**2931.142314**	**2954.767839**
f_{26}	4906.132848	7989.490966	**2900.0**	3346.874039	2900.441895	3653.757741	**2900.0**	**3262.668498**
f_{27}	3200.010703	3792.645588	3143.038057	3184.646353	3158.178238	3397.130323	**3141.010872**	**3176.011524**
f_{28}	3300.010827	3431.570911	**3240.725865**	**3288.253039**	3263.207144	3300.257609	3243.631996	3294.373237
f_{29}	3812.475517	4605.349537	**3533.945743**	**3956.835243**	3955.324537	4364.18129	3653.675553	3966.471956
f_{30}	3673.711968	5813.173755	3916.725719	4869.089335	3730.309354	5143.078706	**3346.483679**	**4747.88675**
$w/t/l$	0/0/30	0/0/30	8/1/21	9/0/21	4/0/26	3/0/27	17/1/12	18/0/12

Table 6: Objective Function Value for Dimension: 100

f_{id}	DE		JADE		PSO-DE		HIDE	
	best	mean	best	mean	best	mean	best	mean
f_1	3427212811.79	13807281895.7	141.263356	13516.698933	6067123.52108	29751976.5091	**122.398748**	**11708.82360**
f_2	4.19617e+84	1.54741e+112	8.73752e+74	2.54362e+87	**6.1536e+66**	**3.2118e+73**	3.8835e+80	8.8914e+114
f_3	228808.969094	262699.687639	312244.360944	332179.290693	241427.723667	257462.977885	**220765.0838**	**251901.1093**
f_4	1975.651157	2752.246068	539.386275	677.054657	777.314462	836.965399	**531.169819**	**621.219143**
f_5	1223.536503	1286.153332	1249.195036	1307.110127	1248.410134	1310.887657	**1068.11742**	**1272.47682**
f_6	651.650133	657.84974	654.709342	659.421427	656.877048	662.318417	**642.33355**	**654.132758**
f_7	1614.003864	1920.797726	1367.066537	1536.357878	**1311.849757**	**1534.207764**	1562.379772	2076.702502
f_8	1595.418732	1736.367379	1672.567849	1768.082435	1678.127263	1761.94051	**1293.552115**	**1592.162983**
f_9	59726.514621	71986.043905	28906.90908	30336.745335	63640.331351	74961.220998	**23466.57501**	**27067.02959**
f_{10}	12005.889721	14725.348334	14227.801909	15355.621891	12937.027857	14972.950738	**11153.58683**	**13298.09210**
f_{11}	7540.617987	11481.260145	40447.548688	57228.683666	**3521.901521**	**4544.804011**	5380.432052	9916.347692
f_{12}	529993877.325	1881773956.29	3893556.27222	**6415173.6097**	26105108.937	41876679.0862	**3680108.181**	10059039.63
f_{13}	7943.9249	508209.562668	4622.698553	**8892.775994**	8246.515295	12675.845535	**2976.841354**	11376.986338
f_{14}	728122.833253	1329183.17224	**132194.7952**	**365560.8816**	548410.338286	941547.524763	234045.940166	867160.306892
f_{15}	2660.465784	181957.060133	**1799.506503**	3362.509604	1899.073444	**2914.44348**	1976.789124	4485.415275
f_{16}	4749.254663	5847.826738	4817.483738	5632.3022	3852.700054	5228.663526	**3519.494945**	**4796.802728**
f_{17}	4397.496352	4958.418182	3842.206015	**4450.177422**	3790.72056	4730.994585	**3582.785882**	5463.216947
f_{18}	1357845.39305	1938893.27972	**146426.2736**	**763318.8226**	1004224.20385	2315010.29868	631040.14635	1335739.59138
f_{19}	2482.170159	26455.706954	2098.9496	4767.529535	2263.725158	3927.459947	**2071.077067**	**3664.159878**
f_{20}	4968.497438	5436.604051	5231.026486	5690.748998	5109.460563	5781.300835	**3627.777893**	**5228.430669**
f_{21}	3180.746656	3355.4783	2921.900122	**3085.692252**	**2885.574085**	3127.356835	2926.350399	3199.986183
f_{22}	17808.897744	19562.986646	19213.375668	20278.929093	18695.522312	20167.413741	**17548.33905**	**19547.15124**
f_{23}	4907.519646	5819.207866	**3352.556985**	4222.436894	3582.043556	4779.921248	3418.983204	**3609.098575**
f_{24}	5173.249408	5946.12042	4060.951302	4095.429519	**3801.368588**	**4042.426859**	3998.054028	4216.824895
f_{25}	4089.118918	4548.285768	**3153.485413**	**3236.61784**	3348.382262	3407.526581	3176.3038	3264.318532
f_{26}	8557.498566	20159.11458	2900.077371	11924.799473	3021.136025	8682.035439	**2900.000382**	**7867.5518**
f_{27}	3200.023355	3772.409153	**3194.809213**	3201.670732	3200.024171	3494.618132	3200.023542	**3200.023953**
f_{28}	4947.745152	5948.213156	**3295.122914**	**3340.280383**	3456.828432	3542.571307	3300.807691	3354.717338
f_{29}	6004.774424	7090.642544	5208.711727	5970.628689	5462.328635	6178.559061	**4541.195471**	**5739.291549**
f_{30}	7798.106217	202435555.594	**3584.974771**	10674.217331	3920.327039	**7139.460728**	3850.317099	15318.554601
$w/t/l$	0/0/30	0/0/30	8/0/22	8/0/22	5/0/25	6/0/24	17/0/13	16/0/14

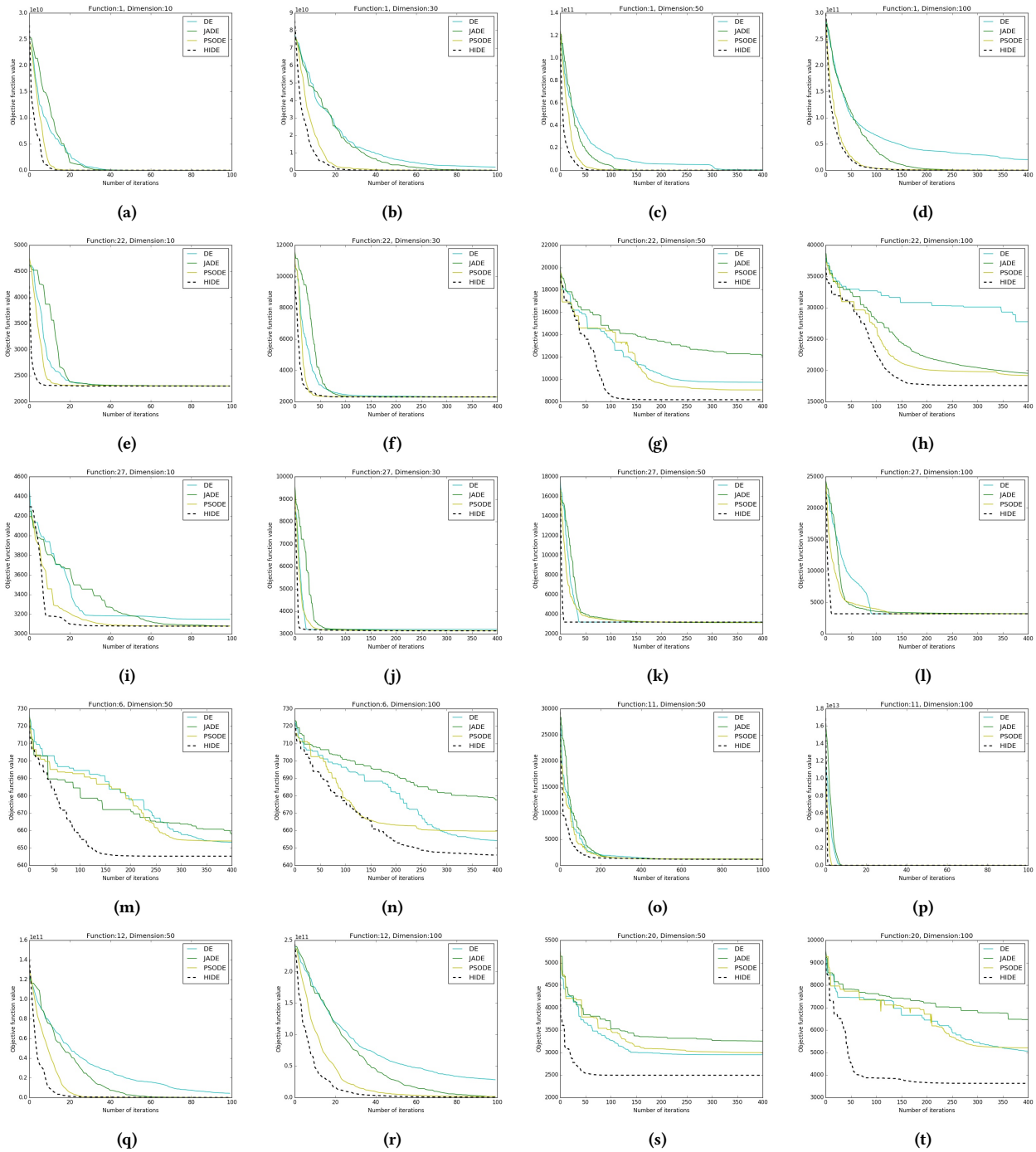


Figure 4: Comparative convergence profiles for test functions from CEC 2017 Benchmark over D = 10,30,50,100

have been summarized in "$w/t/l$" format wherein w represents the number of objective functions where the algorithm outperforms all other algorithms, t specifies the number of objective functions where it is tied as the best algorithm for the objective function and l represents the no of test functions where it does not finish first. The utilization of the evaluation metric facilitates a definitive comparison of the different algorithms under consideration.

Tables 3 and 4 highlight the performance of the algorithms for $D = 10$ and $D = 30$ respectively. For $D = 10$, HIDE depicits impressive performance. It registered a "$w/t/l$" score of 12/7/11 in

the best case and 14/4/12 in the mean of population case. In both these test functions, JADE achieved the second best performance registering a w/t/l of 5/7/18 on the best optimal value case and 9/4/17 on the mean of optimal value case. On $D = 30$, HIDE achieved maximum number of wins in both best and mean case (17 and 18 respectively). JADE achieved second position with 8 and 9 wins in the best and mean case. The decent performance of JADE can be attributed to the adaptive nature of its parameter selection which enables enhancement of its convergence rate.

The results for $D = 50$ and $D = 100$ (higher dimensions) have been summarized in tables 5 and 6. On $D = 50$, HIDE depicted exceptional performance, outperforming all other algorithms. It registered 17 wins in the best case and 18 wins in the mean case. Classical DE shows no wins in any case in high dimensional settings owing to its slow convergence rate and inability to attain global optimum thus highlighting the usefulness of the modifications introduced in the variants including HIDE. Similarly for $D = 100$, HIDE again outperforms all other algorithms by an appreciable margin. From a functional standpoint, It would be worthwhile to highlight that HIDE outperformed the other algorithm on majority on the composite and hybrid functions, particularly on the higher dimensional settings. The efficiency of HIDE can be attributed to the hierarchical nature of crossover selection and concurrency in vector configurations at the higher hierarchy levels. The tabular results reinforce the fact that HIDE outperforms JADE, PSODE and DE. On close analysis, it can be witnessed that HIDE falls behind the other algorithms on a small fraction of unimodal functions such as f_5, f_7 on lower dimensions due to fast convergence during early stages of execution. However, the performance of higher dimensions, particularly on the more involved functions highlights utility for real world problems.

The tabular results are complemented through the graphical representations in Figure 4. For the sake of clarity, representations of higher dimensional problems span more number of iterations than those for lower dimensional settings. Analysis of the plots clearly depicts that HIDE shows better convergence rate as compared to other algorithms. As the analysis transcends to higher dimensional settings, the proposed approach outperforms the other algorithms on majority of the objective functions with respect to both convergence rate and optimality. the superiority of our algorithm on higher dimensions (50 and 100) is clearly evident from Figure 4. (m,n,q,r,s,t). Figure 4. (e,f,g,h) depict that for functions where HIDE and the other variants may depict similar trends on lower dimensions, HIDE eventually excels and surpasses them on higher dimensions in most scenarios. Almost all figures are representative of a faster convergence rate for HIDE on higher dimensions. This remarkable trait in HIDE enhances its utility for high dimensional problems where fast convergence to global optimum value is required, hence making it superior to the other considered algorithms and several variants of the DE algorithm.

5 CONCLUSION

Differential Evolution has been regarded as one of the most successful optimization algorithms and over the years, several variants have been proposed to enhance its convergence rate and performance. In the present work, we introduced a hierarchy influenced variant of the classical DE algorithm and modeled the same on the brain motor operation. The algorithm was characterized by global leader, local leaders and an effector population. The global leader and distributed local leaders interacted to facilitate gross motion via a greedy exploration strategy. The local leaders and their effectors interacted to control intricate motion for smooth convergence. A hierarchical crossover parameter was introduced to characterize the hierarchical transition between the two interactions. The influence of the vector configurations at the higher levels of hierarchy enabled the algorithm to avoid local minima in most objective functions. The same is complemented through our result observations wherein we significantly outperform several popular algorithm on complex multimodal functions in higher dimensional settings. Our proposed approach has sought to establish a viable tradeoff between fast optimization, robust convergence and low number of control parameters. The performance analysis of the algorithm highlights the particular effectiveness of the proposed approach on high dimensional hybrid and composite functions. The observed results provide sufficient motivation to extend the scope of the work to complex high dimensional real life problems including image enhancement, traveling salesman problem and flexible job-shop scheduling.

REFERENCES

[1] NH Awad, MZ Ali, JJ Liang, BY Qu, and PN Suganthan. 2016. Problem Definitions and Evaluation Criteria for the CEC 2017 Special Session and Competition on Single objective Real-Parameter Numerical Optimization. *Technical Report*, (2016).

[2] Swagatam Das and Ponnuthurai Nagaratnam Suganthan. 2011. Differential evolution: A survey of the state-of-the-art. *Evolutionary Computation, IEEE Transactions on* 15, 99 (2011), 4–31.

[3] Marco Dorigo and Thomas Stützle. 2010. Ant colony optimization: overview and recent advances. In *Handbook of metaheuristics*. Springer, 227–263.

[4] J. D. Hunter. 2007. Matplotlib: A 2D graphics environment. *Computing In Science & Engineering* 9, 3 (2007), 90–95.

[5] James Kennedy. 2011. Particle swarm optimization. In *Encyclopedia of machine learning*. Springer, 760–766.

[6] Travis E Oliphant. 2007. Python for scientific computing. *Computing in Science & Engineering* 9, 3 (2007), 10–20.

[7] Godfrey C Onwubolu and BV Babu. 2013. *New optimization techniques in engineering*. Vol. 141. Springer.

[8] Kevin M Passino. 2002. Biomimicry of bacterial foraging for distributed optimization and control. *IEEE control systems* 22, 3 (2002), 52–67.

[9] Kevin M Passino. 2005. *Biomimicry for optimization, control, and automation*. Springer Science & Business Media.

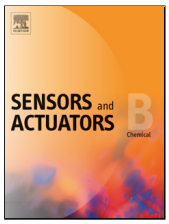
[10] David M. Shaw, A.M.P. Kellam, and R.F. Mottram. 1982. Brain Sciences in Psychiatry. In *Brain Sciences in Psychiatry*, David M. Shaw, A.M.P. Kellam, and R.F. Mottram (Eds.). Butterworth-Heinemann. DOI:http://dx.doi.org/10.1016/B978-0-407-00236-4.50009-4

[11] Rainer Storn and Kenneth Price. 1995. *Differential evolution-a simple and efficient adaptive scheme for global optimization over continuous spaces*. Vol. 3. ICSI Berkeley.

[12] Stefan Van Der Walt, S Chris Colbert, and Gael Varoquaux. 2011. The NumPy array: a structure for efficient numerical computation. *Computing in Science & Engineering* 13, 2 (2011), 22–30.

[13] Jingqiao Zhang and Arthur C Sanderson. 2009. JADE: adaptive differential evolution with optional external archive. *IEEE Transactions on evolutionary computation* 13, 5 (2009), 945–958.

Accepted Manuscript



Title: Highly sensitive porous carbon and metal/carbon conducting nanofiber based enzymatic biosensors for triglyceride detection

Authors: Kunal Mondal, Md. Azahar Ali, Chandan Singh, Gajjala Sumana, Bansi D. Malhotra, Ashutosh Sharma

PII: S0925-4005(17)30270-8
DOI: http://dx.doi.org/doi:10.1016/j.snb.2017.02.050
Reference: SNB 21781

To appear in: *Sensors and Actuators B*

Received date: 8-12-2016
Revised date: 4-2-2017
Accepted date: 9-2-2017

Please cite this article as: Kunal Mondal, Md.Azahar Ali, Chandan Singh, Gajjala Sumana, Bansi D.Malhotra, Ashutosh Sharma, Highly sensitive porous carbon and metal/carbon conducting nanofiber based enzymatic biosensors for triglyceride detection, Sensors and Actuators B: Chemical http://dx.doi.org/10.1016/j.snb.2017.02.050

This is a PDF file of an unedited manuscript that has been accepted for publication. As a service to our customers we are providing this early version of the manuscript. The manuscript will undergo copyediting, typesetting, and review of the resulting proof before it is published in its final form. Please note that during the production process errors may be discovered which could affect the content, and all legal disclaimers that apply to the journal pertain.

ACCEPTED MANUSCRIPT

Highly Sensitive Porous Carbon and Metal/Carbon Conducting Nanofiber Based Enzymatic Biosensors for Triglyceride Detection

Kunal Mondal,[a, #,*] Md. Azahar Ali,[a] Chandan Singh,[b] Gajjala Sumana,[b] Bansi D. Malhotra,[b,c,*] and Ashutosh Sharma[a,*]

[a]Department of Chemical Engineering, Indian Institute of Technology Kanpur, Kanpur-208016, Uttar Pradesh, India

[b]Department of Science and Technology Centre on Biomolecular Electronics, Biomedical Instrumentation Section, National Physical Laboratory, New Delhi-110012, India

[c]Department of Biotechnology, Delhi Technological University, Shahbad Daulatpur, Main Bawana Road, Delhi-110042, India

Corresponding author email: kmondal@ncsu.edu, bansi.malhotra@gmail.com, ashutos@iitk.ac.in[*]

Present Address

[#]Department of Chemical and Biomolecular Engineering, North Carolina State University, 911 Partners Way, Raleigh, NC 27695, USA.

AUTHOR INFORMATION

Corresponding Authors

[*]E-mail: ashutos@iitk.ac.in

[*]E-mail: bansi.malhotra@gmail.com

[*]E-mail: kmondal@ncsu.edu

ACCEPTED MANUSCRIPT

Highlights

1. Electrospun carbon (CNF) and silver/carbon (AgCNF) nanofibers were used to detect triglyceride biomolecules.
2. Silver nanoparticles improved electrical conductivity and graphitization to CNF.
3. Oxygen plasma promoted enhanced enzyme loading on nanofibers.
4. The sensitivity was fourfold higher for the AgCNF (1.232 μA mg/dL^{-1} cm^{-2}) bioelectrode compared with the CNF (0.33 μA mg/dL^{-1} cm^{-2}).
5. Fabricated biosensors exhibited excellent selectivity, good reproducibility, faster response (10 s) over a wide detection range (25–500 mg/dL).

ABSTRACT

Electrospinning was employed to synthesize a Ag nanoparticle (NP)-impregnated partially aligned and free-standing carbon nanofibers (CNFs) mat using a polyacrylonitrile (PAN) and silver nitrate blend followed by carbonization. Pyrolyzation of the PAN/$AgNO_3$ blend produced the nanoporous CNFs, and the Ag NPs were grown within the CNFs via thermal decomposition of $AgNO_3$. The fiber diameters of the synthesized CNFs ranged from 130 to 190 nm, and the size of the impregnated Ag NPs was ~30 nm. The presence of the Ag NPs enhanced the electrical conductivity and promoted graphitization of the CNFs via the templating effect of the Ag NPs. These synthesized CNFs and AgCNFs nanocomposite were electrophoretically deposited onto indium tin oxide electrodes for detection of triglyceride molecules. Oxygen plasma treatment of the CNFs and AgCNFs surfaces resulted in enhanced loading of lipase and glycerol dehydrogenase bienzymes. The AgCNFs nanocomposite exhibited faster electron transfer than the CNFs, as corroborated by electrochemical impedance spectroscopy and cyclic voltammetry studies. Covalent functionalization via 1-ethyl-3-(3-dimethylaminopropyl)carbodiimide/*N*-hydroxysuccinimide coupling chemistry on a nanoporous CNFs surface led to higher stability of

ACCEPTED MANUSCRIPT

the fabricated biosensor toward triglyceride detection. The sensitivity was fourfold higher for the AgCNFs (1.232 μA mg/dL^{-1} cm^{-2}) bioelectrode compared with the CNFs (0.33 μA mg/dL^{-1} cm^{-2}) over a wide detection range (25–500 mg/dL). These biosensors exhibited excellent selectivity, good reproducibility, and faster response (10 s). Thus, enhanced graphitization and electrical conductivity of nanoporous CNFs via incorporation of Ag NPs yields a promising platform for the detection of triglyceride (TG) biomolecules.

Keywords: Carbon nanofibers, Silver-carbon composite nanofibers, Electrospun nanofibers, Biosensor, Triglyceride, Electrochemical technique

1. INTRODUCTION

Metal and metal-oxide nanoparticles (NPs) supported on porous carbon scaffolds have attracted increased interest for gas separation,[1] water purification,[2, 3] catalyst supports,[4-7] fuel cell electrodes,[8] electrochemical double layer capacitors,[9, 10] and biosensors.[11-15] The high surface-to-volume ratio and porosity of carbon are known to result in superior dispersion, and loading of metal NPs has been reported to result in enhanced functionality of the metal/carbon composites.[16] Furthermore, the improved electrical conductivity of graphitized carbon may result in enhanced electron transport for fabrication of an electrochemical biosensor.[17] The porosity of carbon may provide easier transportation of reactants and products during a biochemical reaction.[18]

To synthesize long, one-dimensional (1D) porous carbon materials at relatively low cost is currently a challenge.[19] In this context, the electrospinning technique has been extensively

ACCEPTED MANUSCRIPT

explored for fabricating long and continuous carbon nanofibers (CNFs) because of its easy accessibility and cost-effectiveness.[20-22] Nanofibers of many materials such as polymers, metal oxides, and carbons can be obtained by electrospinning, which is a simple, reliable, and efficient technique.[20, 23] The resultant nanofibers sometimes assemble as an un-woven web of randomly oriented fibers. However, other assembly architectures, such as aligned nanofiber sheets, continuous single nanofiber filaments, nanofiber arrays, and nanofiber yarns, can be used by tailoring the process parameters and controlling the collection of nanofibers during electrospinning.[24-26] CNFs with diameters in the range of tens of nanometers to several micrometers are obtained by carbonization of electrospun fibers of suitable polymeric precursors.[19, 27] Polymer fibers with embedded metal NPs can be fabricated either by mixing the particles in the electrospinning solution or by incorporating a suitable metal salt followed by heat treatment to produce the NPs.[28-30]

Nanostructured Ag particles as nanodisks, nanowires, nanoprisms, and colloidal NPs, among other forms, have prospective applications in nanoelectronics, pharmaceuticals, household appliances, and detection of surface-enhanced Raman spectroscopy (SERS).[31, 32] Recently, research on Ag NPs used in various chemical and biochemical reactions as a catalyst has drawn much interest since these NPs have been found to exhibit unique shape- and size-dependent electro-optical and antimicrobial properties and high electrocatalytic and catalytic activities, particularly in redox reactions.[33-36]

The integration of Ag NPs with CNFs may perhaps improve graphitization and electrical conductivity, which may result in enhanced electron transfer properties between the electrode and electrolyte in a given electrochemical biosensor. In particular, the electrocatalytic property of Ag NPs was utilized for H_2O_2 sensing.[37] Huang et al. reported an electrospun-metal-NP-

ACCEPTED MANUSCRIPT

embedded CNFs platform for the reduction/oxidation of H_2O_2 and NADH.[38] Nafion and hemoglobin combined with CNFs resulted in excellent direct electron transfer between the enzyme and electrode, yielding a mediator-less third-generation H_2O_2 biosensor.[39] In addition, the high surface area and nanoporosity of the CNFs have been found to play important roles in the loading of biomolecules. Various approaches have been reported for the functionalization of biomolecules on CNFs surfaces. However, the covalent functionalization of CNFs provides strong amide bond formation, resulting in higher stability of a biosensor. Munkhbayar *et al*. reported that carbon nanostructured surfaces perhaps acted as a suppor for the uniform and stable dispersion of Ag NPs.[40] Vamvakaki *et al.* demonstrated direct immobilization of glucose oxidase on CNFs for the detection of glucose.[41] CNFs have been shown to be responsible for sensitive, stable, and reproducible electrochemical biosensors compared with CNTs and graphite powder.[41] Thus, CNFs can be used to attain a uniform dispersion of Ag NPs on a biosensor surface, which may lead to improved biosensor characteristics. Ordered mesoporous carbon particles were recently explored for the fabrication of nanocomposites by entrapping magnetic NPs for electrochemical biosensing applications.[42] Although, CNFs have been used as electrode materials for biomolecule immobilization, the use of Ag NP-doped CNFs to develop an electrochemical biosensor has not been yet been investigated.

Quantification of TG in human serum samples has attracted significant interest for health care diagnostics. TG is an ester containing glycerol and three fatty acids that can play a role in the transportation of adipose fat and blood glucose from the liver.[43] A higher concentration (above 200 mg/dL) of TG may cause various diseases including cardiac disease, diabetes mellitus, nephrosis, liver obstruction, and endocrine disorder. To date, various conventional methods have been explored to determine the TG concentration.[44] A state-of-the-art

ACCEPTED MANUSCRIPT

instrument to quantify TG in human plasma and serum has been commercialized as "Cayman's Triglyceride Assay Kit" and is based on the color change due to the enzymatic reaction. Thus, there is an urgent need to develop a highly sensitive, reproducible, low cost, compact electrochemical device with a fast response for the detection of TG.

In this work, a blend of PAN polymer and silver nitrate salt in an *N*, *N*-dimethyl formamide (DMF) solvent was used to prepare nanoporous AgCNFs composites via electrospinning and subsequent thermal treatment. The $AgNO_3$/PAN blend was first electrospun into nanofibers on a rotating collector, and further thermal treatment resulted in the *in situ* formation of Ag NPs because of decomposition of the nitrate salt precursor during the carbonization of PAN, thereby creating porous AgCNFs without the need for any chemical treatments or physical/chemical activation. Removing carbons from AgCNFs produces a structure of Ag nanofibers that may find potential application in nanoelectronic and nanoelectromechanical devices.[45] Furthermore, the synthesized porous, free-standing CNFs and AgCNFs were utilized for covalent interaction with lipase (Lip) and glycerol dehydrogenase (GLDH) bienzyme via 1-ethyl-3-(3-dimethylaminopropyl)carbodiimide/*N*-hydroxysuccinimide (EDC/NHS) coupling chemistry. This bienzyme-modified bioelectrode was also investigated for TG detection.

2. EXPERIMENTAL SECTION

2.1 Materials

Polyacrylonitrile (PAN) (M_w = 150,000), silver nitrate ($AgNO_3$) were purchased from Sigma–Aldrich, USA. N, N-dimethyl formamide (DMF) was purchased from Fischer Scientific, India. Lipase enzyme (specific activity of 48 Umg^{-1}; Lip) was purchased from Fluka.

ACCEPTED MANUSCRIPT

Nicotinamide adenine dinucleotide (NADH), glycerol dehydrogenase (specific activity of 77 Umg^{-1};GLDH),N-N-ethyl-N-(3-dimethylaminopropyl carbodiimide) (EDC), hydroxysuccinimide (NHS), and triglycerides (TG), were obtained from Sigma-Aldrich, USA. The Lip and GLDH enzyme solutions were prepared in phosphate buffer saline (PBS; 50 mM, pH 7.0) prior to being used. Stock solution of TG was prepared in ethanol and it was further diluted to make various concentrations of tributyrin or TG. The Millipore water purification system was utilized for de-ionized water. All chemicals were of analytical grade and used as supplied without further purification.

2.2 Synthesis of carbon nanofibers from PAN polymer

First, an 8 wt.% PAN/DMF blend solution was prepared by heating the solution mixture at 65 $^{\circ}$C with continuous stirring for ~30 min resulting in a clear transparent solution. Then, 2 ml of PAN/DMF solution was taken into a disposable syringe (Dispovan, Hindustan Syringes & Medical Devices Ltd., India) and electrospun on a highly cleaned aluminum foil which was firmly attached on a rotating drum collector (3000 rpm). The flow rate used was 40 microliter/min and 15 kV DC voltage applied between the tip of the syringe and the collector at a distance of 5 cm. The use of a rotating drum collector was to increase the formation of partially aligned nanofibers. Then, the as-spun fibers were stabilized at 250 $^{\circ}$C for 1 h in a vacuum oven. Some of the free standing fiber mats were also collected during the electrospinning process. These electrospun polymer fibers were then carbonized under N_2 atmosphere with a steady flow rate of 0.15 L/min and a heating rate of 5 $^{\circ}$C/min up to 900 $^{\circ}$C and was kept at this temperature for about 2 h followed by ambient cooling to obtain the desired carbon nanofibers.

ACCEPTED MANUSCRIPT

2.3 Synthesis of CNFs with impregnated Ag NPs

Three different AgNP loaded CNFs were synthesized by pursuing the same procedure as mentioned above. However, 0.01, 0.1 and 0.25 equivalents of $AgNO_3$ salt (with respect to the PAN monomer) were also added during the preparation of PAN/DMF solution.

2.4 Fabrication of SU 8 posts

An array of SU 8 posts (120 ×120 µm) was fabricated using standard photolithography on a p- type high resistive Si-wafer with a native SiO_2 layer following the fabrication protocol reported earlier.[46, 47] These fabricated posts were subjected to pyrolysis under the flow of argon at 900 ^oC for 2 h. The height of these fabricated posts after pyrolysis was ~2 µm.

2.5 CNFs based biosensor platform

The electrospun CNFs and AgCNFs were deposited on ITO electrode using electrophoretic deposition (EPD) technique. First, we prepared well-dispersed stock solution, where 10 mg CNFs or AgCNFs powder was dispersed in one mL acetonitrile followed by ultrasonication (40W, 0.25 A) for about 4 h. For EPD, 300 µL of this stock solution was added in 10 mL of acetonitrile to form dilute colloidal suspension of CNFs or AgCNFs. The EPD was conducted using a two-electrode cell by applying a DC voltage of 60 V for 2 min. To create surface charges on CNFs or AgCNFs surface, 10^{-5}–10^{-4} mol of $Mg(NO_3)_2.6H_2O$ was added into the suspension during EPD.[48] A pre-cleaned hydrolyzed ITO electrode acted as the anode and a platinum foil (1 cm × 2 cm) acted as the cathode. The deposited films were then removed from the cell and washed for several times with de-ionized water and dried at 100^oC. For co-immobilization, 20 µL of lipase and GLDH solution (1: 1 ratio) was uniformly spread on the CNFs and AgCNFs electrode surfaces and were then kept in a humid chamber for 4 h and stored

ACCEPTED MANUSCRIPT

at 4ºC for 8 h before experiments. Prior to enzyme co-immobilization, the electrodes surfaces were treated with EDC-NHS solution wherein EDC (0.2M) worked as a coupling agent and NHS (0.05M) activated –COOH groups. Presence of –COOH groups in CNFs perhaps allowed these to covalently interact with $–NH_2$ groups of enzyme molecules resulting in C-N, strong amide bond on transducer surface (Figure 1). These prepared bioelectrodes were then washed with phosphate buffer and stored at 4 ºC, when not in use.

2.6 Characterization

To characterize the surface morphologies of CNFs and the AgCNFs hybrid, the field emission scanning electron microscopy (FESEM, Quanta 200, Zeiss, Germany) was used. The X'Pert Pro, PANanalytical, Netherlands, X-ray system with Cu Kα radiation was used for powder X-ray diffraction (XRD) measurements to obtain the structural information about the desired carbon fibers. Raman spectral analysis was performed to characterize the graphitic nature of the carbon material on WiTec, Germany having a laser light Raman spectra (Raman parameters: laser wavelength (λ) = 532 nm, power = 12 mW, spot size = 500 nm, objective lens = 20X and signal integration time = 5 sec). The surface area and the pore volumes of the fibers were determined by BET (Quantachrome Instruments, USA) having Autosorb 1 software. The total surface area and the pore volume of the pyrolized hybrid samples were calculated based on the amount of nitrogen that was adsorbed and desorbed at -196.15 ºC (77 K) using the Brunauer, Emmett and Teller (*BET*) instrument (Model: AS1-C, Quantachrome, USA). The samples were degassed at 200 °C under vacuum prior to the analysis. The total pore volume of the samples was calculated on the basis of the quantity of N_2 adsorbed at a relative pressure near unity (P/P_o = 0.9965). The electrochemical characterization was performed by an Autolab Potentiostat/Galvanostat (Eco Chemie, Netherlands) using a three-electrode system in phosphate

ACCEPTED MANUSCRIPT

buffer saline (PBS, 50 mM, pH 7.0, 0.9% NaCl) containing 5 mM $[Fe(CN)_6]^{3-/4-}$ redox probe. The whole reaction process was conducted at room temperature (25^{o}C) and at controlled humidity level of 34%.

3. RESULTS AND DISCUSSION

3.1 Electrospinning of AgCNFs

A schematic of the setup used for the electrospinning of AgCNFs is presented in Figure S1 (Supporting Information). A high DC voltage of 15 kV was applied between the metallic needle and grounded rotating drum collector. The polymer drop at the tip of the needle started to elongate because of the high electric field and formed a Taylor cone (shown in Figure S1), and a very thin jet of polymer solution was thrown out from it as soon as the applied electric field overcame the surface tension energy of the polymer. The constant high electric force together with fast solvent evaporation resulted in stretching of the viscoelastic polymer fibril, which further forms polymer nanofibers on the electrically grounded collector surface.

The uniform fibers of the PAN/$AgNO_3$ blend with diameters ranging between 200 and 250 nm were obtained by optimizing the essential parameters for the electrospinning process. At a 80 µL/min solution flow rate, the diameter was observed to shrink upon decreasing the polymer concentration until a critical concentration (~ 1 wt.%) was reached, below which no continuous fiber could be obtained instead of beaded structures (data not shown). Figures 2a and b demonstrate that these nanobeads perhaps continued to form up to 6 wt.% polymer concentration. Low viscosity prevented the formation of the Taylor cone in the polymer solution, which produced these beads.[49, 50] When the viscosity increased to 8 wt.%, bead-free

ACCEPTED MANUSCRIPT

continuous smooth nanofibers were produced, and the diameter also increased (Figures 2c, d). Larger-diameter rough fibers were formed at a higher PAN concentration of 16 wt.%, as observed in Figure 2c, d. Hence, a concentration of 8 wt.% PAN was observed to be the optimum concentration and was thus used for electrospinning because it resulted in easy spinability and bead-free, uniform-diameter, dense nanofiber mats with a typical diameter of ~250 nm.

The average fiber diameters were determined to be ~120 nm and ~1.2 µm for rates of and 180 µL/min, respectively (Figure 2e and 2f), which were observed to increase upon increasing the solution flow rate of the optimized 8 wt.% PAN solution. As discussed earlier, we regulated the flow rates to preserve the Taylor cone. Dry polymer at the needle tip was observed at low flow rates; in contrast, elevated flow resulted in the formation of fibers. However, most of the solution was wasted in the form of large droplets, and thus, no fiber was formed [51]. Thus, the 8 wt.% solution flowing at a flow rate of 40 µL/min (shown in Figure 3a and b) and electrospun at 15-kV electric potential on a rotating drum collector at a 5-cm distance between the syringe tip and collector produced close to optimal dense nanofiber mats. The dependence of the fiber diameter on the amount of polymer and flow rate can be clearly seen in Figure S2 (Supporting Information).

3.2 Surface morphology of the nanofibers

The morphology of the carbon nanofibers before and after pyrolization in an inert N_2 atmosphere is shown in Figure 3. The as-spun nanofibers (Figure 3a, b) exhibited a smooth fibrous morphology and were partially aligned in orientation and pyrolyzed at 900°C (Figure 3c, d), which generated highly porous, long fibers with an average diameter of ~120 nm. Shrinkage

ACCEPTED MANUSCRIPT

of approximately 60% of the fiber diameter was observed after pyrolization of the PAN/$AgNO_3$ electrospun fibers.

The field-emission scanning electron microscopy (FESEM) images (Figure 3d) reveal the presence of Ag NPs with an average diameter of approximately 30 nm that are uniformly distributed on the CNFs surfaces. Further, we also produced free-standing mats of Ag/carbon fibers (Figure 3e). Larger Ag NPs resulted when the loading of the precursor salt ($AgNO_3$) was higher in the PAN polymer. Figure 3f shows CNFs decorated with larger Ag NPs. Analysis of some of the ruptured portion of the composite nanofibers further revealed the presence of metal NPs embedded underneath the fiber skin layers (indicated by the arrow in Figure 3g). During the high-temperature carbonization process, the precursor silver nitrate salt converted into Ag NPs within the carbon fibers and thus produced AgCNFs composite fibers. Moreover, the energy-dispersive X-ray spectroscopy (EDX) data (presented in Figure S3, Supporting Information) confirms the presence of Ag and carbon after carbonization at 900 °C. The composition of the AgCNFs determined using EDX elemental analysis is listed in Table T1 (Supporting Information). The Si peak is perhaps due to the dispersion of AgCNFs on the Si wafer used for the analysis.

We synthesized a metallic Ag NP nanochain architecture by burning the excess carbon present in the AgCNFs composite fibers in air at high temperature (800 °C for 4 h). After complete burning of the AgCNFs, when the temperature started decreasing, Ar gas was allowed to pass to prevent the Ag from oxidation. Calcination of the composite fibers allowed removal of carbon from the fibers as CO_2, leaving behind the metallic chains of the NP architecture (Figures 3h and i). The

ACCEPTED MANUSCRIPT

EDX results confirmed the presence of Ag in the nanochains. The yield for the synthesis of the metallic Ag architecture from the AgCNFs fibers was observed to be 43.11±4.5%.

Lip and GLDH enzymes were immobilized onto CNFs and a AgCNFs surface containing ITO electrodes after oxygen (O_2) plasma treatment (shown in Figure 4). Plasma treatment modified the surface of the CNFs and AgCNFs electrodes by creating functional groups (e.g., -COOH), which allowed enhanced biomolecule loading onto the electrode surface. After bienzyme immobilization, the enzyme molecules covered the CNFs surface, as observed in Figure 4a. These CNFs appeared to become agglomerated because of the incorporation of bienzyme molecules. The enzyme loading was higher on the AgCNFs surface (Figure 4b) compared with on the CNFs because of the high Brunauer–Emmett–Teller (BET) surface area and porosity of the hybrid nanofibers. The high-resolution FESEM image in Figure 4c shows morphology of a single AgCNF, wherein the enzyme molecules are observed to be attached to the pores of the nanofibers due to the covalent interactions between the bienzyme and functionalized CNFs.

Transmission electron microscopy (TEM) images of carbonized nanofibers were acquired to examine the three-dimensional structure of the CNFs and AgCNFs composite fibers. As observed in Figure 5a, the carbon nanofibers are continuous, solid, and uniform in diameter. The thermal decomposition of $AgNO_3$ along with the polymer allowed *in situ* impregnation of Ag NPs into the carbon nanofibers. When the loading of the precursor salt was low, Ag NPs with smaller diameters (average size ~20 nm) were formed (Figure 5b). Figure 5c clearly demonstrates that a few small Ag NPs are present in the CNFs. The density (~12×10^{12} m^{-2} for

ACCEPTED MANUSCRIPT

0.1 equivalent to $AgNO_3$-loaded-PAN/$AgNO_3$-derived AgCNFs) of Ag NPs increased with increased loading of the Ag salt into the fibers, as demonstrated in Figure 5d. Figure 5e shows the uniformly distributed Ag NPs in the porous CNFs. The selected area electron diffraction (SAED) pattern (Figure 5f) reveals that the synthesized Ag NPs were the face-centered cubic (FCC) phase and highly crystalline, which may improve the charge transfer properties. We also estimated the Ag content in the Ag/carbon composite fibers by analyzing the TEM micrographs in Figures 5d, e. By calculating the number of Ag NPs (result shown with the histogram in Figure S4) present in the measured area of a fiber and considering the weight ratio of the Ag particles and carbon fibers, it was observed that a Ag:C ratio of ~4.9:3 was maintained in the composite fiber.

3.3 Surface area measurement

To measure the specific surface area, the Ag/carbon fibers were subjected to degassing at 200 °C for 8 h in vacuum, and then, nitrogen adsorption–desorption isotherms were obtained (Figure 6a). The pore size distribution was evaluated using non-local density functional theory (NLDFT) from the adsorption curve of the isotherm (inset: Figure 6a) of the BET data. The total pore volume was measured from the adsorbed N_2 at a relative pressure, P/P_o, of 0.9994. The total BET surface area and pore volume were observed to be 91.39 m^2/g and 6.49 $\times 10^{-2}$ cc/g, respectively, with an average pore size of 2.84 nm. There were 62.32% micropores, 34.25% mesopores, and 5.16% macropores in the total pore volume calculated based on the recorded BET data. This result indicates that Ag/carbon fibers were porous with dominating micropores.

3.4 Raman spectral analysis of the porous fibers

ACCEPTED MANUSCRIPT

The results of Raman spectroscopy studies conducted on the electrospun-PAN-derived carbon and porous Ag/carbon fibers are presented in Figure 6b. The carbon fibers exhibit two strong bands at approximately 1299 and 1592 cm^{-1}, which correspond to the D and G bands of carbon material, respectively. The G peak represents the E_{2g} mode of graphite because of the sp^2 bonded carbon atoms situated in a 2D hexagonal graphitic plane. The D peak is attributed to the structural defect sites in the hexagonal framework of carbon walls and disorder-induced peak. The D/G band intensity ratio (denoted by I_D/I_G) is frequently used to evaluate the graphitic content in carbon samples. The I_D/I_G ratios for the carbon and Ag/carbon fibers calculated from the Raman spectra as 1.43 and 1.34, respectively, were observed to decrease with metal particles incorporation in the carbon matrix. This result indicates that the metal NPs perhaps induced localized heating to the adjacent carbon layers, decrease some of the disorder, and enhanced graphitic content of the carbon fibers. The crystallinity of the sample could be quantified using an empirical formula proposed by Knight and White[52]:

$$L_a(nm) = \frac{4.4}{I_D/I_G},$$

where L_a (nm) is the in-plane graphitic crystallite size and I_D/I_G is the Raman D and G band intensity ratio. Using this equation, the in-plane graphitic crystallite sizes (L_a) were observed to be increased from 3.08 to 3.20 nm for the carbon and Ag/carbon fibers, respectively. The observed decrease in the ratio indicated the enhancement of the graphite fraction in the CNFs. This finding is most likely because the I_D/I_G ratio is proportional to the number of scattering disordered and ordered sp^2 bonding carbon atoms.[53] The carbon graphitic layer grow, and the spacing between the two graphite layers decreased because of the metal-particle-induced

ACCEPTED MANUSCRIPT

localized heating during high-temperature pyrolysis, which produced the higher graphite domains in the carbonized carbon fibers, as demonstrated in the Raman analysis.

3.5 XRD analysis of porous CNFs and AgCNFs

To investigate the crystalline nature of the as-electrospun PAN-derived carbon and Ag/carbon fibers, X-ray diffraction (XRD) analysis (X-ray wavelength = 1.54060 Å) was performed (Figure 6c).The obtained XRD data was compared with Pearson's crystal data (PCD) (File no. 1819831). The broad diffraction peak of the carbon fibers occured at approximately 2θ = 22.5°, which corresponded to a planar spacing of d = 3.943 Å, indicating the formation of the graphite structure. [54] This peak can be indexed to the (002) reflection plane derived from carbon.[54, 55] The phase composition and crystalline nature of the Ag/carbon fibers were determined by matching the XRD pattern with the PCD reference patterns of pure component carbon (File no. 1819831) and Ag (File no. 261046) substances. The sharp peaks at 2θ=38.11° and 44.31° correspond to the (111) and (200) planes of metallic Ag. The other peaks occur at 57.43°, 64.45°, and 77.48°, which belong to the (222), (220), and (311) reflection planes, respectively; together with the above carbon peak at 2θ=22.5°, these peaks corroborate the presence of Ag NPs in the carbon fibers. All these peaks indicated the presence of the characteristic face-centered cubic (FCC) Ag, which was confirmed by the TEM SAED pattern (Figure 5f). The average crystallite size of the Ag NPs was calculated from the XRD pattern using the Debye–Scherrer equation[56]:

$$D = \frac{0.90\lambda}{\beta cos\theta},$$

ACCEPTED MANUSCRIPT

where β is the full-width at half-maximum (FWHM) corresponding to the diffraction angle (θ), and 0.90 is the Scherrer's constant. The average crystallite size of the Ag NPs was observed to be ~33.73 nm for the (111) reflection plane. The XRD crystallite sizes of the porous carbon and Ag/carbon hybrid fibers along the (111) basal plane determined using Scherrer's formula [57] were ~3.06 and ~3.21 nm, respectively. This result indicates that the graphitic layer grows more because of the metal NP incorporation in the porous carbon matrix.

3.5.2 FTIR studies

Figure S5 (Supporting Information) presents Fourier-transform infrared spectroscopy (FT-IR) spectra of the PAN-derived CNFs, oxygen-plasma-treated AgCNFs, and AgCNFs electrode with and without enzyme immobilization. The spectrum for the CNFs coated on an ITO electrode has strong peaks at 1110 cm^{-1} and 1637 cm^{-1} (curve 'a' in Figure S5), which are assigned to the vibrations of C–O and C=O stretching in the COOH group. The peak observed at 1390 cm^{-1} is due to O–H bending in the COOH group, and the 1844 cm^{-1} peak is assigned to C–H bending vibration. The stretching vibrations observed at 1110 and 1637 cm^{-1} were attributed to the carboxyl group indicating COOH functionalization of the CNFs because of the oxygen plasma treatment. For the AgCNFs, similar FTIR peaks were observed (curve 'b' in Figure S5) with reduced peak intensities because of the impregnated Ag NPs in the CNFs. After Lip–GLDH enzyme immobilization onto the AgCNFs surface, additional peaks were observed at 1650 cm^{-1} and 1260 cm^{-1} due to the N–H bending of amide I and amide III, respectively, present in the enzyme molecules. The peaks arose due to amide I and III, indicating co-immobilization of the enzyme (Lip–GLDH) [curve c in Figure S5].

3.7 Electrical conductivity measurement of the Ag/carbon composite nanofibers

ACCEPTED MANUSCRIPT

The electrical conductivity of the suspended Ag NP-impregnated composite CNFs between two lithographically fabricated SU 8-derived carbon posts was measured using a Keithley 6517A digital electrometer attached to a high-resolution optical microscope (Leica, Germany). The schematic in Figure 7a shows the conductivity measurement setup, where electrical contacts of the single nanofiber suspended between the two carbons micro-posts were made using two sharp tip Au-coated microprobes.

We prepared solutions with three different concentrations of $AgNO_3$ in PAN for electrospinning, which were prepared by mixing 0.01, 0.1, and 0.25 equivalent silver nitrate salt in 8 wt.% PAN in DMF solvent. These solutions were then electrospun at 15 kV DC potential on the lithographically fabricated SU 8 microelectromechanical system (MEMS) structure assembly. The distance between the needle tip and SU 8 MEMS containing the rotating electrode was 5 cm, and the flow rate of the solution was fixed at 2 µL/min. The electrospinning of the PAN and PAN/$AgNO_3$ polymeric blend was performed for a few seconds (~5–10 s) only to restrict the number of fibers and to produced single fibers hanging between the fabricated posts (Figure 7b). The spun fibers on the MEMS were then stabilized in air and subjected to carbonization at 900 °C for 2 h with a slow heating rate to produce carbon nanofibers with worthy interfacial contacts and to minimize the contact resistance between the carbonized fibers and posts. As a result, the current–voltage (I–V) curves of the carbon composite fibers exhibit an ohmic nature. It can thus be concluded that there is very low contact resistance in the nanofibers fabricated using this method. Figure 7c shows a single suspended AgCNFs composite nanofiber. Table 1 summarizes the electrical conductivities of the pure PAN-derived CNFs and Ag-impregnated CNFs. The resistance was calculated from the slope of the I–V curves. The electrical conductivity of CNF

ACCEPTED MANUSCRIPT

and AgCNFs increased upon increasing the Ag loading in the CNFs. The resistivity of the pure PAN-derived CNFs and three different Ag-loaded composite CNFs were determined as (6.59 ± 0.29)×10^{-5}, (1 ± 0.33) ×10^{-5}, (2.76 ± 0.57) ×10^{-6}, and (8.30 ± 1.75)×10^{-07} Ω-m, respectively. Sharma *et al.*[46] reported a comparable value for the resistivity of CNFs (7.68 × 10^{-5} Ω-m). The conductivity of the AgCNFs composite fibers increased upon Ag loading in the CNFs. This increase in conductivity of the composite fibers compared with pure CNFs is in agreement with literature.[46, 47] The impregnated metal NPs in the carbon increased the degree of graphitization, which is in strong agreement with the previously discussed Raman and XRD analysis. It appears that the enhanced graphitic content thus increased the conductivity of the composite fibers. The observed good conductivity and enhanced graphitization in the AgCNFs may perhaps lead to increased electron transfer between the electrode and electrolyte for electrochemical biosensor fabrication. The CNFs are distinguishable from CNTs because of the stacking of graphene sheets present in CNFs with varying shapes and sizes, which perhaps produced additional edge sites on the outer wall of the CNFs compared with those for the CNTs.[11] This phenomenon may perhaps expedite the efficient electron transfer of electroactive analytes.

4. Electrochemical studies

4.1 Cyclic voltammetry studies

Well-defined oxidation and reduction peaks were observed in cyclic voltammetry (CV) studies of the fabricated electrodes recorded in phosphate buffer saline (PBS) containing ferro/ferri cyanide as a mediator in the potential range of -0.7 V to +1.0 V [Figure 8(i)]. The anodic peak current and peak-to-peak potential of the CNT electrode were observed to be 693

ACCEPTED MANUSCRIPT

μA and 0.39 V, respectively. Enhancement of the peak current of 773 μA due to the incorporation of Ag NPs on the CNFs and an additional small peak at lower potential (0.06 V) were observed. The peak-to-peak separation voltage of the AgCNFs electrode was reduced to 0.35 V because of the higher electron transfer kinetics compared with those of the CNFs electrode. The observed higher current and reduced peak-to-peak separation voltage due to improved graphitization for the Ag NP-impregnated CNFs resulted in increased electrochemical conduction between the electrode and electrolyte. Maitra *et al.*[47] observed that graphitization can improve the electrical conductivity of CNFs. After co-immobilization of the Lip-GLDH enzyme on the CNFs surface, the peak current decreased to 559 μA because of the inherent properties of the enzyme molecules, which exhibited an insulating nature during the oxidation and reduction of ferro/ferri cyanide, resulting in decreased current. However, notably, we observed a large peak current (886 μA) for the Lip-GLDH-modified AgCNFs electrode surface compared with the Lip-GLDH/CNFs electrode. This finding is attributed to the fact that Ag NPs acted as a mediator, which activated the electrochemical active sites of enzyme molecules to move electrons toward the electrode.[58] The Ag NPs perhaps established an electronic path between enzyme active sites and the electrode, which may result in increased transport of electrons toward the electrode, yielding an improved current in the presence of enzyme molecules. The diffusion coefficient of the $[Fe(CN)_6]^{3-/4-}$ ions for each electrode was determined using the Randles–Sevcik equation.[59] The electrochemical area (A_{ec}) was estimated using the relation $A_{ec} = q_{ad}/q_m$, where q_{ad} is the charge associated with the electrode with monolayer coverage, and q_m is the charge associated with the known adsorbate on the electrode surface.[60] Table T2 lists the diffusion coefficient and electrochemical area for the fabricated electrode. The surface charge density (Q_{ads}) resulting from protein absorption on the electrode surface was

ACCEPTED MANUSCRIPT

calculated[61] to be 1.37×10^{-7} mol/cm^2 for the AgCNFs electrode, which was higher than that of the CNFs electrode (6.63×10^{-8} mol/cm^2). Figures S6 and S7 (Supplementary Information) present cyclic voltammograms of the CNFs- and AgCNFs-based bioelectrodes obtained as a function of the scan rate (20–100 mV/s). In both cases, the redox peak current/potential increased linearly with the square root of the scan rate, indicating that the redox reaction is a surface-controlled process. Their slopes and intercepts followed the equations, as observed in the inset of Figures S6 and S7 (Supplementary Information).

4.2 Impedance studies

To investigate the impedance of the interfaces between the electrodes and electrolyte, electrochemical impedance spectroscopy (EIS) was used by applying a small AC signal (bias potential = 0.01 V) as a function of frequency (0.01 to 10^5 Hz). Figure 8(ii) presents Nyquist plots for the impedance spectra, where the diameter of the semicircle provides a value of R_{CT} that indicates the electron transfer kinetics of the $[Fe(CN)_6]^{3-/4-}$ redox mediator at the electrode/electrolyte interface. The R_{CT} and Cdl values for bare ITO electrode were estimated to be 1.33 kΩ and 5.64 μF, respectively. The electrophoretic deposition of CNFs and AgCNFs on ITO changed the R_{CT} values (AgCNFs: 1.11 kΩ and CNFs: 1.27 kΩ). The increased R_{CT} value for the AgCNFs electrode compared with that of the CNFs electrode may be due to the incorporation of Ag NPs on the CNFs surface, which promotes electron conduction between the electrode and electrolyte. In addition, the enhanced electrical conductivity may lead to improved electrochemical charge transport thereby leading to a decreased impedance value. The value of the heterogeneous electron transfer (HET) constant for the AgCNFs electrode was determined as 19.3×10^{-8} cm/s, which was higher than that of the CNFs electrode (16.8×10^{-8} cm/s). On co-

ACCEPTED MANUSCRIPT

immobilization of Lip and GLDH on the CNFs surface, the R_{CT} value and HET constant decreased to 1.35 kΩ and 15.8×10^{-8} cm/s, respectively, indicating the absorption of enzyme molecules on the CNF/ITO surface. This result can be attributed to the presence of enzyme molecules on the CNFs surface, which provided hindrance to the diffusion of the ferri/ferro cyanide ions from bulk solutions toward the electrode surface. However, the modification of enzyme molecules on the AgCNFs surface reduced the R_{CT} value to 1.02 kΩ compared with the AgCNFs electrode. AgCNFs perhaps established a conduction pathway in the presence of the enzyme that reduced the tunneling distance to diffuse electrons between the active center of the enzyme and electrode.[59] The HET constant for the Lip-GLDH/AgCNF electrode was higher (20.9×10^{-8} cm/s) than that of the other electrode. Table T2 presents the HET constants and time constants obtained for various fabricated electrodes [62]

4.3 Detection of triglyceride molecules

The cyclic voltammetric responses of CNFs- and AgCNFs-based bioelectrodes were investigated as a function of TG concentration (25–500 mg/dL). The mechanism to quantify TG is explained in Schematic S1 (Supplementary Information). During electrochemical detection, the Lip enzyme on the transducer surface hydrolyzes the triglyceride (tributyrin) molecules, which produce glycerol and three different carbon chain length fatty acids. The produced glycerol was oxidized by GLDH with the participation of NAD+, which acted as an electron acceptor. The production of dihydroxyacetone, NADH, and hydrogen ions occured during this enzymatic reaction on the electrode surface. Thus, glycerol was oxidized using GLDH with NAD^+ to create NADH for the detection of TG molecules. Other than mediator electrons resulting from the ferro/ferri conversion in the electrolyte, the electrons resulting from the

ACCEPTED MANUSCRIPT

enzymatic reaction were responsible for the enhanced electrochemical current. The sensing potential for detecting TG molecules in these biosensors is approximately 0.3 V. Because of the slow charge transfer kinetics, NADH required a large over-potential to oxidize at the electrode surface.

Figures 9 (i) and (ii) present CV curves for various TG concentrations for CNFs- and AgCNFs-based bioelectrodes. The magnitude of the oxidation current increased linearly with increasing TG concentration [Fig. 9(iii)]. The linearity plots between the anodic current and TG concentration for the CNFs- and AgCNFs-based bioelectrodes are presented in Figures 9 (iv) and (v), respectively. This linear nature resulted from the produced electrons during the enzymatic reaction on the transducer surface. Liao et al. incorporated iridium NPs on a carbon paste electrode for electrochemical detection of TG molecules. However, the sensitivity was observed to be 7.5 nA in the detection range of 0 to 10 mM.[44] In our strategy, we incorporated Ag NP-impregnated CNFs for the detection of TG molecules in the range of 25–500 mg/dL. The nanoporous structure of the AgCNFs resulted in improved stability and loading capacity of enzyme absorption, resulting in higher sensitivity and a low detection limit. Table 2 lists the various parameters for TG detection in comparison with those of reported biosensors using other nanomaterials. The range of linearity for the Lip-GLDH/AgCNF bioelectrode is higher (50–400 mg/dL) than that of the Lip-GLDH/CNF bioelectrode (100–400 mg/dL) [Figs. 9(iv and v)]. We observed four-fold enhancement of the sensitivity (1.232 μA mg/dL^{-1} cm^{-2}) for the Ag-imprinted CNFs electrode compared with only using a CNFs electrode (0.33 μA mg/dL^{-1} cm^{-2}). This result may be due to the incorporation of Ag NPs on the CNFs, which improved the electrochemical properties and HET rate of CNFs, resulting in higher sensitivity of the device. Again, the low detection limit of the AgCNFs-based electrode (10.6 mg/dL) compared with that of the CNFs

ACCEPTED MANUSCRIPT

electrode was due to the covalent functionalization of enzyme molecules. Impregnated Ag NPs on CNFs can improve the sensitivity, detection limit, and range to detect TG molecules. The apparent Michaelis–Menten contant constant (K_m) was found to be 1.7 and 3.3 mg/dL, respectively, for the Lip-GLDH/CNF and Lip-GLDH/AgCNF bioelectrodes using a Lineweaver Burke plot, i.e., a plot of 1/concentration vs. 1/current. Thus, in both cases, the observed lower K_m value indicated enhanced affinity of the enzyme to TG molecules on CNFs-based electrodes. Approximately the same response time (10 s) was observed for both bioelectrodes [Figure 9 (vi)].

The stability of the fabricated biosensors was determined by measuring the change in the current response at regular interval of 10 days for approximately 50 days (Figure S8, Supporting Information). The current signal of the Lip-GLDH/AgCNF bioelectrode decreased to a value of 11.7 %, after which only a 2.1 % decrease was observed for up to 50 days. In contrast, for the Lip-GLDH/CNF bioelectrode, the current decreased by 9.6 % from the initial current signal after 50 days. These prepared bioelectrodes were stored at 4 °C when not in use. The effect of selectivity in the presence of potential interferents such as ascorbic acid (AA), urea, glucose (G), cholesterol (Chol), and low-density lipoprotein (LDL) at normal concentrations was tested using the CV technique (Figure S9, Supporting Information). The change in the oxidation current was measured in PBS containing an equal amount (1:1) of TGA (25 mg/dL) and interferents. Compared with the CNFs-based bioelectrode, the Lip-GLDH/AgCNF was more selective, as evident by the low relative standard deviation (RSD: 0.65 %, n=6). The RSD values in the measurement of reproducibility for the Lip-GLDH/AgCNF and Lip-GLDH/CNF bioelectrodes were estimated to be 1.52 % and 1.67 %, respectively (Figure S10, Supporting Information).

ACCEPTED MANUSCRIPT

5. CONCLUSIONS

We have demonstrated an easy, economic, and rapid process for the synthesis of free-standing, partially aligned Ag NP-impregnated porous carbon nanofibers for the detection of TG. This process can be scaled up for the production of CNFs and AgCNFs from a PAN polymer precursor by electrospinning followed by pyrolysis. It is also possible to impregnate Ag NPs into these porous CNFs to enhance their applicability toward enzymatic reactions of significant importance. The removal of carbon from the AgCNFs composite fibers using calcination yielded a nanochain architecture of the Ag NPs. A systemic investigation of the surface morphology and structural properties of the prepared pristine and composite nanofibers has been performed using FESEM, TEM and Raman, BET, EDX, XRD studies, respectively. The bienzyme functionalization of the CNFs and AgCNFs were confirmed by FTIR studies.

The incorporation Ag NPs within the CNFs enhanced the electrochemical characteristics of the fabricated biosensor. The electrical conductivity was higher for the AgCNF-based bioelectrodes than CNFs. Although the CNFs exhibited good electrochemical properties for oxidation and reduction of the ferro/ferri cyanide redox probe, uniform and stabilized Ag NPs within the CNF results in further enhanced electrochemical current, revealing significant improvement of the sensing ability of the TG molecules. In addition, the nanoporous CNFs acted as a template for the growth of Ag nanocrystals, reduced agglomeration of the Ag NPs, and provided uniform dispensability onto the CNFs surface, resulting in enhanced biosensor characteristics. Thus, this hybrid porous AgCNFs nanocomposite is a promising platform for the detection of other biomolecules such as LDL, cholesterol, and urea etc.

ACCEPTED MANUSCRIPT

Author Contributions

The manuscript was written through contributions of all authors.

All authors have given approval to the final version of the manuscript.

Notes

The authors declare no competing financial interest.

Acknowledgements

This work was supported by the DST Unit of Excellence on Soft Nanofabrication at Indian Institute of Technology Kanpur from the Department of Science and Technology, New Delhi, India.

Appendix A. Supplementary data

Electrospinning setup, dependency of various electrospinning parameters on diameter of as-spun nanofiber, Selected area EDX spectra and elemental composition of fibers, histogram for average number of silver particles, FTIR spectra of CNF, AgCNF, and enzyme loaded fibers, CV response, Stability studies of the Lip-GLDH/CNF and Lip-GLDH/AgCNF bioelectrodes, The proposed enzymatic reaction for detection of the triglyceride, value of HET constant and time constant for various fabricated electrodes.

ACCEPTED MANUSCRIPT

REFERENCES

[1] W. Dai, S.J. Kim, W.-K. Seong, S.H. Kim, K.-R. Lee, H.-Y. Kim, et al., Porous carbon nanoparticle networks with tunable absorbability, Sci. Rep., 3(2013) 2524.
[2] K. Mondal, J. Kumar, A. Sharma, TiO_2-nanoparticles-impregnated photocatalytic macroporous carbon films by spin coating, Nanomater. Energy, 2(2013) 121-33.
[3] S. Katiyar, K. Mondal, A. Sharma, One-step sol-gel synthesis of hierarchically porous, flow-through carbon/silica monoliths, RSC Advances, 6(2016) 12298-310.
[4] L. Wang, Z. Tang, W. Yan, H. Yang, Q. Wang, S. Chen, Porous carbon-supported gold nanoparticles for oxygen reduction reaction: effects of nanoparticle size, ACS Appl. Mater. Interfaces, 8(2016) 20635-41.
[5] B. Xia, K. Chen, W. Luo, G. Cheng, NiRh nanoparticles supported on nitrogen-doped porous carbon as highly efficient catalysts for dehydrogenation of hydrazine in alkaline solution, Nano Res., 8(2015) 3472-9.
[6] H. Shin, H.-i. Kim, D.Y. Chung, J.M. Yoo, S. Weon, W. Choi, et al., Scaffold-like titanium nitride nanotubes with a highly conductive porous architecture as a nanoparticle catalyst support for oxygen reduction, ACS Catal., 6(2016) 3914-20.
[7] A.K. Srivastava, K. Mondal, K. Mukhopadhyay, N.E. Prasad, A. Sharma, Facile reduction of para-nitrophenols: catalytic efficiency of silver nanoferns in batch and continuous flow reactors, RSC Adv., 6(2016) 113981-90.
[8] E.S. Cho, A.M. Ruminski, S. Aloni, Y.-S. Liu, J. Guo, J.J. Urban, Graphene oxide/metal nanocrystal multilaminates as the atomic limit for safe and selective hydrogen storage, Nat Commun., 7(2016) Article number: 10804.
[9] S.M. Manocha, Porous carbons, Sadhana, 28(2003) 335–48.
[10] K. Mondal, R. Kumar, A. Sharma, Metal-oxide decorated multilayered three-dimensional (3d) porous carbon thin films for supercapacitor electrodes, Ind. Eng. Chem. Res., 55(2016) 12569-81.
[11] J. Huang, Y. Liu, T. You, Carbon nanofiber based electrochemical biosensors: A review, Anal. Methods, 2(2010) 202–11.

ACCEPTED MANUSCRIPT

[12] M.A. Ali, K. Mondal, Y. Wang, H. Jiang, N.K. Mahal, M.J. Castellano, et al., In situ integration of graphene foam-titanium nitride based bio-scaffolds and microfluidic structures for soil nutrient sensors, Lab Chip, 17(2017) 274-85.
[13] M.A. Ali, C. Singh, K. Mondal, S. Srivastava, A. Sharma, B.D. Malhotra, Mesoporous few-layer graphene platform for affinity biosensing application, ACS Appl. Mater. Interfaces, 8(2016) 7646-56.
[14] M.A. Ali, K. Mondal, Y. Jiao, S. Oren, Z. Xu, A. Sharma, et al., Microfluidic immuno-biochip for detection of breast cancer biomarkers using hierarchical composite of porous graphene and titanium dioxide nanofibers, ACS Appl. Mater. Interfaces, 8(2016) 20570-82.
[15] K. Mondal, M.A. Ali, S. Srivastava, B.D. Malhotra, A. Sharma, Electrospun functional micro/nanochannels embedded in porous carbon electrodes for microfluidic biosensing, Sens. Actuators, B, 229(2016) 82-91.
[16] J.D. Atkinson, M.E. Fortunato, S.A. Dastgheib, M. Rostam-Abadi, M.J. Rood, K.S. Suslick, Synthesis and characterization of iron-impregnated porous carbon spheres prepared by ultrasonic spray pyrolysis, Carbon, 49(2011) 587-98.
[17] P. Kaur, J.T. Hupp, S.T. Nguyen, Porous organic polymers in catalysis: opportunities and challenges, ACS Catal., 1(2011) 819–35.
[18] J.B. Xu, T.S. Zhao, Mesoporous carbon with uniquely combined electrochemical and mass transport characteristics for polymer electrolyte membrane fuel cells, RSC Adv., 3(2013) 16-24.
[19] L. Ji, X. Zhang, Fabrication of porous carbon nanofibers and their application as anode materials for rechargeable lithium-ion batteries, Nanotechnol., 20(2009) 155705.
[20] Z.-M. Huang, Y.-Z. Zhang, M. Kotaki, S. Ramakrishna, A review on polymer nanofibers by electrospinning and their applications in nanocomposites, Composites Sci. Technol., 63(2003) 2223-53.
[21] W.E. Teo, S. Ramakrishna, Areviewonelectrospinning design and nanofibre assemblies, Nanotechnol., 17(2006) R89–R106.
[22] K. Mondal, M.A. Ali, V.V. Agrawal, B.D. Malhotra, A. Sharma, Highly sensitive biofunctionalized mesoporous electrospun tio2 nanofiber based interface for biosensing, ACS Appl. Mater. Interfaces, 6(2014) 2516-27.

ACCEPTED MANUSCRIPT

[23] D. Li, Y. Wang, Y. Xia, Electrospinning of polymeric and ceramic nanofibers as uniaxially aligned arrays, Nano Lett., 3(2003) 1167-71.
[24] P. Singh, K. Mondal, A. Sharma, Reusable electrospun mesoporous ZnO nanofiber mats for photocatalytic degradation of polycyclic aromatic hydrocarbon dyes in wastewater, J. Colloid Interf. Sci., 394(2013) 208–15.
[25] H. Katepalli, M. Bikshapathi, C.S. Sharma, N. Verma, A. Sharma, Synthesis of hierarchical fabrics by electrospinning of PAN nanofibers on activated carbon microfibers for environmental remediation applications, Chem. Eng. J., 171(2011) 1194-200.
[26] F. Dabirian, S.A. Hosseini, Novel method for nanofibre yarn production using two differently charged nozzles, Fibers Text. East. Eur., 17(2009) 45-7.
[27] S.K. Nataraj, B.H. Kim, M.d. Cruz, J. Ferraris, T.M. Aminabhavi, K.S. Yang, Free standing thin webs of porous carbon nanofibers of polyacrylonitrile containing iron-oxide by electrospinning, Mater. Lett., 63(2009) 218–20.
[28] K.P.D. Jong, J.W. Geus, Carbon nanofibers: Catalytic synthesis and applications Catal. Rev-Sci. Eng., 42(2000) 481-510.
[29] W.-J. Jin, H.K. Lee, E.H. Jeong, W.H. Park, J.H. Youk, Preparation of polymer nanofibers containing silver nanoparticles by using poly(n-vinylpyrrolidone), Macromol. Rapid Commun., 26(2005) 1903–7.
[30] S.H. Nam, H.-S. Shim, Y.-S. Kim, M.A. Dar, J.G. Kim, W.B. Kim, Ag or au nanoparticle-embedded one-dimensional composite tio2 nanofibers prepared via electrospinning for use in lithium-ion batteries, ACS Appl. Mater. Interfaces., 2(2010) 2046–52.
[31] X. He, X. Zhao, Y. Li, X. Sui, Shape-controlled synthesis for silver: Triangular/hexagona nanoplates, chain-like nanoplate assemblies, and nanobelts, J. Mater. Res., 24(2009) 2200-9.
[32] Y. Sun, Y. Xia, Shape-controlled synthesis of gold and silver nanoparticles, Science, 298(2002) 2176-9
[33] D. Aherne, D.M. Ledwith, M. Gara, J.M. Kelly, Optical properties and growth aspects of silver nanoprisms produced by a highly reproducible and rapid synthesis at room temperature, Adv. Funct. Mater., 18(2008) 2005–16.
[34] Z.-J. Jiang, C.-Y. Liu, L.-W. Sun, Catalytic properties of silver nanoparticles supported on silica spheres, J. Phys. Chem. B, 109(2005) 1730-5.

ACCEPTED MANUSCRIPT

[35] J.S. Kim, E. Kuk, K.N. Yu, J.-H. Kim, S.J. Park, H.J. Lee, et al., Antimicrobial effects of silver nanoparticles, Nanomed-Nanotechnol., 3(2007) 95–101.
[36] K.M.M.A. El-Nour, A.a. Eftaiha, A. Al-Warthan, R.A.A. Ammar, Synthesis and applications of silver nanoparticles, Arab. J. Chem. 3(2010) 135–40.
[37] A.A. Abdelwahab, Y.-B. Shim, Nonenzymatic H_2O_2 sensing based on silver nanoparticles capped polyterthiophene/MWCNT nanocomposite, Sensor Actuator. B, 201(2014) 51-8.
[38] J. Huang, D. Wang, H. Hou, T. You, Electrospun palladium nanoparticle-loaded carbon nanofibers and their electrocatalytic activities towards hydrogen peroxide and NADH, Adv. Funct. Mater., 18(2008) 441-8.
[39] X. Lu, J. Zhou, WuLu, Q. Liu, J. Li, Carbon nanofiber-based composites for the construction of mediator-free biosensors, Biosens. Bioelectron., 23(2008) 1236–43.
[40] B. Munkhbayar, M.R. Tanshen, J. Jeoun, H. Chung, H. Jeong, Surfactant-free dispersion of silver nanoparticles into MWCNT-aqueous nanofluids prepared by one-step technique and their thermal characteristics, Ceramics Int., 39(2013) 6415–25.
[41] V. Vamvakaki, K. Tsagaraki, N. Chaniotakis, Carbon nanofiber-based glucose biosensor, Anal. Chem., 78(2006) 5538-42
[42] M.I. Kim, Y. Ye, B.Y. Won, S. Shin, J. Lee, H.G. Park, A highly efficient electrochemical biosensing platform by employing conductive nanocomposite entrapping magnetic nanoparticles and oxidase in mesoporous carbon foam, Adv. Funct. Mater., 21(2011) 2868–75.
[43] C. Dhand, P.R. Solanki, K.N. Sood, M. Datta, B.D. Malhotra, Polyaniline nanotubes for impedimetric triglyceride detection, Electrochem. Commun., 11(2009) 1482-6
[44] W.-Y. Liao, C.-C. Liu, T.-C. Chou, Detection of triglyceride using an iridium nano-particle catalyst based amperometric biosensor, Analyst, 133(2008) 1757-63
[45] B. Wu, A. Heidelberg, J.J. Boland, J.E. Sader, X. Sun, Y. Li, Microstructure-hardened silver nanowires, Nano Lett., 6(2006) 468-72.
[46] C.S. Sharma, H. Katepalli, A. Sharma, M. Madou, Fabrication and electrical conductivity of suspended carbon nanofiber arrays, Carbon, 49(2011) 1727 – 32.
[47] T. Maitra, S. Sharma, A. Srivastava, Y.-K. Cho, M. Madou, A. Sharma, Improved graphitization and electrical conductivity of suspended carbon nanofibers derived from carbon nanotube/ polyacrylonitrile composites by directed electrospinning, Carbon, 50(2012) 1753–61.

ACCEPTED MANUSCRIPT

[48] M.A. Ali, K.K. Reza, S. Srivastava, V.V. Agrawal, R. John, B.D. Malhotra, Lipid−lipid interactions in aminated reduced graphene oxide interface for biosensing application, Langmuir, 30(2014) 4192−201.

[49] M.G. McKee, G.L. Wilkes, R.H. Colby, T.E. Long, Correlations of solution rheology with electrospun fiber formation of linear and branched polyesters, Macromolecules, 37(2004) 1760-7.

[50] D.N. Tran, J. Kenneth J. Balkus, Perspective of recent progress in immobilization of enzymes, ACS Catal, 1(2011) 956–68.

[51] J.M. Deitzel, J. Kleinmeyer, D. Harris, N.C.B. Tan, The effect of processing variables on the morphology of electrospun nanofibers and textiles, Polymer, 42(2001) 261-72.

[52] D.S. Knight, W.B. White, Characterization of diamond films by Raman spectroscopy, J. Mater. Res., 4(1989) 385-93.

[53] M.A. Pimenta, G. Dresselhaus, M.S. Dresselhaus, L.G. Cancado, A. Jorioa, R. Saito, Studying disorder in graphite-based systems by Raman spectroscopy, Phys. Chem. Chem. Phys., 9(2007) 1276–91.

[54] J.R. Dahn, Suppression of staging in lithium-intercalated carbon by disorder in the host, Phys. Rev. B, 42(1990) 6424-32

[55] J. Lee, J. Kim, T. Hyeon, Recent progress in the synthesis of porous carbon materials, Adv. Mater., 18(2006) 2073-94.

[56] R.A. Salkar, P. Jeevanandam, S.T. Aruna, Y. Koltypin, A. Gedanken, The sonochemical preparation of amorphous silver nanoparticles, J. Mater. Chem., 9(1999) 1333-5.

[57] M.R. Baldan, E.C. Almeida, A.F. Azevedo, E.S.G. alves, M.C. Rezende, N.G. Ferreira, Raman validity for crystallite size L_a determination on reticulated vitreous carbon with different graphitization index, Appl. Surf. Sci., 254(2007) 600-3.

[58] J. Das, M.A. Aziz, H. Yang, A nanocatalyst-based assay for proteins: DNA-free ultrasensitive electrochemical detection using catalytic reduction of p-nitrophenol by gold-nanoparticle labels, J. Am. Chm. Soc., 128(2006) 16022-3.

[59] M.A. Ali, S. Srivastava, P.R. Solanki, V.V. Agrawal, R. John, B.D. Malhotra, Nanostructured anatase-titanium dioxide based platform for application to microfluidics cholesterol biosensor Appl. Phys. Lett., 101(2012) 084105.

ACCEPTED MANUSCRIPT

[60] M.J. Watt-Smith, J.M. Friedrich, S.P. Rigby, T.R. Ralph, F.C. Walsh, Determination of the electrochemically active surface area of Pt/C PEM fuel cell electrodes using different adsorbates, J. Phys. D, 41(2008) 174004.
[61] F. Manea, C. Radovan, I. Corb, A. Pop, G. Burtica, P. Malchev, et al., Electrochemical oxidation and determination of oxalic acid at an exfoliated graphite-polystyrene composite electrode, Sensors, 7(2007) 615-27.
[62] A. Kaushik, P.R. Solanki, K. Kaneto, C.G. Kim, S. Ahmad, B.D. Malhotra, Nanostructured iron oxide platform for impedimetric cholesterol detection, Electroanalysis, 22(2010) 1045–55.
[63] Minakshi, C.S. Pundir, Construction of an amperometric enzymic sensor for triglyceride determination, Sensor. Actuat. B, 133(2008) 251-5.
[64] C.S. Pundir, B.S. Singh, J. Narang, Construction of an amperometric triglyceride biosensor using PVA membrane bound enzymes, Clinical Biochem., 43(2010) 467–72.
[65] J. Narang, C.S. Pundir, Construction of a triglyceride amperometric biosensor based on chitosan–ZnO nanocomposite film, Int. J. Biol. Macromol., 49(2011) 707-15.
[66] W. Zhang, Y. Tang, J. Liu, Y. Ma, L. Jiang, W. Huang, et al., An electrochemical sensor for detecting triglyceride based on biomimetic polydopamine and gold nanocomposite, J. Mater. Chem. B, 2(2014) 8490-5.
[67] C.Y. Jeong, Y.D. Han, J.H. Yoon, H.C. Yoon, Bioelectrocatalytic sensor for triglycerides in human skin sebum based on enzymatic cascade reaction of lipase, glycerol kinase and glycerophosphate oxidase, J. Biotechnol., 175(2014) 7-14.
[68] J. Narang, N. Chauhan, C.S. Pundir, Construction of triglyceride biosensor based on nickel oxide-chitosan/zinc oxide/zinc hexacyanoferrate film, Int. J. Biol. Macromol., 60(2013) 45-51.

ACCEPTED MANUSCRIPT

Authors Biographies



Kunal Mondal is a post-doctoral research associate at the North Carolina State University, USA, in the Department of Chemical and Biomolecular Engineering. He received his Ph.D from the Indian Institute of Technology Kanpur (2015), his M.Sc and M.Tech. both degrees from the Indian Institute of Engineering Science and Technology, Shibpur (2006-2010). Kunal's research interests are in micro/nano fabrication of functional materials, colloids and interfaces of soft nanostructures, self and directed assembly, nano/micro-electronics, microfluidics, photovoltaics, polymer thin-films, carbon nanomaterials, carbon composites, carbon MEMS/NEMS in health, energy and environmental applications. He has published over 25 peer reviewed papers, 2 book chapters and 4 patents in these areas.



Md. Azahar Ali received his Ph.D. degree from the Biomedical Engineering Department at Indian Institute of Technology Hyderabad, India, in collaboration with the Biomedical Instrumentation Section at National Physical Laboratory, New Delhi, India, in 2014. He also received his Master of Technology degree from the Department of Electronics Engineering at Tezpur University, Assam, India, in 2009. Currently, he is doing Post-Doctoral Associate in the Department of Electrical and Computer Engineering at Iowa State University. He is actively engaged in the area of microfluidic and MEMS sensors in agriculture and biomedicine.

ACCEPTED MANUSCRIPT



Chandan Singh is working as a doctoral candidate at Biomedical Instrumentation section, CSIR-National Physical Laboratory, New Delhi, India. He received his M.Tech. degree in Biotechnology from Jaypee Universityof Information Technology, Waknaghat, H.P. Since 2013 as a CSIR-Senior Research Fellow, he is working on designing of electrochemical immumosensors for the detection of food borne pathogens like salmonella. He is also working on development of microfluidics biosensors for the detection of different bioanalytes.



Dr. Gajjala Sumana received her Ph.D. (1998) from Jiwaji University in Chemistry, India. She is currently working as a principal scientist with the DST Centre on Biomolec-ular Electronics at the National Physical Laboratory, New Delhi, India. She has a research experience of 15 years in controlled drug delivery, liquid crystal polymers, polymer dispersed liquid crystals and biosensors. She has published more than 80 publications in the area of biomedical applications.



B. D. Malhotra received his Ph.D. degree from the University of Delhi, Delhi, India in 1980. He has published more than 275 papers in peer-reviewed journals, filed 10 patents, and edited/co-edited books on biosensors and polymer electronics. After his stint as Chief Scientist and Head of the DST Centre on Biomolecular Electronics at the CSIR-National Physical Laboratory, New Delhi, India, he moved to Delhi Technological University (DTU), India. He has nearly 30 years of research experience in the field of biomolecular

ACCEPTED MANUSCRIPT

electronics and has guided 25 Ph.D. students to date. His current activities include biosensors, nanobiomaterials, conducting polymers, and ordered molecular assemblies including Langmuir–Blodgett films and self-assembled monolayers among others. Dr. Malhotra is a Fellow of the Indian National Science Academy (INSA), the National Academy of Sciences, India (NASI) and an Academician of the Asia-Pacific Academy of Materials (APAM).



Ashutosh Sharma is currently Secretary, Department of Science and Technology, Government of India and an Institute Chair Professor in Chemical Engineering at the Indian Institute of Technology at Kanpur. Ashutosh received his PhD from the State University of New York at Buffalo (1988), his MS from the Pennsylvania State University (1984) and B.Tech. from IIT Kanpur (1982). Ashutosh's research contributions are highly interdisciplinary, spanning a wide range in nanotechnology; thin polymer films; nanocomposites and devices in energy, health and environment; functional interfaces; micro/nano-mechanics of soft matter; nano-patterning and nanofabrication; colloid and interfacial engineering; biomaterials and biosurfaces; wetting and adhesion. He has published over 350 peer reviewed papers in these areas. Ashutosh is an elected Fellow of The Indian National Science Academy, Indian National Academy of Engineering and The World Academy of Sciences (TWAS). He is an associate editor of ACS Applied Materials and Interfaces.

ACCEPTED MANUSCRIPT

Figure Caption

Fig. 1. Schematic representation of synthesis of CNFs and AgCNFs and biosensing platform for triglyceride detection.

Fig. 2. FE-SEM images of the PAN/$AgNO_3$ fibers electrospun with different PAN concentration at constant flow rate of 40 µL/min. (a) Polymer beads with non-uniform diameter polymer fibers at 2 wt.%, (b) higher magnification image of 'a' (c) bead free thicker fibers at 16 wt.% and (d) higher magnification image of 'c'. An 8 wt.% PAN/$AgNO_3$ blend electrospun at a flow rate of (e) 2 µL/min and (f) 180 µL/min.

Fig. 3. FE-SEM images of (a) 8 wt.% PAN/$AgNO_3$ blend electrospun at 40 µL/min flow rate, (b) higher magnification image of 'a', (c) Ag/carbon fibers after carbonization at 900^oC, and (d) higher magnification image of 'c' shows a single composite fiber. (e) FE-SEM micrograph of a porous free-standing Ag/carbon fibers mat, (f) carbon nanofibers reveals the impregnation of silver particles within the porous fibers, (g) ruptured AgCNFs show presence of silver NPs inside the fibers, (h) continuous silver nanoparticles chain structures after burning the carbon form AgCNFs, and (i) higher magnification image of 'c' shows a AgCNFs derived single chain of silver nanoparticles.

Fig. 4. FE-SEM image of (a) Lip-GLDH/CNFs, (b) Lip-GLDH/AgCNFs bioelectrodes surface. (c) Higher magnification image of shows single carbon nanofibers with Lip and GLDH molecules.

Fig. 5. (a) TEM micrograph of (a) carbon nanofiber, (b) porous Ag/carbon fiber impregnated with 0.01 mol. equivalent Ag loading, (c) magnified image of 'b' shows porous morphology of the AgCNFs, (d) Ag/carbon fiber impregnated with 0.1 mol. equivalent Ag loading, (e) magnified image of 'd' shows silver nanoparticles embedded into the porous composite fiber and (f) SAED image shows lattice planes silver nanoparticles.

Fig. 6. (a) Nitrogen adsorption/desorption isotherm and pore size distribution plot (inset) of the Ag/carbon nanofibers.(b) Raman spectral analysis and (c) XRD plot of porous carbon and AgCNFs hybrid fibers.

ACCEPTED MANUSCRIPT

Fig. 7. Schematic shows the electrical conductivity measurement set up for single nanofibers. FE-SEM image of (b) a single suspended AgCNFs between two SU-8 derived carbon posts and (c) higher magnification image of 'b' shows suspended nanofiber.

Fig. 8. (i) CV studies of the CNF, AgCNF, Lip-GLDH/CNF and Lip-GLDH/AgCNF bioelectrodes, (ii) EIS curves of: bare ITO electrode and CNF, AgCNF, Lip-GLDH/CNF, Lip-GLDH/AgCNF bioelectrodes.

Fig. 9. CV response curves for (i) CNF and (ii) AgCNF bioelectrodes as a function of TG concentration, (iii) current response versus TG concentration plots for (a) CNF and (b) AgCNF. Linearity plots for (iv) CNF and (v) AgCNF bioelectrode in presence of TG concentration and (vi) chronoamperometric responses of CNF and AgCNF bioelectrodes.

ACCEPTED MANUSCRIPT

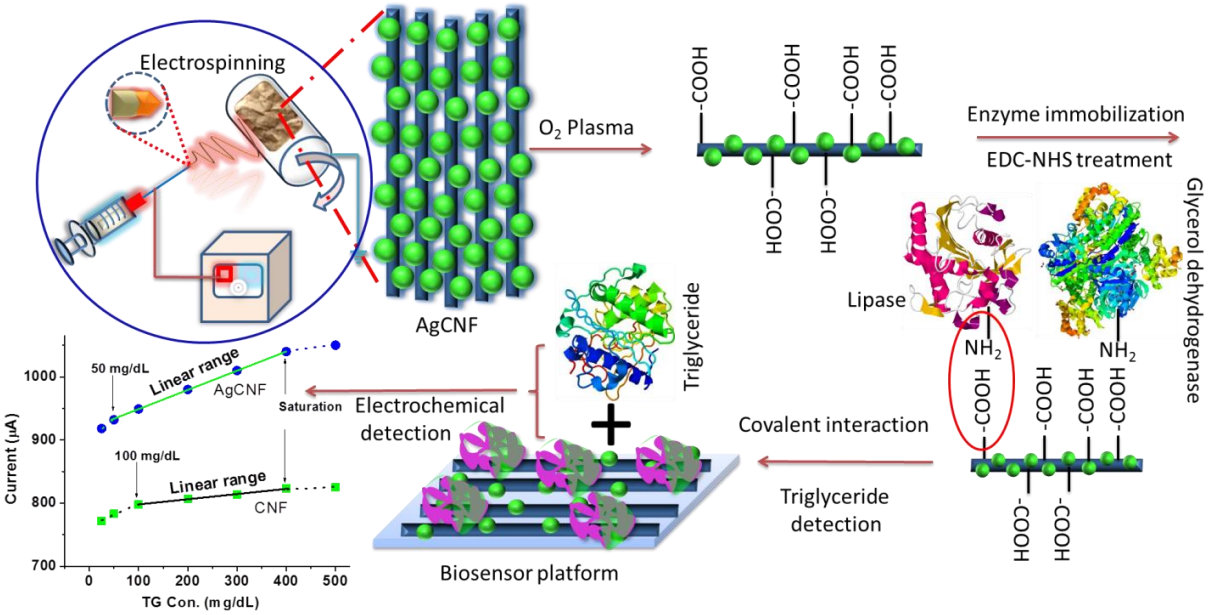


Fig. 1.

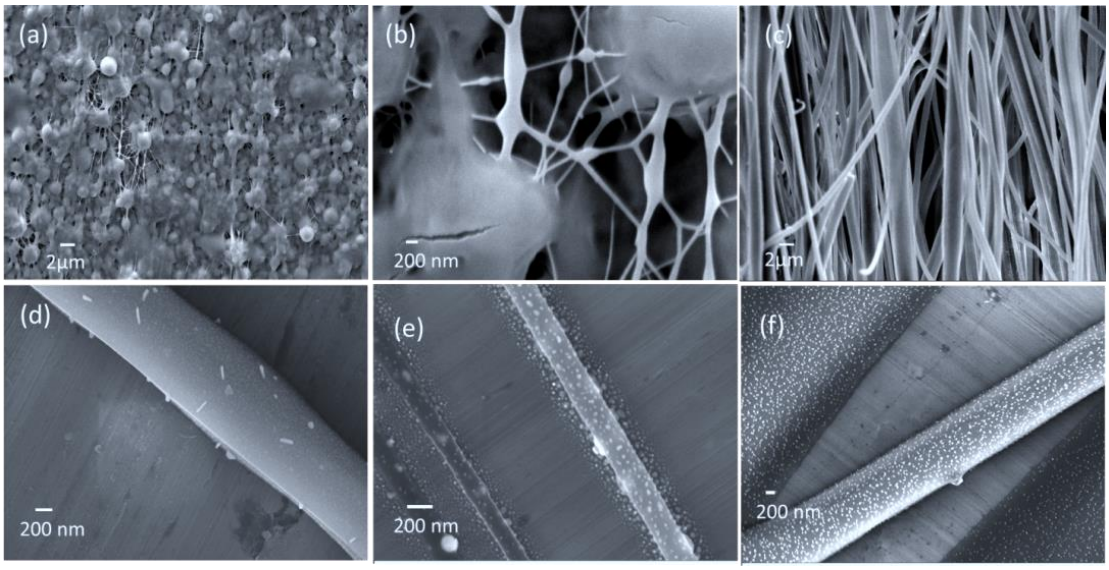


Fig. 2.

ACCEPTED MANUSCRIPT

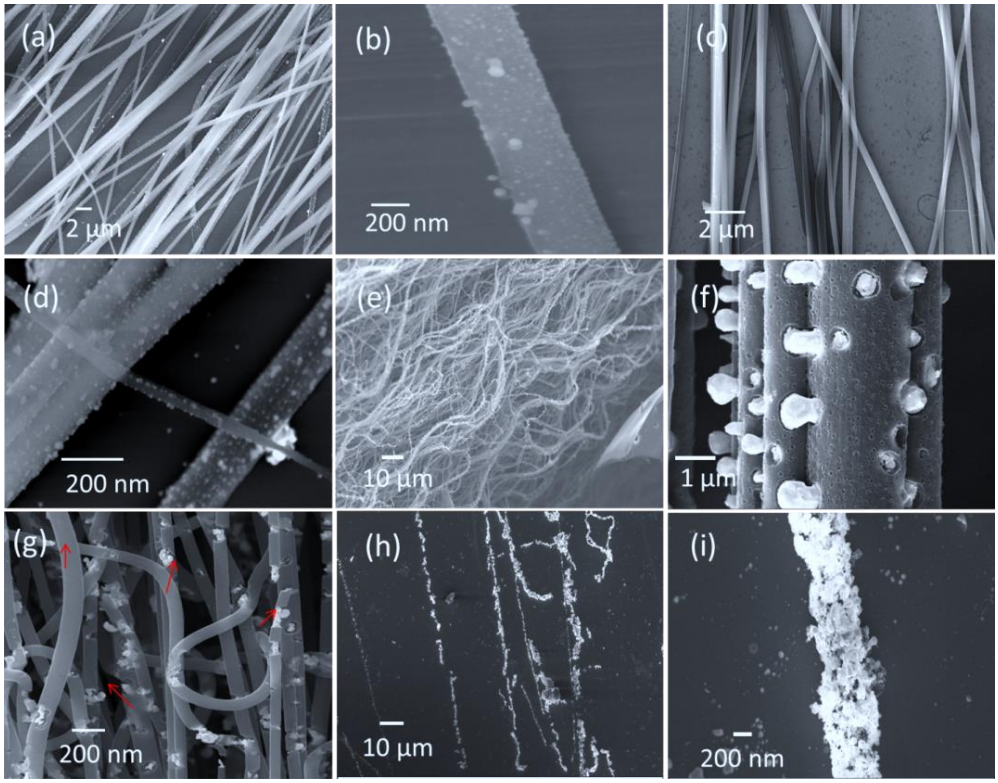


Fig. 3.

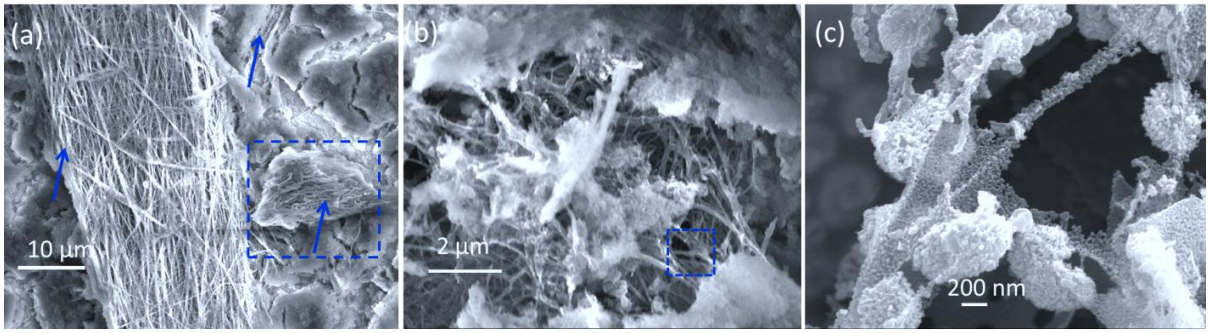


Fig. 4.

ACCEPTED MANUSCRIPT

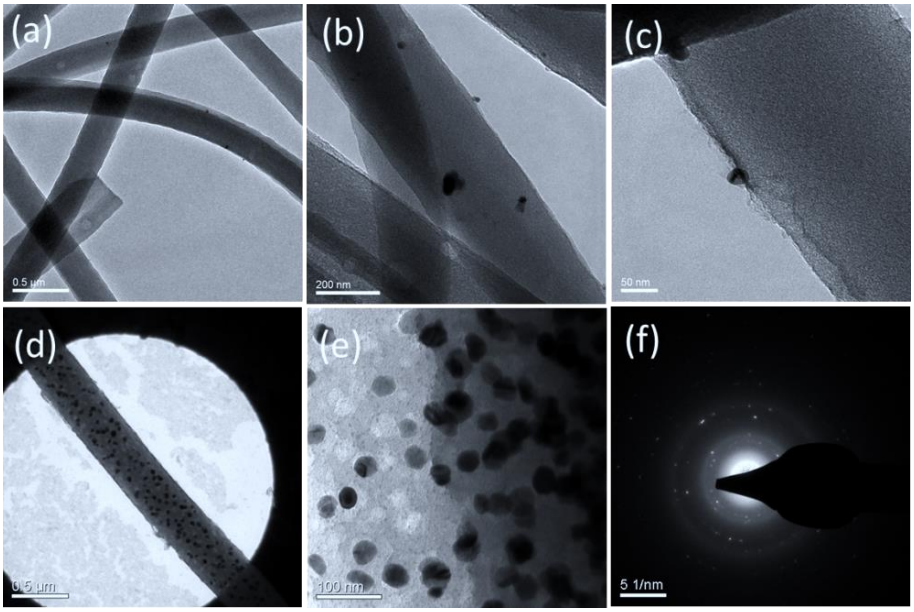


Fig. 5.

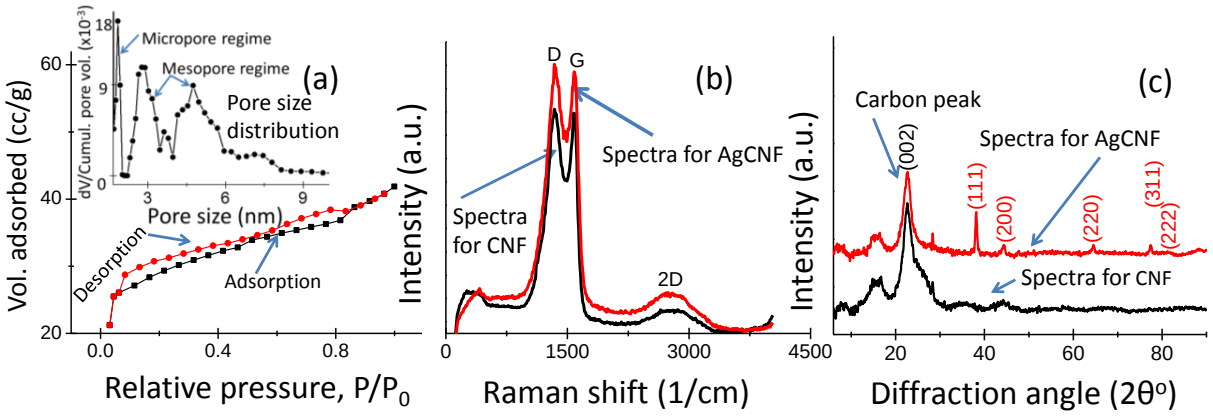


Fig. 6.

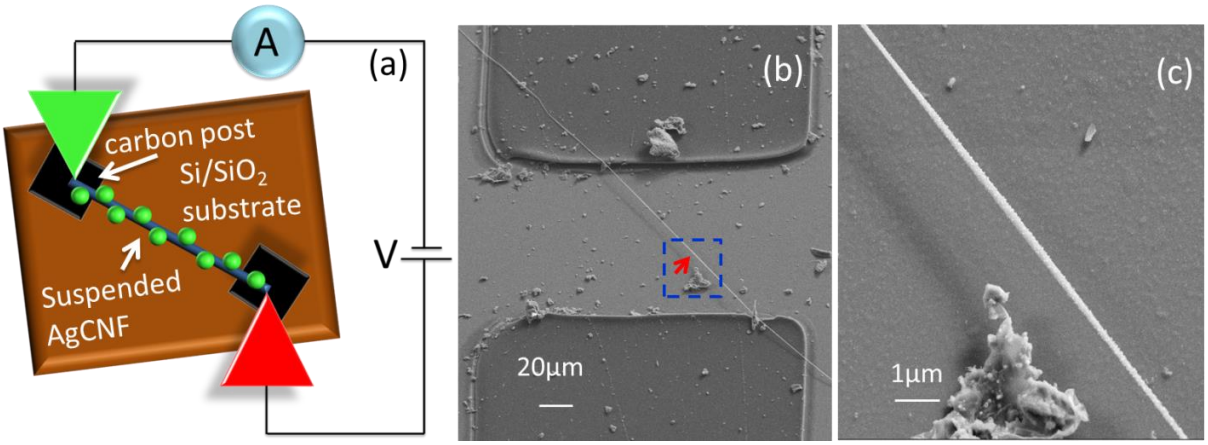

A
(a)
carbon post
Si/SiO2
substrate
Suspended
AgCNF
V
(b)
20µm
(c)
1µm

Fig. 7.

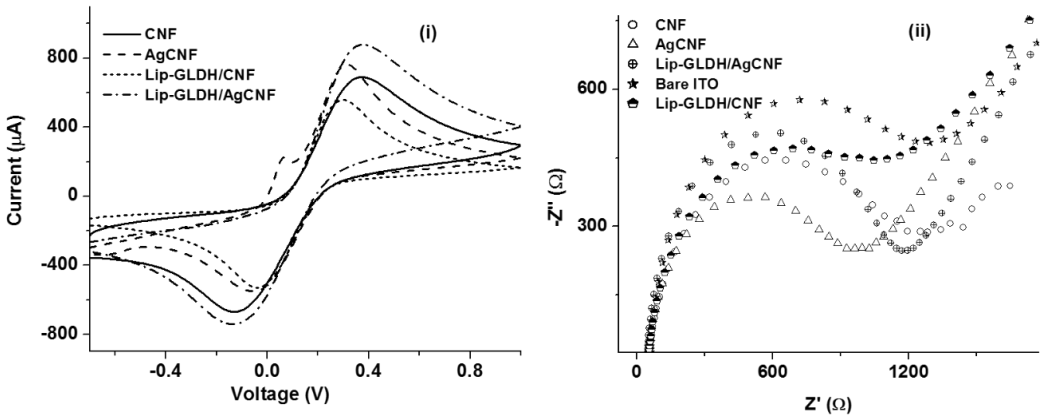

CNF
AgCNF
Lip-GLDH/CNF
Lip-GLDH/AgCNF
(i)
Current (µA)
800
400
0
-400
-800
-0.4
0.0
0.4
0.8
Voltage (V)
CNF
AgCNF
Lip-GLDH/AgCNF
Bare ITO
Lip-GLDH/CNF
(ii)
-Z'' (Ω)
600
300
0
600
1200
Z' (Ω)

Fig. 8.

ACCEPTED MANUSCRIPT

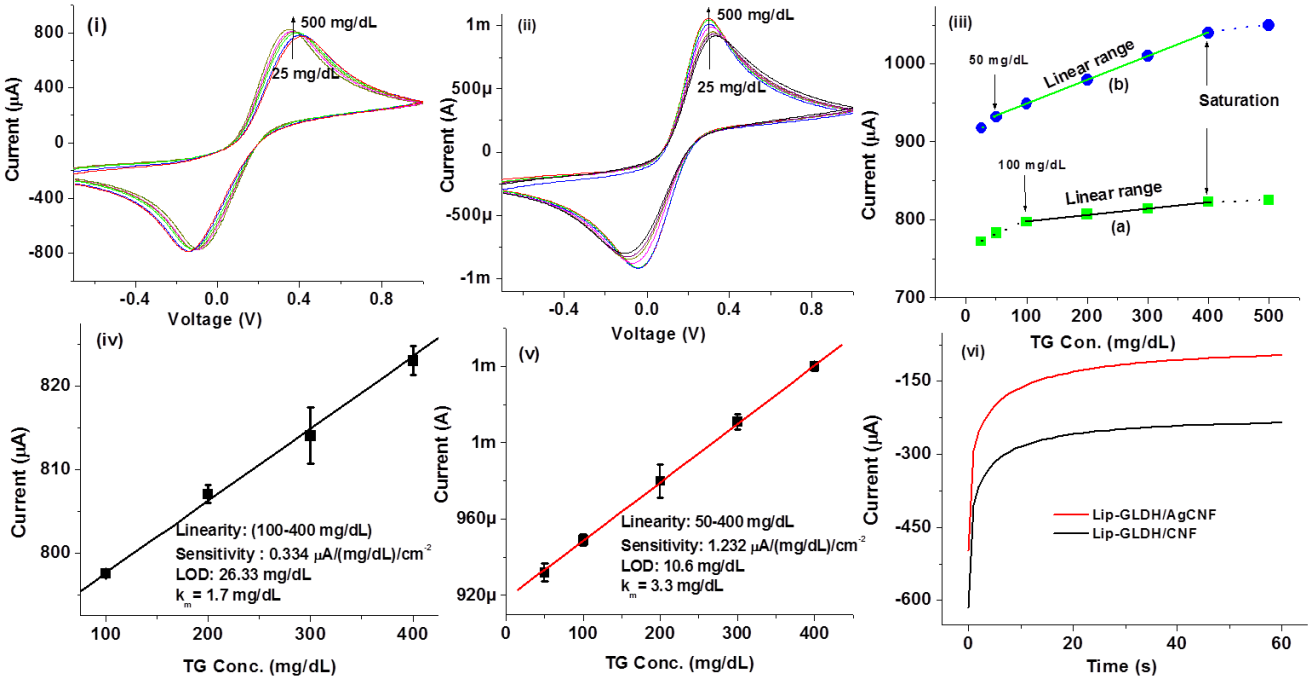


Fig. 9.

ACCEPTED MANUSCRIPT

Table 1

Electrical properties of suspended single CNFs and AgCNFs as measured by I–V curve.

Samples (Carbonized Fiber)	Slope of I-V curve	Resistance (Ω)	Length of the Fiber (μm)	Average Diameter of the Fiber (nm)	Conductivity (S/m)
PAN	0.96×10^{-5}	1.03×10^{5}	185.5	178	$1.51 \pm 0.29 \times 10^{4}$
PAN+0.01 mol. eq $AgNO_3$	1.40×10^{-5}	7.12×10^{4}	180.5	182	$9.74 \pm 0.33 \times 10^{4}$
PAN+0.1 mol. eq $AgNO_3$	5.74×10^{-5}	1.74×10^{4}	178.2	190	$36.10 \pm 0.57 \times 10^{4}$
PAN+0.25 mol. eq $AgNO_3$	2.34×10^{-4}	4.25×10^{3}	177.5	210	$120.35 \pm 1.75 \times 10^{4}$

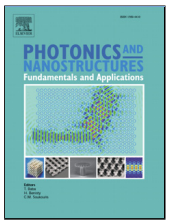
ACCEPTED MANUSCRIPT

Table 2

Summary of sensing characteristics of the CNFs and AgCNFs based biosensor for triglyceride detection along with those reported in the literature.

Working electrodes	Linearity range (mg/dL)	Lower detection limit (mg/dL)	Sensitivity	K_m (mg/dL)	Stability	Reference
Cellulose acetate membrane	8.8-309.7	17.69	---	775.2	---	Minakshi et al.[63]
PVA membrane	49.55–199.11	18.58	---	294.6	50 % loss in 50 days	Pundir et al.[64]
Iridium nano-particle modified carbon paste	0 –884.95	….	84×10^{-6} µA $(mg/dL)^{-1}$	---	---	Liao et al.[44]
Polyanilinenanotubes based film	25–300	25	$2.59\Omega^{-1}(mg/dL)^{-1}$	46.69	---	Dhand et al.[43]
Chitosan–ZnO nanocomposite film	50–650	20	0.89 mg/dL^{-1} μA^{-1}	---	50 % loss in 210 days	Narang et al.[65]
Polydopamine and gold nanoparticle hybrid	50 - 300	0.84	0.38 µA $(mg/dL)^{-1}$ cm^2	7.94	10 % loss in 60 days	Zhang et al.[66]
Evaporated gold surface on a silicon wafer	15–200	15	---	---	30 % loss in 5 days	Jeong et al.[67]
NiO–chitosan/ZnO/zinc hexacyanoferrate film	50-700	10	0.05 µA $(mg/dL)^{-1}$	---	50 % loss in 180 days	Narang et al.[68]
Electrospuncarbon nanofibers (CNFs)	100-400	26.33	0.33 µA $(mg/dL)^{-1}$	1.7	9% loss in 50 days	Present work
Ag impregnated carbon nanofibers (AgCNFs)	50-400	10.6	1.232 µA $(mg/dL)^{-1}$	3.3	13% loss in 50 days	Present work

Accepted Manuscript



Title: High-Quality Laser Cavity based on All-Dielectric Metasurfaces

Author: Nishant Shankhwar Ravindra Kumar Sinha Yogita Kalra Sergey Makarov Alexander Krasnok Pavel Belov

PII: S1569-4410(16)30065-7
DOI: http://dx.doi.org/doi:10.1016/j.photonics.2017.02.003
Reference: PNFA 573

To appear in: *Photonics and Nanostructures – Fundamentals and Applications*

Received date: 4-10-2016
Revised date: 30-12-2016
Accepted date: 1-2-2017

Please cite this article as: Nishant Shankhwar, Ravindra Kumar Sinha, Yogita Kalra, Sergey Makarov, Alexander Krasnok, Pavel Belov, High-Quality Laser Cavity based on All-Dielectric Metasurfaces, *<![CDATA[Photonics and Nanostructures - Fundamentals and Applications]]>* (2017), http://dx.doi.org/10.1016/j.photonics.2017.02.003

This is a PDF file of an unedited manuscript that has been accepted for publication. As a service to our customers we are providing this early version of the manuscript. The manuscript will undergo copyediting, typesetting, and review of the resulting proof before it is published in its final form. Please note that during the production process errors may be discovered which could affect the content, and all legal disclaimers that apply to the journal pertain.

ACCEPTED MANUSCRIPT

High-Quality Laser Cavity based on All-Dielectric Metasurfaces

Nishant Shankhwar[a], Ravindra Kumar Sinha[a,b], Yogita Kalra[a], Sergey Makarov[c], Alexander Krasnok[c,d], Pavel Belov[c]

[a] *TIFAC-Centre of Relevance and Excellence in Fiber Optics and Optical Communication, Department of Applied Physics, Delhi Technological University, Bawana Road, Delhi-110042, India*
[b] *CSIR-Central Scientific Instruments Organisation (CSIO), Chandigarh-160030, India*
[c] *Departament of Nanophotonics and Metamaterials, ITMO University, St. Petersburg 197101, Russia*
[d] *Department of Electrical and Computer Engineering, The University of Texas at Austin, Austin, Texas 78712, USA*

Abstract

In the last few years, all-dielectric metasurfaces cause great interest because of their ability to create broadband perfect reflectors. It opens unique opportunities for designing of optical lenses, reflectors, and cavities for semiconductor lasers. Here, we propose a very compact design for a laser cavity based on all-dielectric metasurface perfect reflectors. We demonstrate that all-dielectric metasurface perfect reflector increases quality factor and reduces threshold power.

1. Introduction

Metasurfaces are two dimensional sheet type metamaterials having thickness several times smaller compared to wavelength of operation. Their subwavelength structure spreads in two dimensions in either periodic or aperiodic arrangement. Metasurfaces can be used to provide such peculiar optical properties to a device which cannot be achieved by thin films of naturally occurring materials [1, 2, 3]. Recently, all-dielectric metamaterials and metasurfaces have been proposed as a more effective counterpart for plasmonic ones

Email address: dr_rk_sinha@yahoo.com (Ravindra Kumar Sinha)

Accepted Manuscript

ACCEPTED MANUSCRIPT

[4, 5, 6]. The principle which lies at the heart of the all-dielectric metamaterials and metasurfaces is an optical response of high-index dielectric nanoparticles. The high-index dielectric nanoparticles possess electric and magnetic resonances in the visible range, providing efficient control of light scattering [7, 8, 9, 10, 11, 12, 13] and strong light enhancement [14, 15, 16, 17]. An advantage of choosing dielectric structures is the very low dissipation losses due to their negligibly small extinction coefficient. Today, such all-dielectric metasurfaces have been implemented for wavefront engineering [18, 19], electromagnetically induced transparency [20], high transmission [21], beam collimators [22], and especially for broadband perfect reflectors [23, 24, 25]. The last one opens new unique opportunities for designing of optical lenses, reflectors and especially cavities for semiconductor lasers.

Semiconductor lasers have revolutionized optical communication system. It has been demonstrated that they are excellent power sources for optical fibers, because of which long distance and high speed communication is now possible. Despite the tremendous development in design of lasers in terms of geometry, wavelength of operation, pulse duration, threshold current, etc, attempts are continuously being made to improve their performance [26]. In particular, further miniaturization of the semiconductor lasers is an important issue to create sub-micron thick highly efficient coherent light sources.

In this article, we propose a compact design of cavity resonator based on all-dielectric metasurfaces. In our design (see Figure 1(a)), mirrors are made up of a two dimensional periodic arrangement of silicon (Si) cylindrical particles having wisely chosen diameter, height and periodicity to operate at a particular wavelength. The cylindrical shape of particles was chosen because its performance in perfect reflection is well studied and it is easy to fabricate by means of electron beam lithography. In Refs. [24, 27, 28, 19, 29] it has been experimentally demonstrated that a perfectly ordered array of the silicon cylinders can reflect nearly 100% of the normally incident radiation. In Refs. [24] it has also been experimentally shown that reflectivity is reduced if there is a slight disorder in the periodic arrangement of cylinders. In our design, the perfectly ordered dielectric array exhibits property of perfect reflection (reflectance $\sim 100\%$) and hence can be used as the first mirror of a cavity. Any type of disorder slightly reduces the reflectance, hence such an array (reflectance $\sim 99.5\%$) can be used as the second mirror of a cavity i.e. the output coupler. Below we compare our metasurface reflector type cavity and a Bragg reflector type cavity, in which former clearly outshines the 25 pairs thick Bragg mirror due to more compact design, 5 times higher quality

ACCEPTED MANUSCRIPT

factor and 80% lesser threshold gain coefficient.

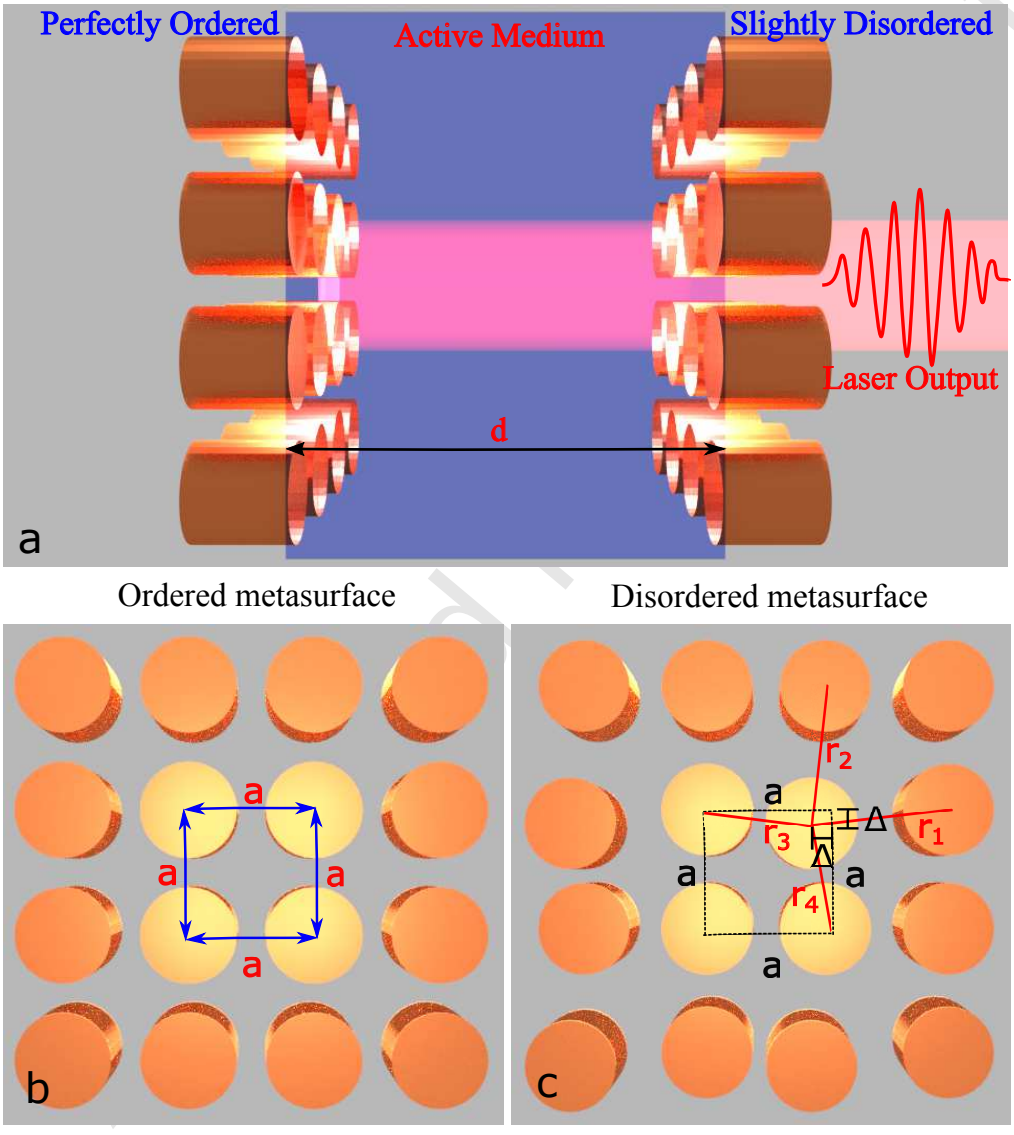


Figure 1: (a) Schematic illustration of laser cavity based on all-dielectric metasurfaces. (b) Design of the first reflector. (c) Design of the second reflector based on a disordered metasurface

ACCEPTED MANUSCRIPT

2. Design and Analysis

Firstly, to determine the value of diameter of the cylinder (D), in order to achieve resonance at the desired wavelength, scattering cross-sections of the silicon cylinder has been calculated at different values λ/D. The results are shown in Figure 2. Here, the peaks at $\lambda/D = 3.47$ and $\lambda/D = 4.3$ correspond to electric and magnetic dipole resonances, respectively (according to figure 1(b) in Ref. [24] for the aspect ratio equal to 1.25). The plot indicates that in order to achieve electric resonance at the desired wavelength (1500 nm in this case), the diameter D should be equal to $\lambda/3.47$. The numerical analysis has been performed in COMSOL Multiphysics. Data for permittivity of silicon ε has been taken from Palik [30]. The imaginary part of permittivity has been ignored due to its negligibly small value in the considered spectral range (1000–2000 nm) and only real part has been considered.

Figure 1(b) shows the scheme of the ordered metasurface. The unit cell of the metasurface is a silicon cylinder. According to figure 2(a), the diameter of the cylinder D should be 430 nm. But it has been observed that when such nanoparticles are periodically arranged, the resulting metasurface resonates at a wavelength higher than that of a single nanoparticle. The reason for this discrepancy is the interference of the fields of neighboring nanoparticles. As a result, the metasurface should be made by nanoparticles which are slightly smaller in diameter than that predicted by figure 2(a), in order to achieve perfect reflection at the desired wavelength. Based on the above observations, diamater D has been chosen to be 420 nm, the height H is 525 nm (aspect ratio = 1.25) and periodicity a is 700 nm. It should be noted that the figure 2(a) estimates the value of the diameter but does not provide any information about the periodicity. The reflection properties depend upon the periodicity of the array as well. Hence the structure has been optimized with respect to periodicity a and the value corresponding to maximum reflectance has been chosen. The structure can be tuned to achieve perfect reflection at different wavelengths by varying height of the cylinder. In Figure 2(b), effective material parameters obtained by field averaging [31] are shown. The results clearly illustrate the presence of the electric resonance around 1600 nm. As a result of which, we get a region of nearly zero effective impedance between 1490 nm and 1640 nm. This band of extremely low effective impedance is the main cause of the perfect reflection [23]. Furthermore, a small peak in the imaginary part of the effective refractive index eradicates the possibility of leakage of power through the metasurface.

ACCEPTED MANUSCRIPT

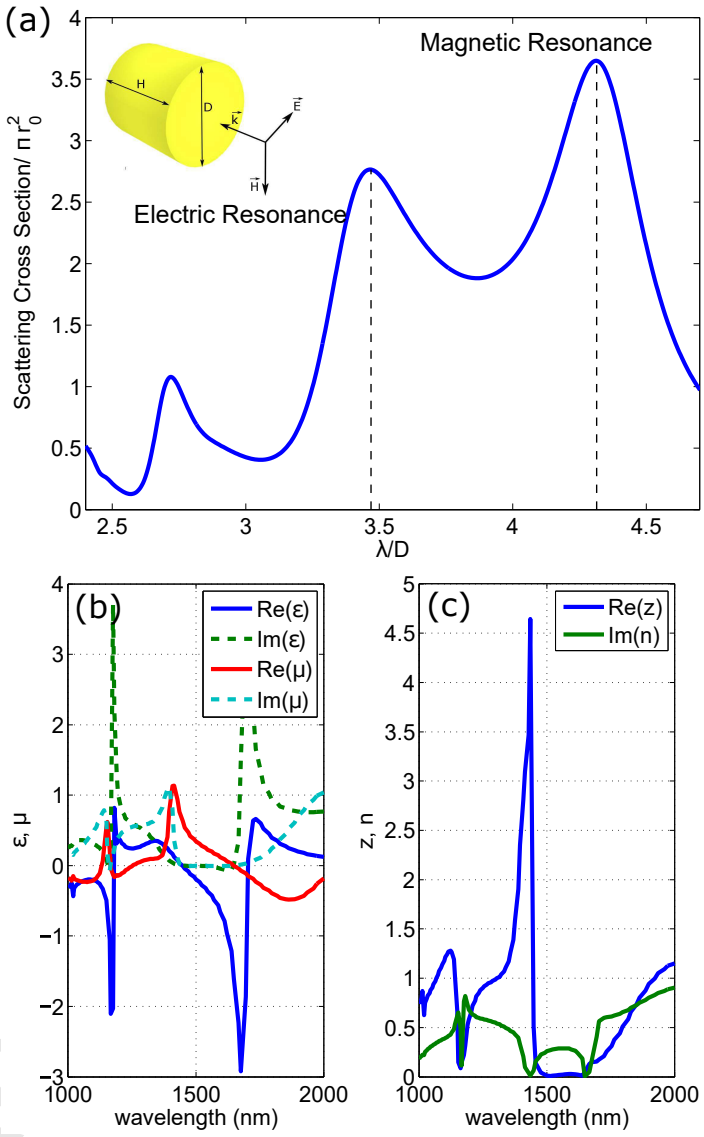


Figure 2: (a) Scattering cross-section vs wavelength for the silicon cylinder with diameter $D = 420$ nm and height $H = 525$ nm. Inset: geometric dimensions of the cylinder and the direction of incidence of the external wave; (b) real and imaginary parts of the effective permittivity 'ϵ' and the effective permeability 'μ'; (c) real part of the effective impedance 'z' and imaginary part of the effective refractive index 'n'

ACCEPTED MANUSCRIPT

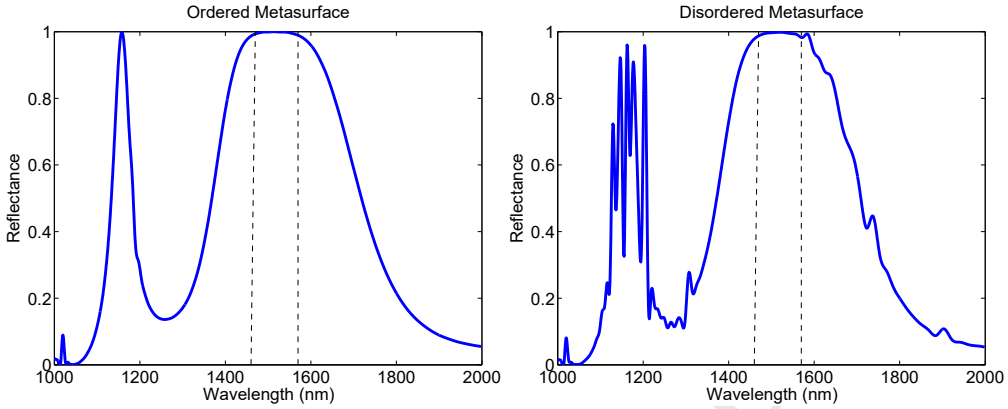


Figure 3: (a) Reflectance vs wavelength for first metasurface reflector. (b) Reflectance vs wavelength plot for second reflector.

For a laser cavity, the linewidth $\Delta\nu = \nu_0/Q$, and the quality factor Q can be written as (as shown in Ref. [32])

$$Q = \frac{4\pi\nu_0 n_0 d}{c(2\alpha d - \ln(R_1 R_2))} \tag{1}$$

where ν_0 is the frequency of the mode, n_0 is the refractive index of the medium inside cavity, d is the length of the cavity, R_1 is the reflectance of the first mirror, R_2 is the reflectance of the second mirror, α is the losses due to other factors except finite reflectivity of the mirrors. Thus, to achieve very high values of quality factor Q the first reflector should have reflectance R_1 as close to 1 as possible (ideally $R_1 = 1$). In other words, it should be a perfectly ordered two dimensional periodic array (see Figure 1(b)). Figure 3(a) shows the reflectance versus wavelength graph of the metasurface array which shows that $R_1 = 0.999$ in the wavelength range from 1490 nm to 1530 nm.

Second reflector should be slightly transmitting with reflectance $\sim 99\%$ but not less than it. An easy way to do this is to deliberately introduce a small disorder in the periodic arrangement of the structure (as it has been shown in Ref. [24]). Though the reflectivity can also be reduced by designing another perfectly ordered array with a slightly different periodicity a, the method of disorder provides a finer control over the reflectivity. It has been observed that increasing the periodicity by 30 nm, reduces the reflectivity by 1%, but shifting the position of every 1 out of 4 cylinders by 70 nm, reduces the reflectivity by 0.5% only. Since the quality factor depends

ACCEPTED MANUSCRIPT

upon the logarithm of the product of R_1 and R_2 according to Eq. (1), small reduction in the reflectivity produces large reduction in the quality factor. Hence precise control on reflectivity of the second mirror is needed. The proposed design of second reflector is shown in Figure 1(c). Percentage disorder can be defined as standard deviation of the distance of a cylinder from the four neighboring cylinders divided by periodicity a of perfectly ordered array multiplied by 100. In this case, if Δ is the small offset introduced in the position of every 1 out of 4 cylinders, then, $r_3 = \sqrt{(a-\Delta)^2+\Delta^2}$, $r_4 = r_3$, $r_1 = \sqrt{(a+\Delta)^2+\Delta^2}$, $r_2 = r_1$. Hence mean $\bar{r} = (r_1+r_2+r_3+r_4)/4$, standard deviation $\sigma = \sqrt{[(r_1-\bar{r})^2+(r_2-\bar{r})^2+(r_3-\bar{r})^2+(r_4-\bar{r})^2]/4}$, and disorder is $100\sigma/a$. For $\Delta = 70$ nm and $a = 700$ nm, we get $r_1 = r_2 = 773.17$ nm, $r_3 = r_4 = 633.87$ nm, $\sigma = 69.65$ nm and disorder=9.94%. Figures 3(a) and 3(b) show the reflectance of the first and the second reflector respectively at different wavelengths.

Using the proposed designs of two reflectors it is possible to create a very high quality cavity. Figure 1(a) shows the design of proposed metasurface-based cavity. For perfect reflection, we intend to keep the dielectric cylinders to be surrounded by air. Thickness of the active medium has been chosen to be $\lambda/2n_0$, where λ (1500 nm in this case) is the wavelength of operation and n_0 is the refractive index of the active medium. According to Ref. [26], for the wavelength range 920 nm – 1700 nm, a double hetrostructure of InP/$In_{1-x}Ga_xAs_yP_{1-y}$/InP can be used as the active medium, where InP is the confining layer and $In_{1-x}Ga_xAs_yP_{1-y}$ acts as the active layer. According to Ref. [33], to minimize lattice mismatch between InP and $In_{1-x}Ga_xAs_yP_{1-y}$, x $\approx$ 0.466y. In this way, beside λ, refractive index depends on y only. For y = 0.6, the refractive index (n_0) of intrinsic $In_{1-x}Ga_xAs_yP_{1-y}$ is 3.43 [33]. The refractive index of confining layer InP is 3.17 [30].

Figure 4(a) shows the normalized electric field distribution profile inside the cavity and figure 4(b) shows intensity distribution along the length of the cavity. Figure 4(c) shows the quality factor of the metasurface laser cavity at different wavelengths with a maximum of 2630 at 1500 nm.

While talking about the performance of a laser it is necessary to discuss its threshold gain coefficient g_{th}. For lasing, $g_{\text{th}} = \alpha + \alpha_R$, where $\alpha_R = -\ln(R_1R_2)/2d$ is the loss due to finite reflectivities of the mirrors and α is the loss attributed to other factors (including diffraction, dissipation, etc) which can be ignored for the sake of simplicity. Hence, threshold gain coefficient

ACCEPTED MANUSCRIPT

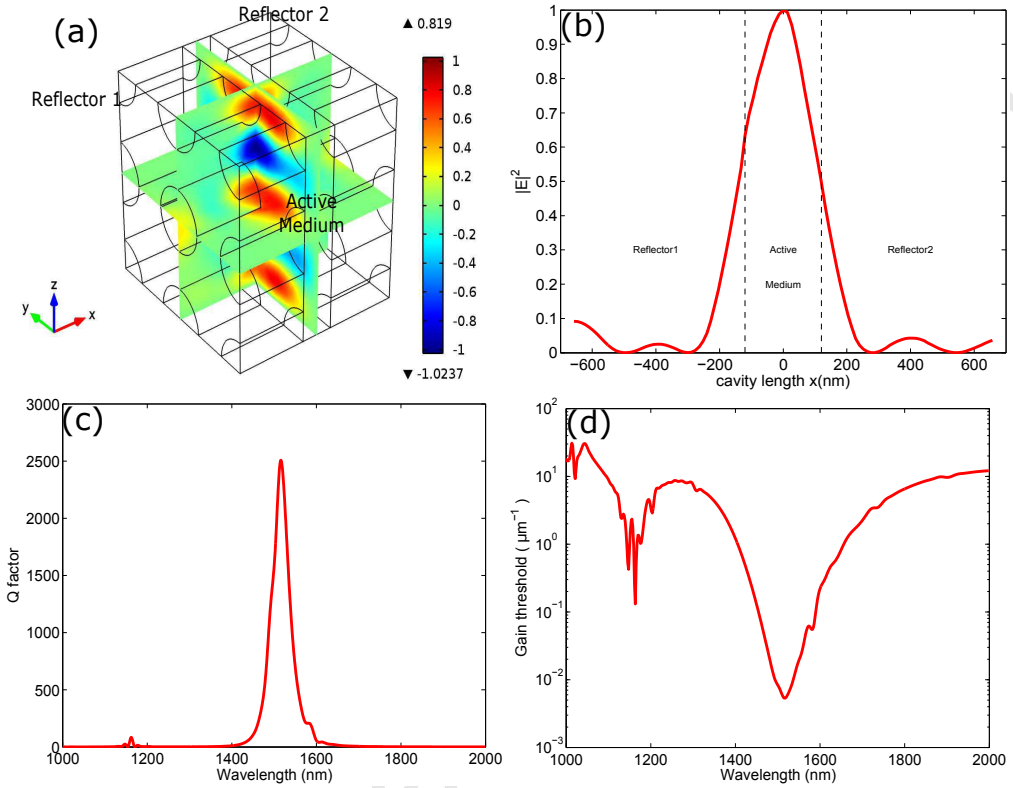


Figure 4: (a) Distribution of the normalized electric field inside the cavity at $\lambda = 1500$ nm and (b) variation of normalized E^2 along the length of the cavity. (c) Quality factor and (d) threshold gain coefficient of Metasurface Laser Cavity at different wavelength.

becomes [26]:

$$g_{\text{th}} = -\frac{\ln(R_1 R_2)}{2d} \tag{2}$$

According to Eq. (2), at 1500 nm threshold gain coefficient $g_{\text{th}} = 0.00557\ \mu m^{-1}$. In figure 4(d), the variation of threshold gain coefficient is shown.

Now we are going to compare our design with a cavity based on Bragg reflectors. The Bragg reflector is a stack of alternating layers of a high refractive index material and a low refractive index material with high refractive index layers at both the ends. Bragg reflector is an excellent reflector with negligible losses because it is made up of dielectrics only. Here, we show that the metasurface perfect reflector proves to have the upper hand because its single layer can provide reflectance equivalent to what is achieved by >25

ACCEPTED MANUSCRIPT

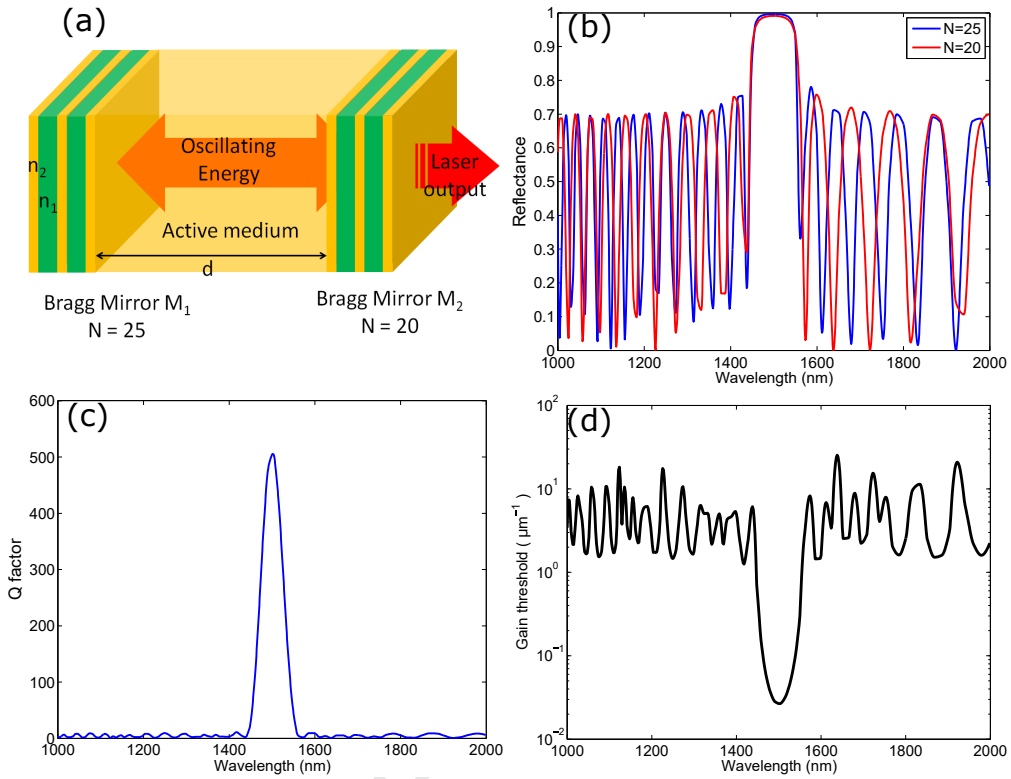


Figure 5: (a) Design of Bragg Cavity. (b) Reflectance for both Bragg mirrors, (c) quality factor and (d) threshold gain coefficient for the laser cavity at different wavelengths.

layers thick Bragg mirror.

We consider a Bragg mirror made up of alternating layers of AlAs ($n_1 = 2.9$) and $Al_{0.1}Ga_{0.9}As$ ($n_2 = 3.57$). For maximum reflection, quaterwave thickness of AlAs and $Al_{0.1}Ga_{0.9}As$ layers are respectively given by: $t_1 = \lambda_0/4n_1$ and $t_2 = \lambda_0/4n_2$. In this way, we get that $t_1 = 130$ nm and $t_2 = 105$ nm. Active medium is again $In_{1-x}Ga_xAs_yP_{1-y}$ (refractive index $n_0 = 3.43$) and length of the cavity d=$\lambda/2n_0$. Here, a 25 pairs stack has been used to make mirror M_1 and a 20 pairs stack has been used to make mirror M_2. Figure 5(a) shows the design of the Bragg cavity, figure 5(b) shows the reflectance vs wavelength graphs for both mirrors, figure 5(c) shows the quality factor of the cavity and figure 5(d) shows variation of threshold gain coefficient at different wavelengths. In our calculations, at 1500 nm quality factor is 505 and threshold gain coefficient g_{th} is 0.0267 μm^{-1}.

ACCEPTED MANUSCRIPT

3. Discussion

Above analysis clearly shows that quality factor achieved using metasurface reflector is 5 times higher and threshold power is 80% lesser than that using Bragg reflector. Since linewidth is inversely proportional to quality factor [32], the higher quality factor also results in reduced linewidth and improved monochromaticity. But most importantly, the design of the metasurface cavity is more compact with just a single layer of dielectric cylinders compared to 20-25 layers of dielectric pairs in case of the Bragg cavity. It should be noted that such impressive results could be seen because the dissipation losses in Silicon are insignificantly small due to negligible value of its extinction coefficient κ around 1500 nm. If the metasurface had been designed for visible spectrum, dissipation loss would be large enough to deteriorate the ability of perfect reflection.

4. Conclusion

In conclusion, we have proposed a very compact design for a laser cavity using all-dielectric metasurface perfect reflectors. We have shown that all-dielectric metasurface perfect reflector reduces threshold power and improves monochromaticity by decreasing linewidth of the laser. Moreover, in a comparative study we have shown that Bragg mirror type reflectors are outperformed by metasurface reflectors which have comparatively simpler design and provide substantially higher quality factor. We believe that our results can be useful for the development of compact laser cavities.

Acknowledgment

The authors gratefully acknowledge (i) the initiatives and support provided by establishment of the TIFAC-Centre of Relevance and Excellence in Fiber Optics and Optical Communication at Delhi Technological University (Formerly Delhi College of Engineering) Delhi, through the "Mission REACH" program of Technology Vision-2020 of the Government of India, (ii) support through DST-RMES (Indo-Russian) joint research project on "All-Dielectric, Plasmonic and Hybrid Photonic Nanostructures", (iii) support through DST-RFBR (Indo-Russian) joint research project entitled "From Plasmonic to Dielectric and Hybrid Nanoantenna: Novel approches to control electromagnetic waves and light". One of the authors (NS) acknowledges the

ACCEPTED MANUSCRIPT

support through Junior Research Fellowship awarded by University Grants Commision (India) under UGC-NET-JRF scheme. This work was supported by the Ministry of Education and Science of the Russian Federation (project 14.584.21.0009 with unique identificator RFMEFI58414X0009)

[1] N. Yu, F. Capasso, Flat optics with designer metasurfaces, Nature Materials 13 (2) (2014) 139–150.

[2] A. V. Kildishev, A. Boltasseva, V. M. Shalaev, Planar photonics with metasurfaces, Science 339 (6125) (2013) 1232009.

[3] C. L. Holloway, E. F. Kuester, J. A. Gordon, J. O. Hara, J. Booth, D. R. Smith, An overview of the theory and applications of metasurfaces: The two-dimensional equivalents of metamaterials, Antennas and Propagation Magazine, IEEE 54 (2) (2012) 10–35.

[4] A. Krasnok, S. Makarov, M. Petrov, R. Savelev, P. Belov, Y. Kivshar, Towards all-dielectric metamaterials and nanophotonics, Proceedings SPIE 9502, Metamaterials X 9502 (2015) 950203.

[5] S. Jahani, Z. Jacob, All-dielectric metamaterials, Nature Nanotechnology 11 (1) (2016) 23–36.

[6] A. Arbabi, Y. Horie, A. J. Ball, M. Bagheri, A. Faraon, Subwavelength-thick lenses with high numerical apertures and large efficiency based on high-contrast transmitarrays, Nature communications 6.

[7] B.-I. Popa, S. A. Cummer, Compact dielectric particles as a building block for low-loss magnetic metamaterials, Physical Review Letters 100 (20) (2008) 207401.

[8] Q. Zhao, J. Zhou, F. Zhang, D. Lippens, Mie resonance-based dielectric metamaterials, Materials Today 12 (12) (2009) 60–69.

[9] A. García-Etxarri, R. Gómez-Medina, L. S. Froufe-Pérez, C. López, L. Chantada, F. Scheffold, J. Aizpurua, M. Nieto-Vesperinas, J. J. Sáenz, Strong magnetic response of submicron silicon particles in the infrared, Optics Express 19 (6) (2011) 4815–4826.

Accepted Manuscript

ACCEPTED MANUSCRIPT

[10] A. B. Evlyukhin, S. M. Novikov, U. Zywietz, R. L. Eriksen, C. Reinhardt, S. I. Bozhevolnyi, B. N. Chichkov, Demonstration of magnetic dipole resonances of dielectric nanospheres in the visible region, Nano Letters 12 (7) (2012) 3749–3755.

[11] A. E. Miroshnichenko, A. B. Evlyukhin, Y. F. Yu, R. M. Bakker, A. Chipouline, A. I. Kuznetsov, B. Lukyanchuk, B. N. Chichkov, Y. S. Kivshar, Nonradiating anapole modes in dielectric nanoparticles, Nature Communications 6 (2015) 8069.

[12] A. Arbabi, Y. Horie, M. Bagheri, A. Faraon, Dielectric metasurfaces for complete control of phase and polarization with subwavelength spatial resolution and high transmission, Nature Nanotechnology 10 (2015) 937–943.

[13] D. Lin, P. Fan, E. Hasman, M. L. Brongersma, Dielectric gradient metasurface optical elements, Science 345 (6194) (2014) 298–302.

[14] R. M. Bakker, D. Permyakov, Y. F. Yu, D. Markovich, R. Paniagua-Domínguez, L. Gonzaga, A. Samusev, Y. Kivshar, B. Lukyanchuk, A. I. Kuznetsov, Magnetic and electric hotspots with silicon nanodimers, Nano Letters 15 (3) (2015) 2137–2142.

[15] M. Caldarola, P. Albella, E. Cortés, M. Rahmani, T. Roschuk, G. Grinblat, R. F. Oulton, A. V. Bragas, S. A. Maier, Non-plasmonic nanoantennas for surface enhanced spectroscopies with ultra-low heat conversion, Nature Communications 6 (2015) 7915.

[16] P. A. Dmitriev, D. G. Baranov, V. A. Milichko, S. V. Makarov, I. S. Mukhin, A. K. Samusev, A. E. Krasnok, P. A. Belov, Y. S. Kivshar, Resonant raman scattering from silicon nanoparticles enhanced by magnetic response, Nanoscale 8 (2016) 9721–9726.

[17] J. Sautter, I. Staude, M. Decker, E. Rusak, D. N. Neshev, I. Brener, Y. S. Kivshar, Active tuning of all-dielectric metasurfaces, ACS Nano 9 (4) (2015) 4308–4315.

[18] M. Decker, I. Staude, M. Falkner, J. Dominguez, D. N. Neshev, I. Brener, T. Pertsch, Y. S. Kivshar, High-efficiency dielectric huygens' surfaces, Advanced Optical Materials 3 (6) (2015) 813–820.

Accepted Manuscript

ACCEPTED MANUSCRIPT

[19] J. Cheng, D. Ansari-Oghol-Beig, H. Mosallaei, Wave manipulation with designer dielectric metasurfaces, Optics Letters 39 (21) (2014) 6285–6288.

[20] Y. Yang, I. I. Kravchenko, D. P. Briggs, J. Valentine, All-dielectric metasurface analogue of electromagnetically induced transparency, Nature Communications 5 (2014) 5753.

[21] Y. F. Yu, A. Y. Zhu, R. Paniagua-Domínguez, Y. H. Fu, B. Luk'yanchuk, A. I. Kuznetsov, High-transmission dielectric metasurface with 2π phase control at visible wavelengths, Laser & Photonics Reviews 9 (4) (2015) 412–418.

[22] A. Arbabi, R. M. Briggs, Y. Horie, M. Bagheri, A. Faraon, Efficient dielectric metasurface collimating lenses for mid-infrared quantum cascade lasers, Optics Express 23 (26) (2015) 33310–33317.

[23] B. Slovick, Z. G. Yu, M. Berding, S. Krishnamurthy, Perfect dielectric-metamaterial reflector, Physical Review B 88 (16) (2013) 165116.

[24] P. Moitra, B. A. Slovick, Z. G. Yu, S. Krishnamurthy, J. Valentine, Experimental demonstration of a broadband all-dielectric metamaterial perfect reflector, Applied Physics Letters 104 (17) (2014) 171102.

[25] N. Bonod, Silicon photonics: Large-scale dielectric metasurfaces, Nature materials 14 (7) (2015) 664–665.

[26] J. M. Senior, M. Y. Jamro, Optical fiber communications: principles and practice, Pearson Education, 2009.

[27] P. Moitra, B. A. Slovick, W. Li, I. I. Kravchencko, D. P. Briggs, S. Krishnamurthy, J. Valentine, Large-scale all-dielectric metamaterial perfect reflectors, ACS Photonics 2 (6) (2015) 692–698.

[28] P. Gutruf, C. Zou, W. Withayachumnankul, M. Bhaskaran, S. Sriram, C. Fumeaux, Mechanically tunable dielectric resonator metasurfaces at visible frequencies, ACS Nano 10 (1) (2015) 133–141.

[29] M. I. Shalaev, J. Sun, A. Tsukernik, A. Pandey, K. Nikolskiy, N. M. Litchinitser, High-efficiency all-dielectric metasurfaces for ultracompact beam manipulation in transmission mode, Nano Letters 15 (9) (2015) 6261–6266.

Accepted Manuscript

ACCEPTED MANUSCRIPT

[30] E. D. Palik, Handbook of optical constants of solids, Vol. 3, Academic press, 1998.

[31] D. R. Smith, J. B. Pendry, Homogenization of metamaterials by field averaging, Journal of Optical Society of America B 23 (3) (2006) 391–402.

[32] A. K. Ghatak, K. Thyagarajan, Optical electronics, Cambridge University Press, 1989.

[33] B. Jensen, A. Torabi, Refractive index of quaternary in1- xgaxasyp1- y lattice matched to inp, Journal of applied physics 54 (6) (1983) 3623–3625.

Accepted Manuscript

ACCEPTED MANUSCRIPT

Highlights:

- **the design of the metasurface cavity is more compact with just a single layer of dielectric cylinders compared to 20-25 layers of dielectric pairs in case of the Bragg cavity**
- **quality factor achieved using metasurface reflector is 5 times higher than that using Bragg reflector**
- **threshold power is 80% lesser than that using Bragg reflector**
- **dissipation losses in the Silicon are insignificantly small due to negligible value of its extinction coefficient κ around 1500 nm**

Accepted Manuscript

Available online at www.ijapie.org

International Journal of Advanced
Production and Industrial Engineering

IJAPIE-SI-OSCM 705 (2017) 17–19

Special Issue on

OPERATIONS
&
SUPPLY CHAIN
MANAGEMENT

Implementation of Lean Manufacturing through Waste Elimination

Sanjeev Jain* , A.K. Madan
(Delhi Technological University, Delhi, India)
**Email: sanjeevjain99@gmail.com*

Abstract- Manufacturing operations are continually striving to increase productivity and output of their processes. Lean manufacturing or Lean technique is more than a cost reduction project or a problem solving approach (Tapping, 2002)James Womack, Daniel Jones, and Daniel Roos coined the term "lean production" in their 1990 book The Machine that Changed the World to describe the manufacturing paradigm established by the Toyota Production System. In the 1950s, the Toyota Motor Company pioneered a collection of advanced manufacturing methods that aimed to minimize the resources it takes for a single product to flow through the entire production process. Inspired by the waste elimination concepts developed by Henry Ford in the early 1900s, Toyota created an organizational culture focused on the systematic identification and elimination of all waste from the production process. Lean manufacturing refers to a manufacturing improvement process based on the fundamental goal of Toyota production system (TPS) in order to reduce or eliminate waste while improving production flow (Tapping, 2002). Many manufacturing organizations realize the importance of using lean methodology. However, few organizations implement lean concept with the necessary knowledge and proven tools to achieve it. The purpose of this study is to develop a process to improve the productivity of line using Lean tool. This particular tool allows the manufacturing plant to document current throughput time, inventory levels and cycle times to determine the ratio of value added work to total lead time of the product line being analysed. The first step will be to measure the current state to make a picture of the production flow and understand the company's current cycle times, process linkages, and machine equipment capacity. This provides the information needed to produce an improved future state map by creating an ideal value flow. The goal is to identify and eliminate the waste, which is any activity that does not add value to the final product, in the production process which will help to achieve the production capacity as per customer demand through Lean manufacturing techniques.

Keywords: Lean Manufacturing; Waste elimination; Value added work; Production Capacity.

INTRODUCTION

Manufacturing operations are continually striving to increase productivity and output of their processes. Lean manufacturing or Lean technique is more than a cost reduction project or a problem solving approaches (Tapping, 2002). The main idea is that an efficient production can be achieved by a comprehensive approach to minimize wastes available in production processes. This means eliminating excess production and inventory, movement of material, waiting and delays in production process, over processing, excess worker movement, and the need for rework and corrections in product during or after production. We did the analysis on an assembly line in an automotive product manufacturing company in Manesar to improve assembly line production capacity by using lean manufacturing technique. During this activity we find detect area of improvement and took action to avoid/ reduce possible non value added work and improve current process of assembly line which will help us to meet increased customer demand through reduced working time.

NECESSITY OF LEAN

In Lean, you pursue understanding the source and rooting out the causes of waste. The practice of Lean as the root-cause eliminator of wastefulness is based on a core set of fundamental assumptions. Follow this logic:

- **You're in business to sell products and services to customers.** The customer has the need and defines the purpose. Everything begins and ends with what the customer requires. Everything else is fluff.
- **The customer is the only true arbiter of value.** The customer is willing to give you their money for your product or service only when they believe it's a fair exchange of value. It has to be the right combination of quality products and services, in the right place, at the right time and at the right price.
- **Value-creation is a process.** A combination of steps — such as marketing, design, production, processing, delivery and support — rightly performed, will result in the creation of products and services that the customer will properly value.

- **Waste diminishes the process of value creation.** Things that naturally creep in and prevent the steps in a process from flowing quickly and effectively will inhibit the creation of customer value.
- **Prepare a perfect process has no waste.** If every step in the process is fully capable, acts only when necessary, flows perfectly, and adapts to perform exactly as needed, the process will develop and deliver products and services without waste.
- **Perfect processes maximize customer value.** The closer to perfection a process becomes, the more effective the creation of value, the more satisfied the customers and the more successful the endeavour.

No one has ever experienced the perfect process, but Lean continually strives for perfection. Lean is the strategy and approach, and it provides the methods and tools for pursuing the perfect process.

To accomplish this, companies employ a variety of advanced manufacturing tools to lower the time intensity, material intensity, and capital intensity of production. When companies implement several or all of these lean methods, several outcomes consistently result:

- Reduced inventory levels (raw material available in store, work-in-progress stock at assembly line, finished product available at Finished Goods store) along with associated carrying costs and loss due to damage, spoilage, off-specification, etc.
- Decreased material usage (product inputs, including energy, water, chemicals, etc. by reducing material requirements and creating less material waste during manufacturing.
- Optimized equipment as per production process helps to reduced capital cost.
- Reduced need for factory facilities by driving down the space required for product production.
- Increased production velocity (the time required to process a product from initial raw material to delivery to a customer) by eliminating / reducing process steps, extra movement, wait times, and downtime available in production process.
- Enhanced production flexibility (the ability to alter or reconfigure products and processes rapidly to adjust to customer needs and changing market circumstances) enable the implementation of a pull production, just-in-time(JIT) oriented system which lowers inventory and capital requirements; and
- Reduced complexity of product (complicated products and processes that increase opportunities for variation and error) by reducing the number of parts/ components and material types in products, and by eliminating unnecessary process steps, movement and equipment with unneeded features.

With the help of all above methods we can achieve the increased profit on product without increase in cost of product as we can understand by Figure 1 & 2. Lean Way not only helps us to gain profit rather than we will achieve customer satisfaction with on time product delivery with right quantity and quality.

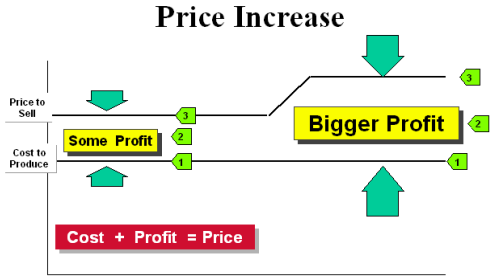


Figure 1. Traditional Way

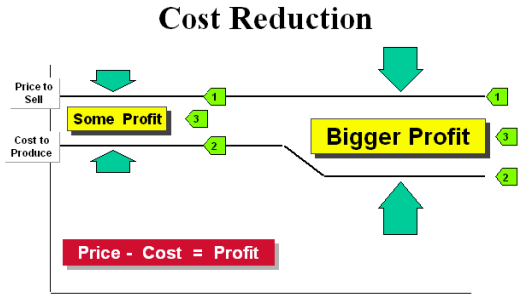


Figure 2. Lean Way or TPS Way

WASTE ELIMINATION

To improve the line capacity and its product quality we visited through the assembly line to find out the possible area of improvement through waste elimination. According to Tapping (2002) "the ultimate lean target is the total elimination of waste. Waste, or Muda, is anything that adds cost to the product without adding value of product" (p. 41).
Sources of waste are available everywhere, we need to focus on production process to find out the available waste in whole Value Stream Mapping. Wastes can be classified into seven categories (Tapping, 2002):

[1] Waste of overproducing: Manufacture components or child parts that are neither intended for stock nor planned for sale immediately will increase only waste at line and waste at stock.
[2] Waste of waiting: Refers to the idle time or waiting time between two operations. We should utilize it to do any other value added work.
[3] Waste of transport: Move material more than necessary will not add any value just un-necessary increase time, cost and fatigue for operator.
[4] Waste of processing: Doing more to the product than required necessary. We should focus on all process to eliminate un-necessary or nonvalue added work.

[5] Waste of inventory: Excess of stock / more than required stock from raw materials to finished goods always loss for any company. It unnecessary increase cost for company and extra space for storage.
[6] Waste of motion: Any motion that is not necessary for the completion of a work.
[7] Waste of defects and spoilage: Defective parts that are produced and need to be reworked after completion of work.

Based upon the above Waste or Muda's we observed at our assembly line and improve the assembly line to improve the line productivity, to reduce cycle time, to reduce operator fatigue, to improve operator safety and to reduce cost.
Area of improved at automotive Switch manufacturing assembly line are:

Before: Location of rivet tray at rivet assembly station is left side of fixture.

After: Location of rivet tray shifted at the right side of rivet assembly station which reduces the Waste of Motion.

Before: Location of Insulator at line is also on left side of machine and inside the deep bin.

After: Location of insulator shifted to right side of machine and reduced the depth of bin it reduces Waste of Motion and operator fatigue.

Before: one station uses 2 different type of rivet and always chances of mix up.

After: Location of rivet tray properly identified by colour coding and process defined to use one rivet by left hand other by right hand. It reduces waste of defect.

Before: at spring assembly station operator always faced problem of spring entangled.

After: Spring separator installed at station, now operate can pick one spring easily it reduces Waste of process.

Before: During illumination checking of switch operator have to bend more than normal which caused high operator fatigue and reduced productivity.

After: Illumination checking process improved as per operator height, it reduces operator fatigue and operator can achieve the production as per standard time. It reduces Waste of Motion and Waste of Process.

Before: Manual assembly and remove coupler for testing Switch require more time and it became bottleneck process.

After: Automatic assembly and remove coupler machine installed to reduce operation time.

Before: Batch code marking and terminal straightness testing done on two different stations.

After: new modified fixture designed which can do both work at one station. It reduces Waste of Over process.

I. CONCLUSIONS

During research, team evaluated where waste or Muda occurs in the production process and analyse observations with team to improve the process and achieve customer demand with right quantity and quality, improve employee satisfaction. After all the improvement we achieved:

- Productivity of line improved by 38.26%.
- Cycle time reduced from 56.9 seconds to 42.9 seconds. This is 24.6 % reduction.
- Able to achieve increased customer demand.
- Knowledge of team for Lean concept improved which will be used at other assembly line to improve.
- Operator fatigue reduced which helps to improve employee more adoptable towards changes.
- Safety of line operator improved.
- Team morale increased for new challenges

REFERENCES

[1] Womack, J., & Jones, D. (1996). *Lean thinking: Banish waste and create wealth in your corporation.* New York, NY: Simon & Schuster.(Book)
[2] Tapping, D., Luyster, T., & Shuker, T. (2002). *Value stream management: Eight steps to planning, mapping, and sustaining lean improvements.* New York, NY: Productivity Press.(Book).
[3] Rachna Shah, Peter T. Ward, "Lean Manufacturing: Context, practices, and performance", *Journal of Operation Management*, 21(2003)129-149 (Article)
[4] J. Ben Naylor, Mohamed M Naim, Danny Berry,"Leagility: Integrating the lean and agile manufacturing paradigms in the total supply chain",Int. *Journal of Production Economics*, 62(1999) 107-118 (Article)
[5] Ohno, T. (1988). *Toyota production system: Beyond large-scale production.* Cambridge, MA: Prod**u**ctivity Press.(Book)
[6] Leonardo Rivera, F. Frank Chen,"Measuring the impact of lean tool on the cost-time investment of a product using cost-time profile", Robotics and computer integrated manufacturing, 23(2007) 684-689 (Article)
[7] James Womack, Daniel Jones, and Daniel Roos (1990) The Machine that Changed the World.(Book).

ResearchGate

See discussions, stats, and author profiles for this publication at: https://www.researchgate.net/publication/309873480

Influence of 100MeV Au+8 ion on photovoltaic response of BiFeO3/BaTiO3 multilayer structures

Article · November 2016

DOI: 10.1016/j.matdes.2016.11.011

CITATION
1

READS
89

6 authors, including:



Monika Tomar
University of Delhi
179 PUBLICATIONS **988** CITATIONS
SEE PROFILE



ASHOK Kumar
National Physical Laboratory - India
221 PUBLICATIONS **2,149** CITATIONS
SEE PROFILE



Fouran Singh
Inter University Accelerator Centre
304 PUBLICATIONS **3,345** CITATIONS
SEE PROFILE



Vinay Gupta
University of Delhi
367 PUBLICATIONS **4,722** CITATIONS
SEE PROFILE

Some of the authors of this publication are also working on these related projects:



Biosensor View project



Synthesis and Characterization of Al2O3 for ion beam dosimetry View project

All content following this page was uploaded by Savita Sharma on 22 November 2016.

The user has requested enhancement of the downloaded file.

ARTICLE IN PRESS
JMADE-02447; No of Pages 10
Materials and Design xxx (2016) xxx–xxx
Contents lists available at ScienceDirect
Materials and Design
journal homepage: www.elsevier.com/locate/matdes

Influence of 100 MeV Au^{+8} ion on photovoltaic response of $BiFeO_3/BaTiO_3$ multilayer structures

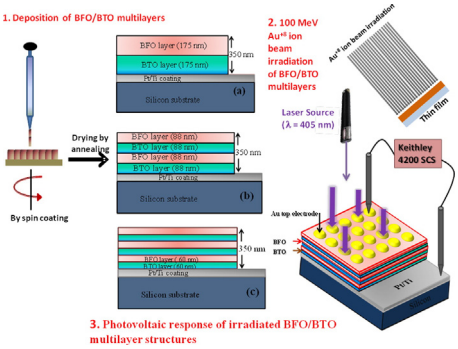
Savita Sharma [a,d], Monika Tomar [b], Ashok Kumar [e], Fouran Singh [c], Nitin K. Puri [d], Vinay Gupta [a,*]

[a] Department of Physics and Astrophysics, University of Delhi, Delhi 110007, India
[b] Physics Department, Miranda House, University of Delhi, Delhi 110007, India
[c] Inter University Accelerator Centre, Aruna Asaf Ali Marg, New Delhi 110067, India
[d] Department of Applied Physics, Delhi Technological University, Delhi 110042, India
[e] CSIR-National Physical Laboratory, Dr. K.S. Krishnan Marg, Delhi, India

HIGHLIGHTS

- BFO/BTO multilayers of varying layer number deposited on Pt/Si using CSD technique
- 100 MeV Au^{+8} irradiation performed at fluences 1×10^{12}, 1×10^{13} and 3×10^{13} ions/cm^2
- Irradiation effects on photovoltaic response studied in MFM capacitor configuration
- Photovoltaic response sustained in multilayer structures post ion beam irradiation

GRAPHICAL ABSTRACT



ARTICLE INFO

Article history:
Received 22 July 2016
Received in revised form 2 November 2016
Accepted 3 November 2016
Available online xxxx

Keywords:
Irradiation
Photovoltaic
Fluence
Ferroelectric

ABSTRACT

This work presents the swift heavy ion (SHI) irradiation induced possible modifications in structural strain and surface morphology of $(BiFeO_3)$BFO/$(BaTiO_3)$BTO multilayer structures prepared by chemical solution deposition technique. Furthermore, the role of structural defects (induced due to irradiation) on the ferroelectric property and photovoltaic response of BFO/BTO multilayer structures having different number of layers has been studied. Significant modifications in the morphological and ferroelectric properties of BFO/BTO (two, four and six layers) multilayer structures due to induced structural defects were observed after SHI irradiation performed using 100 MeV Au^{+8} ion with ion fluence of ~1×10^{12}, 1×10^{13} and 3×10^{13} ions/cm^2. Ferroelectric photovoltaic response decreases with increase in ion fluence from 1×10^{12} to 1×10^{13} ions/cm^2 along with change in open circuit voltage from 0.41 V to 0.23 V, short circuit current density from 5.177 μA/cm^2 to 1.71 μA/cm^2 and I_{on}/I_{off} ratio from 33.02 to 13.02. This study on effect of SHI irradiation on multilayer ferroelectric photovoltaic cell is important to understand the possible application of BFO/BTO multilayer photovoltaic cells in the regions susceptible to radiations. Furthermore, the study of perovskite solar cell performance in the presence of SHI radiation, is essentially required for the development of durable solar energy harvesters.

© 2016 Elsevier Ltd. All rights reserved.

* Corresponding author.
E-mail address: drguptavinay@gmail.com (V. Gupta).

http://dx.doi.org/10.1016/j.matdes.2016.11.011
0264-1275/© 2016 Elsevier Ltd. All rights reserved.

Please cite this article as: S. Sharma, et al., Influence of 100MeV Au+8 ion on photovoltaic response of BiFeO3/BaTiO3 multilayer structures, Materials and Design (2016), http://dx.doi.org/10.1016/j.matdes.2016.11.011

1. Introduction

Energetic ion beams play a significant role in modifying the properties of materials [1–3]. The change in material properties strongly depend on the ion energy, fluence and ion species. Low energy ions having energy up to a few hundred keV available from ion implanters are mainly used in semiconductors for modification of surface and interface and hence the functional properties. The ion beams interact with material in the form of elastic and inelastic scattering of the particles resulting in the excitation and ionization of the atoms. However, it may also trigger a nuclear reaction leading to a disturbance in the structure of matter, which is referred to as radiation damage. The ions entering into a solid having velocity similar to the Bohr velocity of electron (2.18×10^8 m/s), lose their energy while passing through the material either by (a) displacing atoms (of the sample) by elastic collisions where energy transfer takes place directly to target atoms, which is called as the nuclear stopping or nuclear energy loss or (b) exciting the atoms by inelastic collisions between the incoming ions and electrons of the target atoms, which is known as electronic stopping or electronic energy loss [4]. The nuclear energy loss (S_n) is significant at low energies, whereas electronic energy loss (S_e) is dominant at high energies. The heavy ions with very high energies, generally in the range of a few tens of Mega electron volts (MeV) to Giga electron volts (GeV) where the electronic energy loss (S_e) dominates, are called as the swift heavy ions (SHI). SHI generated electronic excitation not only results in the displacement of the lattice atoms, but may also lead to various structural defects [4]. SHI also plays a major role in synthesis and material modification. The passage of SHI involves very rapidly developing processes, which are difficult to observe during or immediately after their occurrence. Hence, a number of modifications can occur in the material including creation of defects, defect annealing, amorphization, crystallization, crystalline-to-crystalline phase transition etc. This is due to the fast energy transfer during the electronic excitation confined to a narrow cylindrical region along the path of the heavy ion beam [5].

Extensive research is in progress for the last two decades, adhering to the SHI induced changes in structural and physical properties of magnetic insulators like ferrites [6–7]. Enormous radiations like low energy ions, high energy ions, fast neutrons etc. are capable of inducing certain crystallographic and magnetic changes in bulk ferrite samples such as spinels, garnets and hexa-ferrites [8–10]. There are reports on the study of material modifications related to surface properties of manganite films and interface behavior due to SHI irradiation. The reports give an insight for better understanding of the localized strain in the films and creation of controlled defects in the lattice [11–14]. Majority of the reports showed that SHI irradiation deteriorates the transport properties and crystallinity of manganite films [12–15]. Considerable efforts have been made to study the effect of SHI irradiation on the property of PLD-grown manganite films, however, limited work is reported on its effect on the multiferroic thin films and their photovoltaic applications [12–14,16]. Therefore, an attempt has been made towards the establishment of BFO/BTO multilayer structure as a renewable source of energy in space where normal detectors are vulnerable to exposure of energetic ions. Significance of the present work is the sustenance of Photovoltaic properties of the prepared multilayer structures post ion beam irradiation.

Based on the reported literature, the effect of SHI irradiation on the structural, electrical and ferroelectric properties of CSD grown BFO/BTO multilayer structures has been studied in the present work. The selection of highly energetic 100 MeV Au^{+8} ions was made by varying the fluence from 1×10^{12} to 3×10^{13} ions/cm^2, and the results are presented in the following sections.

2. Experimental details

BFO/BTO multilayer structures having 2, 4 and 6 alternating layers of BTO and BFO, were deposited onto Pt/Ti coated passivated silicon (Pt/Si) substrates by CSD technique (Deposition details as described in previous reports) [17]. The total thickness of the BFO/BTO structure was maintained as 350 nm and thickness of the individual layer was approximately 175 nm, 88 nm and 60 nm for 2, 4 and 6 layer BFO/BTO structures respectively. All BFO/BTO multilayer samples, of size, 2×1 cm^2, were irradiated with 100 MeV Ag^{+8} ions with varying fluence of 1×10^{12}, 1×10^{13} and 3×10^{13} ions/cm^2, using 15 UD Tandem Accelerator facility at Inter University Accelerator Centre (IUAC), New Delhi. The experimental parameters used for irradiation of samples have been tabulated in Table 1. Ion beam was focused onto a spot of ~1 mm diameter and was continuously scanned over the complete area of the film using a magnetic scanner, to ensure uniform irradiation. Irradiation was performed at low angle with respect to the ion beam direction, to avoid channeling effect.

The electronic energy loss (S_e) and nuclear energy loss (S_n) for BFO and BTO thin films have been calculated using Stopping and Range of Ions in Matter (SRIM) simulation program [18]. The projectile range of 100 MeV Ag^{+8} ions (ion fluencies ~1×10^{12}, 1×10^{13} and 3×10^{13} ions/cm^2) has also been calculated. The calculated values of S_e, S_n and projectile range have been tabulated in Table 2. The calculated value of projectile range was found to be very large as compared to the thicknesses of thin film/multilayer samples (15–20 μm), ensuring that all the ions striking the sample, completely pass through thin film. According to thermal spike model, highly energetic ions, on passing through a thin multilayer multiferroic sample, deposit their energy on to the material resulting in large electronic excitation, and are expected to modify the properties of irradiated samples [19].

Structural and microstructural properties of the pristine and irradiated BFO/BTO multilayer samples were studied using XRD (θ–2θ) and atomic force microscopy (AFM) measurements respectively. Optical properties were studied by UV–Visible spectrophotometer (Make: Perkin Elmer, Model: Lambda 35) in 1100 to 190 nm range of wavelength. For electrical measurement, Au circular top electrodes (200 μm diameter) were deposited on to surface of sample using magnetron sputtering technique. P–E hysteresis loop measurements were carried out using Radiant technologies precession ferroelectric loop tracer. Ferroelectric-Photovoltaic (FE-PV) measurements have been carried out using Keithley 4200 semiconductor characterization unit.

3. Results and discussion

3.1. Structural studies: X-ray diffraction (XRD)

The important properties of the ferroelectric materials are determined by their structure. The crystal symmetry and related strains of these materials have a strong influence on their switching behavior. The structural studies help in establishing a relation between the crystallographic symmetry and ferroelectric switching capability of a material, which in turn plays an important role in its ferroelectric photovoltaic response. Therefore in the following section structural properties of BFO/BTO multilayer structures have been studied in detail.

Fig. 1 (a), (b) and (c) show the XRD patterns of irradiated BFO/BTO multilayer structures having 2, 4 and 6 layers, respectively. XRD patterns obtained for the as prepared pristine BFO/BTO multilayer structures having 2, 4 and 6 layers are also included in the figures for comparison. XRD patterns of the irradiated BFO/BTO multilayer samples

Table 1
Experimental parameters used for irradiation of samples at IUAC, New Delhi.

Selected ion bean parameters	Used
Pelletron	15UD@IUAC New Delhi
Ion bean	Au^{8+}
Fluence	1×10^{12}, 1×10^{13}, 3×10^{13} ions/cm^2
Energy	100 MeV
Current	1 pnA

Please cite this article as: S. Sharma, et al., Influence of 100MeV Au+8 ion on photovoltaic response of BiFeO3/BaTiO3 multilayer structures, Materials and Design (2016), http://dx.doi.org/10.1016/j.matdes.2016.11.011

Table 2
Calculated value S_e, S_n and projectile range.

Thin films	S_e(eV/Å)	S_n(eV/Å)	Projectile range (μm)
BFO	1.266×10^3	3.172×10^1	14.64
BTO	9.558×10^2	1.955×10^1	19.63

show (110) oriented growth of the BTO thin film (Fig. 1). No significant change in the crystalline structure of BFO/BTO multilayer was observed after Au^{8+} irradiation with different fluence (Fig. 1). However, the appearance of new XRD peaks (broad and low intensity) at all fluences (1×10^{12} and 1×10^{13} and 3×10^{13} ions/cm^2) indicates the formation of some impurity phase (related to $Bi_2Fe_4O_9$) in the BFO/BTO multilayer structures (Fig. 1). It has been reported that $BiFeO_3$ is unstable at high temperatures and rapidly decomposes into parasitic phases like $Bi_2Fe_4O_9$ or Fe_2O_3 [20]. The formation of $Bi_2Fe_4O_9$ secondary phase in the present case for irradiated BFO/BTO multilayer samples may be due to the increased temperature in the material medium during the passage of 100 MeV Ag^{+8} ions. The obtained result, thus, supports the applicability of "Thermal spike model" of ion-matter interaction for prepared BFO/BTO samples.

The (110) peak shows a shift towards the lower angle at a fluence of 1×10^{13} ions/cm^2 for all prepared samples, (Fig. 1) depicting the introduction of strain as a result of irradiation. At highest fluence of 3×10^{13} ions/cm^2, (110) peak shifts towards the higher angle showing relaxation of strain. The values of lattice parameters (a, c), c/a distortion ratio and strain induced along 'c' axis at varying fluences for all prepared multilayer structures having 2, 4 and 6 layers are summarized in Tables 3, 4 and 5 respectively. The stress modulus in the BFO/BTO multilayer structures is obtained using equation: stress $= |(c_o - c)|/c_o$ in %, where "c" is the respective lattice constant of BFO or BTO in deposited multilayer film and "c_o" is the corresponding bulk value. Values of crystallite size along the dominant plane, calculated from the Debye Scherrer formula [21] for all the films are tabulated in Table 6. The crystallite size for all the multilayers is seen to be decreasing with increasing the fluence of SHI (Table 6).

The variation in c/a distortion ratio in both BFO and BTO thin films in the pristine and irradiated (a) two layer (b) four layer and (c) six layer multilayer structures as a function of fluence from 1×10^{12} to 3×10^{13} ions/cm^2 shows an oscillating behavior with consecutive depositions of BTO and BFO layers. The large lattice distortion observed for multilayer structure at lowest fluence 1×10^{12} ions/cm^2 is expected to result in improved ferroelectric property than at higher fluences and hence in corresponding ferroelectric photovoltaic response.

3.2. Surface morphology: atomic force microscopy (AFM)

The surface morphology and grain size play an important role in defining the electrical properties of oxide thin films, thus it is necessary to systematically study the effect of irradiation on the surface morphology and grain size of the BFO/BTO multilayer structures.

Modifications in the surface morphology were observed using AFM (2D) images of different multilayer (2, 4 and 6 layers) BFO/BTO structures before and after irradiation, respectively with various ion fluences (1×10^{12}, 1×10^{13} and 3×10^{13} ions/cm^2) are shown in Fig. 2 (a), (b) and (c). Particle fragmentation and agglomeration into bigger grains occurs with the increase in fluence from 1×10^{12} to 3×10^{13} ions/cm^2. With increase in fluence, the spread of energy lost by the SHI is relatively large, thus promotes bigger grain growth.

It may be seen from the AFM images (Fig. 2 (a), (b) and (c)) that the small sized crystallites coalesce with increase in ion fluence in all the samples making bigger globular structures. Values of root mean square (rms) surface roughness (RSR) increase with ion fluence and are listed in Table 6.

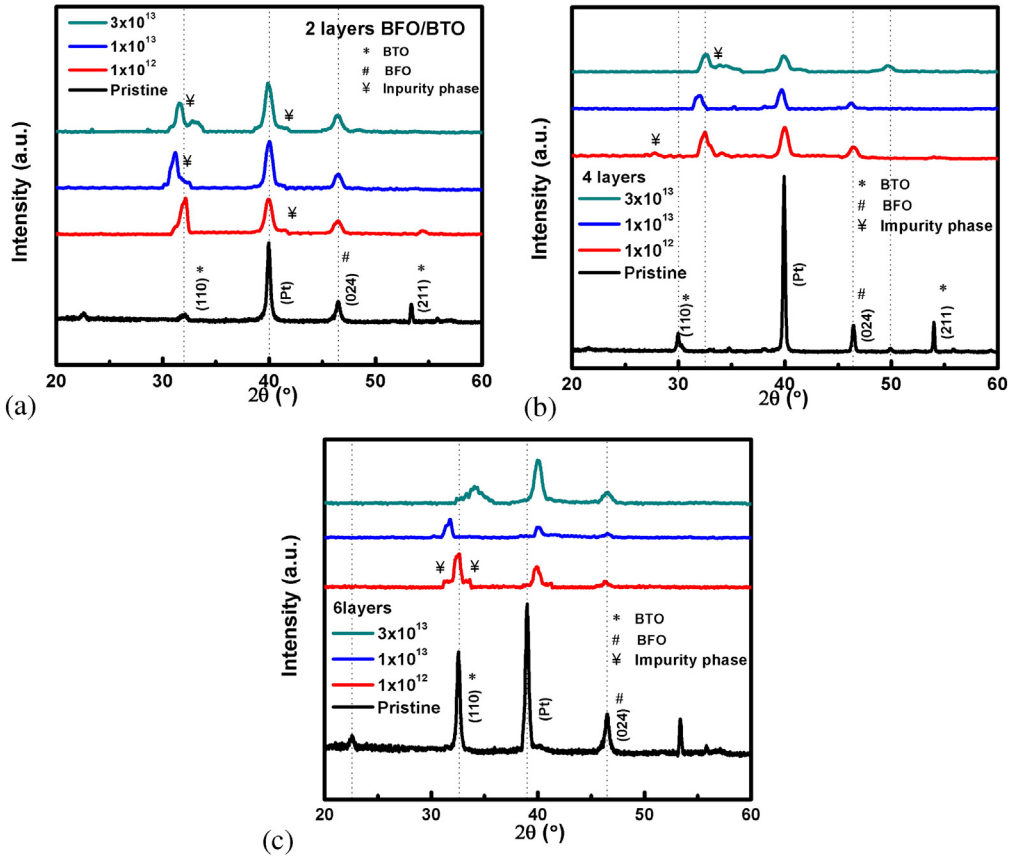


Fig. 1. XRD patterns of bare and irradiated (a) 2 layers (b) 4 layers and (c) 6 layers BFO/BTO multilayer structures.

Please cite this article as: S. Sharma, et al., Influence of 100MeV Au+8 ion on photovoltaic response of BiFeO3/BaTiO3 multilayer structures, Materials and Design (2016), http://dx.doi.org/10.1016/j.matdes.2016.11.011

Table 3
Lattice parameters "a" and "c", c/a distortion ratio and stress modulus along c-axis in BFO/BTO two layers structure after irradiation at varying fluencies.

	BTO				BFO			
	Lattice parameter		Stress modulus	c/a distortion ratio	Lattice parameter		Stress modulus	c/a distortion ratio
	a (Å)	c (Å)			a (Å)	c (Å)		
Bulk	3.999	4.033	–	1.0085	5.876	13.867	–	2.3599
1×10^{12} ions/cm^2	3.981	4.019	0.002	1.009	5.523	13.567	0.0216	2.45645
1×10^{13} ions/cm^2	3.975	3.989	0.010	1.003	5.525	13.571	0.0213	2.45628
3×10^{13} ions/cm^2	3.978	3.998	0.008	1.005	5.526	13.573	0.0212	2.45620
Pristine	3.989	4.028	0.124	1.009	5.520	13.563	2.192	2.4570

Table 4
Lattice parameters "a" and "c", c/a distortion ratio and stress modulus along c-axis in BFO/BTO four layers structure after irradiation at varying fluencies.

	BTO				BFO			
	Lattice parameter		Stress modulus	c/a distortion ratio	Lattice parameter		Stress modulus	c/a distortion ratio
	a (Å)	c (Å)			a (Å)	c (Å)		
Bulk	3.999	4.033	–	1.0085	5.876	13.867	–	2.3599
1×10^{12} ions/cm^2	4.225	4.047	0.003	0.9578	5.521	13.579	0.0207	2.45951
1×10^{13} ions/cm^2	4.199	4.027	0.002	0.9590	5.520	13.574	0.0211	2.45905
3×10^{13} ions/cm^2	4.207	4.027	0.001	0.9572	5.511	13.585	0.0203	2.46506
Pristine	4.229	4.051	0.446	0.9579	5.523	13.582	2.055	2.4591

3.3. Optical studies: UV visible spectroscopy

UV visible spectroscopy is an efficient technique to determine the optical properties of any sample which includes film thickness, refractive index, band gap, color and the reflectance properties in general. Here, the band gap of the pristine and irradiated BFO/BTO multilayer structures have been calculated to check the application of BFO/BTO multilayer structures towards photovoltaic effect in visible region. Also, the effect of ion beam irradiation on the optical properties of prepared samples have been examined.

Fig. 3 (a), (b) and (c) shows the effect of the increasing fluence of irradiation on the optical transmission of BFO/BTO multilayer structures. The average transmittance is seen to be decreasing in the visible region with increase in fluence for all the prepared (2, 4 and 6 layers) BFO/BTO multilayer structures (Fig. 3 (a), (b) and (c)). Pristine sample of 2 layer BFO/BTO structure had 65% transmittance in the visible region, which decreased upto 59% upon ion irradiation at a fluence of 3×10^{13} ions/cm^2 (Fig. 3 (a)). The decrease in transmittance of BFO/BTO multilayer structures after irradiation may be due to increased optical scattering caused by increase in the surface roughness of film as demonstrated by the AFM images (Fig. 2).

It can be observed clearly from Fig. 3 that the band edge shifted towards the higher wavelength upon ion irradiation with increase in ion fluence, in all the BFO/BTO multilayer structures. Shift towards the higher wavelength is due to the formation of defect states producing localized states near the band edges in the forbidden gap. This modification is attributed to the simultaneous lowering of the conduction band edge and uplifting of the valence band edge due to induced defects in the material, post ion irradiation. The Transmittance in the visible region and effect of ion fluencies on pristine and irradiated BFO/BTO multilayer structures have been listed in Table 7.

3.4. Ferroelectric (P–E loop)

For understanding the ferroelectric behavior of pristine and irradiated BFO/BTO multilayer films, room temperature P–E hysteresis loops for 2, 4 and 6 layered structures were obtained at 1 kHz frequency, and are

Table 5
Lattice parameters "a" and "c", c/a distortion ratio and stress modulus along c-axis in BFO/BTO six layers structure after irradiation at varying fluencies.

	BTO				BFO			
	Lattice parameter		Stress modulus	c/a distortion ratio	Lattice parameter		Stress modulus	c/a distortion ratio
	a (Å)	c (Å)			a (Å)	c (Å)		
Bulk	3.999	4.033	–	1.0085	5.876	13.867	–	2.3599
1×10^{12} ions/cm^2	4.249	4.070	0.010	0.957	5.527	13.600	0.0192	2.46064
1×10^{13} ions/cm^2	4.220	3.995	0.009	0.946	5.526	13.597	0.0194	2.46055
3×10^{13} ions/cm^2	4.269	4.090	0.014	0.958	5.525	13.595	0.0196	2.46063
Pristine	4.252	4.079	1.140	0.9586	5.528	13.603	1.903	2.4607

Table 6
Values of grain size and roughness for 2, 4 and 6 layered BFO/BTO structure.

Samples	2 layers BFO/BTO		4 layers BFO/BTO		6 layers BFO/BTO	
	Crystallite size (nm)	Roughness (nm)	Crystallite size (nm)	Roughness (nm)	Crystallite size (nm)	Roughness (nm)
Pristine	25	4.3	28	8.71	29	14.7
1×10^{12} ions/cm^2	22	9.1	18	10.3	26	15.2
1×10^{13} ions/cm^2	20	14.5	17	15.4	24	18.7
3×10^{13} ions/cm^2	19	15.4	16	18.8	15	30.3

Please cite this article as: S. Sharma, et al., Influence of 100MeV Au+8 ion on photovoltaic response of BiFeO3/BaTiO3 multilayer structures, Materials and Design (2016), http://dx.doi.org/10.1016/j.matdes.2016.11.011

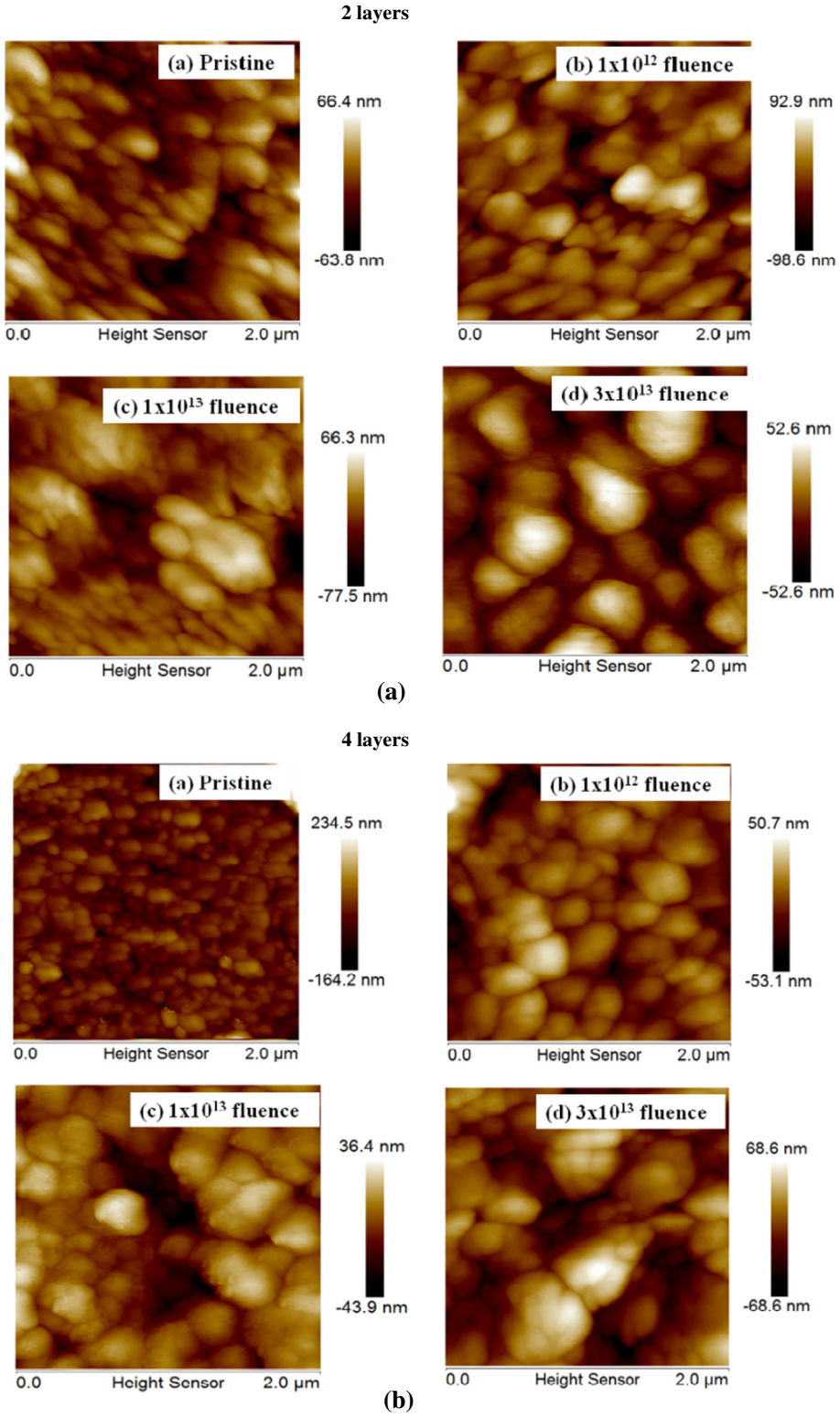


Fig. 2. Surface morphology of pristine and irradiated (a) 2 layers, (b) 4 layers and (c) 6 layers BFO/BTO structures.

shown in Fig. 5 (a), (b) and (c) respectively. All multilayer structures show well defined and saturated PE hysteresis loops without ion irradiation. It can be seen that, all the BFO/BTO multilayer samples exhibit stable P–E loops at low ion fluence upto 1×10^{13} ions/cm^2, whereas, for higher fluence (3×10^{13} ions/cm^2), the leakage current increases. The polarization decreases with increase in ion fluence in all the multilayer structures (Fig. 5 (a) to (c)).

The degradation in hysteresis loops may be correlated with the formation of oxygen vacancies in the multilayer sample due to ion irradiation, resulting in enhanced conductivity. The increase in defects upon ion irradiation can be seen from the large value of rms roughness along with the onset of impurity phases (from XRD analysis) in the BFO/BTO multilayer structure. The 3×10^{13} ions/cm^2 irradiated samples exhibit negligible polarization and lossy PE hysteresis loops; or in other

Please cite this article as: S. Sharma, et al., Influence of 100MeV Au+8 ion on photovoltaic response of BiFeO3/BaTiO3 multilayer structures, Materials and Design (2016), http://dx.doi.org/10.1016/j.matdes.2016.11.011

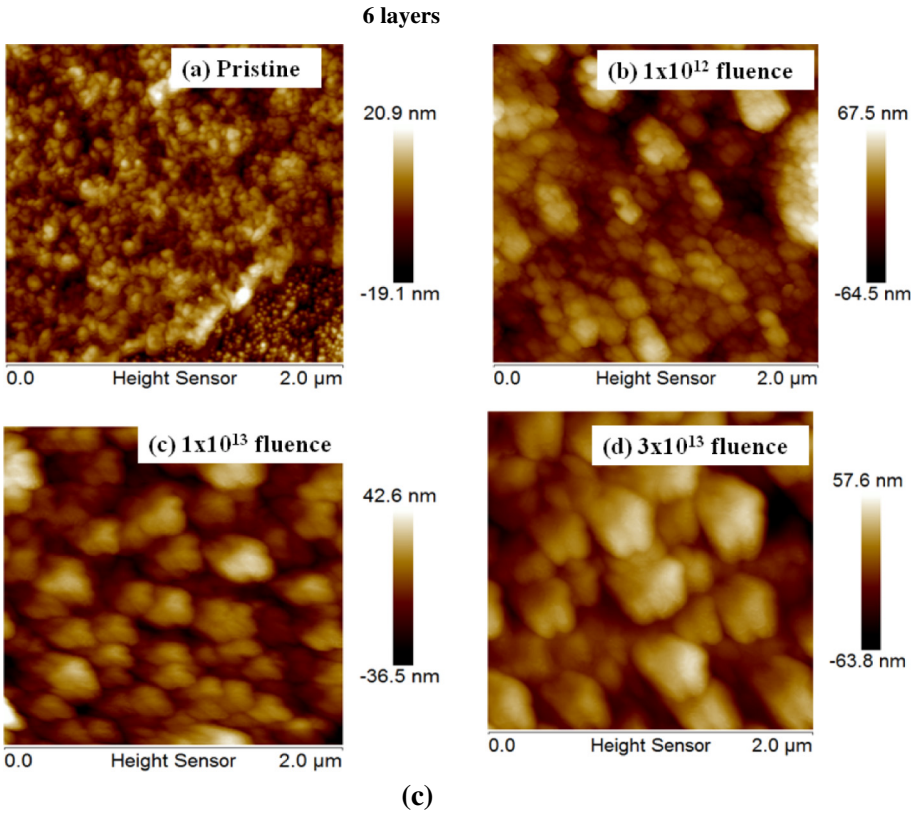


Fig. 2 (*continued*).

words, the ferroelectric property of a material is highly compromised (Fig. 5). For ion beam with high fluence, the passage of highly energetic ions for longer duration creates more defects in the multilayer sample, which increases the leakage current. Values of saturation polarization and remnant polarization for all the multilayer structures before and after irradiation are included in Table 8. The values of P_s obtained for irradiated BFO/BTO multilayer structures are comparatively lower than those reported for BFO films grown on highly conducting Pt/Ti/SiO_2/Si and other substrates [22–25]. A decrease in the value of saturation and remnant polarization has been observed for all multilayer samples upon ion irradiation with increasing fluence.

Hence, it may be inferred that the ion irradiation degrades the ferroelectric properties of the BFO/BTO multilayer structures and at fluence of the order of 3×10^{13} ions/cm^2, the multilayer structure completely loses its ferroelectric behavior. Furthermore, amongst all the multilayer structures prepared, the 6 layered BFO/BTO structure exhibits maximum polarization, which is least degraded even after ion irradiation, i.e. the ferroelectric properties of 6 layer structure are superior to 2 and 4 layered systems, both before and after irradiation (Table 8). Hence, for studying the ferroelectric photovoltaic response, 6 layered structures irradiated with SHI of 1×10^{12} and 1×10^{13} ions/cm^2 fluence have been used. The results are discussed in the subsequent sections.

3.5. Photovoltaic studies

The photovoltaic (PV) measurements of 6-layered BFO/BTO multilayer structures irradiated at 1×10^{12} and 1×10^{13} ions/cm^2 fluence were studied in MFM configuration with Au circular dots (200 μm diameter and 40 nm thin) as the top electrodes. Fig. 5 (a) represents the fluence dependent J-V plots of six layered BFO/BTO pristine structure and irradiated structures, measured at room temperature under dark conditions. Fig. 5 (b) shows the corresponding plots of J versus V under illumination conditions ($\lambda = 405$ nm). It can be noted that the dark current (J_{dark}) increases significantly from 6 nA/cm^2 to 1.12 μA/cm^2 even after irradiation. However, it may be seen from Fig. 5 (b), that both the irradiated samples show degraded photovoltaic response with low value of open circuit voltage and short circuit current.

Photovoltaic response characteristics of six-layered pristine and irradiated BFO/BTO structures at zero bias have been tabulated in Table 9. The dark current (J_{dark}) was found to increase significantly after irradiation and increases further with increase in fluence from 1×10^{12} to 1×10^{13} ions/cm^2 as shown in Fig. 5 (a). The short circuit photocurrent density, J_{sc}, was found to decrease with increase in fluence from 1×10^{12} to 1×10^{13} ions/cm^2 in the six layer BTO/BTO structure (Fig. 5 (b)). The value of open circuit photo voltage, V_{oc}, is also found to decrease from 0.41 V to 0.23 V with increasing fluence. The observed results indicate that after irradiation, ferroelectric-photovoltaic response of multilayer PV cell degraded. The decrease in FE-PV response with increase in fluence from 1×10^{12} to 1×10^{13} ions/cm^2 is in accordance with the ferroelectric PE hysteresis loops obtained in previous section for the six layer BFO/BTO structure (Fig. 4). It may be recalled that, simultaneous increase in dark current (J_{dark}) (Fig. 5 (a)) and decrease in photocurrent (J_{sc}) results in poor $J_{on/off}$ ratio (13.02) (Table 9) of the BFO/BTO irradiated samples as compared to pristine sample (2.955×10^3). It is important to point out that with increase in fluence up to 3×10^{13} ions/cm^2, ferroelectric loops (Fig. 4) become completely lossy and therefore no significant ferroelectric-photovoltaic response was obtained in the corresponding six layered BFO/BTO sample. Fig. 5 (c) shows the repeatability of experiments measuring photocurrent density for BFO/BTO six layer identical samples at different ion beam fluence. Sixteen identical samples (6 layers BFO/BTO thin film structure) were prepared for irradiation. Each batch constituted of 4 identical samples irradiated with same fluence. The photovoltaic response of each sample was studied to ensure repeatability of data. The variation in photocurrent density is found to be less than ±5% at each fluence.

Time-dependent variation of photocurrent density (J) for Au^{+8} irradiated BFO/BTO multilayer structures at 1×10^{12} and 1×10^{13} ions/cm^2 fluences with repeated exposure to light are shown in Fig. 6 (a). For

Please cite this article as: S. Sharma, et al., Influence of 100MeV Au+8 ion on photovoltaic response of BiFeO3/BaTiO3 multilayer structures, Materials and Design (2016), http://dx.doi.org/10.1016/j.matdes.2016.11.011

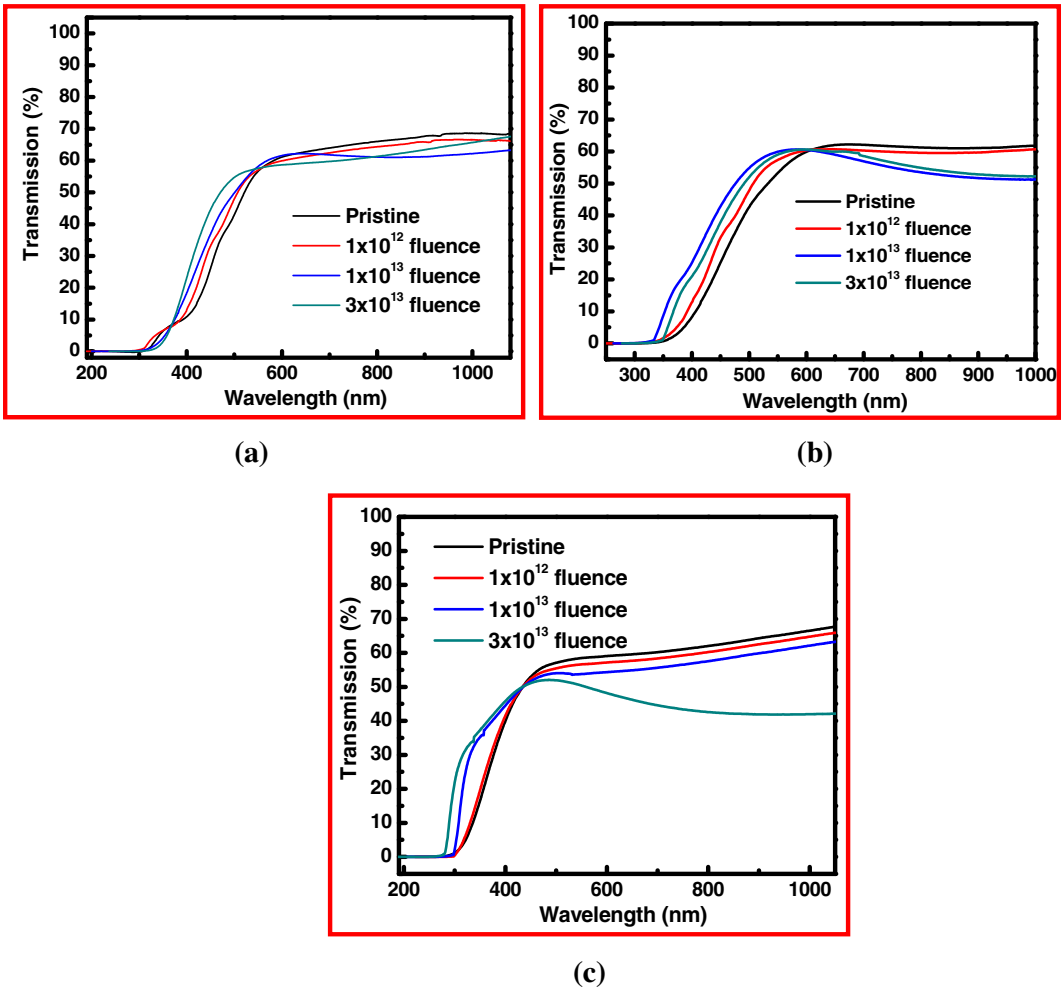


Fig. 3. Uv-visible transmittance spectra of pristine and irradiated (a) 2 layers (b) 4 layers and (c) 6 layers BFO/BTO multilayer structures.

Table 7
Values of % Transmission in the visible region (λ = 686 nm) and effect of ion fluencies on pristine and irradiated BFO/BTO multilayer structures.

Samples	% transmission (λ = 686 nm)		
	2 layers	4 layers	6 layers
Pristine	64	62	60
1×10^{12} ions/cm^2	62	60	58
1×10^{13} ions/cm^2	61	58	55
3×10^{13} ions/cm^2	59	57	45

comparison, time-dependent variation of photocurrent density (J) for pristine BFO/BTO six layer structure is shown in Fig. 6 (b). Both irradiated samples show increase in the photo current density under illumination of violet laser light (405 nm) of intensity 160 mWcm^{-2} on the sample surface with respect to the dark current (Fig. 6 (a)). But it can be seen clearly from Fig. 6 (a), that with increase in Au^{+8} ion fluence from 1×10^{12} to 1×10^{13} ions/cm^2 the photocurrent density decreases from 5.17 μA/cm^2 to 1.71 μA/cm^2, owing to the increased defects and degraded ferroelectric properties, as discussed earlier. Furthermore, the obtained photo-response is not well saturated under light illumination (Fig. 6 (a)) which is also related to the degraded ferroelectric properties of the BFO/BTO multilayer structure post ion irradiation.

The current study is dedicated towards the establishment of BFO/BTO multilayer structure as a renewable source of energy in space where normal detectors are vulnerable to exposure of energetic ions. The present report is also a holistic study of Ferroelectric Photovoltaic sensors and transducers when subjected to adverse conditions (fusion/fission reactors). Most important aspect of the present work is the sustenance of Photovoltaic properties of the prepared multilayer structures post ion beam irradiation. The obtained response in irradiated structures is superior to those reported by other workers for bare thin film Photovoltaic sensors [26–27]. Thus, the present work is

Table 8
Values of saturation polarization (P_s) and remnant polarization (P_r) for different layered BFO/BTO structure after ion irradiation with various fluence.

Samples	2 layers		4 layers		6 layers	
	Ps (μC/cm^2)	2Pr (μC/cm^2)	Ps (μC/cm^2)	2Pr (μC/cm^2)	Ps (μC/cm^2)	2Pr (μC/cm^2)
Pristine	23.77	19.33	47.50	40.56	95.85	108.12
1×10^{12} ions/cm^2	10.06	9.66	25.54	13.62	57.93	24.72
1×10^{13} ions/cm^2	3.91	2.41	13.23	4.38	29.55	20.13
3×10^{13} ions/cm^2	–	–	–	–	–	–

Please cite this article as: S. Sharma, et al., Influence of 100MeV Au+8 ion on photovoltaic response of BiFeO3/BaTiO3 multilayer structures, Materials and Design (2016), http://dx.doi.org/10.1016/j.matdes.2016.11.011

Table 9
Photovoltaic response characteristics of irradiated BFO/BTO six layered structures at varying fluence at zero bias.

Fluence (ions/cm^2)	J_{dark} (μA/cm^2) (at 2 V)	J_{sc} (μA/cm^2)	V_{oc} (V)	I_{on}/I_{off}
Pristine	0.006	17.73	1.806	2.955×10^3
1×10^{12}	0.75	5.17	0.41	33.02
1×10^{13}	1.12	1.71	0.23	13.02

encouraging for the application of BFO/BTO multilayer Photovoltaic sensors in areas susceptible to energetic radiations.

4. Conclusions

Significant modifications in the morphological and ferroelectric properties of BFO/BTO (two, four and six layers) multilayer structures due to induced structural defects were observed after SHI irradiation performed using 100 MeV Au^{+8} ion with ion fluence of ~1×10^{12}, 1×10^{13} and 3×10^{13} ions/cm^2. XRD studies confirm a continuous decrease in crystallite size with increase in fluence from 1×10^{12} to 3×10^{13} ions/cm^2 for all prepared BFO/BTO multilayer structures. Microstructural investigations using AFM, shows formation of agglomerated globular grain morphology in BFO/BTO structures after irradiation. Depending on ion fluences and number of layers in multilayer structures, defects are created and fragmentation and agglomeration effect is observed which results in decrease in grain size and increase in surface roughness.

All multilayer BFO/BTO structures after irradiation exhibit degradation in ferroelectric behavior with increase in ion fluence and at a fluence of 3×10^{13} ions/cm^2, ferroelectricity diminished, giving completely lossy P–E loops. Further, ferroelectric-photovoltaic effect have been studied in six layered BFO/BTO multilayer structure irradiated at different fluences. Ferroelectric photovoltaic response also degraded with increase in ion fluence from 1×10^{12} to 1×10^{13} ions/cm^2 with decrease in open circuit voltage from 0.41 V to 0.23 V, short circuit current density from 5.177 μA/cm^2 to 1.71 μA/cm^2 and I_{on}/I_{off} ratio from 33.02 to 13.02. This irradiation of BFO/BTO multilayer PV cell degraded the PV response due to overall poor ferroelectric property in comparison to the pristine multilayer sample. The study of the effect of SHI irradiation on multilayer ferroelectric photovoltaic cell is important to understand the possibility of application of photovoltaic cell in regions susceptible to high radiation. Hence, it is essentially required to study the effect of SHI irradiation on multilayered BFO/BTO structure for photovoltaic applications. Further, irradiation studies on similar multilayer structures and PV devices will help in engineering the properties of pervoskite materials for other device applications.

Acknowledgments

The authors are thankful to the pelletron group of IUAC, New Delhi for providing good quality scanned beam during irradiation. Authors are also thankful to Nanoscale Research Facility (NRF) for providing AFM facility at Indian Institute of Technology (IIT), New Delhi. The authors wish to thank the University of Delhi for financial support along with providing XRD facility and one of the authors (SS) is thankful to Delhi Technological University (DTU) for teaching assistantship.

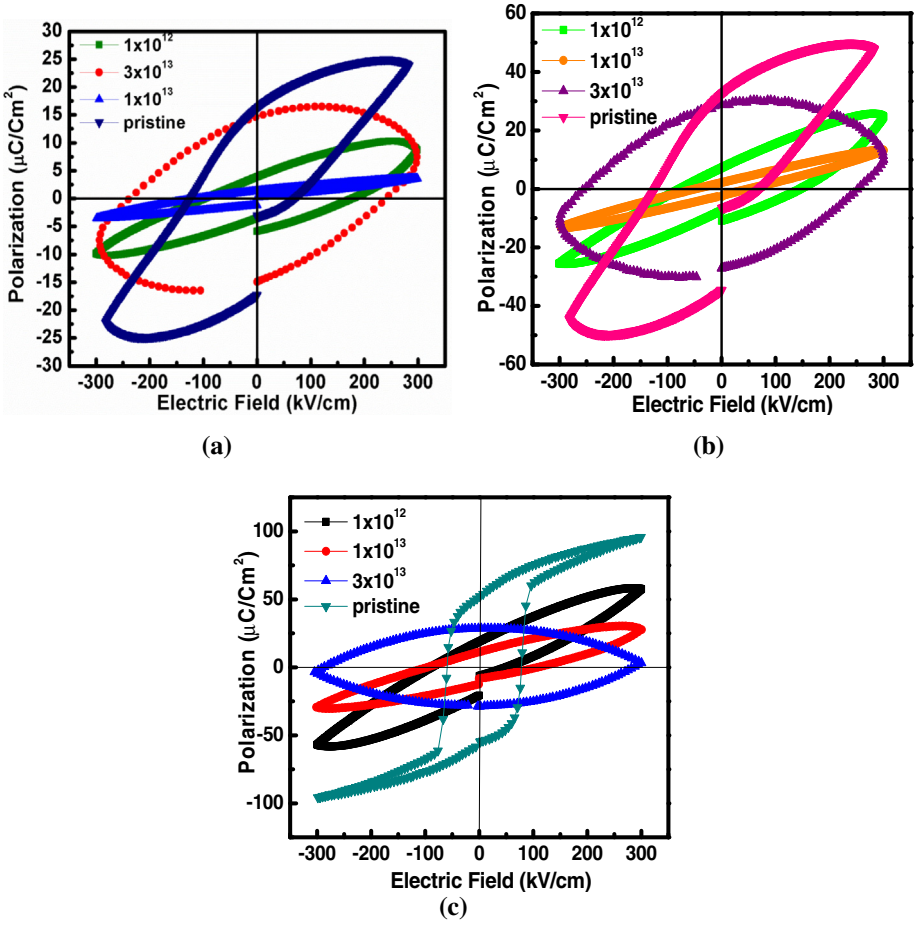
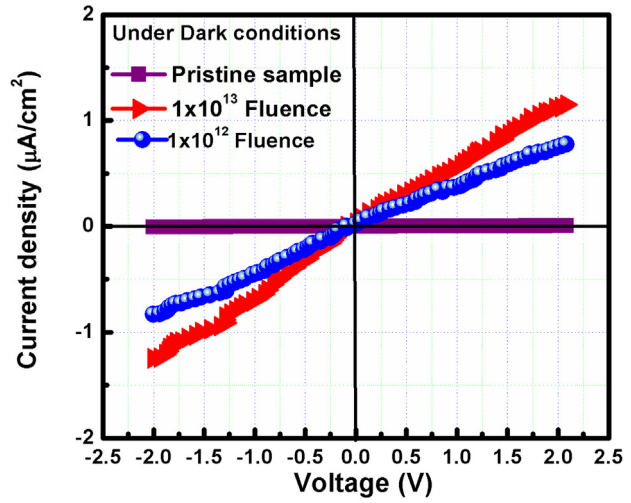
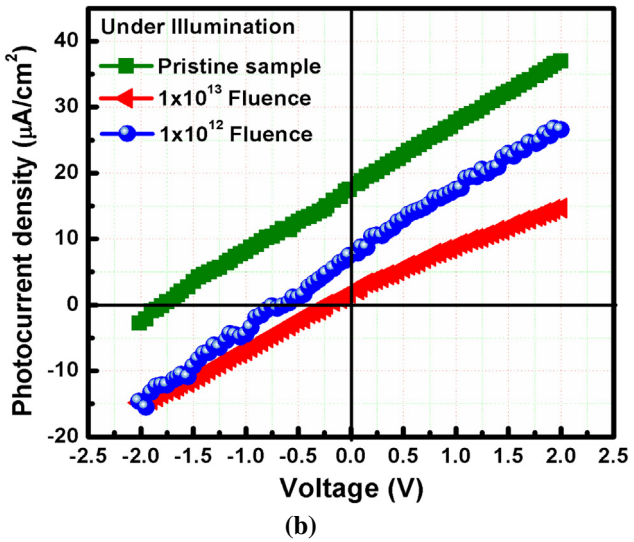


Fig. 4. P–E hysteresis loop of pristine and irradiated (a) 2 layers, (b) 4 layers and (c) 6 layers BFO/BTO structures.

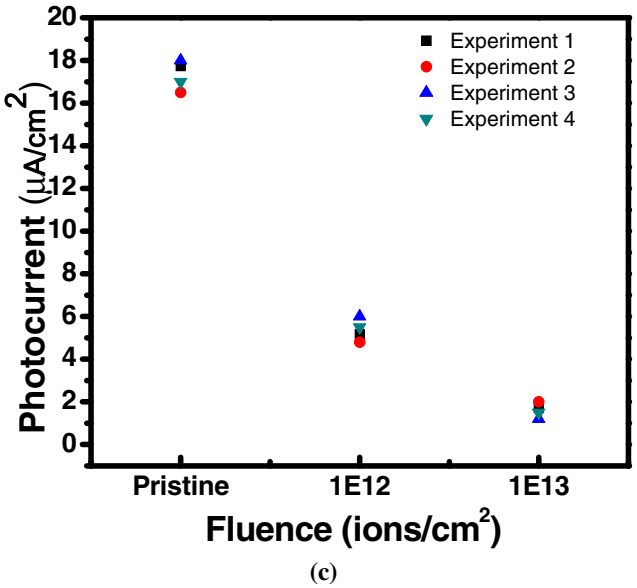
Please cite this article as: S. Sharma, et al., Influence of 100MeV Au+8 ion on photovoltaic response of BiFeO3/BaTiO3 multilayer structures, Materials and Design (2016), http://dx.doi.org/10.1016/j.matdes.2016.11.011



(a)

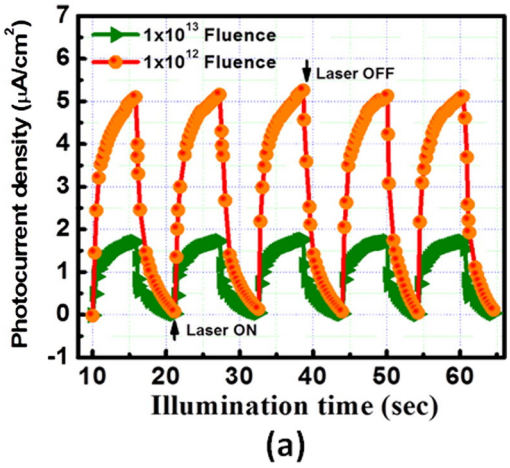


(b)

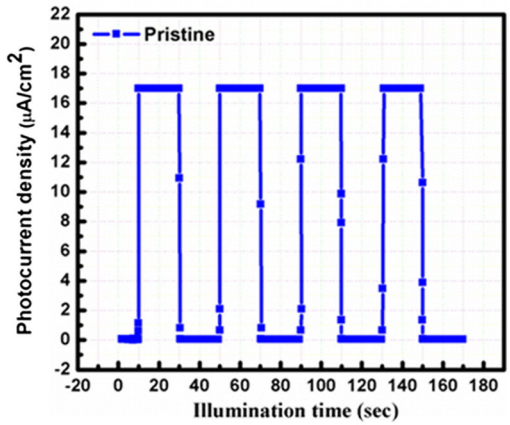


(c)

Fig. 5. J-V curves obtained for the BFO/BTO six layer structure irradiated with different fluences (a) under dark conditions, and (b) under light illumination (λ = 405 nm and intensity = 160 mW/cm^2) showing short circuit photocurrent density and open circuit photo voltage. (c) Repeatability of the experiments measuring photocurrent density for BFO/BTO six layer identical samples at different ion beam fluence.



(a)



(b)

Fig. 6. Transient response curves of short circuit photocurrent density of six layered BFO/BTO structure (a) irradiated at different fluencies (b) without irradiation when laser beam is switched on and off at regular intervals of 20 s.

References

[1] A. M. Vredenberg, A. Polman, P. A. Stolk, E. Snolesand, L. M. Brongersma, Proceedings of 11th International Conference on Ion Beam Modification of Materials Amsterdam, North Holland, Amsterdam, (1998).
[2] S. Klaumuenzer, N. Stolterfoht, Proceedings of the International Conference on Swift Heavy Ions in Matter, North Holland, Berlin, (May 1998).
[3] D. K. Avasthi, D. Kanjilal, Proceedings of the International Conference on Swift Heavy Ions in Materials Engineering and Characterization, New Delhi, North Holland, Amsterdam (October 1998).
[4] D. Kanjilal, Swift heavy ion-induced modification and track formation in materials, Curr. Sci. 80 (2001) 12.
[5] P. Mohanty, V.P. Singh, N.C. Mishra, S. Ojha, D. Kanjilal, C. Rath, Evolution of structural and magnetic properties of Co-doped TiO_2 thin films irradiated with 100 MeV Ag7+ ions, J. Phys. D Appl. Phys. 47 (2014) 315001.
[6] S. Ghosh, S.A. Khan, V. Ganesan, S. Kundu, R. Bhattacharya, Study of 200 MeV Ag^{15+} ion induced amorphisation in nickel ferrite thin films, Nucl. Inst. Methods Phys. Res. B 244 (2006) 34–39.
[7] S.R. Shinde, A. Bhagwat, S.I. Patil, S.B. Ogale, G.K. Mehta, M.K. Singh, R.S. Katiyar, Phonon anomalies near the magnetic phase transitions in $BiFeO_3$ thin films with rhombohedral R_{3c} symmetry, J. Appl. Phys. 109 (2011) 07D916.
[8] F. Studer, A. Meftah, F. Brisard, J.M. Costantini, M. Hage-Ali, J.P. Stoquert, M. Toulemonde, Swift heavy ions in magnetic insulators: a damage-cross-section velocity effect, Phys. Rev. B 48 (1993) 920.
[9] S. Kumar, R.S. Chauhan, S.A. Khan, W. Bolse, D.K. Avasthi, Nucl. Instrum. Methods Phys. Res., Sect. B 244 (2006) 194–197.
[10] R. Kumar, S.K. Sharma, A. Dogra, V.V. Siva Kumar, S.N. Dolia, A. Gupta, M. Knobel, M. Singh, Magnetic study of nanocrystalline ferrites and the effect of swift heavy ion irradiation, Hyperfine Interact. 160 (2005) 143–156.
[11] R.N. Parmar, J.H. Markna, D.G. Kuberkar, R. Kumar, D.S. Rana, C. Bagve, S.K. Vivas, Swift-heavy-ion-irradiation-induced enhancement in electrical conductivity of chemical solution deposited $La_{0.7}Ba_{0.3}MnO_3$ thin films, Appl. Phys. Lett. 89 (2006) 1–3, 202506.
[12] S.B. Ogale, K. Ghosh, G.Y. Gu, G.K. Mehta, Influence of 90 MeV oxygen ion induced disorder on the magnetotransport in epitaxial $La_{0.7}Ca_{0.3}MnO_3$ thin films, J. Appl. Phys. 84 (11) (1998) 6255–6261.

Please cite this article as: S. Sharma, et al., Influence of 100MeV Au+8 ion on photovoltaic response of BiFeO3/BaTiO3 multilayer structures, Materials and Design (2016), http://dx.doi.org/10.1016/j.matdes.2016.11.011

ARTICLE IN PRESS

[13] J.Y. Lee, S.F. Ahmed, M.H. Park, S.k. Ha, J.K. Park, J.H. Yun, S.J. Ahn, K.R. Lee, W.J. Choi, M.W. Moon, C.W. Yang, Self-assembled Cu(In,Ga)Se_2 nanocrystals formed by Ar ion beam irradiation, Sol. Energy Mater. Sol. Cells 105 (2012) 119–124.
[14] R. Sathyamoorthy, S. Chandramohan, P. Sudhagar, D. Kanjilal, D. Kabiraj, K. Asokan, K.P. Vijayakumar, Effect of 80 MeV oxygen ion beam irradiation on the properties of CdTe thin films, J. Mater. Sci. 42 (2007) 6982–6988.
[15] B.L. Belevtsev, V.B. Krasovitsky, V.V. Bobkov, D.G. Naugle, K.D.D. Rathnayaka, A. Parasiris, Influence of high-energy electron irradiation on the transport properties of $La_{1-x}Ca_xMnO_3$ films ($x \approx 1/3$), Eur. Phys. J. B 15 (2000) 461–468.
[16] J.H. Markna, R.N. Parmar, D.G. Kuberkar, R. Kumar, D.S. Rana, S.K. Malik, Thickness dependent swift heavy ion irradiation effects on electronic transport of $La_{0.5}Pr_{0.2}Ba_0MnO_3$ thin films, Appl. Phys. Lett. 88 (2006) 1–3, 152503.
[17] S. Sharma, M. Tomar, A. Kumar, N.K. Puri, V. Gupta, Energy Harvesting and Systems, 2016, http://dx.doi.org/10.1515/ehs-2016-0001.
[18] F. Ziegler, J.P. Biersack, M.D. Ziegler, Program SRIM, 2008.
[19] M. Toulemonde, Swift heavy ions in magnetic insulators: a damage-cross-section velocity effect swift heavy ions in magnetic insulators: a damage-cross-section velocity effect, Phys. Rev. B 48 (1993) 920.
[20] G. Catalan, J.F. Scott, Physics and applications of bismuth ferrite, Adv. Mater. 21 (2009) 2463.
[21] B.D. Cullity, S.R. Stock, Elements of X-ray Diffraction, Prentice Hall, Inc., New Jersey, 2001.
[22] J.M. Park, G. Fumiya, K. Takeshi, O. Masanori, Preparation and characterization of BiFeO3 thin films deposited on ITO substrates by using pulsed laser deposition, J. Korean Phys. Soc. 59 (2011) 2537–2541.
[23] W. Dong, Y. Guo, G. Bing, L. Hongyan, H. Li, L. Hezhou, Enhanced photovoltaic properties in polycrystalline $BiFeO_3$ thin films with rhombohedral perovskite structure deposited on fluorine doped tin oxide substrates, Mater. Lett. 88 (2012) 140–142.
[24] R. Guo, L. You, Y. Zhou, Z.S. Lim, X. Zou, L. Chen, R. Ramesh, J. Wang, Non-volatile memory based on the ferroelectric photovoltaic effect, Nat. Commun. 4 (2013) (1990), http://dx.doi.org/10.1038/ncomms2990.
[25] S. Gupta, M. Tomar, V. Gupta, Ferroelectric photovoltaic properties of Ce and Mn codoped $BiFeO_3$ thin film, J. Appl. Phys. 115 (2014) 014102.
[26] R.K. Katiyar, P. Misra, S. Sahoo, G. Morell, R.S. Katiyar, Enhanced photoresponse in $BiFeO_3/SrRuO_3$ heterostructure, J. Alloys Compd. 609 (2014) 168–172.
[27] R.K. Katiyar, A. Kumar, G. Morell, J.F. Scott, R.S. Katiyar, Photovoltaic effect in a wide-area semiconductor-ferroelectric device, Appl. Phys. Lett. 99 (2011) 092906.

Please cite this article as: S. Sharma, et al., Influence of 100MeV Au+8 ion on photovoltaic response of BiFeO3/BaTiO3 multilayer structures, Materials and Design (2016), http://dx.doi.org/10.1016/j.matdes.2016.11.011

View publication stats

Optical Materials 66 (2017) 142–148

Contents lists available at ScienceDirect

Optical Materials

journal homepage: www.elsevier.com/locate/optmat

Influence of growth temperature on laser molecular beam epitaxy and properties of GaN layers grown on c-plane sapphire

Ripudaman Dixit [a, c], Prashant Tyagi [a, b], Sunil Singh Kushvaha [a], Sreekumar Chockalingam [a], Brajesh Singh Yadav [d], Nita Dilawar Sharma [a], M. Senthil Kumar [a, *]

[a] CSIR- National Physical Laboratory, Dr. K.S. Krishnan Road, New Delhi, 110012, India
[b] Academy of Scientific and Innovative Research (AcSIR), CSIR-NPL Campus, Dr. K.S. Krishnan Road, New Delhi, 110012, India
[c] Department of Applied Physics, Delhi Technological University, Delhi, 110042, India
[d] Solid State Physics Laboratory, Timarpur, Lucknow Road, Delhi, 110054, India

ARTICLE INFO

Article history:
Received 26 August 2016
Received in revised form
20 January 2017
Accepted 31 January 2017

Keywords:
Gallium nitride
Heteroepitaxy
X-ray diffraction
Raman spectroscopy
Photoluminescence
Nanoindentation

ABSTRACT

We have investigated the influence of growth temperature on the in-plane strain, structural, optical and mechanical properties of heteroepitaxially grown GaN layers on sapphire (0001) substrate by laser molecular beam epitaxy (LMBE) technique in the temperature range 500–700 °C. The GaN epitaxial layers are found to have a large in-plane compressive stress of about 1 GPa for low growth temperatures but the strain drastically reduced in the layer grown at 700 °C. The nature of the in-plane strain has been analyzed using high resolution x-ray diffraction, atomic force microscopy (AFM), Raman spectroscopy and photoluminescence (PL) measurements. From AFM, a change in GaN growth mode from grain to island is observed at the high growth temperature above 600 °C. A blue shift of 20–30 meV in near band edge PL emission line has been noticed for the GaN layers containing the large in-plane strain. These observations indicate that the in-plane strain in the GaN layers is dominated by a biaxial strain. Using nanoindentation, it is found that the indentation hardness and Young's modulus of the GaN layers increases with increasing growth temperature. The results disclose the critical role of growth mode in determining the in-plane strain and mechanical properties of the GaN layers grown by LMBE technique.
© 2017 Elsevier B.V. All rights reserved.

1. Introduction

In the last two decades, group III-nitride materials have derived keen research interests and been highly successful in proving their cutting-edge applications in optoelectronics and high power, high frequency electronics due to its wide direct bandgap, high mobility and high breakdown field [1–5]. The performance of group III-nitride devices highly depends on crystal quality and strain of epitaxial layers that are building the device structure. Due to the difficulty in achieving bulk GaN growth, III-nitride layers are normally grown hetero-epitaxially on foreign substrates that lead to generation of a high density of crystalline defects and high strain in the grown epitaxial layers. The crystalline defects play a key role in determining the efficiency of devices, and there are numerous reports related to the studies of quantitative analysis of defect concentrations [6–8]. Thus, the minimization of defects and growth of high quality epitaxial layers are required to promote the production of reliable and high performance devices. The conventional techniques for GaN growth are metal organic chemical vapor deposition (MOCVD), hydride vapor phase epitaxy (HVPE), and plasma assisted molecular beam epitaxy (PAMBE). Laser molecular beam epitaxy (LMBE) is a relatively new and least explored technique for III-nitride growth. But, LMBE has an advantage over other conventional techniques that the growth of GaN films can occur at low temperatures due to the high kinetic energy of film precursors produced by laser ablation [9–11]. Low temperature growth process is critical to further improve GaN epilayer quality by employing thermally vulnerable but closely lattice-matched substrates like ZnO, $LiGa_2O_3$, etc. and also to develop high quality In-rich III-nitride materials.

III-nitrides are grown hetero-epitaxially on different substrates like sapphire, silicon, silicon carbide, etc. But, due to the fact that

* Corresponding author.
E-mail address: senthilmk@nplindia.org (M.S. Kumar).

http://dx.doi.org/10.1016/j.optmat.2017.01.053
0925-3467/© 2017 Elsevier B.V. All rights reserved.

sapphire has a good epitaxial symmetry, high thermal stability, affordable cost and its availability in large wafers, most of the GaN devices are fabricated on sapphire. However, sapphire has a large lattice constant and thermal expansion coefficient mismatch with GaN. Consequently, the grown GaN epitaxial layers are characterized for a high level of in-plane strain and structural defects like dislocations, stacking faults, etc. In general, nitridation of sapphire substrate is carried out before GaN growth as pre-nitridation helps in formation of an intermediate AlN layer for the growth of high quality GaN layers [12,13]. In addition, growth temperature plays a key role in determining the properties of GaN epitaxial layers [14,15]. The reports on LMBE growth of GaN on sapphire substrates are very limited in literature, and the effect of LMBE growth parameters on the physical properties of grown GaN layers is not well understood yet. Particularly, there is no data reported on the mechanical properties of LMBE grown GaN layers using nanoindentation. Considering the advantages of LMBE growth technique in developing III-nitride materials, it is vital to systematically study the effect of experimental parameters on the GaN layer properties. Especially, the in-plane strain in GaN/sapphire lattice mismatched structure determines the characteristics of the grown epilayers and heterostructures [16]. In this paper, we report on the growth temperature dependant in-plane strain, structural, optical and mechanical properties of GaN layers on sapphire (0001) grown by the laser ablation of a HVPE grown GaN solid target using LMBE technique. The properties of GaN layers are found to improve with increasing growth temperature and good quality GaN epitaxial layers have been obtained by growing them above 600 °C.

2. Experimental details

The growth of epitaxial GaN layers were carried out on pre-nitridated sapphire (0001) substrate in a LMBE system equipped with *in-situ* reflection high energy electron diffraction (RHEED), and a radio frequency (RF) nitrogen plasma source. The base pressure of growth chamber was 2×10^{-10} Torr. The low background pressure minimizes the presence of impurities or residual contaminations. The back side of sapphire substrate was coated with 1 μm thick molybdenum layer to increase the absorption of heat and uniform heat distribution. The substrates were cleaned by organic solvents and de-ionized water before loading into the load lock chamber. Prior to growth, the substrate was degassed for several hours at 250 °C in the load-lock chamber of the LMBE system followed by a thermal cleaning at 850 °C for 10 min in the UHV chamber. After thermal cleaning of sapphire substrate, nitridation process was performed at 700 °C with an RF plasma power of 400 W and nitrogen gas flow of 1.2 sccm for 35 min. A high pure HVPE grown GaN solid target (6 N) was ablated using a KrF excimer Laser (248-nm wavelength, 25 ns pulse) with an energy density of about 5 J/cm^2 and a laser frequency of 10 Hz. In the system, nitrogen radicals were supplied through RF nitrogen plasma cell for stochiometric GaN growth. The nitrogen gas flow and the r.f. power were tuned to 0.4 sccm and 250 W during GaN growth. GaN films were grown for a fixed duration of 2 h on nitridated sapphire substrate at various temperatures in the range 500–700 °C keeping all the other experimental parameters constant. The entire growth sequence was monitored through *in-situ* RHEED observations. From the thickness measurement of grown GaN layers, a growth rate of 120–140 nm/h is obtained in the growth temperature range employed in this study.

The irradiation of each KrF laser pulse with GaN target generates plasma plume due to strong absorption of laser energy by the GaN target. The plasma plume is generated continuously as per the designated laser frequency and expands towards the substrate for film deposition. The laser ablated plume contains GaN, GaN_{1-x}, and Ga species [17]. The nitrogen plasma constituents diffuse into the growth zone from the r.f. cell due to pressure gradient and contribute for the growth by supplying additional flux to maintain film stoichiometry. The epitaxial GaN layer growth is achieved by the reaction between the laser plume and the supplied nitrogen radicals on the sapphire substrate under a growth pressure of ~2×10^{-5} Torr [15].

The LMBE grown GaN epitaxial layers have been characterized for their structural properties by high resolution x-ray diffraction (HRXRD) and Raman scattering spectroscopy using a PANalytical HR-XRD system with Cu $K\alpha_1$ source and a triple monochromator spectrometer (T-64000, Jobin-Yvon/Horiba group) with an excitation source of 514.5 nm wavelength, respectively. A multimode-V Veeco atomic force microscopy (AFM) was used to image the surface morphology of the GaN layers while the photoluminescence (PL) characterization was performed using a 266 nm laser line at room temperature to examine their optical emission properties.

The nanoindentation measurements of GaN films deposited on sapphire substrates were performed by high resolution IBIS-nanoindenter (Fischer-Cripps Laboratories Pty. Limited, Australia) equipped with a diamond Berkovich indenter. All measurements were performed with a fixed load of 1 mN. In order to perform the nanoindentation measurements, the samples were mounted with the help of crystal bond wax on a metallic specimen holder with a magnetic base. Extreme care was taken to maintain parallelism while mounting the specimen to the sample holder. The entire system is left for four hours to attain thermal equilibrium before test to eliminate the error due to thermal drift. It is very important to use accurate dimensions of the indenter for the analysis of the results. For the Berkovich indenter, the radius of the tip can vary depending on the quality of the manufacture. To account for these variations in indenter geometry, an area function is applied to the result, which is a ratio expressed as a function of the plastic depth. For best results, a series of indentations were made on the sample and the average values used for the calculation of harness and Young's modulus.

3. Results and discussion

The *in-situ* RHEED showed an epitaxial growth of GaN over sapphire (0001) substrate with a 30° in-plane rotation with respect to the sapphire substrate. The patterns were spotty in all the growth runs exhibiting a three-dimensional growth of GaN layer, which indicated the N-rich flux condition at the growth surface. The ω-2θ XRD scans of the GaN epitaxial layers grown on pre-nitridated sapphire at various temperatures are presented in Fig. 1. The spectra show diffraction peaks only from {0001} family of crystal planes of wurzite GaN and sapphire indicating that single crystalline GaN layers are grown along c-axis. The intensity of GaN (0002) peak increased and the full width at half maximum (FWHM) of the GaN (0002) peak decreased significantly when the growth temperature was raised from 500 to 700 °C. The peak height and width generally depend on the thickness and the mosaic structure of the grown films. Considering the small variation of layer thickness among all samples, i.e. 240–280 nm, the change of XRD peak parameters can be largely related to the crystalline quality of the layers as confirmed by Raman and PL data as discussed below. The sharp and intense XRD peak observed for 700 °C implies that the higher growth temperature improves the crystalline property of the LMBE grown GaN layer. At higher growth temperatures, there is an increase in the kinetic energy of precursor atoms in addition to the laser power which further increases their surface mobility enabling the precursor atoms to find the proper lattice site to get incorporated into the growing layer. As a result, not only the crystalline quality but also the grain size of the GaN crystallites is

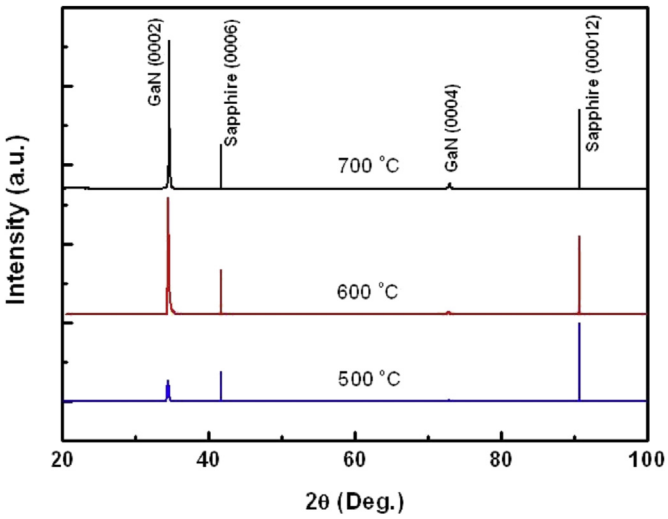


Fig. 1. HRXRD 2θ/ω scans of LMBE GaN layers grown on sapphire (0001) at various temperatures.

improved. Further, the (0002) XRD peaks of GaN layers grown at 500 and 600 °C exhibit a shift towards lower angle, in comparison with stress free bulk GaN implying the presence of a compressive strain. The stress present in the LMBE GaN layers has also been estimated from the HR-XRD ω-2θ scans of (0002) and (10–12) planes of the samples. A typical ω-2θ scan of GaN (10–12) plane is given in Fig. 2. The lattice parameters 'c' and 'a' of the LMBE grown GaN layers were calculated by using the following equations [18]:

$$d_{hkil} = \frac{\lambda}{2Sin(\theta_{hkil} + \Delta\theta)} \tag{1}$$

$$d_{hkil} = \frac{1}{\sqrt{\frac{4}{3}\left(\frac{h^2+hk+k^2}{a^2}\right) + \left(\frac{l}{c}\right)^2}} \tag{2}$$

where, θ_{hkil} is the measured peak position of the (hkil) Bragg reflection, λ is the x-ray wavelength (0.15406 nm) and Δθ is the zero

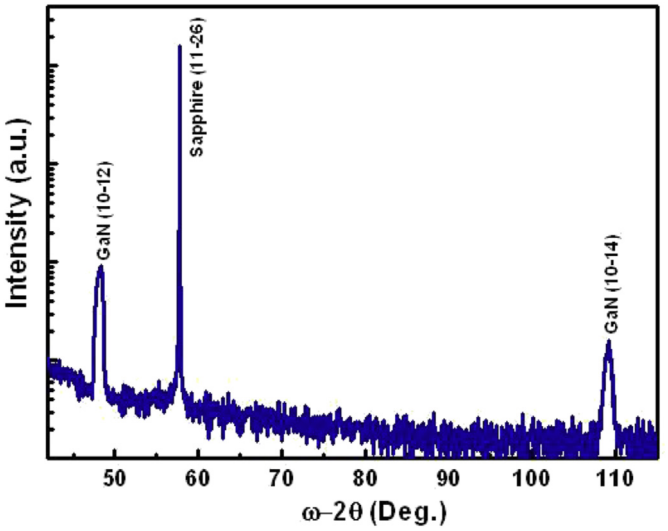


Fig. 2. Typical HRXRD 2θ/ω scan for {10–12} diffraction planes of LMBE GaN layer grown on sapphire (0001). The scan was performed through the centre of GaN (10–12) reflection.

error of the instrument used for HR-XRD measurements. The in-plain strain (ε) was calculated using the equation given below:

$$\varepsilon = \frac{a - a_0}{a_0} \tag{3}$$

where 'ε' is the strain and 'a' is the measured lattice constant. The lattice parameters of strain free GaN are taken as $a_0 = 0.31892$ nm and $c_0 = 0.51850$ nm [19]. The in-plane stress (σ) is obtained by using the following expression:

$$\sigma = \left(\frac{E}{1-\upsilon}\right)\varepsilon \tag{4}$$

where, $(E/1-\upsilon)$ is the biaxial modulus, E is the Young's modulus and υ is the Poisson's ratio. The Young's modulus values of LMBE GaN layers are taken from our nanoindentation measurements (Table 2). The Poisson's ratio value of 0.183 for GaN epilayer grown on sapphire substrate is used for the calculation [20]. The calculated strain and stress values of GaN layers grown at various temperatures are given in Table 1. The obtained strain values indicate the presence of in-plane compressive stress of >1 GPa in the LMBE GaN layers on sapphire grown at ≤ 600 °C and the strain decreased dramatically when the growth temperature was increased to 700 °C.

Room temperature micro-Raman spectroscopy of the GaN epitaxial layers was measured in the back-scattering geometry in order to examine their in-plane stress and structural quality. The Raman spectra of GaN layers grown at different temperatures can be seen in Fig. 3(a). In the backscattering geometry, E_2 (high) and A_1 (LO) are the only active Raman modes in wurtzite GaN (0001) epitaxial layers. The E_g Raman modes of sapphire substrate are also observed in the spectra around 577 and 750 cm^{-1}. The peak intensity and FWHM of E_2 (high) mode can reveal the structural quality of the grown GaN layer. The shift in peak position of E_2 Raman mode is used to further evaluate the in-plane stress present in the layers as the E_2 mode is shifted by stress only [21]. The peak position, magnitude and FWHM of GaN E_2 (high) mode were deduced by deconvolution of experimental data using Lorenztian fitting [Fig. 3(b)]. Here, we observed both E_2 (high) and A_1 (LO) modes in all samples confirming the wurtzite phase GaN grown along the c-axis. The peak intensity of E_2 (high) mode enhanced and the FWHM value decreased considerably when the GaN growth temperature was raised from 500 to 700 °C. The data analysis of E_2 (high) Raman mode is given in Table 1. It indicates that the crystalline quality of the GaN layer improves with increasing growth temperature, which complements the XRD analysis. Additionally, A_1 (TO) Raman mode with a weak intensity appeared in the spectra of GaN layers grown at 500 and 600 °C with a similar intensity ratio of E_2 (high) to A_1 (TO) mode. The A_1 (TO) mode is forbidden in Raman measurement under backscattering geometry of wurtzite GaN (0001) layer but appears in the spectra due to the granular nature of GaN films grown on sapphire as obtained by the AFM imaging, which will be discussed later [22]. The in-plane compressive stress (σ) present in the LMBE GaN epitaxial layers were calculated using the below formula and are presented in Table 1.

$$\sigma = \frac{\Delta\omega}{4.3}\ GPa \tag{5}$$

where, Δω is the Raman shift of E_2 (high) mode [23]. The E_2 (high) peak position for stress-free GaN standard (50–70 μm thick GaN layer grown on sapphire) is taken to be 567.6 cm^{-1} [21,24,25]. An in-plane compressive stress of 0.91–0.95 GPa is obtained in the GaN layers grown at lower temperatures and the layer grown at

Table 1
Structural and optical properties of LMBE GaN epitaxial layers grown on c-plane sapphire at various temperatures.

Growth Temp. (°C)	XRD Analysis		E_2 Mode Raman Analysis			NBE PL Analysis	
	Strain (%)	Stress (GPa)	Peak shift (cm^{-1})	FWHM (cm^{-1})	Stress (GPa)	Peak Position (eV)	FWHM (meV)
500	0.38	1.77 ± 0.52	4.1	8.87	0.95 ± 0.14	3.42	121
600	0.38	1.87 ± 0.55	3.9	6.41	0.91 ± 0.14	3.43	69
700	0.06	0.44 ± 0.20	0.9	6.2	0.21 ± 0.14	3.41	62

Table 2
Mechanical properties of LMBE GaN epitaxial layers grown at various temperatures as studied by nanoindentation measurements.

Growth temperature (°C)	Hardness (GPa)	Young's modulus (GPa)	Degree of elastic recovery (%)
500	19.6	371	46
600	24.3	392	47
700	26.1	477	54

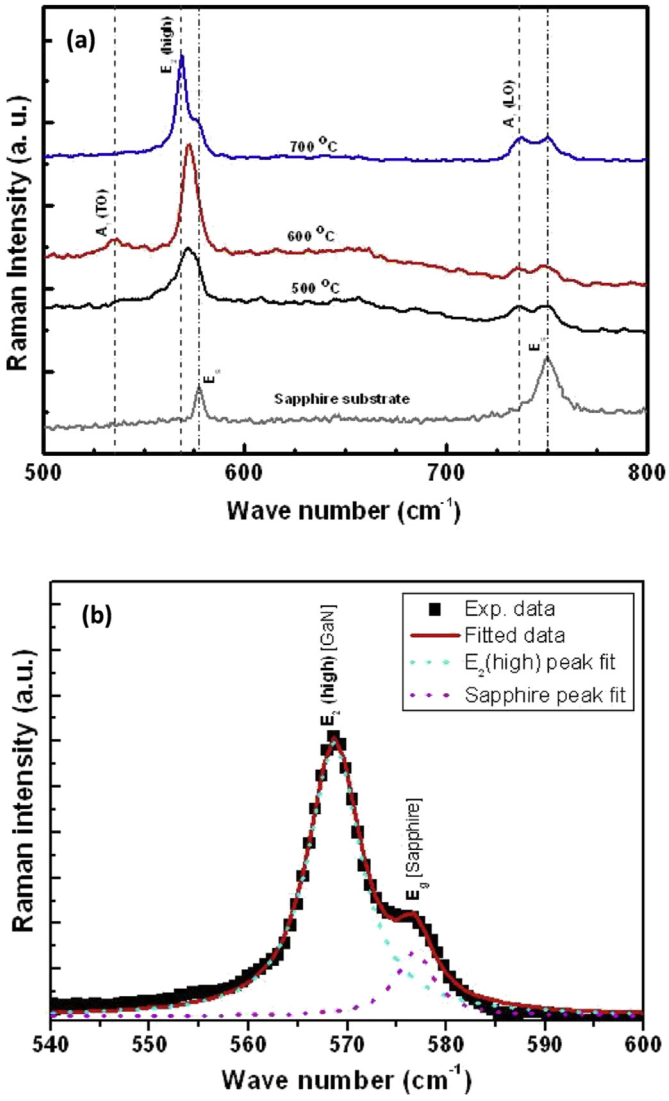


Fig. 3. (a) Room temperature Raman spectra of LMBE GaN layers grown on sapphire (0001) at various temperatures. (b) Typical fitted Raman spectrum for E_2 (high) mode of GaN layer.

700 °C is found to have a stress value of 0.21 GPa. In comparison, the in-plane stress value calculated from XRD analysis is slightly higher that could arise from the large Young's modulus value obtained for LMBE GaN layers, as discussed in the nanoindentation section.

The AFM was conducted in tapping mode on all the samples grown at different temperatures and their surface morphologies are given in Fig. 4. The GaN layers grown at lower temperatures such as 500 and 600 °C revealed a growth of high density fine grains in nanometer scale (60–80 nm) with the surface roughness (rms) values of 8.2 and 4.2 nm, respectively. On the other hand, the layer grown at 700 °C has a flat, smooth surface with large islands of size in the range 250–350 nm as seen in Fig. 4(c). The growth of island mode can be attributed to the enhanced surface mobility of adatoms at the higher growth temperature, as discussed in the XRD section. The AFM image also shows a presence of surface pits that are the remnant of coalescence process of GaN islands. For this case, the rms surface roughness is obtained to be 6.5 nm, mainly due to the surface pits.

In heteroepitaxially grown GaN layers, the in-plane strain is found to have superposition of a biaxial stress and a hydrostatic stress [22]. The biaxial stress occurs due to thermal and lattice related mismatch between GaN and foreign substrate. The biaxial stress can also be caused by growth stress due to island coalescence, grain growth or surface stress. On the other hand, the internal hydrostatic stress is introduced by the presence of various kinds of point defects. Based on the size of the point defects, the related stress could be either compressive or tensile, which makes the stress analysis more complex. The hydrostatic strain is found to mostly depend on the buffer layer stoichiometry and doping [26]. In MOCVD grown GaN on sapphire (0001), Cho et al. have found that the highest temperature growth is most effective in reducing the hydrostatic stress and the in-plane strain is contributed mainly by biaxial strain [27]. In the current study, we observed a drastic decrease of the in-plane residual strain and stress for the layer grown at the higher temperature of 700 °C as seen in Table 1. It can be understood that the growth temperature alters the growth mode of GaN from grain growth to island growth when raised above 600 °C, which can contribute to the reduction of biaxial strain.

Room temperature PL spectroscopy was performed to examine the optical properties of the LMBE GaN layers grown on various temperatures and the respective spectra are presented in Fig. 5(a). We have observed a very strong near band edge (NBE) emission in the range 3.41–3.43 eV for all samples which is mainly due to the band-to-band transition and a negligible yellow luminescence (YL) peak at about 2.2 eV, which has contributions from the intrinsic defect states. The weak YL band emission implies the reduction of crystalline defects responsible for the deep level defect states. The FWHM of NBE peak decreased significantly from 121 to 62 meV

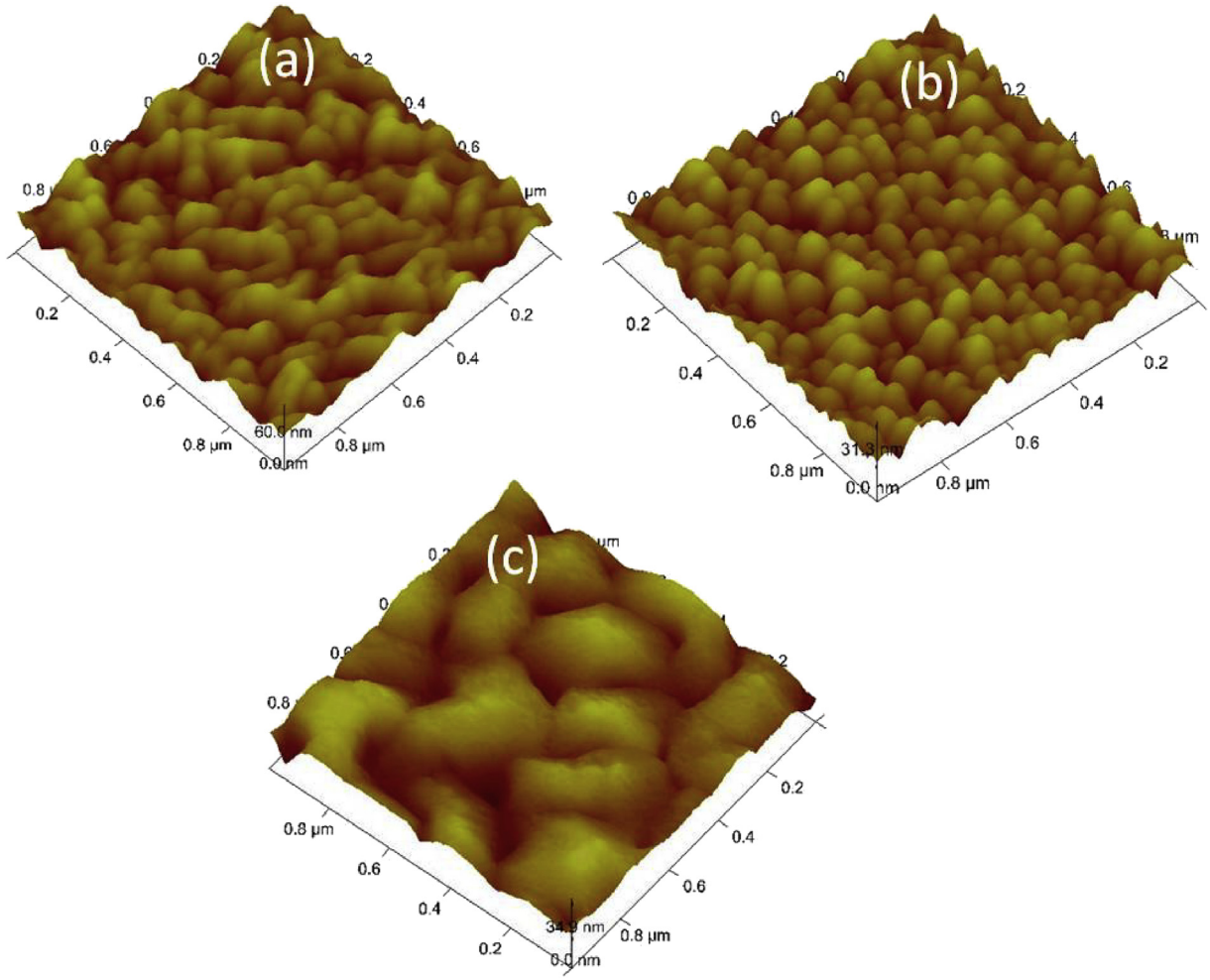


Fig. 4. AFM surface morphology of LMBE GaN layers grown on sapphire (0001) at various growth temperatures: (a) 500, (b) 600, and (c) 700 °C. Scan area: 1 µm × 1 µm.

when the growth temperature was increased from 500 to 700 °C as shown in Fig. 5(b). Li et al. reported a very narrow PL width of 28 meV at room temperature for MOCVD grown GaN on c-sapphire using a low temperature GaN buffer layer [28]. The intensity of the NBE emission also enhanced drastically for the GaN layers grown at 700 °C. The PL parameters of LMBE grown GaN layers are detailed in Table 1. As mentioned, the PL optical properties of LMBE grown GaN layers show a strong, direct dependence on their structural quality.

It is noted that there is a blue shift in NBE peak position that could be a result of in-plane strain present in the LMBE GaN layer. Kisielowski et al. determined that one GPa of in-plane biaxial stress shifts the NBE line by ~27 meV and E_2 Raman mode by ~4.2 cm^{-1} [29]. In our case, a E_2 mode shift of 3.9–4.1 cm^{-1} and a NBE shift of 20–30 meV are observed in the GaN layers grown at 500 and 600 °C having a similar stress of 0.9 GPa. For the 700 °C grown layer, a E_2 mode shift of 0.9 cm^{-1} and a NBE shift of 10 meV are observed under about 0.2 GPa stress. Similarity of the data with Ref.29 indicates that the in-plane stress in LMBE GaN layer could come from the biaxial strain.

To assess the mechanical properties of GaN thin films, a set of nanomechanical tests was quantitatively conducted and the indentation values of hardness (H) and Young's modulus (E) were extracted from the load-displacement curve by using formulas from Olive Pharr model [30].

$$H = \frac{P_{max}}{A} \tag{6}$$

$$E = \frac{1}{2}\frac{\sqrt{\pi}}{\sqrt{A}} S \tag{7}$$

where, P_{max} is maximum load, A is the projected-contact area and S is the slope of unloading curve at maximum load. The measured load versus displacement (P-h) curves of GaN layers grown at different temperatures are shown in Fig. 6. The indentation load of 1 mN was chosen only to probe the top 10–15% thicknesses of the GaN layers in order to avoid any kind of influences from the substrate. The average indentation hardness values are calculated to be 19.6, 24.3 and 26.1 GPa for the GaN layers grown at 500, 600 and 700 °C, respectively. In literature, a range of GaN hardness values, i.e. 17–26 GPa for MOCVD grown GaN and 20–26 GPa for MBE grown GaN on c-sapphire substrates, has been reported using Berkovich indenter as employed in the current study [31,32]. Thus, the hardness values obtained for LMBE GaN lies in the higher side of the values reported for GaN grown by MOCVD and MBE techniques. It should be noted that the LMBE GaN layers are thin and formed just by coalescence of nanoscale islands while the GaN layers by other techniques are micron thick grown under layer-by-layer mode. The nanostructure materials are reported to exhibit higher hardness compared to their microstructure counterparts [33]. In

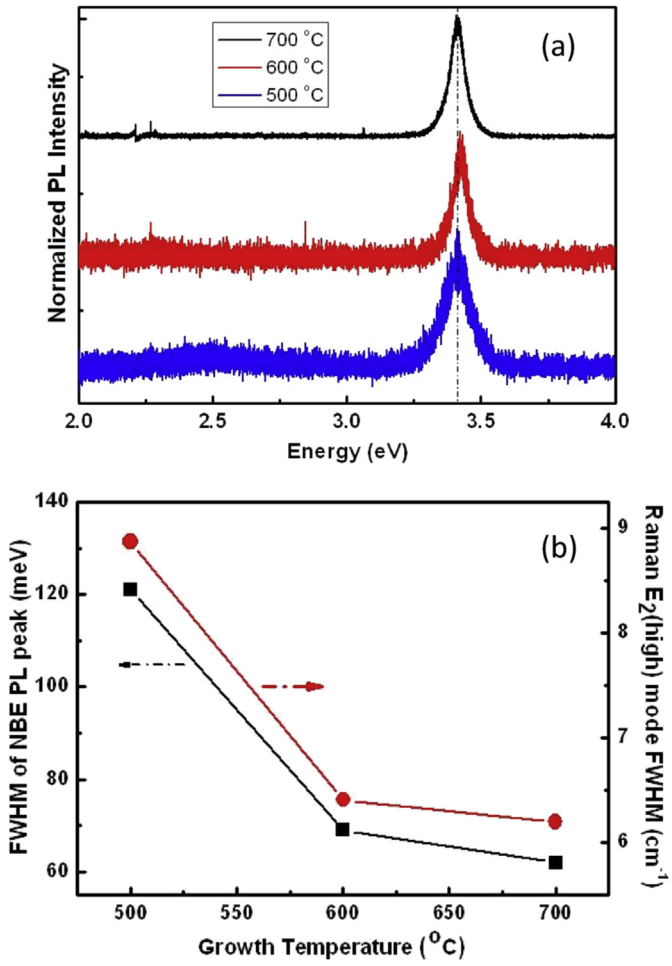


Fig. 5. (a) Room temperature PL spectra of LMBE GaN epitaxial layers grown at various temperatures. (b) FWHM of NBE PL Peak and E_2 (High) Raman mode of GaN epitaxial layers as a function of growth temperature.

addition, we observed discontinuities in the nanoindentation loading curve, which is a reflection of the process of plastic deformation in the material. This phenomenon is commonly known as "pop-in" events associated with hexagonal materials due to nucleation of slip bands or interaction of indentation induced deformed region with pre-existing threading dislocations in GaN epitaxial layers [34,35]. The GaN layers grown at < 700 °C exhibit more than one "pop-in" events in the P-h curve. Also, the initial "pop-in" events are observed at a much smaller threshold load and the penetration depth because the sharp tip of pyramidal (Berkovich) indenter results much higher stress even for smaller loads compared to spherical indenter [31].

The Young's modulus is an important material property which represents the amount of deformation under an external applied force. The greater the value of E under an external applied force the smaller the plastic deformation of the material. The indentation Young's modulus of LMBE grown GaN layers at different temperatures is listed in Table 2. It is clearly evident that the Young's modulus increases from 377 to 471 GPa with increasing growth temperature of GaN layers. The better mechanical property, i.e. increase of harness and Young's modulus, for the GaN layer at 700 °C could be associated with the improved microstructure due to change in growth mode from granular to island growth as discussed before. The island mode growth improves the crystalline quality of the GaN epitaxial layers by reducing the area of defective

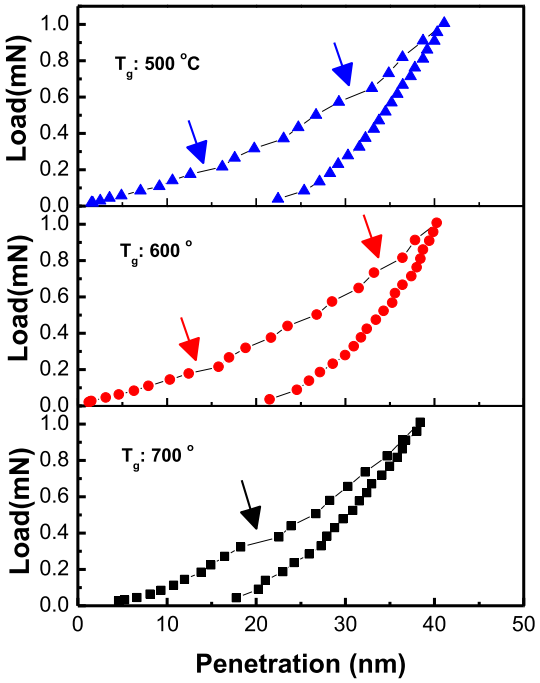


Fig. 6. Load-penetration (P-h) curves of LMBE GaN epitaxial layers grown at varous temperature.

coalescence regions containing dislocations [15]. The Young's modulus reported for GaN grown on c-sapphire by MOCVD and MBE techniques widely varies in the range 250–412 GPa [32]. This large variation is understood based on the layer thickness, growth technique, crystalline property, load applied, etc. However, it should be mentioned that the Young's modulus obtained for LMBE grown GaN layers on c-sapphire is higher than the reported values of MOCVD and MBE grown layers.

It is noticed that the broader nature of the hysteresis between the loading and unloading curves decreases with increasing growth temperature from 500 to 700 °C, indicating that the high temperature growth results an improved elastic recovery. The degree of elastic energy recovery is calculated from the P-h curves using the following equation.

$$\Delta e = \frac{h_{max} - h_{res}}{h_{max}} \times 100\% \quad (8)$$

where h_{max} is the penetration at maximum load and h_{res} is the penetration after unloading. The elastic recovery of GaN layers increased from 46 to 54% with increasing growth temperature from 500 to 700 °C indicating an enhanced elastic nature of high temperature grown GaN layer under island growth mode. Thus, our results clearly indicate that the growth mode of GaN is very crucial in determining the in-built strain and mechanical properties of GaN layers grown by LMBE technique.

4. Conclusion

The in-plane strain in GaN epitaxial layers grown by LMBE technique has been analyzed as a function of growth temperature in the range 500–700 °C, using HRXRD, Raman spectroscopy and PL measurements. It is found that the growth mode of GaN strongly influences the in-plane strain in LMBE GaN layers. The grain growth of GaN at lower temperatures introduces a large in-plane stress about 1 GPa in the layer and the stress value drastically reduced in

the GaN layer grown under island mode at the highest temperature. A strong band-to-band PL emission is obtained with negligible YL band for the GaN layers and the strain induced blue shift of NBE peak is observed in the GaN layers. The mechanical strength also significantly improved for the high temperature grown GaN layer. The obtained results hint that the in-plane strain in LMBE grown GaN layers are predominantly biaxial. This study suggests that the effect of growth temperature should be considered in stain engineering of GaN layers during LMBE growth.

Acknowledgements

The authors would like to thank Dr. K.K. Maurya for the help in x-ray diffraction measurements. The financial support from Council of Scientific and Industrial Research (CSIR) through network project PSC-0109 for carrying out this work is gratefully acknowledged. Mr. Prashant Tyagi is thankful to CSIR for the junior research fellowship (JRF) award.

References

[1] S. Nakamura, G. Fasol, The Blue Laser Diode, Springer, Berlin, 1997.
[2] K.M. Song, J.M. Kim, B.K. Kang, D.H. Yoon, S. Kang, S.W. Lee, S.N. Lee, Characteristics of indium incorporation in InGaN/GaN multiple quantum wells grown on a-plane and c-plane GaN, Appl. Phys. Lett. 100 (2012) 212103.
[3] X.A. Cao, A.A. Syed, H. Piao, Investigation of the electronic properties of nitrogen vacancies in AlGaN, J. Appl. Phys. 105 (2009) 063707.
[4] L. Lewis, B. Corbett, D.O. Mahony, P.P. Maaskant, Low-resistance Ni-based Schottky diodes on freestanding n-GaN, Appl. Phys. Lett. 91 (2007) 162103.
[5] X.G. He, D.G. Zhao, D.S. Jiang, J.J. Zhu, P. Chen, Z.S. Liu, L.C. Le, J. Yang, X.J. Li, J.P. Liu, L.Q. Zhang, H. Yang, GaN high electron mobility transistors with AlInN back barriers, J. Alloy. Compd. 662 (2016) 16–19.
[6] J. Hong, Local magnetic moment induced by Ga vacancy defect in GaN, J. Appl. Phys. 103 (2008) 063907.
[7] S.L. Rhode, W.Y. Fu, M.A. Moram, F.C.-P. Massabuau, M.J. Kappers, C. McAleese, F. Oehler, C.J. Humphreys, R.O. Dusane, S.L. Sahonta, Structure and strain relaxation effects of defects in $In_x Ga_{1-x} N$ epilayers, J. Appl. Phys. 116 (2014) 103513.
[8] A. Uedono, T. Fujishima, D. Piedra, N. Yoshihara, S. Ishibashi, M. Sumiya, O. Laboutin, W. Johnson, T. Palacios, Annealing behaviors of vacancy-type defects near interfaces between metal contacts and GaN probed using a monoenergetic positron beam, Appl. Phys. Lett. 105 (2014) 052108.
[9] A. Kobayashi, J. Ohta, Y. Kawaguchi, H. Fujioka, Room temperature epitaxial growth of AlGaN on ZnO by pulsed laser deposition, Appl. Phys. Lett. 89 (2006) 111918.
[10] A. Kobayashi, S. Kawano, Y. Kawaguchi, Room temperature epitaxial growth of m-plane GaN on lattice-matched ZnO substrates, Appl. Phys. Lett. 90 (2007) 041908.
[11] M.H. Kim, M. Oshima, H. Kinoshita, Y. Shirakura, K. Miyamura, J. Ohta, A. Kobayashi, H. Fujioka, Investigation of the initial stage of GaN epitaxial growth on 6H-SiC (0001) at room temperature, Appl. Phys. Lett. 89 (2006) 031916.
[12] N. Grandjean, J. Massies, M. Leroux, Nitridation of sapphire: effect on the optical properties of GaN epitaxial overlayers, Appl. Phys. Lett. 69 (1996) 2071–2073.
[13] A. Heinlein, J. Grepstad, T. Berge, H. Riechert, Preconditioning of c-plane sapphire for GaN epitaxy by radio frequency plasma nitridation, Appl. Phys. Lett. 71 (1997) 341–343.
[14] M. Senthil Kumar, S.S. Kushvaha, K.K. Maurya, Low temperature growth of GaN epitaxial layers on sapphire (0001) by pulsed laser deposition using liquid gallium target, Sci. Adv. Mater. 6 (2014) 1215–1220.
[15] S.S. Kushvaha, M. Senthil Kumar, K.K. Maurya, M.K. Dalai, N.D. Sharma, Highly c-axis oriented growth of GaN film on sapphire (0001) by laser molecular beam epitaxy using HVPE grown GaN bulk target, AIP Adv. 3 (2013) 092109.
[16] F. Jabli, M.A. Zaidi, M. Gassoumi, H. Mosbahi, M. Charfeddine, T. Alharbi, H. Maaref, Optical analysis of biaxial stress distribution in Al0.26Ga0.74N/GaN/Si HEMT's, J. Alloy. Compd. 650 (2015) 533–536.
[17] R.D. Vispute, V. Talyanksy, R.P. Sharma, S. Choopum, M. Downes, T. Venkatesan, K.A. Jones, A.A. Iliadis, M. Asif Khan, J.W. Yang, Growth of epitaxial GaN films by pulsed laser deposition, Appl. Phys. Lett. 71 (1997) 102–104.
[18] X.H. Zheng, Y.T. Wang, Z.H. Feng, H. Yang, H. Chen, J.M. Zhou, J.W. Liang, Method for measurement of lattice parameter of cubic GaN layers on GaAs (0 0 1), J. Cryst. Growth 250 (2003) 345–348.
[19] W. Shan, R.J. Hauenstein, A.J. Fischer, J.J. Song, W.G. Perry, M.D. Bremser, R.F. Davis, B. Goldenberg, Strain effects on excitonic transitions in GaN: deformation potentials, Phys. Rev. B 54 (1996) 13460–13463.
[20] M.A. Moram, Z.H. Barber, C.J. Humphreys, Accurate experimental determination of the Poisson's ratio of GaN using high-resolution x-ray diffraction, J. Appl. Phys. 102 (2007), 023505 (1-4).
[21] S.S. Kushvaha, M. Senthil Kumar, B.S. Yadav, P.K. Tyagi, S. Ojha, K.K. Maurya, B.P. Singh, Influence of laser repetition rate on the structural and optical properties of GaN layers grown on sapphire (0001) by laser molecular beam epitaxy, CrystEngComm 18 (2016) 744–753.
[22] X. Liu, D. Li, X. Sun, Z. Li, H. Song, H. Jaing, Y. Chen, Stress-induced in situ epitaxial lateral overgrowth of high-quality GaN, Cryst. Eng. Comm. 16 (2014) 8058–8063.
[23] S. Tripathy, S.J. Chua, P. Chen, Z.L. Miao, Micro-Raman investigation of strain in GaN and AlxGa1-xN/GaN heterostructures grown on Si (111), J. Appl. Phys. 92 (2002) 3503–3510.
[24] T. Jiang, S. Xu, J. Zhang, P. Li, J. Huang, Z. Ren, M. Fu, J. Zhu, H. Shan, Y. Zhao, Y. Hao, Spatial distribution of crystalline quality in N-type GaN grown on patterned sapphire substrate, Opt. Mater. Exp. 6 (2016) 1817–1826.
[25] V.Yu Davydov, Yu E. Kitaev, I.N. Goncharuk, A.N. Smirnov, J. Graul, O. Semchinova, D. Uffman, M.B. Smirnov, A.P. Mirgorodsky, R.A. Evarestov, Phonon dispersion and raman scattering in hexagonal GaN and AlN, Phys. Rev. B 58 (1998) 12899–12907.
[26] V.S. Harutyunyan, A.P. Aivazyan, E.R. Weber, Y. Kim, Y. Park, S.G. Subramanya, High-resolution x-ray diffraction strain-stress analysis of GaN/sapphire heterostructures, J. Phys. D. Appl. Phys. 34 (2001) A35–A39.
[27] S.I. Cho, K. Chang, M.S. Kwon, Growth temperature dependence of strain in GaN, grown on c-plane sapphire substrate, J. Mater. Sci. 43 (2008) 406–408.
[28] G. Li, S.J. Chua, S.J. Xu, W. Wang, P. Li, B. Beaumont, P. Gibart, Nature and elimination of yellow-band luminescence and donor-acceptor emission of undoped GaN, Appl. Phys. Lett. 74 (1999) 2821–2823.
[29] A. Kisielowski, J. Kruger, S. Ruvimov, T. Suski, J.W. Ager III, E. Jones, Z. Liliental-Weber, M. Rubin, E.R. Weber, Strain-related phenomena in GaN thin films, Phys. Rev. B 54 (1996) 17745–17753.
[30] W.C. Oliver, G.M. Pharr, An improved technique for determining hardness and elastic modulus using load and displacement sensing indentation experiments, J. Mater. Res. 7 (1992) 1564–1583.
[31] C.-H. Tsai, S.-R. Jian, J.-Y. Juang, Berkovich nanoindentation and deformation mechanisms in GaN thin films, Appl. Surf. Sci. 254 (2008) 1997–2002.
[32] M. Rais-Zadeh, V.J. Gokhale, A. Ansari, M. Faucher, D. Theron, Y. Cordier, L. Buchaillot, Gallium nitride as an electromechanical material, J. Microelectromechanical Syst. 23 (2014) 1252–1271.
[33] Timothy J. Trentler, R. Suryanarayanan Iyer, Shankar M.L. Sastry, William E. Buhro, Preparation of nanocrystalline molybdenum disilicide (MoSi2) by a chlorine-transfer reaction, Chem. Matter 11 (2001) 3962–3968.
[34] S.O. Kucheyev, J.E. Bradby, J.S. Williams, C. Jagadish, M.V. Swain, Mechanical deformation of single-crystal ZnO, Appl. Phys. Lett. 80 (2002) 956–958.
[35] R. Navamathavan, Y.-T. Moon, G.-S. Kim, T.G. Lee, J.-H. Hahn, S.-J. Park, 'Pop-in' phenomenon during nanoindentation in expitaxial GaN thin films on c-plane sapphire substrates', Mater. Chem. Phys. 99 (2006) 410–413.

International Conference on Advanced Material Technologies (ICAMT)-2016

27th and 28th December 2016

Dadi Institute of Engineering and Technology (DIET), Visakhapatnam, Andhra Pradesh, India.

Inscription Image Retrieval Using Bag of Visual Words

N.Jayanthi[1] and S.Indu[2]

1. Assistant Professor, ECE Department, Delhi Technological University, Delhi-110042, India

2. Professor, ECE Department, Delhi Technological University, Delhi-110042, India

Abstract: This paper presents a technique for efficient and veracious retrieval of ancient inscriptions and manuscripts from a large database of images by using the Bag of Visual Words (BoVW) technique. The proposed method can be used to recognize inscription images across the world. SURF (speeded up robust features) is used as an image feature extractor. A visual vocabulary is created by representing the image as a histogram of visual words which helps in the retrieval process. Usage of SURF ensures scalability, faster processing better results with darkened and blurred images. We demonstrate the method on a combination of 300 inscriptions images comprising of several inscription around the world.

Keywords: BoVW, Inscriptions, SURF.

1. INTRODUCTION

Since ancient times inscriptions have been used as a medium of storing and passing the information from one generation to the next. These inscriptions give us an insight into their worlds and carry answers to many of our questions. For ages we have tried to decipher their meanings and determine their origins but with the increasing amount of data and constant digitization of the world it is only natural that this treasure of knowledge is archived as well. Once the inscription images are archived we move to the next step which is the retrieval process. With a database having innumerable images it is necessary to ensure that – i) we have the fastest possible retrieval solution. ii) The retrieval technique is language independent considering the inscriptions from various cultures are inscribed in separate languages. iii) It should be able to perceive images that have undergone damages such as blurring and darkening over time (more resilient to noise).

Different methods have been suggested for efficient retrieval, word spotting is popular for recovering the relevant images without recognition. Various word spotting techniques have been used, such as the Dynamic Time Warping (DTW) algorithm [3], Hidden Markov Model (HMM) [2] etc. DTW compares a series of feature vector for image retrieval, though successful in many cases it has a drawback when it comes to large databases, having a computation time of 1 second for comparing two word images hence it loses its practicality. In [5] Zagoris et al. define a segmentation based word spotting technique using document specific local features that was tested on two historical datasets. In [1] Rajakumar and Bharathi suggest a contour let transform to recognize Tamil characters from stone inscriptions. Sankar and Mamantha [4] have suggested automatic word annotation for document retrieval where the digital image is assigned with a metadata by the system automatically.

The Bag of Visual Words has come across as one of the most efficient techniques for document image retrieval [6], [7], [8], [9], [10]. Augereau et al. [6] talk of combining visual and textural features for document classification and retrieval using BoW and BoVW. Shekhar and Jawahar [13] use the BoVW for image retrieval using SIFT as the feature vector. Aldavert et al. [11] work on the George Washington data set for keyword spotting using BoVW. In [13] it has been observed that SIFT

descriptor is not very robust for all possible image degradations and hence it calls out for the need of a more robust descriptor. Nabeel et al. [12] have summarized the performance of SIFT and SURF on several datasets showing SURF to be outperforming SIFT in case of blurred images and darkened images. SIFT though known to work well with images from different datasets is replaced by SURF here which has proved to be more efficient when it comes to the highly blurred inscription images.

With the inscriptions dating back to medieval times the effect of blurring tends to become very prominent in the inscribed texts or pictorial representations. The biggest problem that then arises is how to retrieve them accurately in the shortest time span possible. To overcome this issue we have come up with an image retrieval procedure that employs the bag of visual words (BoVW) technique using the SURF (Speeded Up Robust Feature) descriptor. SURF has been known to perform exceptionally well with the shortest execution time and hence we have replaced the originally used SIFT (Scale Invariant Feature Transform) with the former technique. SURF works well with blurred and darkened images. The BoVWs technique ensures that the correct output is obtained with its help. The major advantage of our methodology is that its works well with images that have undergone degradation of different forms like darkening or blurring over time and its language independence. Inscriptions from all over the world belonging to separate timelines in any language can be retrieved using this technique making it highly robust.

2. METHODOLOGY

2.1 Bag of Visual Words:

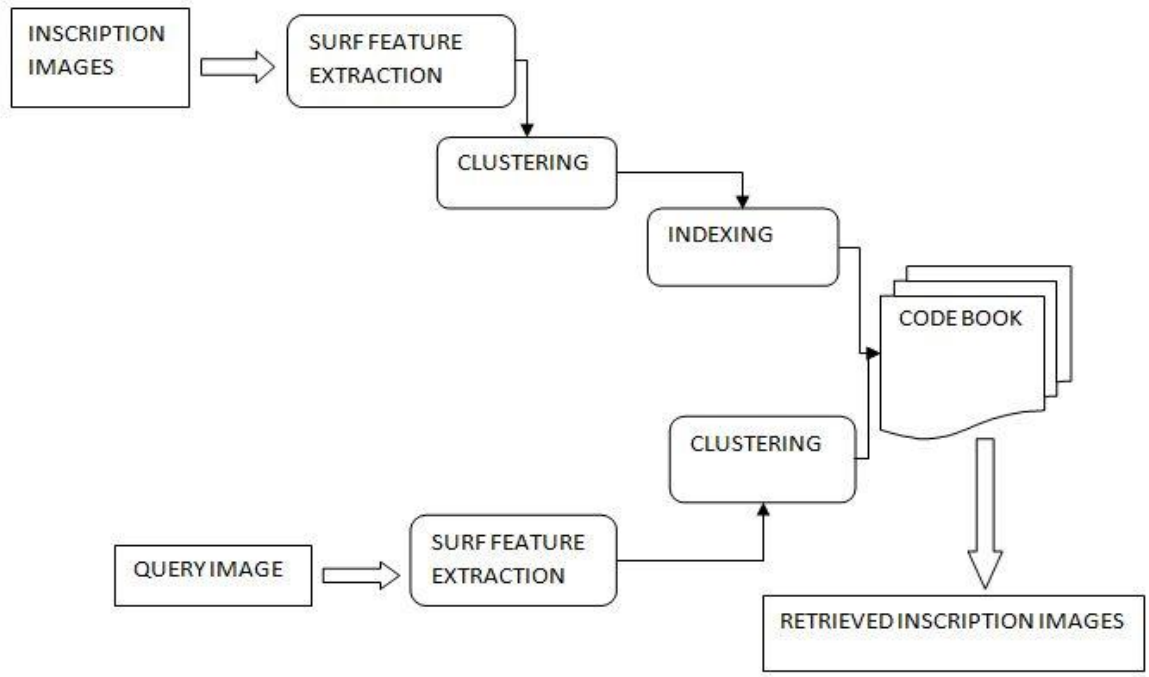


Fig 1: Proposed Image Retrieval system

The bag of visual words technique has evolved from the bag of words technique where we move from document classification in BOWs to image classification in BOVWs. The Bag of Words technique is used for document classification where the documents are represented based on the frequency of word occurrence. The document is considered as a stream of words where punctuation marks and blank spaces are ignored. A vocabulary is created and its size reduced by removing words that occur too often (as they might not hold much significance) or words that occur too less say once or twice. After

filtering the vocabulary to the desired size we proceed further by indexing the documents. The desired document is retrieved from the indexed vocabulary using their histogram (frequency of word occurrence) by comparing the query image with the indexed files. Similar to the BoWs we use the Bag of Visual Words (BoVWs) technique for image classification. Here instead of text words we use visual words to build our vocabulary. An image of an inscription can be represented as a set of non distinctive discrete visual features, where the visual features corresponds to the vocabulary, and the image is defined as a histogram of visual word occurrence.

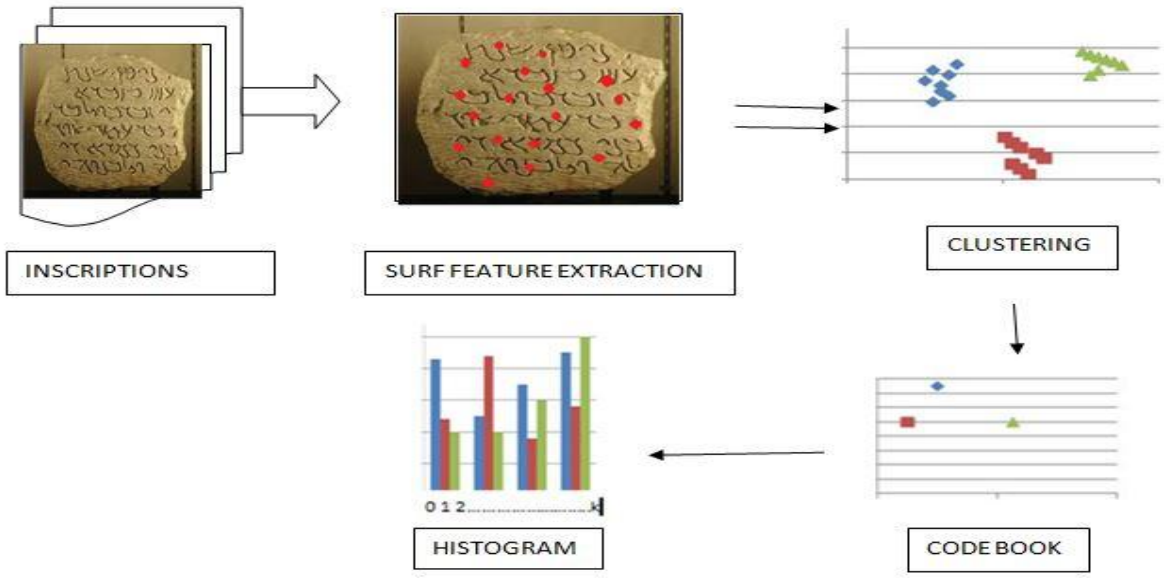


Fig 2 :Code book generation using BOVW

We set off by defining the interest points (either corners or blobs) and then determining the features of those interest points. We have used SURF (speeded up robust features) as our key feature detector. SURF uses an integer approximation of the determinant of Hessian blob detector to find its interest points. After extracting the features we segment those using K mean clustering. This is done to get distinct clusters and then eventually to derive a code book where each cluster is represented by its centroid.

***2.2** K-mean Clustering:*

The k mean clustering is an unsupervised learning algorithm which forms k clusters form M observations. It is a cyclic process where the cluster centroids keep on rearranging their location until they reach a point beyond which they remain in a fixed positions and the clustering process ends. First k centroids are defined and each point of the data set is grouped into clusters based on the nearest centroids. Once this is done we recalculate k new centroids as barycentre of previous clusters and the points are regrouped according to the new centroids. This process is repeated to get k fixed centroids. And these are then used in the codebook generation process. Once the clustering is done the extracted features are given labels of the closest centroid and thus the SURF features are quantized. Figure2. Depicts how from a database of inscription images each image is taken and its SURF extracted followed by generation of a codebook and histogram computation of the quantized SURF features.

***2.3** SURF (speeded up robust features):*

SURF was first introduced by Herbert Bay et al. [12] as a feature detector and descriptor that is both scale and rotation invariant. The SURF algorithm makes use of the Hessian matrix which acts by defining interest points. The Hessian matrix uses the Difference of Gaussian (DoG) which is a basic laplacian based descriptor. The SURF works in four steps, first the Hessian matrix is used to determine interest points, then the major interest point in scale space are found, next feature direction is taken into

account as it should be rotation invariant and finally the feature vectors are generated. Haar transforms are used to assess the direction of the features.

2.4 *Inverted File Indexing:*

Inverted file indexing is introduced as it has proven to enhance the systems efficiency by several orders. The images can be presented as a catalogue of characteristics or attributes. The indexed file then behaves as a sorted list of these attributes and each attribute has a link to the image comprising it. Hence whenever an attribute is recalled all the images from the catalogue comprising of it will be retrieved. The retrieval process as depicted in figure 1 starts with inputting the query image. From our entire collection of images if we want to retrieve an inscription image we need to input a query image which will be used to compare and extract the correct output image. The initial processing on the query image is similar to those on the inscription image from the database. First the SURF features of the query are extracted. Once this is done we cluster them using the k means algorithm. From the vocabulary the closest cluster to the derived cluster of the query image is located and assigned to it. This is represented in the codebook and from the indexed files all the images that are assigned to the given cluster are brought forward of which the best match is retrieved.

3. RESULT AND DISCUSSIONS

In this section we show the result of the inscription retrieval process. Inscriptions written in several languages are taken to form the data set, where the dataset and test images are divided into three categories, namely English, Tamil and other languages. The other language includes inscription images belonging to different periods having different symbols and pictorial representations from all over the world. The results are calculated by finding the precision p, which can be defined as

$$P = \frac{true_positive}{true_positive + false_positive} \qquad (1)$$

Where true positive is means a hit and false positive a miss. Some of the query images taken from different languages have been shown in the figure 3.

3.1 *Performance Statistics:*

Table 1 depicts the precision performance of our algorithm where we have created a database of 72 images in English language, 56 in Tamil and 212 in other languages images in English, Tamil and others respectively. The precisions are as shown. Figure 3. depicts the output taken on several query images. Inscriptions in Tamil, English, symbolic inscriptions have been shown as an example of our methods robustness. Figure 4 shows the algorithm's scale invariant property where the system is able to detect an image from a query image that has been rotated by 90 degrees. Figure 5, 6 and 7 show how the blurring and darkening to a large extent does not affect our retrieval process.

Table I Precision Performance

LANGUAGE	NO. OF IMAGES	QUERY IMAGES	PRECISION
English	72	20	0.781
Tamil	56	15	0.752
Others	212	42	0.734

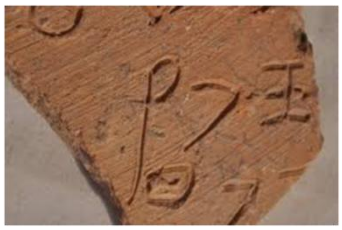
QUERY IMAGE	OUTPUT
	
	
	
	
	

Fig 3. Output for query inputs of Inscriptions

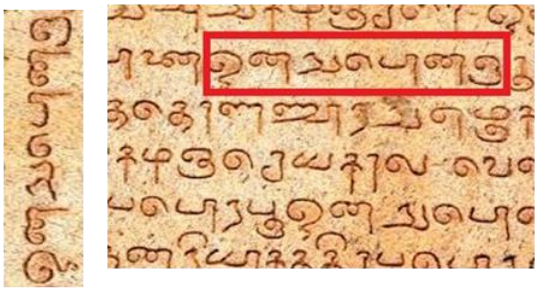


Fig 4. Scale invariant property



(a) (b)

Fig 5. (a) and (b) depict the results when the query image is blurred and the extent of blurring acceptable to give the correct output.



(a) (b)

Fig 6 (a)and(b) depict different degrees of blurring in the image to be retrieved



Query image	Original image	Darkened image

Fig7. Retrieval of a darkened image

4. CONCLUSION

We have proposed an inscription image retrieval system that is based on the Bag of Visual Words technique using SURF as the feature descriptor which has proved to be highly efficient and gives us the advantage of being scale and rotation invariant. It is also a language independent technique making it the best suited for retrieving inscription images considering the ancient inscriptions to be written in varied styles and forms. We have worked with three sets of inscriptions, i) English, ii) Tamil iii) and inscriptions in several other language. The algorithm has proved to work well in all three cases. Usage of SURF has enhanced the scope of the algorithm and enabled us to work with varied forms of image degradation.

ACKNOWLEDGMENT

We would like to thank Arunima Sidhu for the data collection of the inscription images.

REFERENCES

[1] S.Rajakumar, Dr.V.Subbiah Bharathi, “Century Identification and Recognition of Ancient Tamil Character Recognition,” India International Journal of Computer Applications (0975 – 8887) Volume 26– No.4, July 2011.

[2] Rodríguez-Serrano, José A., and Florent Perronnin. "Handwritten word-spotting using hidden Markov models and universal vocabularies." Pattern Recognition 42(9) 2106-2116, (2009).

[3] Brown, M., and L. Rabiner. "Dynamic time warping for isolated word recognition based on ordered graph searching techniques." Acoustics, Speech, and Signal Processing, IEEE International Conference on ICASSP'82. Vol. 7. IEEE, 1982.
[4] K.pramod Sankar, R.Manmatha, C.V Jawahar, "Large scale document image retrieval by automatic word annotation" International Journal on Document Analysis and Recognition archive springer-verlag Berlin, Heildelberg volume 17 Issue 1, March 2014.
[5] Konstantinos Zagoris Ioannis PratikakisBasilis Gatos," Segmentation-based Historical Handwritten Word Spotting using Document-Specific Local Features "14th International Conference on Frontiers in Handwriting Recognition, 2014.
[6] Olivier Augereau, Nicholas Journet, Anne Vialard, Jean-Philippe Domenger," Improving classification of an industrial document image database by combining visual and textual features".
[7] Rusinol, Marcal, et al. "Browsing heterogeneous document collections by a segmentation-free word spotting method." International Conference on Document Analysis and Recognition. IEEE, 2011.
[8] Ataer, Esra, and Pinar Duygulu. "Matching ottoman words: an image retrieval approach to historical document indexing." Proceedings of the 6th ACM international conference on Image and video retrieval. ACM, 2007.
[9] Sankar, P., Jawahar, C., Manmatha, R, "Nearest neighbor based collection OCR" In: Proceedings of the IAPR Workshop on Document Analysis Systems, pp. 207 - 214 (2010).
[10] Rothacker, Leonard, Marcal Rusinol, and Gernot A. Fink. "Bag-of-features HMMs for segmentation-free word spotting in handwritten documents." 2013 12th International Conference on Document Analysis and Recognition. IEEE, 2013.
[11] Aldavert, David, et al. "A study of Bag-of-Visual-Words representations for handwritten keyword spotting." International Journal on Document Analysis and Recognition (IJDAR) 18.3 223-234, (2015).
[12] Bay, Herbert, et al. "Speeded-up robust features (SURF)." Computer vision and image understanding 110(3): 346-359, 2008.
[13] Ravi Shekhar and C.V. Jawahar "Word Image Retrieval using Bag of Visual Words" 10th IAPR International Workshop on Document Analysis Systems, 2012.



N. Jayanthi received her M.Tech. degree in 2007 from Department of Electronics and Communication Engineering, National Institute of Technology, Tiruchirappalli, Tamilnadu. She had been working as a Assistant Professor for the past 8 years in the Department of Electronics and Communication Engineering, Delhi Technological University, Delhi. Currently she is working towards her PhD degree in Image Processing and Applications. Her areas of interest are Image Processing, Machine Learning and Communication System.



Dr. S. Indu received her PhD. degree in 2012 from Department of Electronics and Communication Engineering, Delhi University, Delhi. She is working as Professor having 18 years of teaching experience and presently holds the position of Head of the Department in the Department of Electronics and Communication Engineering, Delhi Technological University, Delhi. Her area of interest is Image Processing, Computer Vision and Wireless Sensor Networks and in these areas she has published several research papers. She also holds position of Branch Counsellor IEEE DTU Branch and worked on several DST sponsored projects.

Accepted Manuscript



Investigation of biocompatible and protein sensitive highly luminescent quantum dots/nanocrystals of CdSe, CdSe/ZnS and CdSe/CdS

R.K. Ratnesh, Mohan Singh Mehata

PII:	S1386-1425(17)30124-5
DOI:	doi: 10.1016/j.saa.2017.02.028
Reference:	SAA 14950
To appear in:	*Spectrochimica Acta Part A: Molecular and Biomolecular Spectroscopy*
Received date:	28 November 2016
Revised date:	10 February 2017
Accepted date:	14 February 2017

Please cite this article as: R.K. Ratnesh, Mohan Singh Mehata , Investigation of biocompatible and protein sensitive highly luminescent quantum dots/nanocrystals of CdSe, CdSe/ZnS and CdSe/CdS. The address for the corresponding author was captured as affiliation for all authors. Please check if appropriate. Saa(2017), doi: 10.1016/j.saa.2017.02.028

This is a PDF file of an unedited manuscript that has been accepted for publication. As a service to our customers we are providing this early version of the manuscript. The manuscript will undergo copyediting, typesetting, and review of the resulting proof before it is published in its final form. Please note that during the production process errors may be discovered which could affect the content, and all legal disclaimers that apply to the journal pertain.

ACCEPTED MANUSCRIPT

Investigation of Biocompatible and Protein Sensitive Highly Luminescent Quantum Dots/Nanocrystals of CdSe, CdSe/ZnS and CdSe/CdS

R. K. Ratnesh and Mohan Singh Mehata*

Laser-Spectroscopy Laboratory, Department of Applied Physics, Delhi Technological University, Bawana Road, Delhi-110042, INDIA.

*Corresponding author E-mail: msmehata@gmail.com; mohan.phy@dce.edu

ACCEPTED MANUSCRIPT

ACCEPTED MANUSCRIPT

ABSTRACT

The size and shape dependent semiconductor quantum dots (1D nanoparticles) with color tunability demonstrating significant influence in a biological system and considered as ideal probes. Here, a non-coordinated colloidal approach was used for the synthesis of CdSe, CdSe/ZnS and CdSe/CdS core-shell quantum dots (QDs) of 3-4 nm. The synthesized nanocrystals show a high crystallinity, examined by X-ray diffraction (XRD) and high-resolution electron microscopy (HRTEM). The core-shell semiconductor QDs exhibit stronger photoluminescence (PL) as compared to the core QDs. The strong PL with small full-width half maximum (FWHM) indicates that the prepared QDs have a nearly uniform size distribution and well dispersibility. The quantum yield (QY) of core-shell QDs increases due to the surface passivation. Further, the PL of BSA is quenched strongly by the presence of core-shell QDs and follow the well-known Stern-Volmer (S-V) relation, whereas the PL lifetime does not follow the S-V relation, demonstrating that the observed quenching is predominantly static in nature. Among CdSe core, CdSe/ZnS and CdSe/CdS core-shell QDs, the CdSe/ZnS QDs shows the least cytotoxicity and most biocompatibility. Thus, the prepared core-shell QDs are biocompatible and exhibit strong sensing ability.

Keywords: Core-Shell quantum dots, optical properties, lifetime, an optical sensor, cytotoxicity.

ACCEPTED MANUSCRIPT

ACCEPTED MANUSCRIPT

1. Introduction

Quantum dots (QDs) and core-shell QDs synthesized by colloidal techniques provide a satisfactory realization of the strong quantum confinement regime. The excellent luminescent properties, stability with an advancement in continuous tunability of the electronic, optical properties with changing the size and relatively low cost and high chemical flexibility makes the subject for the investigation [1-5]. The core-shell semiconductor nanocrystals/QDs have used in various areas of electronics and medical sciences. Currently being explored as light emitting materials, thin-film light emitting devices (LEDs) [5-10], low-threshold lasers [11], optical amplifier media for telecommunication networks and biological label [12,13]. Further, a new field of research has recently been emerged by the use of individual monodisperse nanocrystals as building blocks for the fabrication of quantum dots superstructures and also the investigation of the collective properties of these novel artificial solids [14,15]. In recent years, tremendous advances in colloid chemistry led to the preparation of high-quality nanocrystals of several II-VI [16-18] and III-V [19-20] semiconductors.

The synthesis of CdSe nanocrystals from cadmium oxide and tri-n-octylphosphine selenide (TOPSe) at a high temperature of 250 - 300°C gives highly crystalline CdSe nanocrystals with tunable sizes. Introducing hexadecylamine (HDA) as a co-surfactant to the CdSe nanocrystals during their growth allows a considerable improvement of their PL properties [17]. In the recent past, a relatively greener synthesis approaches have introduced as an alternative to the traditional organometallic route [16]. The classical organometallic route based on highly toxic and expensive materials, e.g., cadmium carbonate ($CdCO_3$), cadmium acetate ($Cd(CH_3CO_2)_2$) and $Cd(CH_3)_2$, which has been replaced by less toxic materials, e.g., cadmium precursors cadmium oxide (CdO) [21-25]. A potential

ACCEPTED MANUSCRIPT

interest using these new materials, cadmium precursors, is to establish the so-called green chemical route and has been inspired by the development of eco-friendly chemical methodologies and materials specially QDs.

The overall interest and motivation are to prepare stable and highly luminescent nanocrystals by the passivation of the surface of the core (CdSe) with an inorganic shell of a semiconductor with a wider bandgap. Numerous II-VI semiconductors have used as shell material for CdSe nanocrystals core. Especially, ZnS, CdS or ZnSe shells prepared around the core enhanced significantly the chemical stability, photostability and PL efficiency of this new class of nanocrystals (core-shell) [17,26-29]. Further, the ZnS shell potentially provides a better stability as compared to the CdS or ZnSe shells. However, the intrinsic strains and lattice mismatch between CdSe and ZnS (~12%) are relatively large as compared with CdSe/CdS, result in defects within the ZnS shell, if the shell thickness exceeds 1.5 monolayers [27]. The PL quantum yield (QY) of CdSe/ZnS nanocrystals decrease with the size of the core. As an example, the QY for red emitting CdSe/ZnS nanocrystals is about 10 - 40% [27,30-32]. On the other hand, the lattice mismatch between CdSe and CdS is considerably lower (~3.9%), which facilitates an epitaxial growth of shell around the core resulting into the higher QY [28], this further leads potential applications in optoelectronic devices (e.g., LEDs [28,33]. It concluded that the two-pot synthesis approach realized when both core and shell could grow in a controlled manner and produces narrow size distribution, in general, the synthesis of CdSe/ZnS and CdSe/CdS core-shell QDs in a controlled manner is rather difficult [28].

In this paper, we present an easy and versatile two port synthesis route for CdSe, CdSe/ZnS and CdSe/CdS core-shell QDs and their applications. In the synthesis process, the HDA - TOP - ODE stabilizing mixture allows perfect control of both core and shell thickness

ACCEPTED MANUSCRIPT

and provides uniform particle size distribution. The prepared CdSe core and core-shell QDs exhibit excellent electronic properties, strong PL with a smaller FWHM and high QY (25 - 43%). We have also demonstrated the biocompatibility and strong sensing ability of the prepared QDs by measuring the toxicity and the interaction of QDs with BSA.

2. Material and Methods

2.1. Chemicals All the chemicals used were of the analytical grade of highest purity. Trioctylphosphine (TOP, 90 %), oleic acid (OA, ≥ 90%) tech grade, selenium powder (99.5%), zinc oxide (ZnO, 99.9995 %), sulfur (≥ 99), hexadecylamine (HDA, 90%) tech grade and Mercaptopropionic acid (MPA, 99 %) were purchased from Aldrich and cadmium oxide (CdO, > 99 %), toluene (99.5 %), methanol (99.93 %), 1- octadecene (ODE, ≥ 95.0%) and bovine serum albumin (BSA, 98.0 %) were purchased from Alfa Aesar, and used without further purification.

2.2. Synthesis of CdSe quantum dots

The synthesis of CdSe core nanocrystals was carried out under nitrogen (N_2) environment [7]. To prepare Cd precursor 0.102 gm of CdO, 1.23 ml of OA, and 14 ml of ODE were mixed in a 50 ml three neck flask and stirred continuously with heating rotamantle at 240° C until the solution becomes colorless. Then the TOPSe solution was injected at 240° C immediately when CdO was dissolved completely in the mixture (the mixture became transparent). For the preparation of the TOPSe solution, 0.0205 gm of Se dissolved in a mixture of solvents (0.2 ml of TOP and 2 ml of ODE) in a glass vial and then the mixture was stir continuously for around one hour. After the injection of a TOPSe solution, the temperature of the solution dropped to 10° C from the attended values. The color of the reaction solution changed, which indicated fast nucleation and growth. After 120 seconds of injection of a TOPSe

ACCEPTED MANUSCRIPT

solution, the heating mantle removed and 30 ml of methanol added to the mixture and after that, the obtained solution centrifuged at 6500 rpm for 15 min. The process is repeated many times to obtained pure CdSe QDs and then obtained eluent was dispersed into toluene for further synthesis.

The method of preparation of CdSe QDs involved the injection of a cold solution of Se precursor into hot liquid (a mixture of CdO+OA+ODE). Upon injection of the prepared Se precursor starts the instantaneous formation of CdSe nuclei. The size of the CdSe nanocrystals increases upon increasing the reaction temperature. The formation of new nuclei prevented by reducing the growth temperature about 10° C. The controlled nucleation process produces nearly monodispersed CdSe QDs. Further, the nucleation process controlled by controlling the reaction temperature and time throughout the synthesis.

2.3. Synthesis of core-shell quantum dots

2.3.1. Preparation of the precursor solution for the SILAR method.

The successive ion layer adsorption and reaction (SILAR) method was chosen for shell growth around the core [34,7]. For the preparation of precursor solution, the metal oxide ZnO, CdO and elemental sulfur were used. Zinc (0.1 M) precursor solution was prepared by dissolving 0.1017 g ZnO in a mixture of oleic acid (3.45 ml) and ODE (9.0 ml) at 300° C. Similarly, the cadmium precursor solution (0.1 M) was prepared by dissolving CdO (0.1602 g) in a mixture of oleic acid (3.45 ml) and ODE (9.0 mL) at 240° C. Sulfur precursor solution (0.1 M) was prepared by dissolving elemental sulfur (0.110 g) in ODE at 180 °C. All the solutions were prepared freshly under N_2 -atmosphere. The prepared Cd, Zn, and Cd/Zn-precursor solutions kept at around 90 - 100 °C, while the sulfur solution was at room temperature

ACCEPTED MANUSCRIPT

before used. For each shell growth, a calculated amount of a given precursor solution injected with a syringe using standard air-free procedures.

2.3.2. Preparation of shell around the CdSe core by SIRAL method

For the preparation of core-shell QDs, the calculated amount of CdSe nanocrystals (diameter 3.4 nm) were dispersed in a mixture of 3.5 ml of ODE and 2.0 ml of HDA and slowly heated up to 235° C under a nitrogen atmosphere. Then, Cd/Zn and sulfur (S) precursor were injected one by one into the solution of CdSe core nanocrystals. The CdSe core QDs concentration is estimated by absorption spectra [35,36]. The optimized temperature for shell growth synthesis was about 180° - 260° C. The amount of Cd and S precursors for the growth of first monolayer (MLs) was taken equally of about 0.33 ml. For the next ML, the amount of Zn and S precursors was calculated based on the size of the core and first ML, as represented in Scheme (S_1). We have taken a period of about 10 min for the addition of one to another ML and found sufficient time to be completed the reaction. After this, the absorption and PL-spectra do not show considerable changes (shifts). Upon completion of each monolayer of CdS or ZnS, the solution kept for another 30 min at 260° C and finally cool to room temperature. To remove the unreacted compound and byproducts from the eluent we added 20 ml of methanol and did centrifugation at 6500 rpm, this process was repeated 3-4 times and finally obtained pure CdSe/CdS QDs. The same process followed for the synthesis of CdSe/ZnS core-shell QDs.

2.3.3. Synthesis of water soluble core-shell QDs

To prepare water-soluble CdSe/ZnS core-shell QDs we use ligand exchange technique which, helps to transform QDs from oil phase into water. During oil phase reaction OA is used and it helps to dissolve the cadmium (Cd) into the reaction and TOP was used as a capping agent. As a result, the nature of QDs became hydrophobic due to TOP and OA. Further, the

ACCEPTED MANUSCRIPT

use of MPA replaced these hydrophobic ligands. For this, a calculated amount of OA/TOP coated CdSe/ZnS QDs mixed in a mixture of estimated amount of deionized (DI) water and MPA and kept for 3 hours with continuous and vigorous stirring [3]. After 3 hrs of continuous stirring, the QDs transferred into the water phase. To remove excess MPA from the supernatant solution centrifugation and decantation were carried out. Successive redispersion of the particles into water especially at pH 8.5, produces a clear solution, which was used for biological applications.

2.4. Experimental Techniques and Methods

The optical spectra of QDs were performed in toluene and water (for water soluble QDs dots) at ambient temperature. Absorption spectra were recorded with the UV/VIS/NIR spectrometer, Lambda-750, Perkin-Elmer. Photoluminescence (PL) spectra were measured by a spectrofluorometer (Fluorolog-3 Horiba Jobin Yvon) equipped with double-grating at excitation as well as at emission monochromators (1200 grooves/mm) and Hamamatsu R928P photomultiplier tube (PMT). The excitation source was a 450W xenon lamp. An auto instrumental correction factor was applied to all PL spectra to correct for the wavenumber/wavelength dependent photomultiplier response and variation in output intensity from the lamp and grating efficiencies. Excitation and emission slit width were chosen about 1.0 nm for all the measurements, and the excitation wavelength was 450 nm. Temperature variation study was performed using Peltier thermocouple device (Model: Fl-3004) with a temperature controller (Model: 350B) provide by Horba Jobin Yvon.

Photoluminescence decay curves were recorded using time-correlated single photon counting (TCSPC) system (DeltaFlex-01-DD, Horiba Jobin Yvon IBH Ltd) coupled with DeltaDiode Laser (450 nm) and PMT (PPD 850) and the data were analyzed using reconvolution and least square fitting method using the commercial software provided by

ACCEPTED MANUSCRIPT

Horiba. The time resolution of the equipment is typically <50 ps with the DeltaDiode laser using the re-convolution method.

HRTEM (high-resolution transmission electron microscopy) images were taken by Tecnai G^2-20 operated at a voltage of about 200 kV. For TEM images, the QDs samples were prepared on 300-mesh carbon coated Cu grids. The EDX (energy-dispersive X-ray) spectra and XRD (X-ray diffraction) pattern were collected by Hitichi-640 at a voltage of 15 kV and BRUKER-D8, respectively. The FTIR (Fourier transform infrared) spectra of the samples were collected with NICOLET-380 (FL-IR) Thermo Scientific. The samples for FTIR measurements were prepared in the form of liquid (i.e. dissolved in water). The spectra were recorded in transmission mode over 32 scans with a resolution of 4 cm^{-1}.

For the measurement of cytotoxicity of QDs, the L929 fibroblast cells seeded with a fixed concentration of different QDs in 96-well tissue culture plate visualized under a confocal microscope (Nikon ECLIPSE-TS100) over 3 days. MTT assay was applied to determine the cytocompatibility of QDs with L929 fibroblast cells. MTT assay is a rapid colorimetric technique, in which yellow MTT reduced into purple formazan following mitochondrial dehydrogenase in cells to assess the cell proliferation. After 1, 2 and 3 days incubation with different QDs, the viability of L929 fibroblast cells determined. Briefly, L929 cells were repeatedly washed (at least three times) with PBS (phosphate buffered saline) for removing unattached cells. Then 100 µl serum free medium and 10 µl MTT stock solution (5 mg/ml in DMEM) were added in each well plate and incubated for 3 hours (37° C) for MTT formazan formation. After 3 hours incubation at 37° C, the reaction solution carefully separated from the each prepared well and after that 100 µl dimethyl sulfoxide added. The well-plates shacked till the formazan precipitate completely dissolved, followed by

ACCEPTED MANUSCRIPT

measurement of absorbance values by spectrophotometry at 595 nm with an ElX-800 Microelisa reader (Bio-Tek Inc., USA) with DMSO as a blank.

3. Results and discussion

Figure 1 shows HRTEM images (a-c) and their size histogram (a' - c') of the CdSe-core and core-shell quantum dots with a different shell and shell thicknesses. The core-shell structure composed of two monolayers (MLs) of ZnS or two monolayers of CdS. A clear difference in the core and core-shell structure is appeared, with increasing the shell monolayer resulting into the increase of the diameter of the QDs. The size histogram of bare CdSe (a'), CdSe/ZnS (b') and CdSe/CdS (c') give the average diameter of the nanocrystals. The average diameter of CdSe QDs is 3.45 nm and increases up to 4.10 nm while adding of MLs of ZnS or CdS. Note that the crystallinity of the crystals remains maintained even in core-shell QDs. The inset of Fig. 1(a) shows the crystallinity with continuous lattice fringes of CdSe QDs. HRTEM images show that the CdSe and core-shell structures (CdSe/ZnS and CdSe/CdS) exhibit narrow size distribution with a standard deviation below 10%.

Figure 2 shows the X-ray diffraction (XRD) pattern of CdSe core and CdSe/ZnS and CdSe/CdS core-shell structures. The broad diffraction pattern together with peaks indicates clearly the nanocrystalline nature of the CdSe, CdSe/ZnS and CdSe/CdS core-shell QDs. The XRD pattern is identical to the hexagonal phase with wurtzite structure. The average crystal sizes (d) of CdSe QDs calculated based on the width of the peak corresponding to (111) plane by using the Scherrer's equation is about 3.7 nm. The EDX spectra of the CdSe and CdSe core covered with a shell composition of ZnS and CdS shown in supporting information Fig.$S_{1,}$ and the percentage amount of elements present in the CdSe, CdSe/ZnS and CdSe/CdS QDs are given in Table 1, demonstrating the formation of core and cores shell QDs.

ACCEPTED MANUSCRIPT

Figure 3 (a,b) shows the absorption and photoluminescence (PL) spectra of CdSe core and CdSe/ZnS core-shell structures including the intermediate stage of core-shell QDs. The absorption maximum of CdSe/ZnS shifted monotonically from 537 to 565 nm as compared to to the CdSe core. The red shift in absorption spectra after coating on CdSe also observed due to partial leakage of the exciton into the ZnS shell matrix [37]. The red shift is more pronounced in smaller dots where the leakage of the exciton into the ZnS shell has a more dramatic effect on the confinement energy of the charge carriers. The absorption edge is relatively sharp, indicating a narrow size distribution of the core and core-shell QDs. The PL spectrum of CdSe core shows a narrow band with a maximum at 557 nm, with the addition of shell over the core in a stepwise fashion, i.e. to prepared CdSe/ZnS, the PL band shifted towards red and peaked at 582 nm. Together with the shift in a peak wavelength, the PL intensity of the core-shell QDs increases. The FWHM of CdSe and CdSe/ZnS core-shell is about 31 and 30 nm, respectively. Thus, the strong PL band and smaller FWHM indicate to the formation of uniform particles distribution both in core and core-shell QDs. The estimated Stokes shift is 20 and 17 nm for core and core-shell QDs, respectively, the difference in Stokes shift may be due to the ZnS shell over the CdSe core [38].

Figure 4 (a,b) shows the absorption and PL spectra of CdSe core and CdSe/CdS core-shell structure together with the spectra of intermediated stage of core-shell. The absorption maximum of CdSe/CdS shifted from 537 to 547 nm in a stepwise fashion as compared to the CdSe core QDs. The PL spectra of CdSe core show a narrow band with a maximum at 557 nm, with the addition of shell over CdSe core, i.e., CdSe/CdS, follow the same trend as CdSe/ZnS, the PL- spectrum shifted towards red and peaked at 563 nm. Together with the shift of peak wavelength, the PL intensity also enhanced. The FWHM of

ACCEPTED MANUSCRIPT

CdSe and CdSe/CdS core-shell is 31 and 29 nm, respectively. The narrow PL band and smaller FWHM clearly indicate to the formation of uniform particle size distributions in both core and core-shell QDs. The Stokes shift is about 20 and 16 nm. The FWHM as well as the Stokes shift is nearly same in both the type of shell coating, which shows the formation of shell over the core is almost same in both the cases. The reduction in Stoke's shift in the core-shell on the cores may be due to passivation of CdS or ZnS onto CdSe core, which takes part into the radiative recombination hence the PL. The small difference in the FWHM and Stokes shift while coating CdSe with ZnS or CdS is due to the lattice mismatch, which is about 12% with ZnS and 3.9% with CdS. The PL (QY) of each core and core-shell QDs defined by (Φ_s) were estimated by the equation:

$$\Phi_S = \Phi_R \left(\frac{\mathrm{I}_S}{\mathrm{I}_R}\right)\left(\frac{1-10^{-A_R}}{1-10^{-A_S}}\right)\left(\frac{n_S^2}{n_R^2}\right) \quad (1)$$

where Φ_R is the absolute QY of standard reference rhodamine 6G (0.95), $\mathrm{I_R}$ and $\mathrm{I_S}$ are the integrated fluorescence intensity of the standard reference (Rhoadmine 6G) and QDs, respectively. $\mathrm{A_R}$ and $\mathrm{A_S}$ are the respective absorbance and $\mathrm{n_R}$ and $\mathrm{n_S}$ are the refractive index of solvent (toluene for QDs and methanol for the dye). The estimated QY for CdSe and CdSe/CdS QDs is about 25 and 43 %, respectively (Table 2). It is important to note that the QY of core-shell QDs is increased after forming shell around the core, this is due the most of the surface vacancies and nonradiative recombination sites are passivated while coating with ZnS or CdS shell resulting into the increase of PL QY [27].

Time-resolved photoluminescence of CdSe Core and Core-shell QDs

Figure 5 shows the time-resolved PL decay curves of CdSe core and CdSe/CdS and CdSe/ZnS core-shell QDs disperse in toluene measured with 450 nm excitation at the peak wavelengths of steady-state PL spectra. The PL decay curve significantly affected by the

ACCEPTED MANUSCRIPT

surface modification of QDs. Upon coating with a shell of CdS and ZnS, the surface of QDs modified with the passivation resulting in the decrease/increase of lifetime and QY [39]. The observed decay curves could not fit with mono-exponential function, however well fitted to a multi-exponential model described by the equation (2):

$$\mathrm{I(t)} = \alpha_1 \exp\left(t/\tau_1\right) + \alpha_2 \exp\left(t/\tau_2\right) + \alpha_3 \exp\left(t/\tau_3\right) \quad (2)$$

where τ_1 , τ_2 and τ_3 represent the lifetimes and α_1, α_2, and α_3 are the corresponding pre-exponential factors, respectively. The multi-exponential lifetimes from the core and core-shell CdSe may be ascribed either due to the distribution of particles or due to the presence of defects. However, the components of lifetime and the corresponding pre-exponential factor varies with core and core-shell structure [40, 41]. The contribution of the fastest component is 59% for CdSe and 68% for CdS/CdS and 77% for CdSe/ZnS. And the contribution of slow component is ~1-5%, which is very small in overall contribution. Further, upon coating core with shell the contribution of the major component is increases and the contribution of other component decreases, resulting into the increase of PL QY. Similar feature were also reported in the case of QDs [40, 41]. The average lifetime, τ_{av} of CdSe, CdSe/CdS and CdSe/ZnS QDs is calculated using the equation (3) and are summarized in Table 3.

$$\tau_{\mathrm{Av}} = (\alpha_1\tau_1^2 + \alpha_2\tau_2^2 + \alpha_3\tau_3^2)/(\alpha_1\tau_1 + \alpha_2\tau_2 + \alpha_3\tau_3) \quad (3)$$

The average lifetimes of CdSe, CdSe/CdS and CdSe/ZnS QDs are 41.84, 21.08 and 11.53 ns, respectively. The τ_{av} decreases while forming the shell around the CdSe core. The average lifetime which was calculated using Eq. 3 depends on both the lifetime and the corresponding amplitude, i.e., pre-exponential factor. It is important to note that when the core is coated with a shell, the amplitude/contribution of longer lifetime component decreases resulting into the decrease of the τ_{av}. Thus, the longer lifetime component is

ACCEPTED MANUSCRIPT

corresponding to the defect state and the reduction in the longer lifetime, and pre-exponential factor clearly indicates the surface passivation. Hence, the shell over core decreased the surface defects and increased the QY. In the case of ZnS shell, Zn atoms serve as surface trapping defect sites as compared to the CdS. There may be two reasons, passivation decreased the surface defects, and decreased surface recombination hence increased the contribution of the faster component. On the other hand, upon increasing the defect at the surface of the QDs, which leads the recombination of the excited carrier on the surface state may decrease the QY of the intrinsic energy level, even with a longer lifetime. Further, recombination of excited carriers on the surface need the participation of phonon, so surface related emission has a longer lifetime, and the fast component of PL decay in NCs is considered to originate from core intrinsic exciton recombination [42]. Furthermore, intrinsic recombination of excited carriers has much higher opportunity to emitting a photon. Recombination of excited carriers on the surface will decrease the possibility of recombination in the core thus decreases entire QY due to a decrease in radiative rate. The reduction in lifetime and increase in QY are consistent with the resulting extension in carrier interaction [40, 41]. Also, CdS transition layer plays a major role in acquiring high-quality QDs, as evidenced by PL measurement. The result can be explained by the fact that the presence of a CdS layer can sufficiently reduce stress between CdSe core and CdS shell and eliminate defects such as dislocation and stress. Meanwhile, according to alloy CdSe/CdS layer helps to decrease large conduction/valence band offsets facilitate excited carrier migration from CdS shell to CdSe core to increases excited carrier number and consequently in favor of the increasing of PL intensity but in case of ZnS layer passivation increase the valance band offsets that decrease the carrier migration from ZnS shell to CdSe core and decrease the number of excited carried [40].

ACCEPTED MANUSCRIPT

Cytotoxicity and biocompatibility of synthesized QDs

The MTT assay was applied to determine the toxicity of the synthesized core (CdSe) and core-shell (CdSe/CdS and CdSe/ZnS) QDs with L929 fibroblast cells. The MTT assay is a rapid calorimetric technique, in which yellow MTT becomes purple formazan following the process of mitochondrial dehydrogenase in cells to assess the cell proliferation. Figure 6 (A,B) shows the phase contrast microscopic images and the corresponding absorbance at 595 nm of L929 fibroblast cells in the presence of three different QDs (CdSe/CdS and CdSe/ZnS) studied by MTT assay over three days. It appears from the Fig. 6A that as the incubation time increases the cells viability increases. However, the cell viability is different for different QDs. Out of there different QDs, the cell viability is maximum for core-shell (CdSe/ZnS). However, the cell viability is the minimum for core (CdSe) QDs. For CdSe/CdS the cell viability lies between the two (6B). Thus core-shell QDs shows less toxicity and higher cell viability than the CdSe QDs and can be used for the other biological application if explored further. When determining the biocompatibility of QDs, together with solubility the biocompatibility also requires to limited toxicity to biological systems, such as interruption to the cell's normal activities. The cell toxicity has directly related to oxidation of the nanoparticles core-shell materials, leading to the release of free cadmium [43]. Cadmium ions have been shown to bind to thiol groups on QDs which cause enough stress and damage in the mitochondria that lead significant cell death [44, 45]. Cadmium is the most widely used material for core QDs. Therefore its release into the cell might be a logical mechanism of toxicity. Toxicity of QDs has been monitored in hepatic cells and found that liver is the primary site for acute damage from cadmium [42] which has been further oxidized by UV light before used [27,46,47]. In addition to air and UV exposure, quantum dot surface oxidation can occur in H_2O_2, i.e., in oxidative solutions, which is relevant because

ACCEPTED MANUSCRIPT

such environments are possible in vivo. Kirchner *et al.* [48] showed that Cd^{2+} was released from CdSe/ZnS QDs into cells at toxic levels over time (48 hours), under standard synthesis and imaging conditions. By examining the effects of the free core materials in solution, cadmium was the primary cause of cytotoxicity however the levels could be reduced or eliminated by adding additional surface coatings [44,48]. In general, the core of quantum dots is prepared with elements that are inherently toxic to cells and living systems. It has been mention [43] that prevention of core material oxidation is necessary for reducing toxicity and increasing biocompatibility of quantum dots. In general, the coatings is used to enhance the QY of the core or solubility and conjugation and thus the cytotoxicity of QDs.

Effects of QDs on BSA photoluminescence

Figure 7 (a,b) shows the absorption and photoluminescence spectra of BSA, CdSe/ZnS core-shell QDs (water soluble) and QDs with BSA at two different concentration. The absorption spectrum of BSA solution exhibits the well-known absorbance maximum at 278 nm assigned to the $\pi \rightarrow \pi^*$ transition of the aromatic amino acids residues and a dilute solution of the QDs exhibit a maximum absorption at 565 nm. The PL spectra measured in the range of 310-650 nm (Fig. 7 (b) using an excitation wavelength of 280 nm. The pure BSA aqueous solution at room temperature exhibits a strong intrinsic PL band centered at 357 nm. On the other hand, the CdSe/ZnS QDs shows a narrow, symmetric band located at 582 nm with an FWHM of 34 nm (Fig. 7b). Upon adding QDs to BSA solution, a decrease in intensity of the BSA characteristic band was observed together with the increase of PL intensity of QDs, which may ascribe due to the energy transfer process. The small shift indicates that BSA residues are in a more hydrophobic environment [49-53].

Further, the PL of BSA is decreased monotonically with increasing the concentration of QDs without any shift in the PL maximum. A small amount of QDs is strong enough to

ACCEPTED MANUSCRIPT

quench the PL of BAS as shown in Fig. 8a. To examine the reason of quenching of PL of BSA in the presence of QDs, we monitored the PL intensity of the BAS in the presence of QDs, which is found decrease progressively with increasing concentration of QDs and becomes relatively very small with a concentration of about 25 nM. The quenching of PL intensity is plotted following the well-known Stern-Volmer (S-V) relation [54].

$$\frac{I_0}{I} = 1 + K_{SV}\,[QDs] \quad (4)$$

where I_0 and I are the PL intensities of BSA in the absence and presence of the quencher, respectively, K_{SV} is S-V constant and [QDs] is the concentration of the quencher. The observed S-V plot, the plot between PL intensity of BSA as a function of the concentration of QDs, is nearly linear as shown in fig. 8 (b). From the linear relation of S-V plot, the S-V constant was calculated and found to be $K_{SV} = 3.26 \times 10^9\ M^{-1}$. The Kq, a bimolecular quenching rate constant can be calculated using the equation (5) [54].

$$K_{SV} = K_q \tau_0 \quad (5)$$

where τ_0 is the lifetime of BSA in the absence of quencher. The average lifetime of the BSA is 5.8 ns, in the absence of quencher. Considering lifetime of BSA in the absence of quencher the value of K_q is about $5.620 \times 10^{17} M^{-1} S^{-1}$. The limit of detection (LOD) was $2.84 \times 10^{-11}\ ML^{-1}$. The calculated K_q is greater as compared with the value obtained for biological macromolecules ($2.0 \times 10^{10}\ M^{-1}S^{-1}$) [55-57], which has been examined by calculating the binding constant between QDs and BSA. The average lifetime of BSA in the absence of quencher (QDs) is about 5.8 ns and decreases slightly (~5%) and do not follow the S-V relation, this demonstrated that the quenching is mainly static in nature.

The binding constant K_b considered between QDs and BSA, where determined from the PL spectra, using the method described by Tedesco *et al.* [58]

ACCEPTED MANUSCRIPT

$$\frac{I_0 - I}{I - I_{Sat}} = \left(\frac{QDs}{K_{diss}}\right)^n \quad (6)$$

where I_0 denotes the PL intensity of pure BSA, I_{Sat} the PL intensity of BSA saturated with QDs and *I* is the PL intensity of intermediate concentrations between I_0 and I_{Sat}. The [QDs] denotes the concentration of QDs, ***n*** is the number of binding sites per particle and K_{diss} is defined as the reciprocal value of K_b. From the slope and intercept of the best fitted line of the plot of log $[I_0 - I/I - I_{Sat}]$ against log ([QDs]), the number of binding sites to be 1.12, whereas the binding constant is 7.91 × 10^7 M^{-1}. It has been reported that at pH>5 the carboxylic group of MPA is deprotonated yielding a negative charge shell at the surface of the QDs resulting into the formation of bioconjugation of CdSe/ZnS QDs with BSA due to the interaction between the negatively charged QDs surfaces and positively charged proteins/protein subdomains [59,60].

Analysis of force acting between CdSe/ZnS core-shell QDs and BSA

To understand the interaction force between CdSe/ZnS QDs and BSA, which may be hydrogen bonds, van der Waals interactions or electrostatic interactions [61,62], the thermodynamic parameters, the enthalpy change (ΔH) and entropy change (ΔS) were calculated from the van't Hoff equation:

$$\ln K_a = -\frac{\Delta H}{RT} + \frac{\Delta S}{R} \quad (7)$$

where R is the gas constant, K_a is the quenching constant at the corresponding temperature. Fig. 9 (a,b) shows plots between $(\frac{I_0}{I} - 1)$ vs concentration of QDs at three different temperature and ($\ln K_a$) vs. temperature (1/T). The K_a, ΔH and ΔS were calculated from the slopes and intercepts of these plots and are given in Table 4. The free energy change (ΔG) can also calculate from the given equation:

$$\Delta G = \Delta H - T\Delta S \quad (8)$$

ACCEPTED MANUSCRIPT

and summarized in Table 4. The negative ΔG, ΔH values and the positive ΔS value representing the binding of MPA-core-shell QDs with BSA is spontaneous and nonbonded (van der Waals) however, electrostatic interaction and hydrogen bonding may play major roles in this binding reaction [62,63].

FTIR analysis of functionalized QDs

Figure 10 shows the FTIR spectra of synthesized CdSe and CdSe/ZnS core-shell quantum dots together with neat MPA. A prominent absorption band at 1639 cm^{-1} indicates the presence of carbonyl (C=O) group and the peaks at 3352 cm^{-1} and 3346.9 cm^{-1} of CdSe and CdSe/ZnS, respectively indicate to the OH group existing in MPA. The appearance of the vibrational band representing to the C=O group in the sample of CdSe/ZnS-MPA showed that the carboxyl group was not involved in coordination to the QDs surface, but MPA was attached to Cd ion on the surface of QD through the thiol group [60]. Further, the absorption peak appeared at 2567 cm^{-1} of MPA is representing the oscillation mode of –SH, which is not observed in the water soluble CdSe, CdSe-ZnS, CdSe-ZnS (BSA) samples and proved that the thiol groups (-SH) reacted with the surface of quantum dots [64].

4. Conclusions

The CdSe and core-shell (CdSe/ZnS, CdSe/CdS) QDs/nanocrystals have been prepared by two port synthesis using non-coordinating solvent. The prepared CdSe and core-shell structure have a hexagonal phase with wurtzite structure. Upon adding 2MLs of ZnS or CdS retain the crystallinity of entire core-shell structure of CdSe/ZnS and CdSe/CdS. The average particle size of the core (CdSe) QDs is about 3.4 nm and increases up to 3.7 and 4.1 nm for

ACCEPTED MANUSCRIPT

CdSe/CdS and CdSe/ZnS core-shell QDs, respectively. Subsequently the absorption and PL maximum shifted towards longer wavelength region. The FWHM of PL spectra is quite small. The QY of the core-shell QDs increased and approached >40% by adding monolayers (MLs) of CdSe and ZnS. The longer lifetime components in the core-shell QDs decreases, due to the reduction of the contribution of defects by surface passivation leading to the strong PL efficiency. The PL of BSA is strongly quenched by the presence of core-shell QDs and follow well known S-V relation. However, the lifetime of BSA did not follow S-V relation in the presence of QDs and demonstrated that the quenching is predominantly static in nature. Out of three QDs, the CdSe/ZnS core-shell QDs shows the least cytotoxicity and most biocompatible. Thus, the prepared core-shell QDs show high sensing ability are biocompatibility.

Acknowledgements

We thank Department of Science and Technology (DST) (SR/FST/PSI-164/2011(C) for providing time-correlated photon counting (TCSPC) system and DAE-BRNS (2012/37P/20/BRNS/765) for financial support, and CDRI, Lucknow for cytocompatibility experiments.

ACCEPTED MANUSCRIPT

ACCEPTED MANUSCRIPT

References

[1] U. Woggon, Optical properties of semiconductor quantum dots, Springer-Verlag: Berlin, Germany (1997).

[2] A. P. Alivisatos, Perspectives on the Physical Chemistry of Semiconductor Nanocrystals, J. Phys. Chem. 100 (1996) 13226 - 13239.

[3] R. K. Ratnesh, M. S. Mehata, Controlled synthesis and optical properties of tunable CdSe quantum dots and effect of pH, AIP Adv. 5 (2015) 097114.

[4] M. S. Mehata, M. Majumder, B. Mallik, N. Ohta, External electric field effects on optical property and excitation dynamics of capped CdS quantum dots embedded in a polymer film, J. Phys. Chem. C 114 (2010) 15594 – 15601.

[5] M. S. Mehata, Enhancement of charge transfer and quenching of photoluminescence of capped CdS Quantum Dots, Sci. Rep. 5 (2015) 12056.

[6] M. S. Mehata, Stark shifts and exciton dissociation in CdSe nanoparticle grafted conjugated polymer, Appl. Phys. Lett. 100 (2012) 151908.

[7] R. K. Ratnesh, M. S. Mehata, Synthesis and optical properties of core-multi-shell CdS/CdS/ZnS quantum dots: surface modification, Opt Mater. 64 (2017) 250 - 256.

ACCEPTED MANUSCRIPT

[8] V. L. Colvin, M. C. Schlamp, A. P. Alivisatos, Light emitting diodes made from cadmium selenide nanocrystals and a semiconducting polymer, Nature 370 (1994) 354 - 357.

[9] N. Tessler, V. Medvedev, M. Kazes, S. H. Kan, U. Banin, Efficient near-infrared polymer nanocrystal light-emitting diodes, Science 295 (2002) 1506 - 1508.

[10] C. F. Du, T. You, L. Jiang, S. Q. Yang, K. Zou, K. L. Han, W. Q. Deng, Controllable synthesis of ultrasmall $CuInSe_2$ quantum dots for photovoltaic application, RSC Adv. 4 (2014) 33855 – 33860.

[11] V. I. Klimov, A. A. Mikhailovsky, S. Xu, J. A. Hollingsworth, C. A. Leatherdale, H. J. Eisler, M. G. Bawendi, Optical gain and stimulated emission in nanocrystal quantum dots, Science 290 (2000) 314 - 317.

[12] M. Jr. Bruchez, M. Moronne, P. Gin, S. Weiss, A. P. Alivisatos, Semiconductor nanocrystals as fluorescent biological labels, Science 281 (1998) 2013 - 2016.

[13] B. Dubertret, P. Skourides, D. J. Norris, V. Noireaux, A. H. Brivanlou, A. Libchaber, In vivo imaging of quantum dots encapsulated in phospholipid micelles, Science 298 (2002) 1759 - 1762.

[14] C. B. Murray, C. R. Kagan, M. G. Bawendi, Self-organization of CdSe Nanocrystallites into Three-dimensional quantum dot superlattices, Science 270 (1995) 1335 - 1338.

[15] A. L. Rogach, D. V. Talapin, E. V. Shevchenko, A. Kornowski, M. Haase, H. Weller, Organization of matter on different size scales: Monodisperse nanocrystals and their superstructures, Adv. Funct. Mater. 12 (2002) 653 - 664.

[16] C. B. Murray, D. J. Norris, M. G. Bawendi, Synthesis and characterization of nearly monodisperse CdE (E =sulfur, selenium, tellurium) semiconductor nanocrystallites, J. Am. Chem. Soc. 115 (1993) 8706 – 8715.

ACCEPTED MANUSCRIPT

[17] D. V. Talapin, A. L. Rogach, A. Kornowski, M. Haase, H. Weller, Highly Luminescent Monodisperse CdSe and CdSe/ZnS nanocrystals synthesized in a hexadecylamine-trioctylphosphine oxide-trioctylphospine mixture, Nano Lett. 1 (2001) 207 - 211.

[18] N. Gaponik, D. V. Talapin, A. L. Rogach, K. Hoppe, E. V. Shevchenko, A. Kornowski, A. Eychmuller, H. Weller, Thiol-capping of CdTe nanocrystals: An alternative to organometallic synthetic soutes, J. Phys. Chem. B 106 (2002) 7177 - 7185.

[19] O. L. Micic, C. J. Curtis, K. M. Jones, J. R. Sprague, A. J. Nozik, Synthesis and characterization of InP quantum dots, J. Phys. Chem. 98 (1994) 4966 - 4969.

[20] A. A. Guzelian, U. Banin, A. V. Kadavanich, X. Peng, A. P. Alivisatos, Colloidal chemical synthesis and characterization of InAs nanocrystal quantum dots, Appl. Phys. Lett. 69 (1996) 1432 - 1434.

[21] L. Qu, X. Peng, Control of photoluminescence properties of CdSe nanocrystals in growth, J. Am. Chem. Soc. 124 (2002) 2049 - 2055.

[22] Z. A. Peng, X. Peng, Formation of high-quality CdTe, CdSe, and CdS nanocrystals using CdO as precursor, J. Am. Chem. Soc. 123 (2001) 183 - 184.

[23] Z. A. Peng, X. Peng, Nearly monodisperse and shape-controlled CdSe nanocrystals via alternative routes: Nucleation and growth, J. Am. Che m. Soc. 124 (2002) 3343 - 3353.

[24] L. Qu, Z. A. Peng, X. Peng, Alternative routes toward high quality CdSe nanocrystals, Nano Lett. 1 (2001) 333 - 337.

[25] J. Aldana, Y. A. Wang, X. Peng, Photochemical instability of CdSe nanocrystals coated by hydrophilic thiols, J. Am. Chem. Soc. 123 (2001) 8844 - 8850.

[26] M. A. Hines, P. Guyot-Sionnest, Synthesis and characterization of strongly luminescing ZnS-capped CdSe nanocrystals, J. Phys. Chem. 100 (1996) 468 - 471.

[27] B. O. Dabbousi, J. Rodriguez-Viejo, F. V. Mikulec, J. R. Heine, H. Mattoussi, R. Ober, K. F. Jensen, M. Bawendi, (CdSe)ZnS Core-shell quantum dots: Synthesis and

ACCEPTED MANUSCRIPT

characterization of a size series of highly luminescent nanocrystallites, J. Phys. Chem. B 101 (1997) 9463 - 9475.

[28] X. Peng, M. C. Schlamp, A. Kadavanich, A. P. Alivisatos, Epitaxial growth of highly luminescent CdSe/CdS core-shell nanocrystals with photostability and electronic accessibility, J. Am. Chem. Soc. 119 (1997) 7019 - 7029.

[29] P. Reiss, J. Bleuse, A. Pron, Highly luminescent CdSe/ZnSe core-shell nanocrystals of low size dispersion, Nano Lett. 2 (2002) 781 - 784.

[30] Y. Ebenstein, T. Mokari, U. Banin, Fluorescence quantum yield of CdSe/ZnS nanocrystals investigated by correlated atomic-force and single-particle fluorescence microscopy, Appl. Phys. Lett. 80 (2002) 4033 - 4035.

[31] J. Lee, V. C Sundar, J. R. Heine, M. G. Bawendi, K. F. Jensen, Full Color Emission from II–VI Semiconductor quantum dot–polymer composites, AdV. Mater. 12 (2000) 1102 - 1105.

[32] D. Gerion, F. Pinaud, S. C. Williams, W. J. Parak, D. Zanchet, S. Weiss, A. P. Alivisatos, Synthesis and properties of biocompatible water-soluble silica-coated CdSe/ZnS semiconductor quantum dots, J. Phys. Chem. B 105 (2001) 8861 - 8871.

[33] M. C. Schlamp, X. Peng, A. P. Alivisatos, Improved efficiencies in light emitting diodes made with CdSe(CdS) core-shell type nanocrystals and a semiconducting polymer, J. Appl. Phys. 82 (1997) 5837 - 5842.

[34] J. J. Li, Y. A. Wang, W. Z. Guo, J. C. Keay, T. D. Mishima, M. B. Johnson, X. G. Peng, Large-scale synthesis of nearly monodisperse CdSe/CdS core-shell nanocrystals using air-stable reagents via successive ion layer adsorption and reaction, J. Am. Chem. Soc. 125 (2003) 12567 - 12575.

[35] O. Schmelz, A. Mews, T. Basche, A. Herrmann, K. Mullen, Supramolecular complexes from CdSe nanocrystals and organic fluorophors, Langmuir 17 (2001) 2861 - 2865.

ACCEPTED MANUSCRIPT

[36] W. W. Yu, L. H. Qu, W. Z. Guo, X. G. Peng, Experimental determination of the extinction coefficient of CdTe, CdSe, and CdS nanocrystals, Chem. Mater. 15 (2003) 2854 - 2860.

[37] D. Schoos, A. Mews, A. Eychmuller, H. Weller, Quantum-dot quantum well CdS/HgS/CdS: Theory and experiment, Phys. Rev. B 49 (1994) 17072 - 17078.

[38] H. Q. Nguyen, Synthesis and optical properties of CdSe nanocrystals and CdSe/ZnS core-shell nanostructures in non-coordinating solvents, Adv. Nat. Sci.: Nanosci. Nanotechnol. 01 (2010) 025004.

[39] C. H. Chuang, S. S. Lo, G. D. Scholes, C. Burda, Charge separation and recombination in CdTe/CdSe core-shell nanocrystals as a function of shell coverage: Probing the onset of the quasi type-II regime, J. Phys. Chem. Lett. 1 (2010) 2530 - 2535.

[40] H. Zhou, G. Zhou, J. Zhou, D. Xu, X. Zhang, P. Kong, Z. Yu, High luminescent core–shell QDs based on noninjection synthesized CdSe QDs: observation of magic sized CdSe quantum dots, RSC Adv. 4 (2014) 42316 - 42325.

[41] M. G. Kotresh, K. S. Adarsh, M. A. Shivkumar, S. R. Inamdar, Study state and time resolved spectroscopy study of CdSe QDs: FRET approach, J Fluoresc 26, (2016) 1249 – 1259

[42] U. Kaiser, D. Jimenez de Aberasturi, R. Malinowski, F. Amin, W. J.Parak, W. Heimbrodt, Multiplexed measurements by time resolved spectroscopy using colloidal CdSe/ZnS quantum dots, Appl. Phys. Lett. 104 (2014) 041901 - 041904.

[43] M. A. Walling, J. A. Novak, J. R. E. Shepard, Quantum dots for live cell and in vivo imaging, Int. J. Mol. Sci. 10 (2009) 441- 491.

[44] A. M. Derfus, W. C. W. Chan, S. N. Bhatia, Probing the cytotoxicity of semiconductor quantum dots, Nano Lett. 4 (2004) 11 - 18.

ACCEPTED MANUSCRIPT

[45] L. E. Rikans, T. Yamano, Mechanisms of cadmium-mediated acute hepatotoxicity, J. Biochem. Mol. Toxicol. 14 (2000) 110 - 117.

[46] J. E. B. Katari, V. L. Colvin, A. P. Alivisatos, X-ray Photoelectron spectroscopy of CdSe nanocrystals with applications to studies of the nanocrystal surface**,** J. Phys. Chem. 98 (1994) 4109 - 4117.

[47] A. P. Alivisatos, Perspectives on the physical chemistry of semiconductor nanocrystals, J. Phys. Chem. 100 (1996) 13226 - 13239.

[48] C. Kirchner, T. Liedl, S. Kudera, T. Pellegrino, A. MunozJavier, H. E. Gaub, S. Stolzle, N. Fertig, W. J. Parak, Cytotoxicity of colloidal CdSe and CdSe/ZnS nanoparticles, Nano Lett. 5 (2005) 331 - 338.

[49] G. Z. Chen, X. Z. Huang, J. G. Xu, Z. Z. Zheng, Z. B. Wang, The methods of fluorescence analysis, second ed., Beijing Science Press, Beijing, (1990).

[50] B. F. Pan, F. Gao, L. M. Ao, Investigation of interactions between dendrimer-coated magnetite nanoparticles and bovine serum albumin, J. Magn. Magn. Mater. 293 (2005) 252 - 258.

[51] Q. Xiao, S. Huang, Z. D. Qi, B. Zhou, Z. K. He, Y. Liu, Conformation, thermodynamics and stoichiometry of HSA adsorbed to colloidal CdSe/ZnS quantum dots, Biochim. Biophys. Acta 1784 (2008) 1020 - 1027.

[52] A. Sułkowska, M. Maciazek, J. Rownicka, B. Bojko, D. Pentak, W. W. Sułkowski, Effect of temperature on the methotrexate – BSA interaction: Spectroscopic study, J. Mol. Struct. 834 – 836 (2007) 162 - 169.

[53] M. Iosin, F. Toderas, P .L. Baldeck, S. Astilean, Study of protein–gold nanoparticle conjugates by fluorescence and surface-enhanced Raman scattering, J. Mol. Struct. 924 –926 (2009) 196 - 200.

ACCEPTED MANUSCRIPT

[54] J. R. Lakowicz, Principles of fluorescence spectroscopy, third ed., Plenum Press, New York, (2006).

[55] J. Liang, Y. Cheng, H. Han, Study on the interaction between bovine serum albumin and CdTe quantum dots with spectroscopic techniques, J. Mol. Struct. 892 (2008) 116 - 120.

[56] S. F. Sun, B. Zhou, H. N. Hou, Y. Liu, G. Y. Xiang, Studies on the interaction between Oxaprozin-E and bovine serum albumin by spectroscopic methods, Int. J. Biol. Macromol. 39 (2006) 197 - 200.

[57] T. Hiratsuka, Conformational changes in the 23-kilodalton NH2-terminal peptide segment of myosin ATPase associated with ATP hydrolysis, J. Biol. Chem. 265 (1990) 18786 - 18790.

[58] A. C. Tedesco, D. M. Oliveira, Z. G. M. Lacava, R. B. Azevedo, E. C. D. Lima, P. C. Morais, Investigation of the binding constant and stoichiometry of biocompatible cobalt ferrite-based magnetic fluids to serum albumin, J. Magn. Magn. Mater. 272 – 276 (2004) 2404 - 2405.

[59] W. J. Parak, T. Pellegrino, C. Plank, Labelling of cells with quantum dots, Nanotechnology 16 (2005) R9 – R25.

[60] M. M. Dzagli, V. Canpean, M. Iosin, M. A. Mohou, S. Astilean, Study of the interaction between CdSe/ZnS core-shell quantum dots and bovine serum albumin by spectroscopic techniques, J. Photochem. Photobiol. A 215 (2010) 118 - 122.

[61] D. Leckband, Measuring the forces that control protein interactions, Annu Rev Biophys. Biomol. Struct. 29 (2000) 1 – 26.

[62] Q. Xiao, S. Huang, J. Ma, W. Su, P. Li, J. Cui, Y. Liu, Systematically investigation of interactions between BSA and different charge-capped CdSe/ZnS quantum dots, J. Photochem. Photobiol. A 249 (2012) 53 - 60.

ACCEPTED MANUSCRIPT

[63] D. P. Ross, S. Subramanian, Thermodynamics of protein association reactions: forces contributing to stability, Biochemistry 20 (1981) 3096 – 3102.

[64] N. T. Vo, H. D. Ngo, D. L. Vu, A. P. Duong, Q. V. Lam, Conjugation of E. coli O157:H7 Antibody to CdSe/ZnS Quantum Dots, J. Nanomaterials Article ID 265315 (2015) 1 - 7.

Table 1: Percentage constituents of each identified element in the CdSe, CdSe/ZnS, and CdSe/CdS QDs obtained from EDX analysis.

QDs	Element	Weight %	Atom %
CdSe	Cd	66.32	58.04
	Se	33.68	41.96
CdSe/ZnS	Cd	63.86	52.48
	Se	27.79	32.52
	Zn	6.16	8.70
	S	2.19	6.30
CdSe/CdS	Cd	68.77	55.77
	Se	26.38	30.45
	S	4.85	13.78

Table 2: Spectral parameters and quantum yield (QY) of different quantum dots at room temperature.

Sample	λ_{abs} (nm)	λ_{PL} (nm)	FWHM (nm)	Diameter (nm)	QY
CdSe	537	557	31	3.4	25
CdSe/CdS	547	563	29	3.7	43
CdSe/ZnS	565	582	30	4.1	40

ACCEPTED MANUSCRIPT

Table 3. Lifetime and pre-exponential factors of various quantum dots at room temperature.

Sample	λ_{ex} (nm)	λ_{em} (nm)	τ_1 (ns)	τ_2 (ns)	τ_3 (ns)	α_1	α_2	α_3	τ_{Av} (ns)
CdSe	450	558	2.35±0.02	20.74±0.13	89.31±0.64	0.59	0.36	0.05	41.84
CdSe/CdS	450	566	2.18±0.03	11.70±0.21	66.69±0.97	0.68	0.30	0.02	21.08
CdSe/ZnS	450	580	1.13± 0.2	7.48±0.17	45.79±0.75	0.77	0.22	0.01	11.53

Table 4. Stern-Volmer association constants K_{SV} and relative thermodynamics parameters of the CdSe/ZnS-BSA QDs.

System	T (K)	K_{SV} ($\times 10^9$ LMol^{-1})	ΔH (kJ Mol^{-1})	ΔG (kJ Mol^{-1})	ΔS (JMol^{-1}K^{-1})	R[a]	S.D.[b]
CdSe/ZnS	293	0.0342	-19.52	-49.37	101.88	0.99	0.096
	308	0.0459		-50.89			
	318	0.0650		-51.91			

ACCEPTED MANUSCRIPT

[a]R is the correlation coefficient, and [b]S.D. is the standard deviation

Figure caption

Scheme 1. Schematic diagram of core (CdSe) and core-shell (CdSe/CdS & CdSe/ZnS) quantum dots.

Figure 1. The HRTEM images (a, b, and c) and corresponding size histogram (a', b', and c') of CdSe, CdSe/ZnS and CdSe/CdS, core-shell Q-dots, respectively. Inset show the continuous lattice fringes.

Figure 2. The XRD pattern of (a) CdSe-core, (b) CdSe/ZnS, and (c) CdSe/CdS core-shell Q-dots. The peak identified with the standard JCPDS software.

Figure 3. The absorption (a) and photoluminescence (b) spectra of CdSe/ZnS core-shell Q-dots dispersed in toluene at room temperatures. The excitation wavelength was 450 nm for PL spectra.

ACCEPTED MANUSCRIPT

Figure 4. The absorption (a) and photoluminescence (b) spectra of CdSe/CdS core-shell Q-dots dispersed in toluene at room temperature. The excitation wavelength was 450 nm for PL spectra.

Figure 5. The time-resolved photoluminescence decay curves (solid lines) together with simulated curves (dotted lines) of CdSe, CdSe/CdS and CdSe/ZnS QDs measured at PL maxima. The excitation wavelength was 450 nm. The dotted line shows the response function.

Figure 6. (A) The phase contrast microscopy of L929 fibroblast cells with CdSe (a,b,c), CdSe/CdS (d,e,f) and CdSe/ZnS (g,h,i) QDs over 1 - 3 days of incubation and (B) MTT assay analysis.

Figure 7. The absorption (a) and photoluminescence (b) spectra of BSA, CdSe/ZnS QDs (water soluble) and CdSe/ZnS QDs + BSA. The excitation wavelength was 278 nm for PL spectra.

Figure 8. (a) Photoluminescence spectra of BSA with various concentration of CdSe/ZnS QDs (water soluble) and (b) Stern-Volmer plot at room temperature. The excitation wavelength was 278 nm for PL spectra.

Figure 9. (a) Stern–Volmer plots for the BSA as a function of the concentration of CdSe/ZnS QDs at different temperatures and (b) Van't Hoff plot for the interaction of BSA with CdSe/ZnS QDs.

Figure 10. The FTIR spectra of surface modified (water soluble) CdSe, CdSe/ZnS and CdSe/ZnS QDs and MPA.

ACCEPTED MANUSCRIPT

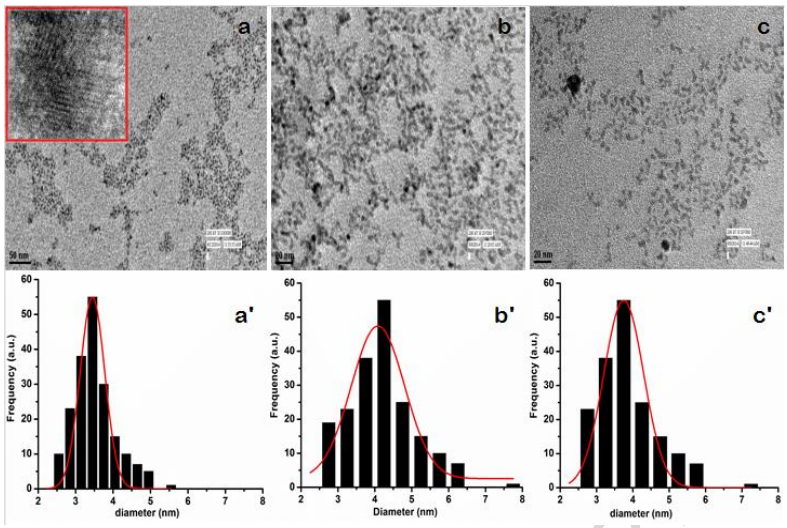


Figure 1

ACCEPTED MANUSCRIPT

ACCEPTED MANUSCRIPT

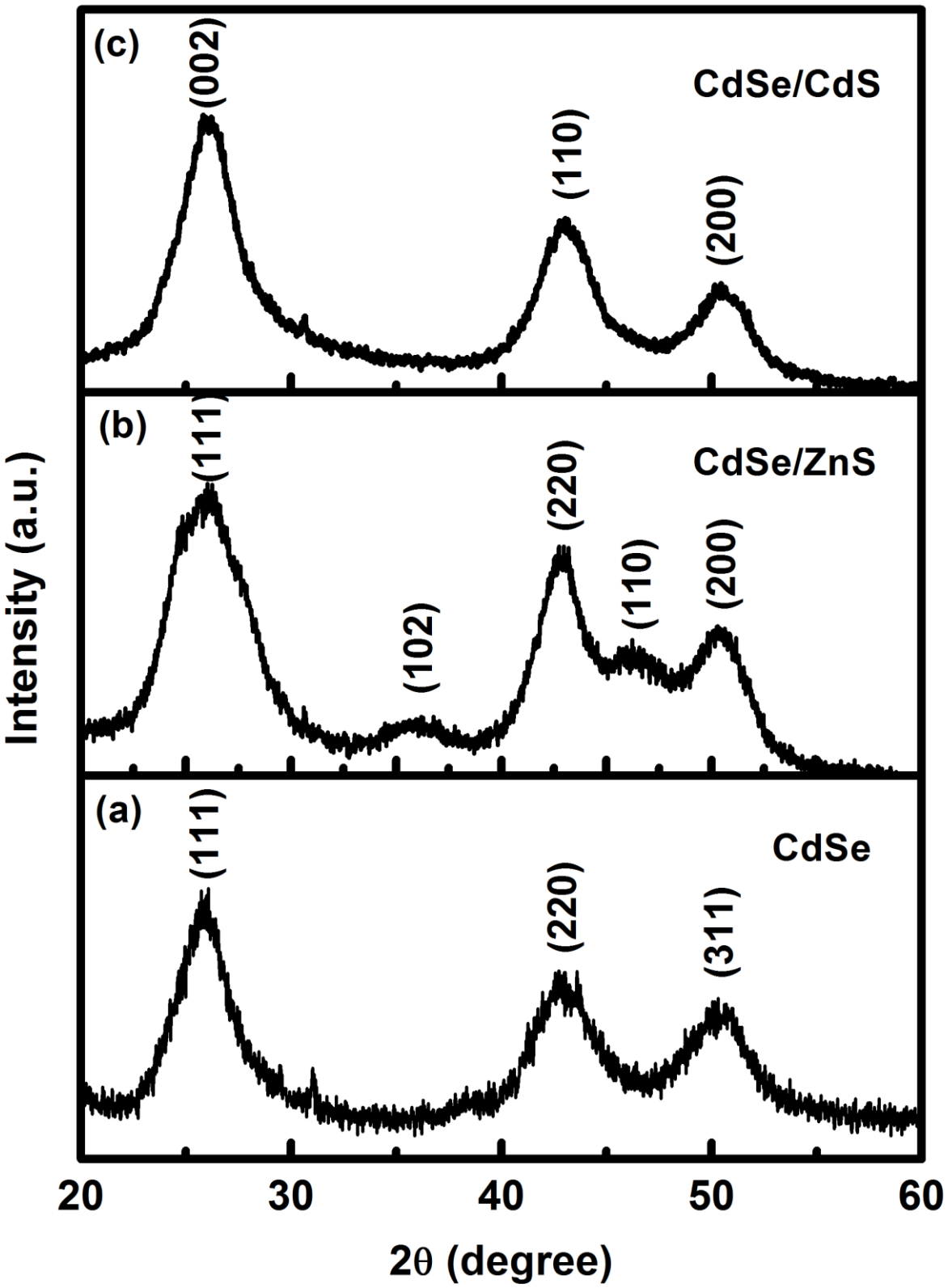


Figure 2

ACCEPTED MANUSCRIPT

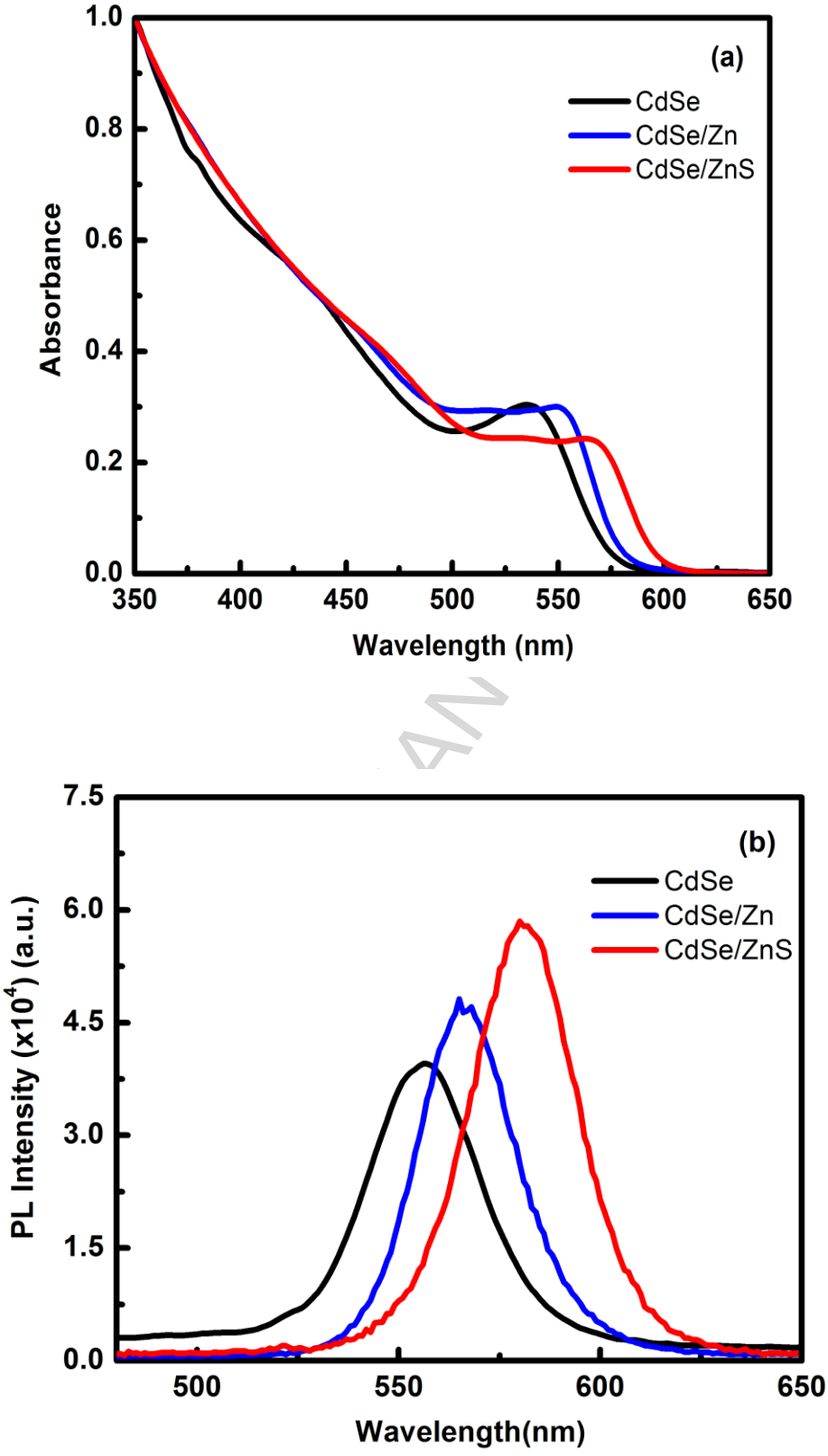


Figure 3

ACCEPTED MANUSCRIPT

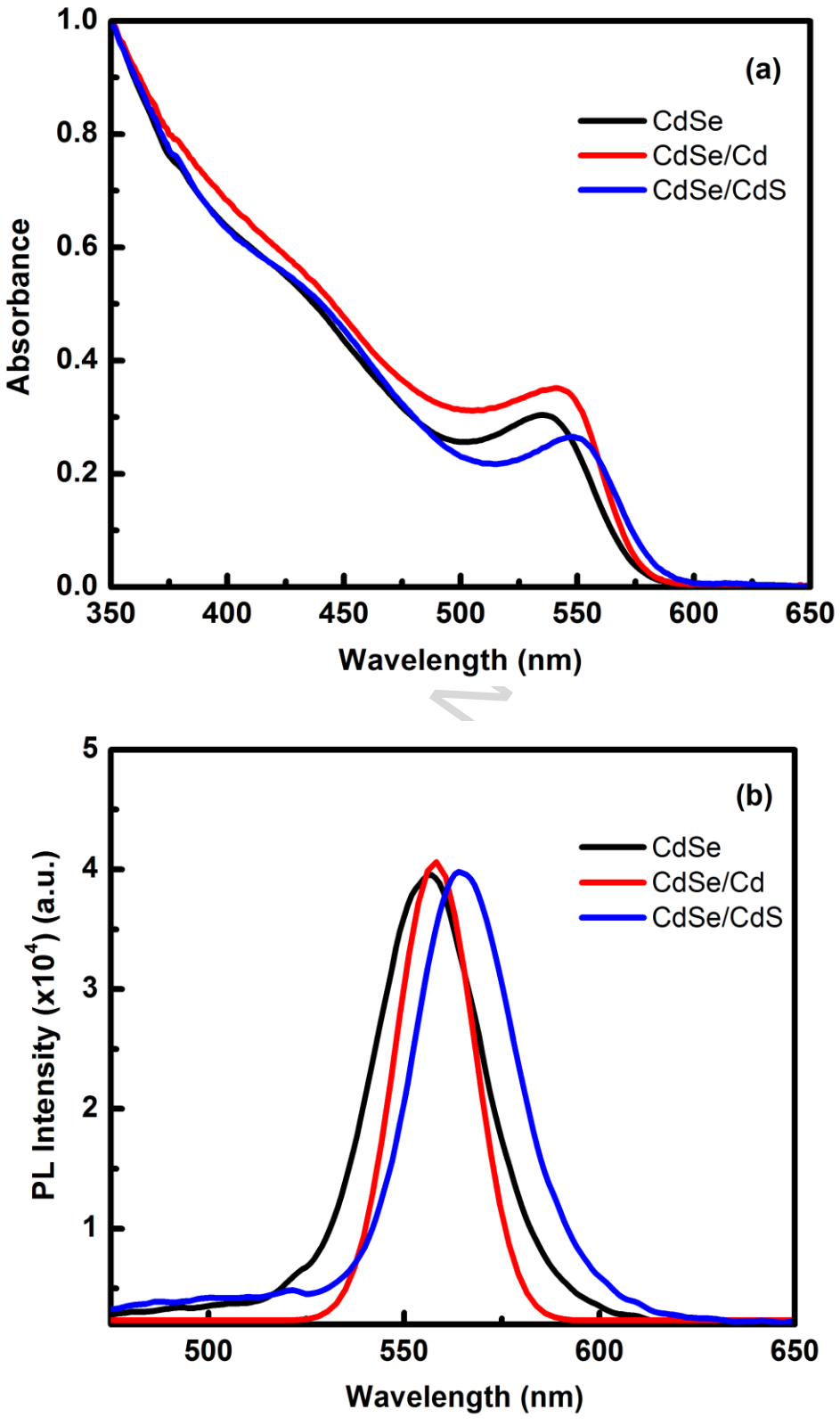


Figure 4

ACCEPTED MANUSCRIPT

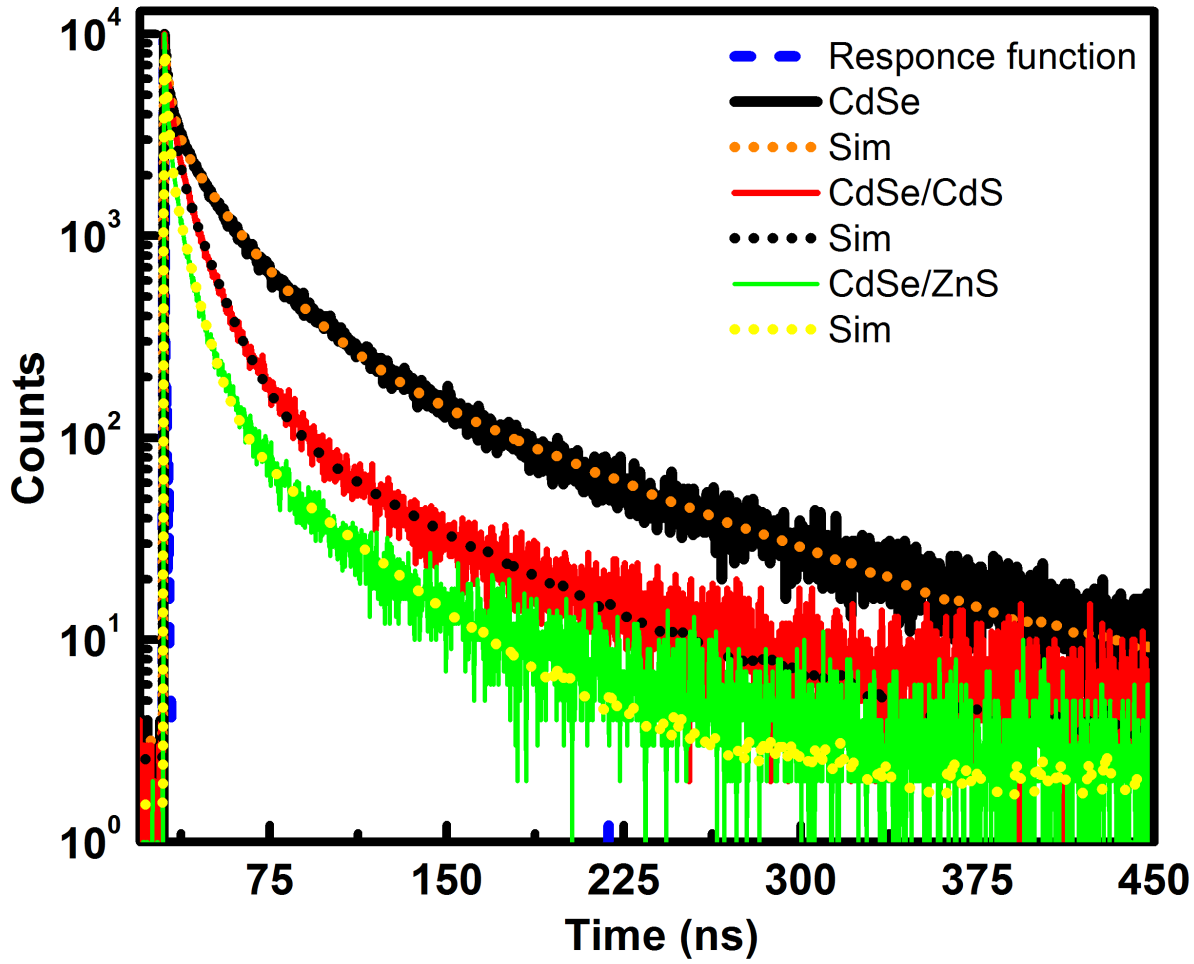


Figure 5

ACCEPTED

ACCEPTED MANUSCRIPT

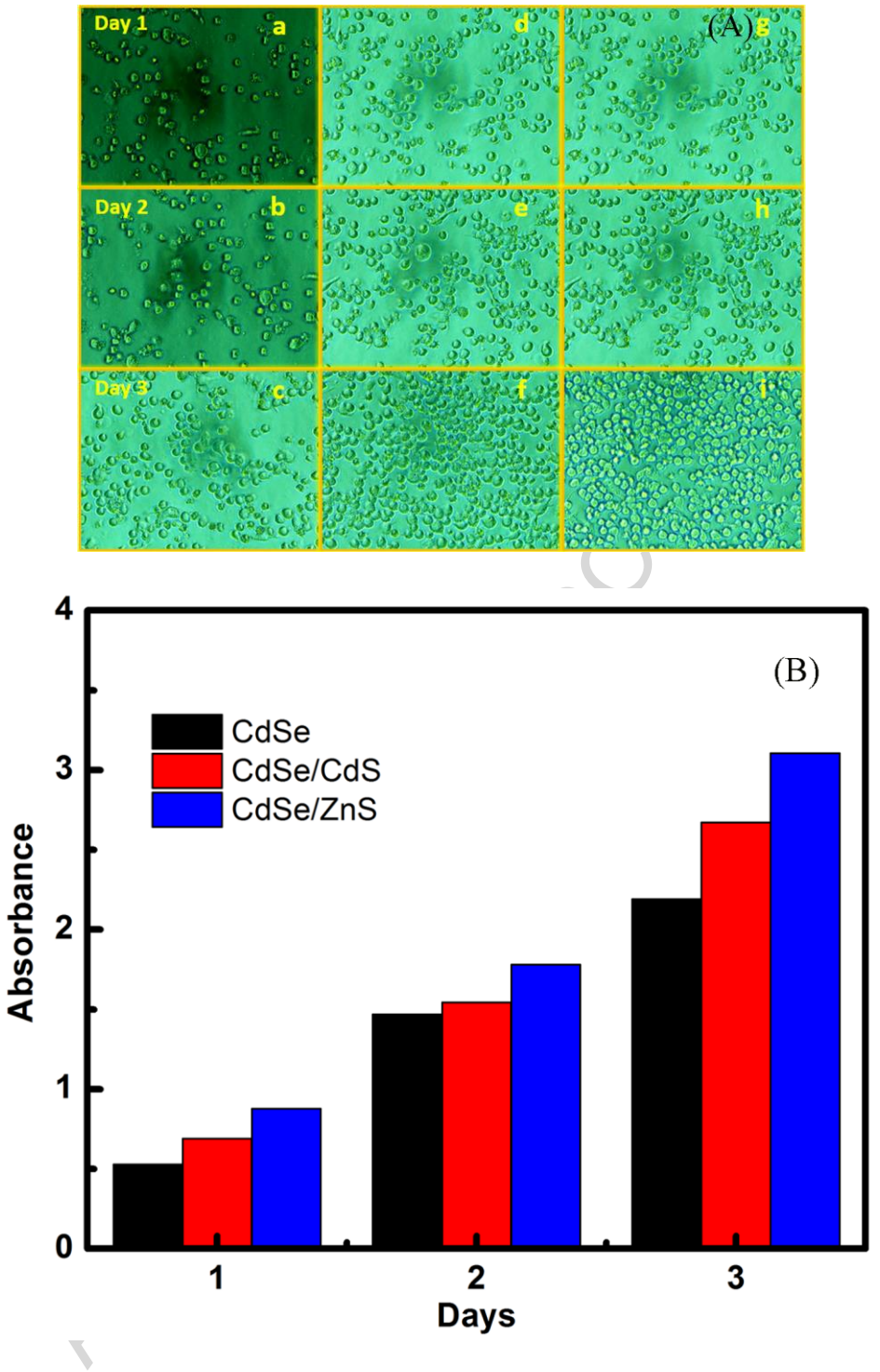


Figure 6

ACCEPTED MANUSCRIPT

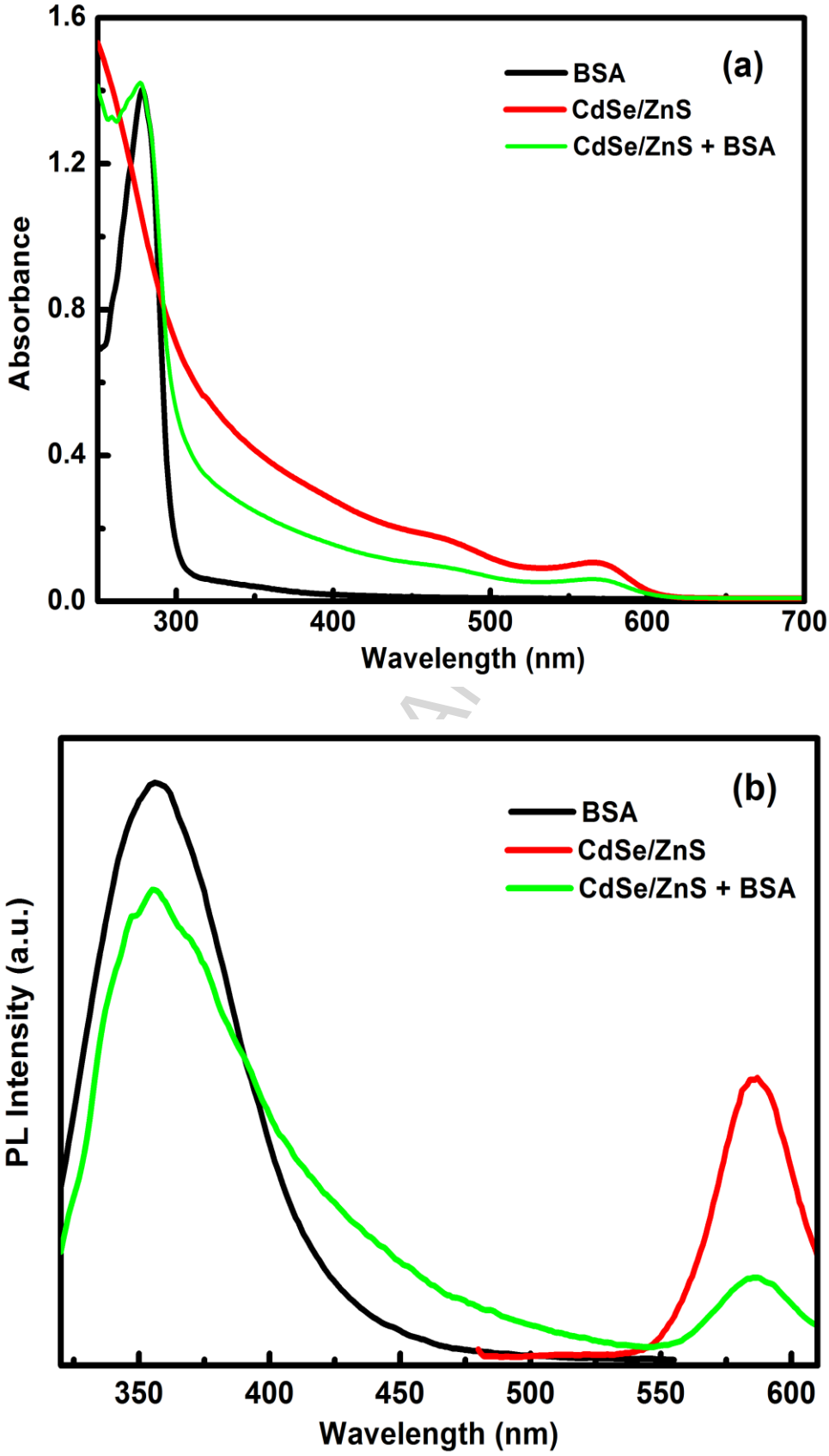


Figure 7

ACCEPTED MANUSCRIPT

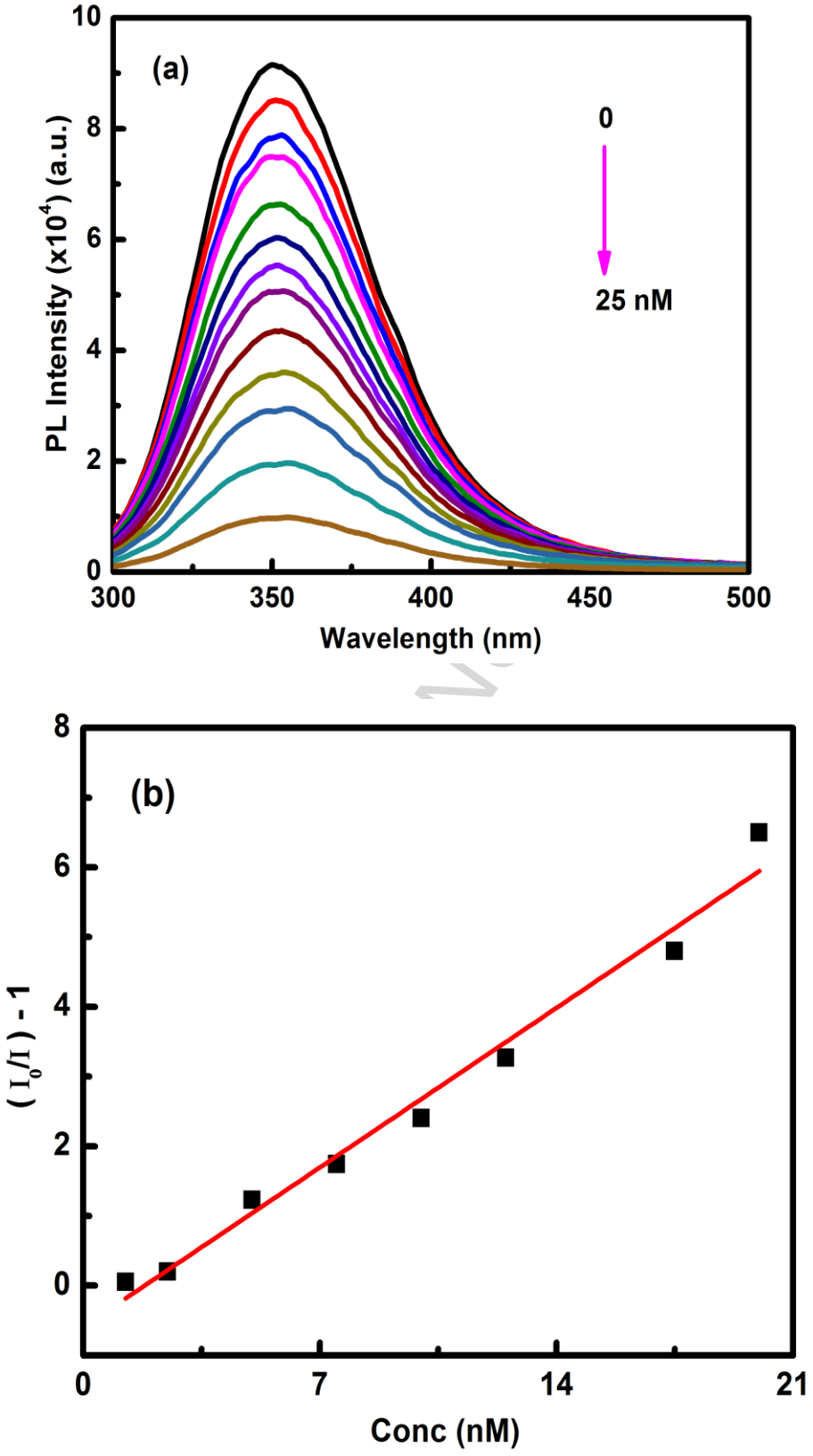


Figure 8

ACCEPTED MANUSCRIPT

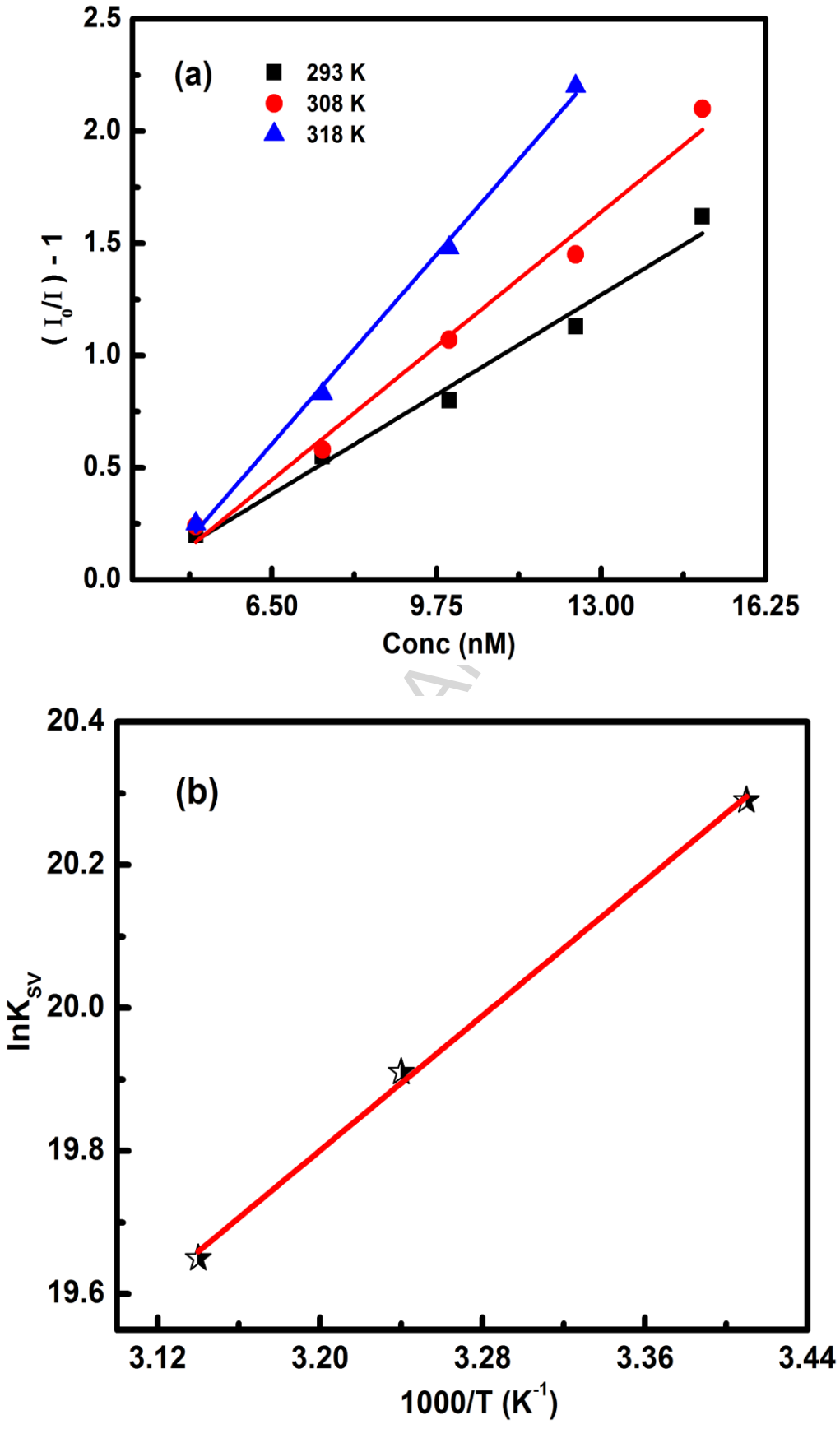


Figure 9

ACCEPTED MANUSCRIPT

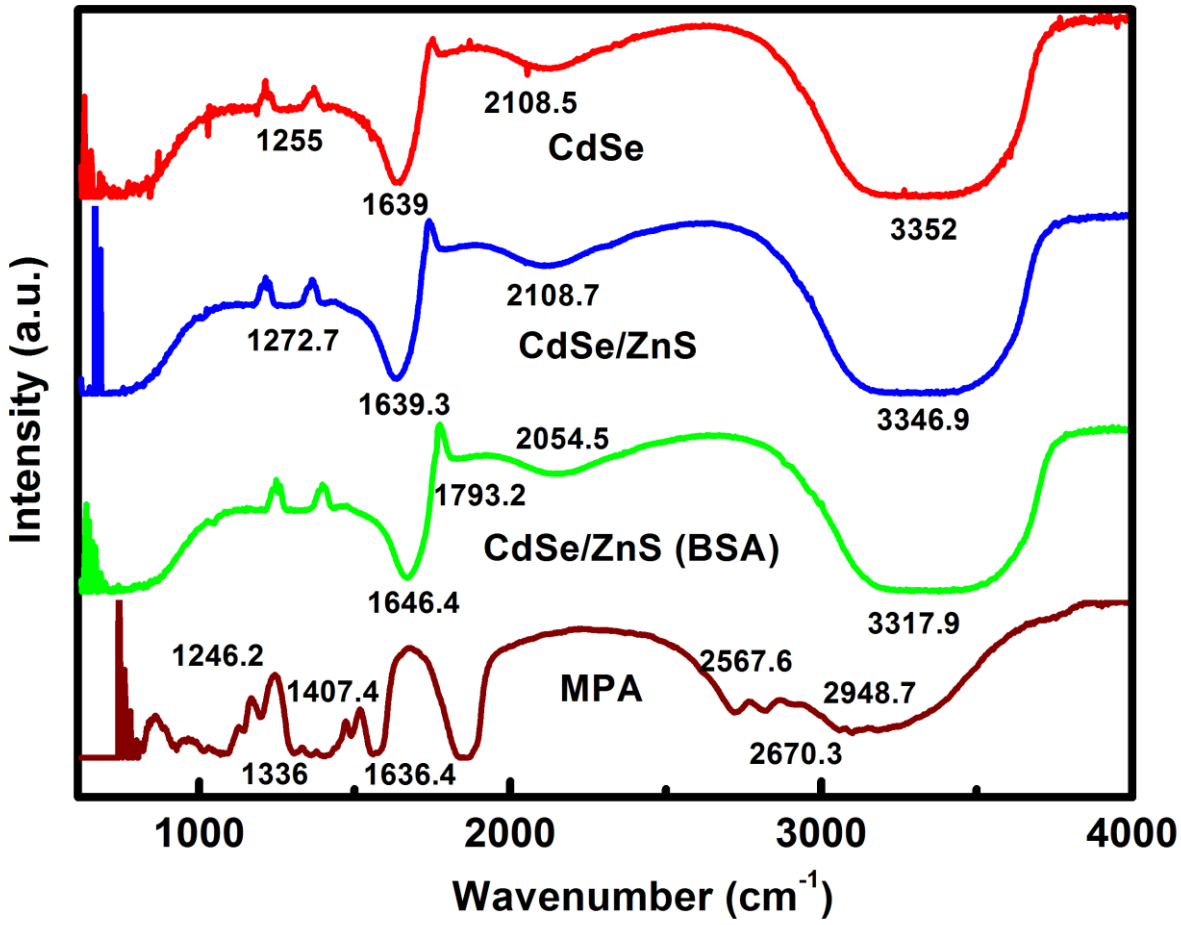
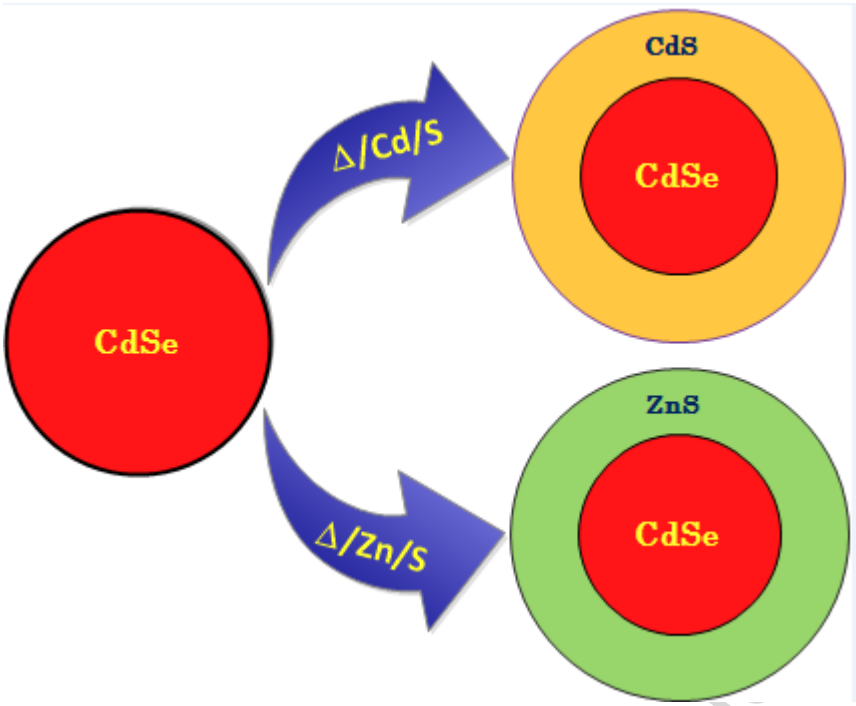


Figure 10

ACCEPTED

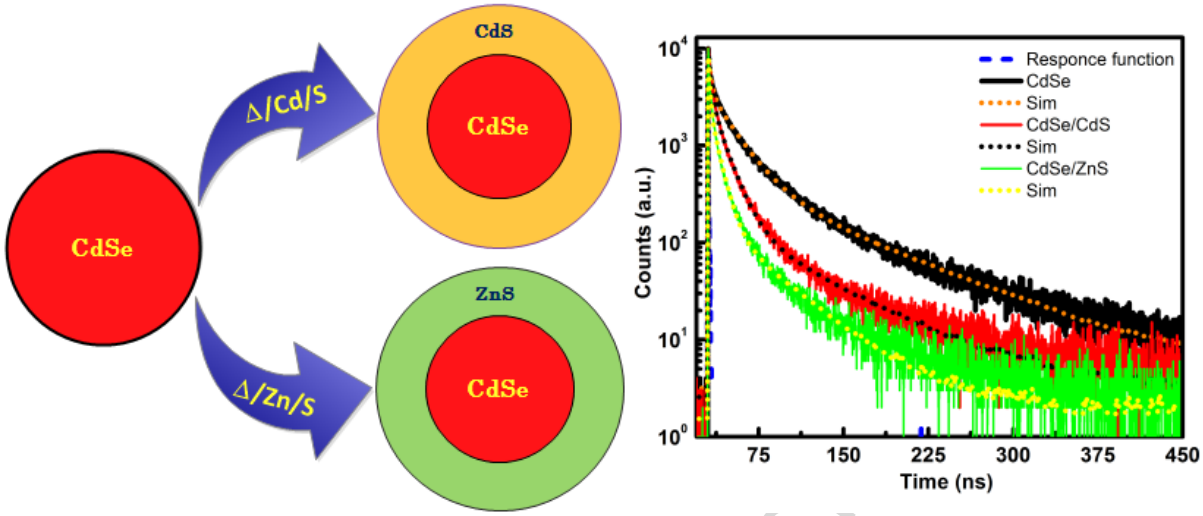
ACCEPTED MANUSCRIPT



Scheme 1

ACCEPTED MANUSCRIPT

ACCEPTED MANUSCRIPT



Graphical abstract

ACCEPTED MANUSCRIPT

ACCEPTED MANUSCRIPT

Research highlights

1. Highly luminescent and stable core-shell QDs were prepared using SILAR technique.
2. Ligand exchange technique was used to convert hydrophobic QDs into hydrophilic.
3. The PL quenching of BSA by QDs is predominantly static in nature.
4. The PL quantum yield of core-shell QDs is higher than the only core QDs.
5. CdSe/ZnS QDs shows the least toxicity/most biocompatibility and sensing ability.

ACCEPTED MANUSCRIPT

Available online at www.ijapie.org

International Journal of Advanced
Production and Industrial Engineering

IJAPIE-SI-IDCM 604 (2017) 16–19

Special Issue on

INNOVATIVE DESIGN
&
COMPUTATIONAL
MODELLING

Modelling and Simulation of Thermoelectric Peltier Effect Cooling Unit

Vineet Mathew*, Akhilesh Arora, B. B. Arora, Saurabh Dubey,
Rayhan Ali, Sushant Sahasrabuddhe
Delhi Technological University, Delhi-110042
Email: vineetdtu@gmail.com

Abstract : Thermoelectric coolers being a Freon free technology with the added advantage of flexibility in mounting position and precise temperature control, are being extensively used in portable applications. The relatively lower efficiency compared to conventional cooling systems is neglected owing to its portability and pollution free nature. The aim of this study is to successfully model a Cooling Unit using a TEC and extended hot side and cold side heat transfer surfaces. The cooling medium is chosen as air. The heat transfer surfaces are Aluminium Extrusions. Modelling and simulation was done on ANSYS Icepak. ANSYS Icepak is a computational package for the thermal management of electronic components. ANSYS Icepak solves for fluid flow and includes all modes of heat transfer i.e. conduction, convection and radiation. In this study the effect of the radiation mode of heat transfer was neglected. A suitable turbulence model is selected that can properly describe flow in the system. After successfully meshing the assembly and setting up the prerequisite conditions, velocity and temperature contours have been plotted to show the nature of flow and temperature distribution across the surroundings as well the cooling elements. The analysis results can assist in the development of cooling strategies to further increase its effectiveness.

Keywords: TEC, Peltier Effect, Cooling Unit, ANSYS Icepak, Heat Transfer, Heat Sinks, CFD, Modelling, Simulation, Turbulence Model

I. INTRODUCTION

Thermoelectric effect refers to the conversion of voltage difference into a temperature gradient or vice-versa. Conversely, a temperature difference will generate a voltage difference. Therefore, by connecting a TEC to a power source, a temperature difference can be generated on either side of the TEC. The thermoelectric effect can be used to generate electricity, measure temperature and also act as a temperature regulator as the hot and cold side of a TEC can be interchanged as it is dictated by the polarity of the applied voltage.

The Thermoelectric effect encompasses mainly two effects, The Seebeck effect and the Peltier Effect. The Peltier effect is named after French physicist Jean Charles Athanase who discovered it in 1834. It is the generation of a hot and cold side at an electrified junction of two different conducting materials. When a current is made to flow through a junction between two conductors A and B, heat may be generated (or removed) at the junction. The heat generated at the junction per unit time, $\dot{Q}$, is given by:

$$\dot{Q} = (\pi_A - \pi_B)I$$

Where Π_A ,Π_B are the Peltier coefficients of conductors A and B respectively, and I is the electric current (from A to B). Joule heating and thermal gradient effects may also effect heat generation. Peltier effect TECs allow cooling below ambient temperature, but unlike other cooling systems that allow this (vapour phase refrigeration), they are less expensive and more compact. Peltier elements are solid-state devices with no moving parts; they are extremely reliable and do not require any maintenance. These are extremely light weight components.

The temperature difference generated by a Peltier TEC is dependent on many variables. The TEC model used in the simulation is Melcor_CP1.0-127-06. The Heat Transfer is inversely proportional to the temperature difference between the Hot side and the Cold side. Hot Side temperature and Ambient Temperature also affect the performance of the Peltier Module.

Ozturk and Tari [1] did a Computational Fluid Dynamics Modelling on a Computer Chassis by mainly concentrating on the comparison of computational results and documented experimental results. The study showed reasonable results with the zero equation turbulence model citing higher computational costs of the k-epsilon model. Yu and Webb [2] used ANSYS Icepak to simulate a 80W CPU to find a probable heat management solution for AGP and PCI cards. The cooling solution was based on a vertical cooling duct. Chang [3] using Icepak was able to reduce the temperature of a 30W CPU socket by 10^{o}C using ducts when compared to a non-ducted setup. Alvin and Chu [5] studies the thermal management of LED lamps by getting a numerical solution using ANSYS Icepak. Additionally heat rejecting materials were also analysed in terms of their effectiveness.

The objective of this study is to successfully model a Portable Cooling Unit using ASYS Icepak by selecting an appropriate turbulent flow model for this application. The Models for Heat Sink and Cold Sink surfaces and TEC is selected from the comprehensive library in ANSYS Icepak.

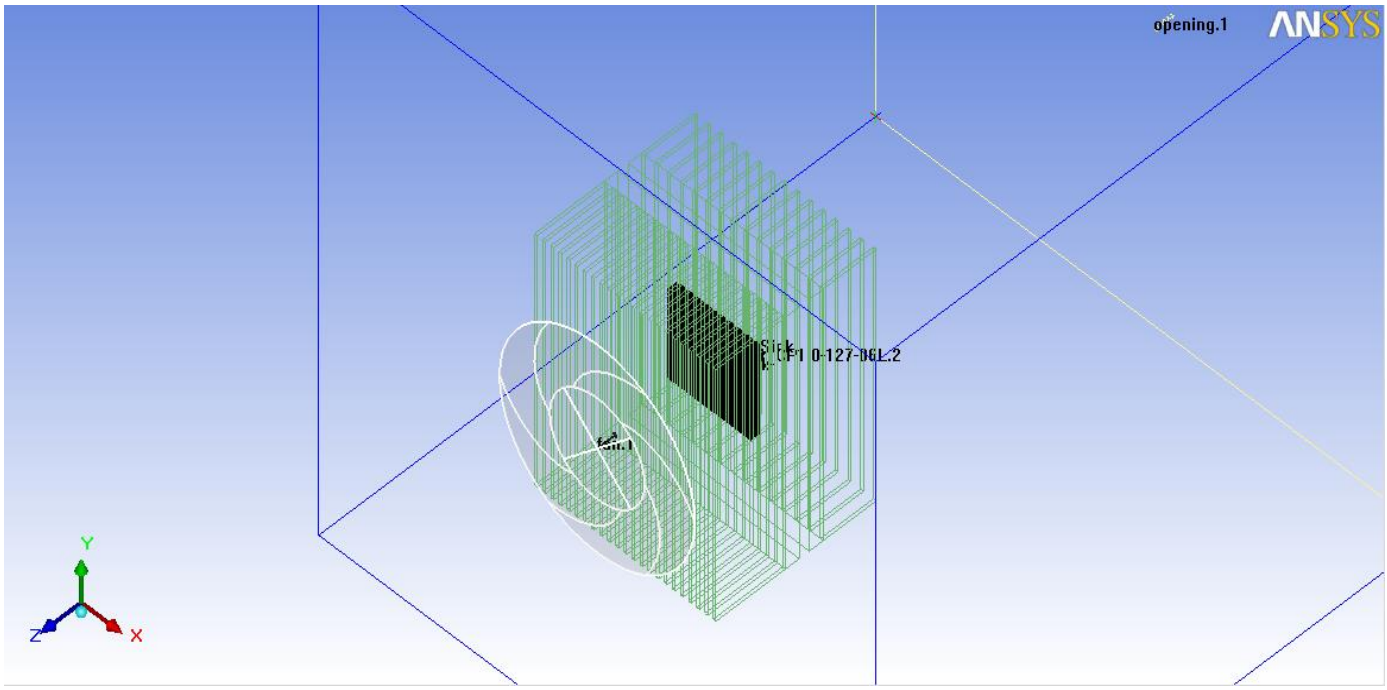


Fig. 1 Isometric view of the assembly

ANSYS Icepak is specifically suited for CFD and Thermal Analysis for electronic components [4]. ANSYS Icepak uses FLUENT as its solver.

II. GEOMETRY

The model consists of a Peltier model Melcor_CP1.0-127-06L.2 from the TECs library in ANSYS Icepak. The dimensions for the heat transfer surfaces are specified in the table below. Cabinet Size is 0.2 X 0.1 X 0.1 (m).

The peltier module is sandwiched between two extended heat transfer surfaces. The interface is assumed to ideal such that no heat is lost at the contact plane. An intake fan is placed at a distance 10mm from the hot side extended heat transfer surface. The flow rate is taken as fixed in terms of volumetric flow rate. This is a reasonable assumption since we are targeting a steady state solution. The fins for both the Heat Sink and the Cold sink are long the Y-Axis.

A. *Extended Heat Transfer Surface Specifications:*

	Heat Sink	**Cold Sink**
Fin Material	Aluminium Extrusion	Aluminium Extrusion
Base Material	Aluminium Extrusion	Aluminium Extrusion
Thermal Conductivity (W/m-K)	204	204
Density (kg/m3)	2800	2800
Dimensions (mm)	85 X 65 X 30	85 X 65 X 24
Base Height (mm)	5	5
Number of Fins	23	15

B. *Cooling Fan Specifications:*

Inner Diameter (mm)	17
Outer Diameter (mm)	35
Flow Rate (cfm)	44

C. *Peltier Module Specifications:*

Hot Side Temperature (^oC)	25	50
Qmax (Watts)	25.7	29.1
Delta Tmax (^oC)	67	77

The specifications for the Heat Sink, Cold Sink as well as the cooling fan have been taken from a CPU cooling unit available in the market.

III. SOLUTION SETUP

ANSYS Icepak is capable of automatic meshing. Non-Conformal Mesh was created using the automatic unstructured Mesher-HD (Hex dominant). The advantage of generating a non-conformal mesh is that the number of elements is relatively lower and the degree of accuracy remains largely unaffected.

- An initial coarse mesh was generated. Mesh was examined for skewness using cut plains in the geometry

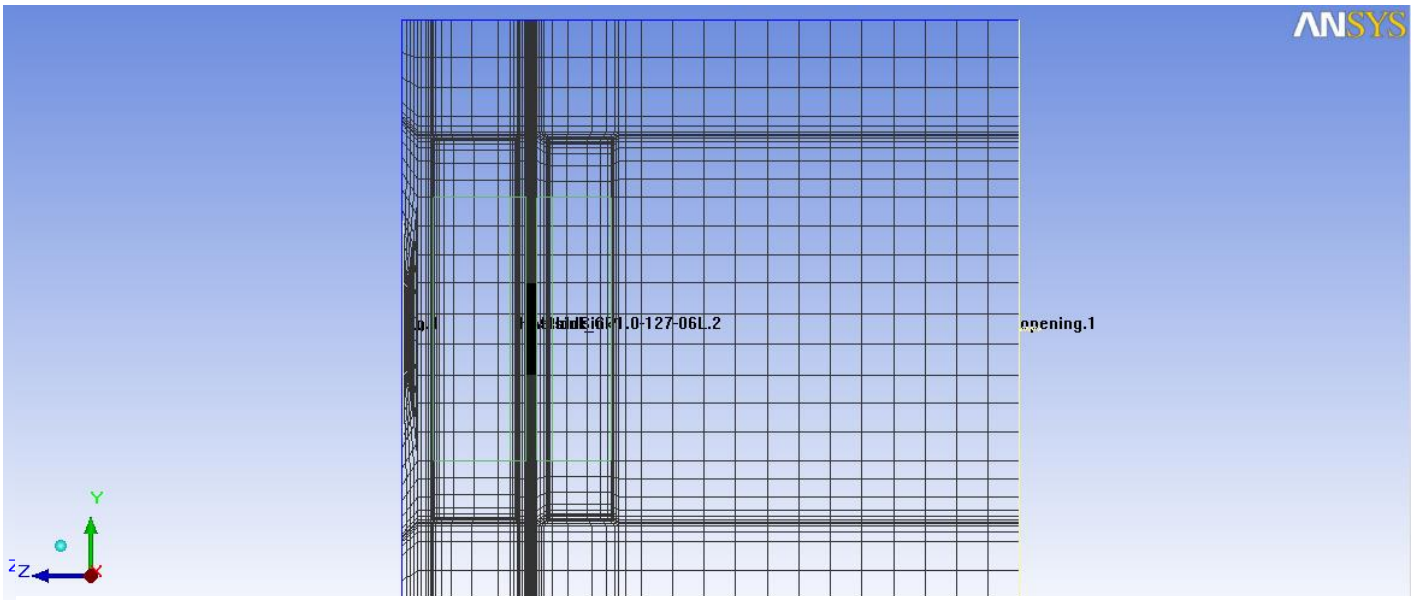


Fig. 2 Y-Z plane view of the generated mesh

- To appropriately capture regions of reversed flow and the formation of wakes, virtual air boxes were placed at such regions and were meshed separately. This is done so that the total number of elements does not exceed the maximum limit and details in the temperature and flow distribution can be accurately visualized.

- Skewness in a few elements is present found near the fan. This is because the unstructured Mesher-HD automatically creates a skewed mesh to better reciprocate the air flow from the fan.

A. *Mesh properties*

Total elements in the mesh are 220330 with the number of nodes 230530. Quality check of the mesh produced a face alignment quality of the range 0.0819063 ->1. Since this is the acceptable range, the mesh is appropriate.

In the study, Flow as well as Temperature was solved for. The effects of radiation were neglected with the scope restricted to conduction and convection. Ambient Temperature selected was 35^{o}C. Examination of the model reveals a clear possibility of flow separation as well reversed flow; therefore the turbulent regime model selected was the Enhanced Realized K-epsilon model [6]. The analysis was conducted to produce a steady state solution.

B. *The following are the convergence criteria:*

Maximum number of iterations	2000
Flow	1e-3
Energy	1e-7
Turbulent Kinetic Energy	1e-3
Turbulent Dissipation Rate	1e-3
Joule heating	1e-7

IV. ASSUMPTIONS

The contact between the TEC, The Heat Sink, and The Cold Sink is assumed to be perfect. The presence of a convective film is neglected. The Cabinet is assumed to be fully insulated from the surrounding. The effects of radiation are neglected. The flow type of the fan is fixed and the intake air is of ambient temperature. Since preliminary investigation reveals the possibility of reversed and separated flow, zero equation turbulence model has not been used since the solution of the simulation may be incomplete or misleading [7].

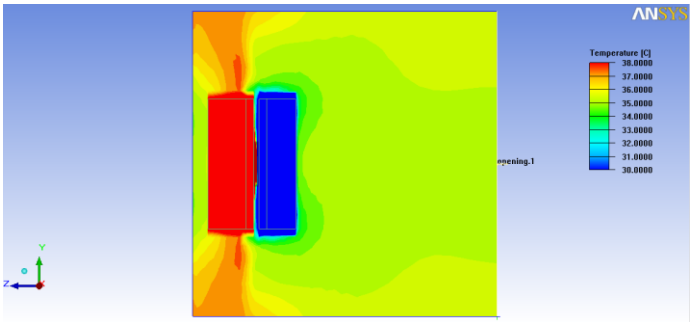


Fig. 2 Temperature Distribution between 30-38 ^{o}C

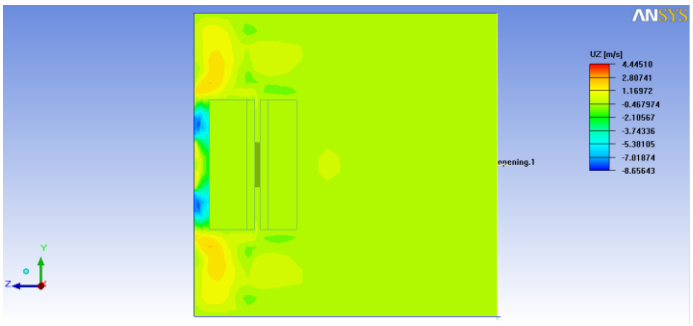


Fig. 4 Y-Z plane z-Velocity contour

Fig. 3 Y-Z plane Temperature Contour

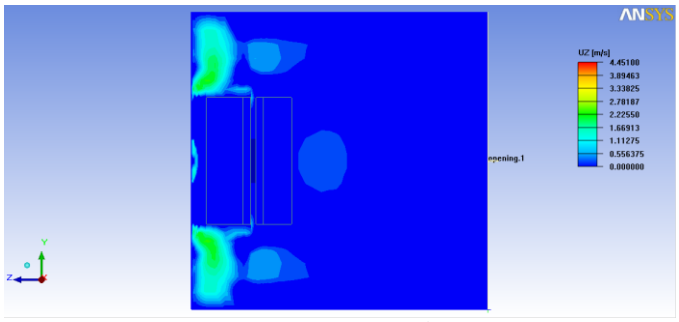


Fig. 5 Y-Z plane reverse flow

The analysis reveals a maximum temperature of 53°C and minimum temperature of 14°C as shown in Fig 2. This is the temperature of the hot side and cold side of the Peltier Module. On further examination in the temperature range of 30°C to 38°C (Fig. 3) the penetration of the cold side temperature of the Peltier Module can be visualized. Velocity Contours in the Z direction (along the model) in Fig 5 show regions of reverse flow (positive values). Further resolution in the reverse flow range can be seen in Fig 6. Reverse flow is generated at the top and bottom of the heat sink which is expected because of the air flow due to the intake fan. A region of reverse flow is also generated right after the cold sink.

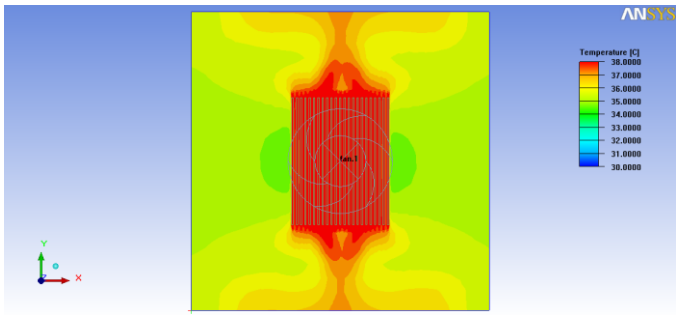


Fig. 6 X-Y plane Temperature Contour at 15% distance from the fan

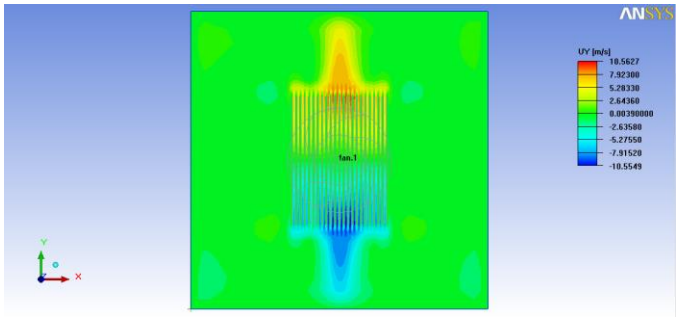


Fig. 7 X-Y plane y-Velocity Contour at 15% distance from the fan

Temperature distribution in the Heat Sink and the Cold Sink shows a concentration at the centre. The temperature bands follow a concave contour with respect to the base of the heat or cold sink. The Heat dissipated from the hot side of the Peltier Module spreads along the length of the fins due the presence of an intake fan. This is also a region of reversed flow. Fig. 7 shows the temperature contour in the X-Y plane at 15% the length of the cabinet. The Y component contour for the velocity closely resembles the temperature contours at the same location (Fig.8). This shows the influence of the intake fan.

V. Conclusion

In this study a TEC cooling unit with Hot Cold extended transfer surfaces was modelled and simulated. The following are the insights that could be drawn from this study.

- The zero equation turbulence model may give suitable results when it comes to maximum and minimum temperatures but for an accurate visualization of the distribution of temperature and velocity across the system the k-epsilon model is more suitable.
- To capture details regarding reverse flow, non-conformal meshing using assemblies should be carried out at regions of interest rather than increasing the elements size throughout the system.
- The effect of radiation can be ignored due to the overbearing influence of forced convection.

The analysis was conducted for the cooling unit in air as the surround medium. The cold sink can be inserted into a container of different medium. The methodology used in the setting up this solution can be extended to a water cooling apparatus.

References

[1] Emre Ozturk & Ilker Tari *CFD Modeling of Forced Cooling of Computer Chassis*, Engineering Applications of Computational Fluid Mechanics, 2007.

[2] C.-W. Yu, and R. L. Webb, "*Thermal Design of a Desktop Computer System Using CFD Analysis*," Seventeenth IEEE-SEMI-THERM Symposium. 2001.

[3] J. Y. Chang, C. W. Yu, and R.L.Webb, "*Identification of Minimum Air Flow Design for a Desktop Computer Using CFD Modelling*", 7th Intersociety Conference on Thermal and Thermomechanical Phenomena in Elec-tronic Systems, Vol.1, pp. 330-338,2000.

[4] Zahn, B., *"Evaluating Thermal Characterization Accuracy Using CFD Codes - A Package Level Benchmark Study of IcePak™ and Flotherm®,"* Proceedings of 6th Inter-society Conference on Thermal and Thermomechanical Phenomena in Electronic Systems (I-THERM), pp. 322-329, 1998.

[5] Christian Alvin, Webber Chu, Ching-Hung Cheng, Jyh-tong Teng, "Thermal analysis of extruded aluminum fin heat sink for LED cooling application", *Microsystems Packaging Assembly and Circuits Technology Conference (IMPACT) 2011 6th International*, pp. 397-400, 2011.

[6] C.C. Liu, Y.M. Ferng, C.K. Shih,"*CFD evaluation of turbulence models for flow simulation of the fuel rod bundle with a spacer assembly*", Applied Thermal Engineering, Volume 40, July 2012, Pages 389-396

[7] http://jullio.pe.kr/fluent6.1/help/html/ug/node402.htm

Astrophys Space Sci (2017) 362:52
DOI 10.1007/s10509-017-3032-0

ORIGINAL ARTICLE

New agegraphic dark energy model in Brans-Dicke theory with logarithmic form of scalar field

Pankaj Kumar[1] · **C.P. Singh**[1]

Received: 1 November 2016 / Accepted: 6 February 2017
© Springer Science+Business Media Dordrecht 2017

Abstract In this paper, the cosmological evolution of new agegraphic dark energy (NADE) model is analyzed in Brans-Dicke theory within the framework of Friedmann-Robertson-Walker Universe. The power-law assumption on Brans-Dicke scalar field is reconsidered by assuming the logarithmic form. We derive the equation of state parameter w_D and deceleration parameter q of NADE model. It is observed that $w_D \to -1$ when $a \to \infty$, i.e., the NADE mimics cosmological constant in the late time evolution. Indeed, due to the assumption of logarithmic form of Brans-Dicke scalar field the NADE in Brans-Dicke theory behaves like NADE in general relativity in the late time evolution. The NADE model shows a phase transition from matter dominated phase in early time to accelerated phase in late time. We further extend NADE model by including the interaction between dark matter and NADE. In this case, w_D definitely crosses the phantom divide line ($w_D = -1$) in the late time evolution. The phase transition from matter dominated to NADE dominated phase may be achieved at early stage in interacting model. Further, we show that the interacting NADE model resolves the cosmic coincidence problem as the energy density ratio may evolve sufficiently slow at present.

Keywords Cosmology · New agegraphic dark energy · Brans-Dicke theory

✉ C.P. Singh
cpsphd@rediffmail.com

P. Kumar
pankaj.11dtu@gmail.com

[1] Department of Applied Mathematics, Delhi Technological University (Formerly Delhi College of Engineering), Bawana Road, Delhi 110 042, India

1 Introduction

The cosmological observations like type Ia supernovae (Riess et al. 1998; Perlmutter et al. 1999) have provided the convincing evidence that our Universe is dominated by two dark components containing dark matter (DM) and dark energy (DE). The nature of DM and DE is one of the most important issues today in modern cosmology. The dark matter plays a role in explaining galactic curves and large scale structure where as dark energy explains the present cosmic accelerated expansion of the Universe. In the literature, the accelerating cosmologies have been described by two ways : dark energy content and modified gravity. In DE models, the accelerated expansion has been explained by modifying the right-hand side of the Einstein field equations, i.e., by modifying the energy-momentum tensor. The modified gravity theory corresponds to modifying the left-hand side of Einstein field equations, i.e., by modifying the geometric part. We refer Copeland et al. (2006) and Bamba et al. (2012) for detail study of DE models and modified gravity.

However, we are still far from a compelling theory which could explain not only the recent accelerated expansion but also the primordial cosmology, structure formation, DM problem etc. without facing any problem. Whatever the way we choose to explain these problems, the quantum effects should be incorporated to come up with an accurate theory of gravity. The gravity theory which incorporates the principles of quantum mechanics, known as quantum theory of gravity. Although, the quantum gravity is not a well established theory, there are some concepts which have been proposed on the principles of quantum gravity. In this context, the holographic dark energy (HDE) and agegraphic dark energy (ADE), which contain some significant properties of the quantum gravity, have been proposed as a candidate of DE to explain the recent accelerated expansion of

Published online: 15 February 2017

the Universe. These DE models are able to present a unified model of the Universe and explain some other problems of the modern cosmology like coincidence problem (Nojiri and Odintsov 2006).

The HDE models are based on the holographic principle ('t Hooft 1993) and have been studied extensively in the literature (Li 2004; Pavón and Zimdahl 2005; Setare 2007; Banerjee and Pavón 2007; Xu et al. 2009; Sheykhi 2009; Li et al. 2013a; Ghaffari et al. 2014). On the other hand, the ADE models are based on the quantum fluctuations of the space-time. Using the concept of quantum fluctuations of space-time, Károlyházy (1966) and Károlyházy et al. (1982, 1986) observed that the distance t in Minkowaski space-time can not be known to a better accuracy than

$$\delta t = \gamma t_p^{2/3} t^{1/3}, \tag{1}$$

where t_p denotes reduced Planck time and γ is a dimensionless constant of order unity. We assume $\hbar = k_b = c = 1$ throughout in this paper. Maziashvili (2007a, 2007b) has argued that the quantum energy density of the metric fluctuations of Minkowaski space-time can be estimated using the relation (1) with the time-energy uncertainty relation. Sasakura (1999) and Maziashvili (2007a, 2007b) have independently obtained the energy density of metric fluctuations of Minkowaski space-time which is given by

$$\rho_D \sim \frac{1}{t_p^2 t^2} \sim \frac{M_p^2}{t^2}, \tag{2}$$

where $M_p^2 = (8\pi G)^{-1}$ represents the reduced Planck mass. This energy density can be viewed as the density of DE, i.e., the ADE. Following the line of the relations (1) and (2), Cai (2007) proposed the original ADE model in which the energy density of the ADE has the form

$$\rho_D = \frac{3n^2 {M_p}^2}{T^2}, \tag{3}$$

where T is age of the Universe. The numerical factor $3n^2$ has been introduced to parameterize some uncertainties like the species of quantum fields in the Universe, the effects of curved space-time, etc. A number of papers on ADE models are available which deal with various aspects of the evolution of the Universe (Wei and Cai 2007, 2009; Kim et al. 2008; Neupane 2009; Lemets et al. 2011). Wei and Cai (2008a) have proposed a new version of this model referred as "new agegraphic dark energy" model, abbreviated as NADE by replacing the cosmic age T with the cosmic conformal age η for the time scale in (3). Thus, in this model, the dark energy density is of the form

$$\rho_D = 3n^2 M_p^2 \eta^{-2}, \tag{4}$$

where the conformal time η is defined as

$$\eta = \int_0^t \frac{dt}{a} = \int_0^a \frac{da}{Ha^2}, \tag{5}$$

where a is the scale factor of the Universe and $H = \dot{a}/a$ is the Hubble parameter. Here, an overdot denotes derivative with respect to the cosmic time t. The most attractive merit of the NADE is that it has been proven to fit the data well. The cosmological constraints and other aspects of NADE models have been studied in the literature (Wei and Cai 2008b; Setare 2010a; Sheykhi and Setare 2011, Saaidi et al. 2012; Zhang et al. 2013). Sheykhi and Setare (2010) have studied NADE model with varying gravitational constant G in a non-flat Universe. They have also generalized to viscous the NADE model in the presence of interacting term between dark components.

The Brans-Dicke (BD) theory (Brans and Dicke 1961), which is a natural alternative and simple generalization of general relativity, provides a suitable framework for dynamical DE models. In this theory, the gravitational constant G is replaced with the inverse of a time-dependent BD scalar field ϕ, namely, $\phi = (8\pi G)^{-1}$ which couples to gravity with a coupling parameter w. One important property of BD theory is that it gives simple expanding solutions for scalar field and scale factor which are compatible with the solar system observations. The BD theory explains the recent accelerated expansion of the Universe and accommodates the observational data as well (Bertolami and Martins 2000; Kim 2005; Clifton and Barrow 2006).

The HDE, ADE or NADE density belongs to a dynamical cosmological constant, we need a dynamical frame to accommodate it instead of Einstein gravity. Therefore, the investigation of the these models of dark energy in the framework of BD theory is well motivated. A number of authors (Setare 2007; Banerjee and Pavón 2007; Xu et al. 2009; Liu and Zhang 2009; Sheykhi 2010; Sheykhi and Jamil 2011) have studied HDE, ADE and NADE models in the framework of BD theory. Thus, it is quite natural to study the NADE in BD theory.

In the BD theory, the NADE models have been studied to discuss the recent accelerated expansion of the Universe (Liu and Zhang 2009; Sheykhi 2010; Sheykhi and Jamil 2011; Pasqua and Chattopadhyay 2013; Fayaz 2016). To the best of our knowledge in all the papers available in the literature on HDE, ADE and NADE models in the framework of BD theory, it has been assumed that the BD scalar field evolves as a power law of scale factor, $\phi \propto a^m$, m is a constant. In Liu and Zhang 2009, Sheykhi (2010) the NADE model have been investigated in detail, but there are some issues that should be re-scrutinized, e.g. power-law form of BD scalar field. One can observe that this relation would always give the constant deceleration parameter (DP) irrespective of the matter content. This means that the

phase transition of the Universe can not be obtained with the power-law form of BD scalar field.

In this paper, we revisit the power-law form of BD scalar field and propose a logarithmic relation between BD scalar field and scale factor of the Universe. We demonstrate that the logarithmic form of BD scalar field is not only suitable to explain the phase transition of the Universe but it also resolves the cosmic coincidence problem in an effective way. We derive the equation of state (EoS) parameter w_D and DP q of NADE model to discuss the evolution of the Universe. We further extend NADE model by including the interaction between dark matter and NADE in BD theory. We show that the interacting NADE model resolves the cosmic coincidence problem as the energy density ratio may evolve sufficiently slow at present.

The paper is organized as follows: In Sect. 2, we present the equations of motion of NADE model in the framework of BD theory. Further, Sect. 2 is divided into two Sects. 2.1 and 2.2. In Sect. 2.1, we discuss the non-interacting NADE model. Section 2.2 is devoted to interacting NADE model. The summary of our findings is presented in Sect. 3.

2 NADE in BD theory with logarithmic scalar field

The action for the BD theory in the Jordan frame (Liu and Zhang 2009) is given by

$$S=\int d^4x\sqrt{-g}\left[\frac{1}{2}\left(-\phi R+\frac{\omega}{\phi}g^{\mu\nu}\partial_\mu\phi\partial_\nu\phi\right)+\mathcal{L}_m\right], \quad (6)$$

where R, g and $\mathcal{L}_m$ represent the Ricci scalar curvature, determinant of the metric tensor $g_{\mu\nu}$ and the matter Lagrangian density, respectively. Here, ϕ and ω denote BD scalar field and BD coupling parameter, respectively. In this theory, the Newtonian constant G is replaced with a time dependent scalar field ϕ such that $\phi=(8\pi G)^{-1}$. The dimensionless parameter ω is introduced to represent a coupling between scalar field and gravity. In Jordan frame, the scalar field and matter field do not interact and matter minimally couples to the metric.

We assume a homogeneous and isotropic FRW spacetime to discuss the evolution of the Universe. The FRW line element is given by

$$ds^2=dt^2-a^2(t)\left[\frac{dr^2}{1-kr^2}+r^2\left(d\theta^2+\sin^2\theta d\phi^2\right)\right], \quad (7)$$

where a is the cosmic scale factor and k is curvature parameter. The curvature parameter has three possible values $k=-1,0,1$ which represent to open, flat and closed geometry of the Universe, respectively. We assume that the Universe is filled with pressureless dark matter (DM) and NADE. We exclude baryonic matter and radiation due to their negligible contribution to total energy budget in the late time evolution.

The variation of the action (6) with respect to the metric tensor, $g_{\mu\nu}$ for the line element (7) yield the following field equations.

$$H^2+\frac{k}{a^2}+H\frac{\dot{\phi}}{\phi}-\frac{\omega}{6}\frac{\dot{\phi}^2}{\phi^2}=\frac{\rho_m+\rho_D}{3\phi}, \quad (8)$$

$$2\frac{\ddot{a}}{a}+H^2+\frac{k}{a^2}+2H\frac{\dot{\phi}}{\phi}+\frac{\omega}{2}\frac{\dot{\phi}^2}{\phi^2}+\frac{\ddot{\phi}}{\phi}=-\frac{p_D}{\phi}, \quad (9)$$

$$\ddot{\phi}+3H\dot{\phi}=\frac{\rho_m+\rho_D-3p_D}{2\omega+3}, \quad (10)$$

where ρ_m and ρ_D denote the energy density of DM and NADE respectively, and p_D is the pressure of NADE. Equation (10) is known as the wave equation of the BD scalar field.

Johri and Sudharsan (1989), Johri and Desikan (1994), Banerjee and Beesham (1996), Singh (2012) have studied the evolution of the Universe in BD theory by assuming a power-law relation between BD scalar field and scale factor of the form $\phi\propto a^m$, where m is a positive constant. They have observed that this assumption leads to a constant value of DP. The constant value of DP can be obtained irrespective of matter content of the Universe. However, some authors (Banerjee and Pavón 2007; Xu et al. 2009; Sheykhi 2009) have studied HDE model in BD theory with the same form of BD scalar field and have obtained a time-dependent DP. Similarly, Liu and Zhang (2009), Sheykhi (2010) and Chattopadhyay et al. (2014) have studied the NADE models in BD theory by assuming the same power-law form of BD scalar field. They have also claimed time dependent DP. Now, the question is that why does the same form of BD scalar field lead to two different values of DP, constant and time-dependent for the same model?

In spite of several advantages of this form of BD scalar field, it seems from the above mentioned works that this may not be a suitable assumption to discuss the evolution of the Universe in HDE or NADE models. In other words, this form may not be suitable for those models where we want to study the phase transition of the Universe. Taking into consideration to this problem, we hereby propose that the BD scalar field evolves as a logarithmic function of the scale factor which is given by

$$\phi=\phi_0\ln(\alpha+\beta a), \quad (11)$$

where ϕ_0, $\alpha>1$ and $\beta>0$ are constants.

In BD theory, the BD scalar field is taken as $\phi=(8\pi G)^{-1}$ which implies $\phi=M_p^2$. Therefore, in this theory the energy density of NADE in (4) is now becomes

$$\rho_D=3n^2\phi\eta^{-2}. \quad (12)$$

The critical energy density ρ_{cr} and energy density of the curvature ρ_k can be defined as follows

$$\rho_{cr} = 3\phi H^2, \qquad \rho_k = 3k\phi a^{-2}. \tag{13}$$

It has been observed that the representation of quantities and equations in the terms of fractional energy densities are useful from the point of view of calculation as well as from the point of view of physical interpretation of the results. The fractional energy densities can be defined in their usual forms as

$$\Omega_m = \frac{\rho_m}{\rho_{cr}} = \frac{\rho_m}{3\phi H^2}, \tag{14}$$

$$\Omega_D = \frac{\rho_D}{\rho_{cr}} = \frac{n^2}{\eta^2 H^2}, \tag{15}$$

$$\Omega_k = \frac{\rho_k}{\rho_{cr}} = \frac{k}{a^2 H^2}. \tag{16}$$

In what follows, we consider the non-interacting and interacting NADE models, and discuss their physical behaviors.

2.1 Non-interacting NADE model

Let us assume that DM and NADE do not interact and their energy densities follow the conservation equations

$$\dot{\rho}_m + 3H\rho_m = 0, \tag{17}$$

$$\dot{\rho}_D + 3H(1 + w_D)\rho_D = 0, \tag{18}$$

where $w_D = p_D/\rho_D$ denotes the equation of state (EoS) parameter of NADE. Using (11), (12) and (15) in the conservation equation (18), one can find the value of w_D as

$$w_D = -1 - \frac{\beta a}{3(\alpha + \beta a)\ln(\alpha + \beta a)} + \frac{2}{3na}\sqrt{\Omega_D}. \tag{19}$$

It is to be noted that the EoS parameter w_D of NADE given by (19) reduces to its respective form in GR (Wei and Cai 2007) for $\beta = 0$, that is,

$$w_D = -1 + \frac{2}{3na}\sqrt{\Omega_D}. \tag{20}$$

From (20) we observe that the w_D does not cross the phantom divide line $w_D = -1$ in the framework of GR.

Let us examine the behavior of the term $\frac{\beta a}{(\alpha+\beta a)\ln(\alpha+\beta a)}$ present in (19) to discuss the behavior of w_D. We observe that the term $\frac{\beta a}{(\alpha+\beta a)\ln(\alpha+\beta a)}$ is zero at $a = 0$, achieves its maximum value during the evolution, and converges to zero as $a \to \infty$ in the late time evolution. The maximum value of the term $\frac{\beta a}{(\alpha+\beta a)\ln(\alpha+\beta a)}$ lies in the interval]0, 1[depending on the value of α. We observe that $\max\{\frac{\beta a}{(\alpha+\beta a)\ln(\alpha+\beta a)}\} \to 1$ as $\alpha \to 1$ and for large value of α we get a small maximum value of the term. It is to be noted that the maximum value does not depend on the value of β. The time when the term will attain its maximum value depends on the values of α and β. For a large value of α, it occurs in the late time and for a large value of β, it will occur in the early time, and vice-versa.

Now, from (19) we observe that $w_D \to -1$ in the late time as the last two terms converge to zero, i.e., the NADE mimics the cosmological constant in the late time evolution. Wei and Cai (2007) have also observed in GR that NADE mimics cosmological constant in the late time evolution. Indeed, the NADE with logarithmic form of BD scalar field in the BD theory behaves like NADE in GR in the late time evolution due to the term $\frac{\beta a}{(\alpha+\beta a)\ln(\alpha+\beta a)}$ which converses to zero as $a \to \infty$. However, in the power law form of BD scalar field the NADE crosses the phantom divide line in the late time evolution because the second term is a constant $\frac{2m}{3}$ for power-law form $\phi \propto a^m$ (Sheykhi 2010). It is also interesting to note that w_D may cross the phantom divide line if $\sqrt{\Omega_D} < [\frac{\beta n a^2}{2(\alpha+\beta a)\ln(\alpha+\beta a)}]$ during the evolution but ultimately it will mimic the cosmological constant in the late time evolution. However, for a sufficiently large value of α and a sufficiently small value of n the phantom divide line crossing is not possible. If α has a small value ($\alpha \to 1$) and n a large value then the value of β is crucial to observe the phantom divide crossing and therefore for sufficiently small value of β the possibility of $w_D < -1$ may be observed.

Let us discuss the evolution of the Universe using the DP which is defined by $q = -\frac{a\ddot{a}}{\dot{a}^2}$. Using (11), (12), (15) and (16) in (9), the DP q can be obtained as

$$q = \frac{1 + 3w_D\Omega_D + \Omega_k - \frac{\beta^2 a^2}{(\alpha+\beta a)^2\ln(\alpha+\beta a)}}{(2 + \frac{\beta a}{(\alpha+\beta a)\ln(\alpha+\beta a)})} + \frac{\frac{2\beta a}{(\alpha+\beta a)\ln(\alpha+\beta a)} + \frac{\omega\beta^2 a^2}{2(\alpha+\beta a)^2\{\ln(\alpha+\beta a)\}^2}}{(2 + \frac{\beta a}{(\alpha+\beta a)\ln(\alpha+\beta a)})} \tag{21}$$

The value of BD parameter ω plays an important role in the value of q. The solar system experiment Cassini gave a very stringent high bound result on w as $|\omega| > 40000$ (Bertotti et al. 2003; Will 2006). However, the cosmological observations put relatively lower bounds on ω (Acquaviva et al. 2005; Wu and Chen 2010; Li et al. 2013b). The term $\frac{\beta^2 a^2}{(\alpha+\beta a)^2\ln(\alpha+\beta a)}$ present in (21) is zero at $a = 0$ which achieves its maximum value during the evolution and converges to zero in the late time evolution like the term $\frac{\beta a}{(\alpha+\beta a)\ln(\alpha+\beta a)}$. The maximum value of this term lies in the interval]0, 0.41[depending on the value of α. Due to a large value of ω suggested by the observations, the last term of the numerator in (21) containing ω will dominate in the early phase of the evolution of the Universe. Thus, we observe a positive value of q, i.e., the Universe evolves

through the decelerated rate of the expansion. It means that the matter dominates the early phase of the expansion of the Universe. Thus, the NADE model with logarithmic form $\phi \propto \ln(\alpha + \beta a)$ explains the matter dominated phase of the Universe. Since, in the late time evolution $w_D \to -1$, and last three terms of numerator and last term of denominator of (21) converge to zero, therefore, we obtain the late time value of q as

$$q \approx \frac{1 - 3\Omega_D + \Omega_k}{2}. \tag{22}$$

It is expected that $\Omega_D \to 1$ in the late time evolution. There are three possibilities for Ω_k: (i) $\Omega_k > 0$ for close Universe ($k > 0$), (ii) $\Omega_k = 0$ for flat Universe ($k = 0$), and (iii) $\Omega_k < 0$ for open Universe ($k < 0$). However, the observations suggest that our Universe is almost flat ($k \approx 0$) at present time. Therefore, if we take $k = 0$, i.e., $\Omega_k = 0$ for late time evolution then we have $q \approx \frac{1-3\Omega_D}{2}$. Thus, we may obtain an accelerated expansion for $\Omega_D > 1/3$. If we take present value $\Omega_D = 0.70$ obtained by resent observations then we get $q = -0.55$ which shows the accelerated expansion. One can observe that the accelerated expansion occurs more easily if we consider the open geometry of the Universe ($\Omega_k < 0$). In the case of close Universe ($\Omega_k > 0$), the accelerated expansion is possible but a relatively large value of Ω_D is required, i.e., a large value of n^2 is required to achieve it.

So far, we have obtained decelerated expansion in the early phase of the evolution which explains the matter dominated phase and accelerated expansion in the late time evolution which explains the NADE dominated phase. Thus, the present model successfully explains the recent phase transition of the Universe from decelerated expansion to accelerated expansion. The time of phase transition depends on the values of the parameters of the model α, β, n^2 and ω. It may be observed from (21) that if phase transition occurs at time t_1 for value ω_1 then it will happen at time t_2 for ω_2 where $t_1 < t_2$ and $\omega_1 < \omega_2$. For a large value of n^2 it occurs at earlier stage. In the similar way, one can see the effects of α and β depending on their effects on the terms $\frac{\beta a}{(\alpha+\beta a)\ln(\alpha+\beta a)}$ and $\frac{\beta^2 a^2}{(\alpha+\beta a)^2\ln(\alpha+\beta a)}$ as discussed above.

The logarithmic form in NADE model is free from the constant DP problem of the power-law form and explains the phase transition of the Universe in the framework of the BD theory. Thus, this form serves our propose well.

Let us discuss the cosmic coincidence problem which has not been addressed for NADE models in the framework of BD theory. Steinhardt (1997) addressed first time the coincidence problem- why are the matter and DE densities comparable at present time? In the conventional ΛCDM model very specific conditions of very early Universe are required to observe the matter and DE densities of the same order today. There are two ways to resolve the coincidence problem. In one of the ways, we should observe the energy density ratio $r_0 \sim \mathcal{O}(1)$ for a wide range of the initial conditions. In the other way, either r should converse to a constant value or evolve very slowly in the late time evolution(including present time) such that $r_0 \sim \mathcal{O}(1)$. In the ΛCDM model, the energy density ratio r evolves as $|\frac{\dot{r}}{r}|_0 = 3H_0$. Here and throughout the paper, the zero subscript denotes the present value of the quantity. Using (17) and (18) one can obtain the evolution of r as

$$\dot{r} = 3rHw_D. \tag{23}$$

As we have observed that NADE mimics cosmological constant in the late time when $a \to \infty$. Therefore, if we take $w_{D0} = -1$, we get $|\frac{\dot{r}}{r}|_0 = 3H_0$ which is same as in the ΛCDM model. Thus, there is no reduction in the acuteness of coincidence problem. However, we have a time-dependent w_D, therefore, it is possible to have a less acute coincidence problem if we have $w_{D0} > -1$. The quintessence like EoS ($w_D > -1$) may be achieved for $\sqrt{\Omega_D} > \frac{\beta n a^2}{2(\alpha+\beta a)\ln(\alpha+\beta a)}$ as can be observed from (19). It is to be noted that Eq. (19) has a time-dependent second term which converses to zero in the late time whereas the second term is a constant in case of power-law form. Therefore, the quintessence like EoS may be achieved more easily with logarithmic form in comparison to the power-law form of BD scalar field in the present time. Thus, the logarithmic form is more suitable to achieve a less acute coincidence problem. The observations also suggest quintessence like EoS of NADE (Wei and Cai 2008b). Let us assume $w_{D0} = -2/3$, we obtain $|\frac{\dot{r}}{r}|_0 = 2H_0$ which is less acute coincidence problem in comparison to the ΛCDM model. On the other hand, the problem is more acute if w_D has phantom like EoS ($w_D < -1$). In this case, the coincidence problem becomes more worse than the ΛCDM model.

In conclusion, the coincidence problem may not be resolved significantly for non-interacting NADE model in the framework of BD theory, however, there are possibilities to achieve a less acute problem. The logarithmic form of BD scalar field is more suitable to have a less acute coincidence problem than power-law form.

2.2 Interacting NADE model

A number of authors (Amendola and Quercellini 2003; Zimdahl and Pavón 2003; Farrar and Peebles 2004; Gumjudpai et al. 2005; Skordis et al. 2015) have studied the interaction between DM and DE and recent cosmological observations (Olivares et al. 2005; Feng et al. 2007; Cao et al. 2011; Costa et al. 2014) also support it. The interacting DE models have also been studied as a possible candidate to resolve the coincidence problem (Berger and Shojaei 2006; del Campo et al. 2006, 2009). Therefore, in this subsection we extend

the NADE model by considering the interaction between DM and NADE.

Assuming that the DM and NADE exchange energy through the interaction Q, the continuity equations become

$$\dot{\rho}_m + 3H\rho_m = Q, \tag{24}$$

$$\dot{\rho}_D + 3(1+w_D)H\rho_D = -Q. \tag{25}$$

The sign of interaction term Q is crucial and defines the direction of the energy transfer, i.e., for $Q > 0$, there is an energy transfer from NADE to DM, and for $Q < 0$, there is an energy transfer from DM to NADE. The interaction between DM and NADE is a quantum scale phenomenon, therefore, the interaction term Q should be defined by the theory of quantum gravity. We do not have a satisfactory theory of quantum gravity, therefore, the dimension of the conservation equation has been used to choose a suitable form of Q in the literature. The conservation equations of DM and NADE imply that the interaction term should has the units of energy density $\times (time)^{-1}$. Therefore, we may have the interaction term of the following forms: (i) $Q \propto H\rho_D$, (ii) $Q \propto H\rho_m$ or (iii) $Q \propto H(\rho_m + \rho_D)$. In this paper, we use the last assumption which is more general than first two. This form can be rewritten as

$$Q = 3b^2 H(\rho_m + \rho_D), \tag{26}$$

where b^2 is a coupling constant. Using (11), (12), (15) and (26) in (25), we get

$$w_D = -1 - b^2(1+r) - \frac{\beta a}{3(\alpha+\beta a)\ln(\alpha+\beta a)} + \frac{2}{3na}\sqrt{\Omega_D}. \tag{27}$$

It is easy to observe that the EoS parameter of NADE achieves its respective form in GR for $\beta = 0$. We observe that w_D contains the third term as time-dependent whereas it is constant term in this place in power-law form of BD scalar field. Therefore, the evolution of w_D in our model will be different from that of power-law form. As discussed in Sect. 2.1, analyzing the terms in w_D in (27), one can observe that w_D will definitely cross the phantom divide in the late time evolution, where $w_D \to -1 - b^2(1+r)$ as $a \to \infty$. The interaction between DM and NADE is the deriving force behind the phantom crossing in the late time. The late time value of w_D depends on the values of coupling constant b^2 and density ratio r. It means that it depends on how DM and NADE interact and what is the ratio of their densities. In the interacting NADE model, we observe that w_D may cross the phantom divide line more easily and earlier in the framework of BD theory than GR. The phantom divide line crossing have been observed in different kind of cosmological models (Setare 2008, 2010b; Nozari et al. 2009; Setare and Vagenas 2010; Lepe and Pena 2010) in the literature.

The expression of q remains same as in the case of non-interacting NADE which is given by (21). However, the evolution of q is different due to different value of w_D for interacting NADE given by (27). From (19) and (27), we observe that the EoS parameter of interacting NADE has an extra term $b^2(1+r)$ with negative sign than non-interacting NADE. Therefore, it is easy to observe from (21) that the recent phase transition of the Universe from matter dominated phase to NADE dominated phase is more easily achieved and we may achieve it at earlier stage in the interacting case. Thus, the interacting NADE model explains the recent phase transition of evolution of the Universe in the framework BD theory with logarithmic form of BD scalar field.

Let us study the evolution of r to check whether the interaction between DM and NADE is able to alleviate the coincidence problem or not. Using (24), (25) and (26), the evolution of r can be obtained as

$$\dot{r} = 3rH\left[w_D + b^2\frac{(1+r)^2}{r}\right]. \tag{28}$$

Here, we have the sum of the terms w_D and $b^2\frac{(1+r)^2}{r}$ which have negative and positive value respectively. Thus, the resultant value of terms within bracket will be less than $|w_D|$. Moreover, for a suitable value of b^2, we may achieve $|w_D + b^2\frac{(1+r)^2}{r}| \ll |w_D|$. Now, it is evident from (23) and (28) that the energy density ratio r may evolve more slowly in interacting NADE model than the ΛCDM model and non-interacting NADE model. Therefore, the interaction between dark components of the Universe may play an important role in the explanation of the coincidence problem. To achieve a soft coincidence we should observe $|\frac{\dot{r}}{r}|_0 \leq H_0$ (del Campo et al. 2008). The condition of soft coincidence may be easily achieved in our model if b^2 satisfies the condition, $b^2 \leq \frac{(1-3w_{D0})r_0}{3(1+r_0)^2}$. If we use the present observational values $r_0 \simeq 3/7$ and $w_{D0} \simeq -1$, we obtain the constraint $b^2 \leq 7/25$ to achieve soft coincidence problem. Even for a suitably small values of b^2, r may evolve more slowly at present which may resolve the coincidence problem more effectively. For example, if we take $b^2 = \frac{1}{5}$ and $w_{D0} = -1$ then we obtain $|\frac{\dot{r}}{r}|_0 \leq \frac{H_0}{7}$ which shows significantly slow variation of r compare to conventional ΛCDM model and condition mentioned above for soft coincidence.

Feng et al. (2008) found that a small coupling constant b^2 is compatible with observation and also required to alleviate the coincidence problem. It also required to satisfy the second law of thermodynamics (also, see references within Feng et al. 2008). We also observe that the coupling constant b^2 should be a small quantity to avoid the coincidence problem which shows the compatibility with the observations. Thus, the interaction between DM and NADE in the

framework of BD theory with logarithmic BD scalar field may resolve the coincidence problem effectively.

3 Conclusion

In this paper, we have investigated how the NADE model evolves in BD theory by assuming the logarithmic form of BD scalar field. The motive is that the existing power-law form of BD scalar field, $\phi = \phi_0 a^m$ gives a constant value of DP whatever may be the energy content. Therefore, it can not describe the phase transition of the Universe. However, many authors have found time-dependent DP by using the same power-law form which shows a contradiction. To overcome from this problem we have proposed and analyzed the logarithmic form of BD scalar field, $\phi = \phi_0 \ln(\alpha + \beta a)$ in NADE model. This form of BD scalar field is free from the above described problem and plays an important role in explaining the evolution of the Universe. It also resolves the cosmic coincidence problem. Therefore, analyzing the importance of this form, we have studied the NADE model within the framework of FRW line element in BD theory. We have discussed the dynamics of non-interacting and interacting NADE models by EoS parameter w_D and DP q. We have also discussed the cosmic coincidence problem. The results of these two models are summarized as follows:

In non-interacting NADE model, we have observed that the NADE model successfully explains the recent phase transition from matter dominated to NADE dominated phase. In this model the NADE mimics cosmological constant in the late time whereas it achieves phantom like behavior for power-law form of BD scalar field (Sheykhi 2010). It has also been observed that w_D may cross the phantom divide line under certain constraint but ultimately it will mimic the cosmological constant in late time evolution. Further, we have shown that a less acute coincidence problem than conventional ΛCDM model may be achieved, however, it is not able to alleviate the problem effectively. The logarithmic form of BD scalar field is more suitable to achieve a less acute coincidence problem than power-law form.

In interacting NADE model, the recent phase transition from decelerated phase to accelerated phase has also been achieved. However, the accelerated expansion may be achieved earlier in this model than non-interacting model. In the late time evolution, it has been analyzed that w_D definitely crosses the phantom divide line. We have shown that the energy density ratio r may evolve sufficiently slow in the present time which resolves the coincidence problem. Thus, the interacting NADE model may be able to alleviate the coincidence problem effectively.

In conclusion, we can say that the logarithmic form of BD scalar field is suitable to explain the recent accelerated expansion of the Universe in NADE model. This model shows the phase transition of the evolution of the Universe as we get the time dependent DP. It also resolves the cosmic coincidence problem effectively. Also, in the limit $\beta \to 0$, the NADE model in general relativity is recovered.

Acknowledgements The authors are thankful to the referee for his constructive suggestions to improve the manuscript. PK also expresses his thanks to UGC, India for providing the financial support to carry out the research under Senior Research Fellowship (SRF).

References

Acquaviva, V., et al.: Phys. Rev. D **71**, 104025 (2005)
Amendola, L., Quercellini, C.: Phys. Rev. D **68**, 023514 (2003)
Bamba, K., et al.: Astrophys. Space Sci. **342**, 155 (2012). arXiv:1205.3421 [gr-qc]
Banerjee, N., Beesham, A.: Aust. J. Phys. **49**, 899 (1996)
Banerjee, N., Pavón, D.: Phys. Lett. B **647**, 477 (2007)
Berger, M.S., Shojaei, H.: Phys. Rev. D **73**, 083528 (2006)
Bertolami, O., Martins, P.J.: Phys. Rev. D **61**, 064007 (2000)
Bertotti, B., Iess, L., Tortora, P.: Nature **426**, 374 (2003)
Brans, C., Dicke, R.H.: Phys. Rev. **124**, 925 (1961)
Cai, R.G.: Phys. Lett. B **657**, 228 (2007)
Cao, S., Liang, N., Zhu, Z.H.: Mon. Not. R. Astron. Soc. **416**, 1099 (2011)
Chattopadhyay, S., Pasqua, A., Khurshudayan, M.: Eur. Phys. J. C **74**, 3080 (2014)
Clifton, T., Barrow, J.D.: Phys. Rev. D **73**, 104022 (2006)
Copeland, E.J., Sami, M., Tsujikawa, S.: Int. J. Mod. Phys. D **15**, 1753 (2006)
Costa, A.A., et al.: Phys. Rev. D **89**, 103531 (2014)
del Campo, S., et al.: Phys. Rev. D **74**, 023501 (2006)
del Campo, S., Herrera, R., Pavón, D.: Phys. Rev. D **78**, 021302 (2008)
del Campo, S., Herrera, R., Pavón, D.: J. Cosmol. Astropart. Phys. **01**, 020 (2009)
Farrar, G., Peebles, P.J.E.: Astrophys. J. **604**, 1 (2004)
Fayaz, V.: Astrophys. Space Sci. **361**, 86 (2016)
Feng, C., et al.: J. Cosmol. Astropart. Phys. **09**, 005 (2007)
Feng, C., et al.: Phys. Lett. B **665**, 111 (2008)
Ghaffari, S., Dehghani, M.H., Sheykhi, A.: Phys. Rev. D **89**, 123009 (2014)
Gumjudpai, B., et al.: J. Cosmol. Astropart. Phys. **06**, 007 (2005)
Johri, V.B., Desikan, K.: Gen. Relativ. Gravit. **26**, 1217 (1994)
Johri, V.B., Sudharsan, R.: Aust. J. Phys. **42**, 215 (1989)
Károlyházy, F.: Nuovo Cimento A **42**, 390 (1966)
Károlyházy, F., Frenkel, A., Lukács, B.: In: Shimony, A., Feschbach, H. (eds.) Physics as Natural Philosophy. MIT Press, Cambridge (1982)
Károlyházy, F., Frenkel, A., Lukács, B.: In: Penrose, R., Isham, C.J. (eds.) Quantum Concepts in Space and Time. Clarendon Press, Oxford (1986)
Kim, H.: Mon. Not. R. Astron. Soc. Lett. **364**, 813 (2005)
Kim, K.Y., Lee, H.W., Myung, Y.S.: Phys. Lett. B **660**, 118 (2008)
Lemets, O.A., Yerokhin, D.A., Zazunov, L.G.: J. Cosmol. Astropart. Phys. **01**, 007 (2011)
Lepe, S., Pena, F.: Eur. Phys. J. C **69**, 575 (2010)
Li, M.: Phys. Lett. B **603**, 1 (2004)
Li, M., et al.: J. Cosmol. Astropart. Phys. **09**, 021 (2013a)
Li, Y.C., Wu, F.Q., Chen, X.: Phys. Rev. D **88**, 084053 (2013b)
Liu, X.L., Zhang, X.: Commun. Theor. Phys. **52**, 761 (2009)
Maziashvili, M.: Int. J. Mod. Phys. D **75**, 1531 (2007a)
Maziashvili, M.: Phys. Lett. B **652**, 165 (2007b)
Neupane, I.P.: Phys. Lett. B **673**, 111 (2009)

Nojiri, S., Odintsov, S.D.: Gen. Relativ. Gravit. **38**, 1285 (2006). arXiv:hep-th/0506212
Nozari, K., Azizi, T., Setare, M.R.: J. Cosmol. Astropart. Phys. **10**, 22 (2009)
Olivares, G., Atrio, F., Pavón, D.: Phys. Rev. D **71**, 063523 (2005)
Pasqua, A., Chattopadhyay, S.: Astrophys. Space Sci. **348**, 284 (2013)
Pavón, D., Zimdahl, W.: Phys. Lett. B **628**, 206 (2005)
Perlmutter, S., et al.: Astrophys. J. **517**, 565 (1999)
Riess, A.G., et al.: Astron. J. **116**, 1009 (1998)
Saaidi, K., Sheikhahmadi, H., Mohammadi, A.H.: Astrophys. Space Sci. **338**, 355 (2012)
Sasakura, N.: Prog. Theor. Phys. **102**, 169 (1999)
Setare, M.R.: Phys. Lett. B **644**, 99 (2007)
Setare, M.R.: Int. J. Mod. Phys. D **17**, 2219 (2008)
Setare, M.R.: Astrophys. Space Sci. **326**, 27 (2010a)
Setare, M.R.: Int. J. Theor. Phys. **49**, 759 (2010b)
Setare, M.R., Vagenas, E.C.: Astrophys. Space Sci. **330**, 145 (2010)
Sheykhi, A.: Phys. Lett. B **681**, 205 (2009)
Sheykhi, A.: Phys. Rev. D **81**, 023525 (2010)
Sheykhi, A., Jamil, M.: Phys. Lett. B **694**, 284 (2011)
Sheykhi, A., Setare, M.R.: Int. J. Theor. Phys. **49**, 2777 (2010)
Sheykhi, A., Setare, M.R.: Mod. Phys. Lett. A **26**, 1897 (2011)
Singh, C.P.: Astrophys. Space Sci. **338**, 411 (2012)
Skordis, C., Pourtsidou, A., Copeland, E.J.: Phys. Rev. D **91**, 083537 (2015)
Steinhardt, P.: In: Fitch, V.L., Marlow, D.R. (eds.) Critical Problems in Physics. Princeton University Press, Princeton (1997)
't Hooft, G.: arXiv:gr-qc/9310026 (1993)
Wei, H., Cai, R.G.: Phys. Lett. B **665**, 1 (2007)
Wei, H., Cai, R.G.: Phys. Lett. B **660**, 113 (2008a)
Wei, H., Cai, R.G.: Phys. Lett. B **663**, 1 (2008b)
Wei, H., Cai, R.G.: Eur. Phys. J. C **59**, 99 (2009)
Will, C.: Living Rev. Relativ. **9**, 3 (2006)
Wu, F.Q., Chen, X.: Phys. Rev. D **82**, 083003 (2010)
Xu, L., Li, W., Lu, J.: Eur. Phys. J. C **60**, 135 (2009)
Zhang, J.F., Lee, Y.H., Zhang, X.: Eur. Phys. J. C **73**, 2280 (2013)
Zimdahl, W., Pavón, D.: Gen. Relativ. Gravit. **35**, 413 (2003)

Available online at www.ijapie.org

International Journal of Advanced
Production and Industrial Engineering

IJAPIE-SI-IDCM 601 (2017) 01–03

Special Issue on

INNOVATIVE DESIGN
&
COMPUTATIONAL
MODELLING

Numerical Simulation of Fluid Flow and Heat Transfer in Wavy Micro-Channel at Different Reynolds Number

Mohammad Zunaid[1*], Afzal Husain[2], NaushadAhmad Ansari[1],
Anant Jindal[1], Avinash Gupchup[1]

[1]*Department of Mechanical Engineering, Delhi Technological University, Bawana Road, Delhi-110042,*

[2]*Department of Mechanical and Industrial Engineering, Sultan Qaboos University, Muscat Oman,*

Email: mzunaid3k@gmail.com

Abstract : Heat performance and overall characteristics of microchannels can be improved by employing different channel structures. In this study wavy microchannel is analysed for its heat transfer and pressure drop characteristics. A three dimensional analysis is performed for different values of Reynolds number. The geometry is first created in Solidworks and then imported in ANSYS for CFD simulation in CFX package. To ensure the accuracy and reliability of the model the results for straight microchannels have been compared with experimental data. They are found to be in great agreement with the experimental results. A constant heat flux of $2*10^6$ W/m^2 is applied at the heat sink bottom. With water taken as coolant, the heat transfer and pressure drop characteristics are analysed for Reynolds number (600, 1000). It is found that both heat transfer and pressure drop increased with the employment of wavy channel as compared to straight microchannel.

Keywords: Microchannel, Wavy, CFD, Heat sink

I. INTRODUCTION

With the developments in electronics in the recent years, electronic devices have become more powerful and small. They also produce a large amount of heat. Microchannel heat sinks are used for removal of large amount of heat from a very small surface area. These are challenging the use of conventional coil technology for heat exchange. Over the past few years, smaller scale machining technology is utilized at a huge rate for the improvement of exceptionally productive cooling gadgets known as micro-channel heat sinks as it possesses greater advantages like small size and less coolant requirements.

Tuckerman and Pease [1], first studied heat transfer in microchannels heat sink. They fabricated a 1×1 cm^2 rectangular microchannel with depth 302 µm and width 50 µm and employing water as the cooling fluid. The microchannel heat sink was capable of dissipating 790 W/cm^2 at the expense of a pressure drop of 2.2 bar. Peng and Peterson [2] investigated the single-phase forced convective heat transfer characteristics in microchannels experimentally with small rectangular channels with hydraulic diameters of 0.134–0.367 mm. P. Mohajeri Khameneh [3] illustrated the effects of geometric parameters on the Nusselt number in a single-phase and forced convective heat transfer of water in microchannels to obtain computational Nusselt number in laminar flow. This study stated that the average Nusselt number is increased by increasing the width or decreasing the height of the microchannel. Roy et al. [4] studied heat transfer using nanofluids as a coolant inside a radial channel between two coaxial and parallel discs. Xu et al. [5] investigated the flow characteristics and heat transfer numerically in microchannels with dimples. Different geometric parameters were independently evaluated under constant Reynolds Number of 500 and a constant heat flux of 1 W/mm^2. It was found that in comparison to straight channels, dimpled surface reduced the local flow resistance and also improved thermal performance of microchannel heat sink. Chai, Xia and Wang [6] studied the laminar flow and heat transfer characteristics in the interrupted microchannel heat sink with ribs in the transverse microchambers. In their study they examined the effect of such ribs on pressure distribution, velocity contour, and temperature distribution. They also observed the pressure drop and heat transfer characteristics in such microchannels. Results portrayed that the ribs in the transverse microchambers would prevent the decline of local heat transfer coefficient along the flow direction.

In the present work the heat transfer and pressure drop characteristics are studied for wavy microchannel at Reynolds number (600,1000). It is clear from the above given literature review that wavy channels have not been studied for heat transfer and pressure drop characteristics before and hence this study is important. To make sure that the model produces desired results, the simulation results of straight microchannel heat sinks have been compared and then validated with Qu and Mudawar's experimental work [7].

Heat transfer and pressure drop characteristics for wavy microchannels are computed for Reynolds number (600,1000). These are then compared with results of the rectangular microchannel heat sink. An increase in heat transfer and pressure drop is seen. The results are used to assess the suitability of macro transport models in depicting the transport characteristics of micro-channel heat sinks.

II. Model Description

The heat sink was created in Solidworks as per the dimensions given in Table I. The wave dimensions were decided in accordance with the length of the channel which is 44.7 mm. A sinusoidal sine wave (Eqn. 1) was constructed in the solid heat sink. The amplitude of the wave was taken as 0.15 mm while the wavelength was taken as 2 mm. However, fluid channel was created of the same dimensions as of the wavy rectangular slot along the length of heat sink.

$$y = A\sin(2\pi x / \lambda) \qquad -(1)$$

Here , 'A' is wave amplitude and 'λ' is wave length.The assembly of the heat sink and fluid channel was created and then imported in ANSYS. The mesh was generated in ANSYS.

TABLE I
Dimensions of the Unit Cell Used for Simulation

W_{wall}(µm)	$W_{channel}$(µm)	H_{wall2}(µm)	$H_{channel}$(µm)	H_{wall1}(µm)	L(mm)
118	231	12700	713	5637	44.7

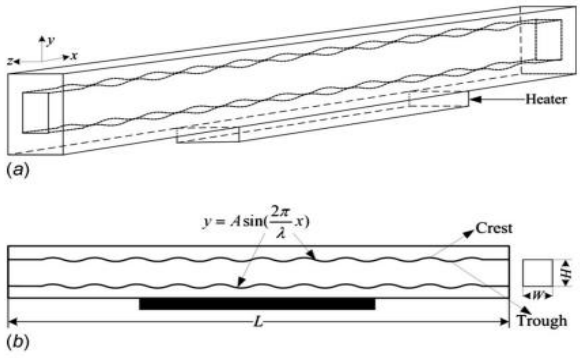


Fig. 1 (a) and (b) Schematic of wavy micro-channel heat sink

As, we have assumed a unitary computational domain, we only need to specify boundary conditions for the unit cell, which are given as: -

Hydraulic Boundary Conditions: -

- Uniform velocity at the inlet of the channel.
- At channel outlet, mass flow rate boundary condition is applied.
- Zero velocity at all other solid boundaries.
- No slip at the surface.

Thermal Boundary Conditions: -

- A uniform heat flux 200 W/ cm^2 of at the bottom wall of the heat sink.

III. Model Validation

To ensure that the model is reliable and accurate, the computational results of a straight rectangular microchannel heat sink were compared with that of the experimental results by Qu and Mudawar [7]. These results are shown in Table II. It can be seen that the computational results comply with that of the experimental results. Hence the model and the boundary conditions chosen are reliable and accurate. The model can be used to assess the characteristics of wavy microchannel heat sink.

TABLE II
Experimental and Computational Pressure Drop and Temperature Rise in Rectangular Microchannel

Reynolds number	Exp. pressure drop (bar)	Comp. pressure drop (bar)	Exp. Temp. rise (°C)	Comp. temp. rise (°C)
600	0.15	0.16	31	28
1000	0.32	0.29	18	16

IV. Results

In this study heat transfer and pressure drop characteristics were studied for a wavy microchannel.

TABLE III
Computational Temperature Rise and Pressure Drop for Wavy Microchannel Heat Sink

Reynolds number	Computational temperature rise (°C)	Computational pressure drop (bar)
600	39	0.204
1000	26	0.390

A. *Pressure drop*

The pressure drop characteristics were studied for a constant heat flux of 200W/cm^2 for two Reynolds number (600,1000). The results are as shown in Table III.

The pressure contours for the two Reynolds number are as shown below in Fig. 2 and Fig. 3.

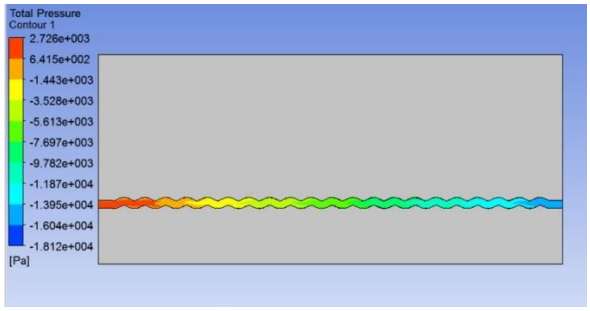


Fig. 2 Pressure contour of water along wavy channel at Re=600

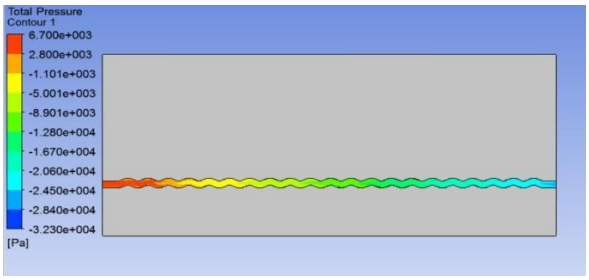


Fig. 3 Pressure contour of water along wavy channel at Re=1000

The pressure drop increases with increase in the Reynolds number. The wavy path obstructs the fluid flow in the direction of motion and hence leads to increased pressure losses as compared to straight microchannel.

B. *Heat Transfer*

The heat transfer characteristics were also studied for a constant heat of 200W/cm^2 for the same Reynolds number (600,1000). The temperature contours for the two Reynolds number are as shown in Fig. 4 and Fig. 5.

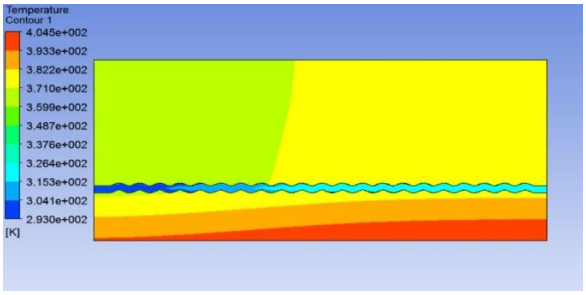


Fig. 4 Temperature contour of water and heat sink at Re=600

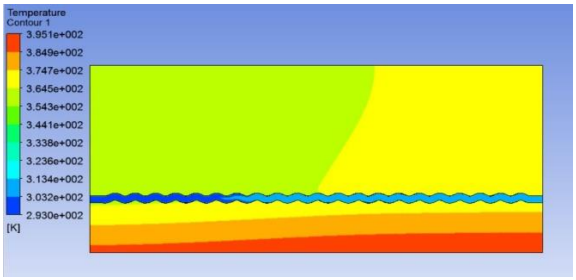


Fig. 5 Temperature contour of water and heat sink at Re=1000

The heat transfer rate decreases with increase in the Reynolds number. Also the heat transfer rate in wavy microchannel is greater than that of straight microchannel for corresponding values of Reynolds number. This can be attributed to the increase in surface area with the help of wavy structure and hence increasing the convective heat transfer.

V. CONCLUSIONS

In this paper, we have investigated, the conjugate heat transfer problem in a wavy microchannel geometry with the assumption of single phase flow. Numerical analysis of pressure drop and heat transfer is conducted and results are laid out. These results are compared with that of a rectangular microchannel heat sink to assess the design of the new geometry. Based on the results following conclusions can be made-

- The heat transfer in wavy microchannel heat sink is greater than that of rectangular microchannel heat sink. This wavy structure increases the convection heat transfer area. It also interrupts thermal boundary layer periodically in the flow direction and hence increases the heat transfer.
- The heat transfer decreases with increase in the Reynolds number as the velocity of coolant (water) flow increases.
- The effect of wavy channel on pressure drop is obvious. This structure hinders the fluid flow in the microchannel. These hindrances lead to a higher pressure loss compared to rectangular microchannel heat sink.
- The pressure drop increases with increase in Reynolds number.
- The computational values for pressure drop and heat transfer are found to be in good agreement with that of the experimental values and hence assures the reliability of the chosen model for analysis.

REFERENCES

[1] D.B. Tuckerman, R.F.W. Pease, High-performance heat sinking for VLSI, IEEE Electron. Dev. Lett. EDL-2 (1981) 126–129.
[2] X.F. Peng, G.P. Peterson, Convective heat transfer and flow friction for water flow in microchannel structures, Int. J. Heat Mass Transfer 39 (1996) 2599–2608.
[3] P. Mohajeri Khameneh et al. A numerical study of single-phase forced convective heat transfer with flow friction in microchannels, International Journal of Engineering 25 (2012) 79-88.
[4] Gilles Roy, Cong Tam Nguyen, Paul-René Lajoie, Numerical investigation of laminar flow and heat transfer in a radial flow cooling system with the use of nanofluids, Superlattices and Microstructures 35 (2004) 497–511.
[5] Minghai Xu, Hui Lu, Liang Gong, John C. Chai, Xinyue Duan, Parametric numerical study of the flow and heat transfer in microchannel with dimples, International Communications in Heat and Mass Transfer 76 (2016) 348–357
[6] Lei Chai, Guo Dong Xia, Hua Sheng Wang, Laminar flow and heat transfer characteristics of interrupted microchannel heat sink with ribs in the transverse microchambers, International Journal of Thermal Sciences 110 (2016) 1-11.
[7] I. Mudawar, W. Qu, Experimental and numerical study of pressure drop and heat transfer in a single-phase micro-channel heat sink, Int. J. Heat and Mass Transfer 45(2002) 2549-2565.
[8] Omar Mokrani, Brahim Bourouga, Cathy Castelain, Hassan Peerhossaini, Fluid flow and convective heat transfer in flat microchannels, Int. J. Heat Mass Transfer 52 (2009) 1337–1352
[9] Hongtao Wang, Zhihua Chen, Jianguo Gao, Influence of geometric parameters on flow and heat transfer performance of micro-channel heat sinks, Applied Thermal Engineering 107 (2016) 870–879
[10] Yunus A.Cengel, John M.Cimbala, Fluid Mechanics, Third edition, McGraw Hill Education, New York(2013)

Egyptian Journal of Petroleum xxx (2017) xxx–xxx

HOSTED BY

Contents lists available at ScienceDirect

Egyptian Journal of Petroleum

journal homepage: www.sciencedirect.com

Full Length Article

Performance and emission characteristics of a stationary diesel engine fuelled by Schleichera Oleosa Oil Methyl Ester (SOME) produced through hydrodynamic cavitation process

Ashok Kumar Yadav [a,*], M. Emran Khan [b], Amit Pal [c], Uttam Ghosh [d]

[a] Department of Mechanical Engineering, Raj Kumar Goel Institute of Technology, Ghaziabad 201003, India
[b] Department of Mechanical Engineering, Faculty of Engineering & Technology, Jamia Millia Islamia, New Delhi 110025, India
[c] Department of Mechanical Engineering, Delhi Technological University, Delhi 110042, India
[d] Department of Production Engineering, Haldia Institute of Technology, Haldia 721657, India

ARTICLE INFO

Article history:
Received 24 August 2016
Revised 3 January 2017
Accepted 23 January 2017
Available online xxxx

Keywords:
Performance
Emission
Diesel engine
Schleichera Oleosa Oil
Biodiesel hydrodynamic cavitation (HC)

ABSTRACT

In this study, the performance and emission characteristics of biodiesel blends of 10, 20, 30 and 50% from Schleichera Oleosa oil based on hydrodynamic cavitation were compared to diesel fuel, and found to be acceptable according to the EN 14214 and ASTM D 6751 standards. The tests have been performed using a single cylinder four stroke diesel engine at different loading condition with the blended fuel at the rated speed of 1500 rpm. SOME (Schleichera Oleosa Oil Methyl Ester) blended with diesel in proportions of 10%, 20%, 30% and 50% by volume and pure diesel was used as fuel. Engine performance (specific fuel consumption and brake thermal efficiency) and exhaust emission (CO, CO_2 and NOx) were measured to evaluate the behaviour of the diesel engine running on biodiesel. The results show that the brake thermal efficiency of diesel is higher and brake specific fuel consumption is lower at all loads followed by blends of SOME and diesel. The performance parameter for B10, B20, B30 and B50 were also closer to diesel and the CO emission was found to be lesser than diesel while there was a slight increase in the CO_2 and NOx. SOME produced by using hydrodynamic cavitation seems to be efficient, time saving and industrially viable. The experimental results revel that SOME-diesel blends up to 50% (v/v) can be used in a diesel engine without modifications.

© 2017 Egyptian Petroleum Research Institute. Production and hosting by Elsevier B.V. This is an open access article under the CC BY-NC-ND license (http://creativecommons.org/licenses/by-nc-nd/4.0/).

1. Introduction

Biodiesel is a clean burning alternative fuel was produced from renewable resources like virgin or used vegetable oils, both edible and non-edible [1]. Biodiesel is obtained from the chemical transformation of oils (triglycerides) by a transesterification process and many oleaginous vegetable species [2]. However, biodiesel produced from edible oils raised the concerns of feedstock competing with food supply in the long-term [3]. Therefore, non-edible oils resources are gaining worldwide attention as it is easily available in many parts of the world especially wastelands that are not suitable for food crops [4]. Besides, the use of biodiesel in diesel engines results in substantial reduction of harmful emission such as unburned hydrocarbons, carbon monoxide and particulate matters [15,16,5,17–20]. There are many ways and procedures to biodiesel fuel from vegetable oil such as pyrolysis, dilution, micro emulsion and transesterification [7,9,14]. All processes are time consuming with high labor cost. Thus, we need a new process i.e. cavitation process for biodiesel production which reduces the reaction time and production cost as well as save the energy. There are four types of cavitation e.g. hydrodynamic, acoustic, optical and particle induced [21]. Hydrodynamic cavitation (HC) has been widely used in waste water treatment and the shipping industry, i.e. ship propellers, pumps and hydrofoils, but only a few works has been reported in the biodiesel field. However, no work has been focused on performance and emission of diesel engine fuelled by Schleichera Oleosa biodiesel.

In this study, biodiesel from Schleichera Oleosa was produced in a HC reactor via transesterification under optimized conditions, such as oil to methanol molar ratio of 1:6 in the presence of 0.75wt% potassium hydroxide as the alkali catalyst at 60 °C operating temperature. Furthermore different blending ratios of SOME, i.e. B0, B10, B20, B30 and B50 were used in the diesel engine in order to study the performance and emission characteristics on

Peer review under responsibility of Egyptian Petroleum Research Institute.
* Corresponding author.
E-mail address: ashokme015@gmail.com (A.K. Yadav).

http://dx.doi.org/10.1016/j.ejpe.2017.01.007
1110-0621/© 2017 Egyptian Petroleum Research Institute. Production and hosting by Elsevier B.V.
This is an open access article under the CC BY-NC-ND license (http://creativecommons.org/licenses/by-nc-nd/4.0/).

Please cite this article in press as: A.K. Yadav et al., Performance and emission characteristics of a stationary diesel engine fuelled by Schleichera Oleosa Oil Methyl Ester (SOME) produced through hydrodynamic cavitation process, Egypt. J. Petrol. (2017), http://dx.doi.org/10.1016/j.ejpe.2017.01.007

single cylinders, four-stroke compression ignition diesel engine without any modification at various loads.

In present study, non-edible Schleichera Oleosa was investigated as a potential feedstock for biodiesel production which has an estimated annual production potential of 66 thousand tons per year in India [11]. Schleichera Oleosa is belonging to Sapindaceae family and also known as Kusum fruit. S. Oleosa is widely found in the sub-Himalayan region, throughout central and Southern India, Burma, Ceylon, Java and Timor. The flowers are yellowish green, fascicled in spike like axillary racemes 7.5–12.5 cm long. The fruits are berry, globose or ovoid, and hard skinned [12]. The seeds are brown, irregularly elliptic, slightly compressed, oily, enclosed in a succulent aril [13]. The oil content of the seed is around 59–72%

2. Materials and method

Schleichera Oleosa oil has been used for biodiesel production in the present study was purchased from an oil industry of Delhi (India) and commercially available petro-diesel was purchased from the nearby petrol pump. Anhydrous methanol (99.8% min.), Sulphuric acid (99% min.) and Potassium hydroxide (85% min.) was purchased from chemical store.

2.1. Biodiesel production

The hydrodynamic cavitation reactor with a 10-L capacity, connected to a reciprocating pump, in a closed loop is used for biodiesel production. The optimized geometry plate with a 1.9 mm diameter and 7 holes was used for this study, whereas the optimal inlet pressure of 3 bars was regulated using main line valve and bypass line valve. The pressure gauges were used to measure the inlet pressure upstream and recovery pressure at the downstream pipe line. 2 kgs of Schleichera Oleosa oil was heated up to the desired optimized temperature (60 °C) in the reactor by circulating the liquid glycerine through the jacket surrounding the holding reactor tank. The schematic diagram of the HC setup is presented in Fig. 1. The optimized conditions of 0.75 wt.% potassium hydroxide as alkali catalyst and 1:6 of oil to methanol molar ratio were used to produce the SOME. The mixture was then passed through the optimized orifice plate for 30 min reaction time with respect to the optimized inlet pressure of 3 bars to generate the constructive cavitation condition. The reactant mixture was allowed to settle down in the reactor by gravity settling for 3 h. The by-products and catalyst were discharged out through the opening of the reactor. The products were washed with the warm water at 50 °C to remove residual catalysts and other by-products. The remaining methanol and water in the product were evaporated under rotary vacuum evaporator.

3. Engine test setup

The engine test setup consists of a single cylinder, four strokes, diesel engine connected to eddy current type dynamometer for loading, facilitated with water cooling jacket. It is provided with necessary instruments for combustion pressure and crank-angle measurements. These signals are interfaced to computer through engine indicator for P-θ and P-V diagrams. Provision is also made for interfacing airflow, fuel flow, temperatures and load measurement. The setup has stand-alone panel box consisting of air box, fuel tank, manometer, fuel measuring unit, transmitters for air and fuel flow measurements, load and speed display. Rota meters are provided for cooling water and calorimeter for water flow measurement. Smoke meter is also attached with the engine set up to measure the smoke opacity of the engine on a particular fuel being used to run it.

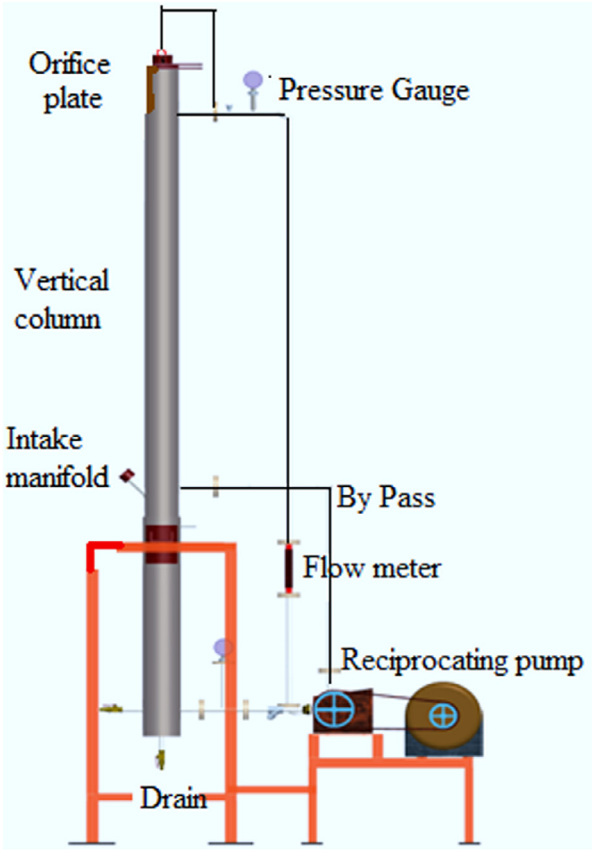


Fig. 1. The schematic diagram of the hydrodynamic setup.

The setup enables study of engine performance for brake power, indicated power, frictional power, brake mean effective pressure, indicated mean effective pressure, brake thermal efficiency, indicated thermal efficiency, mechanical efficiency and brake specific fuel consumption. Windows based Engine Performance Analysis software package "Engine soft" is provided for on line performance evaluation. The detailed specifications of various components are given in Table 1. The main aim of this experiment is to investigate the effects on performance of blending of biodiesel with gasoline diesel fuel in a Kirloskar diesel engine for wide range of operating parameters. The photograph of specified engine set-up for performance and emission testing is shown in Fig. 2.

Table.1
Technical details of the engine.

S. No	Component	Specification
1	Engine make	Kirloskar
2	Engine type	1 cylinder, 4stroke, water cooled
3	Rated Power	3.5 kW at 1500 rpm
4	Cylinder Volume	661 cc
5	Compression Ratio	Variable (12 to 18)
6	Dynamometer	Eddy current, water cooled
7	Piezo Sensors	Range 5000 PSI
8	Crank Sensor	Resolution 1°, Speed 5500 RPM
9	Load Sensor	Load cell, type strain gauge
10	Software	"Engine soft", Engine Performance analysis software

Please cite this article in press as: A.K. Yadav et al., Performance and emission characteristics of a stationary diesel engine fuelled by Schleichera Oleosa Oil Methyl Ester (SOME) produced through hydrodynamic cavitation process, Egypt. J. Petrol. (2017), http://dx.doi.org/10.1016/j.ejpe.2017.01.007

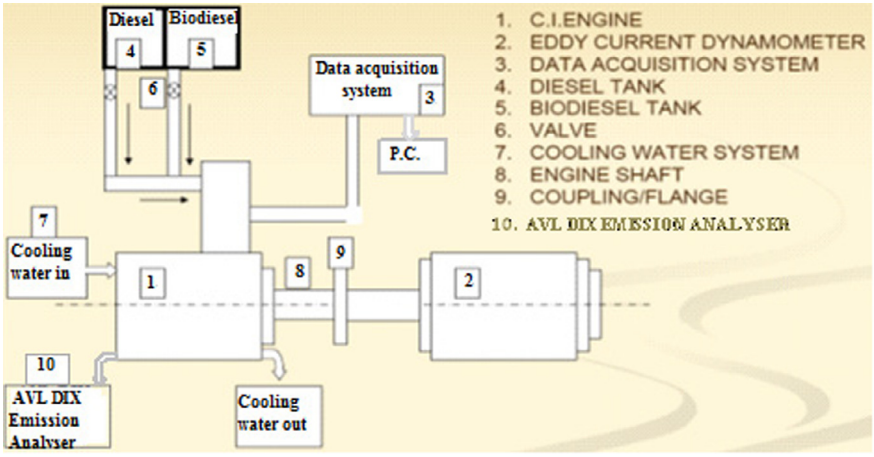


Fig. 2. Line diagram of experimental set up.

The NOx, CO2 and CO emissions were measured with AVL DIX, Emission Diagnostic System. The performance and emission characteristics for different test fuels were compared with the result of baseline diesel operation. All experiments were repeated thrice in order to determine the range and reproducibility of the results.

3.1. Preparation of biodiesel blends and characterization of test fuel properties

Four different blends B-10 (10% biodiesel + 90% diesel v/v), B-20 (20% biodiesel + 80% diesel v/v), B-30 (30% biodiesel + 70% diesel v/v) and B50 (50% biodiesel + 50% diesel v/v) were prepared. Various physico-chemical properties of fuel including density, viscosity, calorific value, cold filter plugging point (CFPP), and fatty acids composition were determined according to standard methods and found to be acceptable according to the EN 14214 and ASTM D 6751 standards. Table 2 presents the average values of the physico-chemical properties of neat SOME, diesel and their blends.

The detailed fatty acids profile of the SOME sample was determined using gas chromatography equipment. Table 3, represents the fatty acids composition. The fatty acids composition indicated that the oil was rich in Oleic and Arachidic acid.

4. Engine performance parameters

4.1. Brake thermal efficiency vs. brake power

Thermal efficiency is the ratio of power output to the energy of injected fuel. Energy of the injected fuel is the product of mass flow rate of fuel and calorific value. Hence BTE is indicating the inverse of BSEC. Fig. 3 is representing the variation of brake thermal efficiency (BTE) with BP. The values of BTE were increased with increasing load in all cases. This was due to reduction in heat losses at higher load. The BTE of SOME blends showed lower brake thermal efficiency compared to diesel fuel. The B10, B20, B30 and B50 blends of SOME showed average reduction of 2.8, 6.5, 7.8 and 14.3% in BTE respectively. This reduction can be attributed to the lower calorific value which leads to increase in the specific fuel consumption [5]. The increase in fuel consumption requires the increase of

Table 3
Fatty acid composition of Schleichera Oleosa oil.

Fatty acids	Chemical formula	Degree of unsaturation	Schleichera Oleosa oil
Palmitic	$C_{16}H_{32}O_2$	16:0	6.73
Palmitoleic	$C_{16}H_{30}O_2$	16:1	2.88
Stearic	$C_{18}H_{34}O_2$	18:1	5.81
Oleic	$C_{18}H_{32}O_2$	18:2	48.51
Linoleic	$C_{20}H_{40}O_2$	20:0	6.57
Arachidic	$C_{20}H_{38}O_2$	20:1	27.21
∑ Saturated fatty acids			40.64
∑ Unsaturated fatty acids			57.96

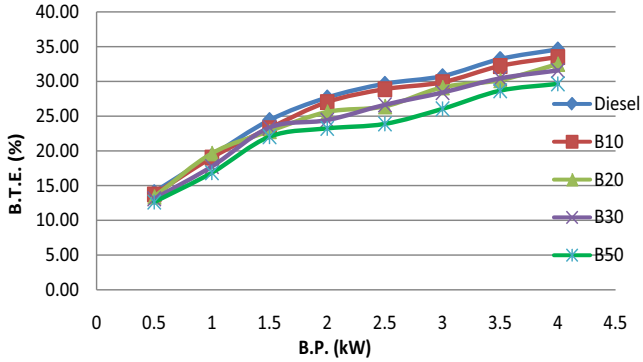


Fig. 3. Variation in brake thermal efficiency with respect to change in BP.

Table 2
Physico-chemical properties of Schleichera Oleosa Methyl Esters.

Type of blend	Kinematic Viscosity at 40 °C (mm^2/s)	Flash Point (°C)	Calorific Value (kJ/kg)	Specific Gravity	CFPP (°C)
Diesel	2.9	60	43,350	0.827	−8
B-10	3.32	68	42,979	0.838	−7
B-20	3.52	76	42,609	0.843	−6
B-30	3.9	83	42,240	0.843	−6
B-50	4.2	98	41,870	0.854	−5
B100	4.4	155	40,000	0.880	−4

Please cite this article in press as: A.K. Yadav et al., Performance and emission characteristics of a stationary diesel engine fuelled by Schleichera Oleosa Oil Methyl Ester (SOME) produced through hydrodynamic cavitation process, Egypt. J. Petrol. (2017), http://dx.doi.org/10.1016/j.ejpe.2017.01.007

volume and duration of fuel injection. Since the fuel was injected at fixed injection timing more fuel was injected during the expansion stroke and leads to more diffusion combustion. Similar results are reported by previous researchers [16,5,17–19].

4.2. Brake specific fuel consumption (BSFC) vs. brake power (B.P.)

BSFC is the ratio of mass flow rate of fuel to brake power output of the engine. Variation in BSFC of blends B10, B20, B30, B50 and diesel with respect to change in load is shown in Fig. 4.

From the graph, it was observed that the brake specific fuel consumptions of diesel as well as the blends were decreasing with increasing load. The reason for this could be that% age increase in fuel required to operate the engine is less than the% age increase in brake power output due to relatively less portion of the heat energy losses at higher loads due to lower temperature gradient at warmed-up condition The values of BSFC of the SME blends were found slightly higher than neat diesel under all range of engine loads. The B10, B20, B30 and B50 reported 4.7, 5.4, 10.6 and 23.9% average increased fuel consumption than the neat diesel fuel. The reason of higher BSFC of SME blend was due to lower calorific value and hence the higher amount of fuel was required to produce the same amount of energy. Higher proportions of Simarouba biodiesel in the blends increase the viscosity which in turn increased the specific fuel consumption due to the poor atomization of the fuel. The variations in the specific fuel consumption with load follow a similar trend with the test results reported in the literature [15,16,5,8].

5. Engine exhaust emissions

5.1. Carbon monoxide vs. brake power

Fig. 5 shows the variation of carbon monoxide (CO) emission with brake power for SOME and diesel. The 10, 20, 30 and 50% blend showed average reduction of 6.8, 12.7, 22.5 and 28.3% respectively compared to diesel fuel. Formation of CO during in-cylinder combustion in diesel engines is primarily attributed to lower air-fuel equivalence ratios of the combustible mixtures as load was increased, there was an increase in CO emission level at higher load due to rich mixture which results in incomplete combustion of fuel. At higher engine loads, the CO emissions of the blended fuels were significantly lower than baseline diesel operation. This is attributed to increase in-cylinder temperature at higher engine load and presence of oxygen in biodiesel fuel, which improves fuel combustion and consequently, reduces CO emissions. This result agreed with Ramadhas et al. [19] emissions compared to diesel fuel and other blends

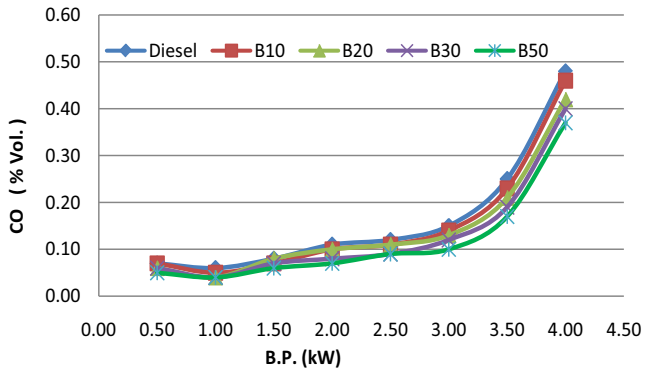


Fig. 5. Variation in quantity of CO with respect to change in BP.

5.2. Carbon dioxide vs. brake power

Fig. 6 shows the variation of carbon dioxide (CO_2) emissions with the load. It can be observed that the carbon dioxide emission increases with increase in load. The carbon dioxide emission is found to increase with an increase in the concentration of biodiesel blends as the fuel. The 10, 20, 30 and 50% SME blend showed average 7.3, 12.8 and 21.3 and 28.3% increased CO_2 emissions compared to average diesel CO_2 emissions. These higher CO_2 emissions of biodiesel blends may be due to their more complete oxidation as compared to diesel. SME of the CO produced during combustion of biodiesel might have converted into CO_2 by taking up the extra oxygen molecules present in the biodiesel chain.

5.3. Oxides of nitrogen vs. brake power

Fig. 7 shows the variation of oxides of nitrogen (NO_x) emission for diesel and SOME blends. Oxides of nitrogen popularly referred as NOx, are the critical diesel engine emissions of major concern owing to their toxicity .It mostly comprises of nitric oxide (NO) and nitrogen dioxide (NO_2). Combustion flame temperature, availability of oxygen, cetane number and time for oxygen-nitrogen reaction are the major factors controlling NOx formation [18,19]. It is observed that the NO_x emission is increased with increase in the load. Emissions of NOx were found to increase with the volume fraction of the SOME in the test fuels for the entire range of engine operation. At full load, SOME10, SOME20, SOME 30 and SOME 50 had NOx emissions of 840 ppm, 875 ppm, 948 ppm and 1056 ppm as compared to 788 ppm for diesel. It is also observed that complete combustion causes higher combustion temperature which results in higher NO_x formation. Similar trends of increasing NO_x were also reported by other researchers [6,10,18–20].

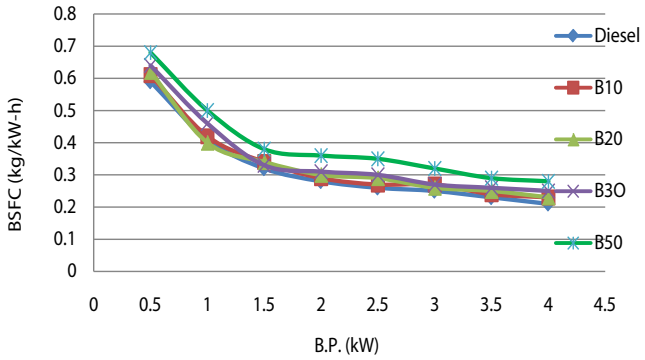


Fig. 4. Variation in brake specific fuel consumption with respect to change in BP.

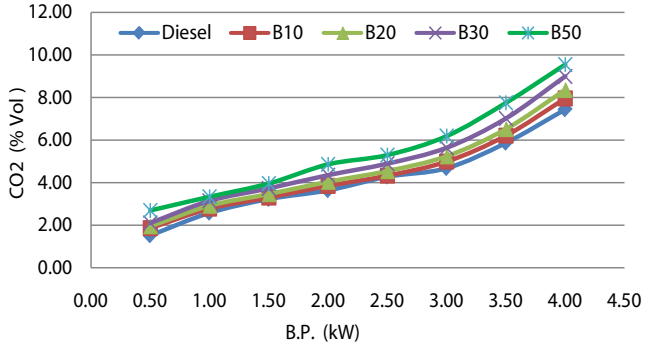


Fig. 6. Variation in quantity of CO_2 with respect to change in BP.

Please cite this article in press as: A.K. Yadav et al., Performance and emission characteristics of a stationary diesel engine fuelled by Schleichera Oleosa Oil Methyl Ester (SOME) produced through hydrodynamic cavitation process, Egypt. J. Petrol. (2017), http://dx.doi.org/10.1016/j.ejpe.2017.01.007

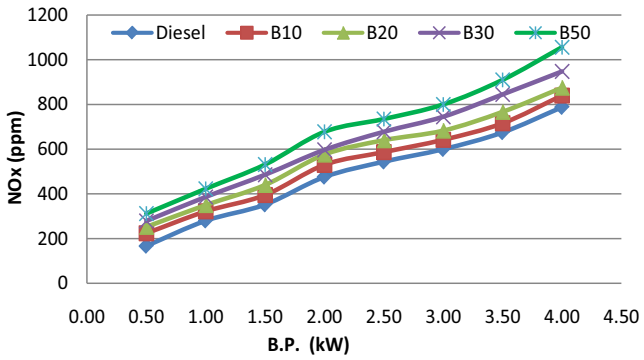


Fig. 7. Variation in quantity of NO_x with respect to change in BP.

6. Conclusions

The performance and emission characteristics of diesel fuel and biodiesel derived from Schleichera Oleosa Oil based on HC and its blends of B10, B20, B30 and B50 were compared. Based on the experimental results found the following conclusions are drawn:

- The better yield (95%) obtained for hydrodynamic cavitation process at the optimized conditions of 0.75 wt.% KOH as alkali catalyst and 1:6 of oil to methanol molar ratio, in very less time (30 min)
- The properties of SOME produced from this reactor conform to both standards of EN 14214 and ASTM D 6751.
- BSFC is lowest for diesel and highest for B50 at all loads. The B10, B20, B30 and B50 reported 4.7, 5.4, 10.6 and 23.9% average increased fuel consumption than the standard diesel fuel.
- BTE dropped marginally with the increase of SOME volume fraction in the test fuel. The B10, B20, B30 and B50 SOME showed average 3.3, 6.5, 7.8 and 14.3% reduction in BTE respectively.
- Blended Biodiesel fuel gives lesser CO emission and higher carbon dioxide and NOx emissions than mineral diesel.

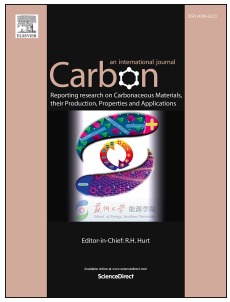
Form the above experimental study it can be concluded that methyl esters of Schleichera Oleosa oil can be successfully used as an alternative fuel in diesel engines without any engine modifications.

References

[1] A. Demirbas, Energy Convers. Manage. 50 (2009) 14–34.
[2] N.N.A.N. Yusuf, S.K. Kamarudin, Z. Yaakub, Overview on the current trends in biodiesel production, Energy Convers. Manage. 52 (2011) 2741–2751.
[3] A.E. Atabani, A.S. Silitonga, H.C. Ong, T.M.I. Mahlia, H.H. Masjuki, I.A. Badruddin, Renew Sust. Energy Rev. 18 (18) (2013) 211–245.
[4] Jagannath B. Hirkude, Atul S. Padalkar, Fuel 119 (2014) 266–273.
[5] A.K. Agarwal, K. Rajamanoharan, Appl. Energy 86 (2009) 106–112.
[6] K. Khiari, S. Awad, K. Loubar, L. Tarabe, R. Mahmoud, M. Tazerout, Energy Convers. Manage. 108 (2016) 392–399.
[7] A. Pal, A. Verma, S.S. Kachhwaha, S. Maji, Renewable Energy 35 (2010) 619–624.
[8] J. Kakati, T.K. Gogoi, Energy Convers. Manage. 121 (2016) 152–161.
[9] A.K. Yadav, M.E. Khan, A. Pal, B. Singh, Biofuels (2016), http://dx.doi.org/10.1080/17597269.2016.1259522.
[10] M.M. Azam, A. Waris, N.M. Nahar, Biomass Bioenergy 29 (2005) 293–302.
[11] C. Palanuvej, N. Vipunngeun, J. Health Res. 22 (2008) 203–212.
[12] M. Gandhi, N. Ramu, S. Bakkiya Raj, Int. J. Pharm. Sci. Res. 2 (2011) 1244–1250.
[13] H. Bhatia, J. Kaur, S. Nandi, V. Gurnani, A. Chowdhury, P.H. Reddy, J. Pharm. Res 6 (6) (2013) 224–229.
[14] A.K. Yadav, M.E. Khan, A. Pal, A.M. Dubey, Energy Sources A: Recovery Utilization Environ. Effects 38 (23) (2016) 3447–3452.
[15] K. Sivaramakrishnan, P. Ravikumar, Thermal Sci. 17 (2013) 179–193.
[16] O.M. Ali, R. Mamat, N.R. Abdullah, A.A. Abdullah, Renewable Energy 86 (2016) 59–67.
[17] A.K. Yadav, M.E. Khan, A. Pal, Egypt J. Petrol. (2016), http://dx.doi.org/10.1016/j.ejpe.2016.07.006.
[18] A. Dhar, R. Kevin, A.K. Agarwal, Fuel Process. Technol. 97 (2012) 118–129.
[19] A.S. Ramadhas, C. Muraleedharan, S. Jayaraj, Renewable Energy 30 (2005) 1789–1800.
[20] A.K. Yadav, M.E. Khan, A. Pal, D. Sharma, Int. J. Sustainable Agri. Manage. Informatics 1 (2015) 285–300.
[21] F. Halek, A. Delavari, A. Kavousi-rahim, Clean Technol. Environ. Policy 15 (2013) 1063–1068.

Please cite this article in press as: A.K. Yadav et al., Performance and emission characteristics of a stationary diesel engine fuelled by Schleichera Oleosa Oil Methyl Ester (SOME) produced through hydrodynamic cavitation process, Egypt. J. Petrol. (2017), http://dx.doi.org/10.1016/j.ejpe.2017.01.007

Accepted Manuscript



P-type multilayer graphene as a highly efficient transparent conducting electrode in silicon heterojunction solar cells

Kamlesh Patel, Pawan K. Tyagi

PII: S0008-6223(17)30171-9

DOI: 10.1016/j.carbon.2017.02.042

Reference: CARBON 11759

To appear in: *Carbon*

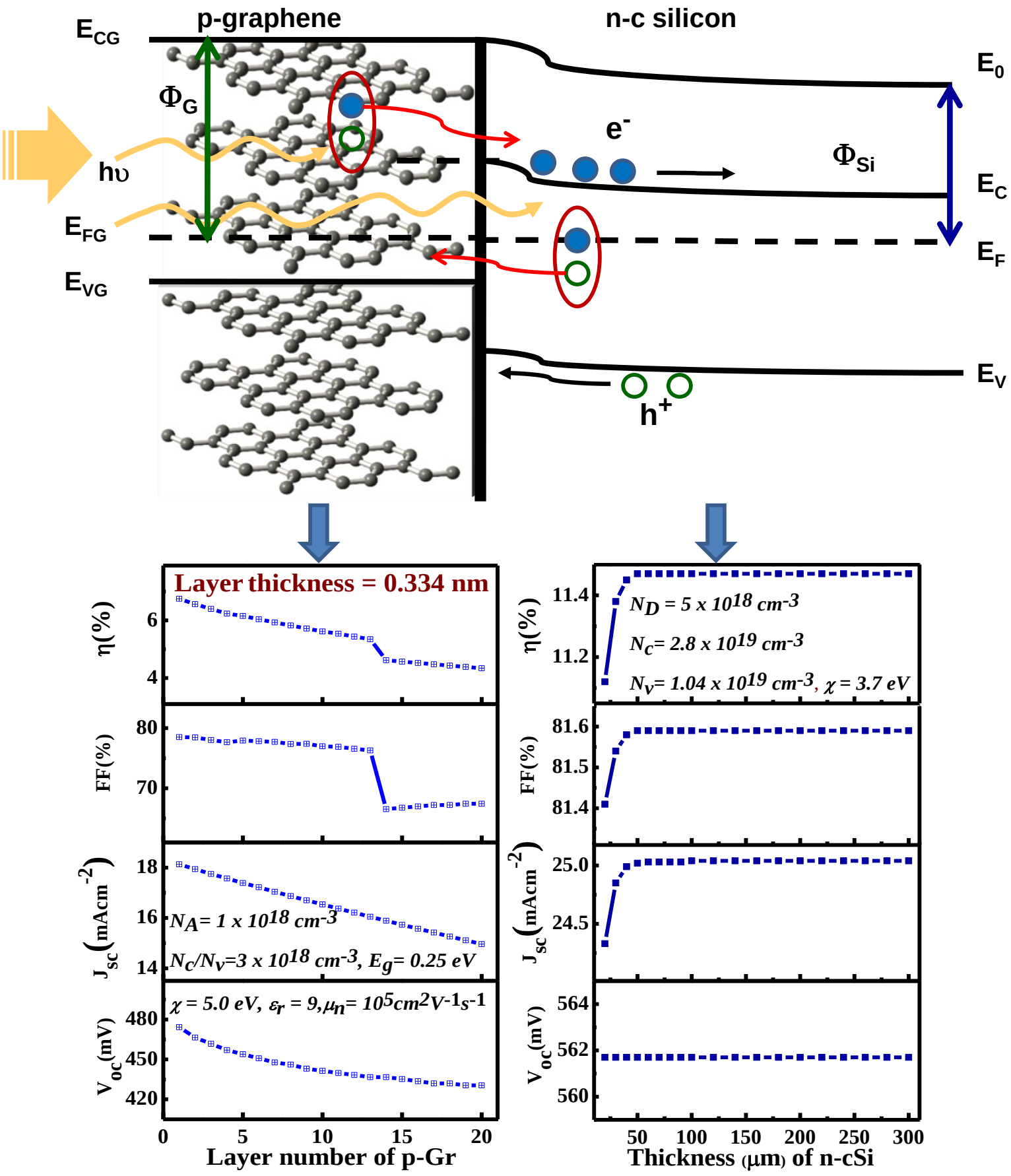
Received Date: 23 August 2016

Revised Date: 29 January 2017

Accepted Date: 15 February 2017

Please cite this article as: K. Patel, P.K. Tyagi, P-type multilayer graphene as a highly efficient transparent conducting electrode in silicon heterojunction solar cells, *Carbon* (2017), doi: 10.1016/j.carbon.2017.02.042.

This is a PDF file of an unedited manuscript that has been accepted for publication. As a service to our customers we are providing this early version of the manuscript. The manuscript will undergo copyediting, typesetting, and review of the resulting proof before it is published in its final form. Please note that during the production process errors may be discovered which could affect the content, and all legal disclaimers that apply to the journal pertain.


p-graphene
n-c silicon
E_{CG}
Φ_G
hυ
E_{FG}
E_{VG}
e^-
Φ_{Si}
E_0
E_C
E_F
E_V
h^+
Layer thickness = 0.334 nm
η(%)
FF(%)
J_{sc} (mAcm^{-2})
V_{oc} (mV)
N_A= 1 x 10^{18} cm^{-3}
N_C/N_V=3 x 10^{18} cm^{-3}, E_g= 0.25 eV
χ = 5.0 eV, ε_r = 9, μ_n= 10^{5}cm^{2}V^{-1}s^{-1}
Layer number of p-Gr
N_D = 5 x 10^{18} cm^{-3}
N_C= 2.8 x 10^{19} cm^{-3}
N_V= 1.04 x 10^{19} cm^{-3}, χ = 3.7 eV
Thickness (μm) of n-cSi

ACCEPTED MANUSCRIPT

P-type multilayer graphene as a highly efficient transparent conducting electrode in silicon heterojunction solar cells

Kamlesh Patel[a,b] and Pawan K. Tyagi[b,*]

[a]Department of Electronic Science, University of Delhi South Campus, New Delhi, 110021, India

[b]Department of Applied Physics, Delhi Technological University, Delhi, 110042, India

Abstract:

In this paper, we have simulated the structure of a p-graphene/n-crystalline silicon solar cell by using AFORS-HET software. Following our recent report (Patel and Tyagi 2015) here also we have considered graphene as 3D in nature. To obtain confinement, boundary conditions have been applied by controlling number of layers. Formation of Schottky junction has been ensured by making of electrical contact along the c-axis to collect the minority carriers. Power conversion efficiency of 6.75 % has been achieved with best-simulated cell's parameters of p-type single layer graphene. Under the illumination conditions of AM1.5G, it has been observed that as layer number increases up to 20 efficiency decreases linearly to 4.34 %. Through the optimization of parameters of n-crystalline silicon layer, a maximum efficiency of 9.812 % has been achieved for 80 μm thick silicon. Such heterojunction photovoltaic device has shown large temperature dependence. Cell performance has been further tested taking parameters of commercial available n-type Si. Optimum efficiency of 11.47 % has been achieved for 100 μm thick silicon layer. Finally, we have demonstrated that p- type multilayer graphene can act as an efficient transparent conducting electrode.

*Corresponding author: pawan.phy@dce.edu, pawankumartyagi@gmail.com (Pawan. K. Tyagi)

ACCEPTED MANUSCRIPT

1. Introduction

Recently, in graphene carrier mobility exceeding 10^5 $cm^2V^{-1}s^{-1}$ has been reported at room temperature. This value closely approaches the estimated value of $>2\times10^5$ $cm^2V^{-1}s^{-1}$ (Mayorov *et al* 2011). In recent advances sheet resistance as low as 8.8 Ωsq^{-1} with 84% optical transparency (Kharpach *et al* 2012), including sheet carrier density as high as 8.9×10^{14} cm^{-2} with mean free path large as ~0.6 μm have been reported for the chemical doped few layer graphene (FLG). These extraordinary properties have led to the applications of multilayer graphene as a transparent conducting electrode. In graphene based heterojunction, transparent conducting electrode (TCE) introduced a built-in electric field near the interface between the electrode and silicon. This field transports the photo-generated charge carriers to the cell terminals. Built-in electric field depends on the work function of graphene as well as silicon that could be enhanced by tuning the work function of either multilayer graphene or silicon. Recently, in both theoretical and experimental reports (Bae *et al* 2010; Kharpach *et al* 2012) it has been demonstrated that chemical doping with HNO_3, $FeCl_3$ and $AuCl_3$ makes the graphene film strongly p-type and modifies the work function (3.5 eV-5.1 eV) (Lin *et al* 2013). In 2013, Li *et al* (2013) reported that in multilayer graphene, if chemical doping was done with $SOCl_2$ and HNO_3 then conversion efficiency increased from 5.52 % to 8.94 % and 9.27 %, respectively. Recently, Meng *et al* (2013) reported that intercalation of $NbCl_5$ and ZnMg in few layer graphene/graphite flake makes effective p- and n-type doping, respectively. During the intercalation process, ZnMg and $NbCl_5$ interact with the FLG and not only transfer charges (electron or holes) to carbon atoms but also increase the disorder in FLG lattice locally. These intercalates are successfully intercalated between FLG layers either forming the cluster or making intercalate layer, as a consequence sp^2 to sp^3 hybridization transformation occurred. Due to this transformation, band of doped FLG might be opened at the Γ point. It was reported that Fermi levels enters the π band of FLG after intercalating with $NbCl_5$ (Meng *et al* 2013). Further advancement was reported by Lin *et al* (2013). They presented a theoretical model considering: graphene work function, layer number modulation and adding an antireflection film where a maximal theoretical efficiency of 9.2 % was achieved. On the other hand, when cell was fabricated with optimized experimental results have demonstrated that by deliberate chemical doping, work function of p-type graphene increases whereas n-type decrease. Albeit p-

graphene/n-silicon configuration has been mostly studied (Lin *et al* 2013; Li *et al* 2010; Miao *et al* 2012; Feng *et al* 2012; Cui *et al* 2013, Ruan *et al* 2015; Shi *et al* 2013) and the maximum simulation efficiency of about 8.6 % (Miao *et al* 2012) without coating and 14.5 % (Shi *et al* 2013) with colloidal anti-reflection coating in Gr/Si heterojunction cell have been reported. Thus, this configuration has been found to be more interesting among the researchers. Motivated by this, in present work we have simulated in p-Gr/n-Si heterojunction using AFORS-HET (Automat FOR Simulation of HETero-structures) software (Stangl *et al* 2008) under air mass 1.5 (AM1.5) illuminations with power density of 100 mWcm^{-2}. Independent effect of the layer's parameters on the performance of cell structure and insights behind the cell responses have been discussed in detail.

2. Simulation Structure

Due to gapless (or small bandgap) nature in graphene, Fermi Level is always either in the conduction or in the valence band. This makes graphene different than the others 2D semiconducting materials those become insulating if Fermi level enters the bandgap. Generally, 2D semiconductor systems exhibit bandgap of > 1 eV (Giannazzo *et al* 2011). This results in completely different electron-doped or hole-doped structures. On the other hand, in graphene the nature of the carrier system changed at the Dirac point from electrons to holes (or vice versa) in a single structure. Recently, a diffusion-drift theory has been developed for understanding the carrier transport in single and multilayer graphene (Ancona 2010). Ideally, a semiconductor system is called 2D only if it possesses one physical dimension in order of Fermi wavelength. As reported by Giannazzo *et al* (2011) and Patel and Tyagi (2015), Fermi wavelength is $\lambda_F = \left(2\times 10^7\sqrt{\pi/n}\right)$ nm for graphene, where n is the sheet carrier density in cm^{-2}. Recently Sarma *et al* (2011) reported that if n approaches to $\sim 10^{15}$ cm^{-2} then λ_F would be $\approx$ 1 nm. Therefore, in doped graphene, even bilayer graphene cannot satisfy the condition $\langle t\rangle \leq \lambda_F$, where $\langle t\rangle$ is the average thickness for a 2D electron system. Recently, it has also been reported that if multilayer or single layer graphene is integrated with silicon wafer then 2D transport equation can be coupled with 3D equations (Ancona 2010). In graphene/crystalline silicon heterojunction solar cell, sheet carrier density (n_{2D}) is in cm^{-2}, which corresponds to doping concentration of $\sim 3.3\times 10^{-8}\times N_A$, where N_A is doping concentration in cm^{-3}. Carrier density can be

controlled by chemical doping and influenced the work function as well as cell resistance. Work function also changed with effective valence band density.

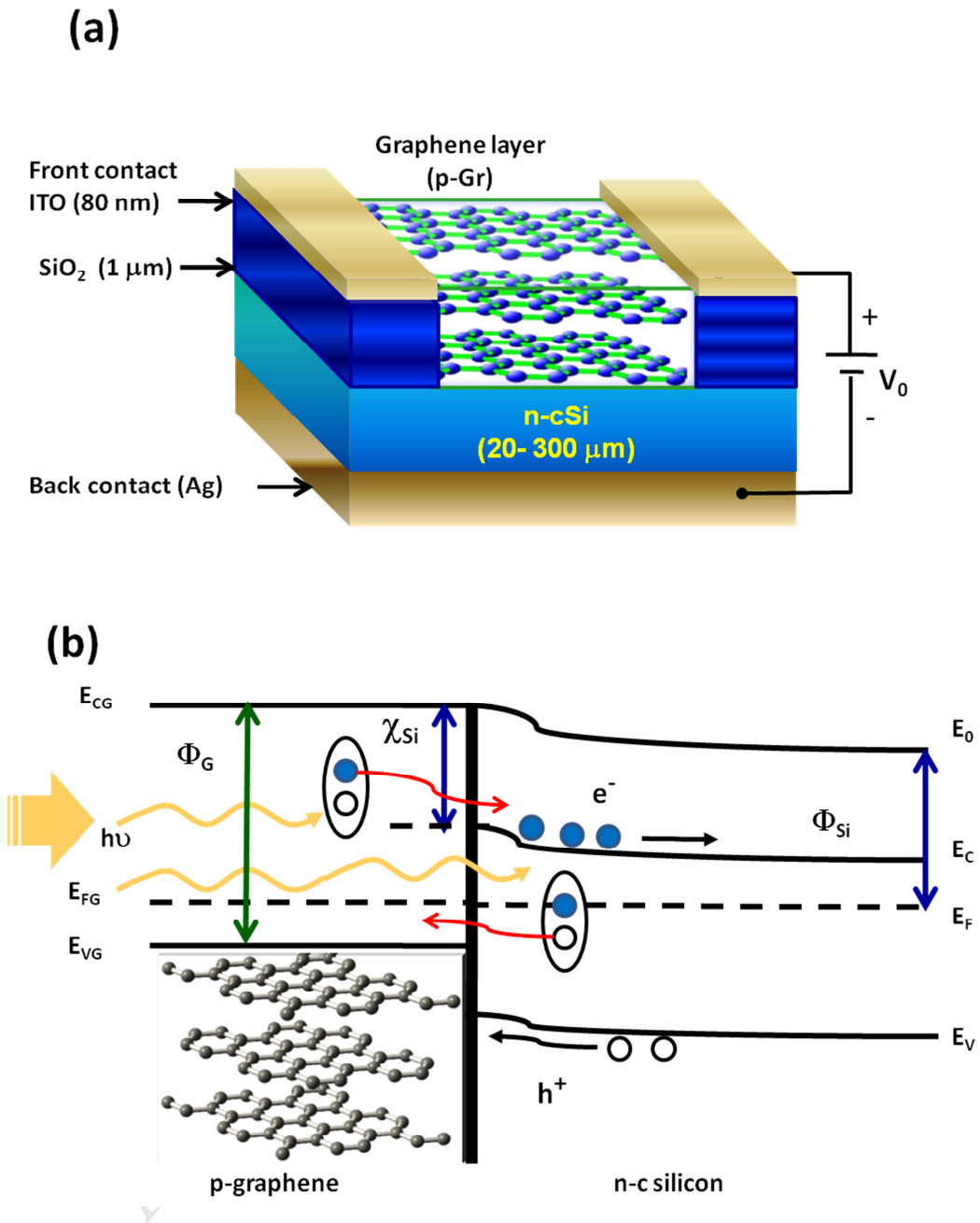


Figure 1. Graphene/silicon heterojunction solar cell. (a) Schematic diagram of simulated structure, where ITO is on the top of graphene (b) Schematic diagram of p-type graphene/ n-c silicon interface, where Φ_G ,Φ_{Si} and χ_{Si} are the graphene work function, silicon work function, and the silicon electron affinity, respectively.

In gapless graphene, carrier density and effective valance band density can be obtained by multiplying the film thickness with the bulk values. Furthermore, in proposed structure as depicted in Figure 1(a), transport of carrier has been made along c-axis of graphene. Therefore, being motivated with facts discussed above, in the simulated work graphene is presumed as quasi 3D in nature. In the present work, basic structure of p-graphene/n- crystalline silicon heterojunction solar cell is configured as TCO (ITO)/p-Gr/n-cSi/Ag and shown in Figure 1(a). Here a layer of SiO_2 is required to insulate the direct carrier transport through transparent conductive oxide (TCO) (contact) to n-cSi layer so that transport will only make through the graphene layer (Lin *et al* 2013; Miao *et al* 2012). Here, we have taken ITO as TCO material and deposited on the top of graphene. ITO can be deposited by using electron beam and pulsed layer deposition (PLD) technique directly on graphene transferred on SiO_2/Si pattern substrate (Abd El-Raheem M M *et al* 2010; Ohshima T *et al* 2010; Zare S *et al* 2016). These deposition techniques will not damage the graphene. Further details of contacts including front as well as back have been tabulated in Table S1. The values and ranges of various parameters are tabulated in Table S2. To simulate the quantum efficiency (QE), the illumination conditions were kept as the monochromatic intensity (photon flux) of 1×10^{16} $cm^{-2}s^{-1}$ with 10 nm spectral width in the range of 300 – 1200 nm. Thickness, refractive index (n) and extinction coefficient (k) of single layer graphene were taken as 0.334 nm, 2.7 and 1.45 respectively, for the initial simulation study (Ni *et al* 2007; Nelson *et al* 2010), and then other six parameters of graphene were varied in the feasible ranges. These parameters were the acceptor concentration (N_A), bandgap (E_g), effective conduction and valance band densities (N_C/N_V), electron affinity (χ), relative permittivity (ε_r) and electron mobility (μ_n). Then the simulation was performed for different layer numbers in multilayer graphene silicon cells, where thickness has been considered as a seventh parameter. After achieving an efficiency around 6.75 % by optimizing the p-Gr layer, we further optimized the parameters of n-type crystalline silicon (n-cSi) like the donor concentration (N_D), effective conduction and valance band densities (N_C/N_V), the electron affinity (χ) and thickness for n-cSi layer. The other parameters of n-cSi layer like the relative permittivity (ε_r), electron mobility (μ_n) and bandgap (E_g) were kept at their standard values in the simulation as per the previous reports (Zhang *et al* 2013; Gangophadhyay *et al* 2012; Wang Lishing *et al* 2011). We have achieved the highest efficiency in single layer p-Gr/n-cSi

heterojunction cell after the complete optimization of the layer parameters of both graphene as well as silicon.

3. Results and discussion

3.1. Optimization and simulation of p-graphene layer

This study has been performed to obtain maximal efficiency in a single layer Gr/Si cell. In the p-Gr/n-cSi solar cell, since the graphene and semiconductor interface barrier is ideally Schottky in nature, a built-in voltage developed in the depletion region of silicon layer due to recombination of the majority charge carriers. The minority charge carriers, i.e. holes in the n-cSi layer, tend to move towards the p-type graphene layer and the energy levels bend upward near the Gr/Si interface (Mohammed *et al* 2012). This voltage (V_{BI}) is the difference of the barrier height (Φ_{BI}) and energy gap (E_g) in the silicon. The barrier height (Φ_{BI}) is defined as a difference of the work function of graphene and silicon as per the following equations (Lin *et al* 2013),

$$\Phi_{BI} = \Phi_G - \Phi_{SI} \tag{1}$$

$$\Phi_{Si}, n-type = \chi_{Si} + k_B T \ln\left(\frac{N_D}{N_C}\right)_{Si} \tag{2}$$

$$\Phi_G, p-type = \chi_G + k_B T \ln\left(\frac{N_A}{N_V}\right)_G \tag{3}$$

where Φ_G, χ_G, Φ_{SI}, and χ_{SI} are the graphene work function and affinity, the silicon work function and the silicon affinity, respectively, k_B (= 1.38×10^{-16} cm^2 kgs^{-1}) is the Boltzmann constant, T is a room temperature (300 K). Here N_D and N_C are the donor concentration and the effective conduction band density of the n-cSi, respectively. In equation (3), N_A and N_V are the acceptor concentration and effective valence band density of the graphene layer, respectively.

On illumination of light, electron and hole, (e-h) pairs are generated in the cell and then separated due to the built in voltage at the interface. These free minority carriers move towards the p-Gr and n-cSi regions, respectively, as shown in Figure 1(b) (Mohammed *et al* 2012). These photo-generated charge carriers enhance the carrier density in the respective regions and develop an open circuit

voltage (V_{oc}) when the cell is open circuited. At the time of short-circuiting, the excess charge carriers are collected at the contact electrodes, which results in a short- circuited current in the external circuit.

ACCEPTED MANUSCRIPT

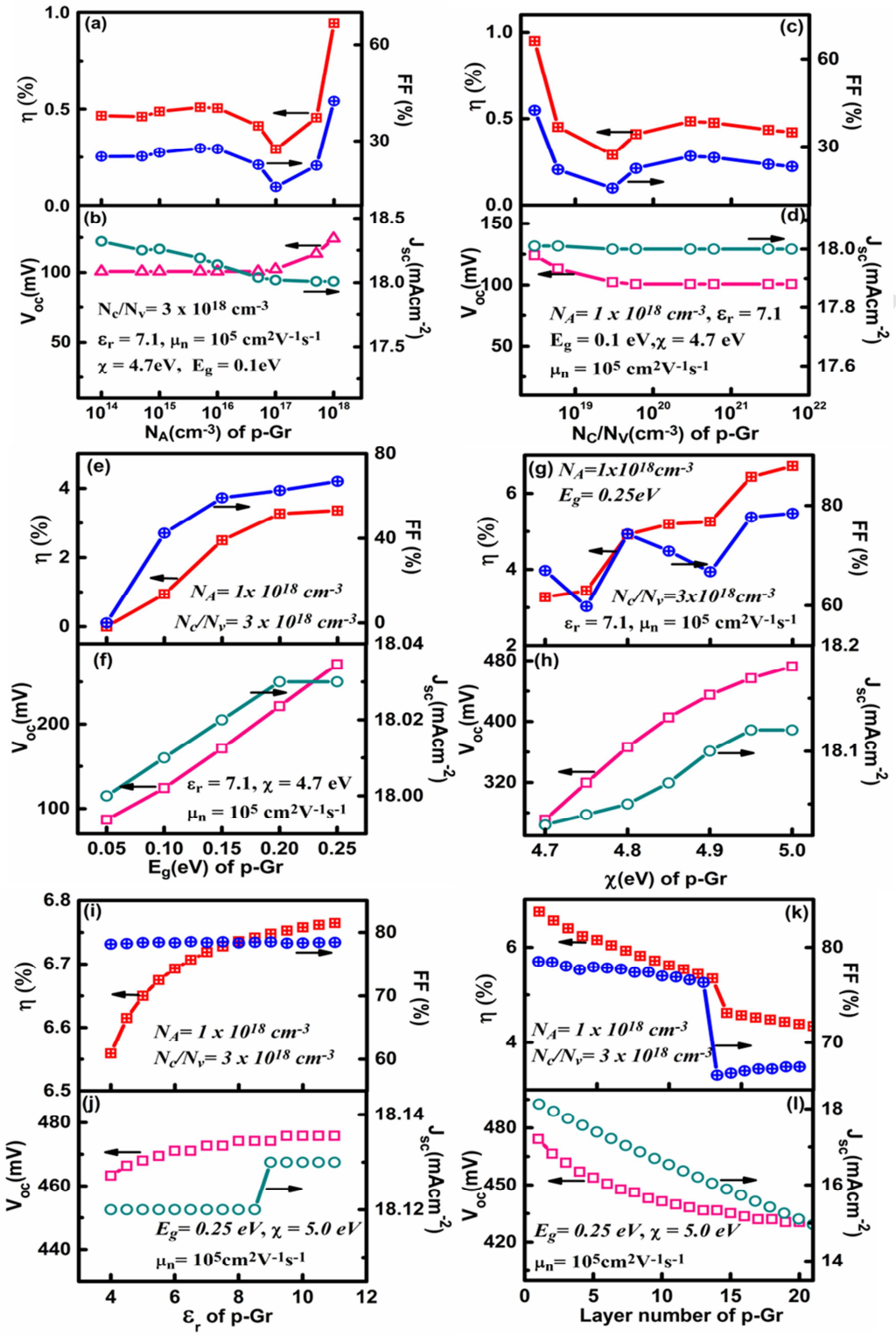


Figure 2. Schematic representation of cell performance with the optimization of the parameters of p-graphene layer, (a-b) the acceptor concentration N_A (cm^{-3}), (c-d) the effective band density N_C/N_V (cm^{-3}), (e-f) the bandgap energy E_g (eV), (g-h) the electron affinity χ (eV), (i-j) the relative permittivity ε_r, and (k-l) layer number. The parameters of n-cSi were kept as, the donor concentration $N_D = 1\times10^{16}$ cm^{-3}, the effective band density $N_C/N_V = 3\times10^{19}$ cm^{-3}, the electron affinity χ= 4.05 eV and thickness 100 µm. The other parameters of silicon as well as p-type graphene are given in Table S2.

In present work, we started the optimization of accepter concentration (N_A) of graphene layer while some significant values have been assigned to other parameters (Tongay *et al* 2012; Tan *et al* 2007; Sarma *et al* 2011; Giannazzo *et al* 2011). The effective conduction and valance band densities (N_C and N_V) were kept to 3×10^{18} cm^{-3} for single layer graphene, which is estimated from the effective electron mass, $m_e^* = 0.012\, m_0$ (Tiras *et al* 2013) and the effective hole mass $m_h^* = 0.0105\, m_0$ (Zou *et al* 2011), where free electron mass $m_0 = 9.1 \times 10^{-31}$Kg. In this case, taking the account of quantum confined effect influenced doping, $N_C^{3D} = N_C^{2D}.t$, where *t* is thickness of graphene layer and $N_C^{2D} = 4\pi\, m_e^* k_B\, T/h$, here *h* (= 6.62 × 10^{-27} cm^2 kgs^{-1}) a Planck's constant. Results are shown in Figure 2(a-b). Doping of $AuCl_3$ has been reported to increase Φ_G from 4.7 eV to 5.1 eV and this tiny shift in Φ_G significantly found to decrease the sheet resistance (R_{sh}) (Lin *et al* 2013). Therefore, as N_A increases, the short-circuited current density (J_{sc}) reduced infinitesimally from 18.19 mA/cm^2 to 18.01 mA/cm^2 until N_A reach to 10^{18} cm^{-3}. After $N_A \approx 10^{17}$ cm^{-3} in p-Gr, the photo-generated electrons moved easily from the graphene layer to n-cSi with high mobility, and increased V_{oc} up to 124.2 mV. Efficiency (η) and fill factor (FF) attained highest values at $N_A > 10^{18}$ cm^{-3}. With further increasing of $N_A > 10^{16}$ cm^{-3}, a little decrement in FF was observed. It may be due to the increase of R_{sh} caused by heavy doping. Although, FF improves after $N_A > 10^{17}$ cm^{-3}, efficiency (η) increased up to 0.95%. This might have happened due to increase in Φ_G, which enhances effective Φ_{BI} and reduces R_{sh}. During this process, V_{oc} was seen to remain constant and increased only after $N_A > 10^{17}$ cm^{-3}.

After optimizing N_A to 10^{18} cm^{-3}, parameter N_C/N_V was optimized in 3×10^{18} cm^{-3} to 6×10^{21} cm^{-3} range for single layer graphene. As N_C/N_V increased minority carrier densities were found to be reduced. This may have happened probably due to the lower lifetime of photo-generated carrier and trapping of free charge carriers. Consequently, J_{sc} was constant to 18 mA/cm^2 at 3×10^{19} cm^{-3} to 6×10^{21} cm^{-3}. As shown in Figure 2 (c-d), V_{oc} reduces sharply with increase of N_C/N_V inside the p-Gr layer. As N_C/N_V increases, significant reduction in barrier height (Φ_{BI}) observed. This resulted in shortage of charge carriers near the junction and the minor built-in voltage offered a lower V_{oc}. Effectively, η dropped to a minimum at 3×10^{19} cm^{-3} of N_C/N_V. However, reducing N_C/N_V to 3×10^{18} cm^{-3}, results movements of free charge carriers to contacts through the respective regions and higher

charge carrier separation near the junction. These all processes collectively maintained V_{oc} and J_{sc} at almost a maximum value on lowering N_C/N_V down to 3×10^{18} cm^{-3}.

After optimizing N_A and N_C/N_V to 10^{18} cm^{-3} and 3×10^{18} cm^{-3}, respectively, we varied the bandgap energy (E_g) of the p-Gr from 0 to 0.25 eV. As E_g increases, V_{oc} was found to enhance as built-in voltage is increased and J_{sc} linearly improved as high barrier voltage separates the photo-generated carriers to cross the p-Gr/n-cSi junction as shown in Figure 2 (e-f). We have found that the fill factor inversely depends on the effective resistance to the charge carriers in layer of p-Gr. The higher values of J_{sc} and FF have increased η from 0.95 % (@ E_g = 0.1 eV) to 3.28 % (@E_g = 0.25 eV). Simulation of the electron affinity (χ) is shown in Figure 2 (m-p). It has been observed that η increased after the initial value of χ = 4.7 eV while J_{sc} and FF increased significantly, and V_{oc} was further improved to the maximum value at χ = 5.0 eV. This might have happened as on increasing χ above 4.7 eV, the barrier height increases which probably higher the transfer of minority charge carriers and results in rising J_{sc}. Thus, η almost linearly increased with higher values of χ in a p-Gr layer and we obtained η~ 6.75 % for χ = 5.0 eV. The value of the relative permittivity (ε_r) for a single layer graphene was reported to be 7.1 ± 3.2 at 540 nm (Pirruccio *et al* 2013), we varied this parameter from 4 to 11 and the cell performances are shown in Figure 2 (i-j). The open-circuit voltage (V_{oc}) is found to be increased for low values of ε_r from 4 to 6, and then nearly become constant with further increase in ε_r. Also FF found to be infinitesimally increased to 78.45 % at $\varepsilon_r \approx 11$ and J_{sc} remained constant, η~ 6.765 % was achieved. The efficiency of this cell was found to be independent of the electron mobility (μ_n) of the p-Gr layer due to very thin layer.

To study the role of p-Gr thickness in the carrier generation due to the photon absorption, with the above-optimized values of the single layer p-Gr, the cell was simulated up to 20 layers of graphene. It has been reported that layer numbers control the transmittance as well as the sheet resistance of the graphene (Lin *et al* 2013). As layer number increases, sheet resistance decreased and η enhanced, but this enhancement is equally compensated by a reduction in the transmittance of p-Gr. Single layer graphene is reported to absorb 2.3 % of the incident light (Pirruccio *et al* 2013). In simulated work, the cell parameters were found to be linearly reduced up to 13 layers of p-Gr and then FF sudden

dropped on its 14th layer, so η reached to 4.57 % only at 14 layers as shown in Figure 2 (k-l). This sudden fall in FF may be indicate that the sheet resistance becomes constant for this thickness of graphene layer and as the layer number becomes larger, FF increased infinitesimally (Lin *et al* 2013). An efficiency of 4.34 % was obtained for 20 layers of p-graphene. Therefore, the thickness of p-Gr does not seem to play an active role in the photo carrier generation in our simulated cell except to provide a Schottky junction for the current movement and as a TCE.

3.2. Optimization and simulation of n-cSi layer

To further enhance the efficiency of the p-Gr/n-cSi heterojunction cells, we focused on the simulation of the parameters of n-cSi layer in order to get better efficiency. When the donor concentration (N_D) in n-cSi layer was raised from 1×10^{14} cm^{-3}, the silicon work function (Φ_{SI}) would increase in accordance to equation (2) and leads to an increase in V_{oc} as shown in Figure 3(a-b). This suggests that the built-in voltage (V_{BI}) increased due to the high value of the barrier height (Φ_{BI}) after doping and the fast reduction in the depletion region led to higher J_{sc}. For $N_D > 10^{17}$ cm^{-3}, V_{oc} starts reducing while J_{sc} continued on increasing, probably due to more minority carrier generation as total carrier density enhanced with doping. In consequence of higher defect density proportional to heavy doping, FF reduced after $N_D \approx 1 \times 10^{18}$ cm^{-3} (Zhong *et al* 2013). However, η has shown the peak value at ~8.61 % at $N_D \approx 5 \times 10^{18}$ cm^{-3}.

ACCEPTED MANUSCRIPT

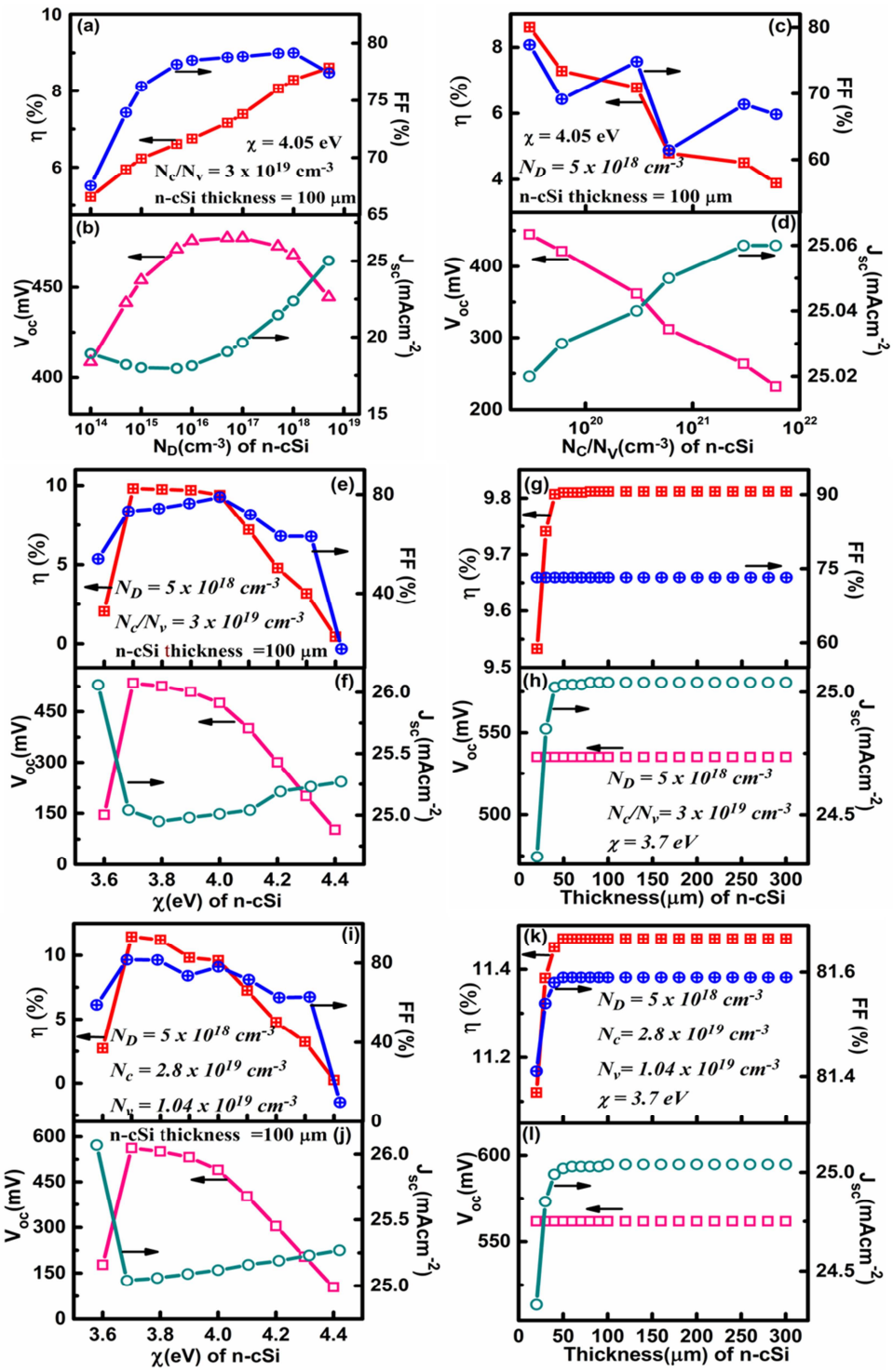


Figure. 3. Schematic representation of cell performance with the optimization of the parameters of n-cSi layer, (a-b) the donor concentration N_D (cm^{-3}), (c-d) the effective band density Nc/Nv (cm^{-3}), (e-f) the electron affinity χ (eV), (g-h) thickness (μm). At $N_D = 5 \times 10^{18}$ cm^{-3}, Nc = 2.8×10^{19} cm^{-3} and Nv = 1.04×10^{19} cm^{-3} for n-cSi, (i-j) the electron affinity χ (eV) and (k-l) thickness (μm). The optimized parameters of p-Gr were $N_A = 1 \times 10^{18}$ cm^{-3}, $N_C/N_V = 3 \times 10^{18}$ cm^{-3}, $E_g = 0.25$ eV, χ = 5.0 eV, $\varepsilon_r = 9$, $\mu_n = 10^5$ $cm^2V^{-1}s^{-1}$.

ACCEPTED MANUSCRIPT

Value of N_C/N_V has been varied in the range of 3×10^{19} to 6×10^{21} cm^{-3} in n-cSi layer and subsequent effects on cell parameters are shown in Figure 3 (c-d). The open circuit voltage (V_{oc}) is found to be decreased, while J_{sc} increased infinitesimally with the variation in N_C/N_V. A variation in V_{oc} kept FF to be changed in the large range of N_C/N_V upto 1×10^{21} cm^{-3}. Further increase in N_C/N_V values of n-cSi layer helped to develop short-interval states for charge carriers, so the voltage dropped significantly in the cell. The efficiency (η) reduced to 3.89 % at Nc/Nv values of 6×10^{21} cm^{-3} in proportion to the drop in V_{oc}. Thus, the higher band density for thick n-cSi layer intends to decrease the silicon work function (Φ_{Si}) with constant χ of silicon, which eventually lowers Φ_{BI}. Thus a drop in built-in voltage V_{BI} and V_{oc} was observed.

After optimizing the n-cSi layer at $N_D \approx 5 \times 10^{18}$ cm^{-3} and $N_C/N_V \approx 3 \times 10^{19}$ cm^{-3}, χ(eV) was varied from 3.6 to 4.4. In this range, V_{oc} was found to be initially increased and then dropped from 535.2 to 102.3 mV and J_{sc} was increased to 25.27 mA/cm^2 from 25.01 mA/cm^2 at χ = 4.4 eV shown in Figure 3(e-f). At χ = 3.7 eV, the maximum efficiency was attained corresponding to 9.812 %. For χ> 3.8 eV, V_{oc} was found to be decreased and J_{sc} changed slightly till χ = 4.4 eV. The changes in these two parameters indicated the significant modification in the work function of n-cSi layer, which leads to the reduction in the rate of carrier transport through the n-cSi layer. This reduction increases the series resistance of n-cSi layer as well as of cell and correspondingly, the fill factor (FF) also significantly reduces and η falls after χ> 4.4 eV. In order to explore the possibility of the lower cost solar cell, the next parameter we have studied was the thickness of the n-cSi by varying from 20 μm to 300 μm. Figure 3(g-h) shows that for 20 μm thick n-cSi layer, η was found to be 9.533 %. Highest efficiency 9.812 % was achieved for 80 μm thickness. The larger thickness significantly increases the number of charge carriers and so J_{sc} becomes higher. In thicker n-cSi layer, the lifetimes of minority charge carriers i.e. holes reduced due to less drift length. In addition, the recombination rate must have been in proportion with excess photo-generated charge carriers in the thick silicon layer, which collectively led to constant V_{oc} and J_{sc}. Thus, the saturated V_{oc} and J_{sc} have produced efficiency of 9.812 %, even on increasing the thickness up to 300 μm.

In reality, 9.812 % efficiency seems practically not feasible for a single layer p-Gr/n-cSi solar cell on 100 μm silicon substrate, as the present simulation does not consider the optical and electrical losses at the interface and contacts. To have a better practical realization, we have further simulated the electron affinity (χ) and thickness of n-cSi layer at most reported experimental values for Si such as $N_D \approx 5 \times 10^{18}$ cm^{-3}, $N_C \approx 2.8\times 10^{19}$ cm^{-3}, $N_V \approx 1.04 \times 10^{19}$ cm^{-3} (Hu 2010). On these values, the simulated responses of cell parameters with χ (eV) are shown in Figure 3 (i-j) which are almost similar to those reported in Figure 3 (e-f). A maximum efficiency found only 11.47 % at χ = 3.7 eV of Si. The short-circuited current density J_{sc} has shown only a little change with large χ, while V_{oc} was decreased only for large χ of 3.9 to 4.5 eV. However, a decrement in FF observed at higher χ values, forces the efficiency η to be drop to 0.256 % at χ = 4.4 eV. Similar to Figure 3(g-h), the thickness of n-cSi has been varied on the new values of N_D, N_C/N_V and χ = 3.7 eV. The trends of cell parameters have shown significant changes in lower thickness range only as illustrated in Figure 3(k-l). For values greater than 50 μm, the high rate of carrier recombination forced V_{oc} and J_{sc} to exhibit a constant value inside the thick n-cSi layer. With thickness, the effective series resistance of the cell remains constant as the total cell area is increased, which results in fill factor independent of silicon layer thickness. The constant cell parameters led the efficiency to the saturated value of 11.47 % irrespective of the layer thickness.

In order to validate our simulated results, a comparison has been done with experimentally reported results as well as simulated result and found much convincing. Recently, Li *et al* (2013) reported that depending on the doping concentration in multilayer graphene (MLG), 4-7 layers, efficiency MLG/Si heterojucntion cell was found between 5.52 to 9.27 %. In our case, this simulated value was nearly 6 %. Our simulated efficiency 6.75 % when single layer was used, was found to nearly match with the experimentally reported values of efficiency 8.6 % (Miao *et al* 2011) and 7.7 %, (Lin *et al* 2013). In their reports, they used the commercial available silicon with doping concentration in range of 8×10^{14} to 1×10^{15} cm^{-3}. Experimentally, Lin *et al* (2013) reported that maximum efficiency of 6 % was achieved for optimized p-type graphene. This value matches with our simulated results 5.22 % and 6.23 % for doped n-type Si of $N_D \approx 1\times10^{14}$ cm^{-3} and 1×10^{15} cm^{-3} ,

respectively as shown in Panel 3(a-b). Later, we have simulated the device performance with the front contact like Au (n=0.27049, k=2.7789), Ti (n=1.96, k=3.06), Ag (the related file is present in AFORS-HET), no significant changes in device performance was found. Previously, other metal (front) contact has been used like Ti/Au, Au, Ag, Au/Cr (Lin et al 2013; Li et al 2010; Miao et al 2012; Feng et al 2012; Cui et al 2013, Ruan et al 2015; Shi et al 2013). These metal contacts were made practically. Here, we preferred TCO to enhance the effective illumination area, as TCO increased the optical absorption rather than reflection as other metal contact do.

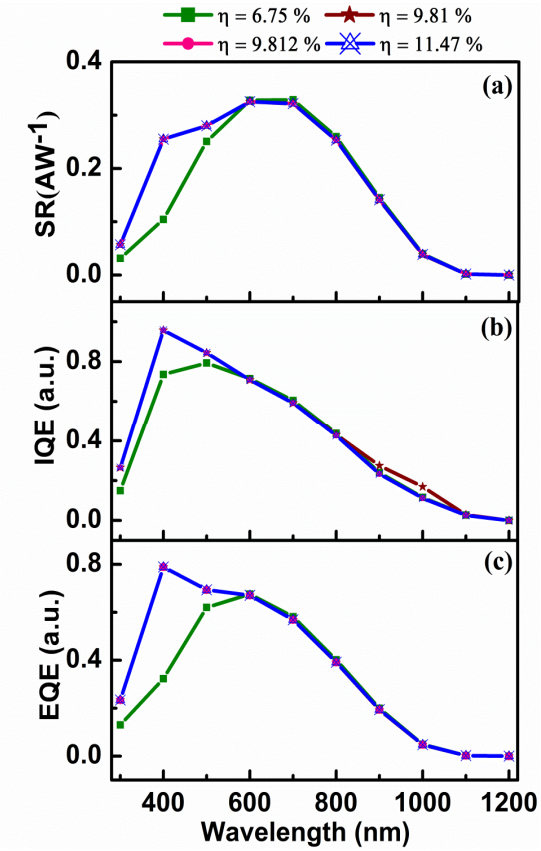


Figure 4. (a) Spectral response (SR), (b) Internal quantum efficiency (IQE), and (c) External quantum efficiency (EQE) of best optimized single layer p-Gr/n-cSi cells (η = 6.75 %, η = 9.81 % and η = 9.812 % with N_D = 5 × 10^{18} cm^{-3} and N_C/N_V = 3 × 10^{19} cm^{-3} for 50 μm and 100 μm n-cSi, respectively, η = 11.47 % with N_D = 5 × 10^{18} cm^{-3}, N_C = 2.8 × 10^{19} cm^{-3} and N_C = 1.04 × 10^{19} cm^{-3} for 100 μm n-cSi).

3.3 Spectral response, quantum efficiency and temperature dependence

The spectral response (SR), ratio of current produced by the solar cell to the optical power incident on the solar cell (Kirchartz *et al* 2011) with the optimized efficiencies 6.75 %, 9.81%, 9.812

ACCEPTED MANUSCRIPT

% and 11.47 % are shown in Figure 4 (a). The graphene layer was found to be absorbing the large fraction of light in the range below 600 nm. This results in less photons reaching to n-cSi layer and subsequent low photocurrent generation in the shorter wavelengths. In the cell design with optimized parameters most of photons in the range from 600 to 1000 nm reach Si layer and their energy matched with silicon bandgap energy, which converts into electrical energy inside Si. So, a smaller efficiency of 6.75 % was achieved on properly tuning the properties of graphene layer. By increasing the doping concentrations in the layers, the SR enhances with higher J_{sc}. Thus, with the optimization of silicon layer, the absorption of the photons by the cell is increased in the shorter wavelengths and the efficiency is enhanced to 9.812 % and 11.47 %, respectively for different N_D and N_C/N_V values of 100 μm Si. As the silicon is an indirect bandgap semiconductor, the cell response falls to zero after approaching the longer wavelength corresponding to its bandgap (E_g = 1.12 eV). For silicon layer > 50 μm ($\eta \approx$ 9.81 %), the effective conversion rate is same and so the SR remains constant even the thickness has been increased to 300 μm.

The internal quantum efficiency (IQE) of cell has been observed increase further at the shorter wavelengths (< 500 nm) after optimizing the parameters silicon layer, as shown in Figure 4 (b). The optical losses are found to be dominant at the shorter wavelengths for graphene optimized cell as revealed by the EQE response in Figure 4 (c). The graphene and silicon optimization led the reduction of reflection and transmission losses of the cells. Hence, higher EQE is obtained for the wavelengths in the range 400 nm < λ < 600 nm. Higher EQE suggests that doping concentration and effective band density optimization significantly increases the electron-hole pair generation and subsequent collections of excess charge carriers, and higher efficiencies have been achieved (Miao *et al* 2012). The IQE and EQE responses of all three cells with efficiencies of 9.81 %, 9.812 % and 11.47 % are found to be almost same, indicating the same number of charge carriers collected at these wavelengths against the photons absorbed into the cells except IQE in the range 800 to 1100 nm. For longer wavelengths, the recombination rates of generated charge carriers are higher and IQE and EQE reduced to zero.

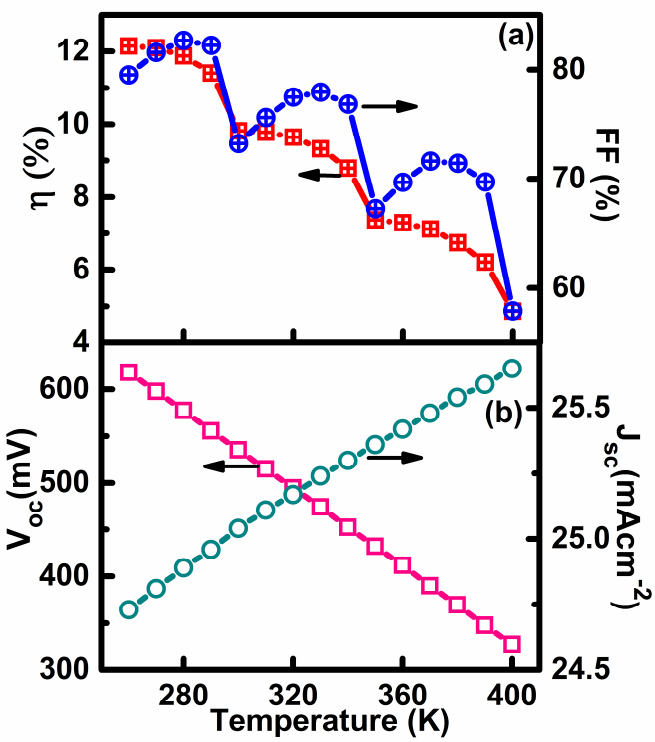


Figure 5. Dependence of cell response for the cell with η = 9.812 % (a) efficiency and fill factor, and (b) V_{oc} and J_{sc} with temperature variation.

The cell response against temperature variation has been studied, shown in Figure 5. As temperature rises from 300 K (RT), band bending reduced at graphene/Si interface. The optical scattering by phonons in graphene layer (Xu and Dong 2011), helps the electrons to move in the conduction band from the valance band through the photoemission. Hence, the photo-generated electrons which are more in the conduction band at the higher temperatures, enhanced J_{sc}. As temperature decreases from RT, carrier generation rate decreased at the interface, which resulted in lower J_{sc}. As V_{oc} and FF were found to be high, a higher efficiency of around 12.15 % was obtained at 260K. For silicon cells, the reverse saturation current density (J_o) controls the effect of temperature on V_{oc}, FF and η, and J_o depends on the material and its bandgap (E_g) (Singh and Ravindra 2012). Exponential increase in J_o with temperature decreases V_{oc} very fast, and FF and η reduced due to lower V_{oc}. Figure 5 represents the rate of change in V_{oc}, J_{sc}, FF and η with temperature and by linear fitting of data, we found, $dV_{oc}/dT \approx -2.07$ mV K^{-1}, $dJ_{sc}/dT \approx 0.0065$ mAcm^{-2} K^{-1}, $dFF/dT \approx -0.124$ % K^{-1} and $d\eta/dT \approx -0.051$ % K^{-1}. The correlation of these cell parameters with temperature for our cell is

in good agreement with those of experimental silicon based cells (Singh and Ravindra 2012). Optimized cell parameters have been summarized in Table 1.

Table 1: Summary of the parameters of the best optimized graphene/silicon cells.

Cell parameters	**p-Graphene layer optimized cell**	**p-Graphene layer and n-cSi layer optimized cell**	
V_{oc} (mV)	474.2	535.2	561.7
J_{sc} (mAcm^{-2})	18.13	25.04	25.04
FF (%)	78.51	73.23	81.54
Efficiency (%)	**6.75**	**9.812**	**11.47**
	(On a n-cSi layer having $N_D = 1\times 10^{16}$ cm^{-3}, $N_C = 3 \times 10^{19}$ cm^{-3}, $N_V = 3 \times 10^{19}$ cm^{-3}, χ = 4.05 eV, thickness = 100 μm)	(On a n-cSi layer having $N_D = 5 \times 10^{18}$ cm^{-3}, $N_C = 3 \times 10^{19}$ cm^{-3}, $N_V = 3 \times 10^{19}$ cm^{-3}, χ = 3.7 eV, thickness = 100 μm)	(On a n-cSi layer having $N_D = 5 \times 10^{18}$ cm^{-3}, $N_C = 2.8 \times 10^{19}$ cm^{-3}, $N_V = 1.04 \times 10^{19}$ cm^{-3}, χ = 3.7 eV, thickness = 100 μm)

4. Conclusions

In this study, we have simulated TCO (ITO)/p-Gr/n-cSi/Ag structure. Independent effects of seven parameters of graphene layer were analyzed and only one parameter i.e. electron mobility (μ_n) was not found to be influencing while others parameters were found to directly affect the cell performance. After optimizing the parameters of graphene and silicon, maximal efficiency of 9.812 % was achieved. Simulated results have also compared with reported experimental values and found to be in accordance. Thicker graphene as well as Si were not found to contribute much in the efficiency suggesting that the cost of cell can be reduced to about 30 %. It has been demonstrated that if experimentally chemical doping can reduce the sheet resistance and enhance work function, then p-

type multilayer graphene can act as a highly efficient transparent conducting electrode than n-type graphene.

Acknowledgements

We thank the financial support from DST-SERB, fast track Program (SR/FTP/PS-055/2012) and DST-FCT, Portugal bilateral Program (INT/PORTUGAL/P-13/2013). The authors gratefully acknowledged Helmholtz-Zentrum Berlin for providing AFORS-HET simulation software.

References

Ancona M G 2010 Electron transport in graphene from a diffusion-drift Perspective *IEEE Trans. Electron Devices* **57 (3)** 681-9.

Bae S, Kim H, Lee Y, Xu X, Park J S, Zheng Y, Balakrishnan J, Lei T, Kim H R, Song Y I, Kim Y J, Kim K S, O¨zyilmaz B, Ahn J H, Hong B H, Iijima S., 2010 Roll-to-roll production of 30-inch graphene films for transparent electrodes *Nature Nanotech.* **5** 574-8.

Cuevas A, Macdonald D, 2004 Measuring and interpreting the lifetime of silicon wafers *Solar Energy* **76** 255–62.

Cui T, Lv R, Huang Z H, Chen S, Zhang Z, Gan X, Jia Y, Li X, Wang K, Wu D, Kang F 2013 Enhanced efficiency of graphene/silicon heterojunction solar cells by molecular doping *J. Mater. Chem. A* **1** 5736-40.

Abd El-Raheem M M, Ali H M, Al-Hosiny N M, Abd El Aal M S 2010 Improvement of the optical properties of ITO/SiO_2/glass films for photovoltaic applications *Journal of Non-oxide Glasses* **2**(1) 67-76.

Feng T, Xie D, Lin Y, Zhao H, Chen Y, Tian H, Ren T, Li X, Li Z, Wang K, Wu D, Zhu H 2012 Efficiency enhancement of graphene/silicon-pillar-array solar cells by HNO_3 and PEDOT-PSS *Nanoscale* **4** 2130–33.

Gangopadhyay U, Roy S, Garain S, Jana S, Das S 2012 Comparative simulation study between n-type and p- type silicon solar cells and the variation of efficiency of n- type solar cell by the application of passivation improvement layer with different thickness using AFORS HET and PC1D *IOSR J. Engineering* **2 (8)** 41-8.

ACCEPTED MANUSCRIPT

Giannazzo F, Sonde S, Raineri V 2011 Electronic properties of graphene probed at the nanoscale, in: Mikhailov S (Ed.) *Physics and Applications of Graphene – Experiments* (InTech) pp. 353 -376.

Hu C C 2010 *Modern Semiconductor Devices for Integrated Circuits* 1st edn Ch 1 (Prentice Hall, United States) pp. 1- 33.

Kirchartz T, Ding K, Rau U 2011 Fundamental Electrical Characterization of Thin-Film Solar Cells, in: Abou-Ras D, Kirchartz T, Rau U (Eds.) *Advanced Characterization Techniques for Thin Film Solar Cells* (Weinheim:Wiley-VCH) pp. 35-60.

Khrapach I, Withers F, Bointon T H , Polyushkin D K, Barnes W L, Russo S, Craciun M F 2012. Novel highly conductive and transparent graphene-based conductors, *Adv. Mater.* **24** 2844 – 49.

Li X, Xie D, Park H, Zhu M, Zeng T H, Wang K, Wei J, Wu D, Kong J, Zhu H 2013. Ion doping of graphene for high-efficiency heterojunction solar cells *Nanoscale* **5** 1945-48.

Li X, Zhu H, Wang K, Cao A, Wei J, Li Z, Jia Y, Li Z, Li X, Wu D 2010 Graphene-on-silicon Schottky junction solar cells *Adv. Mater.* **22** 2743–48.

Lin Y, Li X, Xie D, Feng T, Chen Y, Song R, Tian H, Ren T, Zhong M, Wang K, Zhu H 2013 Graphene/semiconductor heterojunction solar cells with modulated antireflection and graphene work function *Energy Environ. Sci.* **6** 108–15.

Lishing W, Fengxiang C 2011 Simulation of high efficiency bifacial solar cells on n-type substrate with AFORS-HET *J. Optoelectronics and Advance Material* **13 (1)** 81 - 88.

Mayorov A S, Gorbachev R V, Morozov S V, Britnell L, Jalil R, Ponomarenko L A, Blake P, Novoselov K S, Watanabe K, Taniguchi T, Geim A K 2011 Micrometer-Scale Ballistic Transport in Encapsulated Graphene at Room Temperature *Nano Lett.* **11** 2396–99.

Meng X, Tongay S, Kang J, Chen Z, Wu F, Li S S, Xia J B, Li J, Wu J 2013 Stable p- and n-type doping of few-layer graphene/graphite *Carbon* **57** 507-514.

Miao X, Tongay S, Petterson M K, Berke K, Rinzler A G, Appleton B R, Hebard, A F 2012 High efficiency graphene solar cells by chemical doping *Nano Lett.* **12** 2745–50.

Mohammed M, Li Z, Cui J, Chen T 2012 Junction investigation of graphene/silicon Schottky diodes, *Nanoscale Research Letters* **7**: 302.

ACCEPTED MANUSCRIPT

Nelson F J, Kamineni V K, Zhang T, Comfort E S, Lee J U, Diebold A C 2010 Optical properties of large-area polycrystalline chemical vapor deposited graphene by spectroscopic ellipsometry *Appl. Phys. Lett.* **97** 253110.

Ni Z H, Wang H M, Kasim J, Fan H M, Yu T, Wu Y H, Feng Y P, Shen Z X 2007 Graphene Thickness Determination using Reflection and Contrast Spectroscopy *Nano Lett.* **7** 2758–63.

Ohshima T, Matsunaga T, Kawasaki H, Suda Y, Yagyu Y 2010 Preparation of ITO thin films by Pulsed Laser Deposition for use as transparent electrodes in Electronic Display Devices *Transactions of the Material Research Society of Japan* **35**(3) 583-587.

Patel K, Tyagi P K 2015 Multilayer graphene as a transparent conducting electrode in silicon heterojunction solar cells *AIP Advances* **5** 077165.

Pirruccio G, Moreno L M, Lozano G, Rivas J G 2013 Coherent and Broadband Enhanced Optical Absorption in Graphene *ACS Nano* **7 (6)** 4810 –17.

Ruan K, Ding K, Wang Y, Diao S, Shao Z, Zhang X, Jie J 2015 Flexible graphene/silicon heterojunction solar cells *J. Mater. Chem. A* **3** 14370-77.

Sarma S D, Adam S, Hwang E H, Rossi E 2011 Electronic transport in two dimensional graphene, *Rev. Mod. Phy.* **83** 407- 70.

Shi E, Li H, Yang L, Zhang L, Li Z, Li P, Shang Y, Wu S, Li X, Wei J, Wang K, Zhu H, Wu D, Fang Y, Cao A 2013 Colloidal Antireflection Coating Improves Graphene-Silicon Solar Cells, *Nano Lett.* **13** 1776− 81.

Singh P, Ravindra N M 2012 Temperature dependence of solar cell performance—an analysis *Solar Energy Materials & Solar Cells* **101** 36–45.

Stangl R, Kriegel M, Schmidt M 2006 AFORS-HET, Version 2.2, a numerical computer program for simulation of heterojunction solar cells and measurements, in: *Proceedings of the WCPEC-4, Fourth World Conference on Photovoltaic Energy Conversion* (Hawaii, USA) pp. 1350-1353.

Tan Y W, Zhang Y, Bolotin K, Zhao Y, Adam S, Hwang E H, Sarma S D, Stormer H L, Kim P 2007 Measurement of Scattering Rate and Minimum Conductivity in Graphene *Phys. Rev. Lett.* **99** 246803.

ACCEPTED MANUSCRIPT

Tiras E, Ardali S, Tiras T, Arslan E, Cakmakyapan S, Kazar O, Hassan J, Janzén E, Ozbay E 2013 Effective mass of electron in monolayer graphene: Electron-phonon interaction *J. Appl. Phys.* 113 043708.

Tongay S, Lemaitre M, Miao X, Gila B, Appleton B R, Hebard A F 2012 Rectification at graphene-semiconductor interfaces zero- gap semiconductor-based diodes *Phys. Rev. X* **2** 011002.

Xu W, Dong H M 2011 Photo-Induced Carrier Density, Optical Conductance and Transmittance in Graphene in the Presence of Optic-Phonon Scattering, in: Mikhailov S (Ed.) *Physics and Applications of Graphene - Theory* (InTech) pp. 509-12.

Zhong S, Hua X, Shen W 2013 Simulation of high-efficiency crystalline silicon solar cells with homo–hetero junctions *IEEE Trans. Electron Devices* **60 (7)** 2104-10.

Zou K, Hong X, Zhu J 2011 The e□ective mass of bilayer graphene: electron-hole asymmetry and electron-electron interaction *Phys. Rev.* **84** 085408.

Zare S, Izadkhah H, Vittoria C 2016 Deposition of magnetoelectric hexaferrite thin films on substrates of silicon *Journal of Magnetism and Magnetic Materials* **420** 245–248.

ACCEPTED MANUSCRIPT

Figure Captions:

Figure 1. Graphene/silicon heterojunction solar cell. (a) Schematic diagram of simulated structure, where ITO is on the top of graphene (b) Schematic diagram of p-type graphene/ n-c silicon interface, where Φ_G ,Φ_{Si} and χ_{Si} are the graphene work function, silicon work function, and the silicon electron affinity, respectively.

Figure 2. Schematic representation of cell performance with the optimization of the parameters of p-graphene layer, (a-b) the acceptor concentration N_A (cm^{-3}), (c-d) the effective band density N_C/N_V (cm^{-3}), (e-f) the bandgap energy E_g (eV), (g-h) the electron affinity χ (eV), (i-j) the relative permittivity ε_r, and (k-l) layer number. The parameters of n-cSi were kept as, the donor concentration $N_D = 1\times10^{16}$ cm^{-3}, the effective band density $N_C/N_V = 3\times10^{19}$ cm^{-3}, the electron affinity χ= 4.05 eV and thickness 100 μm. The other parameters of silicon as well as p-type graphene are given in Table **S**2.

Figure. 3. Schematic representation of cell performance with the optimization of the parameters of n-cSi layer, (a-b) the donor concentration N_D (cm^{-3}), (c-d) the effective band density Nc/Nv (cm^{-3}), (e-f) the electron affinity χ (eV), (g-h) thickness (μm). At $N_D = 5 \times 10^{18}$ cm^{-3}, $Nc = 2.8 \times 10^{19}$ cm^{-3} and $Nv = 1.04 \times 10^{19}$ cm^{-3} for n-cSi, (i-j) the electron affinity χ (eV) and (k-l) thickness (μm). The optimized parameters of p-Gr were $N_A = 1 \times 10^{18}$ cm^{-3}, $N_C/N_V = 3 \times 10^{18}$ cm^{-3}, $E_g = 0.25$ eV, $\chi = 5.0$ eV, $\varepsilon_r = 9$, $\mu_n = 10^5$ $cm^2V^{-1}s^{-1}$.

Figure 4. (a) Spectral response (SR), (b) Internal quantum efficiency (IQE), and (c) External quantum efficiency (EQE) of best optimized single layer p-Gr/n-cSi cells (η = 6.75 %, η = 9.81 % and η = 9.812 % with $N_D = 5 \times 10^{18}$ cm^{-3} and $N_C/N_V = 3 \times 10^{19}$ cm^{-3} for 50 μm and

ACCEPTED MANUSCRIPT

100 μm n-cSi, respectively, η = 11.47 % with $N_D = 5 \times 10^{18}$ cm^{-3}, $N_C = 2.8 \times 10^{19}$ cm^{-3} and $N_C = 1.04 \times 10^{19}$ cm^{-3} for 100 μm n-cSi).

Figure 5. Dependence of cell response for the cell with η = 9.812 % (a) efficiency and fill factor, and (b) V_{oc} and J_{sc} with temperature variation.

ACCEPTED MANUSCRIPT

ACCEPTED MANUSCRIPT

Table Captions:

Table 1: Summary of the parameters of the best optimized graphene/silicon cells.

ACCEPTED MANUSCRIPT



Review on Morphology and Microstructure Analysis of MGO Reinforced Al Composites For Rame 2016

Surabhi Lata, Nitish Kumar Verma, Chetan Singh, Roop Lal and Ramakant Rana

Abstract - The never-ending demands of advanced materials in the various fields of engineering and manufacturing has significantly increased the development of composite materials. Nowadays a shift is observed from the monolithic materials towards the composite materials. Numbers of ceramic materials are being used to reinforce various grades of aluminium alloy matrices. Metal matrix composites are exhibiting high potential characteristics as aerospace, automobile, defence, and research industries' materials. The properties of aluminium based composites can be easily tailored to achieve the desired strength, hardness, etc. This paper reviews the morphological and microstructural properties of aluminium reinforced with a refractory material i.e. MgO at Nano and micro levels. The input parameters governing the morphology and microstructure were weight and volume fraction of reinforcement and the sintering temperature along with the fabrication technique. The study of morphology included the porous nature of composite and the density measurements with hardness (Brinell Hardness Tester). A detailed review revealed the MgO as reinforcement in a various grades of aluminium is a promising material with a little consideration of its agglomeration and rigid nature during the fabrication process. It can be easily overruled by controlling the sintering temperature at the time of fabrication. Therefore, it can effectively and efficiently be used as a reinforcement with all heat treatable and non- heat treatable aluminium alloys.

Keywords: Aluminum Metal Matrix Composite, Magnesium Oxide, Morphology, Density, Hardness, Microstructure, Sintering, Powder Metallurgy

Introduction Growing technologies demand smart materials and composites on nanoscale possessing all the desired properties. The various components of the composite retains their structure and characteristic, but the composite display better properties such as low density, elastic modulus, stiffness, high specific strength, strength-to-weight ratio, and enhanced wear and creep resistances [1]. The shift from monolithic

Surabhi Lata
Assistant Professor, Department of Mechanical and Automation Engineering, Maharaja Agrasen Institute of Technology, Delhi, India, e-mail: surabhilata.delhi@gmail.com

Nitish Kumar Verma
Student, Department of Mechanical and Automation Engineering, Maharaja Agrasen Institute of Technology Delhi, India, e-mail: nitish28.verma@gmail.com

Chetan Singh
Student, Department of Mechanical and Automation Engineering, Maharaja Agrasen Institute of Technology Delhi, India, e-mail: chetan.singh.95@gmail.com

Roop Lal
Assistant Professor, Department of Mechanical Engineering, Delhi Technological University, Delhi, India, e-mail: rooplalrana@dce.ac.in

Ramakant Rana
Research Scholar, Department of Mechanical Engineering, Delhi Technological University, Delhi, India, e-mail: 7ramakant@gmail.com

PROCEEDINGS OF THE INTERNATIONAL CONFERENCE ON RECENT ADVANCES IN MECHANICAL ENGINEERING, DTU DELHI , INDIA.
(ISBN: 987-194523970-0)

alloys to particle and fibre reinforced composites revolutionised the aerospace and automotive world. The base metal used extensively is aluminium (Al) because of its properties and easy availability. Aluminium is ductile, light and strong material whose mechanical and electrical properties can be tailored. The aluminium based composites exhibits excellent properties such as excellent thermal conductivity, high shear strength, excellent abrasion resistance, high temperature operation, non-flammability, etc. allowing it to be used in various kinds of environment. The various kinds of reinforcements used are SiC, Al2O3, ZrO2, B4C, MgO, industrial wastes and agricultural wastes [2]. These materials possess properties such as refractoriness, high hardness, and high compressive strength, wear resistance, etc. enhancing their suitability as reinforcement in matrix of composites.

This paper reviews the research carried out previously on magnesium oxide reinforced aluminium based composite. Magnesium oxide (MgO) is a refractory material possessing properties such as the good thermal shock resistance, high melting point, low thermal conductivity and excellent thermodynamic stability [2]. MgO has high modulus and high strength refractoriness which when added to low ductile matrix produces composite with properties lying in between matrix and reinforcement. The controlling factors for the composite properties are the processing conditions, distribution of reinforcement and relative amount. Manufacturing of aluminium metal matrix composites can be done by liquid state process (squeeze casting, ultrasonic assisted casting, compo casting and stir casting) and solid state process (friction stir process, vapour deposition technique, powder blending followed by consolidation (PM processing) and diffusion bonding).

2. Density Measurement

M.A. Baghchesaraetal. [2] investigated the variables that affect the density of the fabricated composite having elemental parts as Aluminium powder alloy (A356.1 with D50 = 1 μm) and nano-sized MgO (with D50 = 70 nm). The significant variables were the sintering temperature and volume per cent of Nano MgO. The highest density value were recorded in samples containing 1.5 and 2.5 volume per cent of nanoMgO at three temperatures (575°C, 600°C and 625°C). Increasing volume fraction of MgO particles in aluminium, increases the density of samples adhering to the fact that MgO has higher density. But the increased volume fraction affects the sintering and wettability of MgO in molten Al alloy resulting in particles agglomeration and eventually in reduction of density. The melting point and sintering point temperatures are inter-related and due to this sample compaction is prevented. Hence, increasing the sintering temperature increases particles wettability which helps to reduce the porosities rate thereby increasing the density of samples.

Table 1: Reinforcement with SiC, Al_2O_3, MgO with particle size 0.220 μm for porosity and density after extrusion[4]

x	SiC		Al_2O_3		MgO	
	Density (gm/cm^3)	Porosity	Density (gm/cm^3)	Porosity	Density (gm/cm^3)	Porosity
0	2380	2.01	2380	2.01	2380	2.01
0.05	2421	3.0	2521	3.13	2501	4.0
0.06	2424	2.99	2499	3.12	2522	4.2
0.07	2451	3.2	2525	3.09	2493	4.1
0.08	2462	3.1	2509	3.09	2499	3.79
0.09	2466	3.15	2530	3.11	2507	4.06
0.10	2460	3.4	2533	3.13	2511	4.08

H. Abdizadeh et al. [3] conducted comparative study of density of composite fabricated by stir casting and powder metallurgy process possessing various content of MgO particles by volume. The results exhibited the casted composites were denser than the sintered samples. This occurs due to the high porosity which is encountered in the sintering process. It was clearly discovered that the porosity during the fabrication process

significantly affect the density of the sample. As the volume of MgO is increased from 1.5 to 2.5 volume %, the density increases but above 5% the porous nature resurfaces and the density value goes down. Whereas in sintered samples the increased MgO content decrease the density because of the formation of rigid MgO network in composite.

NripJit et al. [4] analysed the porosity and density for SiC, Al_2O_3 and MgO as reinforcements maintaining the particle size constant at 0.220 in A384.1. A characteristic change was observed in these factors of the Al alloy and MMCs from as-cast to extrusion as a function of reinforcement from x=0 to x=0.10. The porous nature was found to increase with increasing content of reinforcement. The table below shows the high values of porosity are obtained in case of MgO as reinforcement while high values of density are obtained in case of alumina as reinforcement. MgO being a refractory material forms a rigid network in composites resulting in decreased wettability in molten matrix. The decreased value leads to porous nature of composite sample which directly reduces the density.

3. Microstructural Analysis

M.A. Baghchesaraetal. [2] conducted the research on the microstructures of fabricated composites with variable MgO content. The figures below shows the microstructures with the content of 2.5 and 5.0 vol % MgO, sintered at 625 °C. With 5.0 vol% MgO, agglomeration of particles has been initiated which becomes prominent as the sintering temperature is slightly decreased from 625 °C to 575 °C. It is clearly visible from the figures that MgO nanoparticles are well embedded in the aluminium matrix at low MgO content. Similar experiments were conducted to study the effect of reinforcement content through the microstructure analysis at various sintering temperatures. MgO agglomeration displayed the porous behaviour in the composite which is visible in the figures 1.

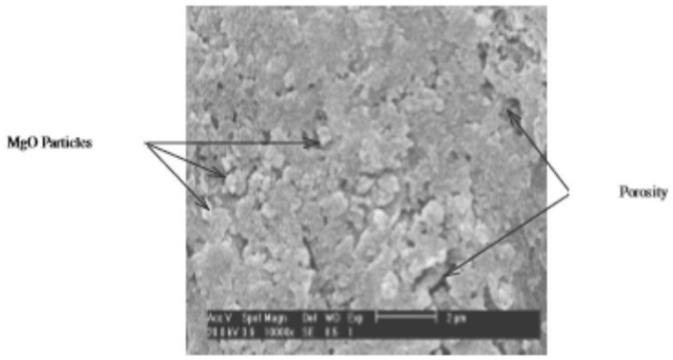


Figure 1 (a): SEM image of composite containing
2.5 vol % MgO sintered at 625 °C[2]

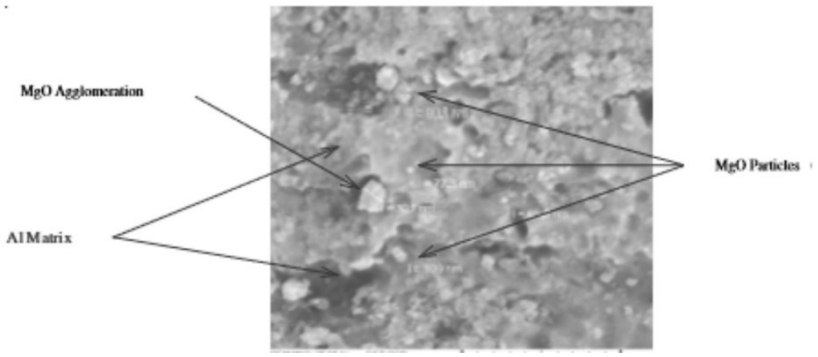


Figure 1 (b): SEM image of composite containing 5 vol % MgO sintered at 625 °C[2]

E. Manikandan et al. [5] studied the microstructural images of MgO reinforced aluminium composite with weight fraction of 2.0 wt.% and 2.5 wt.%. The homogeneity of the composite was excellent at low weight fraction of reinforcement but it was disturbed as the weight fraction was increased. This disturbance occurs due to the rigid behaviour of MgO and low thermal conductivity developing a porous structure.

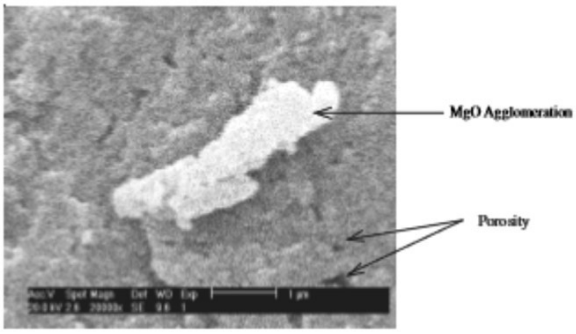


Figure 1 (c): SEM image of composite containing 5 vol % MgO sintered at 625 °C[2]

P. Balaji et al. [6] conducted a comparative research on the microstructure of Al 6061 alloy with Al 6061 – Magnesium Oxide (MgO) composite using SEM. The figures below display the microstructure of aluminium alloy and aluminium composite at 2.0 wt.% of MgO as reinforcement. It was observed that the porosity starts dominantly as the reinforcement content is increased beyond 2.5 wt. %. This can be controlled by increasing the sintering temperature which is directly controlling the wettability property of the reinforcement.

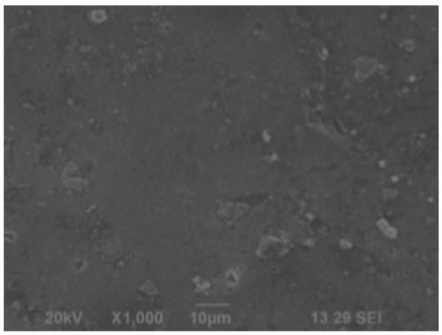


Figure 2 (a): SEM image of aluminium alloy[6]

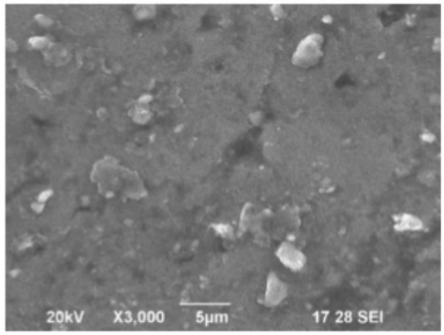


Figure 2 (b): SEM image of Al-MgO composite of 2.0 Wt. %[6]

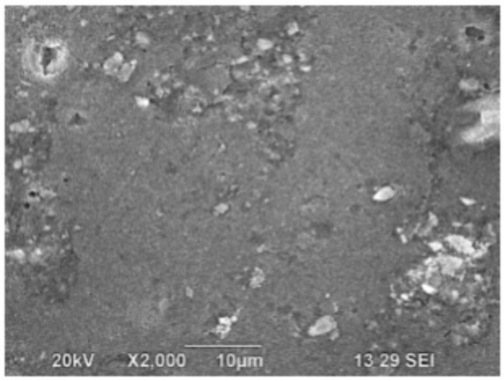


Figure 2 (c): Presence of pores in the Al-MgO composite of 2.5 wt. %[6]

A.R.I. Kheder et al. [7] discussed about the strengthening effect of various reinforcement through the microstructure analysis. Optical microscope was used to analyse the particulate volume fractions, their distribution in the casting and the grain size of the Al matrix at a magnification of X50 [8]. The results displayed that the particulate volume fractions were uniformly present across the casting, horizontally and vertically.
Though a slight difference exist between the volume fractions values in horizontal and vertical direction. The variation in horizontal direction is less than that in vertical direction. These results confirmed that the composite preparation was successfully done with relatively uniform distribution of the particulates within the matrix. It was also observed that the addition of the particulates decreased the grain size which was 897 μm for pure Al in as-cast condition. The largest decrease was viewed at initial additions of the particulates, namely at 5 wt% in all cases, then the decrease diminished and at 20 wt% particulate additions it became almost constant. The composite grain sizes are finer than the base matrix as these particulates act as nuclei for the grain formation during solidification and also inhibit the processes of the grain growth [9].
Harsh Bhadiar et al. [10] worked on the morphology of the fabricated aluminium based composite by varying reinforcement weight percentages. The MgO was studied as reinforcement using the Secondary electron imaging mode of Scanning electron microscopy. SEM image of initial silicon carbide particles are mostly angular at 5% weightage of reinforcement which was destroyed to attain flake shaped particles at 15% of weightage reinforcement of MgO and SiC. This destruction of shape was followed to lead to sub-angular particles generating a rough surface morphology. The X-Ray Diffraction and SEM study shows that the addition of MgO particles in different amount of sizes and varying percentage of particle sizes in the casting strengthens composites particularly, at 10% of MgO as shown in the figure(s) 3.

4. Hardness

Praveen G et al. [11] investigated the hardness of A356.1 Aluminium Alloy Matrix composite reinforced with MgO particles. The Brinell Hardness Tester with a load of 187.5 Kgf and with a Ball Indenter Diameter of 2.5mm was used to test the composite at various Wt. % reinforcements (0.5, 1.0, 1.5, 2.0) for varying temperature and T6 condition of heat treatment. The Hardness Number (BHN) for As cast A356.1 Aluminium alloy at room temperature (280 °C) is 73.61, which gradually increases to 89.97 at 540 °C for As cast material, after heat treatment. Similarly the Hardness Number for 2 Wt.% reinforced A356.1 Aluminium alloy at room temperature (280 °C) is 79.53 while after heat treatment it increases to 98.41 at 540 °C.
Girisha K.B et al. [12] researched the mechanical properties of Al356.1 aluminium alloy matrix composites reinforced with MgO nanoparticles. The base matrix was reinforced with MgO reinforcement with content % as 0.5, 1.0, 1.5 and 2.0. The hardness increases as the reinforcement content increases but shows a dip due to its rigid nature and agglomeration in the composite. This agglomeration enhances the porosity which decrease the strength and hardness of the composite. This is clearly depicted in the graph shown below.
A.R.I. Kheder et al. [7] discussed about the strengthening effect of various reinforcement along with the hardness and impact tests. The graph below displays the result as enhancement in the value of hardness on increasing wt% of the particulates used in this work. These increases can be related to the interaction of the dislocations with the particulates and grain refinement with increasing wt% of the particulates.

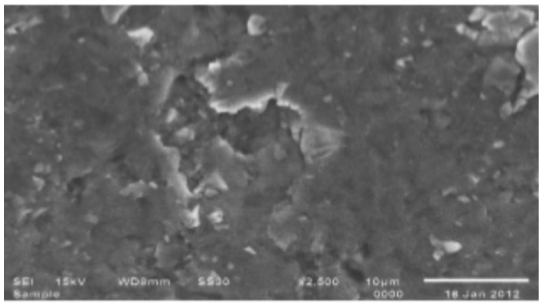


Figure 3 (a):At 5 % (wt.) of MgO-AMMCs[10]

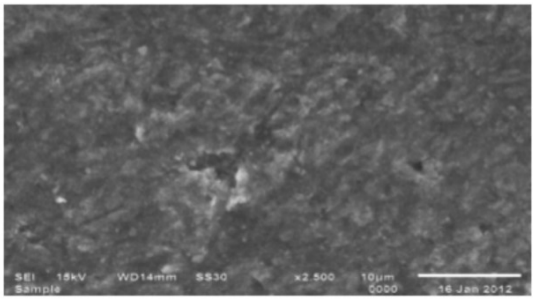


Figure 3 (b):At 10 % (wt.) of MgO-AMMCs [10]

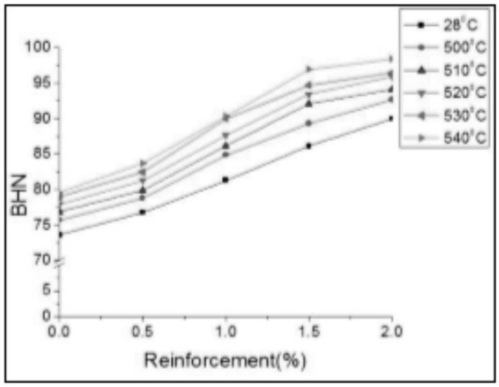


Figure 4 (a): BHN Vs Wt. % Reinforcements at varying temperatures by Praveen G et al. [11]

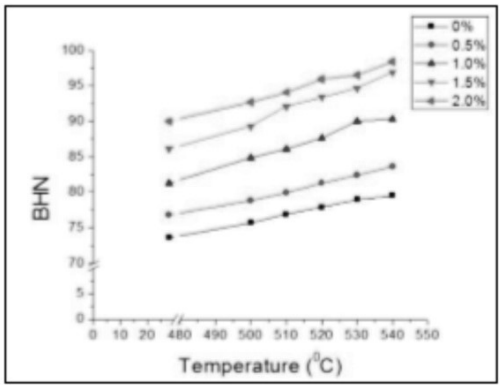


Figure 4 (b): BHN Vs Temperature for Different Wt. % Reinforcements by Praveen G et al. [11]

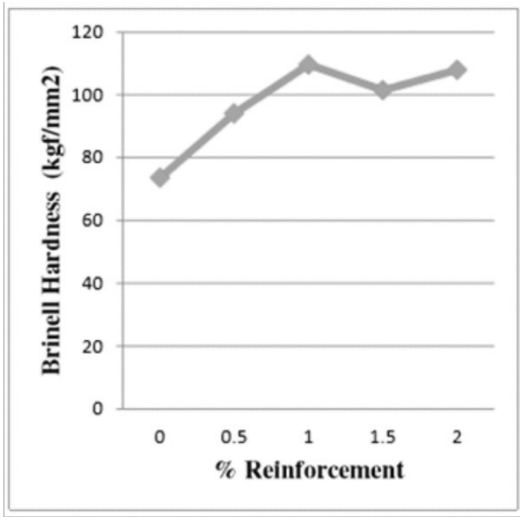


Figure 5 (a):Hardness Vs Reinforcement by Girisha K.B et al. [12]

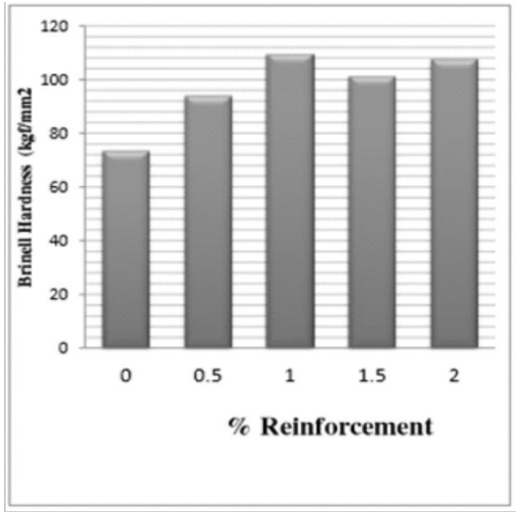


Figure 5 (b): Bar Chart of Hardness Vs % of Reinforcement by Girisha K.B et al. [12]

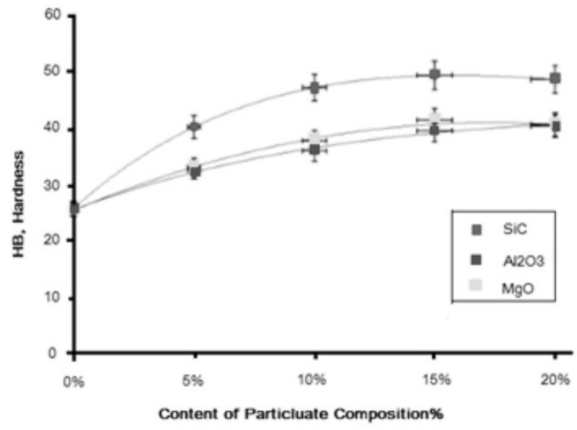


Figure 6: Brinell hardness vs. particulate weight percentage by A.R.I. Kheder et al. [7]

5. Conclusion

A review of the research work on Aluminium Matrix Composites has been presented in this paper. The various grades of aluminium have been studied with various reinforcements and they have been tested for their morphology and mechanical properties for a long time. This paper presents the effect of content of magnesium oxide in various grades of aluminium. Three characteristics have been thoroughly focussed on i.e. density, microstructure and hardness.

It can be concluded from the review that on increasing the MgO content beyond a certain value significantly affect the density and hardness of the composite. The density and hardness shows a dip on increase in content of reinforcement due to the refractoriness behaviour of MgO particles which form a rigid network during the process of fabrication. This creates pores and voids which decrease the strength and density eventually affecting the hardness of the composite. In order to prevent the porous structure of the composite, the sintering temperature is increased which enhance the wettability of the MgO particles in the molten aluminium. Hence, the interpretation of the review explains MgO as a good reinforcement material because of the high hardness, stiffness and strength it imparts to the composite considering a little care of its rigid network formation and the agglomeration process.

MgO nanoparticles when added to base matrix alter the mechanical properties such as hardness, density, surface finish etc. The properties strictly vary on the basis of amount being added in the matrix. It has been observed that composites containing 2.5 and 5 vol. % MgO fabricated at 625˚C showed maximum compressive strength and hardness respectively when compared to other volume %. Among these two variants, 2.5 vol % reflects high reliability as it has maximum density. As the content of MgO is increased composites exhibit a decrease in the mechanical properties [13]. MgO nanoparticles also possess an impressive quality of adsorbing and retaining for a long time (in the order of months) the significant amounts of halogens such as chlorine and bromine due to the extensive porous structure with considerable pore volume. They have the potential properties which enable them to act as a potent disinfectant. These particles have a stronger and faster effect on the killing action of both bacteria and spores [14]. Moreover the antibacterial activity of the MgO nanoparticles is size and concentration dependent [15].

References

[1]. Krishna Murari Pandey , AbhijitDey, “Characterization Of Fly Ash And Its Reinforcement Effect On Metal Matrix Composites: A Review”, Rev. Adv. Mater. Sci. 44 (2016) 168-181

[2]. M.A. Baghchesara, H. Abdizadeh and H.R. Baharvandi,” Microstructure and Mechanical Properties of Aluminum Alloy Matrix Composite Reinforced with Nano MgO Particles”, Asian Journal of Chemistry Vol. 22, No. 9 (2010), 6769-6777

[3]. HosseinAbdizadeh, Reza Ebrahimifard and Mohammad Amin Baghchesara, “Investigation of Microstructure and Mechaincal Properties of Nano MgO reinforced Al Composites manufactured by Stir Casting and Powder Metallurgy Methods: A Comparative Study”, Composites: Part B 56 (2014) 217–221.

[4]. NripJit, Anand K. Tyagi and Nirmal Singh,” Analysis Of Properties For Sic,Al2o3 And Mgo As Reinforcement Keeping Particle Size At 0.220 In (A384.1)1-X [(Reinforcement)p]x”, International Journal of Advanced Engineering Technology, ISSN 0976-3945, Vol. II, Issue III, 2011.

[5]. E. Manikandan, P. Balaji, I. Madhan Ram, G.G. Sozhamannan, K.Velmurugan and V.S.K. Venkatachalapathy, “Tribological Behavior of Aluminium (Al) - Magnesium Oxide (MgO) Composite”, Journal of Material Science and Mechanical Engineering (JMSME) Print ISSN: 2393-9095; Online ISSN: 2393-9109; Volume 2, Number 1; January-March, 2015 pp. 61-65

[6]. P. Balaji, R. Arun, D. Jegath Priyan, I. Madhan Ram, E. Manikandan,” Comparative Study of Al 6061 Alloy with Al 6061 – Magnesium Oxide (MgO) Composite”, International Journal of Scientific & Engineering Research, Volume 6, Issue 4, April-2015, ISSN 2229-5518.

[7]. A.R.I. Kheder, G.S. Marahleh,, D.M.K. Al-Jamea,” Strengthening of Aluminum by SiC, Al2O3 and MgO”, Jordan Journal of Mechanical and Industrial Engineering, Volume 5, Number 6, Dec. 2011 ISSN 1995-6665 Pages 533 – 541.

[8]. Huang, Y.D., Froyen, L., Wevers, M., "Quality Control & Nondestructive Tests in Metal Matrix

Composites, MMCAssess Consortium", Thematic Network, Institute of Materials Science & Testing-Vienna Uni. of Technology MMC-Assess, 2000, vol. 5.

[9]. Daoud, A., El-Bitar, T. and Abd El-Azim, A.N., "Tensile properties & fracture behavior of rolled Al5Mg-Al2O3 or Graphite Particulate Composites", International Conference on Production Engineering, Design & Control, P. 1405 (1999).

[10]. Harsh Bhadiar, Hartaj Singh, Amit Sharma, Pardeep Singh, Kapil Singh, "A fabrication and Micro structural study of A384.1 Metal Matrix Composites", IOSR Journal of Mechanical and Civil Engineering (IOSR-JMCE) e-ISSN: 2278-1684, p-ISSN: 2320-334X, Volume 12, Issue 2 Ver. II (Mar - Apr. 2015), PP 34-38, DOI: 10.9790/1684-12223438

[11]. Praveen G, Girisha K B, Yogeesha H C," Synthesis, Characterization and Mechanical Properties of A356.1 Aluminium Alloy Matrix Composite Reinforced With Mgo Nano Particles", International Journal of Engineering Science Invention ISSN (Online): 2319 – 6734, ISSN (Print): 2319 – 6726, Volume 3, Issue 6, June 2014, PP.53-59

[12]. Girisha K B, H C Chittappa, "Preparation, Characterization and Mechanical Properties of Al356.1 Aluminium Alloy Matrix Composites Reinforced With MgO Nanoparticles", International Journal of Innovative Research in Science, Engineering and Technology, ISSN: 2319-8753, Vol. 2, Issue 10, October 2013.

[13]. Mohammad Amin Baghchesara, Hossein Abdizadeh, Hamid Reza Baharvandi, "Effects of MgO Nano Particles on Microstructural and Mechanical Properties of Aluminum Matrix Composite prepared via Powder Metallurgy Route", 2nd International Conference on Ultrafine Grained & Nanostructured Materials (UFGNSM), International Journal of Modern Physics: Conference Series Vol. 5, 607–614, DOI: 10.1142/S201019451200253X, 2012.

[14]. RavishankarRai V, Jamuna Bai A, "Nanoparticles and their potential application as antimicrobials", Science against microbial pathogens: communicating current research and technological advances.

[15]. Zhen-Xing Tang, Bin-Feng, "MgO Nanoparticles as Antibacterial Agent: Preparation and Activity", Brazilian Journal of Chemical Engineering, ISSN 0104-6632, Vol. 31, No. 03, pp. 591 - 601, dx.doi.org/10.1590/0104-632.20140313s00002813, July - September, 2014.

Accepted Manuscript



Single layer graphene possessing anomalous dispersion with exotic microwave transmission and dielectric properties

Kamlesh Patel, Pawan K. Tyagi

PII: S0925-8388(17)30630-8

DOI: 10.1016/j.jallcom.2017.02.184

Reference: JALCOM 40912

To appear in: *Journal of Alloys and Compounds*

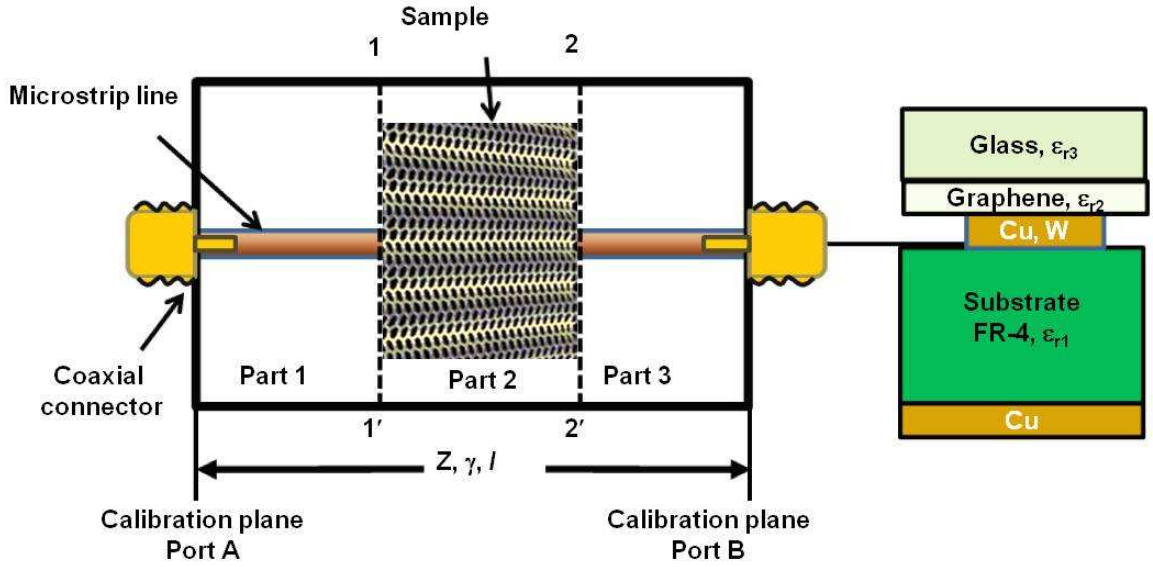
Received Date: 27 October 2016

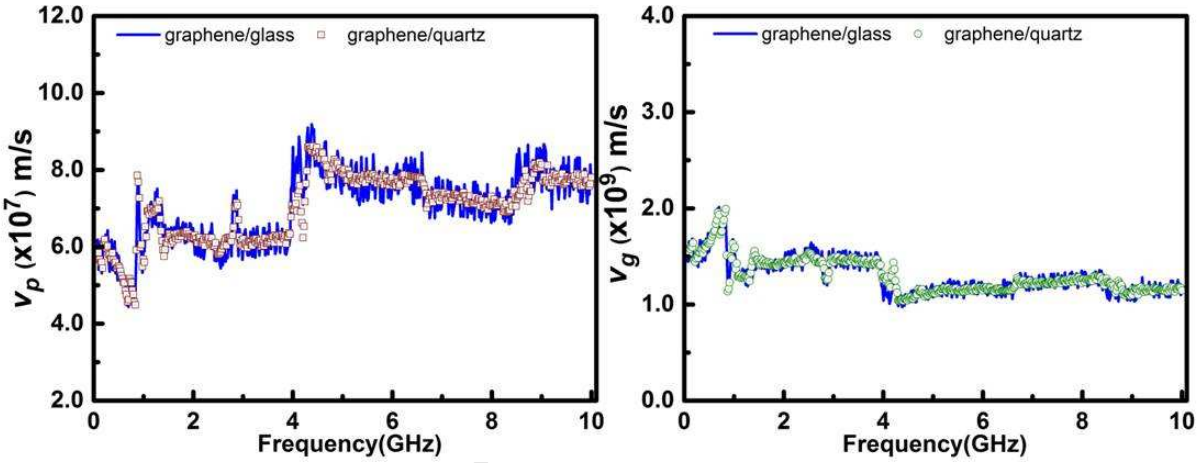
Revised Date: 21 January 2017

Accepted Date: 18 February 2017

Please cite this article as: K. Patel, P.K. Tyagi, Single layer graphene possessing anomalous dispersion with exotic microwave transmission and dielectric properties, *Journal of Alloys and Compounds* (2017), doi: 10.1016/j.jallcom.2017.02.184.

This is a PDF file of an unedited manuscript that has been accepted for publication. As a service to our customers we are providing this early version of the manuscript. The manuscript will undergo copyediting, typesetting, and review of the resulting proof before it is published in its final form. Please note that during the production process errors may be discovered which could affect the content, and all legal disclaimers that apply to the journal pertain.


Sample
1
2
Microstrip line
Glass, ε_{r3}
Graphene, ε_{r2}
Cu, W
Substrate
FR-4, ε_{r1}
Cu
Coaxial
connector
Part 1
Part 2
Part 3
1′
2′
Z, γ, l
Calibration plane
Port A
Calibration plane
Port B


graphene/glass
graphene/quartz
v_p (x10^7) m/s
Frequency(GHz)
v_g (x10^9) m/s

ACCEPTED

ACCEPTED MANUSCRIPT

Single layer graphene possessing anomalous dispersion with exotic microwave transmission and dielectric properties

Kamlesh Patel[a, b] and Pawan K. Tyagi[a#]

[a]Department of Applied Physics, Delhi Technological University, Delhi 110042, India

[b]Department of Electronic Science, University of Delhi South Campus, New Delhi 110021, India

Abstract

The present study aims to experimentally deduce the transmission and dielectric properties of CVD-grown single layer graphene transferred on glass and quartz substrates in wide frequency range from 100 MHz to 10 GHz. First, structural properties of graphene layer have been probed by Raman spectroscopy and then a simple and straightforward de-embedding method based on the propagation constants is adopted to deduce the effective relative permittivity of graphene layer. The graphene layer deposited on the substrate is found to exhibit higher absorption than the bare glass as well as quartz substrate in range of 2 - 10 GHz. The phase and group velocities have been determined and found to be in well agreement with values obtained by using the standard de-embedding method based on ABCD parameters. In both cases, graphene on glass and quartz, the maximum values of phase velocity are found to be ~ 8.57×10^7 m/s at 4.12 GHz and ~ 9.13×10^7 m/s at 4.52 GHz, respectively whereas the respective maximum group velocities for these materials are found to be ~ 2.0×10^9 m/s and ~ 1.9×10^9 m/s at 817 MHz.

Keywords: Single layer graphene, anomalous dispersion, microwave transmission, effective relative permittivity, group and phase velocity

Corresponding author: pawankumartyagi@gmail.com, pawan.phy@dce.edu (Pawan K. Tyagi)

ACCEPTED MANUSCRIPT

1. Introduction

Recent reports on doped few layer graphene (FLG) have shown carrier mobility exceeding 10^5 $cm^2V^{-1}s^{-1}$ at room temperature [1], controllable sheet resistance from 100 to 8.8 Ω/sq (ohms per square) with high optical transparency, sheet carrier density as high as 8.9×10^{14} cm^{-2} with carrier mean free path as large as ~0.6 μm [2], impressive flexibility and controllable conductivity. These properties could lead the application of graphene in the terahertz (THz) and infrared portion of the electromagnetic spectrum. Furthermore, it has been previously demonstrated that carbon nanotube (CNT) cannot be used in microwave devices [3] due to their high impedance greater than 10 kΩ as impedance of 50 Ω is essentially required for such devices. Although this limitation has been overcomed through fabrication of perfectly dense and perfectly aligned arrays of CNT where an impedance drop to 50 Ω has been claimed [3], it is a very difficult process to grow the perfectly dense and perfectly aligned arrays of CNT on a large substrate. These limitations of CNT have been overcomed in graphene. In recent advances, a metallic pattern of coplanar waveguide (CPW) line on graphene was fabricated and 50 Ω impedance and moderate losses in frequency band of 40 MHz- 110 GHz have been demonstrated [4]. This ability to tune the impedance as well as control on mobility and conductivity have triggered the application of graphene in THz devices. Furthermore, in 2D graphene, conductivity has a finite minimum value, whereas in CNT, conductance is quantized and equivalent resistance is 6.3 kΩ, therefore impedance of perfectly dense and aligned arrays of CNTs cannot drop to 50 Ω. [4-5]. In this scenario, graphene may be a realistic solution due to its mobility as high as 15000 cm^2/Vs and ballistic transport even on SiO_2 substrate [6]. This enables the design and fabrication of graphene-FET with cut-off frequency as high as 100 GHz [7-8]. To use the graphene in microwave passive and active components such as patch antenna [9- 11], graphene

microstrip attenuator [12], etc., comprehensive studies on transmission and dielectric properties of graphene are needed to be performed. To measure the transmission and dielectric properties of single layer graphene transferred on glass or quartz substrates, the transmission line i.e. CPW line based non-destructive method has been demonstrated excellently [13] and effective permittivity of graphene on the glass substrates has been reported to be reduced from 5.5 to 3 in 500 MHz to 6 GHz. Electrical permittivity was determined to be 3 from the phase measurements of graphene CPW line [14]. In the present work, a simple and straightforward de-embedding method based on the propagation constants is adopted to evaluate the effective relative permittivity of graphene layer. Here, the test device has been fabricated in a way that microstrip line loaded with the sample is in the central part and surrounded by two identical unloaded parts. Experimentally effective relative permittivity of the microstrip line loaded with graphene on glass substrates (graphene/glass) and graphene on quartz substrate (graphene/quartz) are found to be high than that of microstrip line loaded only with bare glass and quartz in 100 MHz - 10 GHz range.

2. Experimental

2.1 Material characterization

In present study, bare glass and quartz substrates of thickness 0.7 mm and 1.095 mm, respectively was used. Graphene transferred on both the substrates of the dimension 1″×1″ was procured from Graphene Industries, USA. The graphene on glass and quartz substrates were characterized by using a Renishaw inVia Reflex Raman spectrometer, UK (with an excitation source of 514.5 nm and 2.5 mW power).

2.2 Microwave measurements and de-embedding methods

To extract the properties of a single layer graphene, we have used the microstrip line based measurement fixture as shown in Fig. 1a , and the top and front view of the fixture are shown in Figs. 1b and c [15]. The microstrip line has quasi-transverse electromagnetic (TEM) mode of propagation [16]. As shown in Fig. 1b, the fixture is cascaded by three parts in such a way that the central part was loaded (Part 2) whereas others were unloaded (Part 1 & 3). Part 1 and Part 3 have same physical dimensions. The characteristic impedances and propagation constants of these parts are indicated by Z_n and γ_n, where n is part number i.e. 1, 2, 3. In the design fixture, the characteristic impedance and propagation constant in vacuum are denoted by Z_0 (50 Ω) and $\gamma_0 = j2\pi f/c$, respectively, where f is operating frequency in Hz and c is the velocity of light in m/s. In Fig. 1b, the calibration planes of the vector network analyzer (VNA) are port A and port B, whereas the measurement planes for the sample are 1-1′and 2-2′ as marked. The de-embedding method is required to shift the measurement plane from Port A to 1-1′ plane and from Port B to 2-2′ plane. If transmission parameters (ABCD) or transfer scattering parameters (T) -matrix based de-embedding method were used [16], then first S-parameters of microstrip line unloaded and partly loaded over a length (l) were measured individually and then, S-parameters of loaded microstrip line, known as multilayer (Part 2) can be deduced from the corresponding ABCD or T-matrix. Since, the edges of sample kept on the microstrip line denoted by 1-1′and 2-2′ planes, have been presumed to be symmetrical, this assumption of symmetry leads to an error in the extraction of S-parameters of the multilayer microstrip line. This asymmetry occurs due to the increase of effective height of microstrip line in Part 2 as reported previously [17]. In order to minimize asymmetry, first we have deduced impedances Z_1 and Z_3 and then attached to the main test line with impedance Z_2 to get the modified ABCD matrix which is the product of three partial matrices.

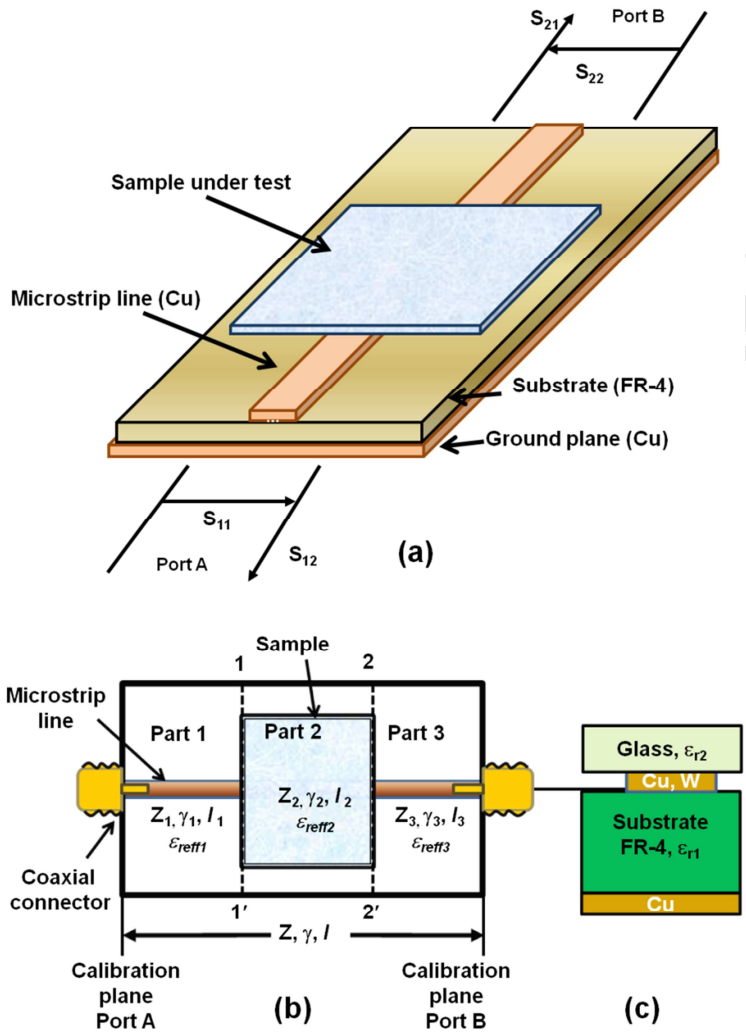


Fig. 1. (a) Microstrip line loaded with sample, (b) Schematic representation of test device and (c) front view

Here, we have proposed a simple de-embedding method, where the propagation constants are directly obtained from the S-parameter measurements taken in both cases when microstrip line is loaded and unloaded. Since, microstrip line is divided into three parts of length l_1, l_2 and l_3 and propagation constants γ_1 , γ_2 and γ_3, respectively. The complex transmission coefficient as a scattering parameter in terms of propagation constant (γ) and length of microstrip line (l), can be expressed as [18],

$$S_{21} = |S_{21}|e^{-\gamma l} = |S_{21}|e^{-(\gamma_1 l_1 + \gamma_2 l_2 + \gamma_3 l_3)} \quad (1)$$

To obtain γ_2 of the second part, we simply use the relation

$$\gamma_2 = \frac{(\gamma l - \gamma_1 l_1 - \gamma_3 l_3)}{l_2} \quad (2)$$

In the cascaded microstrip line, we consider the discontinuity formed at 1-1′ and 2-2′ planes as an open discontinuity and can be modelled as an extra length of line loaded without sample. This extra length of the line '*Δl* 'is estimated by following relation [19],

$$\Delta l = h_S \times 0.412 \frac{\left(\varepsilon_{reff(0)} + 0.3\right)\left(\frac{W}{h} + 0.262\right)}{\left(\varepsilon_{reff(0)} - 0.258\right)\left(\frac{W}{h} + 0.813\right)} \quad (3)$$

where $\varepsilon_{reff(0)}$ is the static value of effective relative permittivity, h_S is thickness of the sample under test, *W* and *h* is the width of microstrip line and height of the substrate. This length is extended to both sides of multilayer microstrip line, as a result effective length of Part 1 and Part 3 were further increased by '*Δl*' whereas effective length of multilayer microstrip line was decreased by twice of '*Δl*'. Therefore, Eq. (4) can be re-written as,

$$\gamma_2 = \frac{\gamma l - \gamma_1 (l_1 + \Delta l) - \gamma_3 (l_3 + \Delta l)}{l_2 - 2\Delta l} \quad (4)$$

For the microwave measurements, a microstrip line of width (*W*) 3.024 mm and length (*l*) 50.8 mm was fabricated on FR-4 (flame retardant epoxy) substrate of relative permittivity $(\varepsilon_r) = 4.4$ and height (*h)* = 1.5 mm with a 18 µm thick copper layer for characteristic impedance 50 Ω. For the S-parameter measurement of microstrip line without sample, Anritsu VNA master model MS2083C/2 was calibrated using an SMA calibration kit by SOLT (Short-Open-Load-

Thru) calibration technique and S-parameters were measured. From the measured S-parameters, the de-embedded S-parameters were extracted using the standard ABCD and the proposed de-embedded (Eq. 6) methods. From the de-embedded S-parameters, the attenuation coefficients and phase constants were calculated for glass, graphene/glass, quartz and graphene/quartz [17, 20]. The effective relative permittivity ε_{reff} in multilayer microstrip line can be determined from the propagation constants as $(\gamma_2/\gamma_0)^2$ [13]. The phase velocity of the waves in a microstrip line is expressed as, $v_p = c/\sqrt{\varepsilon_{reff}}$ in a non-magnetic material (μ_r = 1) and the group velocity of waves is then obtained from $v_g = c^2/v_p$, where c = 2.99× 10^8 m/s, the velocity of the light in a vacuum.

3. Results and discussion

3.1 Raman spectra of graphene transferred on glass and quartz substrates

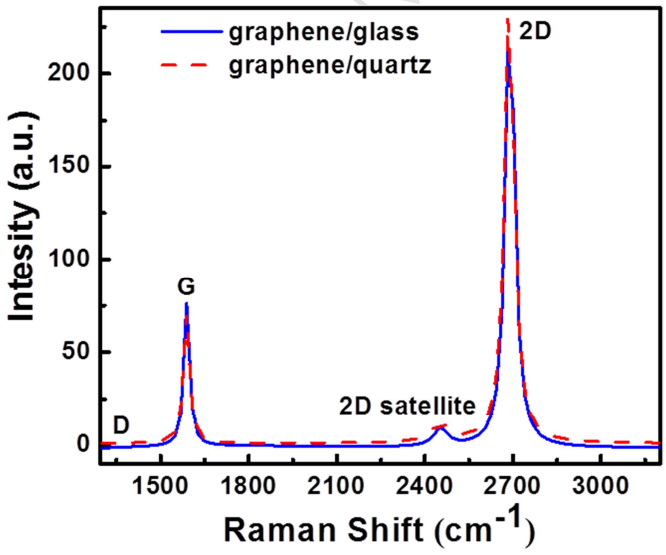


Fig. 2. Raman spectra of graphene transferred on glass and quartz substrates

To determine thickness of single layer graphene, Raman spectra were captured as shown in Fig. 2. In the spectra, three sharp peaks were observed and indexed as G, 2D satellite and 2D

bands. The peak position of the bands are found to be at ω_D ~1341.83 cm^{-1}, ω_G ~1587.12 cm^{-1}, $\omega_{2Dsatelite}$ ~2452.092 cm^{-1}, and ω_{2D} ~2688.67 cm^{-1} for graphene on glass substrate, whereas for graphene on quartz substrate, these values are at ω_D ~1341.83 cm^{-1}, ω_G ~1587.16 cm^{-1}, $\omega_{2Dsatelite}$ ~ 2452.73 cm^{-1}, and ω_{2D} ~2688.82 cm^{-1}. The D-band is barely visible indicating that graphene layers are free from defects. The I_{2D}/I_G ratio is found to be ~3.69 (on glass) and ~4.1 (on quartz), which confirms that a single layer graphene was present on both substrates. In addition, the full width half maxima (FWHM) of 2D band was found to be ~36 cm^{-1}. We have further estimated the thickness of graphene layer. The thickness of the graphene layer (t) can be obtained by $t = n\Delta d$, where n represents the number of layers and Δd is the thickness of single layer graphene (Δd = 0.335 nm). The numbers of layers (n) present in the supplied graphene have been found using the following expressions given in the refs. [21-22], respectively,

$$n_1^{1.6} = \frac{11}{(\omega_G - 1581.6)} - 1 \qquad (5)$$

and,

$$n_2 = \frac{5.5}{(\omega_G - 1581.6)} \qquad (6)$$

The obtained thickness of graphene layer by using Eqs. (7) and (8) are tabulated in Table 1. These results confirm that single layer graphene is present on both substrates.

Table-1: The peak position in G-band and corresponding calculated thickness of graphene layers.

Substrate	**Peak position ω_G (cm^{-1})**	**t_1(nm) (Eq. (7))**	**t_2(nm) (Eq. (8))**
Glass	1587.12	0.334	0.334
Quartz	1587.16	0.330	0.331

ACCEPTED MANUSCRIPT

3.2 Microwave transmission and reflection properties of graphene/glass and graphene/quartz

The measured reflected (S_{11}, S_{22}) and transmitted (S_{12}, S_{21}) parameters of unloaded microstrip line, loaded with glass and graphene/glass substrate have been shown in Figs. 3a-h. As illustrated in Figs. 3a-b, input reflection coefficient (S_{11}) measurements reveal that the magnitude of S_{11} are high for glass and graphene/glass loadings on the microstrip except upper peak at 697 MHz. The lower peaks were observed at 1.6 GHz, 5.38 GHz and 7.7 GHz frequencies and shift towards low frequency. Similar variation and shift were observed for S_{11} phase. In forward (S_{21}) and reverse (S_{12}) transmission characteristics as shown in Figs. 3c-f, the magnitudes decreased as frequency increased. This may have happened due to the lossy behaviour of microstrip line on FR-4 substrate. On comparison with data taken in case of unloaded microstrip line, lower values of S_{21} and S_{12} were seen. This observation further confirmed that the transmission loss is increased in case of loaded microstrip line. In both cases, materials exhibited similar properties up to 5 GHz. In addition, the shift of phase values was found to become prominent with an increase in frequency. As shown in Figs. 3g–h, the values of S_{22} parameters in all the three cases exhibited similar pattern like S_{11}. But, more fluctuations were observed above 4 GHz and magnitude (<15 dB) was found upto 8 GHz. The microstrip line structure became more reflecting above 9 GHz and transmission was blocked, which was also verified by high values of S_{12} and S_{21}.

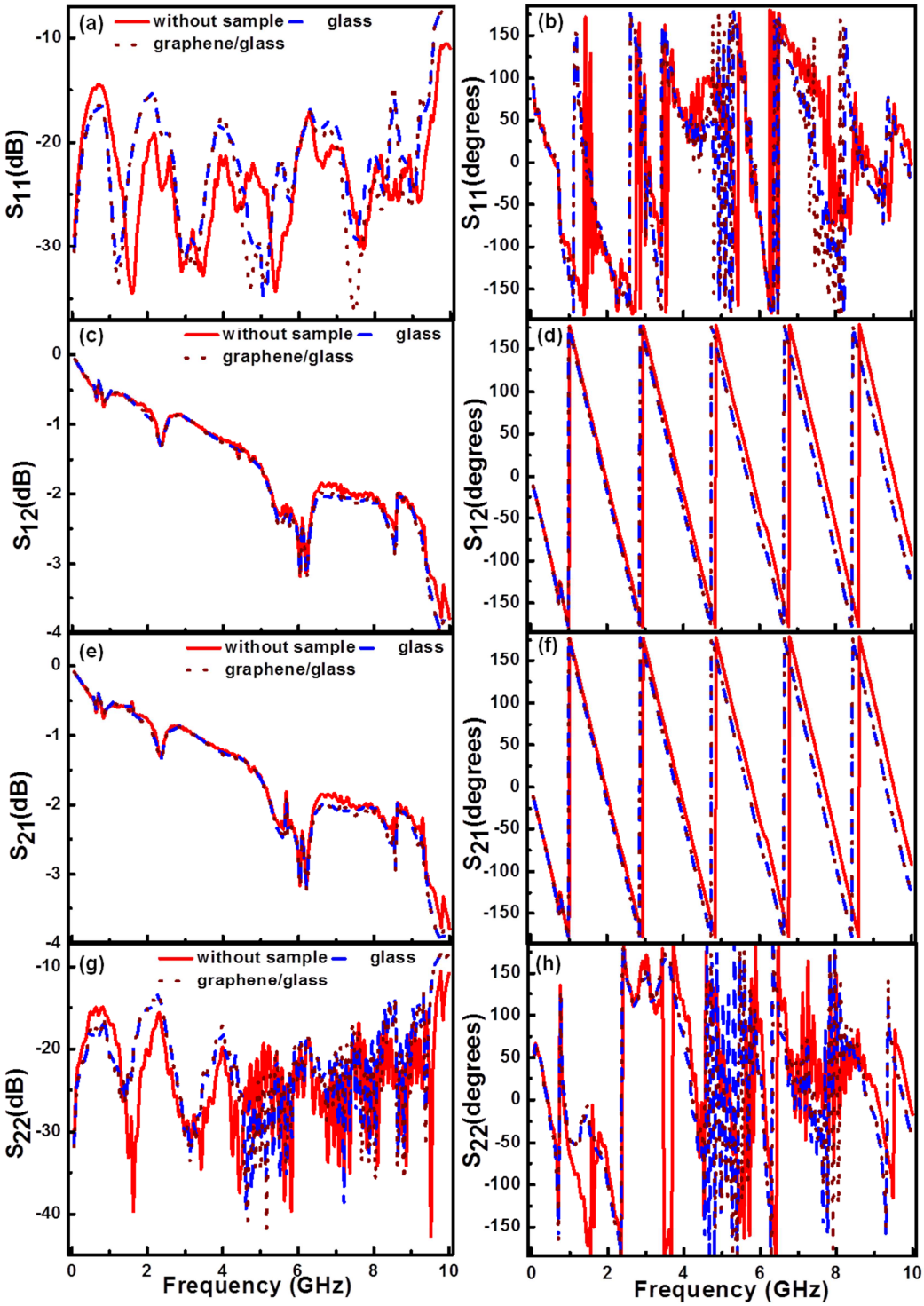


Fig. 3. S-parameters of different measurement configurations for without sample, with glass and graphene/glass, (a) magnitude of S_{11}, (b) phase of S_{11}, (c) magnitude of S_{12}, (d) phase of S_{12}, (e) magnitude of S_{21}, (f) phase of S_{21}, (g) magnitude of S_{22} and (h) phase of S_{22}.

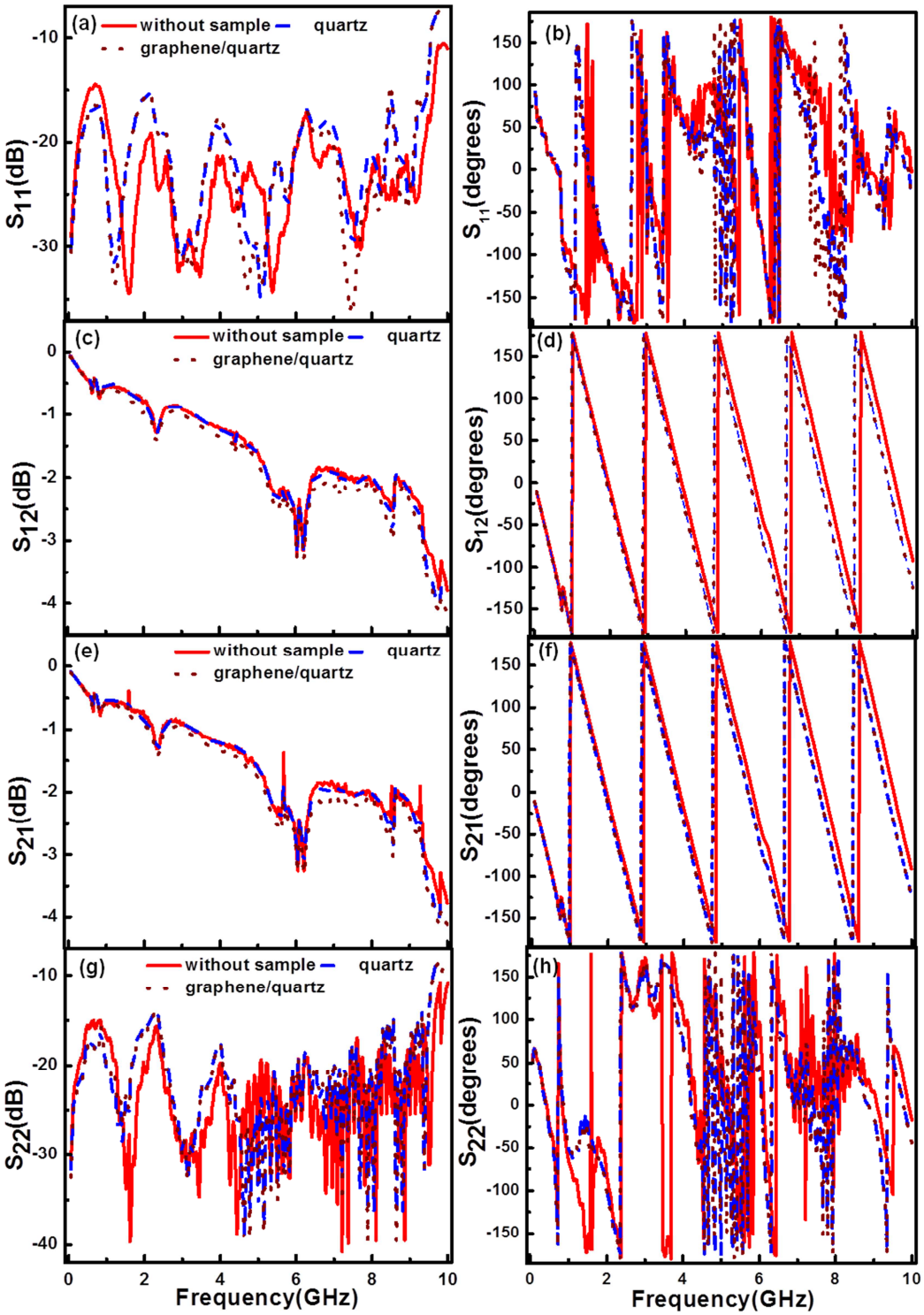


Fig. 4. S-parameters of different measurement configurations for without sample, with quartz and graphene/quartz , (a) magnitude of S_{11}, (b) phase of S_{11}, (c) magnitude of S_{12}, (d) phase of S_{12}, (e) magnitude of S_{21}, (f) phase of S_{21}, (g) magnitude of S_{22} and (h) phase of S_{22}.

ACCEPTED MANUSCRIPT

The S-parameters measured for the unloaded microstrip line and loaded with quartz or graphene/quartz has been shown in Figs. 4a - h. The behaviour of reflection parameters (S_{11} and S_{22}) is analogous to previous case and magnitude was slightly changed at the peaks. Observations in Figs. 4c-f reveals that graphene/quartz have additional losses as compared to quartz, which is known as low loss material. In this case, S_{21} and S_{12} exhibit similar behaviour as compare to unloaded microstrip line. However, the changes in the S_{21} and S_{12} phases are found to be identical for quartz and graphene/quartz and increased with the frequency. For graphene/glass and graphene/quartz, minor variations in reflection coefficients (S_{11} and S_{22}) showed that well-matched characteristic impedance can be obtained with graphene. Identical transmission coefficients (S_{21} and S_{12}) confirmed that graphene is passive and isotropic material, as offering a low dielectric loss even with thickness in nm range. This property of graphene can be utilized in a reciprocal microwave component if a few layer graphene with well-matched characteristic impedance.

3.3 Effective relative permittivity of graphene/glass and graphene/quartz

After de-embedded S-parameters by employing ABCD de-embedding method, the attenuation (α) and phase constant (β) were obtained for glass, graphene/glass, quartz, graphene/quartz. Results are shown in Fig. 5. The peaks in plot of attenuation constants versus frequency were observed at 737 MHz, 2.65 GHz, and 3.98 GHz (lower), 5.54 GHz, 6.61 GHz (lower), 7.96 GHz, 8.43 GHz, 9.02 GHz and 9.18 GHz (lower). These peaks correspond to the peaks observed in S-parameters (Fig. 3 and Fig. 4) and their values were found to depend on the reflection not on the transmission. The attenuation constant was found to be high in both cases graphene/glass and graphene/quartz. This suggests that more microwave absorption takes place

as reported in previous studies [23]. Graphene/glass is also found to be more lossy than the graphene/quartz. Also, as shown in Figs. 5b & d, the phase constant (β) were found to be overlapping. Infinitesimal changes were also observed at the peaks. It can be said that the phase constant of graphene/glass and graphene/quartz are lagging in comparison to the glass and quartz. However, for the graphene/glass, β was found to be larger than that of graphene/quartz, although their phase constant difference varies with frequencies.

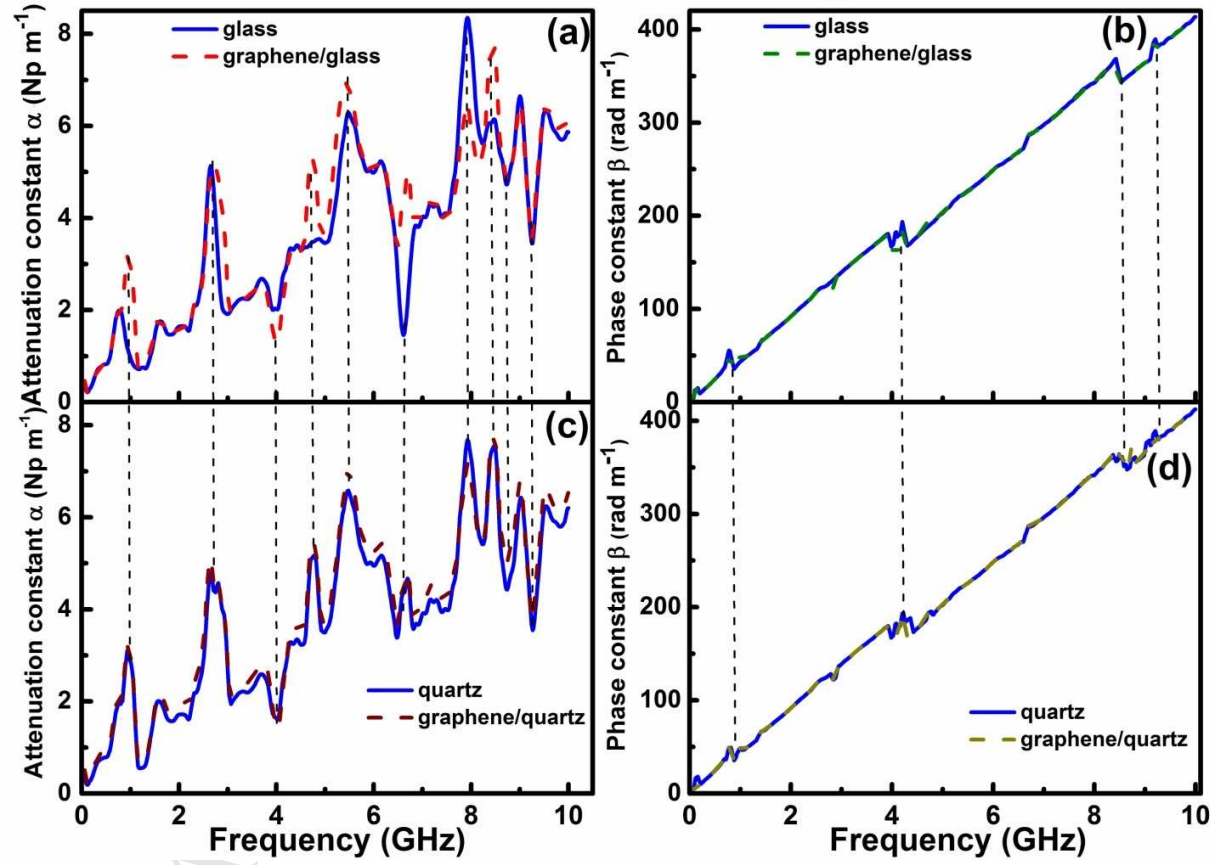


Fig.5. (a) Attenuation constant, (b) phase constant for glass and graphene/glass, and (c) attenuation constant, (d) phase constant for quartz and graphene/quartz.

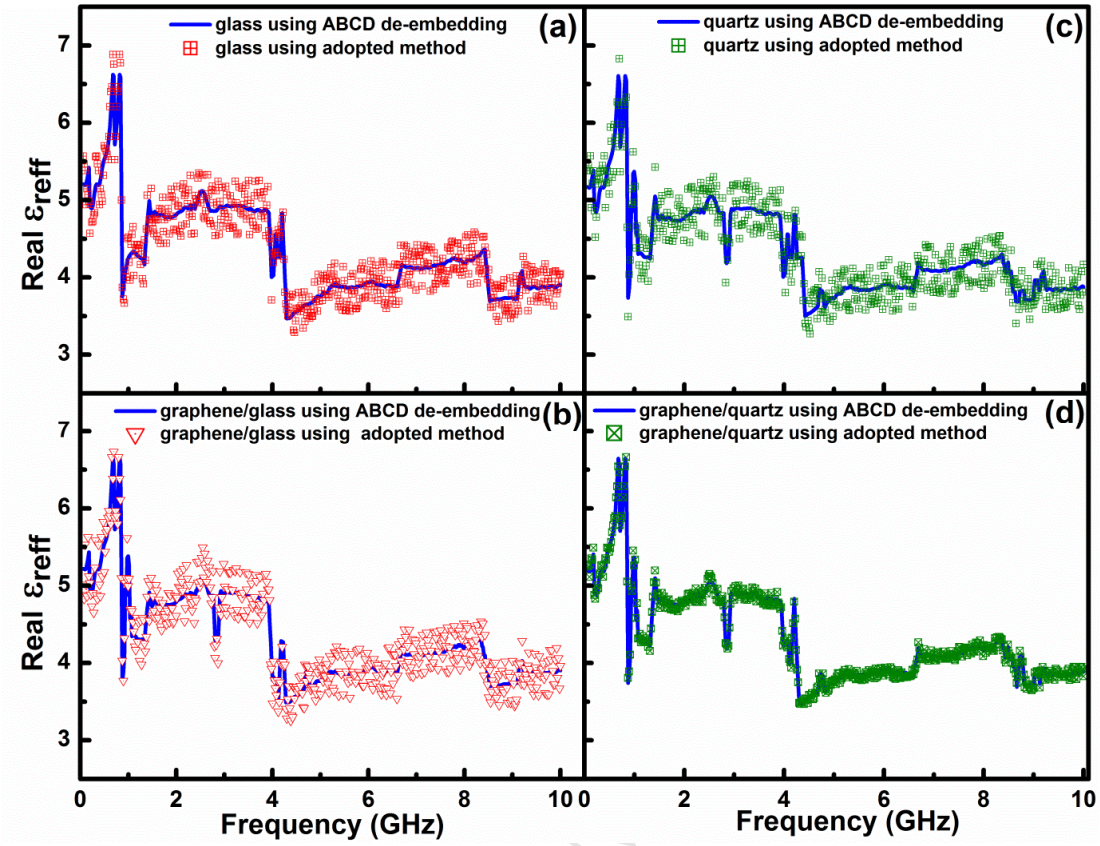


Fig.6. Real ε_{reff} using ABCD and adopted method (a) glass, (b)graphene/glass, (c) quartz and (d) graphene/quartz.

For the multilayer microstrip line, ε_{reff} was then obtained from the frequency dependent complex propagation constant for glass, graphene/glass, quartz and graphene/quartz. The real and imaginary parts of ε_{reff} obtained by the ABCD and adopted de-embedding method were plotted as shown in Fig. 6 and Fig. 7. The real ε_{reff} of glass as well as graphene/glass are found to be in range of 4.80 to 3.89 while these values are in range of 4.76 to 3.87 for quartz and graphene/quartz in frequency range of 2 - 10 GHz. Similar values of real effective permittivity from 5.5 to 3 in 500 MHz to 6 GHz has been reported for graphene/glass earlier [13]. It can be noticed that thickness of quartz (1.095 mm) is larger than glass (0.7 mm). Infinitesimal higher real ε_{reff} for graphene/glass might be due to effective thickness of graphene layer on glass (0.334

nm) than on the quartz (0.331 nm) which may have resulted from the van der Waals attraction between graphene and substrates. Steep and low variations in real ε_{reff} values that were obtained in below 1 GHz as ε_{reff} of the microstrip line are highly dependent on the frequency in lower range. The percent error between the real ε_{reff} values obtained from standard ABCD and adopted de-embedding methods were found to be below 4% for the studied materials, which confirms that adopted method is well within the limits and can be used for fast and simple calculations to obtain the effective relative permittivity and related parameters.

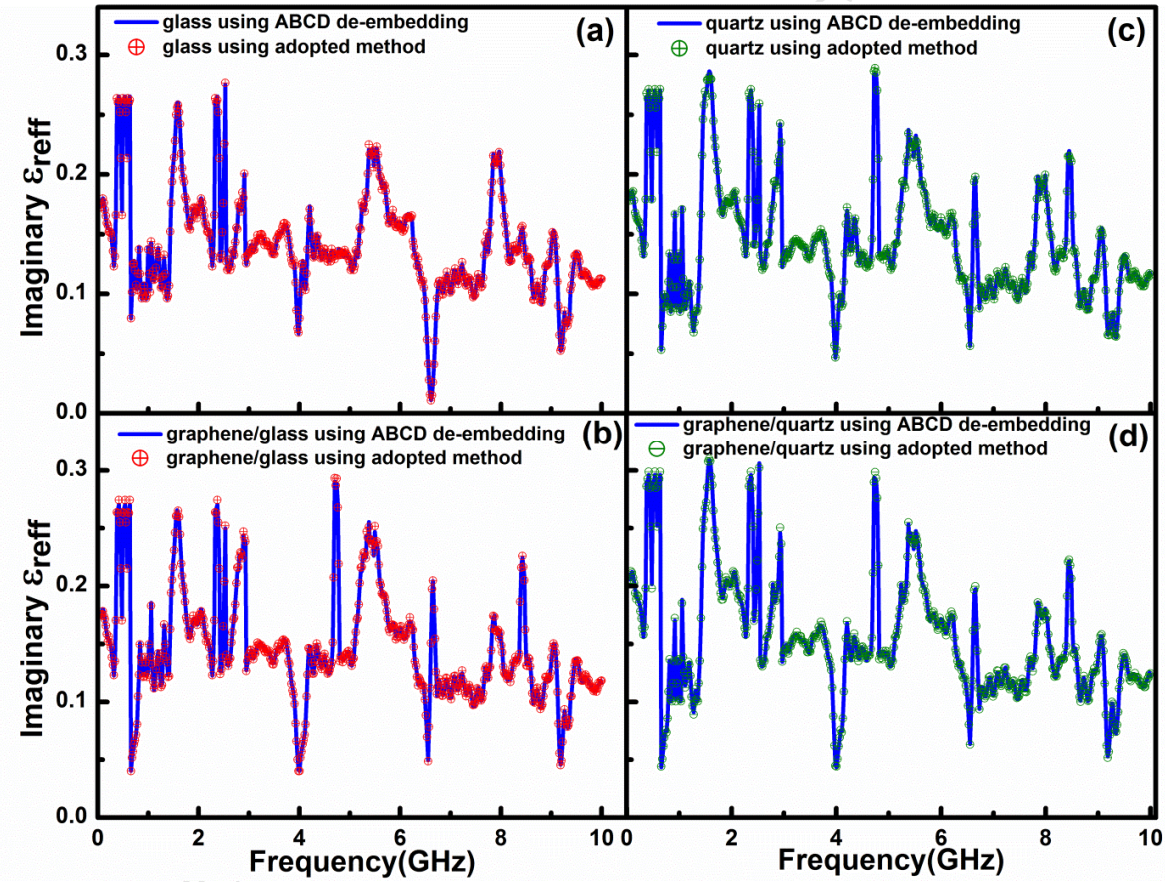


Fig.7. Imaginary ε_{reff} using ABCD and adopted method (a) glass, (b) graphene/glass, (c) quartz and (d) graphene/quartz.

The imaginary part of ε_{reff} for glass, graphene/glass, quartz and graphene/quartz were found to be nearly 0.15 in the entire frequency range from 100 MHz to 10 GHz as illustrated in Fig. 7. However, certain peaks between 0.05 to 0.5 values in imaginary ε_{reff} were observed at 1 GHz (lower), 3 GHz (lower), 4 GHz (upper) and 5 GHz (lower). These abrupt peaks may be attributed to the changes in S_{11} and S_{22} (Fig. 3 and Fig. 4). On analysis of the results, the imaginary ε_{reff} for graphene/glass and graphene/quartz were found to be high and sharp upper and lower peaks at frequency ~ 6.61 GHz were seen, whereas low magnitude of peaks in case of glass substrates was observed. For glass, graphene/glass, quartz and graphene/quartz, the maximum percent error in the imaginary ε_{reff} is found to be below 1%, when results obtained from the standard ABCD and the adopted de-embedding methods were compared.

3.4 Phase and group velocities of graphene/glass and graphene/quartz

On further analysis, phase (v_p) and group (v_g) velocities in presence of graphene layers have been obtained and results have been shown in Fig. 8 and Fig. 9, respectively. As frequency increased, the phase velocities for all materials were increased from 5.74×10^7 m/s @ 100 MHz to 7.67×10^7 m/s @ 10 GHz with some prominent peaks or falls at frequencies 817 MHz (lower), 877 MHz (upper), 2.82 GHz (upper, not observed in case of glass), 4.38 GHz (upper), 6.6 GHz (lower) and 8.53 GHz (upper) as shown in Fig. 8. In case of microstrip line loaded with graphene/glass and graphene/quartz, v_p was found to be lower than that of the microstrip line loaded with bare glass and quartz. This indicates that the propagation of the waves becomes slow with graphene. In addition, the peaks of v_p shifted slightly towards higher frequencies for quartz and graphene/quartz than the glass and graphene/glass that the waves propagate faster in quartz as well as graphene/quartz.

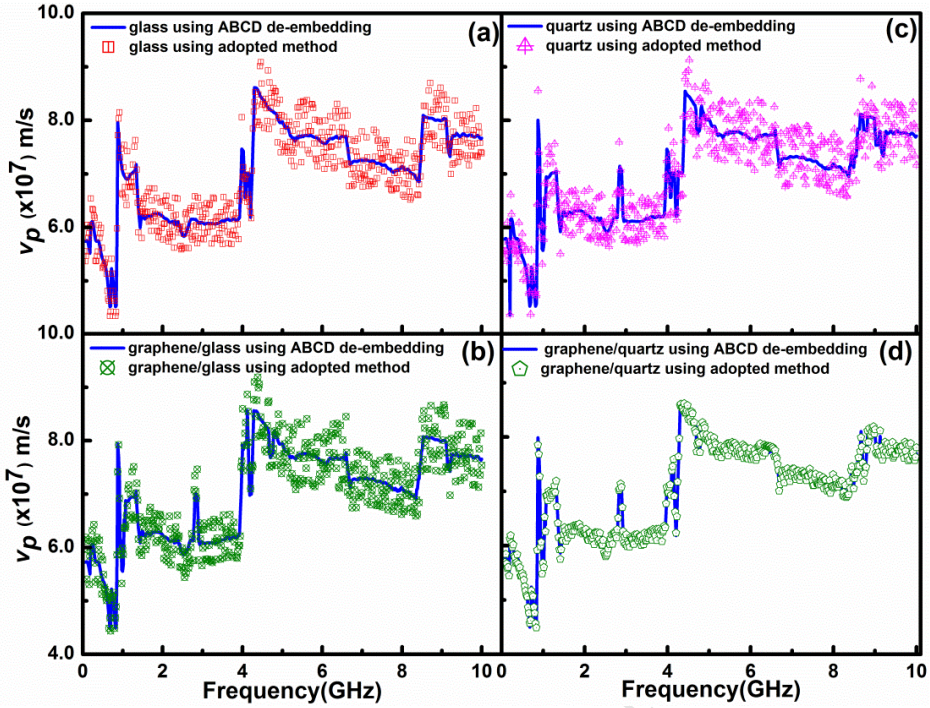


Fig.8. Phase velocity v_p (m/s) using ABCD and adopted method (a) glass, (b)graphene/glass, (c) quartz and (d) graphene/quartz.

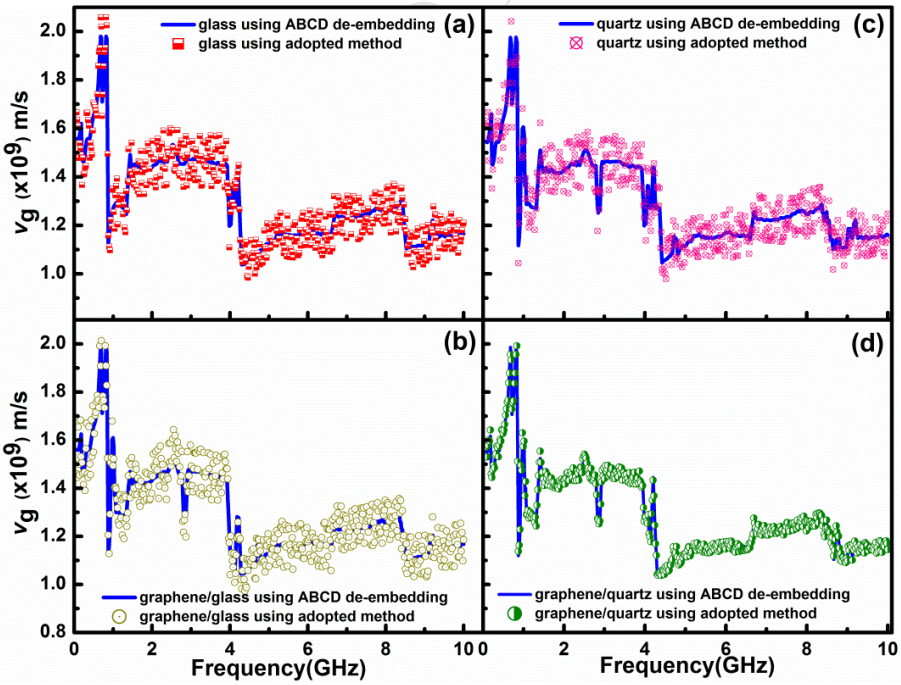


Fig.9. Group velocity v_g (m/s) using ABCD and adopted method (a) glass, (b)graphene/glass, (c) quartz and (d) graphene/quartz.

As shown in Fig. 9, group velocity (v_g) decreased from 1.6×10^9 m/s to 1.1×10^9 m/s. A peak (~2.0×10^9 m/s) at 817 MHz and falls at certain frequencies were obtained in v_g, which may be due to sharp rise in the phase velocity (v_p) as v_g directly depends on v_p. Higher v_g in graphene/glass and graphene/quartz indicates that the wave packets formed within the measured frequency range are moving faster than the wave packets formed in glass and quartz. As, v_g has been found to be larger than the velocity of light (c), it remains higher than v_p too. This confirms that the studied materials are anomalous dispersive and absorb more microwaves in the presence of graphene. Transparent substrates like glass and quartz are known to have selective absorption bands in the infrared and ultraviolet regions and show anomalous dispersion, lower in the microwave region [25, 26]. For graphene/substrate, higher ε_{reff} and v_g indicates that the amount of anomalous dispersion has been increased. Thus, the single graphene layer on glass and quartz is found to possess anomalous dispersion. This might have happened due to lower charge carrier concentration and interelectron interaction in the measured frequency range [27]. Since, group velocity represents the velocity at which the microwave energy is propagated, as v_g is larger than v_p, the wave components with high frequencies travel faster than those with lower frequencies in the single layer graphene/substrate. On comparing v_g and v_p obtained from both de-embedding methods, the percent error for v_g and v_p are found to be below 3%, which further affirms that our de-embedding method can be adopted for obtaining the dispersive behaviour of any material.

4. Conclusions

Microwave transmission and dielectric properties of graphene on glass and quartz substrates were analyzed in frequency range of 100 MHz to 10 GHz. A simple and an efficient

de-embedding method has been adopted, which uses the propagation constants obtained from the measured S-parameters and the physical lengths of the material sample and microstrip line. Comparison with parameters obtained by using standard ABCD de-embedding method and adopted a method confirmed that the latter can be used to estimate the effective relative permittivity accurately. The experimental results show that in graphene, phase velocity of waves decreased whereas the group velocity increased. The observed anomalous dispersion in the graphene causes the absorption of microwaves in the frequency range of 100 MHz - 10 GHz as $v_g > v_p$.We envision that present study would pave way for utilizing the graphene in the microwave passive components as an interconnect or a substrate material and in developing reciprocal microwave components with well-matched characteristic impedance.

Acknowledgments

The work is supported by the DST-SERB, fast track Program (SR/FTP/PS-055/2012) and DST-FCT, Portugal bilateral Program (INT/PORTUGAL/P-13/2013). One of the author (K. Patel) acknowledges the R & D Scheme 2014-15 of University of Delhi for the present work.

References

[1] A. S. Mayorov, R. V. Gorbachev, S. V. Morozov, L. Britnell, R. Jalil, L. A. Ponomarenko, P. Blake, K. S. Novoselov, K. Watanabe, T. Taniguchi, A. K. Geim, Nano Lett. 11(2011) 2396-2399.

[2] I. Khrapach, F. Withers, T. H. Bointon, D. K. Polyushkin, W. L. Barnes, S. Russo, M. F. Craciun, Adv. Mater. 24(2012) 2844-2849.

[3] G. Deligeorgis, M. Dragoman, D. Neculoiu, D. Dragoman, G. Konstantinidis, A. Cismaru, R. Plana, Appl. Phys. Lett. 95(2009) 073107.

ACCEPTED MANUSCRIPT

[4] M. Dragoman, D. Neculoiu, A. Cismaru, A. A. Muller, G. Deligeorgis, G. Konstantinidis, D. Dragoman, R. Plana, Appl. Phys. Lett. 99(2011) 033112.

[5] M. Dragoman, D. Neculoiu, D. Dragoman, G. Deligeorgi, G. Konstantinidis, A. Cismaru, F. Coccetti, R. Plana, IEEE Microw. Mag. 11(2010) 81-86.

[6] J. H. Chen, C. Jang, S. Xiao, M. Ishigami, M. S. Fuhrer, Nature. Nanotechnol 3(2008) 206 - 209.

[7] Y. M. Lin, C. Dimitrakopoulos, K. A. Jenkins, D. B. Farmer, H. Y. Chiu, A. Grill, P. Avouris, Science 327(2010) 662.

[8] L. Liao, Y. C. Lin, M. Bao, R. Cheng, J. Bai, Y. Liu, Y. Qu, K. L. Wang, Y. Huang, X. Duan, Nature 467(2010) 305 -308.

[9] I. Llatser, C. Kremers, A. Cabellos-Aparicio, J. M. Jornet, E. Alarco´n, D. N. Chigrin, Photonics and Nanostructures- Fundamentals and Applications 10(2012) 353-358.

[10] J. S. Gomez-Diaz, J. Perruisseau-Carrier, in Proc. International Symposium On Antennas and Propagation (Isap2012), Nagoya, Japan (2012) 239 -242.

[11] M. Dragoman, A. A. Muller, D. Dragoman, F. Coccetti, R. Plana, J. Appl. Phy. 107(2010) 104313.

[12] L. Pierantoni, D. Mencarelli, M. Bozzi, R. Moro, S. Moscato, L. Perregrini, F. Micciulla, A. Cataldo, S. Bellucci, IEEE Trans on Microwave Theory and Techniques 6 (2015) 2491 - 2497.

[13] Y. Wu, Y. Xu, Z. Wang, C. Xu, Z. Tang, Y. Chen, R. Xu, Appl. Phys. Lett. 101(2012) 053110.

[14] M. Dragoman, A. Cismaru, A. Stefanescu, A. Dinescu, D. Dragoman, in Proc. of the 43rd Euro. Microwave Conf. , Nuremberg, Germany (2013) 530 -532.

ACCEPTED MANUSCRIPT

[15] P. Queffelec, P. Gelin, J. Gieraltowski, J. Loaec, IEEE Trans. Magnetics 30(1994) 224 - 231.

[16] D. M. Pozar, Microwave Engineering, John Wiley & Sons, Inc. 2012, pp.8-10, 147.

[17] Agilent De-embedding and Embedding S-parameter Networks Using a Vector Network Analyzer, Application Note 1364-1, Agilent Technologies, Inc., USA 2004, 5980-2784EN

[18] A. Koul, P. K. R. Anmula, M. Y. Koledintseva, J. L. Drewniak, S. Hinaga, in Proc. of IEEE EMC Symposium, Austin, USA (2009) 191 -196.

[19] U. A. Bakshi, A. V. Bakshi, Network Analysis and Synthesis, 1st ed., Technical Publications Pune, India 2008, pp. 9-3 – 9-4.

[20] E. Hammerstad, in Proc. of EEE MTT-S Intl. Microwave Symp. Digest 1981, 54.

[21] K. Patel, Neha, P. K. Tyagi, in Proc. of Int. Conf. On Condensed Matter and Applied Physics 1728(2016) 020617.

[22] H. Wang, Y. Wang, X. Cao, M. Fenga, G. Lan, J. Raman Spectrosc. 40(2009) 1791-1796.

[23] A. Gupta, G. Chen, P. Joshi, S. Tadigadapa, P. C. Eklund, Nano. Lett. 6(2006) 2667.

[24] B. Wu, H. M. Tuncer, A. Katsounaros, W. Wu, M. T. Cole, K. Ying, L. Zhang, W. I. Milne, Y. Hao, Carbon 77(2014) 814 -822.

[25] J. P. Glusker, M. Lenis, M. Rossi, Crystal Structure Analysis for Chemists and Biologists, Wiley-VCH Inc., Canada 1994, pp. 592.

[26] P. Yadav, Engineering Physics, Discovery Publishing House, New Delhi 2006, pp.109-110.

ACCEPTED MANUSCRIPT

[27] Z. Z. Alisultanova, R. P. Meilanov, On the theory describing graphene in an anomalous-dispersion region, J. Surface Investigation X-ray, Synchrotron and Neutron Techniques 7(2013) 46 -50.

ACCEPTED MANUSCRIPT

ACCEPTED MANUSCRIPT

Figure captions:

Fig.1. (a) Microstrip line loaded with sample, (b) Schematic representation of test device and (c) front view

Fig.2. Raman spectra of graphene transferred on glass and quartz substrates

Fig.3. S-parameters of different measurement configurations for without sample, with glass and graphene/glass, (a) magnitude of S_{11}, (b) phase of S_{11}, (c) magnitude of S_{12}, (d) phase of S_{12}, (e) magnitude of S_{21}, (f) phase of S_{21}, (g) magnitude of S_{22} and (h) phase of S_{22}.

Fig.4. S-parameters of different measurement configurations for without sample, with quartz and graphene/quartz, (a) magnitude of S_{11}, (b) phase of S_{11}, (c) magnitude of S_{12}, (d) phase of S_{12}, (e) magnitude of S_{21}, (f) phase of S_{21}, (g) magnitude of S_{22} and (h) phase of S_{22}.

Fig.5. (a) Attenuation constant, (b) phase constant for glass and graphene/glass, and (c) attenuation constant, (d) phase constant for quartz and graphene/quartz.

Fig.6. Real ε_{reff} using ABCD and adopted method (a) glass, (b)graphene/glass, (c) quartz and (d) graphene/quartz.

Fig.7. Imaginary ε_{reff} using ABCD and adopted method (a) glass, (b) graphene/glass, (c) quartz and (d) graphene/quartz.

Fig.8. Phase velocity v_p (m/s) using ABCD and adopted method (a) glass, (b)graphene/glass, (c) quartz and (d) graphene/quartz.

Fig.9. Group velocity v_g (m/s) using ABCD and adopted method (a) glass, (b)graphene/glass, (c) quartz and (d) graphene/quartz.

ACCEPTED MANUSCRIPT

Table caption

Table-1: The peak position in G-band and corresponding calculated thickness of graphene layers.

ACCEPTED MANUSCRIPT

ACCEPTED MANUSCRIPT

Highlights:

- Microwave transmission and dielectric properties of graphene have been studied
- De-embedding method was used.
- This method is based on the propagation constants, physical length of sample and microstrip line.
- Single layer graphene posseses the anomalous dispersion in 2 to 10 GHz range.

ACCEPTED MANUSCRIPT

Received: 10 June 2016 | Accepted: 19 October 2016

DOI: 10.1111/jace.14668

ORIGINAL ARTICLE

Journal of the American Ceramic Society

Structural and emission properties of Eu^{3+}-doped alkaline earth zinc-phosphate glasses for white LED applications

Kaushal Jha | Mula Jayasimhadri

Luminescent Materials Research Lab (LMRL), Department of Applied Physics, Delhi Technological University, Delhi, India

Correspondence
M. Jayasimhadri, Department of Applied Physics, Delhi Technological University, Delhi, India.
Email: jayaphysics@yahoo.com

Funding information
DST-SERB, University Grants Commission (UGC)

Abstract

Quaternary alkaline earth zinc-phosphate glasses in molar composition $(40 - x)$ $ZnO - 35P_2O_5 - 20RO - 5TiO_2 - xEu_2O_3$ (where x=1 and R=Mg, Ca, Sr, and Ba) were prepared by melt quenching technique. These glasses were studied with respect to their thermal, structural, and photoluminescent properties. The maximum value of the glass transition temperature (T_g) was observed for BaO network modifier mixed glass and minimum was observed for MgO network modifier glass. All the glasses were found to be amorphous in nature. The FT-IR suggested the glasses to be in pyrophosphate structure, which matches with the theoretical estimation of O/P atomic ratio and the maximum depolymerization was observed for glass mixed with BaO network modifier. The intense emission peak was observed at 613 nm ($^5D_0 \rightarrow {}^7F_2$) under excitation of 392 nm, which matches well with excitation of commercial *n*-UV LED chips. The highest emission intensity and quantum efficiency was observed for the glass mixed with BaO network modifier. Based on these results, another set of glass samples was prepared with molar composition $(40 - x)$ $ZnO - 35P_2O_5 - 20BaO - 5TiO_2 - xEu_2O_3$ (x=3, 5, 7, and 9) to investigate the optimized emission intensity in these glasses. The glasses exhibited crystalline features along with amorphous nature and a drastic variation in asymmetric ratio at higher concentration (7 and 9 mol%) of Eu_2O_3. The color of emission also shifted from red to reddish orange with increase in the concentration of Eu_2O_3. These glasses are potential candidates to use as a red photoluminsecent component in the field of solid-state lighting devices.

KEYWORDS
europium, FT-IR, glass, phosphates, photoluminescence

1 | INTRODUCTION

In recent years, rare earth doped inorganic materials have attracted immense attention in all the areas of science and technology such as lighting, lasers, displays, drug carriers, photovoltaics, photocatalysis, telecommunications, and structural analysis due to their intraconfigurational *f-f* transitions.[1-5] Solid-state lighting devices based on white light emitting diodes (w-LEDs) are receiving great attention due to lower power consumption, longer lifetime, and environmentally friendly characteristics as compared with traditional fluorescent and incandescent lamps. However, the commercially available w-LEDs suffer from low color rendering index, which is due to the lack of the red component. Among various rare earth oxides, trivalent europium (Eu^{3+})-doped materials have gained attention due to emission in the red region of the visible spectrum upon excitation via UV/n-UV/blue light. Eu^{3+} with $4f^6$ electronic configuration has application in the field of lighting and display as it depicts narrow, intense, and monochromatic emission due to $^5D_0 \rightarrow {}^7F_2$ transition.[6] Eu^{3+} has also been preferred as a structural probe in

 © 2017 The American Ceramic Society

determining the site occupancy and local symmetry in the host lattice.[7] The luminescent properties and potential applications of Eu^{3+} ions have been reported in many types of glassy host materials, eg, silicates, borates, phosphate, tungstate, and tellurite.[8-10] Glasses are preferred over crystalline materials due to certain unique advantages such as high durability, simpler manufacturing technique, lower production cost, and excellent thermal and mechanical stabilities. In white light emitting devices, glasses serves the purpose of both encapsulant and wavelength converter and is free from the organic resin.[11]

Among various glass-forming oxides, phosphate glasses have been extensively investigated due to their unique characteristics like low melting and softening temperature, transparency in the wide spectral region (UV to IR), and high mechanical and thermal stability.[12] Phosphate glasses have tetrahedral structure described by Q^n (n=0-3) terminology, where n is the number of bridging oxygen per tetrahedron. The phosphate structure consists of various structural units (Q^3, Q^2, Q^1, and Q^0) depending on the oxygen-to-phosphorous (O/P) atomic ratio.[13,14] The rare earth ion solubility for phosphate glasses is 1000 times greater than borate and silicate glasses which make them a suitable candidate as a host material for luminescence applications.[15] However, the hygroscopic nature and poor chemical durability of the phosphate glasses are a major hindrance in their practical applicability for devices. The incorporation of ZnO makes phosphate as moisture resistant due to the formation of P-O-Zn bonds and plays the dual role: either as a glass former in fourfold coordination or as a glass modifier in sixfold coordination.[12,16] ZnO offers special properties that have drawn the significant interest of researchers like low cost, low toxicity, non-hygroscopic, direct band gap, and intrinsic emitting property and large exciton binding energy.[17] The incorporation of alkaline earth metal (Mg, Ca, Sr, and Ba) as a network modifier lowers the melting temperature and leads to disruption of the glass network which enhances the formation of non-bridging oxygen groups.[18,19] TiO_2 is a heavy metal oxide and its incorporation into the phosphate glass significantly improves chemical durability and stabilization of the glass structure.[13]

In this article, Eu^{3+}-doped quaternary zinc-phosphate glasses were prepared by melt quenching technique with different alkaline earth network modifiers (MgO, CaO, SrO, and BaO) for the first time. The thermal, structural, and photoluminescent properties have been explored in detail. Along with this, Judd-Ofelt theory has also been applied on these glasses. The aim is to investigate the applicability of these glasses as the red component for RGB-based white light emitting devices.

2 | EXPERIMENTAL PROCEDURE

The glass samples were prepared by the conventional melt quenching technique. Four set of quaternary alkaline zinc-phosphate glass samples were prepared with molar composition:

$$\mathrm{ZPMT1}:(40-x)\mathrm{ZnO}-35\mathrm{P_2O_5}-20\mathrm{MgO}-5\mathrm{TiO_2}-x\mathrm{Eu_2O_3}$$

$$\mathrm{ZPCT1}:(40-x)\mathrm{ZnO}-35\mathrm{P_2O_5}-20\mathrm{CaO}-5\mathrm{TiO_2}-x\mathrm{Eu_2O_3}$$

$$\mathrm{ZPST1}:(40-x)\mathrm{ZnO}-35\mathrm{P_2O_5}-20\mathrm{SrO}-5\mathrm{TiO_2}-x\mathrm{Eu_2O_3}$$

$$\mathrm{ZPBT1}:(40-x)\mathrm{ZnO}-35\mathrm{P_2O_5}-20\mathrm{BaO}-5\mathrm{TiO_2}-x\mathrm{Eu_2O_3}$$

The value of x was fixed at 1 mol%. Thereafter, another set of glass samples were prepared with BaO network modifier mixed glass in molar composition $(40 - x)$ $ZnO - 35P_2O_5 - 20BaO - 5TiO_2 - xEu_2O_3$ (x=3.0, 5.0, 7.0, and 9.0) and the samples were named as ZPBT3, ZPBT5, ZPBT7, and ZPBT9, respectively. The starting materials were analytical-grade $NH_4H_2PO_4$, ZnO, TiO_2, $MgCO_3$, $CaCO_3$, $SrCO_3$, $BaCO_3$, and high-purity Eu_2O_3. The materials were thoroughly mixed in an agate mortar and pestle with acetone as a wetting medium, and then placed in almina crucible and melted in the temperature range 1150°C-1250°C in a muffle furnace**.** The melt was held for 1 hour and then poured on to preheated brass plate and annealed at 400°C for removal of thermal and mechanical stress and were allowed to cool to room temperature. The glass samples were further cut and polished for characterizations.

The XRD spectra of the glass samples were recorded with high-resolution X-ray diffractometer (Bruker; Model D8 advance) having nickel filtered CuK_α radiation (λ=1.5406 Å) in the 2θ range from 20° to 70°. Differential thermal analysis (DTA) of glass samples was carried out under N_2 atmosphere at heating rate of 10°C/min from ambient temperature to 750°C using TA instrument SDT Q600, New castle, DE. The Fourier transform infrared spectroscopy (FT-IR) was performed by PerkinElmer Frontier FT-IR Spectrometer , Walthman, MA, USA for which the pellets were prepared by mixing the glass samples in powder form with KBr and then compressed mechanically at 1.5 ton. The photoluminescence (PL) Spectra were measured using Shimadzu RF-5301PC spectrofluorophotometer Kyoto, Japan fitted with xenon flash lamp. The decay analysis was performed using an Edinburgh FLSP900 Edinburgh Instruments Ltd, Kirkton Campus, UK, where a xenon lamp was used as an excitation source.

3 | RESULTS AND DISCUSSION

Figure 1 represents the X-ray diffraction patterns of the ZPMT1, ZPCT1, ZPST1, and ZPBT1 glasses. The X-ray

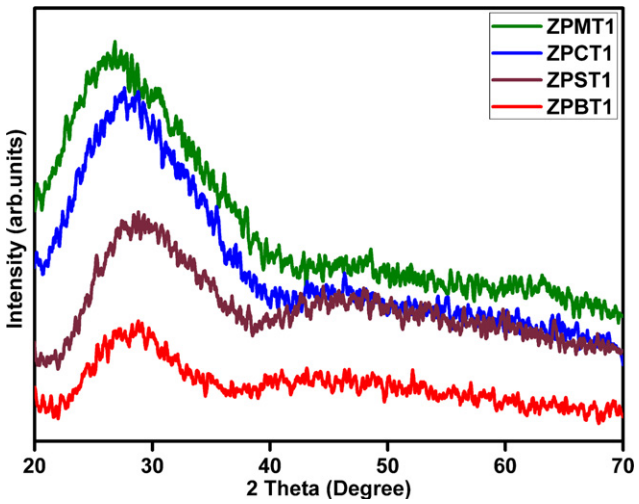


FIGURE 1 XRD spectra of ZPMT1, ZPCT1, ZPST1, and ZPBT1 glasses [Color figure can be viewed at wileyonlinelibrary.com]

diffraction patterns do not indicate any crystalline features, which confirms the amorphous nature of the glass samples.

The DTA curves of the glasses ZPMT1, ZPCT1, ZPST1, and ZPBT1 are shown in Figure 2. All the curves exhibit an endothermic peak associated with the glass transition temperature (T_g) (not always obvious in the graph but found with the help of software). The two sharp exothermic peaks correspond to the peak crystallization temperature and are marked as T_{p1} and T_{p2}. The curves also represent two temperatures related to onset of crystallization, which are marked as T_{x1} and T_{x2}. All these values of T_g, T_{p1}, T_{p2}, T_{x1}, and T_{x2} are given in Table 1. The

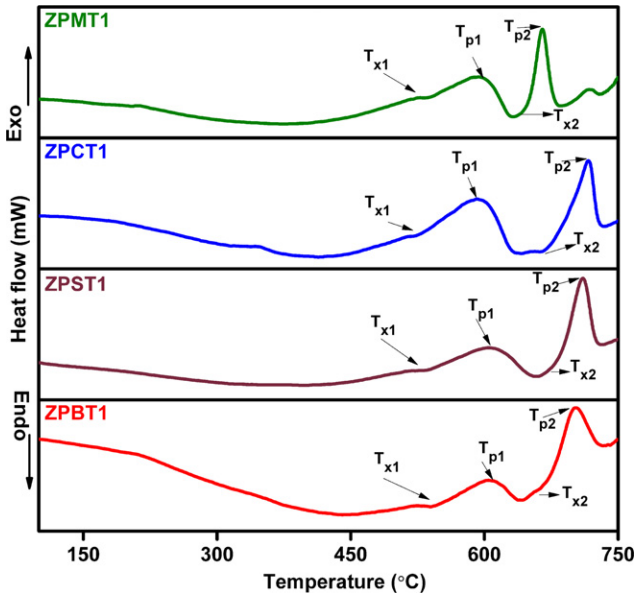


FIGURE 2 DTA Curves of ZPMT1, ZPCT1, ZPST1, and ZPBT1 glasses [Color figure can be viewed at wileyonlinelibrary.com]

TABLE 1 Optical glass transition temperature (T_g), onset of crystallization temperatures (T_{p1}, T_{p2}), peak crystallization temperatures (T_{p1}, T_{p2}), and thermal stability (ΔT) of ZPMT1, ZPCT1, ZPST1, and ZPBT1 glasses

	Glass samples			
Thermal properties (°C)	**ZPMT1**	**ZPCT1**	**ZPST1**	**ZPBT1**
($T_g \pm 3$)	379	390	405	418
($T_{x1} \pm 3$)	525	523	532	542
($T_{p1} \pm 3$)	594	592	606	607
($T_{x2} \pm 3$)	643	669	674	667
($T_{p2} \pm 3$)	665	717	710	702
Thermal stability ($\Delta T \pm 3$)	146	133	127	124

network modifiers directly influence the T_g because glass transition involves modification of chemical bonds between the glass former and glass modifiers.[20] The value of T_g was maximum for the ZPBT1 followed by ZPST1, ZPCT1, and ZPMT1 glasses, which indicates that the higher field strength cations (Ba^{2+}>Sr^{2+}>Ca^{2+}>Mg^{2+}) create a more tightly bonded glass structure.[21] From the DTA curve, the thermal stability of the glasses was calculated by the relation given by dizetel.[22]

$$\Delta T = T_{x1} - T_g \quad (1)$$

where ΔT is the thermal stability and the values are presented in Table 1. For glass to be thermally stable, ΔT value should be greater than 100°C. In this case, the value of ΔT for all the glasses ZPBT1, ZPST1, ZPCT1, and ZPMT1 was found to be greater than 100, which indicates high thermal stability of the all glass samples. The higher the value of ΔT, the lower is the tendency towards crystallization.[22]

The FT-IR spectra for the prepared glasses ZPMT1, ZPCT1, ZPST1, and ZPBT1 are represented in Figure 3 in the range 400-1500 cm^{-1}. The band present in the range 450-650 cm^{-1} may be ascribed to the Zn–O tetrahedral bonds.[20] The presence of ZnO tetrahedral bonds indicates that the ZnO enters the glass structure as a former. The low-frequency absorption band around 476 cm^{-1} is assigned to harmonics of bending vibration of O=P–O.[23] The absorption peak present at 536 cm^{-1} corresponds either to the harmonic of the P–O–P vibrations or the characteristic frequency of $P_2O_7^{4-}$ group. The absorption peaks centered at band 748 and 925 cm^{-1} are attributed to the symmetric stretching, $\upsilon_s(PO_2)$, and antisymmetric stretching, $\upsilon_{as}(PO_2)$, of the P–O–P linkages of the bridging oxygen atoms bonded to the phosphorous, respectively.[24] The simultaneous occurrence of bands present at 748 and 925 cm^{-1} indicate the presence of pyrophosphate structure $(P_2O_7)^{4-}$.[12,20] The band in the region 800-1400 cm^{-1} is broad, and this band consists of several peaks. Therefore,

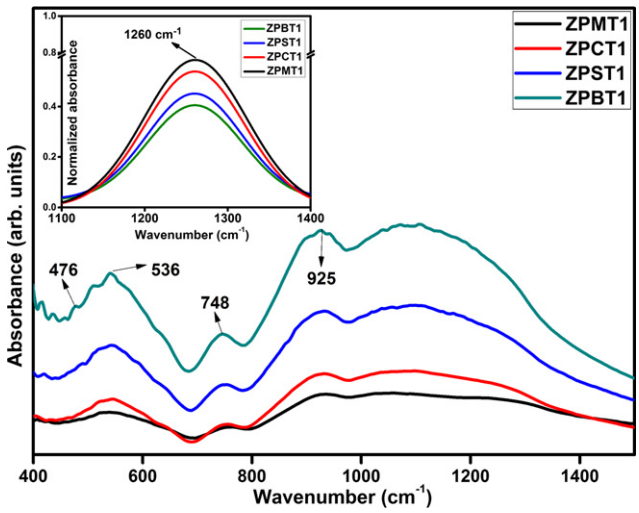


FIGURE 3 FT-IR spectra of ZPMT1, ZPCT1, ZPST1, and ZPBT1 glasses at room temperature. Inset: represents the P=O bond normalized intensity variation [Color figure can be viewed at wileyonlinelibrary.com]

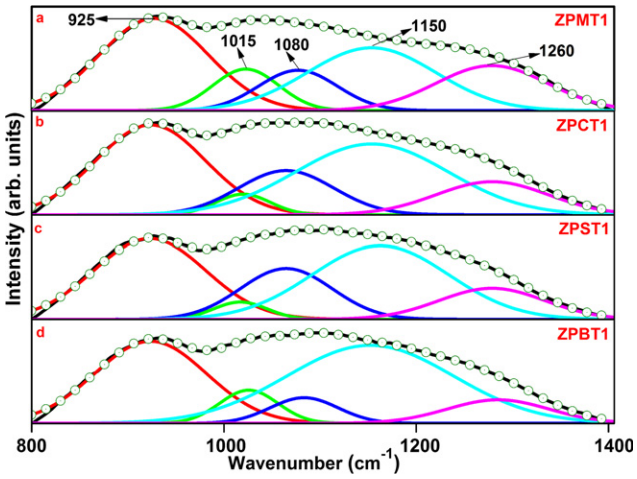


FIGURE 4 D-convoluted spectra FT-IR Spectra of ZPMT1, ZPCT1, ZPST1, and ZPBT1 glasses in the range 800-1400 cm^{-1} at room temperature [Color figure can be viewed at wileyonlinelibrary.com]

deconvolution was performed in this region for all the samples and is shown in Figure 4. The deconvoluted spectra of all the glass samples had peaks at almost the same wavenumbers with slight variation in intensity. The deconvoluted band present around 1015 cm^{-1} is assigned to the symmetric stretching modes of $P–O^-$ in Q^1 structural units.[25] The band around 1080 cm^{-1} corresponds to the asymmetric stretching vibration of $P–O^-$ in Q^2 structural units. Also, this band might be indicative of P–O–Zn linkages. The band located at 1150 cm^{-1} is ascribed to the symmetric stretching vibration of PO_3^{2-} units in Q^1 species. The band located around 1260 cm^{-1} may be ascribed to the symmetric stretching vibrations of P=O double bond. However, this peak exhibited low intensity, which indicates the depolymerization of the phosphate structure.[26,27]

The FT-IR spectra in the range 800-1400 cm^{-1} are broad. The broadening is observed mainly due to the presence of P=O bond at 1260 cm^{-1}. To reveal the structure of P=O bond in different glasses, the absorption spectra were normalized with the most intense peak at 925 cm^{-1}, a graph between normalized absorption vs wavenumber in the range 1100-1400 cm^{-1} is represented in the inset of Figure 3. The inset of the Figure 3 clearly represents that the intensity of the P=O bond at 1260 cm^{-1} follows the sequence: ZPMT1>ZPCT1>ZPST1>ZPBT1. This indicates that the breakage of P=O bond is in the sequence ZPBT1>ZPST1>ZPCT1>ZPMT1 and leads to formation of P–O–Ba, P–O–Sr, P–O–Ca, and P–O–Ma bonds. This indicates that the alkaline earth oxides enter the glass network interstitially as a network modifier and maximum depolymerization is observed for BaO network modifier followed by SrO, CaO, and MgO.[28] The phosphate glasses exhibit different structures based on the oxygen-to-phosphorous (O/P) atomic ratio. The phosphate glasses can be in ultra-phosphate, meta-phosphate, or polyphosphate structure depending on the O/P atomic ratio. For the ultra-phosphate structure, the O/P atomic ratio lies between 2.5 and 3.0 and the networks are dominated by the Q^2 and Q^3 structural units. The O/P atomic ratio is 3.0 for meta-phosphate structure and the network consists of rings and/or long chains of Q^2 structural units. For polyphosphate structure, the O/P atomic ratio is greater than 3.0 and is based on Q^2 chains terminated by Q^1 tetraherda. The polyphosphate structure further can be classified in pyrophosphate and orthophosphate structure. For the present glass systems ZPBT1, ZPST1, ZPCT1, and ZPMT1, the theoretical value of O/P atomic ratio was found to be 3.48, which suggest that it should be in polyphosphate structure. The O/P atomic ratio 3.48 is very near to 3.50, which suggests the presence of pyrophosphate structure.[14,29] The investigated FT-IR spectra clearly indicate about the presence of pyrophosphate structure and Q^1 and Q^2 structural units. Hence, the experimental results were supported by theoretical O/P atomic ratio calculation. Based on the FT-IR spectra, it is confirmed that Mg, Ca, Sr, and Ba act as network modifiers and the glass structure is in pyrophosphate structure.

The excitation spectra of the Eu^{3+}-doped glass samples were obtained by monitoring emission at 613 nm as represented in Figure 5. The excitation spectra consist of a series of bands between 350 and 500 nm, which are attributed to the *f-f* transitions of Eu^{3+} ions.[30] The most intense sharp excitation line was centered at 392 nm attributed to $^7F_0 \rightarrow {}^5L_6$ transition, which matches with emission of *n*-UV LEDs. The other excitation peaks observed at 360, 381, 412,

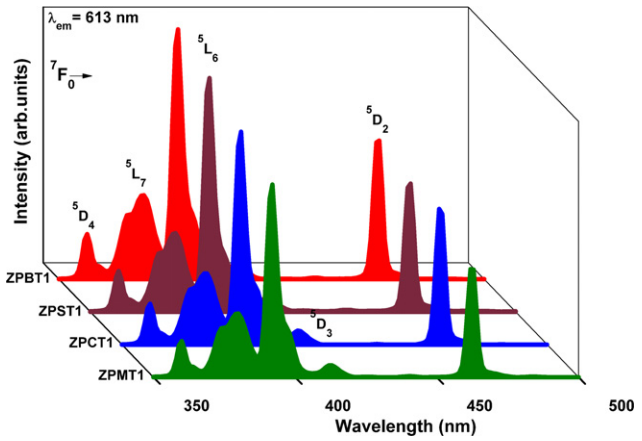


FIGURE 5 Photoluminescence excitation (PLE) spectra of ZPMT1, ZPCT1, ZPST1, and ZPBT1 glasses by monitoring emission at 613 nm [Color figure can be viewed at wileyonlinelibrary.com]

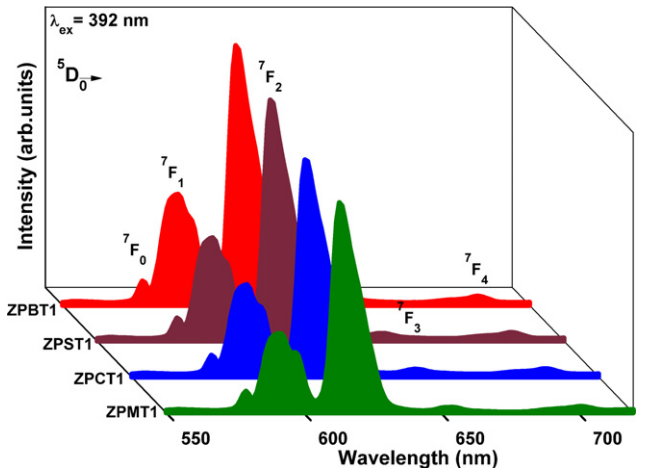


FIGURE 6 Photoluminescence (PL) spectra of ZPMT1, ZPCT1, ZPST1, and ZPBT1 glasses at 392 nm excitation [Color figure can be viewed at wileyonlinelibrary.com]

and 462 nm are attributed to $^7F_0 \rightarrow ^5D_4$, $^7F_0 \rightarrow ^5L_7$, $^7F_0 \rightarrow ^5D_3$, and $^7F_0 \rightarrow ^5D_2$ transitions, respectively.[31] The spectra did not show any notable differences in the peak position and shape of the transitions for the different glasses. However, the intensity of the excitation spectra for ZPBT1 glasses was found to be higher than ZPST1, ZPCT1, and ZPMT1 glasses. The strongest excitation falls in the *n*-UV region of electromagnetic spectrum, suggesting the suitability of these glasses to be excited by n-UV-based LED.

Figure 6 represents the emission spectra of ZPMT1, ZPCT1, ZPST1, and ZPBT1 glasses under excitation of 392 nm. The strongest emission peak in the range 605-635 nm is centered at 613 nm attributed to $^5D_0 \rightarrow ^7F_2$ transition. In addition, this emission bands centered at 577, 591, 655, and 700 nm are assigned to $^5D_0 \rightarrow ^7F_0$, $^5D_0 \rightarrow ^7F_1$, $^5D_0 \rightarrow ^7F_3$, and $^5D_0 \rightarrow ^7F_4$ transitions of Eu^{3+} ions, respectively. The forced electric dipole (ED) transition $^5D_0 \rightarrow ^7F_2$ is hypersensitive in nature, and the emission intensity of this transition is strongly affected by the crystal field of ligand atoms. On the other hand, the magnetic dipole (MD) transition $^5D_0 \rightarrow ^7F_1$ is insensitive to the crystal environment. The transition $^5D_0 \rightarrow ^7F_1$ splits further into two bands, which is due to the stark splitting.[7] According to the selection rules, the MD is allowed, whereas forced ED transition is forbidden. The intensity of forced electric dipole transition dominated over the magnetic dipole transition, which suggested that the local symmetry of Eu^{3+} ion is without an inversion center. Also, the forbidden ED transition $^5D_0 \rightarrow ^7F_2$ becomes parity allowed, due to the odd parity component of the crystal field. This parity allowed transition makes Eu^{3+} ion as an excellent activator for red luminescent materials, which provides a better color purity and brightness. The emission intensity of red to orange ($^5D_0 \rightarrow ^7F_2/^5D_0 \rightarrow ^7F_1$) is known as the asymmetric ratio and is used as a measure of the site symmetry of rare earth ions.

The asymmetric ratio (R_{21}) is represented as[32]

$$R_{21} = \frac{\int_{605}^{635} R_2 d\lambda}{\int_{581}^{604} R_1 d\lambda} \quad (2)$$

The value of the asymmetric ratio was calculated by integrating the area of $^5D_0 \rightarrow ^7F_2$ transition to $^5D_0 \rightarrow ^7F_1$ transition.[30] The value of R_{21} for ZPBT1, ZPST1, ZPCT1, and ZPMT1 glasses was 2.20, 2.23, 2.25, and 2.28, respectively, indicative of red emission stronger than the orange emission. The R_{21} value varies very minutely for different modifier mixed glass samples and follows the order ZPMT1>ZPCT1>ZPST1>ZPBT1. The higher value of this ratio indicates a higher Eu^{3+}–O^{2-} covalence and lower symmetry of Eu^{3+} ions.[33,34] As per Judd-Ofelt (JO) theory, the transition between J=0 levels are strictly forbidden, ie, $^5D_0 \rightarrow ^7F_0$ transition is not allowed. The existence of low-intensity $^5D_0 \rightarrow ^7F_0$ transition is possible due to one of the following reasons: (i) breakage of the closure approximation in JO theory, (ii) either due to parity mixing (d-f mixing) or *J*-*J* mixing due to thermal population at the ground ($F_{J=0,1,2,3 \text{ and } 4}$) state or the excited state ($^5D_{J=0,1,3}$). The parity mixing (d-f) is not feasible due to high energy gap between them, whereas the excited state ($^5D_{J=0,1,3}$) *J*-*J* mixing is ruled out due to the significant energy difference between them.[35,36] However, the possibility of *J*-*J* mixing at ground state ($F_{J=0,1,2,3 \text{ and } 4}$) exists because of the thermal population. The $^5D_0 \rightarrow ^7F_0$ transition arises as the *J*-*J* mixing is most probable between J=0 and 2 at the ground state because the energy difference values between J=0 and J=4, 6 are significantly higher and also the emission intensities are weaker as compared with J=2.[35] The emission intensity ratio between $^5D_0 \rightarrow ^7F_0$ and the $^5D_0 \rightarrow ^7F_2$ transition was determined for the various glass samples. This ratio (R_{02}) is represented as:

$$R_{02} = \frac{\int_{574}^{580} R_0 d\lambda}{\int_{605}^{635} R_2 d\lambda} \quad (3)$$

The R_{02} value for ZPBT1, ZPST1, ZPCT1, and ZPMT1 glasses was found to be 0.0259, 0.0261, 0.0270, and 0.0287, respectively. The increase in R_{02} value indicates the larger *J-J* mixing for ZPMT1 glass samples. The maximum PL intensity was observed for the ZPBT1 followed by ZPST1, ZPCT1, and ZPMT1. The trend depicts that with increasing ionic size or radius of the network modifier ions ($r_{Ba}{}^{2+} > r_{Sr}{}^{2+} > r_{Ca}{}^{2+} > r_{Mg}{}^{2+}$), the PL intensity increases. This trend may be due to greater depolymerization of BaO network modifier oxide, which is in accordance with FT-IR spectra.[18] The PL spectra do not show any peaks from the higher lying states such as $^5D_1$, which is due to the high phonon energy of the phosphate glass.[25,34,37]

Based on the emission spectra of the glasses, Eu^{3+} concentration-dependent emission was recorded for different ZPBT glasses, as they offered intense emission peaks. The concentration-dependent emission spectra are represented in the Figure 7. The emission intensity increased with increasing Eu^{3+} concentration in the prepared glass samples up to 9 mol%; the concentration quenching phenomenon was not observed for the prepared samples. The concentration quenching phenomenon was not observed, as the separation between the Eu^{3+} ions is such that the probability of energy transfer between them ceases.[38] The intensity peaks due to $^5D_0 \rightarrow {}^7F_2$ transition dominated over $^5D_0 \rightarrow {}^7F_1$ transition for ZPBT1 to ZPBT7 samples. However, for ZPBT9 sample $^5D_0 \rightarrow {}^7F_1$ transition dominated over $^5D_0 \rightarrow {}^7F_2$ transition. This result implies that the local symmetry of Eu^{3+} ion is without an inversion center for ZPBT1 to ZPBT7 samples and with an inversion center for ZPBT9 sample. As a result there was variation in the asymmetric ratio for the glass sample. The value of the asymmetric ratio for the glass samples ZPBT1, ZPBT3, ZPBT5, ZPBT7, and ZPBT9 was calculated to be 2.20, 2.19, 2.18, 1.64, and 0.99, respectively. The asymmetric ratio changed drastically for ZPBT7 and ZPBT9 samples. The relatively lower values of the asymmetric ratio for ZPBT7 and ZPBT9 suggest incorporation of Eu^{3+} ions into more symmetric environment with less covalent character. Ideally there should be very minute variation in the asymmetric ratio with increase in concentration of Eu^{3+} ion. To understand the nature of the drastic change in the asymmetric ratio, XRD patterns were recorded for ZPBT1, ZPBT3, ZPBT5, ZPBT7, and ZPBT9 and are represented in Figure 8. ZPBT1, ZPBT3, and ZPBT5 indicated amorphous nature. However, ZPBT7 and ZPBT9 XRD patterns consist of certain crystalline features along with the amorphous nature. This indicates that there is some crystal precipitation in ZPBT7 and ZPBT9. The intense peaks observed at 21.69°, 22.18°, 27.60°, and 35.03° correspond to the (−110), (101), (200), and (−202) planes of $EuPO_4$. The average crystallite size using Debye-Scherrer's formulae ($D=K\lambda/\beta\cos\theta$) was found to be 28.03 and 31.42 nm for ZPBT7 and ZPBT9 glasses, respectively. In Debye-Scherrer's formulae, D represents crystallite size, K is the crystallite shape factor, λ is wavelength of x-ray, β is the pure diffraction broadening, and θ is diffraction angle.[39,40] The variation in the asymmetric ratio and prominent stark splitting for $^5D_0 \rightarrow {}^7F_1$, $^5D_0 \rightarrow {}^7F_2$, and $^5D_0 \rightarrow {}^7F_4$ transitions in both ZPBT7 and ZPBT9 samples may be due to the presence of the crystalline features.[41] Figure 9 represents the SEM images of ZPBT1, ZPBT3, ZPBT5, ZPBT7, and ZPBT9 samples. The homogenous glassy phase is clearly observed for ZPBT1, ZPBT3, and ZPBT5 samples,

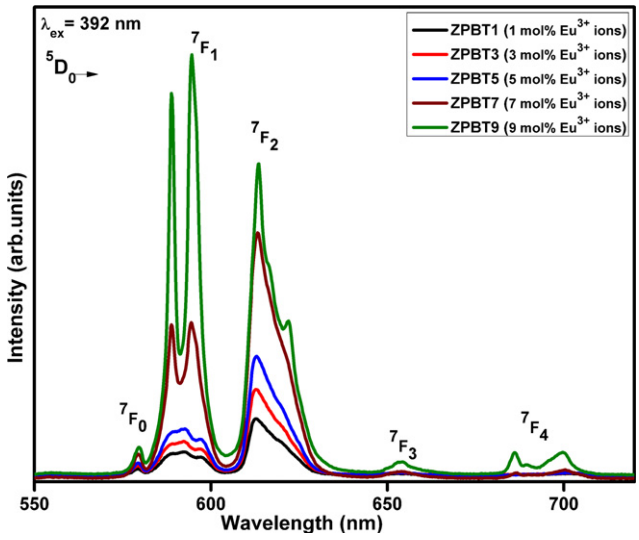


FIGURE 7 PL spectra of ZPBT1, ZPBT3, ZPBT5, ZPBT7, and ZPBT9 glasses at 392 nm excitation [Color figure can be viewed at wileyonlinelibrary.com]

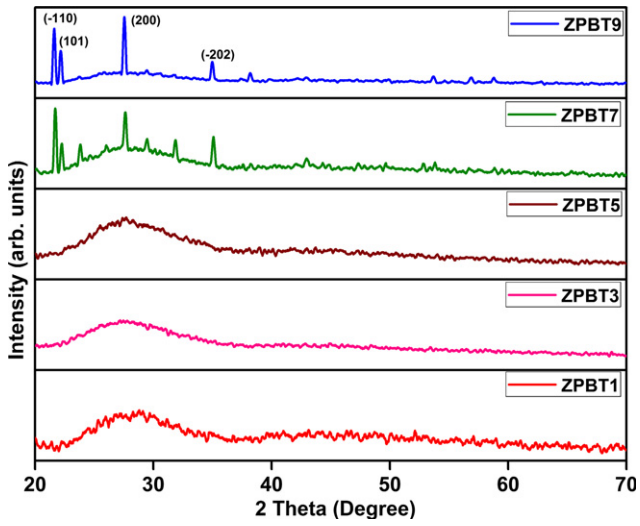


FIGURE 8 XRD spectra of ZPBT1, ZPBT3, ZPBT5, ZPBT7, and ZPBT9 glasses [Color figure can be viewed at wileyonlinelibrary.com]

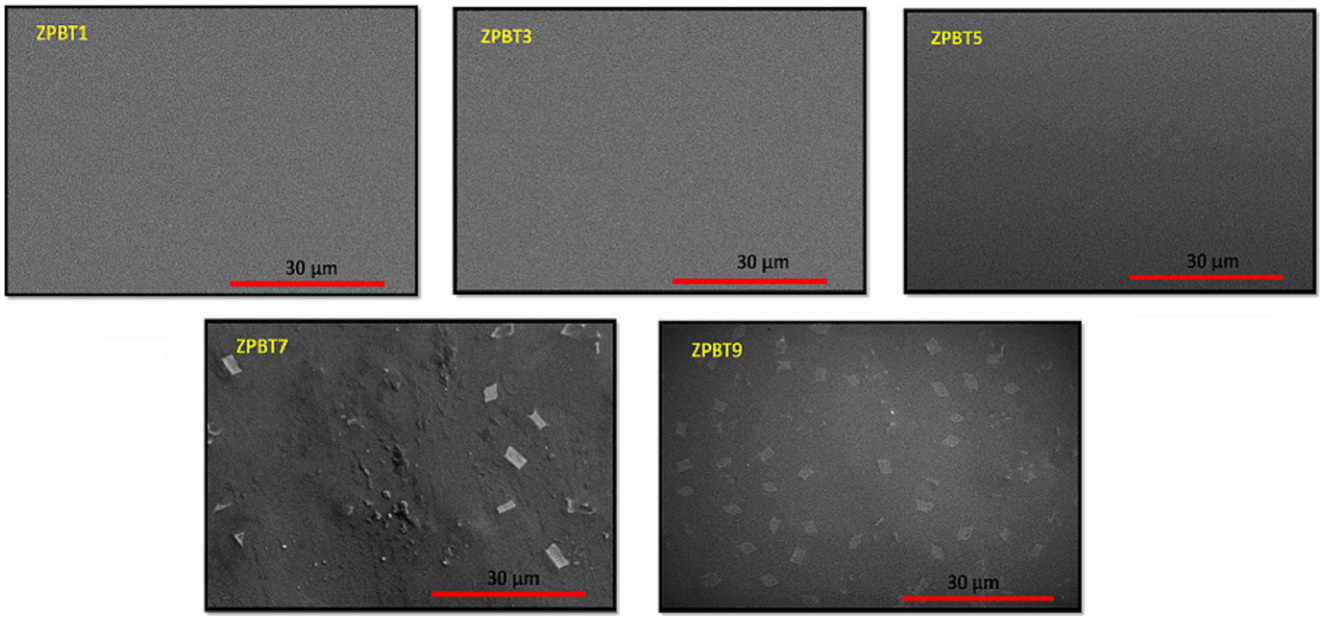


FIGURE 9 SEM micrographs of ZPBT1, ZPBT3, ZPBT5, ZPBT7, and ZPBT9 glasses [Color figure can be viewed at wileyonlinelibrary.com]

whereas microcube crystals were observed for ZPBT7 and ZPBT9 samples. The observed results are in accordance with the XRD, which confirm the existence of crystalline features at higher concentrations of Eu^{3+}.

The Judd-Ofelt parameters (Ω_J, J=2, 4, and 6) and radiative transition rates can be determined from the emission spectra. The radiative transition rate for the $^5D_0 \rightarrow {}^7F_1$ can be obtained by:

$$A_R(5_{D0} \rightarrow 7_{F1}) = \frac{64\pi^4 \upsilon_1^3}{3h(2J+1)} s_{md} n^3 \tag{4}$$

And all the entries have their usual meaning (υ_1—wavenumber of the magnetic dipole transition, h—Planck's constant, n—refractive index). The s_{md} is the magnetic dipole line strength, which is independent of the host lattice and its value is taken to be 7.83×10^{-42} esu (c) cm^2.[32,42,43] The radiative transition rate for the forced electric dipole transition $^5D_0 \rightarrow {}^7F_J$ (J=2, 4, and 6) is expressed as

$$A_R\left(5_{D0} \rightarrow 7_{Fj}\ (J = 2,\ 4,\ 6)\right) = \frac{64\pi^4 \upsilon_J{}^3 e^2}{3h(2J+1)} \frac{n(n^2+2)^2}{9} \sum_{J=2,4,6} \Omega_J \langle 5_{D0} \| U^J \| 7_{FJ} \rangle^2 \tag{5}$$

where υ is the wavenumber of electric dipole transition and $<^5D_0\|U^J\|^7F_J>^2$ is the square reduced matrix element for the J-J' transition. The factor $n(n^2+2)^2/9$ is for consideration that Eu^{3+} ions in not vacuum. The squared values of the reduced matrix element are $<^5D_0\|U^2\|^7F_2>^2$=0.0032, $<^5D_0\|U^4\|^7F_4>^2$=0.0023, and $<^5D_0\|U^6\|^7F_6>^2$=0.0002. The $^5D_0 \rightarrow {}^7F_J$ (J=0, 3, 5) are forbidden transitions, therefore their correlated reduced matrix elements are zero.[44] The transition intensity ratio between the electric and magnetic dipole is expressed by dividing Equation (5) by Equation (4)

$$\frac{A_R\left(5_{D0} \rightarrow 7_{Fj}\ (J = 2,\ 4,\ 6)\right)}{A_R\left(5_{D0} \rightarrow 7_{F1}\right)} = \frac{e^2 \upsilon_j{}^3}{s_{md}\ \upsilon_1{}^3} \frac{n(n^2+2)^2}{9n^3} \Omega_J \| U^J \|^2 \tag{6}$$

The intensity parameters Ω_2, Ω_4, and Ω_6 can then be calculated by the equation mentioned below:

$$A_R\left[\frac{\left(5_{D0} \rightarrow 7_{Fj}\ (J = 2,\ 4,\ 6)\right)}{A_R\left(5_{D0} \rightarrow 7_{F1}\right)}\right] = S\left[\frac{\left(5_{D0} \rightarrow 7_{Fj}\ (J = 2,\ 4,\ 6)\right)}{5_{D0} \rightarrow 7_{F1}}\right] \tag{7}$$

where S is the area under the emission curves related to the different transition $^5D_0 \rightarrow {}^7F_{1,2,4,6}$. The Ω_6 value cannot be calculated in this case as the $^5D_0 \rightarrow {}^7F_6$ transition was not observed from the emission spectra. The Ω_2 and Ω_4 values for all the glass samples are indicated in Table 2. The larger value Ω_2 indicates a higher degree of asymmetry and covalence environment. The values of the Ω_2 are greater than Ω_4 for all the glass samples.[32] The trend of the Ω_2 value is in agreement with R_{21} for all the glass samples.

The CIE chromaticity coordinates were calculated based on the emission spectra for all the glass samples. The value of the CIE chromaticity coordinates for the glasses with different network modifier oxides (ZPMT1, ZPCT1, ZPST1, ZPBT1) has the same value that is (0.65, 0.33) which lies in the pure red region and is represented on the

TABLE 2 *J-O* parameters (Ω_2, Ω_4), radiative transition rates (A_R), radiative transition rates (A_{NR}), average lifetime (τ_{avg}), and efficiency of ZPMT1, ZPCT1, ZPST1, and ZPBT1 glasses

	Glass samples			
Properties	**ZPMT1**	**ZPCT1**	**ZPST1**	**ZPBT1**
Ω_2 ($\times 10^{-20}$) cm^{-2}	2.23	2.27	2.30	2.42
Ω_4 ($\times 10^{-21}$) cm^{-2}	1.15	1.11	1.24	1.02
A_R	215.04	209.66	210.13	219.78
A_{NR}	448.83	475.96	506.84	547.34
Lifetime (ms)	1.827	1.973	2.101	2.228
Quantum efficiency (%)	28.65	29.30	30.58	32.39

CIE plot 1931 as shown in the Figure 10. For simplicity, chromaticity coordinates of ZPBT1 is shown as the value is same as that of ZPMT1, ZPCT1, and ZPST1. This result clearly indicate that the color of emission does not vary with the different modifier oxides (Mg, Ca, Sr, Ba) and the chromaticity coordinates lie on the perimeter of the CIE plot indicating high color purity. The obtained value of the CIE chromaticity coordinates was found to be very close to the commercial red phosphor $Y_2O_2S:Eu^{3+}$ (x=0.647, y=0.343) and National Television Standard Committee standard value of red phosphor (x=0.670, y=0.330). The results indicate that the prepared glass is a potential candidate as the red photoluminescent component for white light emitting devices. The CIE chromaticity coordinates corresponding to ZPBT3, ZPBT5, ZPBT7, and ZPBT9 were found to be (0.65, 0.33), (0.65, 0.33), (0.64, 0.35), and (0.62, 0.37). This suggest that as the concentration of Eu^{3+} is increased for BaO modifier oxide, the chromaticity coordinates start shifting towards the reddish-orange region for ZPBT7 and ZPBT9, which is due to the enhancement in the intensity of the $^5D_0 \rightarrow {}^7F_1$ transition.

The PL decay curve for $^5D_0 \rightarrow {}^7F_2$ (613 nm) transition of Eu^{3+} ions for different glass samples by monitoring excitation at 392 nm is represented in Figure 11. The decay curves were fitted to different exponential equations, and the best fit was obtained for biexponential equation expressed as follows:[45]

$$I = I_0 + A_1 \exp\left(-\frac{t}{\tau_1}\right) + A_2 \exp\left(-\frac{t}{\tau_2}\right) \quad (8)$$

where I and I_0 represent the luminescence intensities at time t and 0, τ_1 and τ_2 represent the two components of the lifetime, corresponding to the fast and slow lifetimes for exponential components, respectively; A_1 and A_2 are fitting constants, and t is the time. The biexponential fitting indicates the energy transfer between Eu^{3+} ions takes place via cross-relaxation process. The value of the average lifetime for different glass samples was calculated using the formulae:[45]

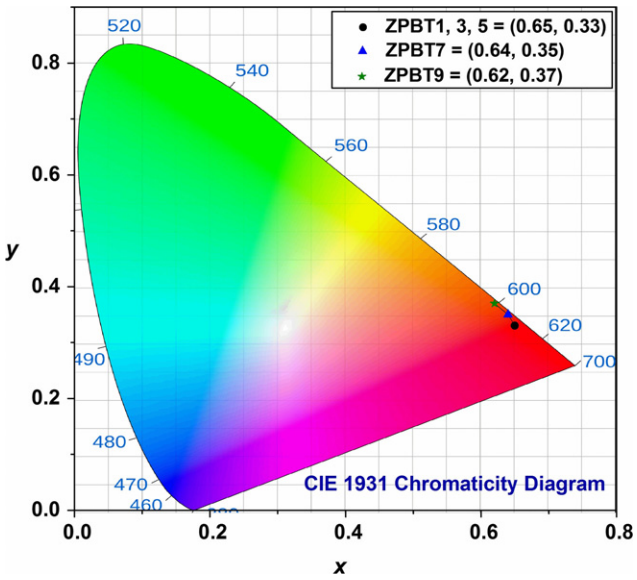


FIGURE 10 CIE chromaticity coordinates of ZPBT1, ZPBT3, ZPBT5, ZPBT7, and ZPBT9 glasses [Color figure can be viewed at wileyonlinelibrary.com]

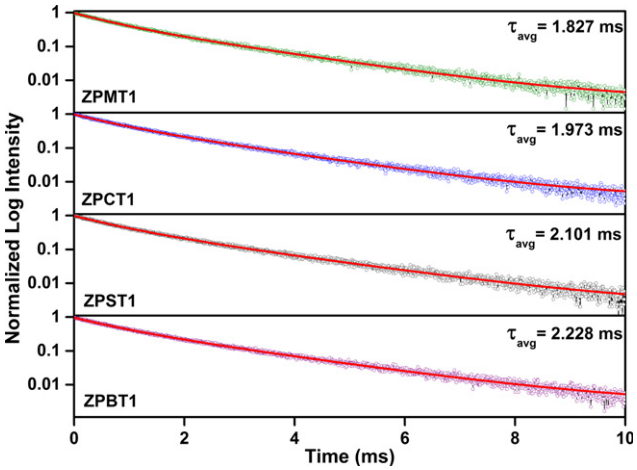


FIGURE 11 PL decay curves of the $^5D_0$ energy level for ZPMT1, ZPCT1, ZPST1, and ZPBT1 glasses [Color figure can be viewed at wileyonlinelibrary.com]

$$\tau_{avg} = \frac{A_1\tau_1^2 + A_2\tau_2^2}{A_1\tau_1 + A_2\tau_2} \quad (9)$$

The average value of the lifetime for ZPMT, ZPCT, ZPST, and ZPBT glasses was 1.827, 1.973, 2.101, and 2.328 ms. The emission quantum efficiencies for all the prepared glass samples were calculated based on the experimental data. The relation among fluorescence life time (τ), total radiative transition rate (A_{TR}), and total nonradiative transition rate (A_{TNR}) for $^5D_0$ level of Eu^{3+} can be expressed as:

$$\frac{1}{\tau} = A_{TNR} + A_{TR} \quad (10)$$

where A_{TR} is sum of total radiative transition rates and A_{TNR} is the total nonradiative transition rates. The quantum efficiency (Q.E) is given by the relation[18]:

$$\eta = \frac{A_{TR}}{A_{TR} + A_{TNR}} = \frac{\tau_{exp}}{\tau_{rad}} \quad (11)$$

τ_{exp} and τ_{rad} are experimental and radiative lifetime. The values of the Q.E for the different glasses are given in Table 2. The maximum value of the Q.E was observed for the ZPBT1 glass sample, which is relatively 13.06% higher than the ZPMT1 glass sample. The highest Q.E for the ZPBT1 glass may be due to the greater depolymerization of this glass batch. Furthermore, the higher Q.E in this glass may also be due to lesser cross-relaxation phenomenon, indicating that the energy transfer between Eu^{3+} ions is less when compared with other glass batches ZPST1, ZPCT1, and ZPMT1.[18]

4 | CONCLUSIONS

The Quaternary alkaline earth zinc-phosphate glasses in molar composition 39 ZnO–35 P_2O_5–20 RO (R=Mg, Ca, Sr, and Ba)–5 TiO_2 doped with 1 mol% Eu_2O_3 were successfully prepared by melt quenching technique. All the glasses were thermally stable and the highest glass transition temperature was found for BaO network modifier mixed glass and the lowest for the MgO network modifier mixed glass. The XRD spectra confirmed the amorphous nature of these glasses and FT-IR spectra indicated depolymerization of the phosphate structure. The glassy network consists of pyrophosphate structure dominated by Q^2 and Q^1 tetrahedra. The other emission lines were observed which were attributed to $^5D_0 \rightarrow {}^7F_{0,\ 1,\ 3,\ \text{and}\ 4}$ transition of Eu^{3+} ions. The asymmetric ratio of all these glasses was almost constant. The quantum efficiency of BaO network modifier glass was maximum, which is 13.06% relatively higher than that of MgO network glass. Based on these results glasses with molar composition $(40-x)$ ZnO35P_2O_5–20 BaO–5TiO_2–xEu_2O_3 (x=3, 5, 7, and 9) were prepared to determine the optimized doping concentration of Eu_2O_3. However, the concentration quenching phenomenon was not observed in these glasses. The glasses at higher Eu_2O_3 concentration (7 and 9 mol%) exhibited certain crystalline features along with amorphous nature and a drastic variation in asymmetric ratio was observed, which in turn shifted the emission color from red to reddish-orange region. However, for the pure glass samples (ZPBT1, ZPBT3, and ZPBT5) the CIE chromaticity coordinates lie in the pure red region, indicating the applicability of these glasses as the red photoluminescent component for white light emitting devices under n-UV excitation.

ACKNOWLEDGMENTS

Kaushal Jha is grateful to the University Grants Commission (UGC) for providing financial support in the form of Junior Research Fellowship (JRF). The author (M. Jayasimhadri) is grateful to DST-SERB, Govt. of India, for the sanction of a research project (No. SB/FTP/PS-082/2014, dt. 02/03/2015).

REFERENCES

1. Yang L, Xu X, Hao L, Yang X, Agathopoulos S. Synthesis and characterization of fast-decaying bluish green phosphors of Tb^{3+}-doped $CaSi_2O_2N_2$ for 2D/3D plasma display panels. *J Lumin*. 2012;132:1540–1543.
2. Liu Z, Li J, Yang L, Chen Q, Chu Y, Dai N. Efficient near-infrared quantum cutting in Ce^{3+}-Yb^{3+} codoped glass for solar photovoltaic. *Sol Energy Mater Sol Cells*. 2014;122:46–50.
3. Jiang WU, Guoliang Z, Jie LIU, Hongbing GAO, Chunxiang S. Synthesis, characteristics, and antibacterial activity of a rare-earth samarium/silver/titanium dioxide inorganic nanomaterials. *J Rare Earths*. 2014;32:727–732.
4. Tanabe S. Rare-earth-doped glasses for fiber amplifiers in broadband telecommunication. *Comptes Rendus Chim*. 2002;5:815–824.
5. Jayasimhadri M, Moorthy LR, Kojima K, Yamamoto K, Wada N, Wada N. Optical properties of Dy^{3+} ions in alkali telluorofluorophosphate glasses for laser materials. *J Phys D Appl Phys*. 2006;39:635–641.
6. Maheshwary, Singh BP, Singh J, Singh RA. Luminescence properties of Eu^{3+} -activated $SrWO_4$ nanophosphors- Concentration and Annealing effect. *RSC Adv*. 2014;4:32605–32621.
7. Gupta SK, Ghosh PS, Sahu M, Bhattacharyya K, Tewari R, Natarajan V. Intense red emitting monoclinic $LaPO_4$:Eu^{3+} nanoparticles: Host–dopant energy transfer dynamics and photoluminescence properties. *RSC Adv*. 2015;5:58832–58842.
8. Wen H, Duan CK, Jia G, Tanner PA, Brik MG. Glass composition and excitation wavelength dependence of the luminescence of Eu^{3+} doped lead borate glass. *J Appl Phys*. 2011;110:1–8.
9. You H, Nogami M. Optical properties and local structure of Eu^{3+} ions in sol–gel TiO_2-SiO_2 glasses. *J Phys Chem B*. 2004;108:12003–12008.
10. Babu AM, Jamalaiah BC, Suhasini T, Rao TS, Moorthy LR. Optical properties of Eu^{3+} ions in lead tungstate tellurite glasses. *Solid State Sci*. 2011;13:574–578.
11. Masai H, Yamada Y, Suzuki Y, Teramura K, Kanemitsu Y, Yoko T. Narrow energy gap between triplet and singlet excited states of Sn^{2+} in borate glass. *Sci Rep*. 2013;3:3541.
12. Omrani RO, Krimi S, Videau JJ, Khattech I, El Jazouli A, Jemal M. Structural and thermochemical study of Na_2O–ZnO–P_2O_5 glasses. *J Non Cryst Solids*. 2014;390:5–12.
13. Silva AMB, Correia RN, Oliveira JMM, Fernandes MHV. Structural characterization of TiO_2-P_2O_5-CaO glasses by spectroscopy. *J Eur Ceram Soc*. 2010;30:1253–1258.
14. Brow RK. Review: The structure of simple phosphate glasses. *J Non Cryst Solids*. 2000;263:1–28.
15. Jha A, Richards B, Jose G, et al. Rare-earth ion doped TeO_2 and GeO_2 glasses as laser materials. *Prog Mater Sci*. 2012;57:1426–1491.

16. Tarafder A, Molla AR, Dey C, Karmakar B. Thermal, structural, and enhanced photoluminescence properties of Eu^{3+}-doped transparent Willemite glass-ceramic nanocomposites. *J Am Ceram Soc*. 2013;96:2424–2431.
17. Jayasimhadri M, Jang K, Lee HS, Chen BJ, Yi SS, Jeong JH. White light generation from Dy^{3+}-doped $ZnO–B_2O_3–P_2O_5$ glasses. *J Appl Phys*. 2009;106:1–4.
18. Raghava Rao P, Murali Krishna G, Brik MG, Gandhi Y, Veeraiah N. Fluorescence features of Sm^{3+} ions in $Na_2SO_4–MO–P_2O_5$ glass system—Influence of modifier oxide. *J Lumin*. 2011;131:212–217.
19. Murthy DVR, Babu AM, Jamalaiah BC, et al. Photoluminescence properties of Er^{3+}-doped alkaline earth titanium phosphate glasses. *J Alloys Compd*. 2010;491:349–353.
20. Sastry SS, Rao BRV. Spectroscopic characterization of manganese-doped alkaline earth lead. *Bull Mater Sci*. 2015;38:475–482.
21. Wilder JA, Shelby JE. Property variation in alkali-earth metaphosphate glasses. *J Am Ceram Soc*. 1845;67:438–444.
22. Wers E, Oudadesse H. Thermal behaviour and excess entropy of bioactive glasses and Zn-doped glasses. *J Therm Anal Calorim*. 2013;115:2137–2144.
23. Abo-Naf SM, El-Amiry MS, Abdel-Khalek AA. FT-IR and UV-Vis optical absorption spectra of γ-irradiated calcium phosphate glasses doped with Cr_2O_3, V_2O_5 and Fe_2O_3. *Opt Mater (Amst)*. 2008;30:900–909.
24. Kiani A, Hanna JV, King SP, et al. Structural characterization and physical properties of P_2O_5-CaO-Na_2O-TiO_2 glasses by Fourier transform infrared, Raman and solid-state magic angle spinning nuclear magnetic resonance spectroscopies. *Acta Biomater*. 2012;8:333–340.
25. Pisarski WA, Żur L, Goryczka T, Sołtys M, Pisarska J. Structure and spectroscopy of rare earth—Doped lead phosphate glasses. *J Alloys Compd*. 2014;587:90–98.
26. Liu HS, Chin TS, Yung SW. FTIR and XPS studies of low-melting PbO–ZnO–P_2O_5 glasses. *Mater Chem Phys*. 1997;50:1–10.
27. Mansour E, El-Damrawi G. Electrical properties and FTIR spectra of ZnO–PbO–P_2O_5 glasses. *Phys B Condens Matter*. 2010;405:2137–2143.
28. Sastry SS, Rao BRV. Spectroscopic studies of copper doped alkaline earth lead zinc phosphate glasses. *Phys B Condens Matter*. 2014;434:159–164.
29. Abou Neel EA, Pickup DM, Valappil SP, Newport RJ, Knowles JC. Bioactive functional materials: A perspective on phosphate-based glasses. *J Mater Chem C*. 2009;19:690–701.
30. Rambabu U, Han S. Luminescence optimization with superior asymmetric ratio (red/orange) and color purity of MBO_3: Eu^{3+}@SiO_2 (M = Y, Gd and Al) nano down-conversion phosphors. *RSC Adv*. 2013;3:1368.
31. Wang Q, Ouyang S, Zhang W, Yang B, Zhang Y, Xia H. Luminescent properties of Eu^{3+}-doped glass ceramics containing $BaGdF_5$ nanocrystals under NUV-excitation for W-LEDs. *J Rare Earths*. 2015;33:13–19.
32. Uma Maheswari D, Suresh Kumar J, Moorthy LR, Jang K, Jayasimhadri M. Emission properties of Eu^{3+} ions in alkali tellurofluorophosphate glasses. *Phys B Condens Matter*. 2008;403:1690–1694.
33. Azeem PA, Kalidasan M, RamaGopal K, Reddy RR. Spectral analysis of Eu^{3+}:$B_2O_3–Al_2O_3–MF_2$ (M=Zn, Ca, Pb) glasses. *J Alloys Compd*. 2009;474:536–540.
34. Gao G, Wei J, Shen Y, Peng M, Wondraczek L. Heavily Eu_2O_3 -doped yttria-aluminoborate glasses for red photoconversion with a high quantum yield: Luminescence quenching and statistics of cluster formation. *J Mater Chem C*. 2014;2:8678–8682.
35. Parchur AK, Ningthoujam RS. Behaviour of electric and magnetic dipole transitions of Eu^{3+}, $5D_0 \rightarrow 7F_0$ and Eu–O charge transfer band in Li+ co-doped YPO_4:Eu^{3+}. *RSC Adv*. 2012;2:10859.
36. Wen H, Jia G, Duan C-K, Tanner PA. 1Understanding Eu^{3+} emission spectra in glass. *Phys Chem Chem Phys*. 2010;12:9933–9937.
37. Linganna K, Sreedhar VB, Jayasankar CK. Luminescence properties of Tb^{3+} ions in zinc fluorophosphate glasses for green laser applications. *Mater Res Bull*. 2015;67:196–200.
38. Katelnikovas A, Plewa J, Sakirzanovas S, et al. Synthesis and optical properties of $Li_3Ba_2La_3(MoO_4)_8$:Eu^{3+} powders and ceramics for pcLEDs. *J Mater Chem C*. 2012;22:22126–22134.
39. Vishwakarma AK, Jha K, Jayasimhadri M, Sivaiah B, Gahtori B, Haranath D. Emerging cool white light emission from Dy^{3+} doped single phase alkaline earth niobate phosphors for indoor lighting applications. *Dalt Trans*. 2015;44:17166–17174.
40. Rawat K, Kim H-J, Shishodia PK. Synthesis of Cu_2ZnSnS_4 nanoparticles and controlling the morphology with polyethylene glycol. *Mater Res Bull*. 2016;77:84–90.
41. Gao G, Reibstein S, Peng M, Wondraczek L. Tunable dual-mode photoluminescence from nanocrystalline Eu-doped Li_2ZnSiO_4 glass ceramic phosphors. *J Mater Chem*. 2011;21:3156.
42. Reisfeld EGR, Brown MGDRN, Jørgensen CK. Fluorescence of europium(III) in a flouride glass containing zirconium. *Chem. Phys. Lett.*. 1983;95:91–94.
43. Reisfeld R. Radiative and non-radiative transitions of rare-earth ions in glasses. *J Rare Earths*. 1975;22:123–175.
44. Li Y, Liu X. Photoluminescence properties of NaY $(MoO_4)_2$: Eu^{3+} phosphor synthesized by microwave assisted hydrothermal method. *Mater Sci Eng, B*. 2014;188:20–25.
45. Li K, Liu X, Zhang Y, Li X, Lian H, Lin J. Host-sensitized luminescence properties in $CaNb_2O_6$: Ln^{3+} (Ln^{3+} = Eu^{3+}/Tb^{3+}/Dy^{3+}/Sm^{3+}) phosphors with abundant colors. *Inorg Chem*. 2015;54:323–333.

How to cite this article: Jha K and Jayasimhadri M. Structural and emission properties of Eu^{3+}-doped alkaline earth zinc–phosphate glasses for white LED applications. *J Am Ceram Soc*. 2017;00:1-10. doi:10.1111/jace.14668.

International Conference on Advanced Material Technologies (ICAMT)-2016

27th and 28th December 2016

Dadi Institute of Engineering and Technology (DIET), Visakhapatnam, Andhra Pradesh, India.

Transadmittance Mode First Order LP/HP/AP Filter and its Application as an Oscillator

Deva Nand[1], Neeta Pandey[2]

Department of ECE, Delhi Technological University, Bawana Road, Delhi, India

[1]devkamboj07@gmail.com, [2]n66pandey@rediffmail.com

Abstract: In this paper new transadmittance mode first order low pass, high pass and all pass filter topologies using operational floating current conveyor (OFCC) is proposed and its application as an oscillator is also put forward. This proposal offers all filter functions at high impedance. Only two OFCCs, two resistors and one grounded capacitor are employed for realization. Workability is verified through SPICE simulations and results conform to the theoretical predictions very well. The proposed circuit is prototyped and tested experimentally for its application as an oscillator.

Keywords: All pass, High pass, Low pass, OFCC, Transadmittance Mode.

1. INTRODUCTION

First order filters specially low pass, high pass and all pass filters are very basic blocks for realization of higher order filter topologies. The first order low pass and high pass filters finds their applications in communication systems while all pass filter is most commonly used analog filter offering capability to modify phase of the input signal with unity magnitude for all frequencies. Over the desired frequency range, phase varies from 0˚ to 180˚ for a one pole filter, due to this frequency dependent time displacement property first order all pass filters may be used in radio systems, communication subsystems such as reconstruction filters and signal generation using multiphase sinusoidal oscillators and quadrature oscillators [1]. As a result a number of such first order filters have been reported earlier [1-16], out of which some are realized in voltage mode (VM) [1-6, 13-15] and in current mode (CM) [5, 7-9, 15, 16] (as well as references cited therein). First order filters with low pass, high pass and all pass functions are reported in VM [4,5] and CM [5] only.

Limited research is available on first order transadmittance mode (TA) filters [10-15] wherein all pass functions are looked into which are useful in baseband receivers. Typically, VM filters are cascaded with CM filters because they does not require any intermittent impedance matching circuitry. Available TA all pass filters are summarized in Table. I and reported implementations use third generation current conveyor (CCIII) [10, 11], modified current backward transconductance amplifier (MCBTA) [12], differential input buffered and transconductance amplifier (DBTA) [13, 14] and z-copy voltage differencing current conveyor (ZC-VDCC) [15]. From above literature survey the following findings are concluded- only all pass responses can be achieved in available first order TA mode filter sections [10-15]; more than one response simultaneously i.e. low pass (LP), high pass (HP) and all pass (AP) from single topology is achieved only in first order VM filter [4, 5] and in CM filter [5], but not available in any first order TA mode filters [10-15]; improper input impedances causing cascadability problem in [10-12], low output impedance [13] puts a limit on its merits as a V-I converter, and high passive and floating component count in [10].

Keeping in view the above facts, a new proposal for TA mode first order filter based on current mode active block operational floating current conveyor (OFCC) offering low pass, high pass and all pass responses, is put forward. The aim of this paper is to contribute towards TA mode first order filters by providing solution for proper input and output impedances to improve cascadability, low passive component count, more than one response simultaneously without any changes in configuration and to introduce an application as a sinusoidal oscillator. The OFCC combines the feature of current conveyor and current feedback opamp (CFOA) and also provides proper inputs with additional current outputs at proper impedances make it suitable for TA mode applications. Significant research efforts has introduced many applications using OFCC such as current mode filter [16,17], voltage mode filter [18-20], TA mode filter [21], instrumentation amplifier [22], wheat stone bridge [23], variable gain amplifier [24], readout circuit [25] and current conveyor realizations [26-28].

Table I Available TA mode first order filters.

Ref.	Active Element count	Passive Component count, R/C	Input Impedance	Output Impedance	No. of simultaneous responses
10	1 CCIII	4/1	Low	High	AP
11	1 CCIII	3/1	Low	High	AP
12	1 MCBTA	1/1	Low	High	AP
13	1 DBTA	2/1	High	Low	AP
14	1 DBTA	1/1	High	High	AP
15	1 ZC-VDCC	0/1	High	High	AP
Proposed	2 OFCC	2/1	High	High	LP, HP or AP, HP

To the best knowledge of authors, none of the literature is reported for TA mode first order LP/HP/AP filter to overcome all or some of the above mentioned problems. To bridge this gap, a TA mode first order LP/HP/AP filter is proposed in this paper. An application namely sinusoidal oscillator is also included. It uses two OFCCs and three passive components.SPICE simulations are carried out using 0.5 µm CMOS process model by MOSIS (AGILENT) and prototyped using commercially available IC AD844. Followings are the key points of proposal- proper input and output impedances that makes it suitable for V-I converter application; availability of two responses at a time, either LP and HP or AP and HP on high output impedance ports; suitable for higher order filter applications.

This paper is divided into four sections where Section 1 showing literature survey and component along with proposed circuit is described in Section 2. Performance analysis including implementation and verification responses are reported in Section 3 and further concluded in Section 4.

2. CIRCUIT DESCRIPTION

2.1 *OFCC Port Relationship*

The symbolic representation of OFCC [26-28] is shown in Fig. 1. The port relationship is given in (1) and describes that $I_Y = 0$, $V_X = V_Y$, $V_W = I_X Z_t$, $I_{Z+} = I_W$, $I_{Z-} = -I_W$. On input ports voltage tracking property exists so voltage at port X follows the voltage at port Y. Similarly current tracking exists at output ports and port W current copied to ports Z+ in phase and Z- out of phase.

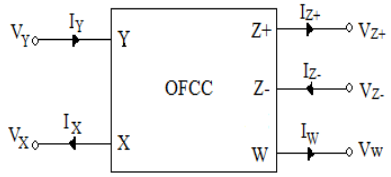


Fig. 1 OFCC Circuit symbol

$$\begin{bmatrix} I_Y \\ V_X \\ V_W \\ I_{Z+} \\ I_{Z-} \end{bmatrix} = \begin{bmatrix} 0 & 0 & 0 & 0 & 0 \\ 1 & 0 & 0 & 0 & 0 \\ 0 & Z_t & 0 & 0 & 0 \\ 0 & 0 & 1 & 0 & 0 \\ 0 & 0 & -1 & 0 & 0 \end{bmatrix} = \begin{bmatrix} V_Y \\ I_X \\ I_W \\ V_{Z+} \\ V_{Z-} \end{bmatrix} \quad (1)$$

Where Z_t is transimpedance gain of OFCC and in practice has a frequency dependent finite value. Port X is low impedance current input and port Y is high impedance voltage input. Port W is low impedance voltage output while Z+ and Z- are high impedance current outputs.

2.2 *Proposed Filter*

In this subsection proposed OFCC based TA mode first order LP/HP/AP filter is described. It emloys two OFCCs, two resistors (one floating and one grounded) and one grounded capacitor is shown in Fig. 2.

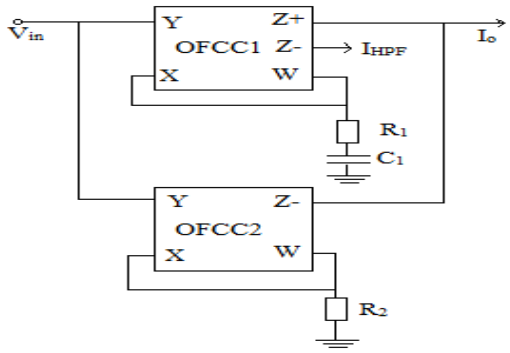


Fig. 2 TA mode first order filter circuit

By applying nodal analysis following filter transfer functions are derived:

$$\frac{I_o}{V_{in}} = \frac{sC_1(R_2 - R_1) - 1}{(sC_1R_1 + 1)R_2} \quad (2)$$

Selecting $R_2 = R_1$ in (2) will provide low pass response,

$$\frac{I_o}{V_{in}} = \frac{I_{LPF}}{V_{in}} = \frac{1}{R_2} \frac{-1}{(sC_1R_1 + 1)} \quad (3)$$

Similarly $R_2 = 2R_1$ will enable all pass function and (2) becomes,

$$\frac{I_o}{V_{in}} = \frac{I_{APF}}{V_{in}} = \frac{1}{R_2} \frac{(sC_1R_1 - 1)}{(sC_1R_1 + 1)} \quad (4)$$

and high pass function is independent of above conditions so will be available along with low pass or all pass, but one response at a time.

$$I_{HPF} = -\frac{sC_1}{(sC_1R_1 + 1)} \quad (5)$$

The pole frequency is given as $\omega_o = \frac{1}{C_1R_1}$ (6)

2.3 *Filter application*

A Sinusoidal Oscillator is implemented using all pass section as shown in Fig. 3. The routine analysis gives the following characteristic equation:

$$s^2C_1C_2R_1R_2 + sC_2R_2 - sC_1(R_2 - R_1) + 1 = 0 \quad (7)$$

The condition of oscillation and frequency of oscillation is derived respectively as:

$$C_1 = 2C_2, R_2 = 2R_1 \quad (8)$$

$$f_o = \frac{1}{8\pi C_2^2 R_1^2} \quad (9)$$

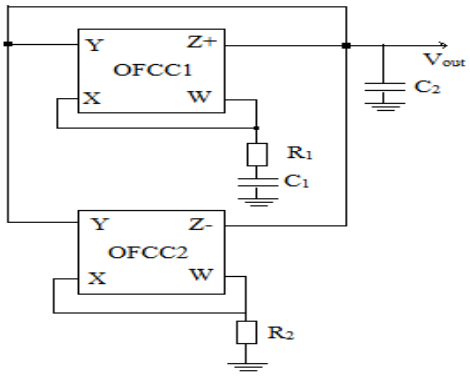


Fig. 3 TA mode first order all pass section as an Oscillator

3. PERFORMANCE ANALYSIS

The proposed filter topology is verified through PSPICE simulation program using MOSIS (AGILENT) 0.5 µm CMOS process parameters. The circuit schematic of OFCC is given in Fig. 4 [24] and W/L parameters for MOS transistors used in simulation are reported in Table II [24]. The supply voltages (V_{DD} and V_{SS}) are taken as ±1.5V and bias voltages (V_{B1} and V_{B2}) of ±0.8V are applied.

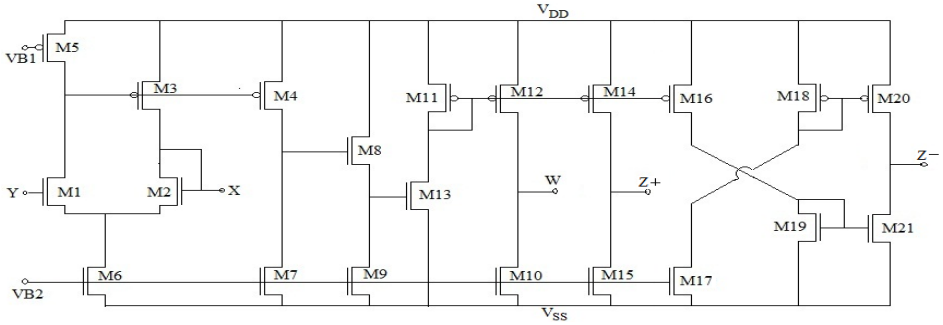


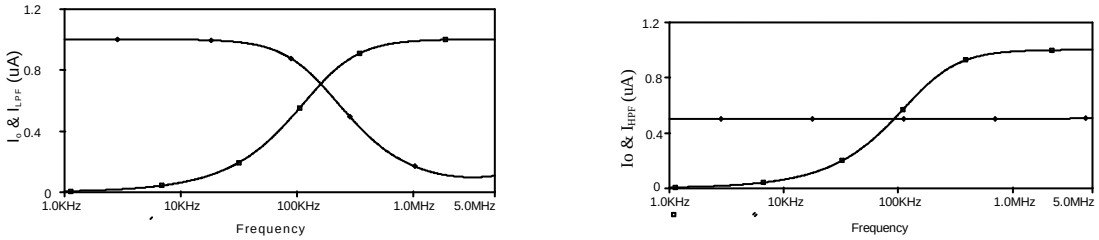
Fig. 4 CMOS schematic of OFCC [24]

Table II Transistors' aspect ratios [24]

Transistor	$W(\mu m)/L(\mu m)$
$M1, M2$	50 / 1
$M3, M4, M11, M12, M14,$ $M16, M18, M20$	50 / 2.5
$M5, M7, M10, M15, M17,$ $M19, M21$	20 / 2.5
$M6, M8$	40 / 2.5
$M9, M13$	100 / 2.5

The pole frequency of 159 KHz is selected for proposed first order filters and corresponding component values found are C_1 = 100pF, $R_1 = R_2$ = 10 kΩ for low pass function while R_1 = 10 kΩ , $R_2 = 2R_1$ = 20 kΩ to obtain all pass response. High pass response is independent of R_2 thus will be available in both conditions. Thus high pass along with either low pass or all pass will be available simultaneously.

The frequency responses of proposed first order low pass and high pass filter are shown in Fig. 5(a) and selecting another component values will facilitate high pass and all pass responses as shown in Fig. 5(b). Fig. 6 showing phase response of all pass filter and is complied with theoretical predictions. Time domain behavior is also verified to confirm the functionality of all the proposed filter topologies by applying sinusoidal signal of amplitude 1 mV, f_o = 159 kHz and corresponding transient responses for low pass, high pass and all pass filter are plotted in Fig. 7 (a), Fig. 7 (b) and Fig. 8 (a). For all pass filter topology Lissagous pattern through simulation is also plotted in Fig. 8 (b).



(a) (b)

Fig. 5 Frequency response of first order (a) low pass and high pass (b) all pass and high pass filter

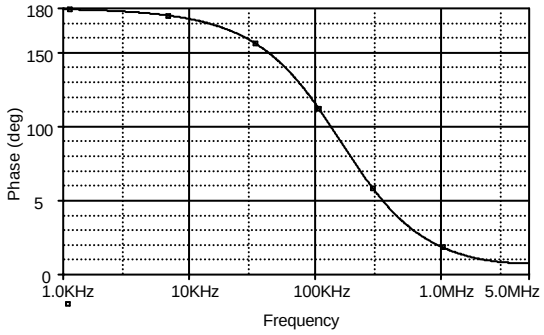
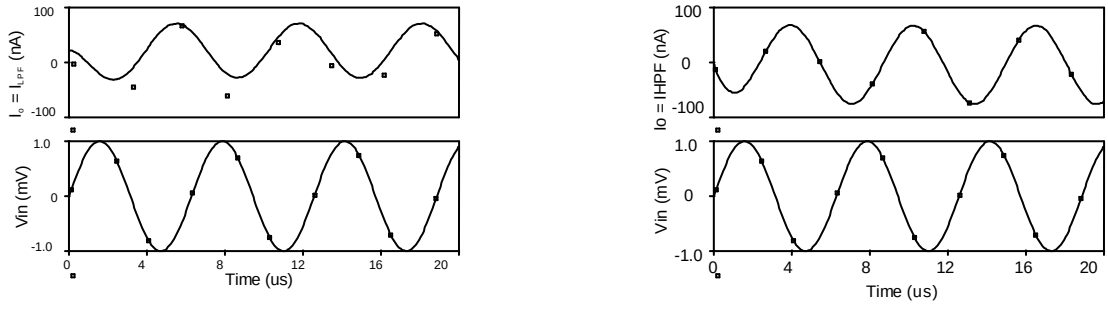


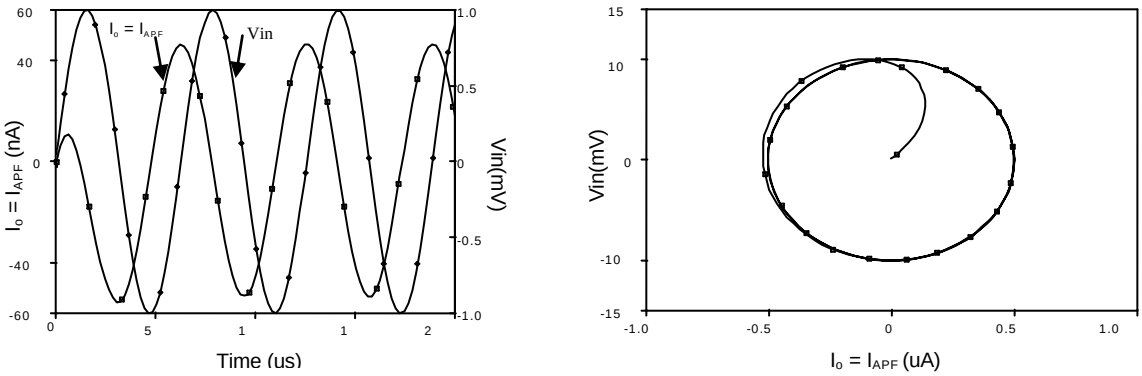
Fig. 6 Phase response of first order all pass filter



(a) (b)

Fig.7 Transient responses for **(a)** low pass output (I_o) **(b)** High Pass output (I_{HPF})

The sinusoidal oscillator as an application of proposed all pass filter section is prototyped using commercially available IC AD844 [29] as shown in Fig. 9 and simulated using CMOS schematic Fig. 4 [24]. Oscillator application is designed for frequency of 859 KHz and corresponding component values chosen are R_1 = 10 kΩ, R_2 = 20 kΩ, C_1 = 0.68 pF and C2 = 1.36 pF. The frequency obtained from simulation is 778.21 KHz while experimental values are 915.23 KHz. Simulated and experimental results are shown in Fig. 10.



(a) (b)

Fig. 8 (a) Transient response and (b) corresponding Lissagous figure for all pass filter

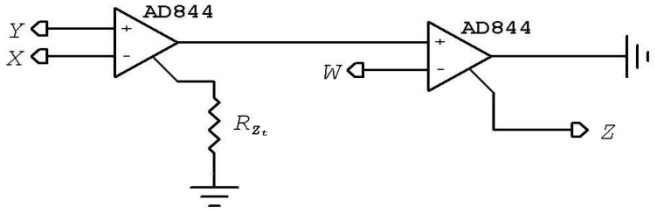
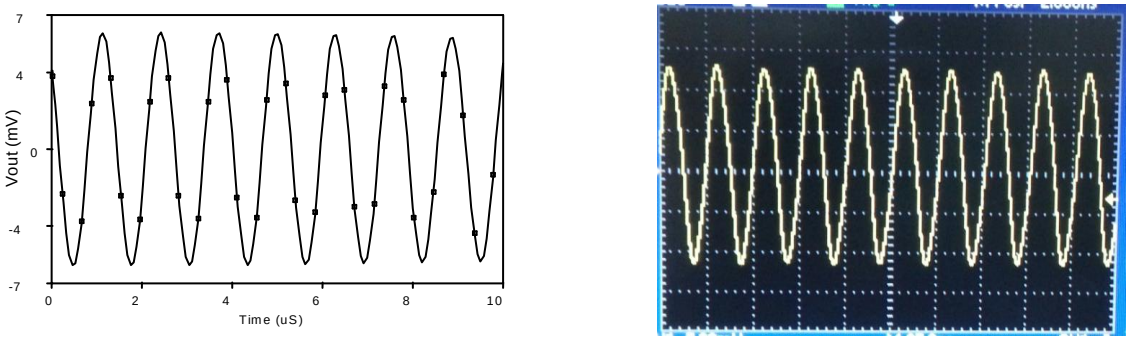


Fig. 9 AD844 realization of OFCC



(a) (b)

Fig. 10 Sinusoidal Oscillator Output (a) Simulated (b) Experimental

4. CONCLUSION

In this paper new TA mode first order LP/HP/AP filter using OFCC and its application as an oscillator is proposed. This proposal offers total three filter functions LP/HP/AP in transadmittance mode at high impedance. Only two OFCCs, two resistors and one grounded capacitor are employed for realization. Workability is verified through PSPICE program and found that simulated results conform the theoretical predictions very well. The proposed circuit is prototyped and tested experimentally for its application as an oscillator.

REFERENCES

[1] S. Maheshwari, "Current conveyor all pass sections: Brief review and novel solution," Scientific world Journal, vol. 2013, pp. 1-6, 2013. http://dx.doi.org/10.1155/2013/429391

[2] H. Cicekli and A. Gokcen, "Synthesis of voltage mode all pass filter employing single current operational amplifier," Int. J. of Comm., vol. 10, pp. 76-79, 2016.

[3] N. Pandey, R. Pandey and S. K. Paul, "A first order all pass filter and its application in a quadrature oscillator," Journal of Electron Devices, vol. 12, pp.-772-777, 2012.

[4] J. W. Horng, "High input impedance first order allpass, highpass and lowpassf ilters with grounded capacitor using single DVCC," Indian J. of engg. and materials sciences, vol. 17, pp. 175-178, 2009.

[5] S. Maheshwari and I. A. Khan, "Novel first order allpass sections using a single CCIII," Int. J. Electronics, vol. 88, no. 7, pp. 773-778, 2001.

[6] A. B. Saied, S. B. Salem and D. S. Masmoudi, "A quadrature oscillator based on a new Optimized DDCC all pass filter," J. of circuits and systems, vol. 4, pp. 498-503, 2013.

[7] W. Tangsrirat, W. Tanjaroen and T. Pukkalanum, "Current mode multiphase sinusoidal oscillator using CDTA based allpass sections," Int. J. Electron. Commun.(AEU), vol. 63, pp. 616-622, 2009.

[8] J. Mohan, "Single active element based current mode allpass filter," Int. J. of Comp. App., vol. 82, no. 1, pp. 23-27, 2013.

[9] J. Mohan and S. Maheshwari, "Cascadable current mode first order allpass filter based on minimal components," Scientific world Journal, vol. 2013, pp. 1-5, 2013.

[10] S. Minaei, "A new high performance CMOS third generation current conveyor (CCIII) and its application," J. of Electrical engineering, Springer Verlag, vol. 85, pp. 147-153, 2003.

[11] U. Cam, "A new transadmittance type first order allpass filter employing single third generation current conveyor," Analog Int. circuits and signal processing, vol. 43, pp. 97-99, 2005.

[12] N. Herencsar, A. Lahiri, J. Koton, M. Sagbas, U. E. Ayten and K. Vrba, "New MOS-C realization of transadmittance type allpass filter using modified CBTA," in Int. conf. on applied electronics, IEEE, pp. 1-4, September, 2011.

[13] N. Herencsar, J. Koton and K. Vrba, "Differential input buffered and transconductance amplifier based new transadmittance and voltage mode first order allpass filters," in Int. conf. on electrical and electronics engg., ELECO-2009, pp. 256-259, December, 2009.

[14] N. Herencsar, J. Koton, K. Vrba and B. Metin, "Fully cascadable dual mode allpass filter based on single DBTA," 35th Int. conf. on telecomm. And signal processing, pp. 374-377, 2012.

[15] R. Sotner, N. Herencsar, J. Jerabek, K. Vrba, T. Dostal, W. Jaikla and B. Metin, "Novel first order allpass filter applications of z-copy voltage differencing current conveyor," Indian J. of pure and applied physics, vol. 53, pp. 537-545, 2015.

[16] T. Parveen, "CMOS compatible current mode high output impedance allpass filter single OFC and grounded passive components," Int. Conf. on Multimedia, Signal Processing and Comm.. Tech., IEEE, pp. 107-109, 2011.

[17] N. Pandey, D. Nand, Z. Khan, "Single Input Four Output Current mode filter using Operational Floating Current Conveyor," J. of Active and Passive Components, vol. 2013, pp. 1-8, 2013.

[18] Y. H. Ghallab, W. Badawy, K. V. I. S. Kaler, M. A. El-Ela, M. H. El-Said, "A New Second-order Active Universal Filter with Single Input and Three Outputs Using Operational Floating Current Conveyor. In: Proceedings of IEEE International Conference on Microelectronics, pp. 42-45, 2002.

[19] Y. H. Ghallab, M. A. El-Ela and M. Elsaid, "A novel universal voltage mode filter with three inputs and single output using only operational floating current conveyor. In: Proceedings of International conference on Microelectronics, pp. 95-98, 2000.

[20] Y. H. Ghallab, and W. Badawy, "The Operational Floating Current Conveyor and its applications" J. of Circuits, Systems, and Computers. Vol. 15, no. 3, pp. 351–372, 2006.

[21] N. Pandey, D. Nand and Z. Khan, "Operational floating current conveyor based single input multiple output transadmittance mode filter," Arab J. Sci. Eng., Springer, vol. 39, pp. 7991-8000, 2014.

[22] Y. H. Ghallab, W. Badawy, K. V. I. S. Kaler and B. J. Maundy, "A Novel Current Mode Instrumentation Amplifier Based on Operational Floating Current Conveyor. IEEE Trans. on Inst. and Meas.. vol. 54, no. 5, pp. 1941-1949, 2005.

[23] Y. H. Ghallab and W. Badawy, "A New Design of a Current-mode Wheatstone Bridge Using Operational Floating Current Conveyor. In: Proceedings of International Conference on MEMS, NANO and Smart Systems, pp. 41-44, 2006.

[24] H. M. Hassan and A. M. Soliman, "Novel CMOS realizations of Operational Floating Current Conveyor and applications," J. of Circuits, Systems, and Computers, vol. 14, no. 6, pp. 1113–1143, 2005.

[25] Y. H. Ghallab and W. Badawy, "A New differential PH Sensor Current Mode Readout circuit using only two Operational Floating Current Conveor" In: Proceedings of IEEE International workshop on Biomedical Circuits & Systems, pp. 13-16, 2004.

[26] C. Toumazou, A. Payne, F. J. Lidgey, "Operational Floating Conveyor. Electronic Letters," vol. 27, no. 8, pp. 651-652, 1991.

[27] A. A. Khan, M. A. Al-Turaigi, M. A. El-Ela, "Operational floating current conveyor: Characteristics, Modeling and applications. In: Proceedings of IEEE Instrumentation and Measurement Technology Conference, Hamamtsu, Japan, pp. 788–790, 1994.

[28] Y. H. Ghallab, M.A. El-Ela, M.H. Elsaid, Operational floating current conveyor: Characteristics, Modeling and Experimental results. In: Proceedings of International Conference on Microelectronics, Kuwait, pp. 59–62, 2000.

[29] "Analog devices, 60 MHz, 2000V/μs, Monolithic Op Amp" Analog Devices Inc., AD844 datasheet, pp. 1-12.



Deva Nand was born in 1982. He did his B.Tech in Electronics and Communication Engineering, M.Tech in Microelectronics and VLSI Design from Kurukshetra University, Kurukshetra, India and he is pursuing Ph.D. from Delhi Technological University, Delhi, India. At present he is Assistant Professor in Department of Electronics and Communication Engineering, Delhi Technological University, Delhi, India. A life member of ISTE, and member of IEEE, USA. His research interests include Analog Mixed Signal VLSI Design.



Neeta Pandey was born in 1966. She did her M. E. in Microelectronics from Birla Institute of Technology and Sciences, Pilani and Ph. D. from Guru Gobind Singh Indraprastha University Delhi. She has served in Central Electronics Engineering Research Institute, Pilani, Indian Institute of Technology, Delhi, Priyadarshini College of Computer Science, Noida and Bharati Vidyapeeth's College of Engineering, Delhi in Various capacities. At present, she is Assistant Professor in ECE department, Delhi Technological University. A life member of ISTE, and member of IEEE, USA. She has published papers in International, National Journals of repute and conferences. Her research interests are Analog and Digital VLSI Design.

Universal biquadratic filter using Operational Floating Current Conveyor (OFCC)

Divyesh Sachan, Deva Nand, Neeta Pandey
Department of Electronics and Communication Engineering
Delhi Technological University
New Delhi, India

***Abstract*— A universal biquadratic filter in voltage mode (VM) and current mode (CM) configuration using single Operation Floating Current Conveyor (OFCC) is presented in this paper. It realizes all standard filter functions i.e. low pass (LP), high pass (HP), band pass (BP), notch and all pass (AP) without changing circuit topology. The proposed multi input multi output (MIMO) circuit has two inputs and two outputs and filter outputs can be obtained simultaneously without modifying circuit topology. Prototype circuit including OFCC has been realized using commercially available IC AD844 and components. Presented circuit has additional advantage of low sensitivity and low components count. Results of both modes are verified through mathematical equations, PSpice simulations and prototype.**

Keywords*— OFCC, Universal Filter, Biquadratic Filter, Voltage Mode, Current Mode, MIMO

I. INTRODUCTION

In recent years multi input and multi output universal biquadratic filters received a considerable interest due to their versatility in terms of their usage in practical applications. A number of voltage mode multi output [1-4] and current mode multi output [4-7] universal biquadratic filter have been proposed earlier using CCII+ [1][4], TOCCII [2], OTA [3], DXCCII [5], Zc-CDTA [6] and OFC [7]. Current conveyor (CC) or current feedback operational amplifier (CFOA) based filters are preferred due to high operational bandwidth, larger dynamic range and greater linearity over OP-AMP or OTA based filters.

OFCC which was introduced in [8] as OFC, combines the feature of current conveyor and CFOA. Literature survey shows that two current mode OFC based universal single input multi output (SIMO) filters has been proposed in [7][9] uses more than 1 active block. In this paper, a single OFCC based MIMO universal biquadratic filter has been proposed which is able to realize all second order filter function such as LP, HP, BP, Notch and AP without changing circuit topology. The proposed universal filter is also able to work in both voltage and current modes and uses only two resistors and capacitors for its operation in either of the mode.

II. CIRCUIT DESCRIPTION

A. OFCC

OFCC is a general purpose building block which features both Second generation current conveyor CCII and Current Feedback Operational amplifier (CFOA) which are widely used in current-mode signal processing circuits.

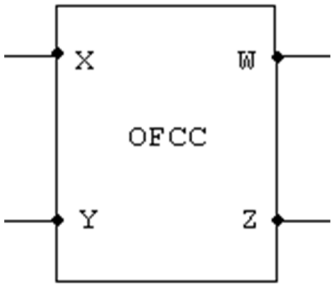


Fig. 1. Block diagram of OFCC

The port relationship matrix of OFCC is

$$\begin{bmatrix} V_x \\ I_y \\ V_w \\ I_z \end{bmatrix} = \begin{bmatrix} 0 & 1 & 0 & 0 \\ 0 & 0 & 0 & 0 \\ Z_t & 0 & 0 & 0 \\ 0 & 0 & 1 & 0 \end{bmatrix} \begin{bmatrix} I_x \\ V_y \\ I_w \\ V_z \end{bmatrix} \quad (1)$$

The output voltage at V_W is product of open loop transimpedance gain Z_t and input current at I_X. Voltage tracking at input port is available since its low impedance current Input port X follows the voltage at high impedance voltage input port Y. Its terminal W is a low impedance voltage output port and terminal Z is a high impedance current output port.

III. PROPOSED CIRCUIT

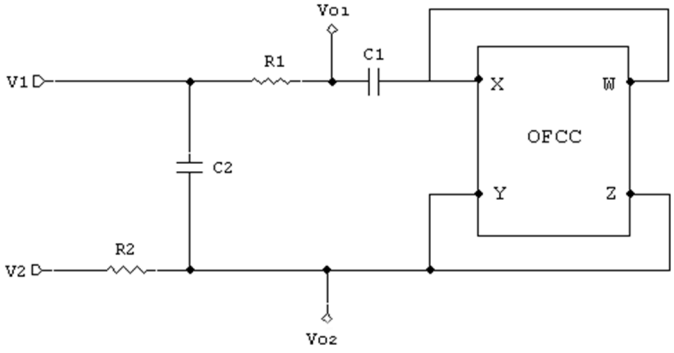


Fig. 2. Proposed Voltage Mode Filter

The proposed voltage mode circuit Fig 2 has two resistors two capacitors with one active component (OFCC). From the circuit output voltages V_{o1} and V_{o2} can be obtained as:

$$V_{o1} = \frac{S^2C_1C_2V_1+S\{C_1G_2V_2+(C_2-C_1)G_1V_1\}+G_1G_2V_1}{S^2C_1C_2+S(C_1G_2+C_2G_1-C_1G_1)+G_1G_2} \quad (1)$$

$$V_{o2} = \frac{S^2C_1C_2V_1+S\{C_1G_2V_2+(C_2-C_1)G_1V_1\}+G_1G_2V_2}{S^2C_1C_2+S(C_1G_2+C_2G_1-C_1G_1)+G_1G_2} \quad (2)$$

From (2) and (3), it is observed that

- If $V_2 = V_{in}$ and $V_1 = 0$ (ground), Band Pass response can be obtained at V_{o1} and Low Pass response can be obtained at V_{o2}.
- If $V_1=V_{IN}$, $V_2 = 0$ (ground) and $C_1=C_2$, Notch response can be obtained at Vo1 and High Pass response can be obtained at V_{o2}.
- If $V_1=V_{IN}$, $V_2 = 0$ (ground) and $C_1=2C_2$, All Pass response can be obtained at V_{o2}.

Therefore, our circuit is able to realize all transfer functions i.e. LP, HP, Band Pass, Notch and All Pass. Without changing the circuit topology same circuit can work in current mode as shown in Fig 3.

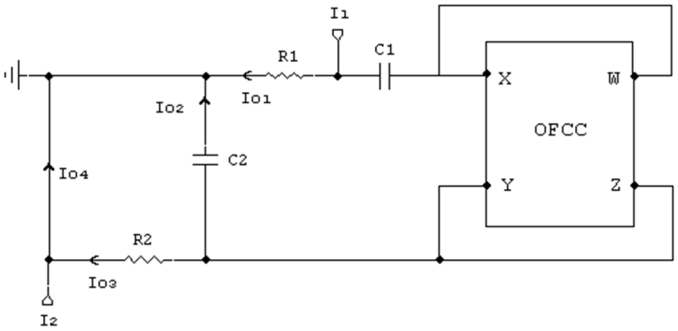


Fig. 3. Proposed Current Mode Filter

From the circuit output current I_{o1}, I_{o2}, I_{o3}, I_{o4} can be calculated as:

$$I_{o1} = \frac{S\{(C_2-C_1)G_1I_1\}+G_1G_2I_1}{S^2C_1C_2+S(C_1G_2+C_2G_1-C_1G_1)+G_1G_2} \quad (3)$$

$$I_{o2} = \frac{-S^2C_1C_2I_1}{S^2C_1C_2+S(C_1G_2+C_2G_1-C_1G_1)+G_1G_2} \quad (4)$$

$$I_{o3} = \frac{-SC_1G_2I_1}{S^2C_1C_2+S(C_1G_2+C_2G_1-C_1G_1)+G_1G_2} \quad (5)$$

$$I_{o4} = \frac{S^2C_1C_2I_2+S\{(C_1G_2+C_2G_1-C_1G_1)I_2-C_1G_2I_1\}+G_1G_2I_2}{S^2C_1C_2+S(C_1G_2+C_2G_1-C_1G_1)+G_1G_2} \quad (6)$$

From (3), (4), (5) and (6), following can be observed

- If $I_1=I_2=I_{IN}$ and $C_1=C_2$, Low Pass response can be obtained at I_{o1}, High Pass response can be obtained at I_{o2}, Band Pass response can be obtained at I_{o3} and Notch response can be obtained at I_{o4}.
- If $I_1=I_2=I_{IN}$ and $C_1=C_2$, All Pass response can be obtained at I_{o4}.

From the above analysis it has been seen that voltage and current mode filter responses can be obtained without changing circuit topology where each of circuit uses two resistors, two capacitors and one OFCC.

Resonant frequency ω_o and Quality factor Q of proposed circuits in Fig. 2 and Fig. 3 are

$$\omega_o = \sqrt{\frac{1}{R_1R_2C_1C_2}} \quad (7)$$

$$Q = \frac{\sqrt{R_1R_2C_1C_2}}{C_1R_1+C_2R_2-C_1R_2} \quad (8)$$

Sensitivity analysis on filter parameters ω_o and Q relating to active and passive parameters R_i and C_i (i=1, 2) can be calculated as

$$S_{R_1}^{\omega_o} = S_{R_2}^{\omega_o} = S_{C_1}^{\omega_o} = S_{C_1}^{\omega_o} = -\frac{1}{2}$$

$$S_{R_1}^{Q} = \frac{1}{2} - \frac{C_1R_1}{C_1R_1+C_2R_2-C_1R_2}$$

$$S_{R_2}^{Q} = \frac{1}{2} + \frac{R_2(C_1-C_2)}{C_1R_1+C_2R_2-C_1R_2}$$

$$S_{C_1}^{Q} = \frac{1}{2} - \frac{C_1(R_1-R_2)}{C_1R_1+C_2R_2-C_1R_2}$$

$$S_{C_2}^{Q} = \frac{1}{2} - \frac{C_2R_2}{C_1R_1+C_2R_2-C_1R_2}$$

For LP, HP, BP, Notch filter response $R_1=R_2$, $C_1=C_2$. Hence,

$$S_{R_1}^{Q} = S_{R_2}^{Q} = S_{C_1}^{Q} = -S_{C_2}^{Q} = \frac{1}{2}$$

Taking account of non-ideal OFCC, transimpedance gain Z_t using single pole model is given by

$$Z_t(s) = \frac{Z_{to}}{1+\frac{s}{\omega_o}}$$

Where Z_{to} is DC open loop transimpedance gain and ω_o is transimpedance cutoff frequency. For high frequency applications, transimpedance gain $Z_t(s)$ will be

$$Z_t(s) = \frac{1}{sC_p}$$

where

$$C_p = \frac{1}{Z_{to}\omega_o}$$

Taking account of single pole model (Z_t), the output voltage equations (1) and (2) can be rewritten as,

$$V_{o1} = \frac{S^2\varepsilon C_1C_2V_1+S\{\varepsilon C_1G_2V_2+(C_2-\varepsilon C_1)G_1V_1\}+G_1G_2V_1}{S^2\varepsilon C_1C_2+S(\varepsilon C_1G_2+C_2G_1-\varepsilon C_1G_1)+G_1G_2} \quad (9)$$

$$V_{o2} = \frac{S^2\varepsilon C_1C_2V_1+S\{\varepsilon C_1G_2V_2+(C_2-\varepsilon C_1)G_1V_1\}+G_1G_2V_2}{S^2\varepsilon C_1C_2+S(\varepsilon C_1G_2+C_2G_1-\varepsilon C_1G_1)+G_1G_2} \quad (10)$$

where

$$\varepsilon(s) = \frac{1}{1+sC_pR_1}$$

IV. Results

A. Realization of OFCC using AD844

AD844 is a combination of CCII+ followed by buffer which is known for its fast signal response, high bandwidth. Current feedback design of AD844 results in improved ac performance, high linearity and remarkably clean output response and due to these features AD844 can be used in place of traditional op amps. Figure 4 shows the block diagram of AD844. The current voltage terminal characteristics of ideal CFOA are almost similar as of CCII+ with a voltage output buffer. However,

voltage tracking error, current tracking error and non-idealities affects circuit performance realized using CFOA[11]. Taking account of all errors and non-idealities current-voltage terminal characteristics of CFOA is defined as

$$\begin{bmatrix} I_y \\ V_x \\ I_z \end{bmatrix} = \begin{bmatrix} 0 & 0 & 0 \\ \beta & 0 & 0 \\ 0 & \alpha & 0 \end{bmatrix} \begin{bmatrix} V_y \\ I_x \\ V_z \end{bmatrix} \quad (2)$$

and $V_o = \gamma V_Z$, where α, β and γ are non-ideal current and voltage gain.

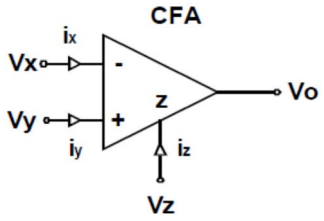


Fig. 4. Symbol of Current Feedback Operational Amplifier (AD844)

OFCC port relationship can be obtained using AD844 as circuit shown in Fig. 4. From the first AD844 and matrix 2 following relations are obtained:

$$V_X = \beta_1 V_Y \quad (11)$$

$$V_{o_AD844_1} = \alpha_1 \gamma_1 I_X . R_{Zt} \quad (12)$$

and from second AD844 and matrix 2, following relations are obtained

$$V_W = \beta_2 V_{o_AD844_1}$$

or it can be rewritten as

$$V_W = \beta_2 \alpha_1 \gamma_1 I_X . R_{Zt} \quad (13)$$

And

$$I_Z = \alpha_2 I_W \quad (14)$$

Rewriting (11), (12), (13) and (14) in matrix form and taking all non-linear gain to unity

$$\begin{bmatrix} V_x \\ I_y \\ V_w \\ I_z \end{bmatrix} = \begin{bmatrix} 0 & 1 & 0 & 0 \\ 0 & 0 & 0 & 0 \\ R_{Zt} & 0 & 0 & 0 \\ 0 & 0 & 1 & 0 \end{bmatrix} \begin{bmatrix} I_x \\ V_y \\ I_w \\ V_z \end{bmatrix} \quad (3)$$

This is same as OFCC port relationship matrix 1. Thus our circuit build using AD844 in Fig 5 realizes OFCC and it is easy to implement than previous realizations in [12-13]. High frequency responses of our realization are better than previous OFCC realization using AD846 and BJT [12] and using CMOS technology [13].

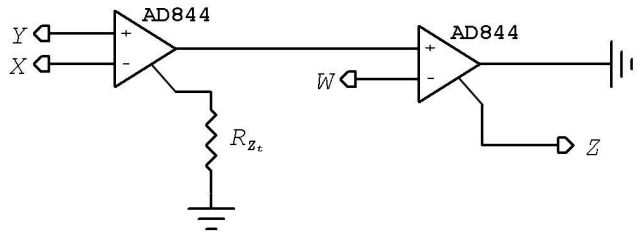


Fig. 5. Implementation of OFCC using AD844

B. Simulation Results

Circuit functionality of the proposed voltage mode and current mode biquad shown in Fig. 2 and Fig. 3 has been simulated using Pspice. OFCC has been implemented using commercially available IC AD844 for feasibility as shown in Fig. 5. Experiment has been formed at supply voltage of $\pm$5V. Fig. 6 and Fig. 7 shows the experimental frequency response of Notch at V_{o1} and High Pass at V_{o2} obtained simultaneously when V_1=V_{in}, V_2= 0 (grounded) and varying C to 1n, 0.5n, 0.25n and 0.1n. Fig. 8 and Fig. 9 shows experimental frequency response of Band Pass at V_{o1} and Low Pass at V_{o2} obtained simultaneously when V_2=V_{in}, V_1=0 (grounded) and varying C to 1n, 0.5n, 0.25n and 0.1n. The values of passive components during simulation were R_1=R_2=1K, C_1=C_2=C. To obtain all pass response at V_{o2} as shown in Fig. 10 value of C_1 should be chosen to double the value of C_2 (C_1=2C_2=0.1n) when V_1=V_{in}, V_2= 0 (grounded) and R_1=R_2=1K.

Notch, HP, BP and LP response curves for f_o=159KHz, f_o=318KHz, f_o=636KHz, f_o=1.59MHz corresponding to C_1=C_2=1n, C_1=C_2=0.5n, C_1=C_2=0.25n and C_1=C_2=0.1n respectively are shown in Fig. 6, Fig. 7, Fig. 8, and Fig. 9. AP response curve corresponding to C_1=2C_2 and C_2=0.1n is shown in Fig. 10. All of these curves illustrate excellent relationship with theoretically calculated values.

Transient analysis has been performed by applying a mixed sinusoidal signal of frequency 150 KHz, 630 KHz and 2 MHz with amplitude of 0.5V each at the input terminal with C=0.25nf. The value of C=0.25nf has been carefully chosen to make cutoff frequency f_o=636KHz. Fig. 11 shows the combined frequency spectrum of input V_{in}, output Notch, HP, BP, LP and All Pass.

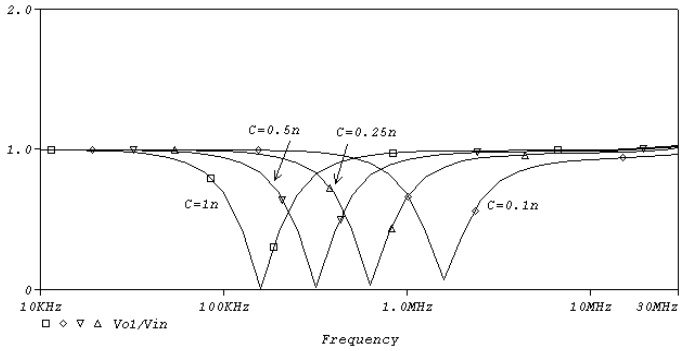


Fig. 6. Notch Response at Vo1 (When V1 = Vin, V2= 0 and C1=C2=C)

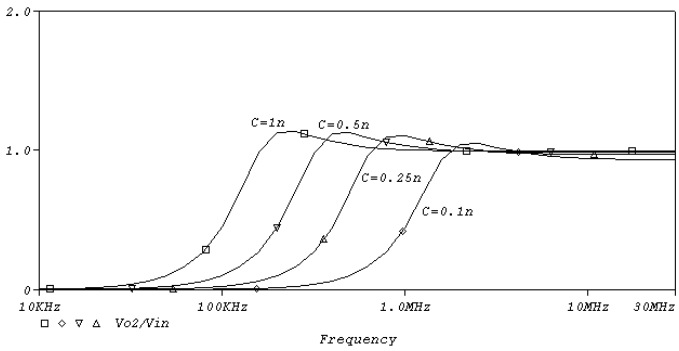


Fig. 7. High Pass Response at Vo2 (When V1 = Vin, V2= 0 and C1=C2=C)

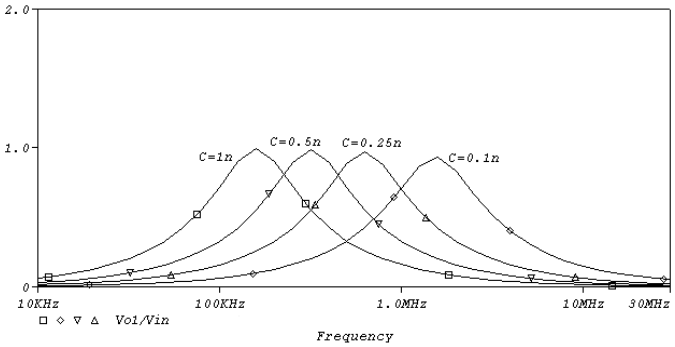


Fig. 8. Band Pass Response at Vo1 (When V1 = 0, V2= Vin and C1=C2=C)

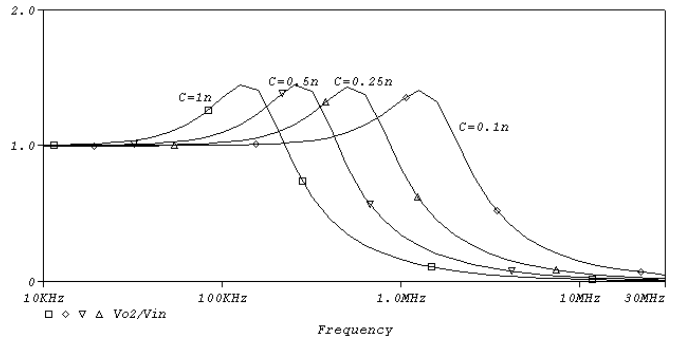


Fig. 9. Low Pass Response at Vo2 (When V1 = 0, V2= Vin and C1=C2=C)

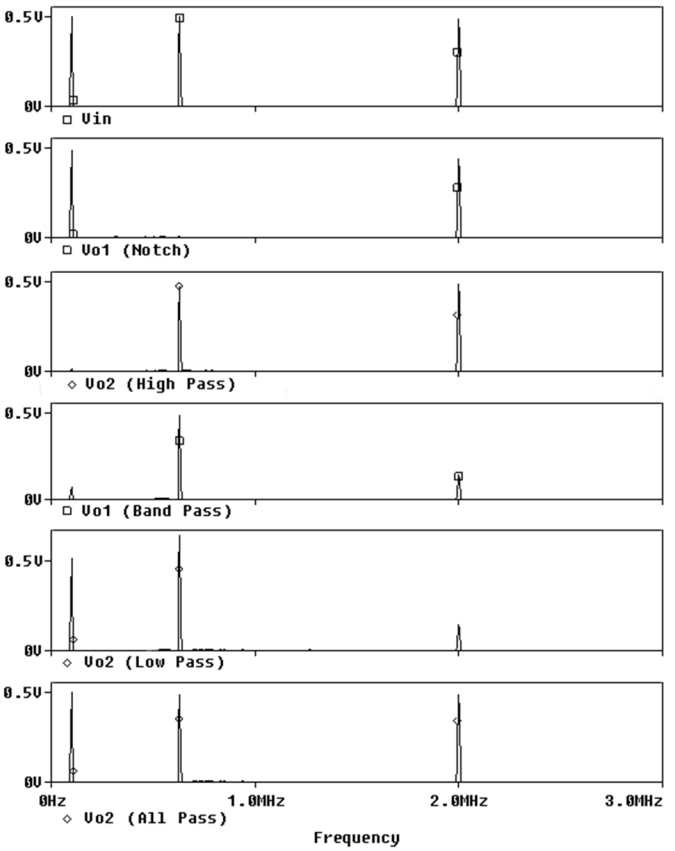


Fig. 11. Spectrum of input signal (Vin) and output signals (Notch, High Pass, Band Pass and Low Pass)

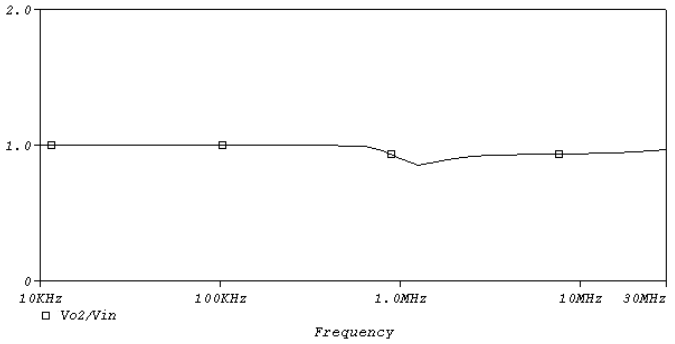


Fig. 10. All Pass Response at Vo2 (When V1=Vin, V2=0 and C1=2C2, C2=0.1n)

V. CONCLUSION

In this paper a new universal biquadratic filter has been proposed using OFCC which is able to realize all standard filter functions. The authenticity of filter function has been verified using prototype circuit. Circuit has an advantage of low sensitivity, less number of passive components and can be built using commercially available components and ICs and doesn't require to manufacture any ASIC.

REFERENCES

[1] S. Ozoguz and E.O. Gunes, "Universal filter with three inputs using CCII+" Electronics Letters, vol. 32, no. 2, Nov. 1996.

[2] S. Minaei and E. Yuc, "TO-CCII Based Voltage-Mode Universal Biquadratic Filter", 24th Canadian Conference on Electrical and Computer Engineering (CCECE), 2011.

[3] K. Kumar, K. Pal and G.K. Gupta, "Realization of multi-function biquad filter using operation Transconductance amplifier", Indian Journal of Pure & Applied Physics, vol.44 pp 71-74, 2006.

[4] J. W. Horng, "Voltage/current mode universal bquardatic filter using CCII+" Indian Journal of Pure & Applied Physics, vol.48 pp 749-756, October 2010.

[5] S. Maheshwari and S. Maheshwari, "Multi Input Multi Output Biquadratic Universal Filter using Dual –X Current Conveyor(DXCCII)", International Conf. on Computer & Communication Technology, 2010.

[6] M. Kumngern and K. Dejhan, "Current-Mode Multifunction Biquad Filter with Three Inputs Five Outputs Using ZC-CDTAs", 2nd Int. Conf. on Digital Information Comm. Tech. and it's Applications (DICTAP), 2012.

[7] T. Parveen, "OFC based High Output Impedance Current Mode SIMO Universal Biquadratic Filter", International Conference on Multimedia, Signal Processing and Communication Technologies, 2011.

[8] C. Toumazou, A. Payne, and F. J. Lidgey, "Operational floating conveyor," Electronics Letters, vol. 27, no. 8, pp. 651–652, 1991.

[9] N. Pandey, D. Nand, and Z. Khan, "Single-Input Four-Output Current Mode Filter Using Operational Floating Current Conveyor", Hindawi Publications, Active and Passive Electronic Components Volume 2013.

[10] A. A. Khan, M. A. Al-Turaigi and M. Abou El-Ela, "Operational Floating Current Conveyor: Characteristics, Modeling and Applications," Instrumentation and Measurement Technology Conference, vol.2, pp.788–791, May 1994.

[11] National Semiconductor, AD844 Datasheet.

[12] H. M. Hassan and A. M. Soliman, "Novel CMOS Realizations of the Operational Floating Conveyor and Applications", World Scientific, Journal of Circuits Systems and Computers, vol. 14, no. 6, pp. 1113–1143, 2005.

[13] N. M. Edward, Y. H. Ghallab, H. M. Hassan and Y. I. Ismail "A CMOS based operational floating current conveyor", International Conference on Electronics Circuits and Systems, pp.157-160, 2015.

International Conference on Advanced Material Technologies (ICAMT)-2016

27th and 28th December 2016

Dadi Institute of Engineering and Technology (DIET), Visakhapatnam, Andhra Pradesh, India.

Voltage Mode Single CDBA Based Multifunction Filter

Priyanka Gupta[1], Rajeshwari Pandey[2], Neeta Pandey[3]

Department of Electronics and Communication Engineering, Delhi Technological University, Main Bawana Road, Delhi, 110042, India, [1]email: priyankagupta09@gmail.com
[2]email: rajeshwaripandey@gmail.com, [3]email: neetapandey06@gmail.com

Abstract: A voltage mode multifunction second order filter topology employing single current differencing buffered amplifier (CDBA) has been proposed in this paper. This topology can be used to synthesize low pass (LP), band pass (BP), and high pass (HP) filter functions with appropriate admittance choices. This configuration is a suitable choice for implementing filters with high quality factor. The demonstration of the proposed configuration is done through PSPICE simulations. The CDBA block is realized using CMOS 0.18µm technology. The simulation results are found in close agreement with the theoretical results.

Keywords: CDBA, Current mode, Multifunction Filter.

1. INTRODUCTION

Electronic filters are the necessary building block of analog signal processing and find extensive applications in communication and instrumentation system. In last few decades The CDBA has emerged as a promising choice [1] for analog filter design [2], [3], [4], [5], [6], [7], [8], [9], [10], [11], [12], [13], [14], [15], [16], [17], [18]. It is characterized by low input impedance terminals which render it free from parasitic capacitances, thereby making it a suitable choice for high frequency operations. Additionally, the CDBA provides both voltage and current outputs which further enhances the design flexibility.

Many biquadratic filters using CDBA were proposed in the literature that can be classified as single input and single output (SISO) [4], [8], [12], [13], [17] multi input single output (MISO) [9], [15], [16] and single input multi output (SIMO) [3], [5], [10], [14]. A detailed comparison of these structures is given in Table 1. For the applications having power consumption as an important design constraint, single active element based filters are the useful choice. A close study of the voltage mode structures based on single CDBA proposed in [4], [8], [9], [13] and [16] shows that

- only single filter response is provided [4], [13]
- Independent adjustment of angular frequency and Q factor is not possible [8], [13]
- filter responses are obtained by lifting of nodes for input excitation [9], [16]
- large component spread is required for obtaining high Q value [8], [9], [13], [16]
- passive component count is large [16]

In this paper a voltage mode generalized second order multifunction filter topology is proposed which employ single CDBA, two capacitors and four resistors. The proposed generalized topology can be used to realize three filter functions namely, low pass (LP), band pass (BP), and high pass (HP), through appropriate component selections, and no component matching condition is needed. The proposed topology can be used to implement high quality factor value with moderate component spread.

The remaining paper is organized as follows: Section 2 presents the description of the proposed configuration. The sensitivity analysis is presented in section 3. The effect of non-idealities of CDBA has been dealt with in section 4. The SPICE simulation results are placed in section 5 followed by conclusion in section 6.

Table 1: Comparison of the proposed work with the previously reported work

Ref	No of CDBA	Type	Standard filter Function	Mode	R+C			Independent ω_o and Q_0
[3]	2	SIMO	LP, BP, HP	CM	4+2			YES
[4]	1	SISO	BP	VM	2+2,3+3 3+3,2+2			YES
[5]	2	SIMO	LP, BP, HP	CM	4+2			YES
[8]	1	SISO	LP, BP, HP		LP	BP	HP	NO
				CM	3+2	2+3	2+3	
				VM	3+2	2+3	2+3	
				TIM	2+2	2+2	NA	
				TAM	3+2	3+2	3+2	
[9]	1	MISO	LP, BP, HP, AP,	VM	4+2			YES
[10]	3	SIMO	LP, BP, BS	VM	7+2			YES
	3		HP, BP, AP	VM	2+7			
[12]	1	SIMO	LP, BP	CM	3+2			YES
	2	SISO	HP	CM	3+2			YES
	2	SISO	HP	CM	3+3			YES
[13]	1	SISO	AP	VM	3+2			NO
[14]	3	SIMO	LP, BP, BS	VM	4+2			YES
	3	SIMO	HP, BP, AP	VM	2+4			YES
[15]	3	MISO	LP, BP, HP, BS,	CM	2+2			YES
[16]	1	MISO	LP, BP, HP, BS,	VM	4+4			YES
[17]	2	SISO	LP, BP, HP, BS,	CM	4+4			YES
Proposed work	1	SISO	LP, BP, HP	VM	4+2			YES

2. CIRCUIT DESCRIPTION

The port characteristics of CDBA are given by matrix (1) and its circuit symbol is shown in Fig. 1.

$$\begin{bmatrix} Iz \\ Vw \\ Vp \\ Vn \end{bmatrix} = \begin{bmatrix} 0 & 0 & 1 & -1 \\ 1 & 0 & 0 & 0 \\ 0 & 0 & 0 & 0 \\ 0 & 0 & 0 & 0 \end{bmatrix} \begin{bmatrix} Vz \\ Iw \\ Ip \\ In \end{bmatrix} \quad (1)$$

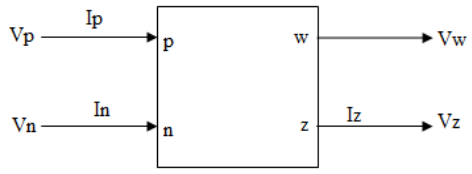


Fig. 1: CDBA symbol

The proposed filter topology is shown in Fig. 2. Using routine analysis the transfer function for the proposed circuit is obtained as

$$\frac{Vo}{Vin} = \frac{KY_1\,Y_2}{D}, \quad (2)$$

Where, $K = \frac{Y_3}{Y_6}$, (3)

$$D = Y_1\,Y_2 + Y_1Y_3 + Y_1Y_4 + Y_2Y_3 + Y_2Y_4 + Y_2Y_5 + Y_3Y_5 + Y_4Y_5 - KY_2Y_5 \quad (4)$$

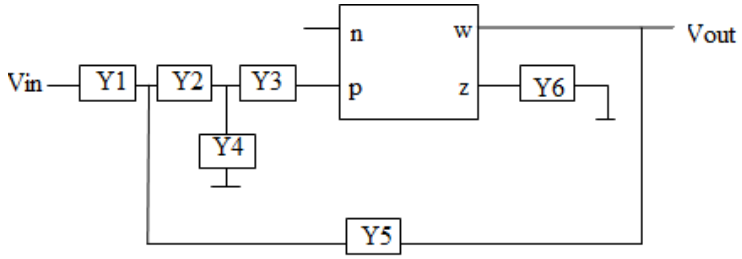


Fig. 2: Proposed Filter Topology

The appropriate admittance choices would result in three required filter responses, as listed in Table 2.

Table 2: Admittance Selection for Proposed Filter Topology

Response Type	Y_1	Y_2	Y_3	Y_4	Y_5	Y_6
LP	G_1	G_2	G_3	sC_4	sC_5	G_6
HP	sC_1	sC_2	G_3	G_4	G_5	G_6
BP	G_1	sC_2	G_3	sC_4	G_5	G_6

For the admittance choices available in Table 2, the transfer function for LP, HP and BP can be expressed as:

$$\left(\frac{V_O}{V_{in}}\right)_{LP} = \frac{K\frac{G_1G_2}{C_4C_5}}{s^2 + s\left(\frac{C_4(G_1+G_2)+G_3C_5+G_2C_5(1-K)}{C_4C_5}\right)+\frac{G_1G_2+(G_1+G_2)G_3}{C_4C_5}} \quad (5)$$

$$\left(\frac{V_O}{V_{in}}\right)_{HP} = \frac{Ks^2}{s^2 + s\left(\frac{(C_1+C_2)G_3+(C_1+C_2)G_4+G_5C_2(1-K)}{C_1C_2}\right)+\frac{G_3G_5+G_4G_5}{C_1C_2}} \quad (6)$$

$$\left(\frac{V_O}{V_{in}}\right)_{BP} = \frac{KS\frac{G_1}{C_4}}{s^2 + s\left(\frac{C_2(G_1+G_3)+C_4(G_1+G_5)+G_5C_2(1-K)}{C_2C_4}\right)+\frac{G_3(G_1+G_5)}{C_2C_4}} \quad (7)$$

From equations (5-7), the resonant angular frequency ω_0, quality factor Q_0 and filter gain H_0 for the three filters are listed in Table 3.

Table 3: Filter Parameters

Filter Type	ω_0	Q_0	H_0
LP	$\sqrt{\frac{G_1G_2+(G_1+G_2)G_3}{C_4C_5}}$	$\frac{\sqrt{C_4C_5(G_1G_2+G_1G_3+G_2G_3)}}{C_4(G_1+G_2)+G_3C_5+G_2C_5(1-K)}$	$\frac{KG_1G_2}{G_1G_2+G_1G_3+G_2G_3}$
HP	$\sqrt{\frac{G_3G_5+G_4G_5}{C_1C_2}}$	$\frac{\sqrt{C_1C_2(G_3G_5+G_4G_5)}}{C_1(G_3+G_4)+C_2(G_3+G_4)+C_2G_5(1-K)}$	K
BP	$\sqrt{\frac{G_1G_3+G_3G_5}{C_2C_4}}$	$\frac{\sqrt{C_2C_4(G_1G_3+G_3G_5)}}{C_2(G_1+G_3)+C_4(G_1+G_5)+C_2G_5(1-K)}$	$\frac{G_1C_2}{C_2(G_1+G_3)+C_4(G_1+G_5)+C_2G_5(1-K)}$

Table 4 lists the filter parameters for all the three responses when all the conductance are set equal to G except G_6 and all capacitors are set equal to C. It may be observed from the Table 4 that ω_0 can be set using appropriate G and C values and the desired Q_0 can be obtained with the help of G_6, the K determining component, thereby making tuning independent.

Table 4: Filter Parameters for Equal Component Design

Filter Type	ω_o	Q_o	H_o
LP	$\sqrt{3}$ G/C	$\sqrt{3}$/(4-K)	K/3
HP	$\sqrt{2}$G/C	$\sqrt{2}$/(5-K)	K
BP	$\sqrt{2}$G/C	$\sqrt{2}$/(5-K)	K/(5-K)

3. SENSITIVITY ANALYSIS

The passive sensitivities of ω_0 and Q_0 for the LP filter configuration can be derived as

$$S_{C_4}^{\omega_0} = S_{C_5}^{\omega_0} = -\frac{1}{2},\ S_{G_1}^{\omega_0} = \frac{1}{2} - \frac{G_2G_3}{2(G_1G_2+G_1G_3+G_2G_3)},\ S_{G_2}^{\omega_0} = \frac{1}{2} - \frac{G_1G_3}{2(G_1G_2+G_1G_3+G_2G_3)},$$

$$S_{G_3}^{\omega_0} = \frac{1}{2} - \frac{G_1G_2}{2(G_1G_2+G_1G_3+G_2G_3)},\ S_{G_1}^{\omega_0} = 0,\ S_{C_4}^{Q_0} = \frac{1}{2} - \frac{C_4(G_1+G_2)}{C_4(G_1+G_2)+G_3C_5+G_2C_5(1-K)},$$

$$S_{C_5}^{Q_0} = \frac{1}{2} - \frac{C_5(G_3+G_2(1-K))}{C_4(G_1+G_2)+G_3C_5+G_2C_5(1-K)} \qquad (8)$$

Similarly the passive sensitivities of ω_0 and Q_0 for the HP and BP filter configuration can be also be computed which have not presented here for the sake of brevity.It may be observed that the filter configurations are insensitive to parameter variations as passive sensitivities for all the responses are less than 0.5 in magnitude.

4. NON-IDEALITY ANALYSIS

In CMOS implementation of CDBA current and voltage tracking errors may exist due device mismatch. Taking these errors into consideration the terminal relationships of the CDBA get modified

$$I_z = \alpha_p I_p - \alpha_n I_n$$

$$V_w = \beta V_z$$

where α_p = (1-ε_p) , α_n = (1-ε_n) and β = (1 - ε_v)

The terms $\varepsilon_p(|\varepsilon_p|<<1)$ and $\varepsilon_n(|\varepsilon_n|<<1)$ denote the current-tracking errors from p and n terminals to z terminal respectively and ε_v ($|\varepsilon_v|<<1$) is the voltage-tracking error from z to w terminal of the CDBA. The modified transfer functions of the proposed filter in the presence of current and voltage tracking errors can be expressed as:

$$\left(\frac{V_O}{V_{in}}\right)_{LP_n} = \frac{\alpha\beta K\frac{G_1G_2}{C_4C_5}}{s^2 + s\left(\frac{C_4(G_1+G_2)+G_3C_5+G_2C_5(1-\alpha\beta K)}{C_4C_5}\right) + \frac{G_1G_2+(G_1+G_2)G_3}{C_4C_5}}$$

$$\left(\frac{V_O}{V_{in}}\right)_{HP_n} = \frac{\alpha\beta Ks^2}{s^2 + s\left(\frac{(C_1+C_2)G_3+(C_1+C_2)G_4+G_5C_2(1-\alpha\beta K)}{C_1C_2}\right) + \frac{G_3G_5+G_4G_5}{C_1C_2}}$$

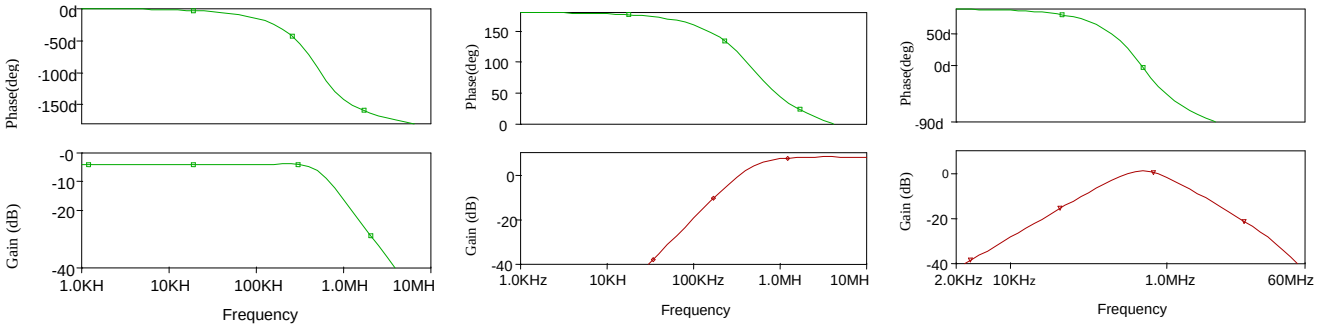
$$\left(\frac{V_O}{V_{in}}\right)_{BP_n} = \frac{\alpha\beta KS\frac{G_1}{C_4}}{s^2 + s\left(\frac{C_2(G_1+G_3)+C_4(G_1+G_5)+G_5C_2(1-\alpha\beta K)}{C_2C_4}\right) + \frac{G_3(G_1+G_5)}{C_2C_4}}$$

So this can be evaluated looking at Table 3 natural frequency of the filter topology is not influenced by tracking errors of the CDBA.

5. SIMULATION RESULTS

The proposed multifunctional filter is verified through simulations using the CMOS implementation of the CDBA as presented in [13]. The SPICE simulations are performed using 0.18µm CMOS process parameters provided by MOSIS (AGILENT). Supply voltages taken are ±0.9 V. The LP, HP and BP filter configurations were designed with Q=1 and f_0 of 500 KHz. For all three filter responses the value of resistances are taken as 10kΩ except for R_6 having a value is 22.68kΩ for LP and 35.86kΩ for HP and BP it is. The values of capacitances for LP are chosen 0.055nF and for HP and BP the values of Capacitances are 0.045nF. The simulated frequency responses of all the three configurations are shown in Figs.3 (a), (b) and (c) respectively. The simulated f0 is observed to be 493 KHz in case of LP whereas in HP and BP it is found to be 484 KHz. The simulated values are in close agreement to the

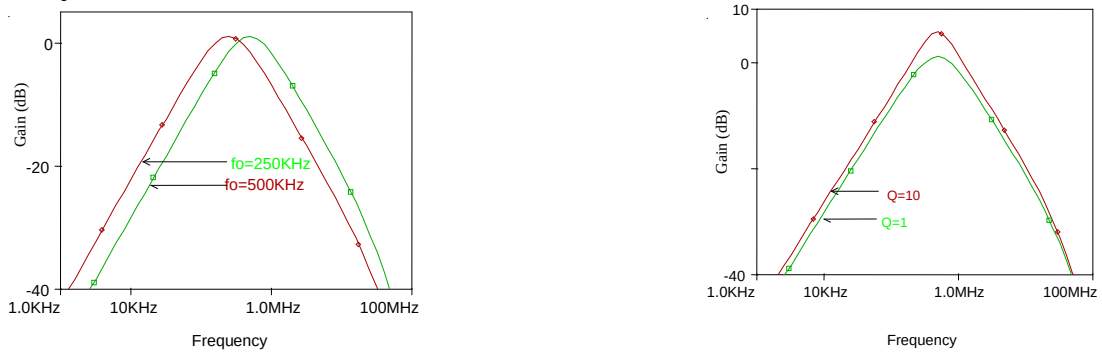
theoretical frequency of 500 KHz.



(a) (b) (c)

Fig. 3: Phase and Gain responses of proposed (a) LP (b) HP (c) BP Filters

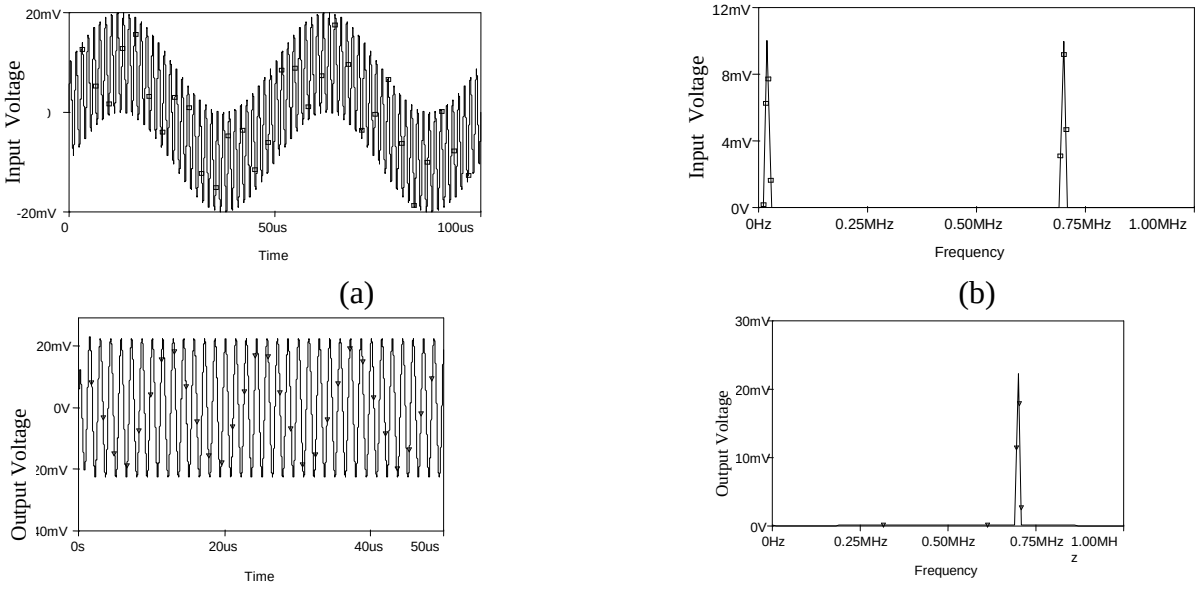
To show the tuning of f_0 BP responses are plotted for two different values of f_0 while keeping Q_0 fixed at 1 as depicted in Fig. 4(a). The independent tunability of Q_0 with R_6 is shown in Fig. 4(b). The center frequency f_0 is taken to be 500 KHz.



(a) (b)

Fig. 4: The BP response depicting independent tunability of (a) f_0 (b) Q_0

Functionality of proposed filter topology is also tested through its time domain response. As a case study the transient response of HPF is observed by applying a composite input sinusoidal signal having frequencies of 20 KHz and 700 KHz.



(a) (b)

(c) (d)

Fig. 5: The HP Filter: Input signal (a) in time domain (b) Frequency spectrum, output signal (c) in time domain (d) Frequency spectrum

The transient responses along with their respective frequency spectrums for input and output signals are

shown in Fig. 5(a)-(d). It may be observed from the response of Fig. 5(d) that the 700 KHz signal is passed without attenuation and 20 KHz signal is significantly attenuated.

The performance of proposed filter topology is also evaluated through well known Monte Carlo statistical analysis. The simulated standard deviation of f_0 is observed to be 122 Hz for BP configuration simulated by setting the values of all passive elements in 5% tolerance. This implies that the proposed filter topology has reasonable sensitivity characteristics. The derived histogram after 50 simulation runs for BP filter is shown in Fig.6.

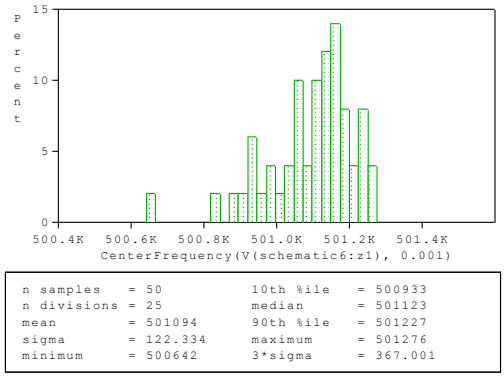


Fig.6: Monte Carlo statistical results BP Filter

6. CONCLUSION

A new voltage mode single CDBA based filter topology is presented in this paper. The configuration can be used to synthesize LP, HP and BP filters with appropriate choices of admittance. The proposed configuration can be extended to obtain the current mode, transadmittance mode and transimpedance mode through appropriate input signal and component selection. The proposed configuration is a suitable choice for high quality factor implementation. Passive sensitivities for the configuration are found low. Extensive SPICE simulations are carried out to observe the performance of the proposed configuration. The simulation and theoretical results are found in close agreement.

REFERENCES

[1] D. Biolek, R. Senani, V. Biolkova, Z, and Kolka, Active Elements for Analog Signal Processing: Classification, Review, and New Proposals", Radio engineering, vol. 17, no. 4, pp. 15-32, 2008.

[2] R. Pal, R. C. Tiwari, R. Pandey, and N. Pandey, "Single CDBA based current mode first order multifunction filter", IJEST, vol. 6, no.7, 2014.

[3] C. Acar, and S. Ozoguz, "A new versatile building block: current differencing buffered amplifier suitable for analog signal processing filters", Microelectronics Journal, vol. 30, no. 2, pp. 157-160, 1999.

[4] A. U. Keskin, "Voltage-mode high-Q band-pass filters and oscillators employing single CDBA and minimum number of components. International Journal of Electronics", vol. 92, no. 8, pp. 479-487, 2005.

[5] S. Ozoguz, A. Toker, and C. Acar, "Current-mode continuous-time fully-integrated universal filter using CDBAs", Electronics Letter, vol. 35, no. 2, 1999.

[6] A. Toker, S. Özoguz, O. Çiçekoglu, and C. Acar, "Current-mode all-pass filters using current differencing Buffered amplifier and a new high- bandpass filter Configuration", IEEE Transactions On Circuits And Systems—II: Analog And Digital Signal Processing, vol. 47, no. 9, pp. 949 -954, 2000.

[7] W. Tangsrirat, N. Fujii, and W. Surakampontorn, "Current-mode leapfrog ladder filters using CDBAs", Proceedings of the IEEE International Symposium on Circuits and Systems (ISCAS), pp. 57-60, 2002.

[8] M. Koksal, S. E. Oner, and M. Sagbas, "A new second-order multi-mode multi-funtion filter using a single CDBA", European Conference on Circuit Theory and Design, Antalya/Turkiye, IEEE, pp. 699-702, 2009.

[9] S. A. Bashir, and N. A. Shah, "Voltage mode universal filter using current differencing buffered amplifier as an active device", Circuits and Systems, vol. 3, no.3, pp. 278-281, 2012.

[10] S. Pisitchalermpong, T. Pukkalanun, W. Tangsrirat, and W. Surakampontom, "Current differencing buffered amplifier based multiple-output biquadratic filters", Electron. Devices and Solid-State Circuits, IEEE, pp. 521-524, 2005.

[11] F. Kaçar, and S. Menekay, "Realization of a CMOS current differencing buffer amplifier and its filter application", Electrical and Electronics Engineering (ELECO) Conference, Bursa IEEE, 358-361, 2011.

[12] S. Özcan, H. Kuntman, and O. Çiçekoglu, "Cascadable current mode multipurpose filters employing current differencing buffered amplifier (CDBA)", International Journal of. Electronic. and Communication, vol. 56, no. 2, pp. 67-72, 2002.

[13] C. Cakir, S. Minaei, and O. Cicekoglu, "Low voltage low power CMOS current differencing buffered amplifier", Analog Integrated Circuit Signal Process, vol. 62, no. 2, pp. 237–244, 2010.

[14] W. Tangsrirat, and W. Surakampontorn, "Realization of multiple-output biquadratic filters using current differencing buffered amplifiers", International Journal of Electronics, vol. 92, no. 6, pp. 313–325, 2005.

[15] V. Sawangarom, T. Dumawipata, W. Tangsrirat, and W. Surakampontorn, "Cascadable three-input single-output current-mode universal filter using CDBAs", The ECTI International Conference, 2007.

[16] A. U. Keskin, "Multi-function biquad using single CDBA", Electrical Engineering, vol. 88, no. 5, pp. 353–356, 2006.

[17] A. U. Keskin, and E. Hancioglu, "Current Mode Multifunction Filter Using Two CDBAs", International Journal of Electronics & Communications. vol. 59, no. 8, pp. 495-498, 2005.

[18] R. Pandey, N. Pandey, T. Negi, and V. Garg, "CDBA based universal inverse filter". ISRN Electronics, Article ID 181869, vol. 2013, 2013.



Priyanka Gupta did B.E (Hons.) and M.Tech in Electronics and Communication Engineering from Maharshi Dayanand University, Rohtak. She is having teaching experience of three years. Currently she is pursuing her Ph.D from Delhi Technological University, Delhi. Her research interests are Analog Integrated Circuits and signal processing.



Rajeshwari Pandey did her B.Tech (Electronics and Telecommunication) from University of Allahabad, M.E. (Electronics and Control) from BITS, Pilani, Rajasthan and Ph.D. from Delhi University. Currently, she is Associate Professor in Department of Electronics and Communication Engineering, Delhi Technological University, Delhi. Her research interests include Analog Integrated Circuits, and Microelectronics.



Neeta Pandey did M. E. in Microelectronics from Birla Institute of Technology and Sciences, Pilani, Rajasthan, India and Ph.D. from GGSIPU Delhi, India. At present she is Associate Professor in Department of Electronics and Communication Engineering, Delhi Technological University, Delhi. A life member of ISTE, and member of IEEE, USA, she has published papers in International, National Journals of repute and conferences. Her research interests are in Analog and Digital VLSI Design.